

**Electrode Reaction and Mass-
Transport Mechanisms Associated
with the I^-/I_2 and H^+/H_2 Redox
Couples in Ionic Liquid Media**

By:

Cameron L. Bentley

B. Sc. (Hons.)

A thesis submitted to the Faculty of Science, Monash University, in fulfilment
of the requirements for the degree of *Doctor of Philosophy*.

School of Chemistry

Monash University

Australia

June 2015

© The author 2015. Except as provided in the Copyright Act 1968, this thesis may not be reproduced in any form without the written permission of the author.

I certify that I have made all reasonable efforts to secure copyright permissions for third-party content included in this thesis and have not knowingly added copyright content to my work without the owner's permission.

Contents

Abstract	iii
General Declaration	v
Acknowledgements	vi
List of Figures	vii
Symbols	ix
Glossary of Terms	xi
1. Introduction	1
1.1 Ionic Liquids	3
1.1.1 History.....	3
1.1.2 Structure	5
1.1.3 Physicochemical Properties	9
1.1.4 Applications	10
1.2 Ionic Liquids as Electrolytes	11
1.2.1 Electrolyte Properties	11
1.2.2 Application in Electrochemical Devices.....	12
1.3 Fundamentals of Electrochemistry.....	20
1.3.1 Kinetics of Electrode Reactions.....	21
1.3.2 Electrode Reaction Mechanisms.....	23
1.3.3 Mass-transport.....	25
1.4 Electrochemical Methods.....	30
1.4.1 Chronoamperometry	30
1.4.2 Potential Sweep Voltammetry	31
1.4.3 Convolution Voltammetry	33
1.4.4 Practical Considerations in Ionic Liquids	35
1.5 Model Redox Systems.....	37
1.5.1 I ⁻ /I ₂ Couple.....	38
1.5.2 H ⁺ /H ₂ Couple	46
1.6 Research Objectives	60

2. Experimental.....	78
2.1 Materials and Preparation	78
2.1.1 Glovebox and Schlenk Line	78
2.1.2 Ionic Liquids	78
2.1.3 Solvents and Supporting Electrolytes	79
2.1.4 Electroactive Species	80
2.2 Electrochemical Systems and Procedures.....	82
2.2.1 Potentiostats.....	82
2.2.2 Electrodes	83
2.2.3 Setup	84
2.2.4 Semiintegration and Convolution.....	85
2.2.5 Numerical Simulation.....	85
2.2.6 Miscellaneous Techniques.....	86
3. Electroanalytical Applications of Semiintegral and Convolution Voltammetry in Ionic Liquid Media	91
4. Electrode Reaction and Mass-Transport Mechanisms Associated with the I^-/I_2 Redox Couple in Ionic Liquid Media	123
5. Proton Transport, Hydrogen Evolution and Equilibrium Acidity (pK_a) in Ionic Liquid Media	177
6. Conclusions and Future Work.....	319
7. Publications.....	327

Abstract

Room temperature ionic liquids have received considerable attention over the past two decades as promising replacements for volatile molecular solvents in a range of applications. As the use of these neoteric solvents in electrochemical devices and in a growing range of processing technologies continues to expand, the limits to our knowledge of some of the fundamental underlying processes has become apparent. For this reason, the fundamentals of heterogeneous electron transfer reactions (*i.e.*, thermodynamics, kinetics and mechanisms) and mass-transport have been investigated in ionic liquid media, focusing on the technologically relevant I^-/I_2 and H^+/H_2 redox systems.

Initially, the utility of several voltammetric methods was evaluated for the purpose of quantifying the parameters associated with a range of electroactive species (*i.e.* diffusivity, stoichiometric number of electrons, and/or bulk concentration) in ionic liquid media. Conventional steady-state voltammetric methods (*i.e.*, microelectrode or rotating disk electrode) are difficult to apply under highly viscous conditions and the peak currents of dc cyclic voltammograms are sensitive to heterogeneous kinetics/uncompensated resistance, limiting the application of these techniques for quantitative analysis in ionic liquid media. Semiintegral voltammetry and related convolutive techniques were shown to be powerful and also robust electroanalytical methods, which can be readily applied under highly viscous conditions to quantify the diffusivity of a range of electroactive species.

Following the development of suitable electroanalytical methodology, the electrode reaction and mass-transport mechanisms associated with the I^-/I_2 redox couple was investigated in 1-ethyl-3-methylimidazolium bis(trifluoromethanesulfonyl)imide. The iodide oxidation and iodine reduction processes were found to proceed in two steps on platinum, *via* a triiodide, I_3^- , intermediate. These processes were simulated by combining a termolecular heterogeneous charge transfer reaction (*i.e.*, $2I^- \rightleftharpoons I_2 + 2e^-$) with a

homogeneous process (*i.e.*, triiodide formation, $\text{I}^- + \text{I}_2 \rightleftharpoons \text{I}_3^-$). An analogous electrode reaction mechanism was observed on glassy carbon and boron-doped diamond electrodes, albeit with significant overpotentials when compared with the behaviour at platinum. Iodide oxidation on gold also proceeds in two steps, however the predominant intermediate species was found to be the diiodaurate complex anion, $[\text{AuI}_2]^-$, rather than triiodide. Finally, the diffusivity of iodide was found to be directly proportional to the concentration of triiodide present, showing up to a 50% enhancement under the conditions investigated. This enhancement in mass transport could not be explained by a decrease in solution viscosity (as predicted by the Stokes-Einstein equation), and was therefore attributed to electron-hopping and/or a Grothuss-type bond-exchange reaction between iodide and triiodide.

In the final body of work, proton transport, hydrogen evolution (at a platinum electrode) and equilibrium acidity ($\text{p}K_{\text{a}}$) was investigated in a broad range of ionic liquids. In bis(trifluoromethanesulfonyl)imide containing ionic liquids, when the conjugate acid of the anion (*i.e.*, $\text{H}[\text{NTf}_2]$) is used as the proton source, proton diffusivity was found to be inversely proportional to medium viscosity, as predicted by the Stokes-Einstein equation. Furthermore, it was found that the ‘proton’ diffusion coefficient (derived electrochemically) is equal to the bis(trifluoromethanesulfonyl)imide anion self-diffusion coefficient (derived with ^{19}F NMR), indicating that the acid is not dissociated in this environment (*i.e.*, the protons diffuse as $\text{H}[\text{NTf}_2]$). The hydrogen evolution reaction from both $\text{H}[\text{NTf}_2]$ and a range of weak acids (sulfonamides, protonated amines, phenols, carboxylic acids or sulfonic acids) was simulated by combining the classical Volmer (rate determining step), Tafel and Heyrovsky reactions. Finally, a straightforward voltammetric method for calculating $\text{p}K_{\text{a}}$ values was devised and the equilibrium acidities ($\text{p}K_{\text{a}}$) of twenty weak acids, covering eighteen orders of magnitude in acid strength ($2.0 \leq \text{p}K_{\text{a}} \leq 19.5$) was quantified in 1-ethyl-3-methylimidazolium bis(trifluoromethanesulfonyl)imide.

PART A: General Declaration

Monash University

Declaration for thesis based or partially based on conjointly published or unpublished work

General Declaration

In accordance with Monash University Doctorate Regulation 17.2 Doctor of Philosophy and Research Master's regulations the following declarations are made:

I hereby declare that this thesis contains no material which has been accepted for the award of any other degree or diploma at any university or equivalent institution and that, to the best of my knowledge and belief, this thesis contains no material previously published or written by another person, except where due reference is made in the text of the thesis.

This thesis includes 6 original papers published in peer reviewed journals and 2 unpublished publications. The core theme of the thesis is electroanalytical chemistry in ionic liquids. The ideas, development and writing up of all the papers in the thesis were the principal responsibility of myself, the candidate, working within the School of Chemistry under the supervision of Dr. Jie Zhang.

The inclusion of co-authors reflects the fact that the work came from active collaboration between researchers and acknowledges input into team-based research.

In the case of Chapter 3 to 5, my contribution to the work involved the following:

Thesis chapter	Publication title	Publication status*	Nature and extent of candidate's contribution
3	Advantages Available in the Application of the Semi-Integral Electroanalysis Technique for the Determination of Diffusion Coefficients in the Highly Viscous Ionic Liquid 1-Methyl-3-Octylimidazolium Hexafluorophosphate	Published	In all cases, the experimental work and manuscript writing was carried out solely by the candidate, Cameron L Bentley. Editing/proof-reading of the manuscript was jointly performed by all co-authors.
3	Applications of Convolution Voltammetry in Electroanalytical Chemistry	Published	
4	Concentration and Electrode Material Dependence of the Voltammetric Response of Iodide on Platinum, Glassy Carbon and Boron-doped Diamond in the Room Temperature Ionic Liquid 1-ethyl-3-methylimidazolium Bis(trifluoromethanesulfonyl)imide	Published	
4	Unexpected Complexity in the Electro-Oxidation of Iodide on Gold in the Ionic Liquid 1-Ethyl-3-methylimidazolium bis(trifluoromethanesulfonyl)imide	Published	
4	Electrode Reaction and Mass-Transport Mechanisms Associated with the Iodide/Triiodide Couple in the Ionic Liquid 1-Ethyl-3-methylimidazolium Bis(trifluoromethanesulfonyl)imide	Published	
5	Mass Transport Studies and Hydrogen Evolution at a Platinum Electrode Using Bis(trifluoromethanesulfonyl)imide as the Proton Source in Ionic Liquids and Conventional Solvents	Published	
5	Electrochemical Proton Reduction and Equilibrium Acidity (pK_a) in Aprotic Ionic Liquids: Phenols, Carboxylic Acids and Sulfonic Acids	In preparation	
5	Electrochemical Proton Reduction and Equilibrium Acidity (pK_a) in Aprotic Ionic Liquids: Protonated Amines and Sulfonamide Acids	In preparation	

I have / have not (circle that which applies) renumbered sections of submitted or published papers in order to generate a consistent presentation within the thesis.

Signed: _____

Date: _____

05/03/2015

Acknowledgements

I would like to express my sincere thanks to my supervisors, Dr. Jie Zhang, Prof. Alan Bond, Dr. Tony Hollenkamp and Dr. Peter Mahon for their time, patience and expertise throughout the duration of my doctoral studies. Through their continued guidance and support, I have been able to develop my skills as a researcher while also advancing science.

I would like to thank all of the members of the Monash electrochemistry group for their assistance and support. Special thanks to Dr. Stephen Feldberg for his valuable discussions on simulations and electrode-reaction mechanisms.

I would like to thank all of the members of the energy storage team at CSIRO. Special thanks to Dr. Thomas R  ther, who was always willing to answer my questions and lend a hand along the way.

Special thanks to Dr. Iko Burgar and Dr. Roger Mulder in the Materials Science and Engineering Division at CSIRO for performing the NMR experiments and for their expert assistance in interpreting the results.

I would like to recognize the support of the Monash University School of Chemistry and CSIRO Energy Flagship, which has made this work possible. I also acknowledge the support of the Monash University Institute of Graduate Research for providing travel grants to present my research at the ACES 9th Annual International Electromaterials Science Symposium (Wollongong, Australia) and the 65th Annual ISE Meeting (Lausanne, Switzerland).

Finally, I would like to thank my family and friends for their moral support and most importantly for keeping me sane along the way.

List of Figures

- Figure 1.** Names, abbreviations and structures of a range of commonly encountered AIL cations and anions. R = alkyl chain.....6
- Figure 2.** Names, abbreviations and structures of a range of commonly encountered PIL cations and anions. R = H or alkyl chain.....8
- Figure 3.** Rapid growth in the number of publications on the topic “ionic liquid*” over the period 1994 to 2014. Data was obtained from a literature search using the ISI Web of Knowledge database.....10
- Figure 4.** Schematic diagram showing the basic structure and operation of a dye-sensitized solar cell. Figure 4 was adapted from Hagfeldt *et al.* (2009)⁵⁰.14
- Figure 5.** Schematic diagram showing the basic structure and operation of a proton-exchange membrane fuel cell. Figure 5 was taken from Rana *et al.* (2012).²⁹17
- Figure 6.** Schematic diagram of the electrochemical processes occurring during the discharge of a Li-ion battery. Figure 6 was taken from Dunn *et al.* (2011).⁶¹19
- Figure 7.** Schematic representation of the reaction pathways possible following the (a) reduction or (b) oxidation of the electroactive species “RX”. “E” represents an electron transfer at the electrode surface, and “C” represents a homogeneous chemical reaction. The general species, RX, is an organic compound, where R is a hydrocarbon moiety (*e.g.*, alkyl, aryl) and X is a substituent (*e.g.*, H, OH, Cl, Br, NH₂, NO₂, CN, CO₂⁻). Figure 7 was adapted from Bard and Falkner (2001).⁶24
- Figure 8.** Schematic diagram showing the diffusion pattern at an inlaid (a) macrodisk electrode and (b) microdisk electrode during an electrochemical perturbation. Figure 8 was adapted from Forster (2006).⁸¹29
- Figure 9.** (a) *E-t* and (b) *I-E* curves showing the proton reduction process obtained from 41.6 mM *p*-toluenesulfonic acid in [C₂mim][NTf₂] at a 1.6 mm dia. Pt macrodisk electrode with a scan rate of 50 mV s⁻¹. The peak splitting seen in (b) is indicative of an *ECE* mechanism. Figure 9 was adapted from Bentley *et al.* (2015).⁸⁵33

Figure 10. (a) Mixed transient/steady-state cyclic voltammogram obtained from the oxidation of 4.3 mM I ⁻ in [C ₂ mim][NTf ₂] using a 25 μm dia. Pt microdisk electrode with a scan rate of 50 mV s ⁻¹ . (b) The convolved current of the voltammogram (forward sweep) shown in (a). Figure 10 was adapted from Bentley <i>et al.</i> (2014). ¹¹²	35
Figure 11. Cyclic voltammograms obtained from the oxidation of ferrocene in (a) acetonitrile + 0.1 M tetrabutylammonium hexafluorophosphate (near steady-state) and (b) [C ₂ mim][NTf ₂] (mixed transient/steady-state) using a 25 μm dia. Pt microdisk electrode with a scan rate of 50 mV s ⁻¹	36
Figure 12. The Grotthuss-type homogeneous bond-exchange mechanism proposed to occur between I ⁻ /I ₃ ⁻ in IL media. Figure 12 was adapted from Thorsmolle <i>et al.</i> (2011). ¹⁴⁸	42
Figure 13. Plots showing the (a) steady-state limiting current (<i>I</i> _{lim}) and (b) apparent diffusion coefficient (<i>D</i> _{app}) of the I ⁻ /I ₃ ⁻ redox couple as a function of the concentration of redox species (1/3[I ⁻] + [I ₃ ⁻]). The molar ratio of [I ⁻]:[I ₂] is indicated on the plots. The experiments shown above were carried out in [C ₂ mim][NTf ₂] or polyethylene glycol dimethylether at a 12 μm dia. Pt microdisk electrode with [C ₂ mim]I as the iodide source. Figure 13(a) and (b) were taken from Kawano and Watanabe (2003) ⁷⁹ and (2005) ⁴² , respectively.	44
Figure 14. Illustration of proton transport in acidic aqueous solution. <i>Top:</i> Grotthuss mechanism, where protons ‘hop’ <i>via</i> a network of hydrogen bonds. <i>Bottom:</i> Vehicle mechanism, where proton movement occurs with the aid of a moving ‘vehicle’ (<i>i.e.</i> , H ₂ O). Figure 14 was taken from Ueki and Watanabe (2008) ¹⁹²	56

Symbols

Symbol	Meaning	Usual Units
A	electrode area	cm^2
a or r_0	electrode radius	μm
C	concentration	mol dm^{-3}
C_{dl}	double layer capacitance	F
D	diffusion coefficient or diffusivity	$\text{cm}^2 \text{s}^{-1}$
d	medium density	g cm^{-3}
D_{app}	apparent diffusion coefficient	$\text{cm}^2 \text{s}^{-1}$
D_{ex}	exchange diffusion coefficient	$\text{cm}^2 \text{s}^{-1}$
D_{phys}	physical diffusion coefficient	$\text{cm}^2 \text{s}^{-1}$
E	potential of an electrode vs. a reference	V
E^0	formal potential	V
E_i	initial potential	V
E_p	(transient) voltammetric peak potential	V
$E_{p,\text{ox}}$	oxidation peak potential	V
$E_{p,\text{red}}$	reduction peak potential	V
E_s	step potential	V
F	Faraday's constant	96485 C mol^{-1}
f	F/RT	V^{-1}
f_0	resonant frequency	MHz
I	current	μA ($\mu\text{C s}^{-1}$)
I_{lim}	steady-state limiting current	nA
I_p	(transient) voltammetric peak current	μA
J_j	flux of species j	$\text{mol s}^{-1} \text{cm}^{-2}$
K_a	acid dissociation constant	
k_b	(a) homogeneous rate constant for 'backward' reaction	s^{-1} or $\text{L mol}^{-1} \text{s}^{-1}$
	(b) heterogeneous rate constant for oxidation	cm s^{-1}
k_B	Boltzmann constant	$1.3806488 \times 10^{-23} \text{ J K}^{-1}$
k_{ex}	exchange reaction bimolecular rate constant	$\text{L mol}^{-1} \text{s}^{-1}$
k_f	(a) homogeneous rate constant for 'forward' reaction	s^{-1} or $\text{L mol}^{-1} \text{s}^{-1}$
	(b) heterogeneous rate constant for reduction	cm s^{-1}

k_s or k^0	standard heterogeneous rate constant	cm s^{-1}
M	semiintegrated or convolved current	$\mu\text{A s}^{1/2}$
M_L	limiting semiintegrated or convolved current	$\mu\text{A s}^{1/2}$
n	stoichiometric number of electrons	
N_A	Avogadro constant	mol^{-1}
Q	charge	C
r	rate of an electrode reaction	$\text{mol s}^{-1} \text{cm}^{-2}$
r_H	Stokes or hydrodynamic radius	\AA
R_u	uncompensated resistance	Ω
T	temperature	K
t	time	s
T_m	melting point	$^{\circ}\text{C}$
x_q	thickness of quartz crystal	mm
z_j	valence (charge) of species j	
α	transfer coefficient	
δ	diffusion layer thickness	nm
ΔE_p	voltammetric peak-to-peak separation	mV
δ_{int}	centre-to-centre intersite distance at the site of reaction	\AA
η	medium viscosity	cP (mPa.s)
ν	voltammetric scan rate	V s^{-1}
ν_L	linear velocity of solution flow	cm s^{-1}
ρ_q	density of quartz crystal	g cm^{-3}
σ	sphericity factor	
τ	$4Dt/r_0^2$	
Ω	angular rotation rate	rad s^{-1}
κ	conductivity	mS cm^{-1}
ϕ	electrostatic potential	V

Glossary of Terms

Abbreviation	Meaning
$[\text{C}_x\text{dmim}]^+$	1-alkyl-2,3-methylimidazolium
$[\text{C}_x\text{mim}]^+$	1-alkyl-3-methylimidazolium
$[\text{C}_x\text{mpyr}]^+$	1-alkyl-1-methylpyrrolidinium
$[\text{FAP}]^-$	Tris(perfluoroethyl)trifluorophosphate
$[\text{NBu}_4]^+$ or TBA	Tetrabutylammonium
$[\text{NEt}_4]^+$	Tetraethylammonium
$[\text{NTf}_2]^-$	Bis(trifluoromethanesulfonyl)imide
$[\text{N}_{x,x,x,x}]^+$	Tetraalkylammonium
$[\text{OTf}]^-$	Trifluoromethanesulfonate
$[\text{P}_{x,x,x,x}]^+$	Tetraalkylphosphonium
$[\text{S}_{x,x,x}]^+$	Trialkylsulfonium
$\text{A}_{\text{IL}}^-/\text{HA}_{\text{IL}}$	Constituent anion/conjugate neutral acid of an IL
AIL	Aprotic Ionic Liquid
B/BH^+	General neutral base/conjugate cation acid
BDD	Boron Doped Diamond
Cc^+/Cc	Cobaltocenium/Cobaltocene
Cp	Cyclopentadienyl
DC	Direct Current
DR	Direct Reduction
DSSC	Dye-sensitized Solar Cell
EQCM	Electrochemical Quartz Crystal Microbalance
Fc/Fc^+	Ferrocene/Ferrocenium
GC	Glassy Carbon
HA/A^-	General neutral acid/conjugate anion base
HER	Hydrogen Evolution Reaction
HOR	Hydrogen Oxidation Reaction
IL	Ionic Liquid
Li-ion	Lithium Ion
ME	Microelectrode
NMR	Nuclear Magnetic Resonance

OTTLE cell	Optically Transparent Thin Layer Electrochemical cell
PEGDE	Polyethylene Glycol Dimethyl Ether
PEM	Proton Exchange Membrane
PEMFC	Proton Exchange Membrane Fuel Cell
PFSA	Perfluorinated Sulfonic Acid
PGSE–NMR	Pulsed Field Gradient Spin-Echo NMR
PIL	Protic Ionic Liquid
PRE	Pseudo-Reference Electrode
RDE	Rotating Disk Electrode
rpm	Revolutions Per Minute
RTIL	Room Temperature Ionic Liquid
UME	Ultramicroelectrode
UPD	Under Potential Deposition
UV/vis or UV–vis	UV/Visible
VOC	Volatile Organic Compound

1. Introduction

Fossil fuels are an unsustainable long-term energy source due to depleting reserves and CO₂ emissions contributing to global climate change. Worldwide reliance on fossil fuels has been a strong driving force for the development of renewable energy sources (*e.g.*, solar, wind, hydroelectric) and high efficiency energy storage technologies (*e.g.*, low/zero emission fuels, batteries). Intensive research efforts have focused on designing electrochemical devices which are suitable for large-scale renewable energy generation (*e.g.*, dye-sensitized solar cells), storage (*e.g.*, lithium-ion/lithium batteries) and conversion (*e.g.*, proton exchange membrane fuel cells).¹⁻⁴

Electrochemical devices are composed of one or more electrochemical cells, which, in their simplest form, are made up of two electronic conductors known as electrodes and an ionic conductor known as the electrolyte.^{5,6} Conventional electrolytes are composed of one or more ionic compounds (salts) dissolved in a molecular solvent, which may be protic (*e.g.*, water) or aprotic (*e.g.*, acetonitrile), depending on the nature of the electrochemical device. Unfortunately, the use of volatile molecular solvents in electrolytes can cause safety (solvent flammability) and stability (solvent volatility) issues, limiting the conditions (*i.e.*, temperature range) under which these electrochemical devices can be operated.

Since the conception of air/water stable non-haloaluminate ionic liquids (ILs) over two decades ago⁷, there has been growing interest in using these neoteric solvents as replacements for volatile molecular solvents in a range of applications. Although the only property common to all ILs is intrinsic ionic conductivity⁸, many possess other favourable properties which make them suitable electrolytes, including high thermal/chemical/electrochemical stability and the ability to dissolve a wide range of electroactive species.⁹⁻¹¹ Unfortunately, due to the relatively strong cohesive (electrostatic)

forces operating within an IL, they are typically 10 to 1000 times more viscous than conventional molecular solvents, resulting in sluggish physical mass-transport.¹² Despite this limitation, ILs have been successfully employed as electrolytes in dye-sensitized solar cells^{13, 14}, lithium batteries¹⁵, fuel cells¹⁶ and supercapacitors¹⁷.

As the use of ILs in electrochemical devices and in a growing range of processing technologies continues to expand, the limits to our knowledge of some of the fundamental underlying processes become more apparent. In the past, long-established theory developed in conventional solute/solvent electrolyte systems governing fundamental processes such as mass-transport, reaction kinetics, reaction thermodynamics and reaction mechanisms was often assumed to be analogous in ILs. As research in the field matures, it has become apparent that there are nuances which must be accounted for when investigated such fundamental phenomena, owing to the unique ionic environment of ILs. Indeed, some studies have revealed anomalous behaviour which is only seen in this type of medium.

In this work, the fundamentals of heterogeneous electron transfer reactions (*i.e.*, thermodynamics, kinetics and mechanisms) and mass-transport in ionic liquid media have been investigated. In order to accomplish this, two ‘model’ redox systems have been studied in detail; the Γ/I_2 couple, which finds application in current dye-sensitized solar cell technology; and the H^+/H_2 couple, which finds application in a myriad of green energy technologies (*i.e.*, fuel cells, water splitting). Comparisons have been made with conventional molecular solvent-based electrolytes where possible. Electroanalytical methodology which is suitable for quantifying the parameters (diffusivity, stoichiometric number of electrons and/or bulk concentration) associated with a redox system under highly viscous conditions has also been developed.

1.1 Ionic Liquids

ILs are known by many names in the literature, including room temperature ionic liquids, room temperature molten salts, low temperature molten salts, ambient-temperature molten salts or liquid organic salts. Their physicochemical properties are identical to those of ‘molten salts’, however practical aspects regarding their use, maintenance and handling are different enough to warrant a distinction.^{7, 12} ILs are arbitrarily defined as any ionic compound (salt) with a melting point or glass transition below the boiling point of water (100°C).¹⁸ Below is an overview of the history, structure, physicochemical properties and applications of ILs.

1.1.1 History

The first known observation of an IL occurred during the mid-19th century; a ‘red oil’ formed during a Friedel-Crafts reaction between chloromethane and benzene using AlCl_3 (or a similar Lewis acidic compound) as a catalyst to form toluene.^{7, 18} It wasn’t until the widespread use of NMR spectroscopy by chemists that the ‘red oil’ was identified as an ionic compound, composed of a stable aromatic carbocation and an anion originating from the Lewis acidic catalyst. Ethylammonium nitrate, $[\text{CH}_3\text{CH}_2\text{NH}_3][\text{NO}_3]$, was first observed in 1914¹², a compound that certainly qualifies as an IL by today’s definition ($T_m = 12^\circ\text{C}$). Other low-melting alkylammonium nitrates were also discovered during the early-20th century and were investigated for use as liquid propellants in naval guns and artillery.⁷

Hurley and Wier described the first haloaluminate ILs in 1951 (used for aluminium electrodeposition), which were mixtures of 1-ethylpyridinium halides (mainly bromide) and AlCl_3 .¹⁹ These mixtures are often dubbed as the ‘first generation’ of ILs¹¹ and from this work the modern era of ILs was born. The pyridinium-based cation was later replaced by 1,3-dialkylimidazolium, which was less easily reduced and thus produced electrolytes with greatly improved electrochemical windows.⁷ The Lewis acidity/basicity of these ILs can be

adjusted by controlling the ratio of 1,3-dialkylimidazolium chloride (Lewis base) to aluminium chloride (Lewis acid).⁹ During the 1980's, systematic studies on the 1,3-dialkylimidazolium chloroaluminate ILs spawned interest in these novel solvents as alternative electrolytes in a range of applications, including batteries²⁰ and metal electroplating baths.¹²

Although the 1,3-dialkylimidazolium chloroaluminate ILs possess a number of desirable physicochemical properties, widespread use of these novel solvents was hindered by their sensitivity to moisture (AlX_3 reacts to liberate corrosive HX in the presence of water).^{7, 18, 20} Consequently, air and water stable "Lewis neutral" ILs were investigated during the 1990's using the 1,3-dialkylimidazolium cation and water stable anions.⁷ The 'second generation' of ILs were based on the anions tetrafluoroborate, $[BF_4]^-$, and hexafluorophosphate, $[PF_6]^-$, which are resistant to hydrolysis at room temperature. Nonetheless, the susceptibility of these anions to hydrolysis at elevated temperatures shifted attention to larger, more hydrolytically stable anions, such as bis(trifluoromethanesulfonyl)imide, $[NTf_2]^-$, trifluoromethanesulfonate (triflate), $[OTf]^-$, and dicyanamide, $[N(CN)_2]^-$, which make up the 'modern generation' of ILs.¹¹ These anions are the primary focus of modern IL research, along with an expanded range of cations including di/tri-alkylimidazolium, dialkyl-pyrrolidinium, tetraalkylammonium, tetraalkylphosphonium and triethylsulfonium, with each combination of anion/cation producing an IL with a unique set of physicochemical properties.^{7, 11, 18}

1.1.2 Structure

Aprotic Ionic Liquids. Aprotic ionic liquids (AILs) are those which contain no dissociable protons in their structures. The cation of AILs tend to be organic, bulky and asymmetric, with extensively shielded or delocalized charge (*i.e.*, they are weak Lewis acids). They can be three-dimensional (tetraalkylammonium), planar (imidazolium) or intermediate between the two (pyrrolidinium). Asymmetry is achieved by having at least one relatively large alkyl chain substituent, which lowers the lattice energy of the salt by disrupting the crystal lattice structure. Altering the chain length of the alkyl substituents on the cation influences the physicochemical properties of the resulting IL (melting point, hydrophobicity and viscosity), allowing for fine-tuning to a particular application.^{10, 18}

The anions of AILs tend to be inorganic with highly diffuse or delocalized charge. They are typically weak Lewis bases and poor hydrogen bond acceptors. IL anions also tend to be fluorinated, which, by virtue of the strong electron-withdrawing nature of fluorine, further reduces the tendency to form hydrogen bonds and increases the thermal/electrochemical stability of the anion. The hydrophilicity/hydrophobicity and, as a result, the water-miscibility of an IL is largely determined by the choice of anion.^{18, 21}

The diffuse, shielded or delocalized charge on the constituent anion and/or cation of an IL results in intermolecular forces which are relatively weak compared to ‘traditional’ ionic compounds (*i.e.*, NaCl, $T_m = 801^\circ\text{C}$). This translates to a relatively low lattice energy (further lowered by inefficient packing due to cation asymmetry), which is why these compounds are liquid at or below 100°C . It is important to note however, that the cohesive forces operating within an IL are strong relative to those operating in most conventional molecular solvents. For this reason, ILs often possess negligible vapor pressures and, unfortunately, relatively high viscosities, usually in the range of 20 to 1000 cP.^{12, 18} The

names, abbreviations and structures of a range of commonly encountered AIL cations and anions are shown in Figure 1.

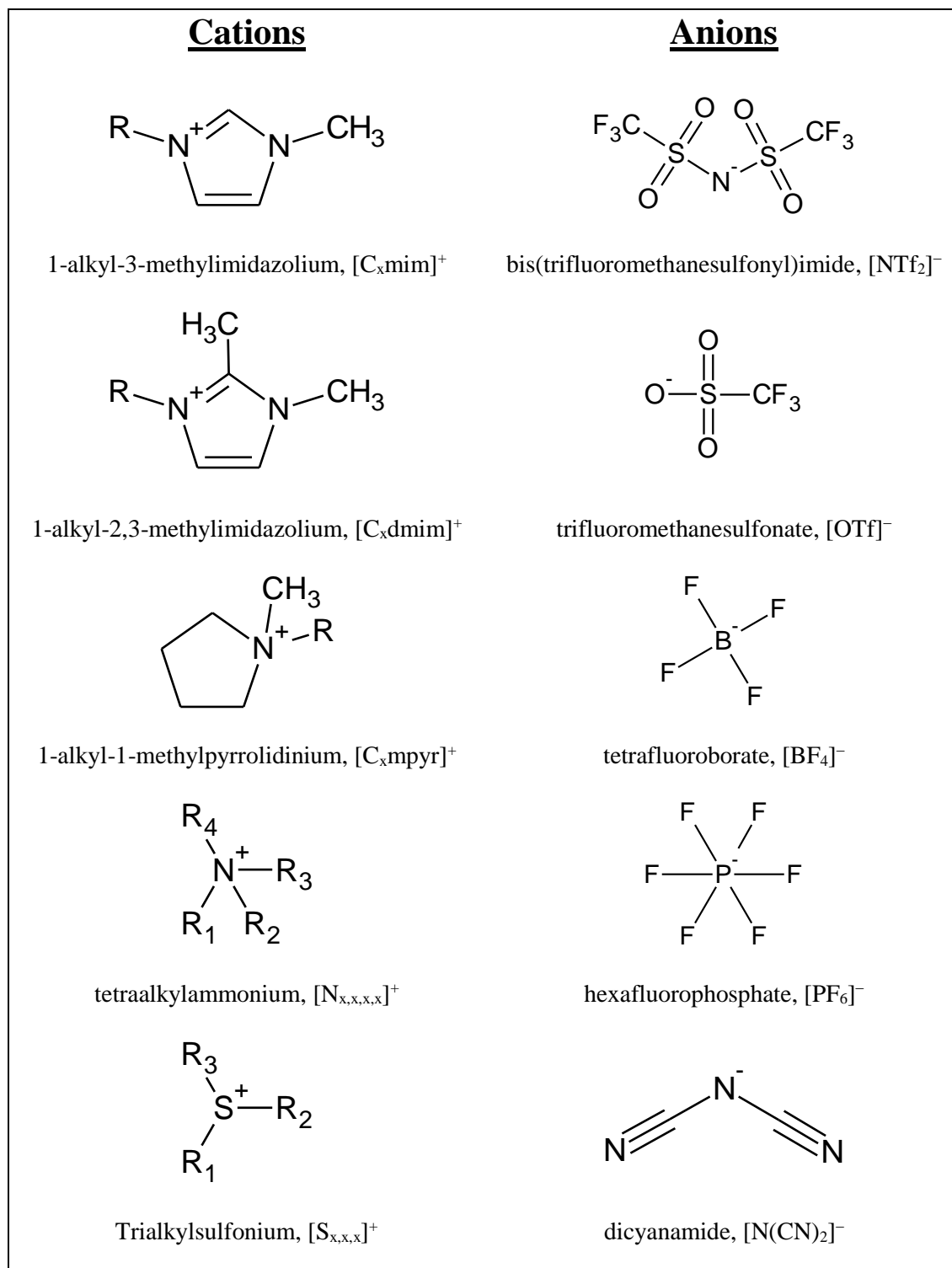


Figure 1. Names, abbreviations and structures of a range of commonly encountered AIL cations and anions. R = alkyl chain.

Protic Ionic Liquids. Protic ionic liquids (PILs) are formed through the transfer of a proton from a Brønsted acid to a Brønsted base:



They contain dissociable (acidic) protons and possess intrinsic (anhydrous) proton conductivity. The proton activity in PILs varies depending on the identity of the constituent Brønsted acid/base, analogous to pH in aqueous systems, allowing some control over proton-mediated chemical/electrochemical processes. When complete transfer of the proton from HA to B occurs, the properties of PILs are generally not discernible from those of AILs (discussed below). This is often the case when the HA is a strong acid and B is a strong base in aqueous media, for example if triflic acid was combined with a tertiary amine.²²⁻²⁸

When proton transfer from HA to B does not go to completion, the melt may contain a significant amount of neutral species (*i.e.*, HA/B). This is often the case when HA is a weak aqueous acid and/or B is a weak aqueous base, for example if a carboxylic acid was combined with imidazole or pyridine. Proton-donor (*i.e.*, HA or BH⁺) and -acceptor (*i.e.*, B or A⁻) sites establish a hydrogen-bonded cation/anion network, often resulting in water-like properties. In addition, when the proton transfer is reversible (*i.e.*, does not go to completion), it is possible that the boiling temperature of [BH][A] (achieved through the backwards reaction shown in Eq. 1.1) is below its decomposition temperature, thereby allowing the PIL to be readily distilled.^{22, 29} There is some controversy as to whether or not PILs containing a large proportion of neutral species (*i.e.*, due to incomplete proton-transfer equilibria) should be thought of as ‘true’ ILs or a mixture (solution) of ionic and molecular species. Macfarlane and Seddon⁸ recommend that for a PIL to be considered a ‘pure IL’, less than 1% of the neutral species should be present at equilibrium. The names, abbreviations and structures of commonly encountered PIL cations and anions are shown in Figure 2.

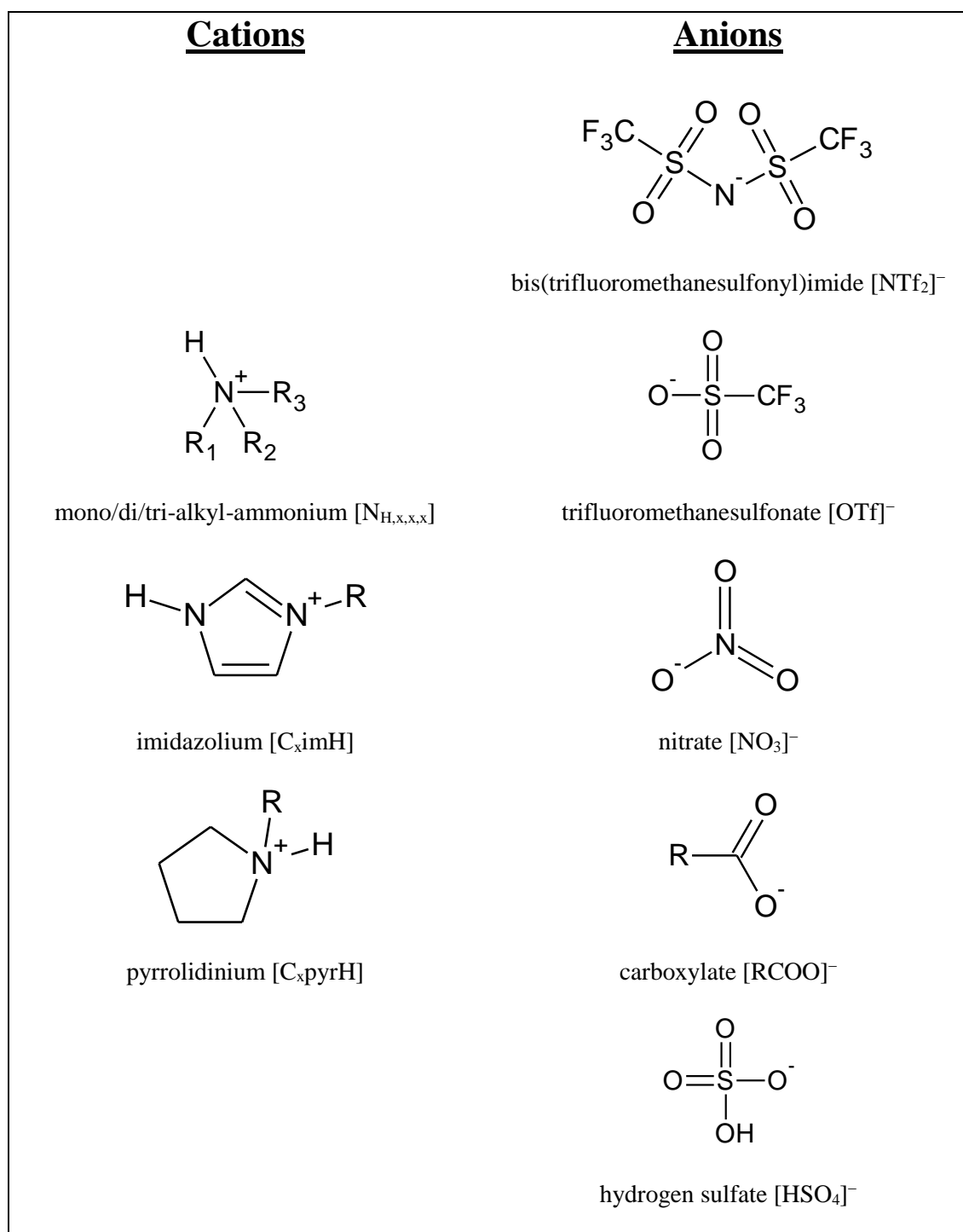


Figure 2. Names, abbreviations and structures of a range of commonly encountered PIL cations and anions. $R = H$ or alkyl chain.

1.1.3 Physicochemical Properties

One of the biggest selling points of ILs is their great versatility; it has been estimated that 10^{18} different ILs could be prepared by varying the combination of anion and cation. Indeed, they are commonly referred to as ‘designer solvents’ because their physicochemical properties can be ‘tuned’ to an extent by changing their constituent cation and/or anion. ILs display complex phase behaviour, being prone to supercooling and forming metastable amorphous glass or plastic crystal phases. ILs may display hydrophilic or hydrophobic character and thus range from being completely miscible to completely immiscible with water. Regardless of their degree of hydrophobicity, ILs are generally hygroscopic, readily absorbing water upon exposure to the atmosphere.^{9, 10, 12, 18, 30, 31}

The only truly ubiquitous property shared by all ILs is intrinsic ionic conductivity.⁸ Nonetheless, in the broad chemical literature^{1, 3, 6, 11-13}, ILs are often claimed to possess a number of generic properties, including:

- Negligible vapour pressures and non-flammability;
- High solvating ability and non-coordinating;
- High thermal, chemical and electrochemical stability;
- High ionic conductivity;
- Large liquidus range;
- Non-toxic and environmentally friendly (biodegradable);

In reality, the unique physicochemical properties of an IL are decided by the identity of its constituent cation and anion.¹¹ Although ILs do often possess *some* of the above attributes, there are many exceptions, for example, the so-called distillable ILs³² do possess a significant vapour pressure. Furthermore, despite the fact that ILs are often claimed to be ‘non-toxic’ and ‘biodegradable’, there is usually very little data available to back up such claims.⁸

1.1.4 Applications

Interest in ILs in both academia and industry for use in a range of applications has increased dramatically over the last two decades. This is illustrated in Figure 3; the number of publications on the topic was over 500-fold higher in 2014 compared to 1994. ILs are versatile solvents, and have been employed as replacements for volatile organic compounds (VOCs) in ‘green’ synthesis³³, separations³⁴, ‘clean catalysis’³⁵, and as electrolytes.¹² ILs have also found application in the bio-sciences, being employed as media for enzymatic reactions^{36, 37} and solubilisation of biomolecules (*i.e.*, cellulose, DNA and proteins).⁹ The application of ILs as a solvent/electrolyte in electrochemical energy conversion and storage technologies is the main focus herein.

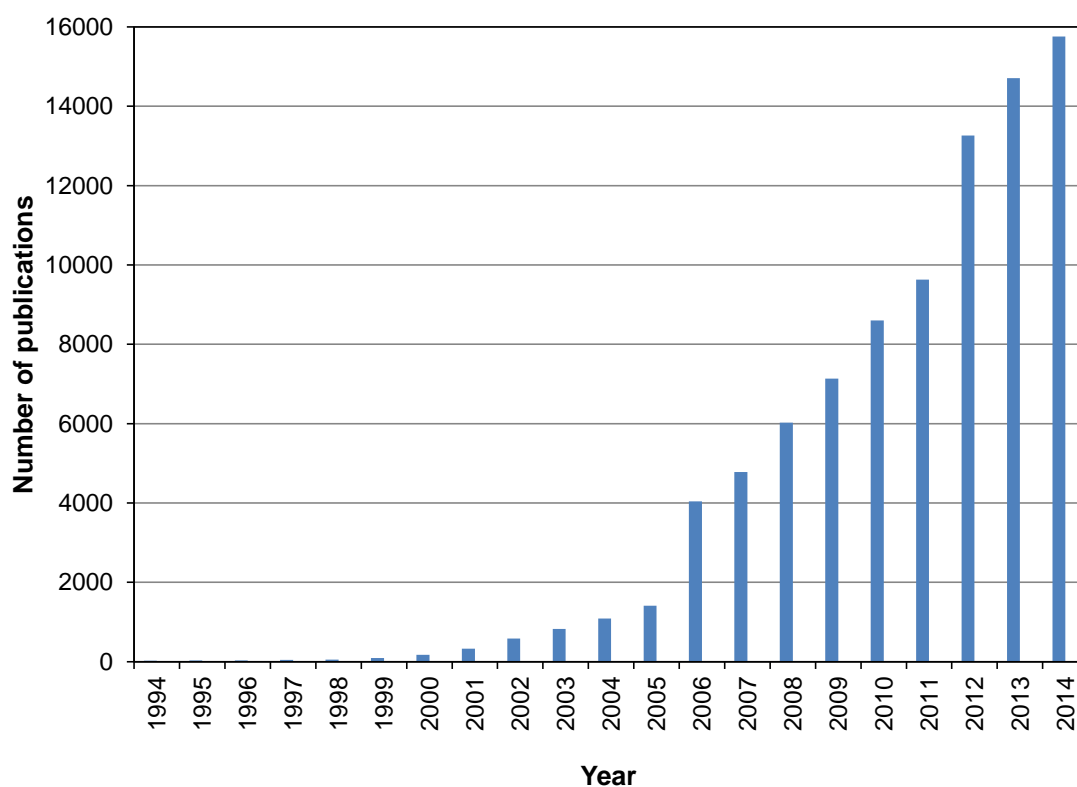


Figure 3. Rapid growth in the number of publications on the topic “ionic liquid*” over the period 1994 to 2014. Data was obtained from a literature search using the ISI Web of Knowledge database.

1.2 Ionic Liquids as Electrolytes

1.2.1 Electrolyte Properties

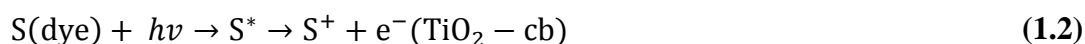
A conventional electrolyte formulation consists of one or more salts dissolved in a molecular solvent. In an IL electrolyte formulation on the other hand, there is no such distinction between ‘salt’ and ‘solvent’: the system is composed purely of ions.^{12, 38} AILs often possess wide electrochemical windows (*ca.* 4.0 to 6.0 V) due to the resilience of their constituent cations toward reduction and anions toward oxidation. However, the electrochemical window is highly conditional on the exact combination of cation/anion, the presence/absence of impurities (such as water and halides) and the identity of the electrode material.^{11, 38} In general, PILs tend to have narrower electrochemical windows than AILs due to the ease of proton reduction, although this can be averted somewhat through careful choice of electrode material.³⁹

As previously alluded to, ILs are typically 10 to 1000 times more viscous than conventional electrolyte solutions.^{11, 12} The strong cohesive forces operating within an IL impede physical mass-transport, resulting in low diffusivities, often in the 10^{-9} to 10^{-7} $\text{cm}^2 \text{s}^{-1}$ range.^{12, 23} Despite the high-ionic strength of ILs, low ionic mobility means they often possess modest conductivities, typically in the range of $0.1 - 18 \text{ mS cm}^{-1}$ at room temperature, compared to $500 - 700 \text{ mS cm}^{-1}$ for aqueous electrolytes and $10 - 60 \text{ mS cm}^{-1}$ for non-aqueous electrolytes. Mass-transport is an important factor for the application of ILs in electrochemical energy storage and conversion technologies, since it directly influences the ultimate speed and/or efficiency at which an electrochemical device can operate. Despite the obvious mass-transport limitations imposed by their use, ILs have shown promise as replacement electrolytes in batteries¹⁵, supercapacitors¹⁷, fuel cells^{16, 40, 41} and dye-sensitized solar cells.⁴²⁻⁴⁴ Some applications are discussed in detail below.

1.2.2 Application in Electrochemical Devices

Dye-Sensitized Solar Cells. Since first reported by O'Regan and Grätzel⁴⁵ over twenty years ago, intensive research efforts have focused on improving and optimizing the performance of the dye-sensitized solar cell (DSSC). Owing to the low manufacturing cost and design versatility (*i.e.*, size, shape and flexibility) of DSSCs, they are considered to be promising candidates to replace traditional (*p*-/*n*-) silicon photovoltaics in a range of applications. In essence, a prototypical DSSC has three fundamental components: (1) a TiO₂ semiconductor photoanode with an adsorbed photoactive dye; (2) a platinized counter electrode (cathode) and; (3) an electrolyte solution containing the oxidized and reduced forms of a suitable redox couple so as to establish a redox shuttle system that regenerates the reduced form of the dye.¹⁴

The I⁻/I₃⁻ redox couple dissolved in a VOC (such as acetonitrile) is the most commonly employed redox mediator or 'shuttle' system in DSSCs.^{13, 14} During operation, dye molecules at the photoanode are excited by incident photons and inject electrons into the conduction band of a semi-conductor (TiO₂), leaving them in an oxidised state:



The dye is regenerated (reduced) at the photoanode by I⁻ in the electrolyte, forming I₃⁻ in the process:



I₃⁻ subsequently diffuses a short distance through the electrolyte to the platinized counter electrode, where it is reduced back to I⁻ by electrons previously 'injected' by the dye molecules at the photoanode after flowing through an external circuit.^{14, 46} A schematic diagram showing the basic operation of a DSSC is shown in Figure 4. I⁻ is always present in excess relative to I₃⁻ and thus the photocurrent achievable in a particular DSSC is largely

dependent upon how facile I_3^- transport is in the electrolyte.⁴⁶ It is therefore desirable to minimize the distance between the photoanode and the counter electrode and to employ electrolytes in which I_3^- has a relatively large diffusion coefficient. The operating voltage generated by a DSSC under illumination is, as with any electrochemical device, determined by the difference in electrochemical potential of an electron at the anode and cathode. This corresponds to the difference in the Fermi potential of the semiconductor anode (TiO_2) and the redox potential of the active shuttle.¹⁴ Evidently, the operational voltage of a DSSC can be theoretically increased by choosing a mediator system with a more positive redox potential than the I^-/I_3^- couple.^{14, 47}

There is no net chemical change during the operation of a DSSC, in theory allowing these devices to generate electrical power without permanent chemical transformation indefinitely. In reality, as with any electrochemical device, degradation processes limit the cycle life of DSSCs, although with the use of stable electrolytes/dyes, life-times of greater than 15 years have been predicted.¹⁴ Unfortunately, unless the DSSC is properly sealed, VOC-based electrolytes impose restrictions on device performance due to the poor long term stability (solvent volatility) and safety (solvent flammability) under light soaking conditions.^{13, 14, 48}

In this regard, ILs are promising alternatives, because, as previously discussed, they often possess negligible vapour pressures and are electrochemically/chemically/thermally stable. Unfortunately, due to the relatively high viscosity of ILs, I_3^- transport is expected to be sluggish, limiting the photocurrent achievable during DSSC operation.^{14, 49} Fortunately, non-Stokesian diffusion achieved through a Grotthuss-type bond-exchange mechanism between I^- and I_3^- (discussed in Section 1.3.3) can partially compensate for the intrinsically low physical mass-transport in ILs.¹⁴ Key studies on the electrode reaction and mass-transport mechanisms associated with the I^-/I_3^- couple in ILs are discussed in Section 1.5.1.

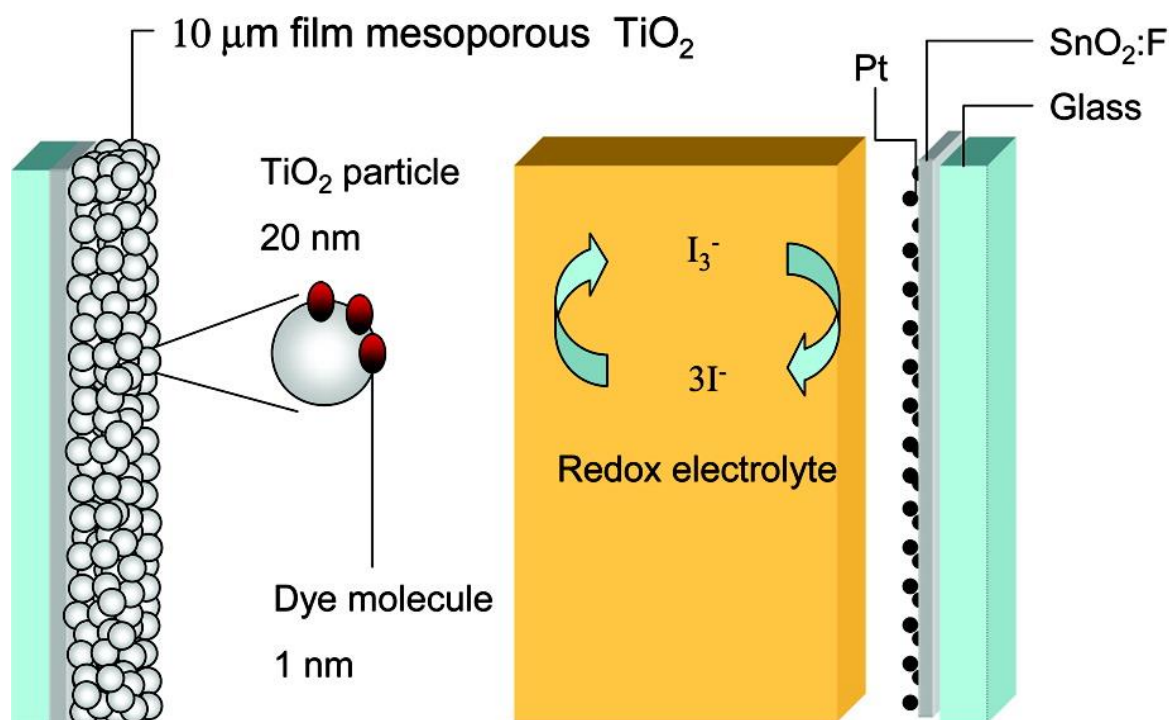


Figure 4. Schematic diagram showing the basic structure and operation of a dye-sensitized solar cell. Figure 4 was adapted from Hagfeldt *et al.* (2009)⁵⁰.

Proton Exchange Membrane Fuel Cells. The first application of the proton-exchange membrane fuel cell (PEMFC) was as an auxiliary power source in the Gemini space flights during the 1960's.⁵¹ This type of fuel cell possesses many favourable properties, including high power density, rapid start up, high efficiency and zero greenhouse gas emissions (H₂O is the only by-product).⁵² In recent years, intensive research efforts have focused on: optimizing PEMFC fabrication, design and layout; developing new electrode materials with reduced cost and optimized performance and; developing novel proton conducting materials with improved performance and resilience.⁵¹

In essence, a PEMFC consists of two electrodes, one where H₂ oxidation to H⁺ occurs (negative electrode) and one where O₂ reduction to H₂O occurs (positive electrode), with proton conduction occurring through a proton exchange membrane (PEM) separating the two electrodes⁵¹:



The PEM is necessarily an ionic (proton) conductor and an electronic insulator (electrons flow through an external circuit). The basic operation and structure of a PEMFC is shown schematically in Figure 5.

At the heart of any PEMFC is the membrane electrode assembly, which is composed of the gas diffusion layers, catalyst layers and the PEM. The catalyst is composed of platinum or platinum alloys and the gas diffusion layer (not shown in Figure 5) is an electronic conductor, often porous carbon paper or carbon cloth. The structure and properties of the PEM is discussed below. There are three fundamental transport processes that occur during the operation of a PEMFC:

- Transport of protons through the PEM from the negative electrode to the positive electrode;
- Transport of electrons to/from the current collectors through the gas diffusion layer from/to the catalyst layers;
- Transport of the reactants (H₂ + O₂) and product (H₂O) from the catalyst layers through the gas diffusion layer.

The three processes described above are all equally important and must be correctly balanced to optimize the performance of a PEMFC.⁵¹

The PEM is composed of a hydrated polyelectrolyte, most commonly a perfluorosulfonic acid (PFSA) such as Nafion. Hydrated PFSA-based membranes possess relatively high proton conductivity at intermediate temperatures (70 - 90°C). Unfortunately, the proton conducting properties and mechanical stability of PFSA-based membranes is humidity dependent, limiting operation to temperatures below 100°C (typically $\leq 80^\circ\text{C}$). In addition, when operating a PEMFC with a PFSA-based membrane, there is a need to constantly replace water lost through evaporation.^{52, 53} Increasing the operating temperature of PEMFCs to above 100°C offers a number of advantages, including:

- Accelerated heterogeneous kinetics at both electrodes (significant for the kinetically sluggish oxygen-reduction reaction, see Eq. 1.5);
- Increased tolerance of the Pt catalysts to carbon monoxide (CO) poisoning, allowing the use of less-pure H₂ feed stocks;
- Simplified water management (H₂O is only present in the gaseous state above 100°C);
- Improved gas diffusion.

Due to the perceived advantages listed above, there has been a drive to develop novel humidity-independent proton-conducting materials which are stable at temperatures above 100°C.^{52, 54}

PILs have been identified as promising candidates for this application, as they are generally non-volatile and thermally/chemically stable, facilitating anhydrous proton conduction at temperatures well above 100°C.^{22, 29, 54} Both stoichiometric and non-stoichiometric combinations of Brønsted acid/base have been investigated for this purpose.²² PIL formulations which exhibit fast proton transport and facile hydrogen oxidation/oxygen reduction kinetics have been reported.⁵⁵ As is the case in aqueous media, proton conduction has been proposed to occur by a combination of vehicular (physical) transport and the

Grotthuss mechanism in PILs.^{40, 41} Proton conduction *via* the Grotthuss mechanism may serve to offset limited physical transport as a result of the high viscosity of PIL-based electrolytes.^{22, 40} Key studies on the electrode reaction and mass-transport mechanisms associated with the H^+/H_2 couple in ILs are discussed in Section 1.5.2.

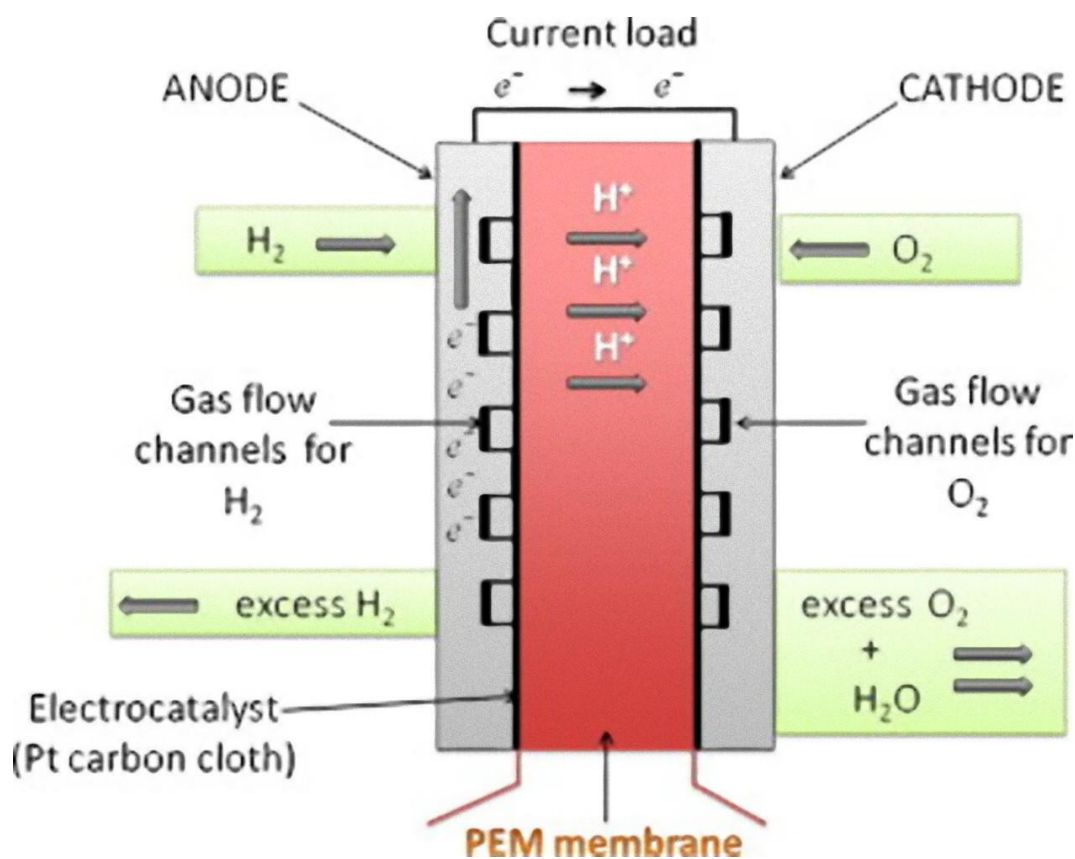


Figure 5. Schematic diagram showing the basic structure and operation of a proton-exchange membrane fuel cell. Figure 5 was taken from Rana *et al.* (2012).²⁹

Lithium Batteries. Both lithium-ion (Li-ion) and lithium metal battery technology has developed over the past two decades from research and development interests to high-sales consumer products that have become the standard power source in a diverse range of markets. They have replaced conventional battery technologies (such as nickel-cadmium and nickel metal-hydride) in a range of applications, owing to their comparatively high volumetric/gravimetric energy density and desirable performance characteristics (*i.e.*, high charge/discharge rate capability, high operating voltage and lack of memory effect).^{2, 5}

In a prototypical secondary (rechargeable) Li-ion battery, the positive electrode is a transition metal oxide (*e.g.*, LiCoO₂) and the negative electrode is graphite.^{56, 57} Both of the electrodes are intercalation compounds which operate by reversibly incorporating Li⁺ from the electrolyte:



to give the overall reaction:



where LiMO₂ is the positive electrode transition metal oxide and C₆ is the graphitic negative electrode.^{5, 58} The forward direction of the reactions shown above occur during discharge and the reverse occur during charge. The electrochemical processes occurring during the discharge of a Li-ion battery are shown schematically in Figure 6.

Lithium metal batteries contain positive electrode materials identical to those in Li-ion batteries, but contain a Li-metal negative electrode. In a commercial setting, Li-metal batteries are only employed as primary (non-rechargeable) batteries due to the difficulty associated with reversibly cycling lithium at the negative electrode:



When cycled in conventional molecular solvent based electrolytes (see below), dendritic lithium grows on the surface of the negative electrode, causing internal short circuits to form between the electrodes, resulting in poor cycle life. This also poses a safety issue, as internal short circuiting can cause heating and thermal runaway, leading to an explosion.^{3, 4, 15, 59}

The conventional electrolyte found in most commercially available lithium batteries is composed of a solution of lithium salt in a mixture of organic solvents, typically carbonates, ethers or esters. There has been growing interest in replacing these volatile and

flammable organic-solvent based electrolytes due to issues with safety, electrochemical instability and toxicity.^{1, 60} ILs have been shown to be promising replacement electrolytes in this application, as they offer obvious practical advantages, often being non-flammable, non-volatile and electrochemically/chemically stable. Additionally, certain ILs have been shown to interact uniquely with lithium metal, suppressing lithium dendrite growth and thus allowing long-term cycling with Li-metal negative electrodes. Based on this fact, it has been proposed that implementation of ILs as electrolytes would allow the widespread commercialization of secondary Li-metal batteries.^{46, 51, 52}

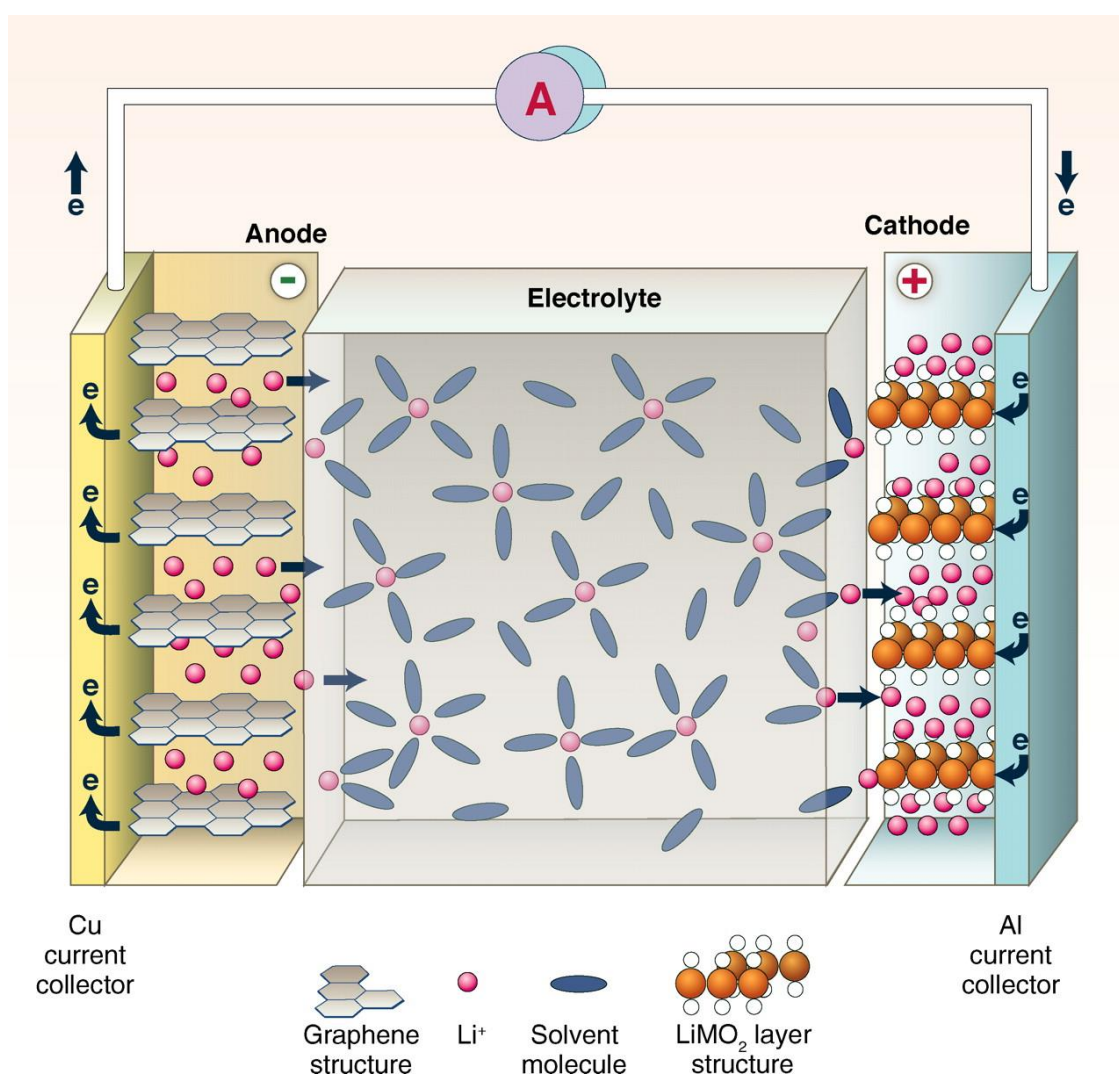


Figure 6. Schematic diagram of the electrochemical processes occurring during the discharge of a Li-ion battery. Figure 6 was taken from Dunn *et al.* (2011).⁶¹

The main disadvantage of ILs in this application relates to mass-transport limitations imparted by their high intrinsic viscosity. This limitation is snowballed by the fact that addition of a lithium salt to an IL electrolyte further increases viscosity.²⁴ During the operation of lithium batteries, Li⁺ ions are transported between the electrodes by a combination of physical diffusion and electromigration. In conventional electrolytes, low-polarity, low-viscosity solvents (*i.e.*, dimethylcarbonate) are often mixed with high-polarity solvents (*i.e.*, ethylene carbonate) to form electrolytes with a good balance of Li⁺ transport and Li⁺ solvation properties.⁵ This approach is obviously not feasible when using IL electrolytes and for this reason there has been a push to develop novel low-viscosity ILs for this application.²⁴ Nonetheless, despite the mass-transport limitations, ILs have successfully been employed as electrolytes with both graphitic^{62, 63} and Li-metal negative electrodes.^{56, 57}

1.3 Fundamentals of Electrochemistry

Electrochemistry is the branch of chemistry concerned with the interrelation of electrical and chemical phenomena. Electrochemical processes are those which involve the transfer of charge across an interface between two or more chemical phases. The most frequently studied interface is that formed between an electronic conductor, known as the electrode, and an ionic conductor, known as the electrolyte. The net rate of an electrode reaction, r , is proportional to the current (I) flowing across the interface:

$$r = \frac{I}{nFA} \tag{1.10}$$

where n is the stoichiometric number of electrons involved in the charge transfer, F is Faraday's constant (96485 C mol⁻¹) and A is the area of the electrode.⁶ Many factors influence the rate of charge transfer (*i.e.*, current flowing) across this electrode/electrolyte interface, including:

-
- Mass-transport to/from the interface;
 - Electron transfer across the interface;
 - Reactions preceding/proceeding the electron transfer;
 - Surface reactions, including adsorption, desorption, or crystallization.

As previously outlined, in this work the aim is to elucidate the electrode reaction and mass-transport mechanisms associated with a number of ‘model’ redox species in IL media using electrochemical methods. To this end, the fundamentals of heterogeneous electron transfer kinetics, electrode reaction mechanisms and mass-transport are outlined in brief below.

1.3.1 Kinetics of Electrode Reactions

The following discussion refers to the classical Butler-Volmer formalism⁶ of electrode kinetics, which has been employed in all numerical simulations herein. Take the following general redox reaction:



Where O is the oxidised form, R is the reduced form and k is a heterogeneous rate constant (cm s^{-1}), where the subscripts f and b signify the forward (reduction) and backward (oxidation) reaction pathways respectively. The k_f and k_b reaction components shown in Eq. 1.11 proceed at rates (see Eq. 1.10) proportional to the surface concentration of O and R respectively, and thus the net reaction rate is given by:

$$r_{\text{net}} = r_f - r_b = k_f C_O(0, t) - k_b C_R(0, t) = \frac{I_{\text{net}}}{nFA} \quad (1.12)$$

where $C_j(x, t)$ is the concentration of species j at distance x from the electrode surface at time t . From Eq. 1.10, the overall current, I_{net} , is:

$$I_{\text{net}} = I_{\text{red}} - I_{\text{ox}} = nFA[k_f C_O(0, t) - k_b C_R(0, t)] \quad (1.13)$$

where the subscripts *red* and *ox* signify the reduction (forward) and oxidation (backward) processes respectively.

If the simplest possible (one electron) electrode process is considered:



and it is assumed that k_f and k_b have an Arrhenius form, it can be shown that⁶:

$$k_f = k_s \exp[-\alpha f(E - E^{0'})] \quad (1.15)$$

$$k_b = k_s \exp[(1 - \alpha)f(E - E^{0'})] \quad (1.16)$$

where k_s is the standard heterogeneous rate constant, α is the charge-transfer coefficient, $E^{0'}$ is the formal potential and $f = F/RT$ (R is the constant and T is temperature). Evidently, unlike homogeneous rate constants, the heterogeneous rate constants, k_f and k_b , are exponentially related to the applied potential (or more specifically, $E - E^{0'}$). One consequence of this relationship is that at the rate of the forward (reduction) reaction component shown in Eq. 1.14 can be made insignificant relative to the backward (oxidation) reaction component (or vice versa) through careful control of the applied potential. Substituting Eqs. 1.15 and 1.16 into Eq. 1.13 yields the complete current-potential characteristic:

$$I_{net} = F A k_s [C_O(0, t) e^{-\alpha f(E - E^{0'})} - C_R(0, t) e^{(1-\alpha)f(E - E^{0'})}] \quad (1.17)$$

This relationship is the cornerstone of the Butler-Volmer treatment of electrode kinetics.

For a heterogeneous electron-transfer reaction of the type shown in Eq. 1.11 or 1.14, in the absence of net current flow (*i.e.*, the system is at equilibrium), the potential adopted by the electrode is governed by the Nernst equation:

$$E = E^{0'} + \frac{RT}{nF} \ln \left(\frac{C_O(\infty, t)}{C_R(\infty, t)} \right) \quad (1.18)$$

The Nernst equation is a thermodynamic expression, linking the electrode potential to the bulk concentrations of redox species, irrespective of electrode kinetics. On the other hand, k_s is a kinetic parameter, numerically equal to k_f and k_b when $E = E^0$. It is a measure of the kinetic facility of a redox process. If k_s is large, the process is termed ‘electrochemically reversible’, as it is able to achieve equilibrium on the timescale of the experiment. If the reaction shown in Eq. 1.14 is assumed to be electrochemically reversible (*i.e.*, k_s is large), the Butler-Volmer expression (Eq. 1.17) reduces to:

$$E = E^{0'} + \frac{RT}{F} \ln \left(\frac{C_O(0, t)}{C_R(0, t)} \right) \quad (1.19)$$

In other words, the surface concentrations of O and R and electrode potential are linked by an equation of the Nernst form, regardless of the current flow.

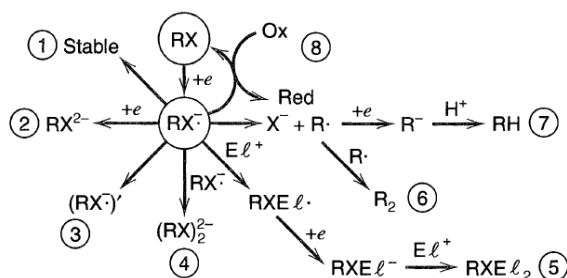
In reality, redox processes are considerably more complex than shown in Eq. 1.14, featuring several elementary reactions which may or may not be heterogeneous electron transfer steps (see Section 1.3.2). The overall rate of reaction is controlled by the most sluggish step of the mechanism, termed the rate-determining step (RDS). In theory, if the RDS is a heterogeneous electron transfer reaction, a Butler-Volmer type current-potential relationship (see Eq. 1.17) can be employed. In practice however, this is often not true, requiring intricate knowledge of the reactions preceding the RDS in order to establish the complete theory that applies. For this reason, computational simulation is widely employed in the literature to solve complex electrochemical problems.

1.3.2 Electrode Reaction Mechanisms

The previous section dealt with relatively simple electrode reactions (see Eqs. 1.11 and 1.14), where the oxidized electroactive species, O , is converted to the reduced electroactive species, R , in a heterogeneous electron transfer step. In reality, heterogeneous electron transfer reactions are often coupled to one or more homogeneous processes that

involve species O or R . A number of general reaction pathways which may be followed after the reduction or oxidation of species ‘RX’ are shown schematically in Figure 7.

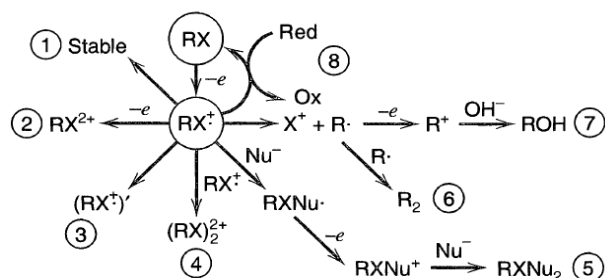
(a) General reduction pathways.



Reduction pathways leading to:

- ① a stable reduced species (E)
- ② uptake of a second electron (EE)
- ③ rearrangement (EC)
- ④ dimerization (EC_2)
- ⑤ reaction with an electrophile, $E\ell^+$, to produce a radical followed by an additional electron transfer and further reaction ($ECEC$)
- ⑥ loss of X^- followed by dimerization (ECC_2)
- ⑦ loss of X^- followed by a second electron transfer and protonation ($ECEC$)
- ⑧ reaction with an oxidized species, Ox , in solution (EC')

(b) General oxidation pathways.



Oxidation pathways leading to:

- ① a stable oxidized species (E)
- ② loss of a second electron (EE)
- ③ rearrangement (EC)
- ④ dimerization (EC_2)
- ⑤ reaction with an electrophile, Nu^- , to produce a radical followed by an additional electron transfer and further reaction ($ECEC$)
- ⑥ loss of X^+ followed by dimerization (ECC_2)
- ⑦ loss of X^+ followed by a second electron transfer and reaction with OH^- ($ECEC$)
- ⑧ reaction with a reduced species, Red , in solution (EC')

Figure 7. Schematic representation of examples of reaction pathways following (a) reduction or (b) oxidation of the electroactive species “RX”. “ E ” represents an electron transfer at the electrode surface, and “ C ” represents a homogeneous chemical reaction. The general species, RX , is an organic compound, where R is a hydrocarbon moiety (*e.g.*, alkyl, aryl) and X is a substituent (*e.g.*, H , OH , Cl , Br , NH_2 , NO_2 , CN , CO_2^-). Figure 7 was adapted from Bard and Falkner (2001).⁶

Cyclic voltammetry (often in tandem with numerical simulation) is a powerful method for mechanistic studies, since each of the reaction pathways shown in Figure 7 ideally will give rise to an I - E data set with unique characteristics.⁶ This is explored in further detail below.

1.3.3 Mass-transport

Stokesian Diffusion. In the discussion about the kinetics of electrode reactions (see Section 1.3.1) it was assumed that mass-transport is not limiting. In practice, due to the exponential nature of the relationship between the rate of an electrode reaction and the applied potential (see Eqs. 1.15 and 1.16), mass-transport often becomes limiting on the experimental timescale. Mass-transport to an electrode surface is described generally by the Nernst-Planck equation:

$$J_j = -D_j \nabla C_j - \frac{z_j F}{RT} D_j C_j \nabla \phi + C_j v_L \quad (1.20)$$

where J_j is the flux density of species j , D_j is the diffusion coefficient of species j , z_j is the valence of species j , ϕ is electrostatic potential and v_L is the linear velocity of solution flow. ∇ is a Laplacian operator, the form of which depends on the electrode geometry.⁶

When mass-transport to the electrode surface occurs in one dimension (*i.e.*, to a planar electrode), Eq. 1.20 becomes:

$$J_j(x, t) = -D_j \frac{\partial C_j(x, t)}{\partial x} - \frac{z_j F}{RT} D_j C_j \frac{\partial \phi(x, t)}{\partial x} + C_j v_L(x, t) \quad (1.21)$$

where $\frac{\partial C_i(x, t)}{\partial x}$ and $\frac{\partial \phi(x, t)}{\partial x}$ are concentration and potential gradients respectively. In the above equations, the contributions of diffusion, migration and convection makeup the first, second and third terms respectively. A rigorous solution to Eq. 1.21 is difficult when all three modes of mass-transport are in effect and hence electrochemical experiments are often designed to make the contribution of one or more of the processes to the total flux negligible.^{6, 64} For example, electrochemical experiments are often carried out in the presence of large

concentrations of supporting electrolyte, making the migrational component of mass-transport negligible. In addition, convection can be easily avoided by preventing stirring or vibrations in the electrochemical cell.

Unless otherwise stated, the results discussed herein have been carried out under conditions where mass-transport is governed solely by diffusion. Diffusion is the movement of a species under the influence of a concentration (chemical potential) gradient. The chemical conversion of electroactive species brought about by charge transfer processes at the electrode/electrolyte interface necessarily give rise to concentration gradients. The diffusion coefficient or diffusivity, D , is the proportionality constant between molar flux due to diffusion and the concentration gradient of a species (see Eq. 1.21). The diffusivity of a solute in solution is inversely proportional to the frictional force acting upon it:

$$D = \frac{k_{\text{B}}T}{f_{\text{c}}} \quad (1.22)$$

This is a form of the Einstein-relation, where k_{B} is the Boltzmann constant and f_{c} is a friction coefficient.⁶⁵ By likening the dissolved solute to a rigid solid sphere with a radius, r_{H} , diffusing in a continuum of solvent with a viscosity, η , f_{c} can be calculated using Stokes-Law^{66, 67}:

$$f_{\text{c}} = 4\pi\eta r_{\text{H}} + 2\pi\eta r_{\text{H}} = 6\pi\eta r_{\text{H}} \quad (1.23)$$

The first term represents a force due to pressure built up in front of a diffusing solute and the second term is a frictional force parallel to its surface.^{66, 68, 69} Combining Eqs. 1.22 and 1.23 gives the Stokes-Einstein equation⁶⁵:

$$D = \frac{k_{\text{B}}T}{6\pi\eta r_{\text{H}}} \quad (1.24)$$

The Stokes-Einstein equation, as written in Eq. 1.24, is strictly only valid when the size of the solute is large compared to the size of the solvent (*i.e.*, when $r_{\text{solute}}/r_{\text{solvent}} > 5$). To accommodate this fact, the Stokes-Einstein equation is often written in the form:

$$D = \frac{k_{\text{B}}T}{c\pi\eta r_{\text{H}}} \quad (1.25)$$

where c is a constant with a value of 4 ('perfect slip') or 6 ('perfect stick').⁶⁶ The value of 4 arises because the second term of Eq. 1.23 (arising from frictional force parallel to the solute surface) disappears when the solvent is able to 'slip past' the surface of a small solute particle (typically when $r_{\text{solute}} < 0.5$ nm).^{66, 70} In practice, an empirical constant with a value between 4 and 6 is often used for small solutes in conventional solvents^{66, 68, 69} and ILs.^{71, 72}

Non-Stokesian Diffusion. Diffusion processes arising from homogeneous bond-exchange reactions (*i.e.*, electron hopping) cannot be categorized into any of the physical mass-transport processes discussed so far in Section 1.3.3. These processes are not governed by any form of the Stokes-Einstein equation (see Eq. 1.22) and are therefore broadly termed non-Stokesian diffusion. The most commonly-cited example of non-Stokesian diffusion is the Grotthuss mechanism⁷³, which explains why the diffusion coefficient of H^+ in water is five times larger than what would be expected based on the dimensions of the hydronium ion (H_3O^+).^{74, 75}

Non-Stokesian diffusion is thought to be facilitated by a bimolecular exchange reaction between chemically identical species, written generally below for the species A:



where X is an atom, radical, ion, molecule or electron that can be exchanged between A/A* and the asterisks serve only to distinguish between the two identical molecules.⁷⁶ In the above reaction scheme, displacement of AX (*e.g.*, H_3O^+) and A* (*e.g.*, H_2O) effectively occurs without physical mass-transport and because the exchange process is favored in the

direction of any existing chemical potential gradients, this additional transport mechanism is additive with physical mass-transport processes, enhancing the flux density of the species involved.⁷⁶

Enhanced mass-transport *via* electron/bond-exchange mechanisms is predicted to occur in electrolytes containing mixtures of both the oxidized and reduced species (*e.g.*, $\text{Fe}^{2+}/\text{Fe}^{3+}$ or I^-/I_3^-) of a redox couple, as reported by Dahms⁷⁷ and Ruff *et al.*^{76, 78}. The relationship between the apparent diffusion coefficient (D_{app}), physical diffusion coefficient (D_{phys}) and the exchange-reaction diffusion coefficient (D_{ex}) is described by the Dahms-Ruff equation:

$$D_{\text{app}} = D_{\text{phys}} + D_{\text{ex}} = D_{\text{phys}} + \frac{1}{6} k_{\text{ex}} \delta_{\text{int}}^2 C \quad (1.27)$$

where k_{ex} is the bimolecular exchange reaction rate constant and δ_{int} is the centre-to-centre intersite distance at the time of the exchange reaction.^{42, 77, 79, 80} The 1/6 term arises from the fact that physical diffusion takes place in three-dimensions (*i.e.*, x, y and z planes).⁸⁰

Diffusion Patterns. The geometry of an electrode governs the shape of the diffusion field that develops adjacent to its surface during an electrochemical perturbation. In a planar (or linear) diffusion field, mass-transport takes place in one dimension at all points normal (perpendicular) to the electrodes surface. In a spherical (or two dimensional) diffusion field, mass-transport takes place radially with respect to the electrodes axis of symmetry at the edges of its surface. These processes are shown schematically in Figure 8. At macrodisk electrodes, spherical (radial) diffusion is negligible and planar (linear) diffusion dominates (shown in Figure 8a). At microdisk electrodes, under steady-state conditions, planar diffusion is negligible and radial diffusion dominates (shown in Figure 8b). The enhanced mass-transport at the edges of microdisk electrodes resulting from the spherical diffusion field gives rise to enhanced current densities relative to macrodisk electrodes.

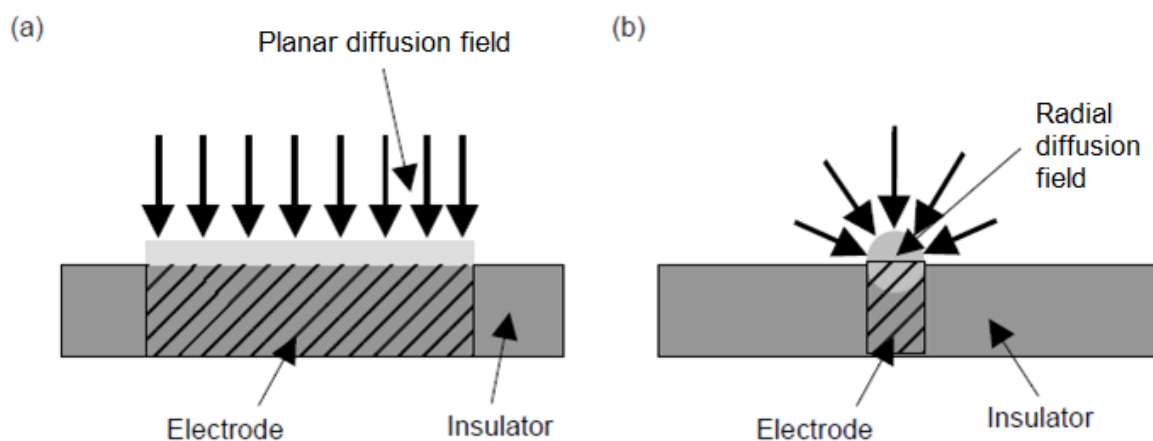


Figure 8. Schematic diagram showing the diffusion pattern at an inlaid (a) macrodisk electrode and (b) microdisk electrode during an electrochemical perturbation. Figure 8 was adapted from Forster (2006).⁸¹

At an inlaid disk electrode, conditions under which mass-transport is governed solely by planar diffusion are known as transient conditions. The term transient implies a time dependence, referring to the fact that the Nernst diffusion layer thickness (δ) is a time dependent parameter:

$$\delta(t) \propto \sqrt{D_j t} \quad (1.28)$$

As the diffusion layer extends further in the bulk solution, electroactive species must diffuse from greater distances to reach the electrode surface (*i.e.*, concentration gradients become shallower, see Eq. 1.21), resulting in a decrease in molar flux with time. Since current is proportional to molar flux, under transient mass-transport controlled conditions, I decays with $t^{-1/2}$ (discussed in further detail below).

At an inlaid disk electrode, conditions under which mass-transport is governed predominantly by radial diffusion are known as steady-state conditions. Under steady-state conditions, the thickness of the Nernst diffusion layer is time independent and comparable to the radius of the disk electrode (r_0). Logically, when δ is constant, molar flux to the electrode surface (and the concentration gradient across the diffusion layer) is constant, and

current is therefore independent of time. From Eq. 1.28, it is obvious that the time-lapse before the ‘steady-state’ is achieved (*i.e.*, $\delta \approx r_0$) must be dependent upon both the electrode geometry and the diffusion coefficient of the electroactive species. Steady-state conditions are readily achieved at microdisk electrodes (μsec to sec), whereas at macrodisk electrodes, convective effects dominate mass-transport over the timescale required to achieve the steady-state (min to hour).^{6, 11, 82, 83}

1.4 Electrochemical Methods

1.4.1 Chronoamperometry

During chronoamperometry, the working electrode potential is stepped from the initial potential (E_i) to the step potential (E_s) and the resulting current is measured as a function of time. At an inlaid disk electrode, under conditions where planar diffusion dominates (*i.e.*, transient regime), the current response can be described by the Cottrell equation:

$$I(t) = \frac{nFA\sqrt{DC(\infty, t)}}{\sqrt{\pi t}} \quad (1.29)$$

In the above equation, it is assumed that (i) no faradaic current can flow at E_i and (ii) E_s corresponds to a potential at which the concentration of electroactive species at the electrode surface is equal to zero (*i.e.*, diffusion controlled conditions).^{6, 11, 82}

At a microdisk electrode, the mode of diffusion depends on the timescale of the measurement (see Eq. 1.28). During the short-time regime (also known as the early transient regime), when $r_0 \gg \delta$, planar diffusion dominates, hence the $I-t$ response can be modelled using the Cottrell equation (see Eq. 1.29). During the intermediate-time regime, when $r_0 \geq \delta$, contribution by radial diffusion becomes comparable to that by planar diffusion.

During the long-time regime (also known as the steady-state regime), when $r_0 \approx \delta$, radial diffusion dominates and $I(t)$ approaches its steady-state value:

$$I_{\text{lim}} = 4nFDC(\infty, t)r_0 \quad (1.30)$$

The $I-t$ response at a microdisk electrode can be modelled using the equations proposed by Shoup and Szabo⁸⁴, which sufficiently describe the current response over the entire time domain, with a maximum error of less than 0.6%:

$$I(t) = 4nFDC(\infty, t)r_0f(t) \quad (1.31)$$

$$f(t) = 0.7854 + 0.8862\tau^{-\frac{1}{2}} + 0.2146 \exp\left(-0.7823\tau^{-\frac{1}{2}}\right) \quad (1.32)$$

where the dimensionless time parameter, τ , is given by:

$$\tau = \frac{4Dt}{r_0^2} \quad (1.33)$$

As $\tau \rightarrow \infty$, $f(\tau) \rightarrow 1$ and therefore Eq. 1.31 approaches Eq. 1.30, the steady-state limiting current.

1.4.2 Potential Sweep Voltammetry

During potential sweep voltammetry, the potential applied at the working electrode is varied (usually linearly) with time and the current is measured as a function of the applied potential. The experimental timescale can be readily controlled by varying the voltammetric sweep rate, also known as the scan rate, v .⁸² The applied potential waveform may: (i) terminate at a given potential on the forward sweep, which is known as linear sweep voltammetry or; (ii) switch direction at a given potential, which is known as cyclic voltammetry.

Under transient conditions, where mass-transport is governed solely by planar diffusion (*i.e.*, at a macrodisk electrode), a ‘peak-shaped’ voltammogram is generated. In a fully electrochemically reversible redox system (described in Section 1.3.1), in an electrolyte

devoid of uncompensated resistance (R_u), peak potentials (E_p) are independent of scan rate and peak currents (I_p) are proportional to the square-root of scan rate as per the Randles-Sevcik equation^{6, 11}:

$$I_p = 0.4663nFAC(\infty, t) \sqrt{\frac{nFDv}{RT}} \quad (1.34)$$

In reality, very few electrochemical systems fulfil the above criteria, so Eq. 1.34 is of limited quantitative use. For this reason, more complex theory is usually needed, so transient cyclic voltammetric data is often treated qualitatively or semi-quantitatively, where mechanistic, thermodynamic and kinetic information is inferred from the characteristic shape of the $I-E$ curve. An example of an experimental cyclic voltammogram is shown in Figure 9. Numerical simulation of the theory is often performed in tandem with experimental cyclic voltammetry in mechanistic studies.

Under true steady-state conditions, where mass-transport occurs solely by radial diffusion (*i.e.*, at a microdisk electrode at low scan rates), a sigmoidal cyclic voltammogram is generated. The steady-state limiting current, which is approached under mass-transport controlled conditions (see Eq. 1.30), is insensitive to k_s and R_u and is therefore more suitable than I_p (see Eq. 1.34) for quantitative purposes. In order to approach a true-steady state during potential sweep voltammetry, the following inequality must be satisfied:

$$v \ll \frac{RTD}{nFr_0^2} \quad (1.35)$$

This relationship has important practical implications when working in highly viscous media, such as ILs, as is explored in greater detail below.¹¹

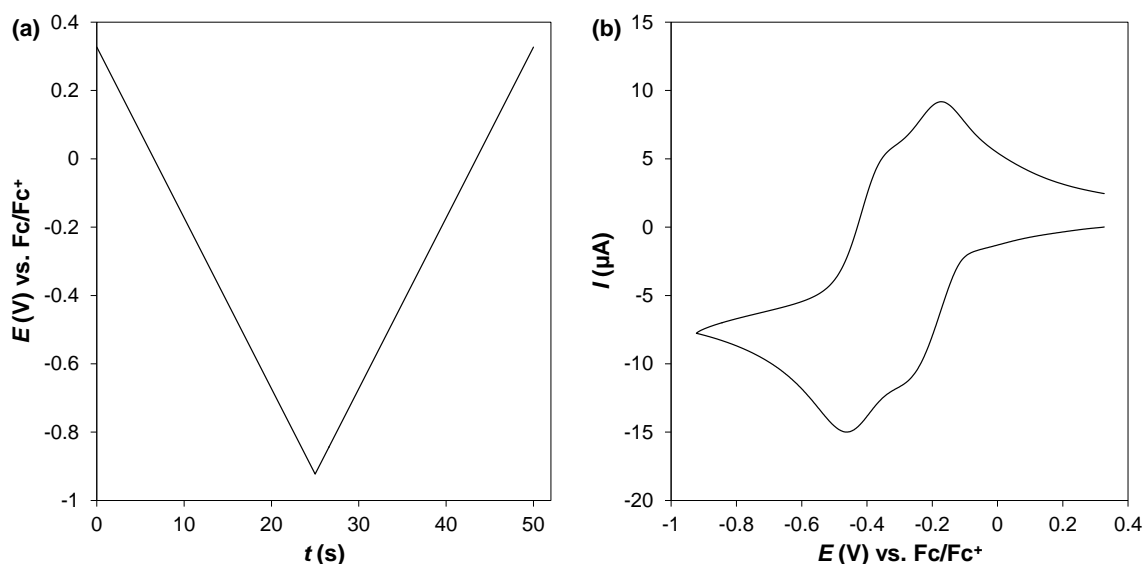


Figure 9. (a) $E-t$ and (b) $I-E$ curves showing the proton reduction process obtained from 41.6 mM *p*-toluenesulfonic acid in [C₂mim][NTf₂] at a 1.6 mm dia. Pt macrodisk electrode with a scan rate of 50 mV s⁻¹. The peak splitting seen in (b) is indicative of an *ECE* mechanism. Figure 9 was adapted from Bentley *et al.* (2015).⁸⁵

1.4.3 Convolution Voltammetry

Post-measurement data processing techniques which can be applied to voltammetric $I-t$ or $I-E$ data can greatly enhance the ability to extract information from the raw data. One such data transformation approach makes use of the general convolution procedure initially described by Savéant and co-workers⁸⁶⁻⁹⁴, where semiintegral voltammetry⁹⁵ is a subset of a range of techniques collectively known as convolution voltammetry. As described by Oldham and co-workers⁹⁵⁻¹⁰⁵, semiintegration is specific to conditions under which mass-transport to the electrode surface occurs solely by planar diffusion and gives rise to a function, $M(t)$, which is the 1/2 order fractional integral of current, $I(t)$, where:

$$M(t) = \frac{d^{-1/2}I(t)}{dt^{-1/2}} = I(t) * \frac{1}{\sqrt{\pi t}} \quad (1.36)$$

and the asterisk represents the convolution operation. In Eq. 1.36, the current, $I(t)$ is said to have been semiintegrated with respect to time or convolved with the function $1/\sqrt{\pi t}$. The function, $M(t)$, known as the semiintegral of the current, is related to the concentration of electroactive species at the electrode surface:

$$C(0, t) = C(\infty, t) - \frac{M(t)}{nAF\sqrt{D}} \quad (1.37)$$

It follows that under purely diffusion controlled conditions [*i.e.* $C(0, t) = 0$], $M(t)$ reaches its maximum or limiting value, M_L :

$$M_L = nAFC(\infty, t)\sqrt{D} \quad (1.38)$$

Semiintegrating a peak-shaped transient voltammogram ($I-E$) gives rise to a sigmoidal $M-E$ curve which superficially resembles a steady-state voltammogram, which in some circumstances is more amenable to data analysis.⁶ Indeed, just like the I_L plateau of a steady-state voltammogram, the magnitude of the M_L plateau is insensitive to k_s or R_u .

The fully planar diffusion restrictions associated with semiintegral voltammetry can be relaxed by replacing the function, $1/\sqrt{\pi t}$, in Eq. 1.36 with the generalized function, $g(t)$, whose form is dependent upon the details of the mechanism (*e.g.*, electron transfer with coupled chemical reactions) and the geometry of the electrode¹⁰⁶:

$$M(t) = I(t) * g(t) \quad (1.39)$$

Herein $M(t)$ will be referred to as the semiintegrated current when calculated based on Eq. 1.36 under planar diffusion conditions and as the convolved current for other electrode geometries when calculated more generally based on Eq. 1.39 taking into account the contribution of spherical diffusion to the mass-transport. For all intents and purposes, semiintegration and convolution can effectively be thought of as “black box” data analysis methods, as the required transformations can be readily performed offline on voltammetric

$I-t$ or $I-E$ data using programmable digital algorithms available in the literature.¹⁰⁷⁻¹¹¹ An example of an experimental convolved current voltammogram is shown in Figure 10.

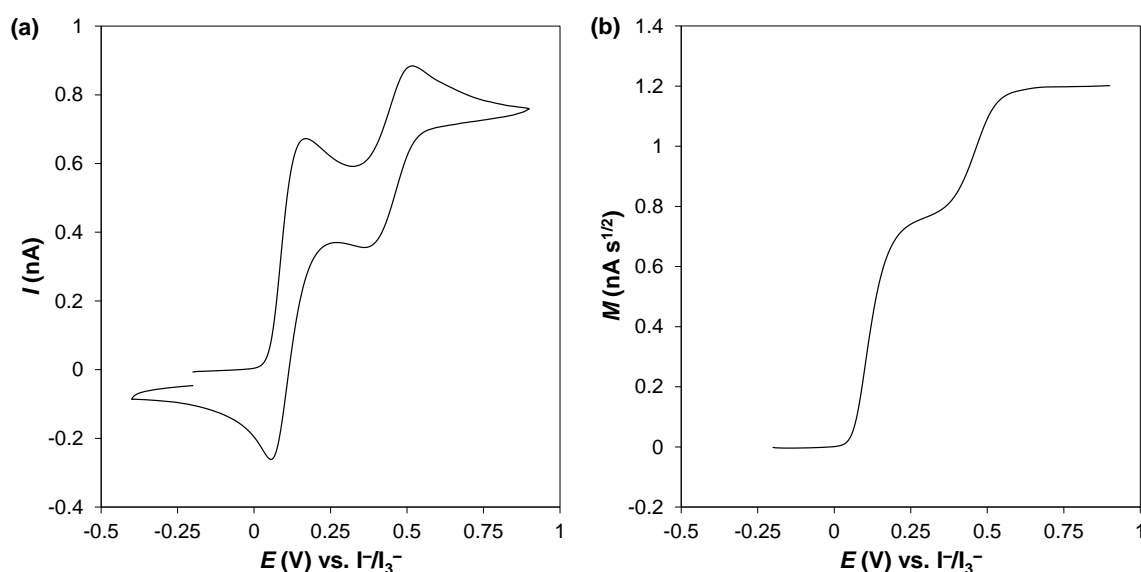


Figure 10. (a) Mixed transient/steady-state cyclic voltammogram obtained from the oxidation of 4.3 mM I^- in $[C_2mim][NTf_2]$ using a 25 μm dia. Pt microdisk electrode with a scan rate of 50 mV s^{-1} . (b) The convolved current of the voltammogram (forward sweep) shown in (a). Figure 10 was adapted from Bentley *et al.* (2014).¹¹²

1.4.4 Practical Considerations in Ionic Liquids

The high viscosity of ILs compared to conventional molecular solvents poses a number of practical challenges when applying classical voltammetric methods. The low diffusivity of electroactive species in viscous IL media (as per the Stokes-Einstein equation, see Eq. 1.24) results in an extremely contracted diffusion layer (see Eq. 1.28), favouring a planar diffusion field (see Figure 8). Furthermore, Eq. 1.35 predicts that when D is approximately $10^{-7} \text{ cm}^2 \text{ s}^{-1}$, steady-state conditions can only be achieved with slow sweep rates ($< 5 \text{ mV s}^{-1}$) at extremely small microdisk electrodes ($r_0 < 5 \mu\text{m}$).¹¹ In practice, voltammograms displaying both transient ('peak-shaped') and steady-state ('sigmoidal') characteristics are observed under conditions where a steady-state response would be expected in molecular-solvent based media. This outcome is demonstrated in Figure 11.

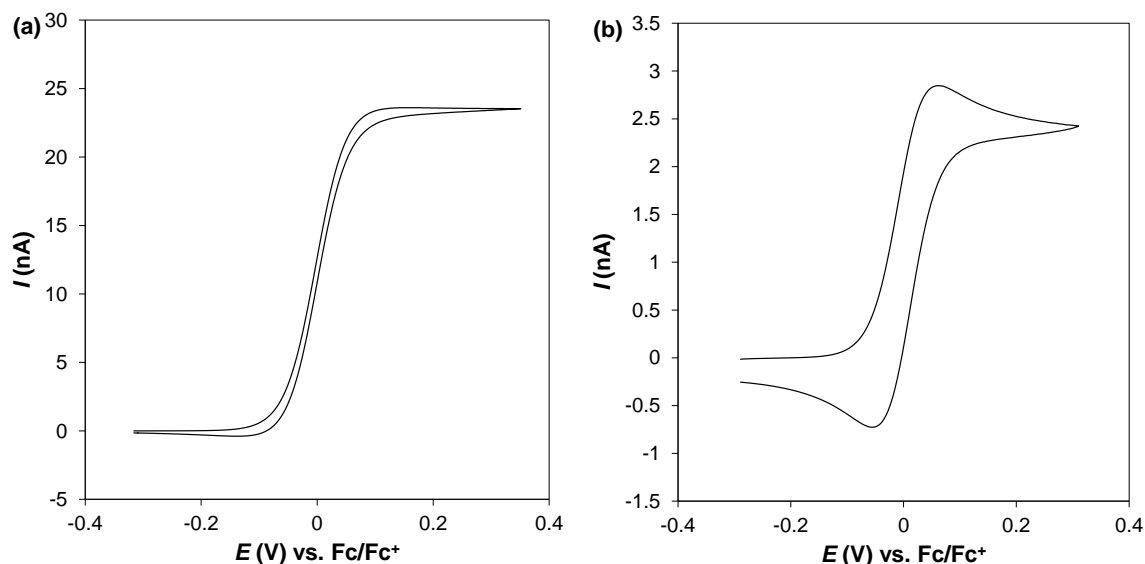


Figure 11. Cyclic voltammograms obtained from the oxidation of ferrocene in (a) acetonitrile + 0.1 M tetrabutylammonium hexafluorophosphate (near steady-state) and (b) $[\text{C}_2\text{mim}][\text{NTf}_2]$ (mixed transient/steady-state) using a 25 μm dia. Pt microdisk electrode with a scan rate of 50 mV s^{-1} .

Unfortunately, in practice it is often found that an impractically small electrode (difficulty in both electrode fabrication and current measurement¹¹³) or slow scan rate would be required to achieve a good approximation to true steady-state measurements, ruling out the use of steady-state microelectrode voltammetry for quantitative analysis in IL media.¹¹⁴ It has also been shown that it is similarly difficult to achieve a true steady-state at a rotating disk electrode in ILs, arising from the difficulty in rotating the electrode at sufficiently high rates under highly-viscous conditions.^{11, 39, 114} Quantitative analysis using the Randles-Sevcik equation (see Eq. 1.34) and the peak currents from a transient cyclic voltammogram is often not feasible in practice, due to the sensitivity of I_p to k_s and R_u .⁶ Finally, in some instances a best-fit approach with numerical simulation is a viable option, although even this method has its limitations, as mechanistic complexities or other uncertainties can make the modelling process difficult.¹¹⁴

In light of the difficulties outlined above, a considerable amount of time was invested into finding a suitable electroanalytical technique to calculate D , n and/or C under highly viscous conditions. Semiintegral/convolution forms of voltammetry were found to be suitable methods for this purpose, as they share a number of advantages with steady-state techniques (*i.e.*, M_L is insensitive to k_s and R_u) without the need to achieve conditions under which spherical diffusion dominates.^{80, 82} Application of these methods for quantitation of D , n and/or C in IL media is the focus of Chapter 3.

1.5 Model Redox Systems

As previously highlighted, in this work the electrode reaction and mass-transport mechanisms associated with a number of ‘model’ redox systems will be investigated in IL media. The ideal ‘model’ redox system should possess the following characteristics:

- Have well-defined and well-understood electrochemistry in conventional (molecular solvent) media, so comparisons can be readily made with the results collected in IL media;
- Be relevant to current energy conversion and storage technologies;
- Have workable physicochemical properties, for example the relevant redox species should be reasonably soluble in IL media.

The first model redox system, and the focus of Chapter 4, is the I^-/I_2 couple, which is technologically relevant due to the role of the I^-/I_3^- couple in DSSCs. The second model redox system, and the focus of Chapter 5, is the H^+/H_2 couple, which plays a crucial role in a wide range of technologically important reactions, for example water electrolysis or PEMFC operation. The electrochemical and mass-transport phenomena associated with the I^-/I_2 (Section 1.5.1) and the H^+/H_2 (Section 1.5.2) redox couples are discussed in detail below.

1.5.1 I⁻/I₂ Couple

Electrochemistry in Conventional Solvents. The I⁻/I₂ redox process has been studied extensively in a range of conventional solvents, most notably water¹¹⁵⁻¹¹⁷ and acetonitrile¹¹⁸⁻¹²³. The heterogeneous electron transfer kinetics of the I⁻/I₂ redox process are strongly dependent upon the identity and state (*i.e.*, cleanliness, microstructure and surface chemistry) of the electrode material. Irrespective of the solvent, platinum is by far the most widely studied electrode material, on which it is well known that halides chemisorb.¹²⁴⁻¹²⁷ On platinum, iodide is oxidized to molecular iodine in an overall one-electron per iodide ion process:



Iodide and iodine combine homogeneously to form the polyhalogen complex anion, triiodide:



The equilibrium (stability) constant of this reaction is highly solvent dependent, ranging from *ca.* 10³ in water¹²⁸ to *ca.* 10⁷ in acetonitrile^{129, 130} and has a strong bearing on the observed iodide oxidation mechanism.¹²⁹ The overall oxidation process shown in Eq. 1.40 may occur in one step, giving rise to a single voltammetric process (as observed in aqueous media^{129, 131-133}) or in two steps (*via* an I₃⁻ intermediate), giving rise to two voltammetric processes (as observed in acetonitrile^{120, 129, 131}):



The potential gap separating the two voltammetric processes is proportional to the magnitude of K_{eq} for the reaction shown in Eq. 1.41.^{129, 131}

As previously noted, platinum is the most commonly employed counter-electrode (cathode) material in current DSSC technology, where it acts as an electrocatalyst for the redox shuttle reaction given in Eq. 1.42. Obviously the high-cost of noble metals is a significant driving force for the development of cheaper counter electrodes, notably carbon-based materials.^{14, 134, 135} In comparison to platinum, the electrochemical behaviour of the Γ^-/I_2 couple has not been extensively explored on carbon electrodes, with a few studies available with pyrolytic carbon electrodes in water^{132, 133} and acetonitrile¹²⁰. Iodide oxidation on pyrolytic carbon is qualitatively similar to that seen on platinum: a single process is observed in aqueous media, corresponding to Eq. 1.40 and two processes are observed in acetonitrile, corresponding to Eqs. 1.42 and 1.43.¹²⁰

Unlike platinum and carbon, which act as a simple electron source or sink (*i.e.*, an inert electrode) during I_2 reduction and Γ^- oxidation respectively, mercury is known to participate directly in the charge transfer process:



Analogous behaviour is also observed with Cl^- and Br^- . In non-aqueous media, when investigated using DC polarography, Γ^- gives rise to two well-defined oxidation processes on a mercury electrode, the first being assigned to the reversible oxidation of mercury to soluble triiodomercurate (Eq. 1.44) and the second to the reversible oxidation of mercury to soluble mercuric iodide (Eq. 1.45).¹³⁶ The limited number of studies available¹³⁷⁻¹³⁹ (all undertaken in ‘conventional’ media) also suggest that the Γ^-/I_2 process on gold is appreciably more complicated than that observed on platinum or carbon. A myriad of reaction pathways are thought to be possible due to significant overlap between the standard potentials for Γ^- and Au oxidation.^{138, 139} Gold-halide complexes of the type $[\text{AuX}_2]^-$ and $[\text{AuX}_4]^-$ (where X^-

= Cl⁻, Br⁻ and I⁻) reportedly form during oxidative polarization of gold electrodes in aqueous halide media.¹³⁷

Mechanistic Studies in Ionic Liquids. Zhang and Zheng¹⁴⁰ investigated the electro-oxidation of iodide at a platinum electrode in [C₄mim][NTf₂]. The authors report I⁻/I₂ electrochemistry analogous to that observed in aprotic molecular solvents such as acetonitrile, with iodide oxidation occurring in two steps *via* a triiodide intermediate, as shown in Eqs. 1.42 and 1.43 respectively. The heterogeneous kinetics of the I⁻/I₃⁻ process (see Eq. 1.42) were found to be sluggish (electrochemically irreversible) relative to the I₃⁻/I₂ process (electrochemically reversible, see Eq. 1.43).

Compton and co-workers¹⁴¹ investigated the electro-oxidation of multiple iodide salts ([C₄mim]I, LiI, NaI, KI, RbI and CsI) at a platinum electrode in [C₄mim][NTf₂].¹⁴¹ As expected, the iodide oxidation process was found to occur in two steps *via* a triiodide intermediate (see Eqs. 1.42 and 1.43), regardless of the identity of the iodide-salt counter-cation. At elevated iodide concentrations (>100 mM), the peak for the I₃⁻/I₂ oxidation process (see Eq. 1.43) became distorted, with a marked ‘crossover’ being evident at extreme concentrations (>7,000 mM), characteristic of a nucleation-growth process. The authors attributed this to the deposition of sparingly soluble I₂ on the platinum electrode surface. The electro-oxidation of iodide (low concentrations) was simulated using the following mechanism:



By treating Eq. 1.47 as a homogeneous process, and setting the parameters K_{dim} , k_{dim} and k_f to be fictitiously large, the forward (oxidative) sweep was simulated. From the simulations, the stability constant of I₃⁻ was estimated to be ~8700.

The same research group have investigated the electro-reduction of molecular iodine in [C₄mim][NTf₂].¹⁴² As expected, the iodine reduction process was found to be the reverse of the iodide oxidation process, occurring *via* a triiodide intermediate (see Eqs. 1.43 and 1.42). The authors also report that I₂ is sparingly soluble in [C₄mim][NTf₂], with a thermodynamic solubility of *ca.* 1.7 mM at room temperature, in agreement with their previous report.¹⁴¹ The I₂/I₃⁻ process was modelled using the following *EC* mechanism:



where I*(ads) is an adsorbed iodine atom. From the simulated data, the authors concluded that Eq. 1.49 is the rate-limiting step and that the equilibrium shown in Eq. 1.50 lies to the left at potentials corresponding to the I⁻/I₂ process, so that the surface coverage of I*(ads) is saturated.

Walsh and co-workers¹⁴³ studied the I⁻/I₃⁻ processes in [C_{*x*}mim][NTf₂] (*x* = 2, 4 or 8). Mirroring the results discussed above, two processes were observed in all of the investigated ILs, which was attributed to the reactions shown in Eqs. 1.42 and 1.43. The I⁻/I₃⁻ process (see Eq. 1.42) was found to possess relatively sluggish heterogeneous kinetics, with the voltammetric peak-to-peak separation (ΔE_p) increasing with scan rate and decreasing at elevated temperatures. By comparison, the I₃⁻/I₂ process was found to be more kinetically facile, with ΔE_p being independent of both scan rate and temperature.

Homogeneous Bond-Exchange. As outlined in Section 1.2.2, the I⁻/I₃⁻ couple is the most commonly employed redox mediator in conventional DSSC electrolytes. ILs have shown promise as replacement electrolytes for this application, however physical mass-transport limitations as a result of their high viscosity remains a challenge. Nevertheless, several research groups^{42-44, 79, 144-147} have reported significantly greater mass-transport of

the Γ/I_3^- redox couple in IL electrolytes than expected, which is often attributed to a rapid exchange process establishing a Grotthuss-like extension of diffusion:



where I_2 is exchanged between Γ^- and I_3^- , displacing them without physical mass-transfer, as shown schematically in Figure 12. According to the proposed mechanism, when in close proximity, Γ^- forms a partial bond with I_3^- which is subsequently strengthened by the exchange-reaction, liberating Γ^- from the other end of the I_3^- chain. This effectively displaces Γ^- and I_3^- by the distances δ_{Γ^-} and $\delta_{I_3^-}$ respectively.¹⁴⁸ In effect, with each successful collision, I_3^- is displaced by the length of approximately one I–I bond (~ 2.9 Å) without having to physically cross that distance.^{46, 149}

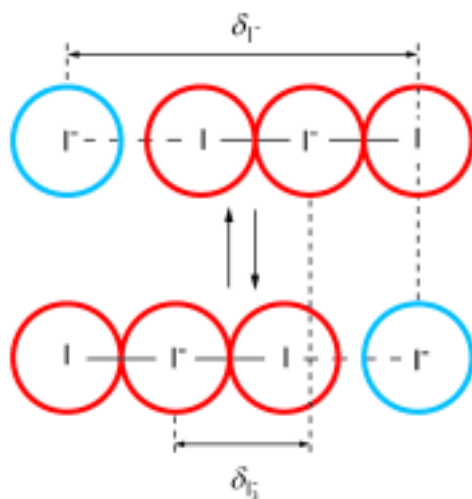


Figure 12. The Grotthuss-type homogeneous bond-exchange mechanism proposed to occur between Γ/I_3^- in IL media. Figure 12 was adapted from Thorsmolle *et al.* (2011).¹⁴⁸

In order for I_2 to be ‘exchanged’ as shown in Figure 12, Γ^- and I_3^- must be within close proximity of one another. In molecular solvents of moderate Γ/I_3^- concentrations (*i.e.*, low to moderate ionic strength), this reaction would be kinetically constrained, since both of the reacting species are negatively charged and would thus give rise to an energetically disadvantageous transition state. The collision of ions of like charge (*i.e.*, Γ/I_3^-) is more

favourable under conditions of high ionic strength due to a phenomenon known as the ‘kinetic salt effect’⁶⁵, making the process shown in Eq. 1.52 more feasible in ILs due to charge screening.^{43, 44, 74, 144} Supporting this hypothesis is the fact that Γ/I_3^- exchange diffusion only makes a significant contribution to mass-transport in aqueous solutions of extremely high ionic strengths (approx. 5 M).¹⁵⁰ The high-ionic strength of ILs therefore offers an alternative route to achieving facile I_3^- transport *via* the Grotthuss-type exchange reaction shown in Eq. 1.52. Elucidation of this phenomenon is of the utmost importance if practical application of ILs as DSSC electrolytes is ever to be realised; key studies are discussed below.

Mass-transport Studies in Ionic Liquids. Studies by Kawano and Watanabe^{42, 79} on the voltammetric behaviour of the Γ/I_3^- couple in $[\text{C}_2\text{mim}][\text{NTf}_2]$ revealed exceptionally fast mass-transport. As shown in Figure 13, the apparent diffusion coefficient increased with the total concentration of Γ and I_3^- , to values that were much higher than could be explained by physical diffusion alone. Shown in Figure 13a, in a single component system (*e.g.*, 1:1 or 10:0), the steady-state limiting current (I_{lim}) increases linearly as a function of concentration, in accordance with Eq. 1.30. In a dual component system however, when $[\Gamma]$ and $[\text{I}_3^-]$ are comparable, I_{lim} displays a non-linear (second-order) concentration dependence:

$$I_{\text{lim}} = 4nFr_0(D_{\text{phys}}C + \frac{1}{6}k_{\text{ex}}\delta_{\text{int}}^2C^2) \quad (1.53)$$

where C is taken to be equal to $1/3[\Gamma] + [\text{I}_3^-]$. Eq. 1.47 was derived by combining Eq. 1.30 with the Dahms-Ruff equation (Eq. 1.27).

Shown in Figure 13b is a plot of D_{app} (calculated using Eq. 1.30) versus concentration ($1/3[\Gamma] + [\text{I}_3^-]$). At low concentrations, D_{app} was found to be comparable in $[\text{C}_2\text{mim}][\text{NTf}_2]$ ($\eta_{\text{neat}} = 27$ cP at 30°C) and the molecular solvent, polyethylene glycol dimethylether (PEGDE, $\eta_{\text{neat}} = 19$ cP at 30°C). Doping the respective solvents with $[\text{C}_2\text{mim}]\text{I} + \text{I}_2$ increases viscosity (*i.e.*, $\eta \propto C$), which, based on the Stokes-Einstein equation, is expected to lead to

a decrease in diffusivity ($D \propto 1/\eta$, see Eq. 1.24). This trend is observed in the PEGDE electrolyte; D_{app} decreases as a function of C at both of the investigated $[I^-]:[I_2]$ ratios. The opposite trend is observed in the $[C_2mim][NTf_2]$ electrolyte; D_{app} increases as a function of C . The authors concluded that this non-Stokesian ‘enhancement’ in mass-transport must arise from a Grotthuss-like exchange process between I^- and I_3^- , facilitated by the high-ionic strength of $[C_2mim][NTf_2]$.

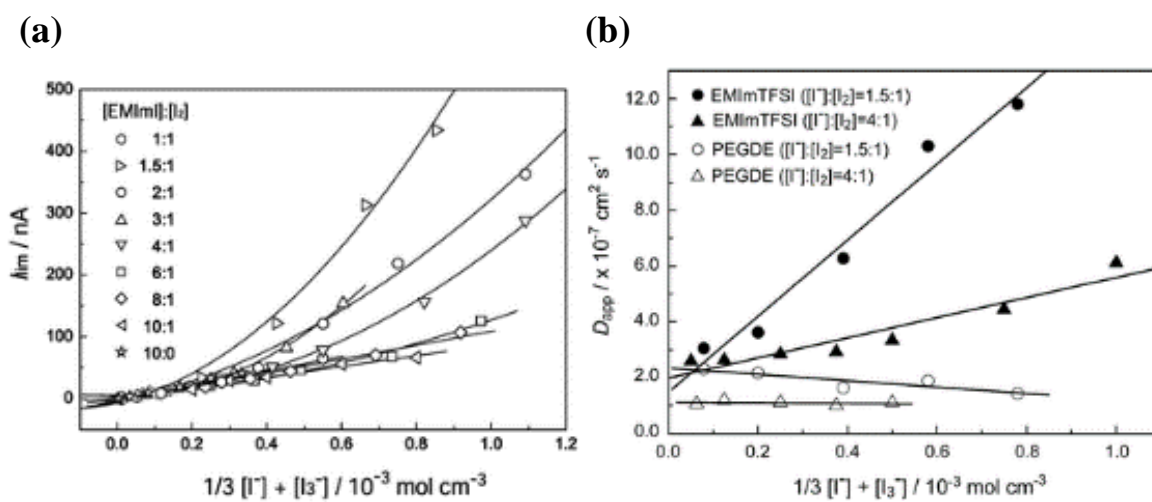


Figure 13. Plots showing the (a) steady-state limiting current (I_{lim}) and (b) apparent diffusion coefficient (D_{app}) of the I^-/I_3^- redox couple as a function of the concentration of redox species ($1/3[I^-] + [I_3^-]$). The molar ratio of $[I^-]:[I_2]$ is indicated on the plots. The experiments shown above were carried out in $[C_2mim][NTf_2]$ or polyethylene glycol dimethylether at a $12 \mu\text{m}$ dia. Pt microdisk electrode with $[C_2mim]I$ as the iodide source. Figure 13(a) and (b) were taken from Kawano and Watanabe (2003)⁷⁹ and (2005)⁴², respectively.

The enhanced effective mass-transport afforded by the homogeneous bond-exchange mechanism between I^- and I_3^- obviously translates to enhanced performance in a DSSC, despite the high viscosity of IL electrolytes.^{13, 42, 44, 79} Indeed, the Watanabe group⁴⁹ have also reported DSSCs employing IL electrolytes with short-circuit currents greater than 80% of that achievable in cells employing conventional organic electrolytes, despite the viscosity of the former electrolytes being greater than 10-fold higher than the latter. The most promising results were achieved with a low-viscosity electrolyte based on $[C_2mim][N(CN)_2]$

($\eta = 21$ cP at 21°C), which highlights the need to balance the Stokesian and non-Stokesian mass-transport processes.⁴⁹

More recently, Gores and co-workers^{43, 44, 74, 144} have investigated the mass-transport of I^-/I_3^- in a variety of imidazolium-based ionic liquids. The concentration of I_3^- was typically fixed ≈ 0.05 M and the concentration of I^- was varied over a large range, achieved by adding a variable mole fraction of highly viscous $[\text{C}_3\text{mim}]\text{I}$ ($\eta = 880$ cP at 25°C). The authors provide strong evidence for an exchange-reaction mediated enhancement in mass-transport, with the increase in viscosity as a result of increasing the mole fraction of $[\text{C}_3\text{mim}]\text{I}$ being several times larger than the observed decrease in $D_{\text{I}_3^-}$, contrary to what is predicted based on the Stokes-Einstein equation. The authors also report that the overall contribution of non-Stokesian transport to total mass-transport decreases with increasing temperature, which was attributed to the breakdown in IL ordering at elevated temperatures.^{44, 144}

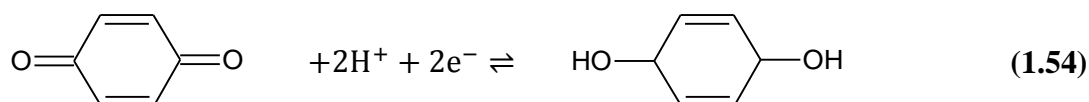
A recent study by Grätzel and co-workers¹⁴⁸ also demonstrated that the conductivity of $[\text{C}_3\text{mim}]\text{I}$ increases significantly upon adding molecular iodine to values beyond which can be explained by a simple decrease in medium viscosity. The order-of-magnitude increase in ionic conductivity was attributed to the enhancement of the mobility of I^-/I_3^- as a result of a Grotthuss-like bond-exchange process. In addition, the authors found that the conductivity of the $[\text{C}_3\text{mim}]\text{I}/\text{I}_2$ mixture increased abruptly when $[\text{I}_2]$ was raised above ~ 4.2 M, which was attributed to the formation of higher polyiodides (*i.e.*, I_5^- , I_7^- etc.). The authors postulate that long-chain polyiodides enable higher packing densities, which reduces the distance between adjacent iodide/polyiodide species (*i.e.*, ‘exchange sites’), and thereby accelerates the homogeneous exchange reaction, leading to enhanced mobility (and increased ionic conductivity).¹⁵¹

Lin and co-workers¹⁵² studied the relative contributions of physical diffusion and exchange diffusion to the mass-transport of I_3^- in $[\text{C}_2\text{mim}][\text{N}(\text{CN})_2]:[\text{C}_3\text{mim}]\text{I}$ electrolytes

(at a fixed $[I_2]$) by varying the ratio of the two constituents. Increasing the volume fraction of the low viscosity, electro-inactive component $[C_2mim][N(CN)_2]$ up to 40% (v/v) in the binary electrolyte system increased D_{app} , which was attributed to accelerated physical (Stokesian) diffusion. Interestingly, further increasing the volume fraction of $[C_2mim][N(CN)_2]$ above 40% (v/v) decreased D_{app} , which was attributed to hindered non-Stokesian (exchange) diffusion. The 40% (v/v) $[C_2mim][N(CN)_2]$ electrolyte therefore offered the best compromise between exchange diffusion and physical diffusion, resulting in the highest apparent diffusion coefficient of I_3^- . These observations translated directly to DSSC performance; the 40% (v/v) $[C_2mim][N(CN)_2]$ electrolyte gave rise to the highest short-circuit current and photo-conversion efficiency of any of the investigated mixtures.

1.5.2 H^+/H_2 Couple

Electrochemistry. Proton (H^+) transfer is an important step in a plethora of (electro)chemical reactions, one example being the reduction of benzoquinone to 1,4-hydroquinone in aqueous media⁶:



The proton reduction reaction (or hydrogen evolution reaction, HER), is of wide technological importance and has therefore been studied extensively at many electrode surfaces in a range of media¹⁵³⁻¹⁵⁵, predominantly aqueous¹⁵⁶⁻¹⁵⁸:



The H^+/H_2 couple also forms the basis of the fundamental reference potential scale in aqueous electrochemistry, the Normal (NHE) or Standard (SHE) Hydrogen Electrode.⁶ Although Eq. 1.55 is conceptually simple, involving the transfer of one electron per proton, it is subject to significant kinetic barriers, and therefore requires a suitable electrode (electrocatalyst) to proceed at an economically viable rate. Indeed, it has been well

established that different metals display vastly different catalytic activities towards proton reduction/hydrogen oxidation, with exchange current densities ranging from approximately 10^{-8} mA cm $^{-2}$ on Pb, a ‘poor’ electrocatalyst; to 100 mA cm $^{-2}$ on Pt, a ‘good’ electrocatalyst.¹⁵⁹

In acidic aqueous media, proton reduction is thought to proceed *via* a combination of the following three elementary reactions^{154, 156, 159}:



where H_{ads} is a chemisorbed hydrogen atom and Eqs. 1.56, 1.57 and 1.58 are known as the Volmer (or discharge), Tafel (or combination) and Heyrovsky (or ion + atom) reactions respectively. Thus, the formation of H_{ads} on the electrode surface (Eq. 1.56) by electron transfer (reduction) is followed either by surface migration and dimerization of H_{ads} (Eq. 1.57) to form H_2 or the direct formation of H_2 from H_{ads} and H^+ (solution) by electron-transfer (Eq. 1.58). The preferred reaction pathway depends on the identity of the metallic electrode and is thought to be governed by whether Eq. 1.56 is sluggish or facile relative to H_{ads} migration across the electrode surface.¹⁵⁴

Mechanistic Studies in Ionic Liquids. Compton and co-workers¹⁶⁰ have investigated the hydrogen oxidation reaction (HOR) in $[\text{C}_2\text{mim}][\text{NTf}_2]$, $[\text{C}_4\text{mim}][\text{NTf}_2]$, $[\text{N}_{6,2,2,2}][\text{NTf}_2]$, $[\text{P}_{14,6,6,6}][\text{NTf}_2]$, $[\text{C}_4\text{mpyr}][\text{NTf}_2]$, $[\text{C}_4\text{mim}][\text{OTf}]$, $[\text{C}_4\text{mim}][\text{BF}_4]$, $[\text{C}_4\text{mim}][\text{PF}_6]$ and $[\text{C}_6\text{mim}]\text{Cl}$. No oxidation process was observable on gold in any of the ILs, indicating that this metal is electrocatalytically inactive for the HOR. On platinum, a broad (*i.e.*, large ΔE_p), chemically reversible process was observed in the $[\text{NTf}_2]^-$ and $[\text{OTf}]^-$ ILs, which the authors attributed to the following process:



where S signifies the IL anion. The HOR is inhibited at oxidative potentials above ~1.0 V vs. Ag pseudo-reference electrode (PRE), which the authors attributed to blocking of the catalytically active sites on the platinum electrode surface by a platinum-oxide layer, formed from the oxidation of residual water in the IL. Interestingly, if the electrode is ‘preanodized’ at strongly oxidizing potentials (*i.e.*, 2.0 V vs. Ag PRE), the kinetics of the HOR are greatly improved in the potential range where the surface oxide is not present (0.1 – 1.0 V vs. Ag PRE), presumably due to the formation of a catalytically active ‘pristine’ platinum surface after oxide layer formation/dissolution. This hypothesis is supported by the results from an XPS study performed by Walsh and co-workers.¹⁶¹ In [C₄mim][BF₄], [C₄mim][PF₆] and [C₆mim]Cl, the HOR is only partially chemically reversible, which the authors attributed to instability of the protonated anion (see Eq. 1.59). In the case of [PF₆]⁻ and [BF₄]⁻, it is thought that the anion undergoes acid-catalyzed dissociation (decomposition) on the voltammetric timescale:



In the case of Cl⁻, it is thought that HCl (formed from hydrogen oxidation, see Eq. 1.59) reacts to form stable H[Cl₂]⁻ as highlighted in a first principles simulation study by Del Popolo and co-workers.¹⁶²

In a follow-up publication, the Compton group¹⁶³ investigated the HOR at an activated platinum electrode in an expanded range of ILs: [C₂mim][NTf₂], [C₄mim][NTf₂], [N_{6,2,2,2}][NTf₂], [P_{14,6,6,6}][NTf₂], [C₄mim][OTf], [C₄mim][BF₄], [C₄mim][PF₆], [C₄mim][NO₃], [C₆mim]Cl and [C₆mim][FAP]. As was the case in the previous study, chemically reversible and electrochemically quasi-reversible voltammetry was observed in [C₂mim][NTf₂], [C₄mim][NTf₂], [N_{6,2,2,2}][NTf₂], [P_{14,6,6,6}][NTf₂], [C₄mim][OTf] and [C₆mim][FAP]. Again, the HOR only possesses partial chemical reversibility in

[C₄mim][BF₄], [C₄mim][PF₆], [C₄mim][NO₃] and [C₆mim]Cl, attributable to protonated anion instability. It is thought that H[NO₃]₂⁻ is formed following hydrogen oxidation in [C₄mim][NO₃], analogous to the chloride case. In addition hydrogen gas was found to be sparingly soluble (*ca.* 3 to 10 mM) in all of the investigated ILs. Finally, the formal potential of the H⁺/H₂ process (calibrated against a cobaltocenium/cobaltocene internal reference) was found to depend strongly on the identity of the IL anion, increasing in the order [OTf]⁻ < [NTf₂]⁻ < [PF₆]⁻.

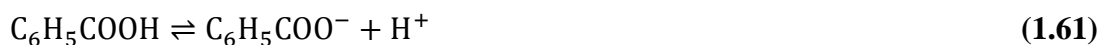
The Compton group¹⁶⁴ have also investigated the proton reduction process from H[NTf₂] and HCl in [C₄mim][NTf₂]. A chemically reversible proton reduction process is observed on platinum, which is thought to proceed *via* the combination of reactions outlined in Eqs. 1.56 to 1.58. On gold, proton reduction occurs irreversibly at potentials negative of those on platinum and on glassy carbon (GC), an irreversible, broad reduction process is observed just prior to solvent breakdown. These results are in accordance with the relative hydrogen overpotentials of the electrode materials: GC >> Au > Pt. On platinum, proton reduction from HCl is chemically reversible, occurring at potentials negative of the H[NTf₂]/H₂ process, in accordance with the relative acidities of HCl and H[NTf₂] (*vide infra*). Additional peaks are also observed at positive potentials, which correspond to the oxidation of Cl⁻ to Cl₃⁻/Cl₂. The authors also postulate that H[Cl₂]⁻ forms as an intermediate during proton reduction, at potentials where the concentrations of both HCl and Cl⁻ are significant.

In later studies, the Compton group^{154, 165} investigated electrochemical proton reduction (from H[NTf₂] as the proton source) on a range of metallic electrodes (Au, Mo, Ni, Ti and Pt) in [C₂mim][NTf₂]. Irreversible proton reduction was observed on all of the metal surfaces except platinum, with no H₂ process being observed on the reverse cyclic voltammetric sweep. The apparent charge-transfer coefficient (α_{app}) was found to be ≤ 0.5 on all metal surfaces, indicating that the Volmer reaction (Eq. 1.56) is the rate determining

step in all cases. Finally, the heterogeneous kinetics of the HER (estimated by numerical simulation) was found to be strongly dependent on the identity of the metallic electrode, with the electrocatalytic trend being different ($\text{Pt} > \text{Mo} > \text{Au} > \text{Ni} > \text{Ti}$) to that observed in aqueous media ($\text{Pt} > \text{Ni} > \text{Au} > \text{Mo} > \text{Ti}$).

In a follow-up study¹⁵⁵, the same authors investigated electrochemical proton reduction on platinum in $[\text{C}_2\text{mim}][\text{NTf}_2]$, $[\text{C}_4\text{mim}][\text{NTf}_2]$, $[\text{C}_4\text{mpyr}][\text{NTf}_2]$, $[\text{C}_4\text{dmim}][\text{NTf}_2]$, $[\text{C}_4\text{mim}][\text{OTf}]$ and $[\text{C}_4\text{mim}][\text{BF}_4]$. α_{app} was found to be ≤ 0.55 in all of the investigated ILs, indicating once again that the Volmer reaction (Eq. 1.56) is the rate determining step in all instances. The heterogeneous rate constant (estimated by numerical simulation) was found to be an order of magnitude lower in the $[\text{BF}_4]^-$ IL compared to the $[\text{NTf}_2]^-$ and $[\text{OTf}]^-$ ILs. In addition, $E^0(\text{H}^+/\text{H}_2)$ was found to be essentially independent of the identity of the IL cation and strongly dependent upon the identity of the IL anion (*vide infra*), increasing in the order $[\text{BF}_4]^- < [\text{OTf}]^- < [\text{NTf}_2]^-$. Finally, by measuring proton diffusivity in each of the ILs, it was found that proton transport is Stokesian ($D \propto 1/\eta$, see Eq. 1.24) in AIL media.

Compton and co-workers¹⁶⁶⁻¹⁶⁸ have also investigated the proton reduction process from benzoic acid (BZA) on a platinum electrode in $[\text{C}_2\text{mim}][\text{NTf}_2]$, $[\text{C}_4\text{mim}][\text{NTf}_2]$, $[\text{C}_4\text{mpyr}][\text{NTf}_2]$, $[\text{C}_4\text{mim}][\text{OTf}]$, $[\text{C}_4\text{mim}][\text{BF}_4]$, $[\text{C}_4\text{mim}][\text{NO}_3]$ and $[\text{C}_4\text{mim}][\text{PF}_6]$. Proton reduction from BZA occurred at potentials negative of the $\text{H}^+_{\text{solvated}}/\text{H}_2$ process, and is thought to proceed *via* a generic *CE* mechanism:



where the electron transfer step (*E*) is preceded by a fast chemical (dissociation) step (*C*). A reductive pre-peak was observed prior to the main reduction peak in all of the investigated ILs, which was assigned to the formation of adsorbed $\text{H}\bullet$ on the platinum electrode surface.

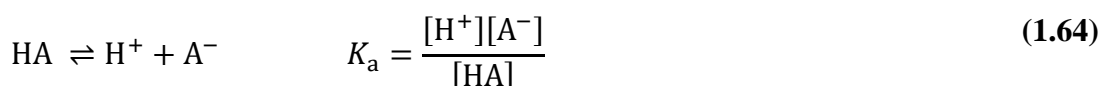
The potential region in which proton reduction from BZA occurs was also found to be dependent on the identity of the IL anion, consistent with their previous studies.

Doherty and co-workers¹⁶⁹ investigated proton reduction from a range of protonated amines (pyridine; 3-picoline; 2,6-lutidine; 2,4,6-collidine and triethylamine) at a platinum electrode in [C₄mim][NTf₂]. In all cases, proton reduction from the protonated amines (BH⁺) was reported to be a quasi-reversible process:

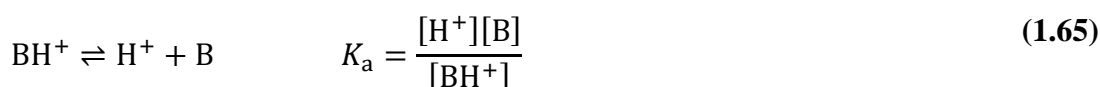


where B is a general base (amine). In addition, the authors applied the Nernst Equation (see Eq. 1.18) to show that the potential at which the BH⁺/H₂ process occurs relative to the H⁺_{solvated}/H₂ process is proportional to the pK_a of BH⁺. The relative strength of the bases (estimated using cyclic voltammetry, *vide infra*) was found to be the same as that previously reported in molecular solvents: pyridine ≈ 3-picoline < 2,6-lutidine < 2,4,6-collidine ≈ triethylamine.

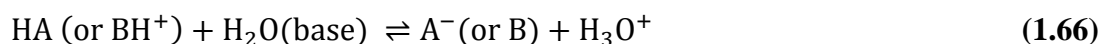
Equilibrium Acidity (pK_a). The acid dissociation constant (K_a) of a Brønsted acid, HA, formally defined as follows, is a quantitative measure of acid strength in solution:



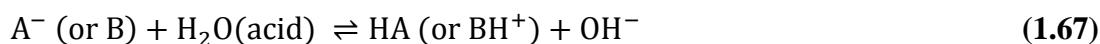
Although the acid is taken to be a neutral species (HA) in Eq. 1.64, the expression for K_a is equally valid for a cationic acid species, BH⁺ (*i.e.*, a protonated neutral base, B):



Brønsted acidity/basicity is a well-established concept in aqueous media¹⁷⁰, where water, an amphoteric species, can act as a Brønsted base and accept a proton:



or as a Brønsted acid and donate a proton:



From Eq. 1.66, it is clear that the hydronium ion (also known as a hydrated/solvated proton), H_3O^+ , which has a pK_a of -1.74 (where $pK_a = -\log_{10}K_a$), is the strongest acid that can exist in aqueous media. In other words, the process shown in Eq. 1.66 effectively ‘levels’ the acidity of all strong acids ($pK_a < -1.74$) in aqueous media and is the origin of the aqueous pK_a scale.^{169, 171}

Many organic compounds contain acidic and/or basic functional groups that dictate their physical, chemical and biological properties. Indeed, bond transformations in solution frequently involve the cleavage or formation of ‘R–H’ bonds. As described above, pK_a describes the free energy change of ‘R–H’ bond heterolysis, making it a critically important thermodynamic parameter in synthetic chemistry and related fields.¹⁷²⁻¹⁷⁴ Equilibrium acidities (pK_a) are media-dependent, being dictated by the ability of the solvent to solvate each of the species outlined in Eqs. 1.64 (*i.e.*, HA, A^- and H^+) or 1.65 (*i.e.*, BH^+ , B and H^+). It follows that solvent acidity/basicity, dielectric properties and ability to donate/accept hydrogen bonds can all influence the pK_a of an acid in solution.^{174, 175} Although pK_a data is most readily available in water^{176, 177}, pK_a scales have been established in a range of non-aqueous solvents, including acetonitrile¹⁷⁸, dimethylsulfoxide^{174, 179, 180} and 1,2-dichloroethane¹⁷⁸. A variety of methods¹⁸¹ are employed to quantify pK_a in conventional media, including potentiometry¹⁸², spectrophotometry^{174, 183} and voltammetry^{175, 179, 180}.

The protons released from the dissociation of a Brønsted acid in IL media must associate with (or be ‘solvated’ by) the most basic component of the IL, most commonly the anion (A_{IL}^-):



where HA_{IL} is the strongest acid that may exist in a given IL. HA_{IL} effectively levels the acidity of strong acids in IL media, comparable to H_3O^+ in aqueous media. In other words,

HA_{IL} is the origin of the $\text{p}K_{\text{a}}$ scale in IL media and for this reason $\text{p}K_{\text{a}}$ data are not directly comparable between ILs with different constituent anions.^{169, 172, 173}

At this point in time, absolute $\text{p}K_{\text{a}}$ data for weak acids in IL media is scarce, with only a few key studies available.^{169, 172, 173} Cheng *et al.*^{172, 173} have previously established the equilibrium acidity of 18 carbon acids¹⁷² and 15 substituted benzoic acids¹⁷³ in $[\text{C}_4\text{mim}][\text{OTf}]$, $[\text{C}_4\text{mim}][\text{NTf}_2]$, $[\text{C}_4\text{mpyr}][\text{NTf}_2]$ and $[\text{C}_4\text{dmim}][\text{NTf}_2]$ using a spectrophotometric (overlapping indicator) method. After carefully calibrating for intermolecular hydrogen bonding interactions between the oxy-acids and oxyanions (*i.e.*, anionic homoassociation), the authors found that the $\text{p}K_{\text{a}}$ (IL) data correlated linearly with corresponding $\text{p}K_{\text{a}}$ (DMSO) and $\text{p}K_{\text{a}}$ (GP) data (where GP signifies ‘gas phase’, determined using mass spectrometry¹⁸⁴). In addition, the identity of both the IL anion and, to a lesser extent, cation was found to influence the $\text{p}K_{\text{a}}$ of a given acid, with the effect being more prominent for the benzoic acids than for the carbon acids.

$\text{p}K_{\text{a}}$ can be conveniently calculated using electrochemical methods such as cyclic voltammetry from the following relationship^{54, 149, 154}:

$$\text{p}K_{\text{a}} = F[E^{0'}(\text{H}^+/\text{H}_2) - E^{0'}(\text{HA}/\text{H}_2)]/(2.303RT) \quad (1.69)$$

where H^+ is taken to be a ‘solvated’ proton, equivalent to HA_{IL} in the present context and $E^{0'}(\text{HA}/\text{H}_2)$ is the formal potential for the following process:



Indeed, this method was used by Doherty and co-workers¹⁶⁹ to estimate to $\text{p}K_{\text{a}}$ of protonated pyridine ($[\text{PyrH}]^+$) in $[\text{C}_4\text{mim}][\text{NTf}_2]$, $[\text{C}_4\text{mpyr}][\text{NTf}_2]$, $[\text{C}_4\text{mim}][\text{BF}_4]$ and $[\text{C}_2\text{mim}][\text{C}_2\text{F}_5\text{BF}_3]$. The strength of $[\text{PyrH}]^+$ (estimated directly from the cyclic voltammogram) was found to depend strongly on the constituent anion of the IL, although, as previously discussed, direct comparison between ILs with different constituent anions is not thermodynamically rigorous.

Protic Ionic Liquids. As addressed in Section 1.1.2, PILs are formed through the transfer of a proton from a Brønsted acid to a Brønsted base (see Eq. 1.1). The extent of proton transfer (*i.e.*, how strongly a proton will be transferred from the acid to a given base) is governed by the relative pK_a of the acid and base (*i.e.*, ΔpK_a), and has a strong bearing on the physicochemical properties of the resulting PIL. Since pK_a data is scarcely available in IL media, the pK_a values measured in dilute aqueous media are often used to predict the extent of proton transfer.^{28, 32}

Angell and co-workers^{26, 28} have investigated the physicochemical properties of a range of PILs, and correlated the observed trends with ΔpK_a (aq). The authors report that boiling point excess (*i.e.*, the excess over the value expected from simple additivity of the boiling points of acid and base components) and ionicity (a measure of ion dissociation) of a PIL is positively correlated to ΔpK_a (aq). PILs with ΔpK_a (aq) values greater than ~ 10 typically possess AIL-like properties, with high ionicities and low vapour pressures. In addition, the authors note that when ΔpK_a (aq) > 10 , PIL decomposition typically precedes boiling (*i.e.*, the PIL is non-distillable).

The Angell group²⁵ also have investigated the HER and HOR in the following H₂-saturated PILs: [N_{H,1,2,2}][NTf₂], [N_{H,1,2,2}][AlCl₄], [N_{H,1,2,2}][OTf], [N_{H,2,2,2}][OTf], [N_{H,1,1,2}][OTf], [N_{H,H,H,2}][NO₃], [PyrH][CH₃COO], [N_{H,2,2,2}][CH₃SO₃], [N_{H,1,2,2}][CH₃SO₃] and [α -MePyrH][OTf]. Starting from the equilibrium potential, proton reduction (from BH⁺) occurs when sweeping to negative potentials:



and hydrogen oxidation (supported by protonation of A⁻) occurs when sweeping to positive potentials:



The potential gap between these two processes is proportional to the differences in the proton free energy between the Brønsted couples HA/A⁻ and BH⁺/B and correlates well with $\Delta pK_a(\text{aq})$.

Proton Conduction. Proton transport (conduction) is fundamental step in many biologically and technologically important processes^{53, 185}, including photosynthesis⁵³, electrochemical CO₂ fixation¹⁸⁶, methanol oxidation¹⁸⁷ and water (photo)electrolysis¹⁸⁸. Proton conduction in aqueous solution occurs by a combination of a vehicle mechanism (*i.e.*, physical diffusion of H₃O⁺) and the Grotthuss mechanism (*i.e.*, proton exchange between H₃O⁺ and H₂O).^{53, 75, 189} These two processes are illustrated in Figure 14. As previously discussed, vehicular transport *via* the physical movement of the H₃O⁺ ion only contributes ~20% to the total mobility of H⁺ in aqueous media. In other words, proton diffusivity in aqueous media ($8.0 \times 10^{-5} \text{ cm}^2 \text{ s}^{-1}$)¹⁹⁰ is five times larger than what would be expected based on the dimensions of the hydronium ion (H₃O⁺).^{75, 191} Facile proton conduction is a key consideration when choosing the electrolyte for a fuel cell (*i.e.*, a PEMFC), as it influences the ultimate speed/efficiency at which the device can operate. Key studies on proton conduction in ILs are summarized below.

Watanabe and co-workers⁴¹ have studied the properties of a range of neutral salts formed between organic amines and H[NTf₂] for potential application as anhydrous proton conductors at elevated temperatures in fuel cells. Of the compounds studied, only a select few were found to be PILs, of which, the [ImH][NTf₂] neutral salt (1:1 ratio, $T_m = 73.0^\circ\text{C}$) was characterized using cyclic voltammetry at a temperature of 130°C. [ImH][NTf₂] was found to support molecular hydrogen oxidation/proton reduction at platinum under a H₂ atmosphere:



The electrolyte was also found to support oxygen reduction (albeit at a large overpotential) upon switching to an O₂ atmosphere:



Preliminary results employing this electrolyte in a crude H₂/O₂ fuel cell also were promising.

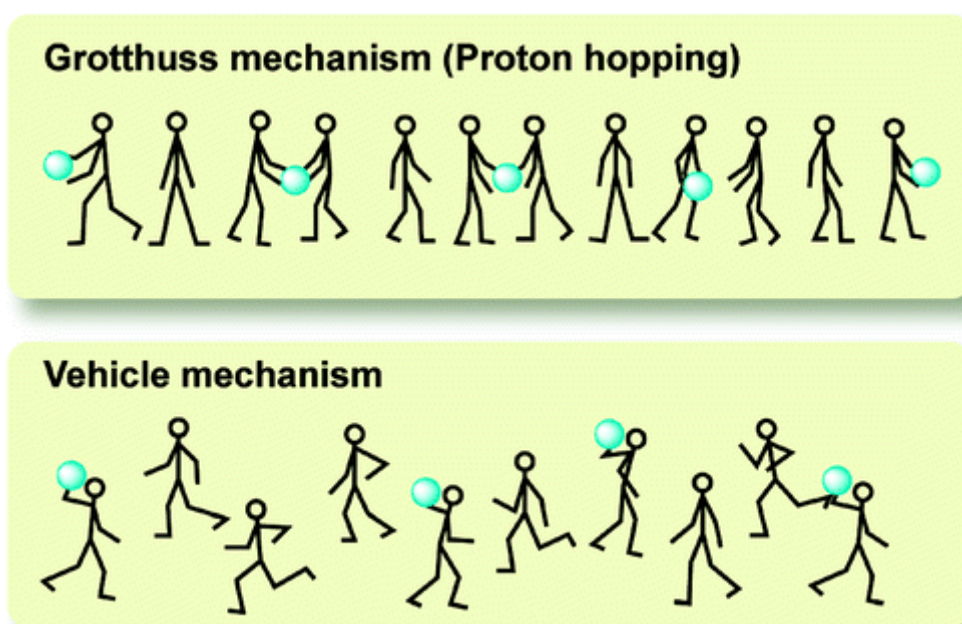


Figure 14. Illustration of proton transport in acidic aqueous solution. *Top:* Grotthuss mechanism, where protons ‘hop’ *via* a network of hydrogen bonds. *Bottom:* Vehicle mechanism, where proton movement occurs with the aid of a moving ‘vehicle’ (*i.e.*, H₂O). Figure 14 was taken from Ueki and Watanabe (2008)¹⁹².

In a later study⁴⁰, proton transport was investigated in non-stoichiometric mixtures of Im and H[N Tf₂]. In stoichiometric (*i.e.*, [HA] = [B]) or acid rich (*i.e.*, [HA] > [B]) mixtures, the diffusivity of the mobile proton (calculated using NMR) is equal to that of the base (Im), suggesting that proton conduction occurs exclusively *via* a vehicular-type mechanism as [ImH]⁺. On the other hand, in base-rich (*i.e.*, [HA] < [B]) mixtures, the mobile proton possesses a greater diffusivity than that of the base, suggesting that proton transport is enhanced by a Grotthuss-type mechanism. The authors suggested that rapid proton exchange occurs between [ImH]⁺ and the free basic site on excess (*i.e.*, unprotonated) Im.

The base-rich mixtures were also found to support H^+ reduction/ H_2 oxidation and O_2 reduction on a platinum electrode at elevated temperatures, which once again demonstrates the promise of this system for application as an electrolyte in fuel cells under non-humidifying conditions. A similar set of observations were made by the same group¹⁹³ when investigating mixtures of $H[NTf_2]$ and benzimidazole (PhIm) at various molar ratios. Compared to the Im + $H[NTf_2]$ mixtures, the PhIm + $H[NTf_2]$ mixtures possessed superior thermal stabilities and performed better under fuel cell polarization conditions.

Since then, a comprehensive study characterizing the thermal properties, ionic conductivity and oxygen reduction overpotential of more than seventy stoichiometric PILs has been carried out by the Watanabe group.⁵⁵ The acids were oxyacids or imides and the bases were imidazole/piperidine/tertiary amine based. Of all of the PILs investigated, $[N_{H,1,2,2}][OTf]$ had the most promising properties for application as a fuel cell electrolyte, with a low melting point ($-13.1^\circ C$), high thermal stability ($360^\circ C$) and reasonably high ionic conductivity at $120^\circ C$ (43.3 mS cm^{-1}). Self-diffusion studies by NMR revealed that the dissociated active proton from $H[OTf]$ is predominantly conducted *via* a vehicular mechanism as $[N_{H,1,2,2}]^+$ (*i.e.*, there was no Grotthuss-like mechanism). $[N_{H,1,2,2}][OTf]$ was also found to support H^+ reduction/ H_2 oxidation and O_2 reduction on a platinum electrode (at relatively low overpotentials) under non-humidifying conditions. When tested in a crude fuel cell at $150^\circ C$ under polarizing conditions, $[N_{H,1,2,2}][OTf]$ was found to give rise to a high OCP ($> 1 \text{ V}$ for at least 300 hours) and was able to sustain the highest currents of any of the tested systems.

Angell and co-workers^{23, 25-27, 194} have prepared and characterized the physicochemical properties of a diverse range of PILs. They have reported PILs with ionic conductivities comparable to aqueous media²⁷, which is usually attributed to high ionic dissociation (*i.e.*, high ionicity) and mobility (*i.e.*, low viscosity) rather than a Grotthuss-type mechanism, although in certain cases it is thought that a proton hopping may make a

non-negligible contribution to proton transport. For example, in a recent study¹⁹⁵, the Angell group characterized the PILs formed from the neutralization reaction between decahydroisoquinoline (DHiQ) and a range of Brønsted acids. While most DHiQ-acid combinations produced either ‘poor’ (*i.e.*, low ionicity) or ‘good’ (*i.e.*, high ionicity) PILs, the $[\text{HSO}_4]^-$ salt displayed ‘superionic’ character, which was attributed to a Grotthuss-like proton exchange mechanism facilitated by the extended hydrogen bond network that is set-up by the anion.

Ohno and co-workers¹⁹⁶ have prepared and characterized the electrochemical and thermal properties of a range of proton conducting ILs with an alkyylimidazolium cation ($[\text{C}_2\text{mim}]^+$, $[\text{C}_1\text{imH}]^+$ or $[\text{C}_2\text{imH}]^+$) and a multivalent anion that itself can dissociate to release a proton ($[\text{HSO}_4]^-$, $[\text{HPO}_3]^-$, $[\text{HPO}_4]^-$ or $[\text{H}_3\text{P}_2\text{O}_7]^-$). The $[\text{HSO}_4]^-$ ILs displayed superior thermal stability and ionic conductivity compared to any of the phosphate derivatives. Within the group of $[\text{HSO}_4]^-$ ILs, conductivity increased in the order $[\text{C}_2\text{imH}]^+ \ll [\text{C}_2\text{mim}]^+ < [\text{C}_1\text{imH}]^+$. The temperature dependence of the ionic conductivities of the $[\text{C}_2\text{mim}]^+$ salts strongly suggests that proton conduction occurs *via* a vehicular mechanism (associated with the anion) and not by a Grotthuss-type mechanism when the cation contains no dissociable protons (*i.e.*, is aprotic).

More recently, Lemordant and co-workers¹⁹⁷ investigated the ionic conductivity, viscosity and proton conduction properties of two PILs: $[\text{PyrH}][\text{CF}_3\text{COO}]$ and $[\text{PyrH}][\text{HSO}_4]$. In both PILs, the self-diffusion coefficient of the mobile proton was found to be much greater than that of either the cation or the anion, suggesting that proton conduction occurs *via* a Grotthuss-type mechanism. The diffusivity of the mobile proton relative to the cation was found to be approximately five-fold higher in $[\text{PyrH}][\text{HSO}_4]$ compared to only two-fold higher in $[\text{PyrH}][\text{CF}_3\text{COO}]$. This explains why $[\text{PyrH}][\text{HSO}_4]$ and $[\text{PyrH}][\text{CF}_3\text{COO}]$ possess similar ionic conductivities, despite the viscosity of the former (187.6 cP at 25°C) being approximately seven-fold higher (25.7 cP at 25°C) than the

latter. The comparatively greater ‘enhancement’ in proton conductivity in [PyrH][HSO₄] is thought to be due to the dual Brønsted acidic/basic nature of [HSO₄]⁻. In addition, the uptake of water into the PILs further enhanced proton mobility, consistent with a Grotthuss-type transport mechanism.

In a recent publication, Sanchez and co-workers¹⁹⁸ investigated the physicochemical properties of more than twenty proton conducting ILs derived from monoamines or half-neutralized diamines in combination with H[OTf]. The viscosities of the PILs derived from the half-neutralized diamines were higher than those derived from the monoamines, although the ionic conductivities were comparable. In the PILs derived from monoamines, the proton self-diffusion coefficient is equal to that of the monoamine, indicating that proton transport occurs exclusively by a vehicular mechanism. By contrast, in the PILs derived from the half-neutralized diamines, the proton self-diffusion coefficient is higher than that of the parent diamine, indicating that an additional mechanism (*i.e.* a Grotthuss-type mechanism) contributes to proton transport (consistent with the trend in ionic conductivity). Interestingly, at elevated temperatures, when water is introduced into the monoamine salt, [N_{H,2,2,2}][OTf], proton diffusivity drastically increases, being intermediate between that of water and the parent amine, suggesting that proton transport is able to occur *via* a mixed Grotthuss-vehicular mechanism.

1.6 Research Objectives

- To develop electroanalytical methodology which is suitable for quantifying the parameters associated with an electrochemical system (*i.e.*, diffusivity, stoichiometric number of electrons and/or bulk concentration) under highly viscous conditions.
- To study the fundamentals of mass-transport in ionic liquids by quantifying the diffusivity of a number of ‘model’ redox active species.
- To investigate the impact that the ionic environment of ionic liquids has on the electrode reaction mechanisms of the investigated redox systems by drawing comparisons with conventional electrolyte media.
- To gain an insight into how the physicochemical properties and intermolecular ordering of the ionic liquid influences fundamental processes such as heterogeneous charge transfer and mass-transport.

References

- (1) Scrosati, B.; Garche, J., Lithium Batteries: Status, Prospects and Future. *J. Power Sources* **2010**, *195*, 2419-2430.
- (2) Soloveichik, G. L., Battery Technologies for Large-Scale Stationary Energy Storage. In *Annual Review of Chemical and Biomolecular Engineering, Vol 2*, Prausnitz, J. M., Ed. Annual Reviews: Palo Alto, 2011; Vol. 2, p 503-527.
- (3) Ellis, B. L.; Lee, K. T.; Nazar, L. F., Positive Electrode Materials for Li-Ion and Li-Batteries. *Chem. Mat.* **2010**, *22*, 691-714.
- (4) MacFarlane, D. R.; Tachikawa, N.; Forsyth, M.; Pringle, J. M.; Howlett, P. C.; Elliott, G. D.; Davis, J. H.; Watanabe, M.; Simon, P.; Angell, C. A., Energy Applications of Ionic Liquids. *Energy Environ. Sci.* **2014**, *7*, 232-250.
- (5) Linden, D.; Reddy, T. B., *Handbook of Batteries*. 3rd ed.; McGraw-Hill: New York, 2002.
- (6) Bard, A. J.; Faulkner, L. R., *Electrochemical Methods : Fundamentals and Applications*. 2nd ed.; Wiley: New York, 2001.
- (7) Wilkes, J. S., A Short History of Ionic Liquids - from Molten Salts to Neoteric Solvents. *Green Chem.* **2002**, *4*, 73-80.
- (8) MacFarlane, D. R.; Seddon, K. R., Ionic Liquids - Progress on the Fundamental Issues. *Aust. J. Chem.* **2007**, *60*, 3-5.
- (9) Armand, M.; Endres, F.; MacFarlane, D. R.; Ohno, H.; Scrosati, B., Ionic-liquid materials for the electrochemical challenges of the future. *Nat Mater* **2009**, *8*, 621-629.
- (10) Buzzeo, M. C.; Evans, R. G.; Compton, R. G., Non-haloaluminate Room-Temperature Ionic Liquids in Electrochemistry - a Review. *ChemPhysChem* **2004**, *5*, 1106-1120.
- (11) Barrosse-Antle, L. E.; Bond, A. M.; Compton, R. G.; O'Mahony, A. M.; Rogers, E. I.; Silvester, D. S., Voltammetry in Room Temperature Ionic Liquids: Comparisons and Contrasts with Conventional Electrochemical Solvents. *Chem.-Asian J.* **2010**, *5*, 202-230.
- (12) Galinski, M.; Lewandowski, A.; Stepniak, I., Ionic Liquids as Electrolytes. *Electrochim. Acta* **2006**, *51*, 5567-5580.

(13) Papageorgiou, N.; Athanassov, Y.; Armand, M.; Bonhote, P.; Pettersson, H.; Azam, A.; Grätzel, M., The Performance and Stability of Ambient Temperature Molten Salts for Solar Cell Applications. *J. Electrochem. Soc.* **1996**, *143*, 3099-3108.

(14) Hagfeldt, A.; Boschloo, G.; Sun, L. C.; Kloo, L.; Pettersson, H., Dye-Sensitized Solar Cells. *Chem. Rev.* **2010**, *110*, 6595-6663.

(15) Howlett, P. C.; MacFarlane, D. R.; Hollenkamp, A. F., High Lithium Metal Cycling Efficiency in a Room-Temperature Ionic Liquid. *Electrochem. Solid State Lett.* **2004**, *7*, A97-A101.

(16) de Souza, R. F.; Padilha, J. C.; Goncalves, R. S.; Dupont, J., Room Temperature Dialkylimidazolium Ionic Liquid-Based Fuel Cells. *Electrochem. Commun.* **2003**, *5*, 728-731.

(17) Balducci, A.; Dugas, R.; Taberna, P. L.; Simon, P.; Plee, D.; Mastragostino, M.; Passerini, S., High Temperature Carbon-Carbon Supercapacitor Using Ionic Liquid as Electrolyte. *J. Power Sources* **2007**, *165*, 922-927.

(18) Dean, P. M.; Pringle, J. M.; MacFarlane, D. R., Structural Analysis of Low Melting Organic Salts: Perspectives on Ionic Liquids. *Phys. Chem. Chem. Phys.* **2010**, *12*, 9144-9153.

(19) Hurley, F. H.; Wier, T. P., The Electrodeposition of Aluminum from Nonaqueous Solutions at Room Temperature. *J. Electrochem. Soc.* **1951**, *98*, 207-212.

(20) Li, Q. F.; Bjerrum, N. J., Aluminum as Anode for Energy Storage and Conversion: a Review. *J. Power Sources* **2002**, *110*, 1-10.

(21) Huddleston, J. G.; Visser, A. E.; Reichert, W. M.; Willauer, H. D.; Broker, G. A.; Rogers, R. D., Characterization and Comparison of Hydrophilic and Hydrophobic Room Temperature Ionic Liquids Incorporating the Imidazolium Cation. *Green Chem.* **2001**, *3*, 156-164.

(22) Greaves, T. L.; Drummond, C. J., Protic Ionic Liquids: Properties and Applications. *Chem. Rev.* **2008**, *108*, 206-237.

(23) Angell, C. A.; Ansari, Y.; Zhao, Z. F., Ionic Liquids: Past, Present and Future. *Faraday Discuss.* **2012**, *154*, 9-27.

(24) Fericola, A.; Scrosati, B.; Ohno, H., Potentialities of Ionic Liquids as New Electrolyte Media in Advanced Electrochemical Devices. *Ionics* **2006**, *12*, 95-102.

-
- (25) Bautista-Martinez, J. A.; Tang, L.; Belieres, J. P.; Zeller, R.; Angell, C. A.; Friesen, C., Hydrogen Redox in Protic Ionic Liquids and a Direct Measurement of Proton Thermodynamics. *J. Phys. Chem. C* **2009**, *113*, 12586-12593.
- (26) Belieres, J.-P.; Angell, C. A., Protic Ionic Liquids: Preparation, Characterization, and Proton Free Energy Level Representation. *J. Phys. Chem. B* **2007**, *111*, 4926-4937.
- (27) Xu, W.; Angell, C. A., Solvent-Free Electrolytes with Aqueous Solution-Like Conductivities. *Science* **2003**, *302*, 422-425.
- (28) Yoshizawa, M.; Xu, W.; Angell, C. A., Ionic Liquids by Proton Transfer: Vapor Pressure, Conductivity, and the Relevance of Delta pK_a from Aqueous Solutions. *J. Am. Chem. Soc.* **2003**, *125*, 15411-15419.
- (29) Rana, U. A.; Forsyth, M.; MacFarlane, D. R.; Pringle, J. M., Toward Protic Ionic Liquid and Organic Ionic Plastic Crystal Electrolytes for Fuel Cells. *Electrochim. Acta* **2012**, *84*, 213-222.
- (30) Seddon, K. R., Ionic Liquids for Clean Technology. *J. Chem. Technol. Biotechnol.* **1997**, *68*, 351-356.
- (31) Schroder, U.; Wadhawan, J. D.; Compton, R. G.; Marken, F.; Suarez, P. A. Z.; Consorti, C. S.; de Souza, R. F.; Dupont, J., Water-induced Accelerated Ion Diffusion: Voltammetric Studies in 1-Methyl-3-[2,6-(S)-dimethylocten-2-yl]-Imidazolium Tetrafluoroborate, 1-Butyl-3-Methylimidazolium Tetrafluoroborate and Hexafluorophosphate Ionic Liquids. *New J. Chem.* **2000**, *24*, 1009-1015.
- (32) MacFarlane, D. R.; Pringle, J. M.; Johansson, K. M.; Forsyth, S. A.; Forsyth, M., Lewis Base Ionic Liquids. *Chem. Commun.* **2006**, 1905-1917.
- (33) Welton, T., Room-Temperature Ionic Liquids. Solvents for Synthesis and Catalysis. *Chem. Rev.* **1999**, *99*, 2071-2083.
- (34) Cull, S. G.; Holbrey, J. D.; Vargas-Mora, V.; Seddon, K. R.; Lye, G. J., Room-Temperature Ionic Liquids as Replacements for Organic Solvents in Multiphase Bioprocess Operations. *Biotechnol. Bioeng.* **2000**, *69*, 227-233.
- (35) Zhao, D., Ionic Liquids: Applications in Catalysis. *Catalysis today* **2002**, *74*, 157-189.
- (36) Kragl, U.; Eckstein, M.; Kaftzik, N., Enzyme Catalysis in Ionic Liquids. *Curr. Opin. Biotechnol.* **2002**, *13*, 565-571.
-

(37) van Rantwijk, F.; Sheldon, R. A., Biocatalysis in Ionic Liquids. *Chem. Rev.* **2007**, *107*, 2757-2785.

(38) Zhang, J.; Bond, A. M., Practical Considerations Associated with Voltammetric Studies in Room Temperature Ionic Liquids. *Analyst* **2005**, *130*, 1132-1147.

(39) Zhao, C.; Burrell, G.; Torriero, A. A. J.; Separovic, F.; Dunlop, N. F.; MacFarlane, D. R.; Bond, A. M., Electrochemistry of Room Temperature Protic Ionic Liquids. *J. Phys. Chem. B* **2008**, *112*, 6923-6936.

(40) Noda, A.; Susan, A. B.; Kudo, K.; Mitsushima, S.; Hayamizu, K.; Watanabe, M., Bronsted Acid-Base Ionic Liquids as Proton-Conducting Nonaqueous Electrolytes. *J. Phys. Chem. B* **2003**, *107*, 4024-4033.

(41) Susan, M.; Noda, A.; Mitsushima, S.; Watanabe, M., Bronsted Acid-Base Ionic Liquids and Their Use as New Materials for Anhydrous Proton Conductors. *Chem. Commun.* **2003**, 938-939.

(42) Kawano, R.; Watanabe, M., Anomaly of Charge Transport of an Iodide/Tri-iodide Redox Couple in an Ionic Liquid and Its Importance in Dye-Sensitized Solar Cells. *Chem. Commun.* **2005**, 2107-2109.

(43) Wachter, P.; Schreiner, C.; Zistler, M.; Gerhard, D.; Wasserscheid, P.; Gores, H. J., A Microelectrode Study of Triiodide Diffusion Coefficients in Mixtures of Room Temperature Ionic Liquids, Useful for Dye-Sensitised Solar Cells. *Microchim. Acta* **2008**, *160*, 125-133.

(44) Zistler, M.; Wachter, P.; Schreiner, C.; Gores, H. J., Electrochemical Measurement of Triiodide Diffusion Coefficients in Blends of Ionic Liquids Results for Improving a Critical Parameter of Dye-Sensitized Solar Cells. *J. Mol. Liq.* **2010**, *156*, 52-57.

(45) O'Regan, B.; Grätzel, M., A Low-Cost, High-Efficiency Solar-Cell Based on Dye-Sensitized Colloidal TiO₂ Films. *Nature* **1991**, *353*, 737-740.

(46) Pringle, J. M.; Armel, V., The Influence of Ionic Liquid and Plastic Crystal Electrolytes on the Photovoltaic Characteristics of Dye-Sensitised Solar Cells. *Int. Rev. Phys. Chem.* **2011**, *30*, 371-407.

(47) Oskam, G.; Bergeron, B. V.; Meyer, G. J.; Searson, P. C., Pseudohalogens for Dye-Sensitized TiO₂ Photoelectrochemical Cells. *J. Phys. Chem. B* **2001**, *105*, 6867-6873.

-
- (48) Wang, P.; Zakeeruddin, S. M.; Moser, J. E.; Humphry-Baker, R.; Grätzel, M., A Solvent-Free, $\text{SeCN}^-/(\text{SeCN})_3^-$ Based Ionic Liquid Electrolyte for High-Efficiency Dye-Sensitized Nanocrystalline Solar Cells. *J. Am. Chem. Soc.* **2004**, *126*, 7164-7165.
- (49) Kawano, R.; Matsui, H.; Matsuyama, C.; Sato, A.; Susan, M.; Tanabe, N.; Watanabe, M., High Performance Dye-sensitized Solar Cells Using Ionic Liquids as Their Electrolytes. *J. Photochem. Photobiol. A-Chem.* **2004**, *164*, 87-92.
- (50) Boschloo, G.; Hagfeldt, A., Characteristics of the Iodide/Triiodide Redox Mediator in Dye-Sensitized Solar Cells. *Acc. Chem. Res.* **2009**, *42*, 1819-1826.
- (51) Litster, S.; McLean, G., PEM Fuel Cell Electrodes. *J. Power Sources* **2004**, *130*, 61-76.
- (52) Zhang, J. L.; Xie, Z.; Zhang, J. J.; Tanga, Y. H.; Song, C. J.; Navessin, T.; Shi, Z. Q.; Song, D. T.; Wang, H. J.; Wilkinson, D. P.; Liu, Z. S.; Holdcroft, S., High Temperature PEM Fuel Cells. *J. Power Sources* **2006**, *160*, 872-891.
- (53) Kreuer, K. D., Proton Conductivity: Materials and Applications. *Chem. Mat.* **1996**, *8*, 610-641.
- (54) Lee, S. Y.; Ogawa, A.; Kanno, M.; Nakamoto, H.; Yasuda, T.; Watanabe, M., Nonhumidified Intermediate Temperature Fuel Cells Using Protic Ionic Liquids. *J. Am. Chem. Soc.* **2010**, *132*, 9764-9773.
- (55) Nakamoto, H.; Watanabe, M., Bronsted Acid-Base Ionic Liquids for Fuel Cell Electrolytes. *Chem. Commun.* **2007**, 2539-2541.
- (56) Lewandowski, A. P.; Hollenkamp, A. F.; Donne, S. W.; Best, A. S., Cycling and Rate Performance of Li-LiFePO₄ Cells in Mixed FSI-TFSI Room Temperature Ionic Liquids. *J. Power Sources* **2010**, *195*, 2029-2035.
- (57) Best, A. S.; Bhatt, A. I.; Hollenkamp, A. F., Ionic Liquids with the Bis(fluorosulfonyl)imide Anion: Electrochemical Properties and Applications in Battery Technology. *J. Electrochem. Soc.* **2010**, *157*, A903-A911.
- (58) Verma, P.; Maire, P.; Novak, P., A Review of the Features and Analyses of the Solid Electrolyte Interphase in Li-ion Batteries. *Electrochim. Acta* **2010**, *55*, 6332-6341.
- (59) Lewandowski, A.; Swiderska-Mocek, A., Ionic Liquids as Electrolytes for Li-ion Batteries-An Overview of Electrochemical Studies. *J. Power Sources* **2009**, *194*, 601-609.
-

- (60) Xu, K., Nonaqueous Liquid Electrolytes for Lithium-Based Rechargeable Batteries. *Chem. Rev.* **2004**, *104*, 4303-4417.
- (61) Dunn, B.; Kamath, H.; Tarascon, J.-M., Electrical Energy Storage for the Grid: A Battery of Choices. *Science* **2011**, *334*, 928-935.
- (62) Ishikawa, M.; Sugimoto, T.; Kikuta, M.; Ishiko, E.; Kono, M., Pure Ionic Liquid Electrolytes Compatible with a Graphitized Carbon Negative Electrode in Rechargeable Lithium-Ion Batteries. *J. Power Sources* **2006**, *162*, 658-662.
- (63) Guerfi, A.; Duchesne, S.; Kobayashi, Y.; Vijn, A.; Zaghbi, K., LiFePO₄ and Graphite Electrodes with Ionic Liquids Based on Bis(Fluorosulfonyl)Imide (FSI) for Li-ion Batteries. *J. Power Sources* **2008**, *175*, 866-873.
- (64) Oldham, K. B.; Myland, J. C., *Fundamentals of Electrochemical Science*. Academic Press: San Diego, 1994.
- (65) Atkins, P. W.; De Paula, J., *Atkins' Physical Chemistry*. 9th ed.; Oxford University Press: Oxford, 2010.
- (66) Ue, M., Mobility and Ionic Association of Lithium and Quaternary Ammonium Salts in Propylene Carbonate and γ -Butyrolactone. *J. Electrochem. Soc.* **1994**, *141*, 3336-3342.
- (67) Robinson, R. A.; Stokes, R. H., *Electrolyte Solutions. The Measurement and Interpretation of Conductance, Chemical Potential and Diffusion in Solutions of Simple Electrolytes*. 2nd ed.; Butterworths Scientific Publications: London, 1959.
- (68) Matsuura, N.; Umemoto, K.; Takeda, Y., Formulation of Stokes Radii in DMF, DMSO and Propylene Carbonate with Solvent Structure Cavity Size as Parameter. *Bull. Chem. Soc. Jpn.* **1975**, *48*, 2253-2257.
- (69) Edward, J. T., Molecular Volumes and Stokes-Einstein Equation. *J. Chem. Educ.* **1970**, *47*, 261-270.
- (70) Cussler, E. L., *Diffusion: Mass Transfer in Fluid Systems*. 3rd ed.; Cambridge University Press: New York, 2009.
- (71) Tokuda, H.; Hayamizu, K.; Ishii, K.; Susan, M. A. B. H.; Watanabe, M., Physicochemical Properties and Structures of Room Temperature Ionic Liquids. 2. Variation of Alkyl Chain Length in Imidazolium Cation. *J. Phys. Chem. B* **2005**, *109*, 6103-6110.
- (72) Hapiot, P.; Lagrost, C., Electrochemical Reactivity in Room-Temperature Ionic Liquids. *Chem. Rev.* **2008**, *108*, 2238-2264.
-

-
- (73) Bernal, J.; Fowler, R. E., A Theory of Water and Ionic Solution, with Particular Reference to Hydrogen and Hydroxyl Ions. *J. Chem. Phys.* **1933**, *1*, 515–548.
- (74) Zistler, M.; Wachter, P.; Wasserscheid, P.; Gerhard, D.; Hinsch, A.; Sastrawan, R.; Gores, H. J., Comparison of Electrochemical Methods for Triiodide Diffusion Coefficient Measurements and Observation of Non-stokesian Diffusion Behaviour In Binary Mixtures of Two Ionic Liquids. *Electrochim. Acta* **2006**, *52*, 161-169.
- (75) Agmon, N., The Grotthuss Mechanism. *Chem. Phys. Lett.* **1995**, *244*, 456-462.
- (76) Ruff, I.; Friedrich, V. J., Transfer Diffusion. I. Theoretical. *J. Phys. Chem.* **1971**, *75*, 3297-3302.
- (77) Dahms, H., Electronic Conduction in Aqueous Solution. *J. Phys. Chem.* **1968**, *72*, 362-364.
- (78) Ruff, I., Transfer Diffusion. II. Kinetics of Electron Exchange Reaction Between Ferrocene and Ferricinium Ion in Alcohols. *J. Phys. Chem.* **1971**, *75*, 3303-3309.
- (79) Kawano, R.; Watanabe, M., Equilibrium Potentials and Charge Transport of an I/I_3^- Redox Couple in an Ionic Liquid. *Chem. Commun.* **2003**, 330-331.
- (80) Ruff, I.; Botar, L., Effect of Exchange-Reactions on Transport Processes - a Comparison of Thermodynamic Treatment with Random-walk on Lattice Points. *J. Chem. Phys.* **1985**, *83*, 1292-1297.
- (81) Forster, R. J., Ultrafast Electrochemical Techniques. In *Encyclopedia of Analytical Chemistry*, John Wiley & Sons, Ltd: 2006.
- (82) Heinze, J., Ultramicroelectrodes in Electrochemistry. *Angew. Chem.-Int. Edit. Engl.* **1993**, *32*, 1268-1288.
- (83) Bond, A. M.; Oldham, K. B.; Zoski, C. G., Steady-State Voltammetry. *Anal. Chim. Acta* **1989**, *216*, 177-230.
- (84) Shoup, D.; Szabo, A., Chronoamperometric Current at Finite Disk Electrodes. *J. Electroanal. Chem.* **1982**, *140*, 237-245.
- (85) Bentley, C. L.; Bond, A. M.; Hollenkamp, A. F.; Mahon, P. J.; Zhang, J., Electrochemical Proton Reduction and Equilibrium Acidity (pK_a) in Aprotic Ionic Liquids: Phenols, Carboxylic Acids and Sulfonic Acids. *In preparation* **2015**.
-

(86) Imbeaux, J. C.; Savéant, J. M., Convolution Potential Sweep Voltammetry. I. Introduction. *J. Electroanal. Chem.* **1973**, *44*, 169-187.

(87) Savéant, J. M.; Vianello, E., Potential-Sweep Voltammetry: Theoretical Analysis of Monomerization and Dimerization Mechanisms. *Electrochim. Acta* **1967**, *12*, 1545-1561.

(88) Savéant, J. M.; Vianello, E., Potential-Sweep Voltammetry - General Theory of Chemical Polarization. *Electrochim. Acta* **1967**, *12*, 629-646.

(89) Mastragostino, M.; Nadjo, L.; Savéant, J. M., Disproportionation and ECE Mechanisms—I. Theoretical Analysis. Relationships for Linear Sweep Voltammetry. *Electrochim. Acta* **1968**, *13*, 721-749.

(90) Ammar, F.; Savéant, J. M., Convolution Potential Sweep Voltammetry: II. Multistep Nernstian Waves. *J. Electroanal. Chem.* **1973**, *47*, 215-221.

(91) Nadjo, L.; Savéant, J. M.; Tessier, D., Convolution Potential Sweep Voltammetry: III. Effect of Sweep Rate Cyclic Voltammetry. *J. Electroanal. Chem.* **1974**, *52*, 403-412.

(92) Savéant, J. M.; Tessier, D., Convolution Potential Sweep Voltammetry V. Determination of Charge Transfer Kinetics Deviating from the Butler-Volmer Behaviour. *J. Electroanal. Chem.* **1975**, *65*, 57-66.

(93) Savéant, J. M.; Tessier, D., Convolution Potential Sweep Voltammetry: Part IV. Homogeneous Follow-Up Chemical Reactions. *J. Electroanal. Chem.* **1975**, *61*, 251-263.

(94) Amatore, C.; Nadjo, L.; Savéant, J. M., Convolution and Finite Difference Approach: Application to Cyclic Voltammetry and Spectroelectrochemistry. *J. Electroanal. Chem.* **1978**, *90*, 321-331.

(95) Grenness, M.; Oldham, K. B., Semiintegral Electroanalysis: Theory and Verification. *Anal. Chem.* **1972**, *44*, 1121-1129.

(96) Oldham, K. B., Signal-Independent Electroanalytical Method. *Anal. Chem.* **1972**, *44*, 196-198.

(97) Goto, M.; Oldham, K. B., Semiintegral Electroanalysis: Shapes of Neopolarograms. *Anal. Chem.* **1973**, *45*, 2043-2050.

(98) Goto, M.; Oldham, K. B., Semiintegral Electroanalysis: Studies on the Neopolarographic Plateau. *Anal. Chem.* **1974**, *46*, 1522-1530.

-
- (99) Oldham, K. B., Semi-Integration of Cyclic Voltammograms. *J. Electroanal. Chem.* **1976**, *72*, 371-378.
- (100) Goto, M.; Oldham, K. B., Semiintegral Electroanalysis: The Shape of Irreversible Neopolarograms. *Anal. Chem.* **1976**, *48*, 1671-1676.
- (101) Dalrymple-Alford, P.; Goto, M.; Oldham, K. B., Shapes of Derivative Neopolarograms. *J. Electroanal. Chem.* **1977**, *85*, 1-15.
- (102) Dalrymple-Alford, P.; Goto, M.; Oldham, K. B., Peak Shapes in Semi-Differential Electroanalysis. *Anal. Chem.* **1977**, *49*, 1390-1394.
- (103) Oldham, K. B., Semiintegral Electroanalysis. Analog Implementation. *Anal. Chem.* **1973**, *45*, 39-47.
- (104) Oldham, K. B.; Zoski, C. G., Semiintegral Electroanalysis with Discrimination Against Charging Current. *J. Electroanal. Chem.* **1983**, *145*, 265-278.
- (105) Oldham, K. B., Tables of Semiintegrals. *J. Electroanal. Chem.* **1997**, *430*, 1-14.
- (106) Mahon, P. J.; Oldham, K. B., Convulsive Modelling of Electrochemical Processes Based on the Relationship Between the Current and the Surface Concentration. *J. Electroanal. Chem.* **1999**, *464*, 1-13.
- (107) Oldham, K. B.; Spanier, J., The Replacement of Fick's Laws by a Formulation Involving Semidifferentiation. *J. Electroanal. Chem.* **1970**, *26*, 331-341.
- (108) Oldham, K. B.; Spanier, J., *The Fractional Calculus: Theory and Applications of Differentiation and Integration to Arbitrary Order*. Academic Press: US, 1974.
- (109) Bond, A. M.; Oldham, K. B.; Snook, G. A., Use of the Ferrocene Oxidation Process to Provide Both Reference Electrode Potential Calibration and a Simple Measurement (via Semiintegration) of the Uncompensated Resistance in Cyclic Voltammetric Studies in High Resistance Organic Solvents. *Anal. Chem.* **2000**, *72*, 3492-3496.
- (110) Oldham, K. B., Convolution: A General Electrochemical Procedure Implemented by a Universal Algorithm. *Anal. Chem.* **1986**, *58*, 2296-2300.
- (111) Aoki, K.; Osteryoung, J., Formulation of the Diffusion-controlled Current at Very Small Stationary Disk Electrodes. *J. Electroanal. Chem.* **1984**, *160*, 335-339.

(112) Bentley, C. L.; Bond, A. M.; Hollenkamp, A. F.; Mahon, P. J.; Zhang, J., Applications of Convolution Voltammetry in Electroanalytical Chemistry. *Anal. Chem.* **2014**, *86*, 2073–2081.

(113) Mauzeroll, J.; LeSuer, R. J., 6.3.3 - Laser-Pulled Ultramicroelectrodes. In *Handbook of Electrochemistry*, Zoski, C. G., Ed. Elsevier: Amsterdam, 2007; p 199-211.

(114) Bentley, C. L.; Bond, A. M.; Hollenkamp, A. F.; Mahon, P. J.; Zhang, J., Advantages Available in the Application of the Semi-Integral Electroanalysis Technique for the Determination of Diffusion Coefficients in the Highly Viscous Ionic Liquid 1-Methyl-3-Octylimidazolium Hexafluorophosphate. *Anal. Chem.* **2012**, *85*, 2239-2245.

(115) Dane, L. M.; Janssen, L. J. J.; Hoogland, J. G., Iodine/Iodide Redox Couple at a Platinum Electrode. *Electrochim. Acta* **1968**, *13*, 507-&.

(116) Bruckenstein, S., Ring-Disk Electrode Studies of the Open-Circuit Dissolution of Iodine Films Formed During the Anodic Oxidation of Iodide on Platinum. *J. Electroanal. Chem.* **1981**, *125*, 63-71.

(117) Swathirajan, S.; Bruckenstein, S., The Anodic Behavior of Iodide at Platinum in the Presence of an Iodine Film under Potentiostatic Steady-State and Hydrodynamic Modulation Conditions. *J. Electroanal. Chem.* **1983**, *143*, 167-178.

(118) Popov, A. I.; Geske, D. H., Studies on the Chemistry of Halogen and of Polyhalides .13. Voltammetry of Iodine Species in Acetonitrile. *J. Am. Chem. Soc.* **1958**, *80*, 1340-1352.

(119) Nelson, I. V.; Iwamoto, R. T., Voltammetric Evaluation of the Stability of Trichloride, Tribromide, and Triiodide Ions in Nitromethane, Acetone, and Acetonitrile. *J. Electroanal. Chem.* **1964**, *7*, 218-221.

(120) Elving, P. J., Electrooxidation of Halides at Pyrolytic Graphite Electrode in Aqueous and Acetonitrile Solutions. *Anal. Chem.* **1967**, *39*, 606-615.

(121) Macagno, V. A.; Giordano, M. C.; Arvia, A. J., Kinetics and Mechanisms of Electrochemical Reactions on Platinum with Solutions of Iodine-Sodium Iodide in Acetonitrile. *Electrochim. Acta* **1969**, *14*, 335-357.

(122) Sereno, L.; Macagno, V. A.; Giordano, M. C., Electrochemical Behaviour of the Chloride/Chlorine System at Platinum Electrodes in Acetonitrile Solutions. *Electrochim. Acta* **1972**, *17*, 561-575.

-
- (123) Magno, F.; Mazzocch.Ga; Bontempe.G, Electrochemical Behavior of Bromide Ion at a Platinum-Electrode in Acetonitrile Solvent. *J. Electroanal. Chem.* **1973**, *47*, 461-468.
- (124) Hubbard, A. T., Electrochemistry of Chemisorbed Molecules. III. Determination of the Oxidation State of Halides Chemisorbed on Platinum. Reactivity and Catalytic Properties of Adsorbed Species. *J. Phys. Chem.* **1975**, *79*, 808-815.
- (125) Swain, G. M., 5 - Solid Electrode Materials: Pretreatment and Activation. In *Handbook of Electrochemistry*, 1st ed.; Zoski, C. G., Ed. Elsevier: Amsterdam, 2007; p 111-153.
- (126) Mebrahtu, T.; Rodriguez, J. F.; Bravo, B. G.; Soriaga, M. P., Hydrogenative/Cathodic Stripping of Iodine Chemisorbed on Smooth Polycrystalline Platinum Electrodes. *J. Electroanal. Chem.* **1987**, *219*, 327-333.
- (127) Bravo, B. G.; Mebrahtu, T.; Rodriguez, J. F.; Soriaga, M. P., Electroactivity of Strongly-Absorbed Redox Centers: Reduction of Iodine Chemisorbed on Platinum in Aprotic Solvent. *J. Electroanal. Chem.* **1987**, *221*, 281-287.
- (128) Gebert, E., Solvent Effects in the Iodide Iodine Triiodide Complex Equilibrium. *J. Am. Chem. Soc.* **1954**, *76*, 2049-2054.
- (129) Guidelli, R.; Piccardi, G., The Dissociation Constant of I_3^- in the Voltammetric Behaviour of the Iodine-Iodide Couple. *Electrochim. Acta* **1967**, *12*, 1085-1095.
- (130) Popov, A. I.; Rygg, R. H.; Skelly, N. E., Studies on the Chemistry of Halogens and of Polyhalides .9. Electrical Conductance Study of Higher Polyiodide Complex Ions in Acetonitrile Solutions. *J. Am. Chem. Soc.* **1956**, *78*, 5740-5744.
- (131) Iwamoto, R. T., Solvent Effects on the Electro-Oxidation of Iodide Ion. *Anal. Chem.* **1959**, *31*, 955-955.
- (132) Zittel, H. E., Voltammetry of the Iodine System in Aqueous Medium at the Pyrolytic Graphite Electrode. *J. Electroanal. Chem.* **1966**, *11*, 85-93.
- (133) Dryhurst, G.; Elving, P. J., Voltammetric Determination of Iodide and Bromide at Rotating Pyrolytic Graphite Electrode. *J. Electroanal. Chem.* **1966**, *12*, 416-&.
- (134) Kay, A.; Grätzel, M., Low Cost Photovoltaic Modules Based on Dye Sensitized Nanocrystalline Titanium Dioxide and Carbon Powder. *Sol. Energy Mater. Sol. Cells* **1996**, *44*, 99-117.
-

(135) Murakami, T. N.; Ito, S.; Wang, Q.; Nazeeruddin, M. K.; Bessho, T., Highly Efficient Dye-Sensitized Solar Cells Based on Carbon Black Counter Electrodes. *J. Electrochem. Soc.* **2006**, *153*, A2255-A2261.

(136) Matsui, Y.; Kurosaki, Y.; Date, Y., Polarography of Halides in Dimethylformamide .2. Iodide Ion, Triiodomercurate Ion, and Mercuric Iodide. *Bull. Chem. Soc. Jpn.* **1970**, *43*, 1707-1714.

(137) Loo, B. H., In Situ Identification of Halide-Complexes on Gold Electrode by Surface-Enhanced Raman-Spectroscopy. *J. Phys. Chem.* **1982**, *86*, 433-437.

(138) Qi, P. H.; Hiskey, J. B., Electrochemical-Behavior of Gold in Iodide Solutions. *Hydrometallurgy* **1993**, *32*, 161-179.

(139) Zhao, S. F.; Lu, J. X.; Bond, A. M.; Zhang, J., Remarkable Sensitivity of the Electrochemical Reduction of Benzophenone to Proton Availability in Ionic Liquids. *Chem.-Eur. J.* **2012**, *18*, 5290-5301.

(140) Zhang, Y.; Zheng, J. B., Investigation on the Electro-Oxidation of Iodide in the Room Temperature Ionic Liquid, 1-Butyl-3-Methylimidazolium Tetrafluoroborate at Platinum Electrode. *Electrochim. Acta* **2007**, *52*, 4082-4086.

(141) Silvester, D. S.; Aldous, L.; Hardacre, C.; Compton, R. G., Electrooxidation of the Iodides [C₄mim]I, LiI, NaI, KI, RbI, and CsI in the Room Temperature Ionic Liquid [C₄mim][NTf₂]. *J. Phys. Chem. C* **2008**, *112*, 6551-6557.

(142) Rogers, E. I.; Streeter, I.; Aldous, L.; Hardacre, C.; Compton, R. G., Electrode Kinetics and Mechanism of Iodine Reduction in the Room-Temperature Ionic Liquid [C₄mim][NTf₂]. *J. Phys. Chem. C* **2008**, *112*, 10976-10981.

(143) Ejigu, A.; Lovelock, K. R. J.; Licence, P.; Walsh, D. A., Iodide/Triiodide Electrochemistry in Ionic Liquids: Effect of Viscosity on Mass Transport, Voltammetry and Scanning Electrochemical Microscopy. *Electrochim. Acta* **2011**, *56*, 10313-10320.

(144) Wachter, P.; Zistler, M.; Schreiner, C.; Fleischmann, M.; Gerhard, D.; Wasserscheid, P.; Barthel, J.; Gores, H. J., Temperature Dependence of the Non-Stokesian Charge Transport in Binary Blends of Ionic Liquids. *J. Chem. Eng. Data* **2009**, *54*, 491-497.

(145) Zistler, M.; Schreiner, C.; Wachter, P.; Wasserscheid, P.; Gerhard, D.; Gores, H. J., Electrochemical Characterization of 1-Ethyl-3-Methylimidazolium Thiocyanate and

Measurement of Triiodide Diffusion Coefficients in Blends of Two Ionic Liquids. *Int. J. Electrochem. Sci.* **2008**, *3*, 236-245.

(146) Thapa, R.; Park, N., First-Principles Identification of Iodine Exchange Mechanism in Iodide Ionic Liquid. *J. Phys. Chem. Lett.* **2012**, *3*, 3065-3069.

(147) Kubo, W.; Murakoshi, K.; Kitamura, T.; Yoshida, S.; Haruki, M.; Hanabusa, K.; Shirai, H.; Wada, Y.; Yanagida, S., Quasi-Solid-State Dye-Sensitized TiO₂ Solar Cells: Effective Charge Transport in Mesoporous Space Filled with Gel Electrolytes Containing Iodide and Iodine. *J. Phys. Chem. B* **2001**, *105*, 12809-12815.

(148) Thorsmolle, V. K.; Rothenberger, G.; Topgaard, D.; Brauer, J. C.; Kuang, D. B.; Zakeeruddin, S. M.; Lindman, B.; Grätzel, M.; Moser, J. E., Extraordinarily Efficient Conduction in a Redox-Active Ionic Liquid. *Chemphyschem* **2011**, *12*, 145-149.

(149) Cao, Y. M.; Zhang, J.; Bai, Y.; Li, R. Z.; Zakeeruddin, S. M.; Gratzel, M.; Wang, P., Dye-sensitized solar cells with solvent-free ionic liquid electrolytes. *J. Phys. Chem. C* **2008**, *112*, 13775-13781.

(150) Ruff, I.; Friedric.Vj; Csillag, K., Transfer Diffusion .3. Kinetics and Mechanism of Triiodide-Iodide Exchange-Reaction. *J. Phys. Chem.* **1972**, *76*, 162-165.

(151) Thorsmolle, V. K.; Brauer, J. C.; Zakeeruddin, S. M.; Grätzel, M.; Moser, J. E., Temperature-Dependent Ordering Phenomena of a Polyiodide System in a Redox-Active Ionic Liquid. *J. Phys. Chem. C* **2012**, *116*, 7989-7992.

(152) Hao, F.; Lin, H.; Zhang, J.; Li, J. B., Balance Between the Physical Diffusion and the Exchange Reaction on Binary Ionic Liquid Electrolyte for Dye-Sensitized Solar Cells. *J. Power Sources* **2011**, *196*, 1645-1650.

(153) Barrette, W. C.; Sawyer, D. T., Determination of Dissolved Hydrogen and Effects of Media and Electrode Materials on the Electrochemical Oxidation of Molecular-Hydrogen. *Anal. Chem.* **1984**, *56*, 653-657.

(154) Meng, Y.; Aldous, L.; Belding, S. R.; Compton, R. G., The Hydrogen Evolution Reaction in a Room Temperature Ionic Liquid: Mechanism and Electrocatalyst Trends. *Phys. Chem. Chem. Phys.* **2012**, *14*, 5222-5228.

(155) Meng, Y.; Aldous, L.; Belding, S. R.; Compton, R. G., The Formal Potentials and Electrode Kinetics of the Proton/Hydrogen Couple in Various Room Temperature Ionic Liquids. *Chem. Commun.* **2012**, *48*, 5572-5574.

- (156) Kibler, L. A., Hydrogen Electrocatalysis. *Chemphyschem* **2006**, *7*, 985-991.
- (157) Jaworski, A.; Donten, M.; Stojek, Z.; Osteryoung, J. G., Conditions of Strict Voltammetric Reversibility of the H⁺/H₂ Couple at Platinum Electrodes. *Anal. Chem.* **1999**, *71*, 243-246.
- (158) Conway, B. E.; Tilak, B. V., Interfacial Processes Involving Electrocatalytic Evolution and Oxidation of H₂, and the Role of Chemisorbed H. *Electrochim. Acta* **2002**, *47*, 3571-3594.
- (159) Rieger, P. H., *Electrochemistry*. 2nd ed.; Chapman & Hall: New York, 1994.
- (160) Silvester, D. S.; Aldous, L.; Hardacre, C.; Compton, R. G., An Electrochemical Study of the Oxidation of Hydrogen at Platinum Electrodes in Several Room Temperature Ionic Liquids. *J. Phys. Chem. B* **2007**, *111*, 5000-5007.
- (161) Johnson, L.; Ejigu, A.; Licence, P.; Walsh, D. A., Hydrogen Oxidation and Oxygen Reduction at Platinum in Protic Ionic Liquids. *J. Phys. Chem. C* **2012**, *116*, 18048-18056.
- (162) Del Popolo, M. G.; Kohanoff, J.; Lynden-Bell, R. M., Solvation Structure and Transport of Acidic Protons in Ionic Liquids: a First-Principles Simulation Study. *J. Phys. Chem. B* **2006**, *110*, 8798-8803.
- (163) Silvester, D. S.; Ward, K. R.; Aldous, L.; Hardacre, C.; Compton, R. G., The Electrochemical Oxidation of Hydrogen at Activated Platinum Electrodes in Room Temperature Ionic Liquids as Solvents. *J. Electroanal. Chem.* **2008**, *618*, 53-60.
- (164) Aldous, L.; Silvester, D. S.; Pitner, W. R.; Compton, R. G.; Lagunas, M. C.; Hardacre, C., Voltammetric Studies of Gold, Protons, and HCl₂⁻ in Ionic Liquids. *J. Phys. Chem. C* **2007**, *111*, 8496-8503.
- (165) Meng, Y.; Aldous, L.; Compton, R. G., Electrochemistry of Hydrogen in the Room Temperature Ionic Liquid 1-Butyl-3-methylimidazolium Bis(trifluoromethylsulfonyl)imide: Dissolved Hydrogen "Lubricates" Diffusional Transport. *J. Phys. Chem. C* **2011**, *115*, 14334-14340.
- (166) He, W.; Silvester, D. S.; Streeter, I.; Aldous, L.; Hardacre, C.; Compton, R. G., Measuring the Solubility of Benzoic Acid in Room Temperature Ionic Liquids Using Chronoamperometric Techniques. *J. Phys. Org. Chem.* **2009**, *22*, 69-76.

-
- (167) Silvester, D. S.; He, W.; Aldous, L.; Hardacre, C.; Compton, R. G., Electrochemical Reduction of Benzoic Acid and Substituted Benzoic Acids in Some Room Temperature Ionic Liquids. *J. Phys. Chem. C* **2008**, *112*, 12966-12973.
- (168) Meng, Y.; Norman, S.; Hardacre, C.; Compton, R. G., The Electroreduction of Benzoic Acid: Voltammetric Observation of Adsorbed Hydrogen at a Platinum Microelectrode in Room Temperature Ionic Liquids. *Phys. Chem. Chem. Phys.* **2013**, *15*, 2031-2036.
- (169) Barhdadi, R.; Troupel, M.; Comminges, C.; Laurent, M.; Doherty, A., Electrochemical Determination of pK_a of N-Bases in Ionic Liquid Media. *J. Phys. Chem. B* **2012**, *116*, 277-282.
- (170) Perrin, D. D.; Dempsey, B.; Serjeant, E. P., *pK_a Prediction for Organic Acids and Bases*. Chapman and Hall: New York, 1981.
- (171) Campbell, M. L.; Waite, B. A., The K_a Values of Water and the Hydronium Ion for Comparison with Other Acids. *J. Chem. Educ.* **1990**, *67*, 386.
- (172) Deng, H.; Li, X.; Chu, Y.; He, J.; Cheng, J.-P., Standard pK_a Scales of Carbon-Centered Indicator Acids in Ionic Liquids: Effect of Media and Structural Implication. *J. Org. Chem.* **2012**, *77*, 7291-7298.
- (173) Wang, Z.; Deng, H.; Li, X.; Ji, P. J.; Cheng, J. P., Standard and Absolute pK_a Scales of Substituted Benzoic Acids in Room Temperature Ionic Liquids. *J. Org. Chem.* **2013**, *78*, 12487-12493.
- (174) Bordwell, F. G., Equilibrium Acidities in Dimethyl Sulfoxide Solution. *Acc. Chem. Res.* **1988**, *21*, 456-463.
- (175) Barrette, W. C.; Johnson, H. W.; Sawyer, D. T., Voltammetric Evaluation of the Effective Acidities (pK_a') for Bronsted Acids in Aprotic-Solvents. *Anal. Chem.* **1984**, *56*, 1890-1898.
- (176) Slater, A. M., The IUPAC Aqueous and Non-Aqueous Experimental pK_a Data Repositories of Organic Acids and Bases. *J. Comput.-Aided Mol. Des.* **2014**, *28*, 1031-1034.
- (177) Haynes, W., *CRC Handbook of Chemistry and Physics : a Ready-Reference Book of Chemical and Physical Data* 95th ed.; CRC Press: Boca Raton, Florida, 2014.
-

(178) Kütt, A.; Leito, I.; Kaljurand, I.; Sooväli, L.; Vlasov, V. M.; Yagupolskii, L. M.; Koppel, I. A., A Comprehensive Self-Consistent Spectrophotometric Acidity Scale of Neutral Brønsted Acids in Acetonitrile. *J. Org. Chem.* **2006**, *71*, 2829-2838.

(179) Treimer, S. E.; Evans, D. H., Electrochemical Reduction of Acids in Dimethyl Sulfoxide. CE Mechanisms and Beyond. *J. Electroanal. Chem.* **1998**, *449*, 39-48.

(180) Treimer, S. E.; Evans, D. H., Electrochemical Reduction of Acids in Dimethyl Sulfoxide. Comparison of Weak C-H, N-H and O-H Acids. *J. Electroanal. Chem.* **1998**, *455*, 19-28.

(181) Serjeant, E. P.; Dempsey, B., *Ionisation Constants of Organic Acids in Aqueous Solution*. Pergamon: Oxford, 1979.

(182) Qiang, Z.; Adams, C., Potentiometric Determination of Acid Dissociation Constants (pK_a) for Human and Veterinary Antibiotics. *Water Res.* **2004**, *38*, 2874-2890.

(183) Kütt, A.; Rodima, T.; Saame, J.; Raamat, E.; Mäemets, V.; Kaljurand, I.; Koppel, I. A.; Garlyauskayte, R. Y.; Yagupolskii, Y. L.; Yagupolskii, L. M.; Bernhardt, E.; Willner, H.; Leito, I., Equilibrium Acidities of Superacids. *J. Org. Chem.* **2010**, *76*, 391-395.

(184) McMahon, T. B.; Kebarle, P., Intrinsic Acidities of Substituted Phenols and Benzoic Acids Determined by Gas-Phase Proton-Transfer Equilibriums. *J. Am. Chem. Soc.* **1977**, *99*, 2222-2230.

(185) Migliore, A.; Polizzi, N. F.; Therien, M. J.; Beratan, D. N., Biochemistry and Theory of Proton-Coupled Electron Transfer. *Chem. Rev.* **2014**.

(186) Mikkelsen, M.; Jorgensen, M.; Krebs, F. C., The Teraton Challenge. A Review of Fixation and Transformation of Carbon Dioxide. *Energy Environ. Sci.* **2010**, *3*, 43-81.

(187) Arico, A. S.; Srinivasan, S.; Antonucci, V., DMFCs: From Fundamental Aspects to Technology Development. *Fuel Cells* **2001**, *1*, 133-161.

(188) Bard, A. J.; Fox, M. A., Artificial Photosynthesis - Solar Splitting of Water to Hydrogen and Oxygen. *Acc. Chem. Res.* **1995**, *28*, 141-145.

(189) Kreuer, K. D., Fast Proton Conductivity: a Phenomenon Between the Solid and the Liquid State? *Solid State Ionics* **1997**, *94*, 55-62.

(190) Slevin, C. J.; Unwin, P. R., Lateral Proton Diffusion Rates along Stearic Acid Monolayers. *J. Am. Chem. Soc.* **2000**, *122*, 2597-2602.

- (191) Bard, A. J.; Lund, H., *Encyclopedia of Electrochemistry of the Elements*. M. Dekker: New York,, 1973.
- (192) Ueki, T.; Watanabe, M., Macromolecules in Ionic Liquids: Progress, Challenges, and Opportunities. *Macromolecules* **2008**, *41*, 3739-3749.
- (193) Nakamoto, H.; Noda, A.; Hayamizu, K.; Hayashi, S.; Hamaguchi, H. O.; Watanabe, M., Proton-conducting Properties of a Bronsted Acid-Base Ionic Liquid and Ionic Melts Consisting of Bis(Trifluoromethanesulfonyl)Imide and Benzimidazole for Fuel Cell Electrolytes. *J. Phys. Chem. C* **2007**, *111*, 1541-1548.
- (194) Zhao, Z. F.; Ueno, K.; Angell, C. A., High Conductivity, and "Dry" Proton Motion, in Guanidinium Salt Melts and Binary Solutions. *J. Phys. Chem. B* **2011**, *115*, 13467-13472.
- (195) Ueno, K.; Zhao, Z. F.; Watanabe, M.; Angell, C. A., Protic Ionic Liquids Based on Decahydroisoquinoline: Lost Superfragility and Ionicity-Fragility Correlation. *J. Phys. Chem. B* **2012**, *116*, 63-70.
- (196) Ogihara, W.; Kosukegawa, H.; Ohno, H., Proton-Conducting Ionic Liquids Based upon Multivalent Anions and Alkylimidazolium Cations. *Chem. Commun.* **2006**, 3637-3639.
- (197) Anouti, M.; Porion, P.; Brigouleix, C.; Galiano, H.; Lernordant, D., Transport Properties in Two Pyrrolidinium-Based Protic Ionic Liquids as Determined by Conductivity, Viscosity and NMR Self-diffusion Measurements. *Fluid Phase Equilib.* **2010**, *299*, 229-237.
- (198) Iojoiu, C.; Hana, M.; Molmeret, Y.; Martinez, M.; Cointeaux, L.; El Kissi, N.; Teles, J.; Leprêtre, J. C.; Judeinstein, P.; Sanchez, J. Y., Ionic Liquids and Their Hosting by Polymers for HT-PEMFC Membranes. *Fuel Cells* **2010**, *10*, 778-789.

2. Experimental

2.1 Materials and Preparation

2.1.1 Glovebox and Schlenk Line

The preparation and handling of hygroscopic materials such as ionic liquids, non-aqueous solvents and supporting electrolytes was carried out in an argon filled glovebox (KIYON, Korea). Materials were admitted into the glovebox through an antechamber, which was subsequently evacuated and refilled three times with high-purity argon. The glovebox atmosphere was maintained by passing it through a series of columns containing molecular sieves (4 Å) and copper/copper oxide, responsible for scrubbing water and oxygen respectively. In addition, the glovebox was fitted with oxygen and moisture sensors to monitor the quality of the atmosphere.

A Schlenk line was also employed to carry out reactions and procedures (*i.e.*, moisture removal) in the absence of air. One manifold was connected to a nitrogen gas source, while the other was connected to a high-vacuum pump (Edwards, UK).

2.1.2 Ionic Liquids

1-methyl-3-octylimidazolium hexafluorophosphate ([C₈mim][PF₆], Solvent Innovation), 1-ethyl-3-methylimidazolium bis(trifluoromethanesulfonyl)imide ([C₂mim][NTf₂], Io-li-tec), triethylsulfonium bis(trifluoromethanesulfonyl)imide ([S_{2,2,2}][NTf₂], Solvent Innovation), 1-methyl-1-butylpyrrolidinium bis(trifluoromethanesulfonyl)imide ([C₄mpyr][NTf₂], Merck), 1-butyl-2,3-dimethylimidazolium bis(trifluoromethanesulfonyl)imide ([C₄dmim][NTf₂], Solvent Innovation), dimethylethylpropylammonium bis(trifluoromethanesulfonyl)imide ([N_{1,1,2,3}][NTf₂], Merck), 1-ethyl-3-methylimidazolium trifluoromethanesulfonate

([C₂mim][OTf], Merck) and 1-ethyl-3-methylimidazolium dicyanamide ([C₂mim][N(CN)₂], Solvent Innovation) were commercial samples.

Tributylmethylammonium bis(trifluoromethanesulfonyl)imide, [N_{1,4,4,4}][NTf₂], was prepared by a metathesis reaction between lithium bis(trifluoromethanesulfonyl)imide, (Li[NTf₂], 3M) and tributylmethylammonium methylsulfate ([N_{1,4,4,4}][CH₃OSO₃], Sigma-Aldrich) in de-ionized water. Following preparation, [N_{1,4,4,4}][NTf₂] was taken up in dichloromethane and rinsed repeatedly with water to extract residual Li[CH₃OSO₃]. Triethylammonium bis(trifluoromethanesulfonyl)imide, [N_{H,2,2,2}][NTf₂], was prepared by a metathesis reaction between Li[NTf₂] and triethylammonium chloride ([N_{H,2,2,2}]Cl, Sigma-Aldrich, recrystallized from ethanol) in de-ionized water. Following preparation, [N_{H,2,2,2}][NTf₂] was taken up in dichloromethane and rinsed repeatedly with water to extract residual LiCl until the aqueous phase passed the silver nitrate test. 1-ethyl-3-methylimidazolium *p*-toluenesulfonate, [C₂mim][OTs], was prepared by alkylation of *N*-methylimidazole (Sigma-Aldrich, vacuum distilled over lithium) with ethyl *p*-toluenesulfonate (Sigma-Aldrich, recrystallized from *n*-pentane) in toluene, as reported in the literature.¹

Before use, each of the ILs was dried under high vacuum ($\leq 10^{-1}$ mbar) on a Schlenk line at 45°C for 48 hours. The residual water content was less than 100 ppm by Karl Fischer titration (Metrohm 831 KF Coulometer).

2.1.3 Solvents and Supporting Electrolytes

Ethyl acetate, isopropanol, acetone, *n*-pentane, toluene, dichloromethane, ethanol, diethyl ether and methanol were used in preparation/purification procedures and were all EMSURE grade from Merck. The dichloromethane used in electrochemical experiments was from Sigma-Aldrich (anhydrous, 99.8%). The acetonitrile used in electrochemical experiments was from Sigma-Aldrich (anhydrous, 99.8%) or Alfa-Aesar (anhydrous, 99.7%).

Propylene carbonate was from Sigma-Aldrich (anhydrous, 99.8%). 1,2-propanediol (propylene glycol, Acros, 99%) was distilled under high vacuum over lithium. De-ionized water was collected from a Milli-Q water purification system (Millipore, Milli-Q Plus 185).

Tetraethylammonium tetrafluoroborate ([NEt₄][BF₄], Stella Chemifa, 99.9%) was recrystallised twice from methanol and dried at 50°C for 72 hours under vacuum. Tetra-*n*-butylammonium hexafluorophosphate ([NBu₄][PF₆], Sigma-Aldrich) and lithium tetrafluoroborate (Li[BF₄], Stella Chemifa) were used as supplied by the manufacturer.

2.1.4 Electroactive Species

Metallocenes and metal salts. Ferrocene (Fc or Fe(Cp)₂, Fluka, >98%) was recrystallized from *n*-pentane. Cobaltocenium hexafluorophosphate ([Co(Cp)₂][PF₆] or CcPF₆, Sigma-Aldrich) and silver nitrate (AgNO₃, BDH, 99.9%) were used as supplied by the manufacturer.

Iodide and Iodine. 1-ethyl-3-methylimidazolium iodide ([C₂mim]I, Io-li-tec, >98%) was recrystallized twice from a 2:1 mixture of ethyl acetate and isopropanol and then dried under high vacuum for 48 hours. Care was taken during handling and storage of [C₂mim]I to avoid exposure to light. Iodine (Sigma-Aldrich, 99.8%) was used as supplied by the manufacturer. Tetra-*n*-butylammonium diiodoaurate ([NBu₄][AuI₂]) was prepared by suspending gold foil (0.53 g, Sigma Aldrich, ≥99.9%), iodine (0.39 g, Sigma-Aldrich, 99.8%) and tetra-*n*-butylammonium iodide (1.08 g, [NBu₄]I, Sigma-Aldrich, ≥99%) in absolute ethanol (8 cm³, Merck, EMSURE) and refluxing for 72 hours.² The following reaction took place:

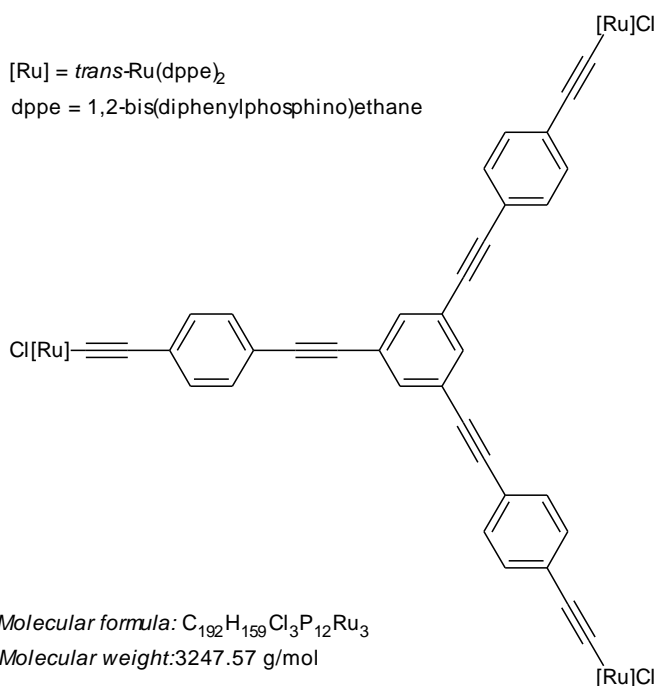


The crude product, [NBu₄][AuI₂] (confirmed by electrospray ionization mass spectrometry) was recrystallised twice from dry ethyl acetate³, washed with diethyl ether and dried under

vacuum, for a final yield of 77%. This procedure was carried out under an atmosphere of dry N₂ using standard Schlenk techniques.

Dinitrodurene. 1,4-dinitro-2,3,5,6-tetramethylbenzene (dinitrodurene) was prepared by forming a homogeneous slurry of powdered 1,2,4,5-tetramethylbenzene (1.2 g, Sigma-Aldrich, 98%) in 98% H₂SO₄ (7.5 mL, Univar) and adding dropwise a mixture of 70% HNO₃ (Scharlau) and 98% H₂SO₄ (5 mL total, 1:3 v/v) over a period of 2 hours, ensuring the temperature of the reaction mixture remained between 5 and 10°C.⁴ The reaction mixture was subsequently quenched in ice water and the crude product was filtered, rinsed and recrystallised from absolute ethanol. The recrystallised dinitrodurene was finally dried at 65°C for 2 hours ($T_m = 207\text{-}208^\circ\text{C}$), for a final yield of 49%.

Alkynylruthenium complex. The alkynylruthenium complex (see Structure 1), 1,3,5-C₆H₃{4-C≡CC₆H₄C≡C-*trans*-[RuCl(dppe)₂]}₃, had previously been prepared at the Research School of Chemistry at The Australian National University⁵ and was used as received.



Structure 1. The alkynylruthenium complex investigated in this work.

Acids and Bases. Bis(trifluoromethanesulfonyl)imide (H[NTf₂], Sigma-Aldrich, 95%) was purified by sublimation under high vacuum. N-methylimidazole (Sigma-Aldrich) was purified by vacuum distillation over lithium. Aniline (Sigma-Aldrich) was purified by vacuum distillation over potassium hydroxide (Merck). The protonated amine salts were prepared in methanol by adding a stoichiometric amount of H[NTf₂] and stirring for several hours. Methanol was subsequently removed on a rotary evaporator and the remaining salt was dried under high vacuum at 45°C for at least 12 hours before use. *p*-toluenesulfonic acid monohydrate (Acros, 99%) was recrystallized from ethyl acetate. Trifluoromethanesulfonic (triflic) acid (H[OTf], Sigma-Aldrich, 98%), N-methylpyrrolidine (Sigma-Aldrich, 99%), pyridine (BDH, 99.8%), saccharin (Fluka, >99%), di(benzenesulfonyl)amide (TCI, 97%), 2-chloropyridine (Sigma-Aldrich, 99%), 2,4-dichloropyridine (Combi-Blocks, 98%), *o*-phenylenediamine (Sigma-Aldrich, 99.5%), naphthalene-2-sulfonic acid monohydrate (TCI, 98%), methanesulfonic acid (Sigma-Aldrich, ≥ 99.5%), dichloroacetic acid (Fluka, 99.5%), trichloroacetic acid (Univar, 99%), *o*-hydroxybenzoic acid (Univar, 99.9%), glycolic acid (Sigma-Aldrich, 99%), malonic acid (Sigma-Aldrich, 99%), pentachlorophenol (Sigma-Aldrich, 99%) and 2,3,4-trichlorophenol (Sigma-Aldrich, 99%) were used as supplied by the manufacturer.

2.2 Electrochemical Systems and Procedures

2.2.1 Potentiostats

Voltammetric experiments at high scan rates ($\geq 10 \text{ V s}^{-1}$) were carried out with a CH Instruments 760D Potentiostat (CH Instruments, USA). Unless otherwise stated, all other voltammetric experiments were undertaken with a Gamry Reference 600 Potentiostat/Galvanostat/ZRA (Gamry Instruments, USA).

2.2.2 Electrodes

Working Electrodes. The platinum macrodisk (nominal diameter = 1.6 mm), gold macrodisk (nominal diameter = 1.6 mm), glassy carbon macrodisk (nominal diameter = 3.0 mm), platinum microdisk (nominal diameter = 10 μm) and glassy carbon microdisk (nominal diameter = 11 μm) were purchased from BASi (Bioanalytical Systems, USA). The platinum rotating disk electrode (nominal diameter = 3.0 mm), platinum macrodisk electrode (nominal diameter = 2.0 mm), gold macrodisk electrode (nominal diameter = 3.0 mm), platinum microdisk electrodes (nominal diameters = 20 and 100 μm) and gold microdisk electrode (nominal diameter = 25 μm) were purchased from Metrohm (Switzerland). The boron-doped diamond macrodisk (nominal diameter = 3.0 mm) was purchased from Windsor Scientific (UK). The 25 μm dia. platinum microdisk electrode was fabricated by sealing a wire of the appropriate dimensions in glass. The 2 μm dia. platinum microdisk electrode was fabricated by sealing a Wollaston wire of the appropriate dimensions in a glass capillary.⁶

Auxiliary Electrodes. The auxiliary electrode used in all electrochemical experiments was either platinum wire, foil or mesh.

Reference Electrodes. The reference electrode employed in IL media was either a platinum/silver wire pseudo-reference electrode or an Γ/I_3^- reference electrode (Pt | 400 mM $[\text{C}_2\text{mim}]\text{I} + 100 \text{ mM } \text{I}_2$ in $[\text{C}_2\text{mim}][\text{NTf}_2]$). The reference electrode employed in aprotic media was either a silver wire pseudo-reference electrode or an Ag/Ag⁺ quasi-reference electrode (10 mM AgNO₃ + 0.1 M $[\text{NBu}_4][\text{PF}_6]$ in acetonitrile). The pseudo-reference electrode was constructed by immersing the platinum/silver wire in the electrolyte under investigation and sealing it in a fritted (Vycor) glass tube. The pseudo-reference electrode potential was calibrated against the formal potential of the recommended Fc/Fc⁺ or Cc⁺/Cc

process^{7, 8} in the electrolyte of interest. A Metrohm double junction Ag/AgCl (3 M KCl) reference electrode was employed during experiments carried out in aqueous media.

Electrode Preparation. Macrodisk electrodes were activated by polishing with successively smaller (1 and 0.3 μm) aqueous alumina slurries (Kemet, UK) on a clean polishing cloth (Buehler, USA). Adherent alumina was removed by sonication in de-ionized water. Microdisk electrodes were activated by polishing with an aqueous slurry of 0.3 μm alumina and rinsing thoroughly with de-ionized water. The active electrode area of each of the electrodes was calibrated regularly with convolution voltammetry⁹⁻¹¹, using the oxidation of a Fc solution of known concentration (2.0 mM in acetonitrile containing 0.10 M [NBu₄][PF₆]) and adopting a diffusion coefficient of $2.4 \times 10^{-5} \text{ cm}^2 \text{ s}^{-1}$, as published under these conditions.¹² During studies on the Γ/I_2 system, the working electrode was preconditioned in 0.1 M aqueous sulfuric acid by scanning between the oxygen and hydrogen evolution reactions¹³ with subsequent rinsing in deionized water and acetone. During studies on the H^+/H_2 system, the working electrode was preconditioned by oxidative polarization at 1.5 to 2.2 V vs. Fc/Fc⁺ for ≤ 10 msec as has been previously reported.¹⁴

2.2.3 Setup

All electrochemical experiments were carried out under benchtop conditions at ambient temperature ($24 \pm 1^\circ\text{C}$) in a Faraday cage. All solvents were degassed with N_2 prior to experimentation, and a blanket of N_2 was maintained during the course of the electrochemical experiments. Positive feedback IR_u compensation (R_u = uncompensated resistance) was employed in macroelectrode experiments (R_u was estimated by electrochemical impedance). Unless otherwise stated, all electrochemical experiments were carried out using a standard 3-electrode arrangement with a working, auxiliary and reference electrode as described above. All electrochemical experiments were carried out in glass cells, ranging in size from 1 – 2 mL (IL media) to 50 mL (aqueous media).

2.2.4 Semiintegration and Convolution

Semiintegration of the I - t data was performed using an algorithm from de Levie¹⁵, which was adapted from Oldham and Myland.¹⁶ A Microsoft Excel macro that includes this algorithm is available free online.¹⁷ Convolved currents for the inlaid disk geometry were calculated using an efficient convolution algorithm applicable to data with regularly spaced time intervals¹⁸:

$$M(t) = [I(t) * g(t)]_{t=j\Delta} = \frac{1}{\Delta} \left(I_j G_1 + \sum_{j=1}^{J-1} I_{j-j} (G_{j-1} - 2G_j + G_{j+1}) \right) \quad (2.2)$$

where Δ is a small increment of the total time, $G(t) = \int_0^t \int_0^t g(t) dt dt$ and the abbreviations I_j and G_j refer to $I(j\Delta)$ and $G(j\Delta)$. The *double* integral of $g(t)$ at short times for use in the convolution algorithm is obtained from:

$$G(t) = \frac{r_0^3}{D^{3/2}} \sum_{j=1}^5 a_j \theta^{(j+2)/2} \quad (2.3)$$

and for the long time series:

$$G(t) = \frac{r_0^3}{D^{3/2}} \left(\sum_{j=1}^3 b_j \theta^{(3-j)/2} + \sum_{j=4}^8 b_j \theta^{(7-2j)/2} \right) \quad (2.4)$$

with transition occurring when $\theta = 1.368$. The coefficients b_1 and b_3 are integration constants obtained from Aoki *et al.*¹⁹ The double integral of the long-time expression contains eight terms due to the addition of the integration constant for each integration step. The values for the a_j and b_j coefficients are available elsewhere.¹⁰

2.2.5 Numerical Simulation

Cyclic voltammetric simulations were carried out using the commercially available DigiElch software package²⁰⁻²⁴ (v. 7F, Elchsoft, Germany) on a dual core Dell Laptop

running Windows 7. Inlaid disk electrode geometry was assumed in all simulations and two-dimensional (radial) diffusion was considered. In all simulations, uncompensated resistance and double layer capacitance were assumed to be negligible.

2.2.6 Miscellaneous Techniques

Optical Microscopy. The working electrode surface was imaged *in situ* using a Nikon Epiphot bright/dark field inverted optical microscope (Nikon Instruments, Japan). A specially designed glass electrochemical cell (~5 mL) with an optically transparent, circular microscope coverslip (19 mm dia.) for a base was used in these experiments.

UV/Visible Spectrophotometry. UV/Visible spectroscopy was performed *in situ* with a Varian Cary 50 Bio UV/Visible Spectrophotometer (Agilent, USA) in a quartz optically transparent thin layer electrochemical (OTTLE) cell with a platinum mesh working electrode.

Electrochemical Quartz Crystal Microbalance. The electrochemical quartz crystal microbalance (EQCM) experiments were carried out using an impedance method (passive EQCM) on an Agilent E5061A ENA Series Network Analyser (USA) coupled to an Autolab PGSTAT302N potentiostat (Metrohm, Switzerland) with a commercially available EQCM cell (CH instruments, USA). The EQCM working electrode was a 13 mm diameter AT-cut α -quartz crystal (Bright Star Crystals, Australia), which had gold disks (5.0 mm diameter) vapour deposited on each side; the electrode resonated in air at 10 ± 0.05 MHz. The change in resonant frequency (Δf_0) in the quartz crystal electrode is related to the change in mass (Δm) by the Sauerbrey equation^{25, 26}:

$$\Delta f_0 = f_0(m + \Delta m) - f_0(m) = -\left(\frac{f_0(m)}{Ax_q\rho_q}\right)\Delta m = -S\Delta m \quad (2.5)$$

where x_q is the thickness of the quartz crystal, ρ_q is the density of the quartz crystal (2.645 g cm⁻³ at 20°C), A is the active electrode surface area and S is the Sauerbrey constant. Before

each experiment, the EQCM working electrode was cleaned using concentrated nitric acid and rinsed successively with distilled water and acetone.

Viscosity and Density. Density was measured with an Anton Paar DMA 4500M Density Meter. Viscosity was measured using the falling ball method with an Anton Paar Automated Microviscometer (AMVn).

Nuclear Magnetic Resonance (NMR) Spectroscopy. Standard NMR experiments were carried out on a Bruker Av400 NMR spectrometer equipped with a triple resonance broadband observe (TBO) probe operating at 400.13 MHz for ^1H , 376.50 MHz for ^{19}F and 100.62 MHz for ^{13}C . NMR self-diffusion coefficients were determined using the pulsed field gradients spin echo (PGSE) method utilising a Bruker Av500 NMR spectrometer equipped with a 5 mm Bruker CryoProbe Prodigy H/F-C/N-D probe operating at 500.13 MHz for ^1H and 470.55 MHz for ^{19}F with a 6.6 G/mm z -gradient. Samples were maintained at 25°C and at least 30 mins was allowed for each sample to thermally equilibrate before any measurements were made. The diffusion coefficients were measured with a stimulated echo sequence with one spoil gradient. The diffusion time (Δ) and the gradient pulse length (δ) were optimised for each sample; Δ was either 50 or 100 ms while δ was between 1 and 10 ms. Gradient pulses were smoothed square chirp shape. Experiments were performed as Pseudo-2D with a linear variation of the gradient from 2 to 95% of maximum intensity in 32 steps. The PGSE-NMR data were processed and the peak areas (integrals) were used to fit the following equation to determine the diffusion coefficient:

$$I = I_0 \exp(-D(2\pi\gamma G\delta)^2 \left(\frac{\Delta - \delta}{3}\right)) \quad (2.6)$$

where I is the signal intensity, I_0 is the initial intensity, γ is the gyromagnetic ratio (4258 s⁻¹ G⁻¹ for ^1H and 4005 s⁻¹ G⁻¹ for ^{19}F) and G is the gradient strength.

References

- (1) Holbrey, J. D.; Reichert, W. M.; Swatoski, R. P.; Broker, G. A.; Pitner, W. R.; Seddon, K. R.; Rogers, R. D., Efficient, Halide Free Synthesis of New, Low Cost Ionic Liquids: 1,3-Dialkylimidazolium Salts Containing Methyl- and Ethyl-Sulfate Anions *Green Chem.* **2002**, *4*, 407-413.
- (2) Baker, L. J.; Bott, R. C.; Bowmaker, G. A.; Healy, P. C.; Skelton, B. W.; Schwerdtfeger, P.; White, A. H., Structural, Far-infrared and P-31 Nuclear-Magnetic-Resonance Studies of 2-Co-ordinate Complexes of Tris(2,4,6-trimethoxyphenyl)Phosphine with Gold(I) Halides. *J. Chem. Soc.-Dalton Trans.* **1995**, 1341-1347.
- (3) Ohtsuka, I.; Nakayama, H.; Ishii, K., Raman-Spectra of the Tetrabutylammonium Diiodaurate(I) Crystal, TBA-AuI₂, Without I₃⁻ impurity Bands. *J. Raman Spectrosc.* **1989**, *20*, 489-492.
- (4) Lind, C. J.; Warren, C. A. Production of 1, 4-dinitro-2, 3, 5, 6-tetraalkylbenzenes. 1964.
- (5) McDonagh, A. M.; Powell, C. E.; Morrall, J. P.; Cifuentes, M. P.; Humphrey, M. G., Convergent Synthesis of Alkynylbis(Bidentate Phosphine)Ruthenium Dendrimers. *Organometallics* **2003**, *22*, 1402-1413.
- (6) Liu, B., 6.3.2 - Platinum and Gold Inlaid Disks ≤5 μm Diameter. In *Handbook of Electrochemistry*, Zoski, C. G., Ed. Elsevier: Amsterdam, 2007; p 197-199.
- (7) Gritzner, G.; Kuta, J., Recommendations on Reporting Electrode-Potentials in Nonaqueous Solvents. *Pure Appl. Chem.* **1984**, *56*, 461-466.
- (8) Stojanovic, R. S.; Bond, A. M., Examination of Conditions under Which the Reduction of the Cobaltocenium Cation Can Be Used as a Standard Voltammetric Reference Process in Organic and Aqueous Solvents. *Anal. Chem.* **1993**, *65*, 56-64.
- (9) Mahon, P. J.; Oldham, K. B., Convolution Modelling of Electrochemical Processes Based on the Relationship Between the Current and the Surface Concentration. *J. Electroanal. Chem.* **1999**, *464*, 1-13.
- (10) Bentley, C. L.; Bond, A. M.; Hollenkamp, A. F.; Mahon, P. J.; Zhang, J., Applications of Convolution Voltammetry in Electroanalytical Chemistry. *Anal. Chem.* **2014**, *86*, 2073–2081.
- (11) Bentley, C. L.; Bond, A. M.; Hollenkamp, A. F.; Mahon, P. J.; Zhang, J., Electrode Reaction and Mass-Transport Mechanisms Associated with the Iodide/Triiodide Couple in

the Ionic Liquid 1-Ethyl-3-methylimidazolium Bis(trifluoromethanesulfonyl)imide. *J. Phys. Chem. C* **2014**, *118*, 29663–29673.

(12) Bard, A. J.; Faulkner, L. R., *Electrochemical Methods : Fundamentals and Applications*. 2nd ed.; Wiley: New York, 2001.

(13) Swain, G. M., 5 - Solid Electrode Materials: Pretreatment and Activation. In *Handbook of Electrochemistry*, 1st ed.; Zoski, C. G., Ed. Elsevier: Amsterdam, 2007; p 111-153.

(14) Bentley, C. L.; Bond, A. M.; Hollenkamp, A. F.; Mahon, P. J.; Zhang, J., Mass Transport Studies and Hydrogen Evolution at a Platinum Electrode Using Bis(trifluoromethanesulfonyl)imide as the Proton Source in Ionic Liquids and Conventional Solvents. *J. Phys. Chem. C* **2014**, *118*, 22439–22449.

(15) de Levie, R., *How to Use Excel® in Analytical Chemistry and in General Scientific Data Analysis*. Cambridge University Press: Cambridge, 2001.

(16) Oldham, K. B.; Myland, J. C., *Fundamentals of Electrochemical Science*. Academic Press: San Diego, 1994.

(17) de Levie, R. Excellaneous. <http://www.bowdoin.edu/~rdelevie/excellaneous/> (accessed March 11, 2015).

(18) Oldham, K. B., Convolution: A General Electrochemical Procedure Implemented by a Universal Algorithm. *Anal. Chem.* **1986**, *58*, 2296-2300.

(19) Aoki, K.; Osteryoung, J., Formulation of the Diffusion-controlled Current at Very Small Stationary Disk Electrodes. *J. Electroanal. Chem.* **1984**, *160*, 335-339.

(20) Rudolph, M., Digital Simulations with the Fast Implicit Finite-Difference (FIFD) Algorithm .2. An Improved Treatment of Electrochemical Mechanisms with 2nd-Order Reactions. *J. Electroanal. Chem.* **1992**, *338*, 85-98.

(21) Rudolph, M., Digital Simulations on Unequally Spaced Grids. Part 3. Attaining Exponential Convergence for the Discretisation Error of the Flux as a New Strategy in Digital Simulations of Electrochemical Experiments. *J. Electroanal. Chem.* **2004**, *571*, 289-307.

(22) Rudolph, M., Attaining Exponential Convergence for the Flux Error with Second- and Fourth-Order Accurate Finite-Difference Equations. Part 3. Application to Electrochemical Systems Comprising Second-Order Chemical Reactions. *J. Comput. Chem.* **2005**, *26*, 1193-1204.

(23) Rudolph, M., Attaining Exponential Convergence for the Flux Error with Second- and Fourth-Order Accurate Finite-Difference Equations. I. Presentation of the Basic Concept and Application to a Pure Diffusion System. *J. Comput. Chem.* **2005**, *26*, 619-632.

(24) Rudolph, M., Attaining Exponential Convergence for the Flux Error with Second- and Fourth-Order Accurate Finite-Difference Equations. II. Application to Systems Comprising First-Order Chemical Reactions. *J. Comput. Chem.* **2005**, *26*, 633-641.

(25) Sauerbrey, G., Verwendung Von Schwingquarzen Zur Wagung Dunner Schichten Und Zur Mikrowagung. *Zeitschrift Fur Physik* **1959**, *155*, 206-222.

(26) Snook, G. A.; Bond, A. M.; Fletcher, S., The Use of Massograms and Voltammograms for Distinguishing Five Basic Combinations of Charge Transfer and Mass Transfer at Electrode Surfaces. *J. Electroanal. Chem.* **2002**, *526*, 1-9.

3. Electroanalytical Applications of Semiintegral and Convolution Voltammetry in Ionic Liquid Media

This chapter is concerned with the development of electroanalytical methodology which is suitable for quantifying the parameters associated with an electrochemical system (*i.e.*, D , n and/or C) under highly viscous conditions. Semiintegral voltammetry is a powerful and robust electroanalytical method, which has not been widely adopted in the literature. My studies revealed that this method is applicable under highly viscous conditions, where the direct use of conventional steady-state and transient voltammetry is severely limited. Further detail can be found in the following publication:

Bentley, C. L.; Bond, A. M.; Hollenkamp, A. F.; Mahon, P. J.; Zhang, J., *Anal. Chem.* **2012**, *85*, 2239-2245.

Semiintegral voltammetry is a subset of a range of techniques collectively known as convolution voltammetry. Following on from the previous study, electroanalytical applications of the more general convolution procedure were explored in a range of electrolyte media, including ionic liquids. Further detail can be found in the following publication:

Bentley, C. L.; Bond, A. M.; Hollenkamp, A. F.; Mahon, P. J.; Zhang, J., *Anal. Chem.* **2014**, *86*, 2073–2081.

After publication, the findings from these research articles were summarized in a review-style article, titled “*Electroanalytical Applications of Semiintegral and Convolution Voltammetry in Room Temperature Ionic Liquids*“, which has been accepted for publication as a book chapter in the Springer book “*Electrochemistry in Ionic Liquids*”.

Part B: Specific Declaration

Monash University

Declaration for Thesis Chapter 3**Declaration by candidate**

In the case of Chapter 3, the nature and extent of my contribution to the work was the following:

Nature of contribution	Extent of contribution (%)
Experimental work, Manuscript writing/preparation	100%

The following co-authors contributed to the work. If co-authors are students at Monash University, the extent of their contribution in percentage terms must be stated:

Name	Nature of contribution	Extent of contribution (%) for student co-authors only
Cameron L. Bentley	Experimental work, manuscript writing/preparation, editing.	100%
Alan M. Bond	Supervision, proof-reading, editing.	
Anthony F. Hollenkamp	Supervision, proof-reading, editing.	
Peter J. Mahon	Supervision, proof-reading, editing.	
Jie Zhang	Supervision, proof-reading, editing.	

The undersigned hereby certify that the above declaration correctly reflects the nature and extent of the candidate's and co-authors' contributions to this work*.

Candidate's
Signature

	Date 02/03/2015
---	--------------------

Main
Supervisor's
Signature

	Date 02/03/2015
---	--------------------

Advantages Available in the Application of the Semi-Integral Electroanalysis Technique for the Determination of Diffusion Coefficients in the Highly Viscous Ionic Liquid 1-Methyl-3-Octylimidazolium Hexafluorophosphate

Cameron L. Bentley,^{†,‡} Alan M. Bond,^{*,‡} Anthony F. Hollenkamp,[‡] Peter J. Mahon,[§] and Jie Zhang^{*,†}

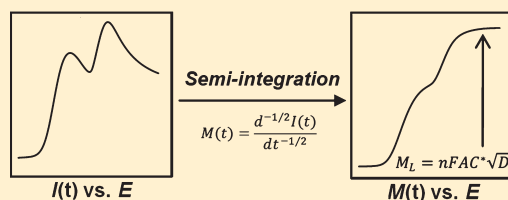
[†]School of Chemistry, Monash University, Clayton, Victoria 3800, Australia

[‡]CSIRO Energy Technology, Box 312, Clayton South, Victoria 3169, Australia

[§]Faculty of Life and Social Sciences, Swinburne University of Technology, Hawthorn, Victoria 3122, Australia

Supporting Information

ABSTRACT: While it is common to determine diffusion coefficients from steady-state voltammetric limiting current values, derived from microelectrode/rotating disk electrode measurements or transient peak currents at macroelectrodes, application of these methods is problematic in highly viscous ionic liquids. This study shows that the semi-integral electroanalysis technique is highly advantageous under these circumstances, and it has allowed the diffusion coefficient of cobaltocenium, $[\text{Co}(\text{Cp})_2]^+$ (simple redox process), and iodide, I^- (complex redox mechanism), to be determined in the highly viscous ionic liquid 1-methyl-3-octylimidazolium hexafluorophosphate (viscosity = 866 cP at 20 °C) from transient voltammograms obtained using a 1.6 mm diameter Pt electrode. In such a viscous medium, a near-steady-state current is not attainable with a 10 μm diameter microdisk electrode or a 3 mm diameter Pt rotating disk electrode, while peak currents at a macrodisk are subject to ohmic drop problems and the analysis is hampered by difficulties in modeling the processes involved in the oxidation of iodide. The diffusion coefficients of $[\text{Co}(\text{Cp})_2]^+$ and I^- were determined to be $9.4 (\pm 0.3) \times 10^{-9} \text{ cm}^2 \text{ s}^{-1}$ and $7.3 (\pm 0.3) \times 10^{-9} \text{ cm}^2 \text{ s}^{-1}$, respectively. These results highlight the utility of the semi-integral electroanalysis technique for quantifying the diffusivity of electroactive species in high viscosity media, where the use of steady-state techniques and transient peak currents is often limited.



In recent years, there has been growing interest in replacing volatile molecular solvents with room temperature ionic liquids (RTILs) in a range of applications. Although the only truly ubiquitous property of RTILs is intrinsic ionic conductivity,¹ nonhaloaluminate ionic liquids often possess a number of attractive qualities, including negligible vapor pressure and high chemical, electrochemical, and thermal stability.² The physicochemical properties of a particular RTIL are determined by its constituent anion/cation and can therefore be tailored to suit specific applications.³ One research area where RTILs have found application is in electrochemistry, where they have been successfully employed as alternative electrolytes in a range of electrochemical devices, including dye-sensitized solar cells, lithium batteries, and supercapacitors.^{2,4,5}

The investigation and quantification of mass-transport (in the present case diffusivity) is of interest in any solvent, especially those employed in electrochemical devices, as it influences the ultimate rate/speed at which the device can operate. Potential sweep⁶ or potential step⁷ techniques are often employed to quantify the diffusivity of electroactive species in RTILs. In low viscosity molecular solvents, steady-state techniques, such as ultramicroelectrode (UME) voltammetry or rotating disk electrode (RDE) voltammetry, are

generally advantageous over transient techniques as the measured steady-state mass transport limited currents are unaffected by sluggish electrode kinetics and/or high levels of uncompensated resistance. This allows the diffusion coefficient of the electroactive species to be determined using well-established theories.⁸

The viscosities of RTILs are typically 10–10 000 times higher than conventional molecular solvent (electrolyte) media. As a result, mass transport is significantly slower in RTILs, with diffusion coefficients often being in the range of 10^{-7} to $10^{-9} \text{ cm}^2 \text{ s}^{-1}$ compared to 10^{-5} to $10^{-6} \text{ cm}^2 \text{ s}^{-1}$ in molecular solvents. Consequently, in RTIL electrolytes, especially those with high viscosity, it is much more difficult to achieve a true steady state (at a disk UME), preventing the diffusion coefficient from being determined from the mass transport limited current.^{9,10} It has also been shown that the RDE method suffers from similar problems,^{10,11} arising from the difficulty in rotating the electrode at the sufficiently high rates

Received: October 18, 2012

Accepted: December 18, 2012

Published: December 18, 2012

that are needed to achieve steady state under the highly viscous conditions.

In principle, diffusion coefficients can be calculated from the peak current of a dc linear sweep or cyclic voltammogram by employing the relationships described by the Randles–Sevcik equation for a reversible electron transfer process of the kind $\text{Ox} + ne^- \rightleftharpoons \text{Red}$ when the effect of uncompensated resistance is negligible.⁸ In reality, very few of the electrochemical systems of interest in a viscous RTIL fulfill these criteria, limiting the direct application of dc voltammetry in the determination of diffusivity. Semi-integral electroanalysis is a technique pioneered by Oldham,^{12–16} with semi-integration being specific for semi-infinite planar diffusion. It is related to the more general convolution procedure initially described by Savéant and co-workers¹⁷ and later extended to other electrode geometries.¹⁸ The technique involves semi-integrating the measured current with respect to time, giving rise to the function, $M(t)$, which is related to the concentration of the electroactive species at the electrode surface.

$$M(t) = \frac{d^{-1/2}I(t)}{dt^{-1/2}} \quad (1)$$

Semi-integrating a peak-shaped transient voltammogram ($I-E$) gives rise to a sigmoidal $M-E$ curve resembling a steady-state voltammogram.⁸ As described in the theory of semi-integral electroanalysis, under purely diffusion controlled conditions (i.e., the concentration of analyte at the electrode surface is equal to zero), $M(t)$ reaches its limiting or maximum value, M_L :

$$M_L = nAFC^* \sqrt{D} \quad (2)$$

The diffusion coefficient, D , can therefore be determined from the M_L plateau by transposing eq 2 if the stoichiometric number of electrons, n , active electrode area, A , and bulk concentration of electroactive species, C^* , are known along with the use of Faraday's constant, F .^{8,13} The semi-integral electroanalysis technique shares a number of advantages with the previously discussed steady-state techniques without the need to record experimental data under steady-state conditions.

To demonstrate the advantage of using the semi-integral electroanalysis technique, this study aims to quantify diffusivity in a highly viscous RTIL, 1-methyl-3-octylimidazolium hexafluorophosphate, $[\text{C}_8\text{mim}][\text{PF}_6]$ ($\eta = 866$ cP at 20 °C¹⁹), where the use of UME or RDE methods is impractical due to the difficulty in achieving a true steady state and IR_u drop compromises peak current measurements with transient techniques at macrodisk electrodes. Two redox active species were the subject of investigations: cobaltocenium, $[\text{Co}(\text{Cp})_2]^+$ ($\text{Cp}^- = \text{C}_5\text{H}_5^-$), which is known to undergo a mechanistically simple and electrochemically reversible one-electron reduction in RTILs⁶ and iodide, I^- , which is known to undergo two oxidation processes with various degrees of reversibility in RTILs.^{20–22}

EXPERIMENTAL SECTION

Reagents. 1-Methyl-3-octylimidazolium hexafluorophosphate ($[\text{C}_8\text{mim}][\text{PF}_6]$, Solvent Innovation) was dried under high vacuum ($\leq 10^{-2}$ mbar) at 45 °C for 48 h and stored under lithium. The residual water was less than 25 ppm by Karl Fischer titration (Metrohm 831 KF Coulometer). 1-Ethyl-3-methylimidazolium iodide ($[\text{C}_2\text{mim}]\text{I}$, Io-li-tec GmbH, >98%) was recrystallized from a 2:1 mixture of ethyl acetate (Merck) and isopropanol (Merck) and then dried under high vacuum

for 48 h. Care was taken during handling and storage of $[\text{C}_2\text{mim}]\text{I}$ to avoid exposure to light. Cobaltocenium hexafluorophosphate ($[\text{Co}(\text{Cp})_2][\text{PF}_6]$, Sigma-Aldrich) was used as supplied by the manufacturer. Acetonitrile was dried over activated alumina (Al_2O_3). Tetrabutylammonium hexafluorophosphate (TBAPF₆, Sigma) was dried under vacuum at 80 °C for 24 h. Ferrocene ($[\text{Fe}(\text{Cp})_2]$, Fluka, >98%) and acetone (Merck) were used as supplied by the respective manufacturers. All of the above chemicals were stored and handled under a dry argon atmosphere in a glovebox.

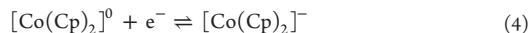
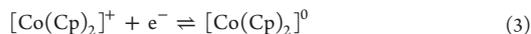
Electrochemical Systems and Procedures. All voltammetric experiments were undertaken with a Gamry Reference 600 Potentiostat/Galvanostat/ZRA (Gamry Instruments, Warminster, PA). All experiments were carried out at ambient temperature (24 ± 1 °C). The solutions were degassed for at least 30 min with N_2 prior to experimentation and a blanket of N_2 was maintained over the electrolytes during the respective experiments. Microelectrode experiments were carried out inside a faraday cage using a 2-electrode arrangement with an Ag-wire quasi-reference electrode. Stationary macroelectrode and RDE experiments were carried out using a standard 3-electrode arrangement with a platinum flag auxiliary electrode and an Ag-wire or a Pt-wire quasi-reference electrode. All voltammetric measurements were carried out in at least triplicate. After performing the required voltammetric scans, the potential of the quasi-reference electrode was calibrated against the recommended $[\text{Fe}(\text{Cp})_2]^{0/+}$ or $[\text{Co}(\text{Cp})_2]^{+/0}$ process.^{23,24}

The platinum macroelectrode (nominal diameter = 1.6 mm) and platinum UME (nominal diameter = 10 μm) were purchased from BASi (Bioanalytical systems, West Lafayette, IN) with the platinum rotating disk electrode (nominal diameter = 3.0 mm) purchased from Metrohm (Herisau, Switzerland). Prior to each new series of experiments, the pertinent electrodes were polished with aqueous 0.05 μm alumina slurry (Kemet Ltd., Kent, UK) on a clean polishing cloth (Buehler, Lake Bluff, IL). To remove adherent alumina, the electrodes were rinsed thoroughly with deionized water, rinsed with acetone, and allowed to dry at ambient temperature. Consistency of the electrode surfaces was checked using an optical microscope. The effective electrochemical area of the platinum macroelectrode was determined to be 0.0215 cm^2 by measuring the peak current obtained as a function of scan rate under linear sweep voltammetric conditions for the oxidation of $[\text{Fe}(\text{Cp})_2]$ (2.0 mM in acetonitrile [0.1 M TBAPF₆]) and the use of the Randles–Sevcik equation [see eq 7]. The diffusion coefficient of $[\text{Fe}(\text{Cp})_2]$ was taken to be 2.24×10^{-5} $\text{cm}^2 \text{s}^{-1}$ under these conditions as published.⁷

Voltammetric simulations were undertaken using the DigiElch software (v. 4.0, Elchsoft, Germany). The algorithm used for semi-integration of the $I-t$ data was from de Levie,²⁵ which was adapted from Oldham and Myland.²⁶ A Microsoft Excel macro including this algorithm is available free online.²⁷ Experimental uncertainties were estimated by propagation of the standard deviations in the variables of interest.²⁸

RESULTS AND DISCUSSION

$[\text{Co}(\text{Cp})_2]^{+/0}$ Process. The $[\text{Co}(\text{Cp})_2]^{+/0}$ process has been characterized in a range of molecular solvents and RTILs and has been demonstrated to be a broadly useful reference scale by Bond and co-workers.²⁹ In some molecular solvents and RTILs, the $[\text{Co}(\text{Cp})_2]^+$ cation has been shown to undergo two reversible one-electron reduction processes:



The second reduction process, $[\text{Co}(\text{Cp})_2]^{0/-}$, is reportedly solvent dependent,²³ and for this reason, only the first process was the subject of investigations in this study.

Ultramicroelectrode Studies. In principle, the diffusion coefficient (D) of an electroactive species can be calculated from the steady-state limiting current (I_L) measured at a disk UME using the expression:⁵

$$I_L = 4nFC^*aD \quad (5)$$

where a is the radius of the electrode. A cyclic voltammogram obtained from 9.96 mM $[\text{Co}(\text{Cp})_2][\text{PF}_6]$ in $[\text{C}_8\text{mim}][\text{PF}_6]$ at a 10 μm diameter Pt UME is shown in Figure 1. The waveshape

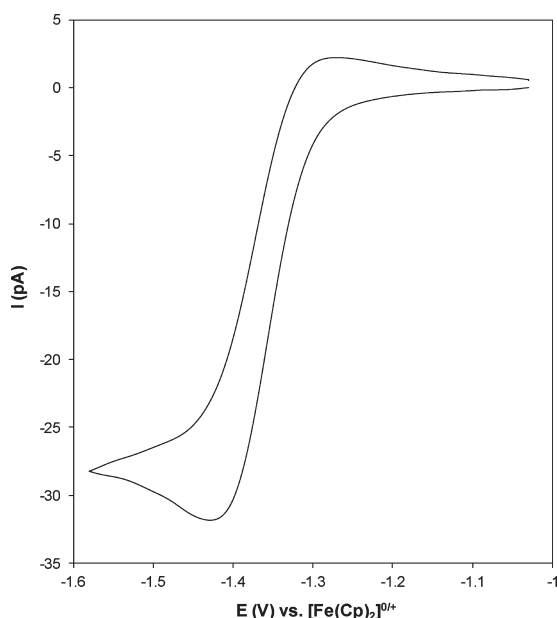


Figure 1. Cyclic voltammogram obtained from 9.96 mM $[\text{Co}(\text{Cp})_2][\text{PF}_6]$ in $[\text{C}_8\text{mim}][\text{PF}_6]$ at a 5 μm radius Pt UME with a scan rate of 5 mV s^{-1} .

in this RTIL is intermediate between a sigmoidal and a peak-shaped voltammogram, implying that radial diffusion contributes significantly to mass transport. Despite the small electrode size ($a = 5 \mu\text{m}$) and slow voltammetric scan rate (5 mV s^{-1}), even near steady-state conditions have not been attained and for this reason calculating the diffusion coefficient using eq 5 is not possible. Attempting to extract a “limiting current” from a voltammogram obtained under these mixed transient/steady-state conditions leads to an overestimate of the true steady-state limiting current.³⁰ The true steady-state current could be predicted using a procedure known as convolutive forecasting; however, in order to apply the convolving function, it is necessary to know the values of D and a , whereas semi-integration only requires the current.³¹ Alternatively, the diffusion coefficient could be estimated from this mixed transient/steady-state voltammogram using a “best-fit” approach via numerical simulation with DigiElch.

In principle, in order to approach a true steady state, either a much smaller electrode or a slower scan rate can be employed. However, these approaches are generally impractical due to the high viscosity of RTILs which can result in a diffusion coefficient of the order of $10^{-9} \text{ cm}^2 \text{ s}^{-1}$. Under these conditions, an impractically small electrode (difficulty in both electrode fabrication and current measurement) or slow scan rate would have to be used for true steady-state measurements (see detailed discussion in the Supporting Information section).

Rotating Disk Electrode Studies. In theory, the diffusion coefficient of an electroactive species can also be calculated from the steady-state limiting current measured at the RDE using the Levich equation:²⁶

$$I_L = 0.620nFA \left(\frac{d}{\eta} \right)^{1/6} D^{2/3} \omega^{1/2} C^* \quad (6)$$

where d is the density of the electrolyte, η is the dynamic viscosity of the electrolyte, and ω is the angular rotation rate of the electrode. Cyclic voltammograms obtained from 10.1 mM $[\text{Co}(\text{Cp})_2][\text{PF}_6]$ in $[\text{C}_8\text{mim}][\text{PF}_6]$ at a 3.0 mm diameter Pt RDE are shown in Figure 2. The waveshape in this RTIL at 500

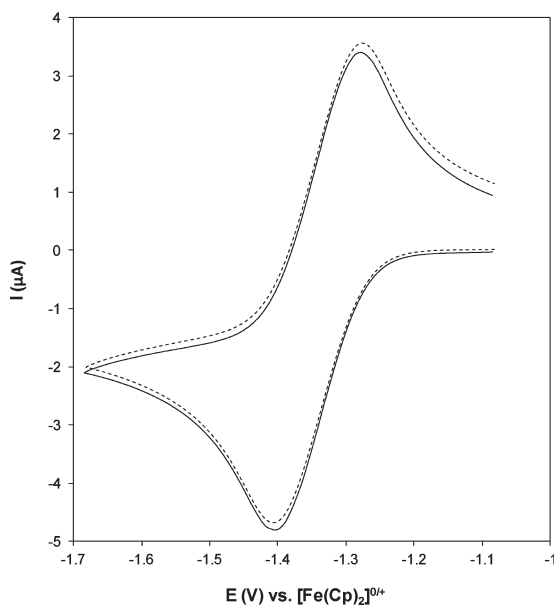


Figure 2. Cyclic voltammograms obtained from 10.1 mM $[\text{Co}(\text{Cp})_2][\text{PF}_6]$ in $[\text{C}_8\text{mim}][\text{PF}_6]$ at a 1.5 mm radius Pt RDE with a scan rate of 50 mV s^{-1} and rotation speeds of 0 rpm (dashed trace) and 500 rpm (solid trace).

rpm is almost identical to when the electrode is stationary (0 rpm) implying that mass transport is governed predominantly by planar diffusion at this rotation speed, accentuating the fact that forced convection is relatively ineffective in high viscosity fluids. Once again, because steady-state conditions have not been attained, the diffusion coefficient cannot be calculated using eq 6 and would have to be estimated using a “best-fit” approach with numerical simulation.

In principle, in order to approach a true steady state, much higher rotation speeds could be employed. In practice, however, this approach is not feasible, as it was found that air bubbles

become trapped at the electrode–electrolyte interface at high rotation speeds (>500 rpm), giving rise to noisy and irreproducible current data (see Figure S2, Supporting Information). Similar problems were encountered by Zhao et al.¹¹ when performing RDE experiments in a range of high viscosity room temperature protic ionic liquids (RTPILs). Simulations revealed that rotation speeds in excess of 5000 rpm would be required to approach a true steady state in RTPILs with viscosities that are lower than that of [C₈mim][PF₆].

Macrodisc Electrode Studies. In light of the practical difficulties in approaching true steady-state conditions in [C₈mim][PF₆], transient voltammetric techniques were applied in order to quantify the diffusivity of [Co(Cp)₂]⁺ in this RTIL. Since [Co(Cp)₂]⁺⁰ is a well-known reversible process, *D* can be calculated from the transient peak current (*I*_p) using the Randles–Sevcik equation when the *IR*_u effect is negligible:⁸

$$I_p = 0.4463nFA \left(\frac{nFD\nu}{RT} \right)^{1/2} C^* \quad (7)$$

where *R* is universal gas constant, ν is the voltammetric scan rate, and *T* is the temperature.

Cyclic voltammograms obtained from 9.96 mM [Co(Cp)₂]-[PF₆] in [C₈mim][PF₆] at multiple scan rates at a Pt macroelectrode are shown in Figure 3a. As expected, a chemically reversible reduction process corresponding to eq 3 was observed at all of the investigated scan rates. Peak separations (ΔE_p) were larger than the expected 56.8 mV for a reversible process at 24 °C and increased significantly with increasing scan rate with values of 67, 83, and 100 mV at 10, 25, and 50 mV s⁻¹, respectively. Given that it has been demonstrated that the [Co(Cp)₂]⁺⁰ process displays ideal electrochemical reversibility in a range of molecular solvents²³ and RTILs,^{6,32} the large ΔE_p values are likely due to the effect of uncompensated resistance (*IR*_u). On the basis of the geometry of the electrode (*a* = 0.8 cm) and the ionic conductivity (κ) of [C₈mim][PF₆], 0.26 mS cm⁻¹ at 25 °C,³³ uncompensated resistance is estimated ($R_u \approx 1/4\kappa r$)³⁴ to be ~12 kΩ, which accounts for the significant distortion seen in the voltammograms shown in Figure 3a.

The peak current is predicted to be proportional to the square root of scan rate, which was not the case for the data shown in Figure 3a, evidenced by the nonzero intercept of the linear plot shown in Figure 3b. Nevertheless, the diffusion coefficient of [Co(Cp)₂]⁺ was determined to be 7.6 (±0.2) × 10⁻⁹ cm² s⁻¹ from the slope of the *I*_p vs $\nu^{1/2}$ curve, obtained by linear regression of the experimental data, by substituting the appropriate values of known parameters into eq 7. As expected, the calculated diffusion coefficient of [Co(Cp)₂]⁺ in [C₈mim]-[PF₆] is orders of magnitude lower than that reported in acetonitrile, 1.64 × 10⁻⁵ cm² s⁻¹ at 23 °C³² and [C₂mim]-[NTf₂], 3.27 × 10⁻⁷ cm² s⁻¹ at 23 °C⁶ in accordance with the relative viscosities of the respective solvents. However, it should be noted that, due to the presence of significant *IR*_u effect, the diffusion coefficient obtained on the basis of peak current and application of eq 7 is expected to be smaller than the true value with the presence of uncompensated resistance resulting in a nonzero intercept in Figure 3b. Forcing the linear line of best fit through the origin lowers the coefficient of determination (*R*² = 0.9968) and changes the slope of the *I*_p vs $\nu^{1/2}$ curve, demonstrating that this approach is unsuitable under the circumstances. In order to obtain a more accurate *D* value, numerical simulations that accommodate the contribution from

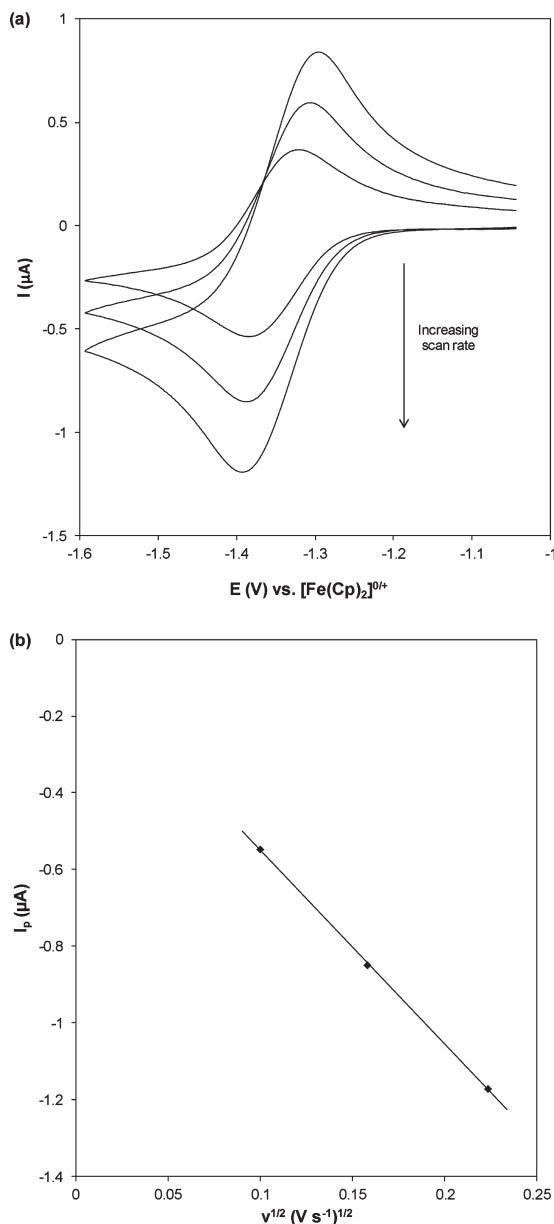


Figure 3. (a) Cyclic voltammograms obtained from 9.96 mM [Co(Cp)₂][PF₆] in [C₈mim][PF₆] at a 0.8 mm radius Pt macroelectrode with scan rates (from top to bottom) of 50, 25, and 10 mV s⁻¹. (b) Linear plot of mean peak current (from triplicate experiments) vs the square root of the scan rate (*R*² = 0.9998).

*R*_u were undertaken and a *D* value of 9.0 (±0.2) × 10⁻⁹ cm² s⁻¹ was obtained from simulation/experiment comparison (see Figure S3, Supporting Information). This is significantly greater than the value obtained from the direct use of the peak currents and demonstrates the effect of uncompensated resistance when using peak currents to estimate the diffusion coefficient.

Semi-integral Analysis Studies. The semi-integral electroanalysis technique is unaffected by sluggish electrode kinetics or

I_{R_u} and does not require comparison with a simulation, making it preferable to the Randles–Sevcik method. M – E curves before and after background subtraction for the $[\text{Co}(\text{Cp})_2]^{+/0}$ process are shown in Figure 4. As can be seen in this figure,

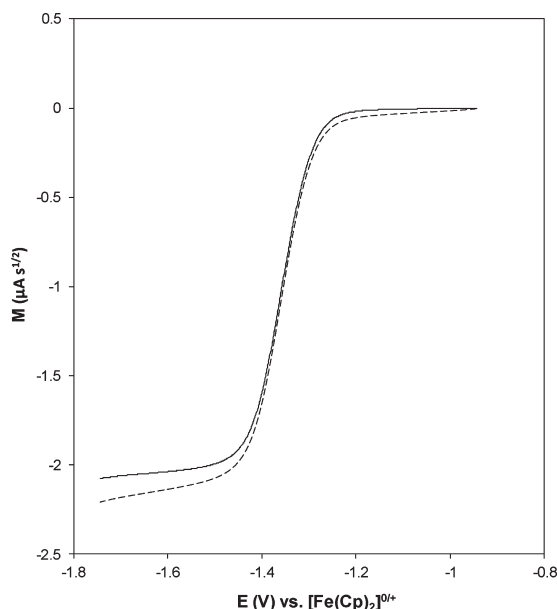


Figure 4. M – E curves obtained from 9.96 mM $[\text{Co}(\text{Cp})_2][\text{PF}_6]$ in $[\text{C}_8\text{mim}][\text{PF}_6]$ at a 0.8 mm radius Pt macroelectrode with a scan rate of 50 mV s^{-1} before (dashed curve) and after (solid curve) background subtraction.

there is a significant slope in the M_L plateau prior to background subtraction, which can be attributed to charging of the electrical double layer at the stationary electrode. At the analyte concentration used, the contribution from double layer charging current to the total current can be significant. If the double layer capacitance is potential independent, the M_C – E (M_C = semi-integration of capacitance current) curve will not be potential independent as the semi-integration of a constant introduces a $t^{1/2}$ dependence. This becomes more complicated when the capacitance is potential dependent.¹³ Therefore, the background current was measured in the absence of $[\text{Co}(\text{Cp})_2]^+$ and subtracted from the total current. The diffusion coefficient of $[\text{Co}(\text{Cp})_2]^+$ was then determined to be $9.4 (\pm 0.3) \times 10^{-9} \text{ cm}^2 \text{ s}^{-1}$ using the M_L value taken at -1.55 V vs $[\text{Fe}(\text{Cp})_2]^{0/+}$ and by substituting the appropriate values into eq 2. This D value is in good agreement with that of $9.0 (\pm 0.2) \times 10^{-9} \text{ cm}^2 \text{ s}^{-1}$ obtained using transient cyclic voltammetry with numerical simulation.

$I^-/I_3^-/I_2$ Processes. Semi-integral Analysis Studies. Analogous to its behavior in aprotic solvents such as acetonitrile,^{35,36} iodide has been shown to undergo two oxidation processes in a range of RTILs to produce molecular iodine as per eqs 8 and 9:^{8,14,24}



The reaction mechanism is complicated by the following homogeneous equilibrium process:



Overall, it is a one-electron per iodine atom process with much greater mechanistic complexity than the previously investigated $[\text{Co}(\text{Cp})_2]^{+/0}$ process.

Cyclic voltammograms obtained from 14.3 mM $[\text{C}_2\text{mim}]\text{I}$ in $[\text{C}_8\text{mim}][\text{PF}_6]$ at multiple scan rates at a Pt macroelectrode are shown in Figure 5. At all of the investigated scan rates, there are

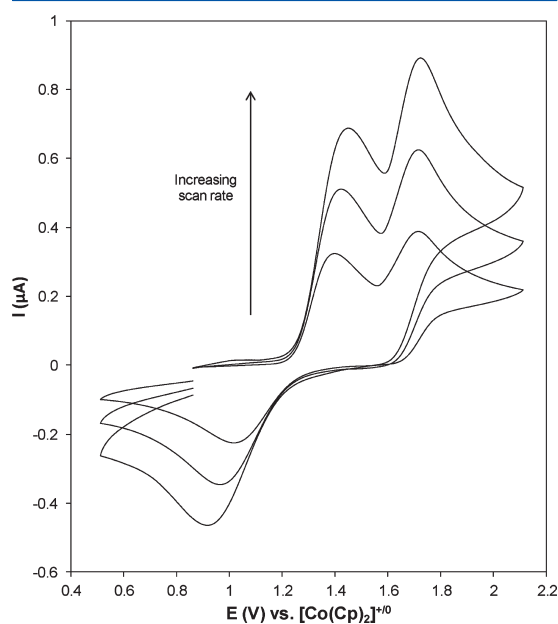


Figure 5. Cyclic voltammograms obtained from 14.3 mM $[\text{C}_2\text{mim}]\text{I}$ in $[\text{C}_8\text{mim}][\text{PF}_6]$ at a 0.8 mm radius Pt macroelectrode with scan rates (from top to bottom) of 50, 25, and 10 mV s^{-1} .

two peaks on the forward sweep, corresponding to the I^-/I_3^- and I_3^-/I_2 processes shown in eqs 8 and 9, respectively. On the reverse sweep, the reduction peak for the I_2/I_3^- process, eq 9, is not well-defined, and the reduction peak associated with the I_3^-/I^- process, eq 8, is asymmetric with respect to the oxidation peak, with large ΔE_p values of 383, 460, and 536 mV at 10, 25, and 50 mV s^{-1} , respectively. Indeed, the first oxidation process has been reported to be kinetically sluggish and electrochemically irreversible in a range of imidazolium RTILs.^{20–22}

The mechanistic complexity and sluggish heterogeneous kinetics of the iodide oxidation process precludes the direct application of the relationship described by the Randles–Sevcik equation and the use of numerical simulation to quantify diffusivity. Consequently, the semi-integral electroanalysis technique was applied; M – E curves before and after background subtraction obtained from 14.3 mM $[\text{C}_2\text{mim}]\text{I}$ in $[\text{C}_8\text{mim}][\text{PF}_6]$ are shown in Figure 6. There are two plateaus on the M – E curve corresponding to the I^-/I_3^- and I_3^-/I_2 processes shown in eqs 8 and 9, respectively. The size of the plateaus relative to each other are expected to be proportional to the number of electrons involved in each redox process (2:1); however, it is difficult to accurately measure the magnitude of the first plateau due to overlap caused by the

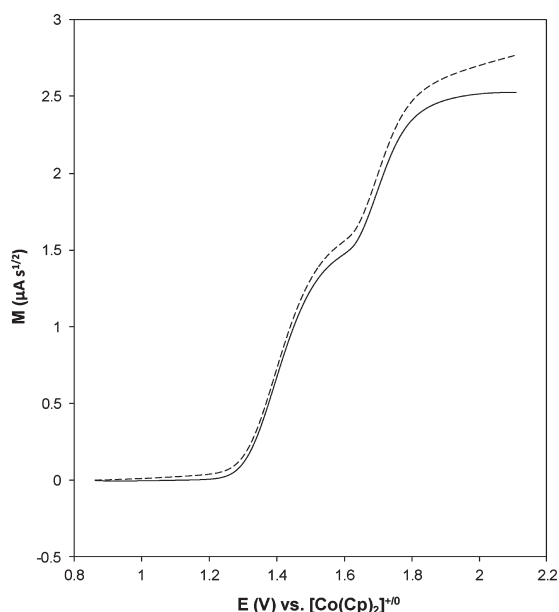


Figure 6. M - E curves obtained from 14.3 mM $[\text{C}_2\text{mim}]\text{I}$ in $[\text{C}_8\text{mim}][\text{PF}_6]$ at a 0.8 mm radius Pt macroelectrode with a scan rate of 50 mV s^{-1} before (dashed curve) and after (solid curve) background subtraction.

closeness of half-wave potentials, resulting in the observation of a $\sim 3:2$ ratio. Attempting to extract a M_L value from such a poorly defined “plateau” would inevitably lead to an inaccurate determination of D . Once again, there is quite a significant slope in the M_L plateau prior to background subtraction, which was corrected for in the same way as previously described. The diffusion coefficient of I^- was determined to be $7.3 (\pm 0.3) \times 10^{-9} \text{ cm}^2 \text{ s}^{-1}$ using the M_L value taken at 2.0 V vs $[\text{Co}(\text{Cp})_2]^{+/0}$ and by substituting the appropriate values into eq 2. Unsurprisingly, the calculated diffusion coefficient of I^- in $[\text{C}_8\text{mim}][\text{PF}_6]$ is orders of magnitude lower than that reported in acetonitrile, $1.68 \times 10^{-5} \text{ cm}^2 \text{ s}^{-1}$ at 25°C ,³⁶ and $[\text{C}_2\text{mim}][\text{NTf}_2]$, $2.68 \times 10^{-7} \text{ cm}^2 \text{ s}^{-1}$ at 25°C ³⁷ in accordance with the relative viscosities of the respective electrolytes.

Microelectrode measurements in this system again do not approach the near-steady-state condition, and RDE methods cannot be used for the reasons noted above. The determination of the diffusion coefficients of both $[\text{Co}(\text{Cp})_2]^+$ and I^- using transient techniques without resorting to numerical simulation is therefore highly advantageous.

CONCLUSIONS

The relative merits of several voltammetric methods have been evaluated for the purposes of determining the diffusion coefficient of cobaltocenium and iodide in the high viscosity room temperature ionic liquid 1-methyl-3-octylimidazolium hexafluorophosphate. It was found that the viscosity of the electrolyte was too high to practically approach true steady-state conditions over a reasonable experimental time scale, ruling out the use of steady-state UME theory to quantify diffusivity. Similarly, the steady-state RDE theory was unable to be applied due to the difficulties associated with rotating the electrode at sufficient rates in the high viscosity electrolyte. The

diffusion coefficient of cobaltocenium measured using transient voltammetry and the Randles–Sevcik method was significantly underestimated due to the effect of uncompensated resistance. Therefore, a reliable D value under these circumstances requires comparison of the experimental cyclic voltammogram with a simulated one. In contrast, the semi-integral electroanalysis method does not suffer from the effect of uncompensated resistance, allowing the D value to be determined efficiently with high accuracy, with the use of a simple equation. The advantages of using the semi-integral electroanalysis method are even more important when used for the successful determination of the D value of I^- in a $\text{I}^-/\text{I}_3^-/\text{I}_2$ model system, where the application of the Randles–Sevcik method is invalid and numerical simulations are problematic due to the mechanistic complexity and kinetic sluggishness of the iodide oxidation process.

ASSOCIATED CONTENT

Supporting Information

Further discussion on the applicability of steady-state techniques in RTILs (Figure S1), demonstration of the practical difficulties in rotating the RDE at high rates in viscous media (Figure S2), and numerical simulations of the $[\text{Co}(\text{Cp})_2]^{+/0}$ process (Figure S3). This material is available free of charge via the Internet at <http://pubs.acs.org>

AUTHOR INFORMATION

Corresponding Author

[REDACTED]

Notes

The authors declare no competing financial interest.

ACKNOWLEDGMENTS

We thank Dr. Thomas Ruether for assistance with the drying of $[\text{C}_8\text{mim}][\text{PF}_6]$ and the recrystallization of $[\text{C}_2\text{mim}]\text{I}$.

REFERENCES

- (1) MacFarlane, D. R.; Seddon, K. R. *Aust. J. Chem.* **2007**, *60*, 3–5.
- (2) Armand, M.; Endres, F.; MacFarlane, D. R.; Ohno, H.; Scrosati, B. *Nat. Mater.* **2009**, *8*, 621–629.
- (3) Dean, P. M.; Pringle, J. M.; MacFarlane, D. R. *Phys. Chem. Chem. Phys.* **2010**, *12*, 9144–9153.
- (4) Galinski, M.; Lewandowski, A.; Stepniak, I. *Electrochim. Acta* **2006**, *51*, 5567–5580.
- (5) Fernicola, A.; Scrosati, B.; Ohno, H. *Ionics* **2006**, *12*, 95–102.
- (6) Sukardi, S. K.; Zhang, J.; Burgar, I.; Horne, M. D.; Hollenkamp, A. F.; MacFarlane, D. R.; Bond, A. M. *Electrochem. Commun.* **2008**, *10*, 250–254.
- (7) Rogers, E. I.; Silvester, D. S.; Poole, D. L.; Aldous, L.; Hardacre, C.; Compton, R. G. *J. Phys. Chem. C* **2008**, *112*, 2729–2735.
- (8) Bard, A. J.; Faulkner, L. R. *Electrochemical methods: fundamentals and applications*, 2nd ed.; Wiley: New York, 2001.
- (9) Zhang, J.; Bond, A. M. *Analyst* **2005**, *130*, 1132–1147.
- (10) Barrosse-Antle, L. E.; Bond, A. M.; Compton, R. G.; O’Mahony, A. M.; Rogers, E. I.; Silvester, D. S. *Chem.-Asian J.* **2010**, *5*, 202–230.
- (11) Zhao, C.; Burrell, G.; Torriero, A. A. J.; Separovic, F.; Dunlop, N. F.; MacFarlane, D. R.; Bond, A. M. *J. Phys. Chem. B* **2008**, *112*, 6923–6936.
- (12) Grenness, M.; Oldham, K. B. *Anal. Chem.* **1972**, *44*, 1121–1129.
- (13) Oldham, K. B. *Anal. Chem.* **1972**, *44*, 196–198.
- (14) Goto, M.; Oldham, K. B. *Anal. Chem.* **1973**, *45*, 2043–2050.
- (15) Goto, M.; Oldham, K. B. *Anal. Chem.* **1974**, *46*, 1522–1530.
- (16) Oldham, K. B. *J. Electroanal. Chem.* **1976**, *72*, 371–378.
- (17) Saveant, J. M. *J. Electroanal. Chem.* **1973**, *44*, 169–187.

- (18) Mahon, P. J.; Oldham, K. B. *J. Electroanal. Chem.* **1999**, *464*, 1–13.
- (19) Seddon, K. R.; Stark, A.; Torres, M. J. Viscosity and density of 1-alkyl-3-methylimidazolium ionic liquids. In *Clean Solvents: Alternative Media for Chemical Reactions and Processing*; Abraham, M. A., Moens, L., Eds.; American Chemical Society: Washington, DC, 2002; Vol. 819, p 34–49.
- (20) Zhang, Y.; Zheng, J. B. *Electrochim. Acta* **2007**, *52*, 4082–4086.
- (21) Ejigu, A.; Lovelock, K. R. J.; Licence, P.; Walsh, D. A. *Electrochim. Acta* **2011**, *56*, 10313–10320.
- (22) Silvester, D. S.; Aldous, L.; Hardacre, C.; Compton, R. G. *J. Phys. Chem. C* **2008**, *112*, 6551–6557.
- (23) Stojanovic, R. S.; Bond, A. M. *Anal. Chem.* **1993**, *65*, 56–64.
- (24) Gritzner, G.; Kuta, J. *Pure Appl. Chem.* **1984**, *56*, 461–466.
- (25) de Levie, R. *How to Use Excel® in Analytical Chemistry and in General Scientific Data Analysis*; Cambridge University Press: Cambridge, 2001.
- (26) Oldham, K. B.; Myland, J. C. *Fundamentals of electrochemical science*; Academic Press: San Diego, 1994.
- (27) de Levie, R. *Excellaneous*. <http://www.bowdoin.edu/~rdelevie/excellaneous/> (accessed June 18, 2012).
- (28) Skoog, D. A.; West, D. M.; Holler, F. J.; Crouch, S. R. *Fundamentals of analytical chemistry*, 8th ed.; Thomson-Brooks/Cole: Belmont, CA, 2004.
- (29) Hultgren, V. M.; Mariotti, A. W. A.; Bond, A. M.; Wedd, A. G. *Anal. Chem.* **2002**, *74*, 3151–3156.
- (30) Buzzeo, M. C.; Evans, R. G.; Compton, R. G. *ChemPhysChem* **2004**, *5*, 1106–1120.
- (31) Mahon, P. J. *J. Solid State Electrochem.* **2009**, *13*, 573–582.
- (32) Shiddiky, M. J. A.; Torriero, A. A. J.; Zhao, C.; Burgar, I.; Kennedy, G.; Bond, A. M. *J. Am. Chem. Soc.* **2009**, *131*, 7976–7989.
- (33) Kanakubo, M.; Harris, K. R.; Tsuchihashi, N.; Ibuki, K.; Ueno, M. *Fluid Phase Equilib.* **2007**, *261*, 414–420.
- (34) Creager, S. Solvents and Supporting Electrolytes. In *Handbook of Electrochemistry*; Zoski, C. G., Ed.; Elsevier: Amsterdam, 2007; Chapter 3, p 57–72.
- (35) Hanson, K. J.; Tobias, C. W. *J. Electrochem. Soc.* **1987**, *134*, 2204–2210.
- (36) Macagno, V. A.; Giordano, M. C.; Arvia, A. J. *Electrochim. Acta* **1969**, *14*, 335.
- (37) Kawano, R.; Watanabe, M. *Chem. Commun.* **2003**, 330–331.

Supporting information for

Advantages available in the application of the semi-
integral electroanalysis technique for the
determination of diffusion coefficients in the highly
viscous ionic liquid 1-methyl-3-octylimidazolium
hexafluorophosphate

*Cameron L. Bentley,^{†,‡} Alan M. Bond,[†] Anthony F. Hollenkamp,[‡] Peter J. Mahon[§] and Jie
Zhang[†]*

[†]School of Chemistry, Monash University, Clayton, Vic 3800, Australia

[‡]CSIRO Energy Technology, Box 312, Clayton South, Vic 3169, Australia

[§]Faculty of Life and Social Sciences, Swinburne University of Technology, Hawthorne, Vic
3122, Australia

Application of steady-state voltammetric techniques in highly viscous electrolytes:

In order to approach a true steady state at an ultramicroelectrode (UME) during potential sweep voltammetry, the following inequality must be satisfied:

$$v \ll \frac{RTD}{nFa^2} \quad (\text{S1})$$

where F is Faraday's constant, a is the electrode radius, v is the voltammetric scan rate, R is the universal gas constant, T is the temperature, n is the number of electrons transferred and D is the diffusion coefficient of the electroactive species under investigation. Under conditions where the above inequality is satisfied, convergent diffusion dominates and sigmoidal voltammograms will be observed.

Evident from Eq. (S1), a true steady-state can often be approached in relatively fluid RTIL electrolytes ($D \geq 10^{-7} \text{ cm}^2 \text{ s}^{-1}$) by using electrodes of very small radius ($a \leq 5 \text{ }\mu\text{m}$) and slow voltammetric scan rates ($v \leq 10 \text{ mV s}^{-1}$).¹ Linear sweep voltammograms generated from DigiElch voltammetric simulation software which demonstrate the effect of varying these parameters are shown in Figure S1. The simulations reveal how practicably unfeasible it is to approach a true-steady state at an UME when diffusivity is in the low $10^{-8} \text{ cm}^2 \text{ s}^{-1}$ range.

At a scan rate of 10 mV s^{-1} , peak-shaped voltammograms are observed at electrodes with radii as small as $0.5 \text{ }\mu\text{m}$, with true steady state voltammograms only being observed when $a \leq 100 \text{ nm}$. It should be noted that the current data shown in Figure S1a are normalized with respect to electrode radius in order to contrast the shape of the respective scans. Disk UMEs with $a \geq 5 \text{ }\mu\text{m}$ are commercially available from manufacturers such as BASi (Bioanalytical systems, West Lafayette, IN) and CHi (CH Instruments, Austin, TX). UMEs with $5 \text{ }\mu\text{m} < a \leq 0.5 \text{ }\mu\text{m}$ can be fabricated by sealing wires of the appropriate dimensions in glass capillaries.^{2, 3} Fabrication of electrodes with sub-micron (nanometer) diameters is generally more problematic however,

requiring significant user skill and capital investment.⁴ In addition, substituting values of 1, 1×10^{-5} mol cm⁻³ (10 mM), 1×10^{-5} cm (0.1 μ m) and 1×10^{-8} cm² s⁻¹ for the values of n , C , a and D respectively into Eq. (S2) gives a steady-state limiting current of 3.9×10^{-13} A:

$$I_L = 4nFC^*aD \quad (\text{S2})$$

Measuring sub-picoampere currents (0.39 pA) accurately is, in itself a major experimental challenge, as it is well below the capabilities of many commercial potentiostats.

At an electrode with a radius of 5 μ m, peak-shaped voltammograms are observed at voltammetric scan rates as low as 100 μ V s⁻¹, with scan rates < 10 μ V s⁻¹ being required to observe true-steady state behavior (see Figure S1b). As well as being extremely time consuming (a typical scan spanning 800 mV would take more than 20 hours at 10 μ V s⁻¹), these low voltammetric scan rates are practicably unfeasible, as environmental factors (temperature, vibrations etc.), natural convection and adsorption processes at the electrode surface would become significant factors at such prolonged experimental time scales.

It should also be noted that although the viscosity, η , of [C₈mim][PF₆] is relatively high compared to classical molecular solvents, such as acetonitrile ($\eta = 0.34$ cP containing 0.1 M TBAClO₄ at 22°C) or more ‘fluid’ RTILs, such as [C₂mim][NTf₂] ($\eta = 34$ cP at 20°C), RTILs with viscosities in excess of 1000 cP have been reported, such as [C₆mim]Cl ($\eta = 7453$ cP at 20°C).⁵ Diffusion coefficients in these RTILs would be expected to be roughly another order of magnitude lower than in [C₈mim][PF₆] (i.e. in the 10⁻⁹ cm² s⁻¹ range), which would make achieving close to true steady-state conditions practically impossible.

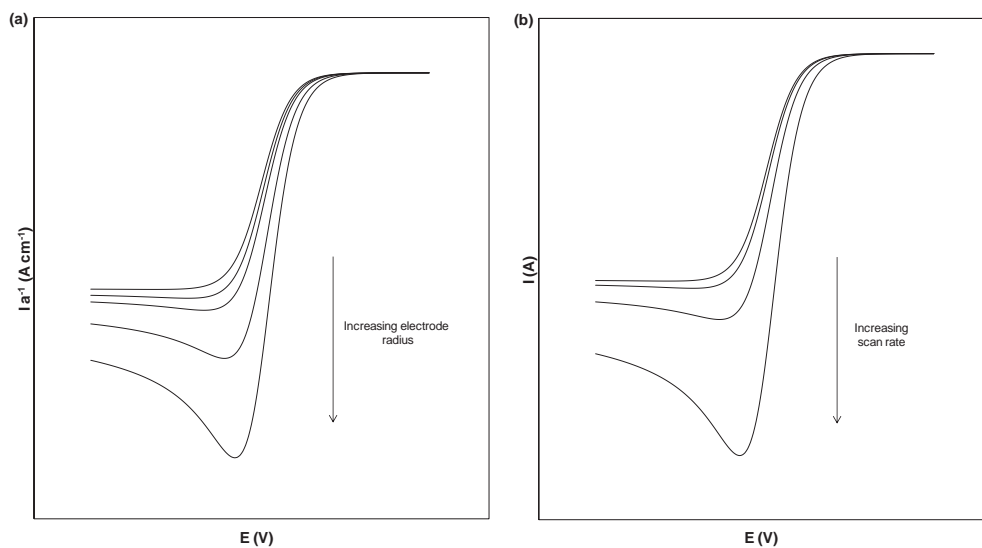


Figure S1. Simulated linear sweep voltammograms generated with: (a) variable electrode radii (5 μm , 2.5 μm , 1 μm , 0.5 μm and 0.1 μm) with a constant scan rate (10 mV s^{-1}) and (b) variable voltammetric scan rates (10 mV s^{-1} , 1 mV s^{-1} , 0.1 mV s^{-1} and 0.01 mV s^{-1}) with a constant electrode radius (5 μm). In all cases, the following simulation parameters were used: $D_{\text{ox}} = D_{\text{red}} = 1 \times 10^{-8} \text{ cm}^2 \text{ s}^{-1}$, $k_s = 10,000 \text{ cm s}^{-1}$, $\alpha = 0.5$, $C_{\text{dl}} = 0 \text{ F}$ and $R_u = 0 \text{ }\Omega$.

RDE voltammetry at high rotation rates ($\omega > 500$ rpm):

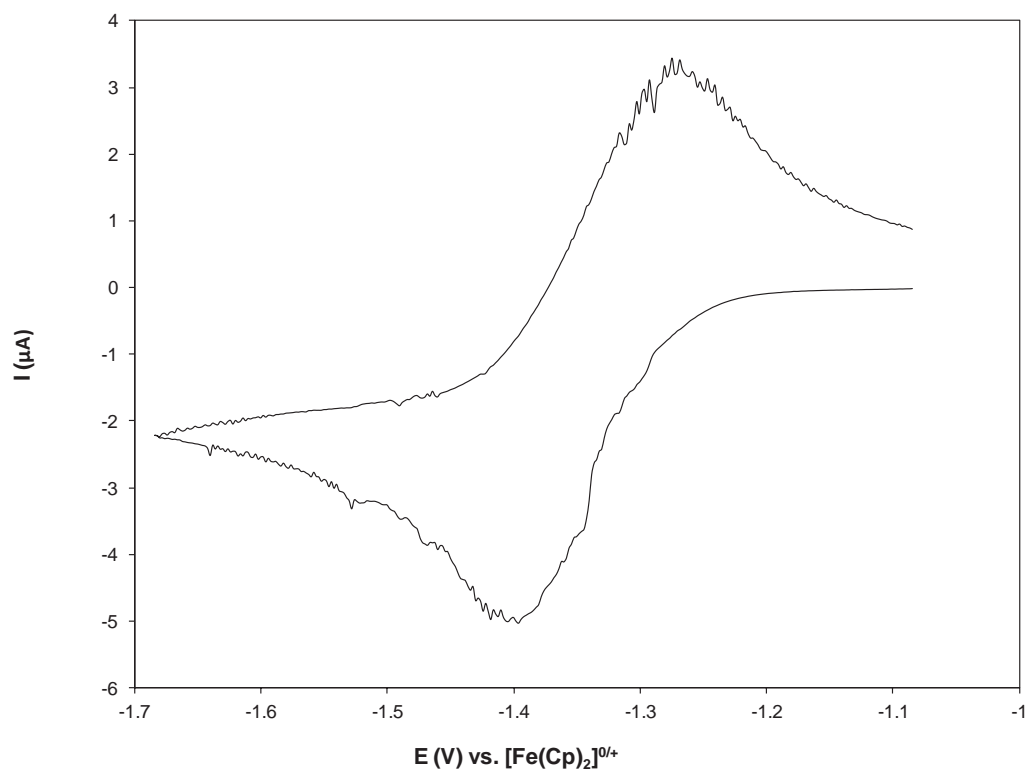


Figure S2. Rotating disk electrode voltammogram obtained from 10.1 mM $[\text{Co}(\text{Cp})_2][\text{PF}_6]$ in $[\text{C}_8\text{mim}][\text{PF}_6]$ at a 1.5 mm radius Pt RDE with a scan rate of 50 mV s^{-1} and a rotation speed of 1000 rpm.

Numerical simulation of the $[\text{Co}(\text{Cp})_2]^{+/0}$ process:

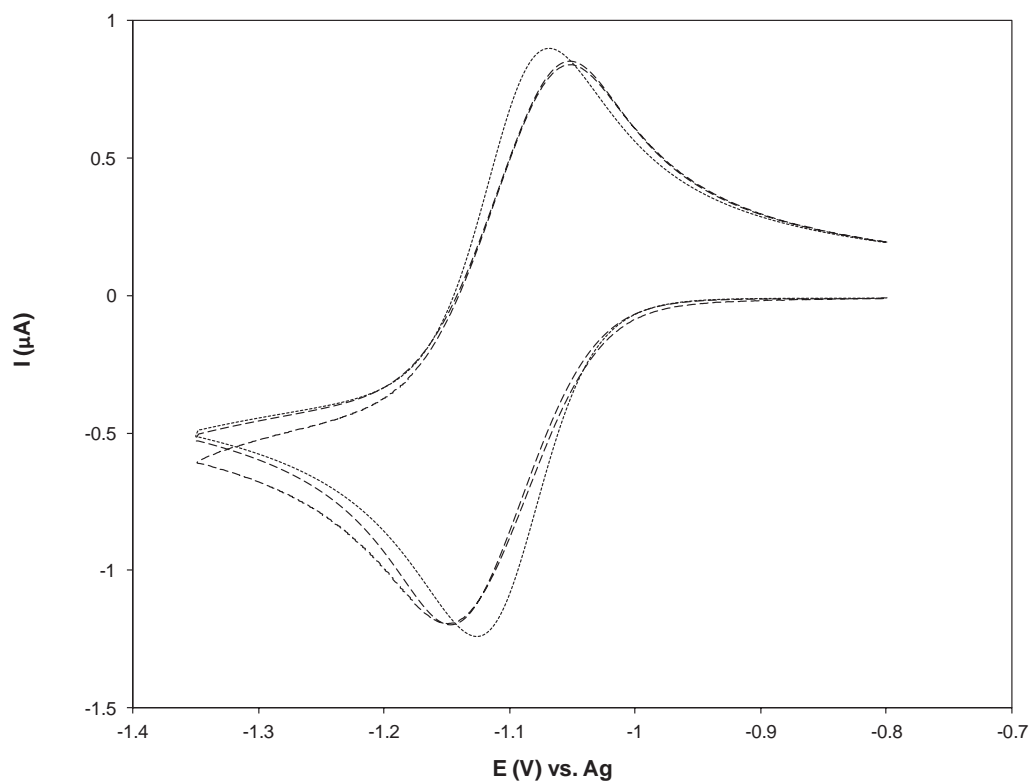


Figure S3. Comparison of an experimental voltammogram (solid curve) obtained from 9.96 mM $[\text{Co}(\text{Cp})_2][\text{PF}_6]$ in $[\text{C}_8\text{mim}][\text{PF}_6]$ at a Pt macroelectrode ($A = 0.0215 \text{ cm}^2$) with a scan rate of 50 mV s^{-1} and simulated voltammograms for a reversible process with no uncompensated resistance (dotted curve) and $13,000 \text{ } \Omega$ uncompensated resistance (dashed curve). Other simulation parameters used were: $D_{\text{ox}} = 9.1 \times 10^{-9} \text{ cm}^2 \text{ s}^{-1}$, $D_{\text{red}} = 1.5 \times 10^{-8} \text{ cm}^2 \text{ s}^{-1}$, $k_s = 1 \text{ cm s}^{-1}$, $\alpha = 0.5$, $C_{\text{dl}} = 2 \times 10^{-7} \text{ F}$, $E^0 = -1.104 \text{ V}$ and $T = 297 \text{ K}$.

REFERENCES

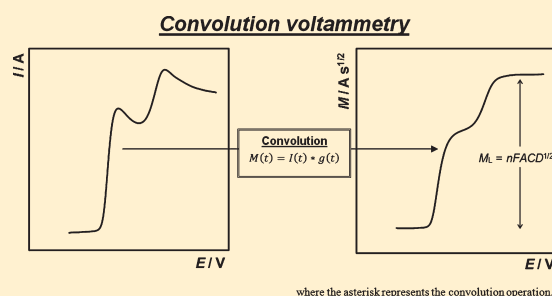
- (1) Buzzeo, M. C.; Evans, R. G.; Compton, R. G., *ChemPhysChem* **2004**, *5*, 1106-1120.
- (2) Fan, F.-R. F.; Fernandez, J.; Liu, B.; Mauzeroll, J.; Zoski, C. G., 6.3.1 - Platinum and gold inlaid disks ≥ 5 μm diameter. In *Handbook of Electrochemistry*, Zoski, C. G., Ed. Elsevier: Amsterdam, 2007; p 189-197.
- (3) Liu, B., 6.3.2 - Platinum and gold inlaid disks ≤ 5 μm diameter. In *Handbook of Electrochemistry*, Zoski, C. G., Ed. Elsevier: Amsterdam, 2007; p 197-199.
- (4) Mauzeroll, J.; LeSuer, R. J., 6.3.3 - Laser-pulled ultramicroelectrodes. In *Handbook of Electrochemistry*, Zoski, C. G., Ed. Elsevier: Amsterdam, 2007; p 199-211.
- (5) Barrosse-Antle, L. E.; Bond, A. M.; Compton, R. G.; O'Mahony, A. M.; Rogers, E. I.; Silvester, D. S., *Chem.-Asian J.* **2010**, *5*, 202-230.

Applications of Convolution Voltammetry in Electroanalytical Chemistry

Cameron L. Bentley,^{†,‡} Alan M. Bond,^{*,†} Anthony F. Hollenkamp,[‡] Peter J. Mahon,^{*,§} and Jie Zhang[†][†]School of Chemistry, Monash University, Clayton, Vic 3800, Australia[‡]CSIRO Energy Technology, Box 312, Clayton South, Victoria 3169, Australia[§]Faculty of Life and Social Sciences, Swinburne University of Technology, Hawthorn, Victoria 3122, Australia

Supporting Information

ABSTRACT: The robustness of convolution voltammetry for determining accurate values of the diffusivity (D), bulk concentration (C^b), and stoichiometric number of electrons (n) has been demonstrated by applying the technique to a series of electrode reactions in molecular solvents and room temperature ionic liquids (RTILs). In acetonitrile, the relatively minor contribution of nonfaradaic current facilitates analysis with macrodisk electrodes, thus moderate scan rates can be used without the need to perform background subtraction to quantify the diffusivity of iodide [$D = 1.75 (\pm 0.02) \times 10^{-5} \text{ cm}^2 \text{ s}^{-1}$] in this solvent. In the RTIL 1-ethyl-3-methylimidazolium bis(trifluoromethanesulfonyl)imide, background subtraction is necessary at a macrodisk electrode but can be avoided at a microdisk electrode, thereby simplifying the analytical procedure and allowing the diffusivity of iodide [$D = 2.70 (\pm 0.03) \times 10^{-7} \text{ cm}^2 \text{ s}^{-1}$] to be quantified. Use of a convolutive procedure which simultaneously allows D and nC^b values to be determined is also demonstrated. Three conditions under which a technique of this kind may be applied are explored and are related to electroactive species which display slow dissolution kinetics, undergo a single multielectron transfer step, or contain multiple noninteracting redox centers using ferrocene in an RTIL, 1,4-dinitro-2,3,5,6-tetramethylbenzene, and an alkynylruthenium trimer, respectively, as examples. The results highlight the advantages of convolution voltammetry over steady-state techniques such as rotating disk electrode voltammetry and microdisk electrode voltammetry, as it is not restricted by the mode of diffusion (planar or radial), hence removing limitations on solvent viscosity, electrode geometry, and voltammetric scan rate.



As with any form of analysis, the ideal electroanalytical technique should be selective, accurate, reproducible, and applicable under a wide range of experimental conditions. In many respects, voltammetric methods meet these requirements, since they are applicable to a diverse range of electroactive species (exhibiting a wide range of electrode mechanisms) and can be applied in a wide range of electrolyte media. At stationary macroelectrodes, transient voltammetric responses are scan rate dependent and hence steady-state techniques, such as microdisk electrode (ME) or rotating disk electrode (RDE) voltammetry that are independent of scan rate are often advantageous over transient voltammetric techniques for analytical purposes, as the limiting current (I_L), in contrast to the transient peak current (I_p), is insensitive to both sluggish heterogeneous electron transfer kinetics and high levels of uncompensated resistance (R_u), that give rise to IR_u drop effects.¹ Fundamental parameters, such as the diffusion coefficient (D), the stoichiometric number of electrons (n), or the bulk concentration of electroactive species (C^b) can therefore be calculated from the voltammetric I_L plateau at a ME or RDE using the appropriate equation:^{1,2}

$$I_L^{\text{ME}} = 4nFC^bDr \quad (1)$$

$$I_L^{\text{RDE}} = 0.620nFA(d/\eta)^{1/6}D^{2/3}\omega^{1/2}C^b \quad (2)$$

where F is Faraday's constant, r is the electrode radius for a disk, A is the electrode area, d is the density of the solvent (electrolyte), η is the dynamic viscosity of the solvent (electrolyte), and ω is the angular rotation rate of the electrode.

Even though the application of steady-state ME or RDE voltammetry in conventional electrolytes (i.e., salt in molecular solvent) has been successful, there have been difficulties in applying them in highly viscous media, as encountered in room temperature ionic liquids (RTILs).^{3–5} RTILs are nonvolatile, nonflammable, intrinsic ionic conductors which often possess viscosities 10–10 000 times higher than conventional molecular solvent (electrolyte) media, resulting in much slower mass-transport.^{6,7} Indeed, the viscosity of many RTILs is often too

Received: November 5, 2013

Accepted: January 20, 2014

Published: January 20, 2014

high to allow true steady-state conditions to be approached over a reasonable experimental time scale, which rules out the application of eqs 1 or 2. Under these circumstances, a best-fit approach with numerical simulation may be a viable alternative; however, even this method has its limitations, as mechanistic complexities or other uncertainties can make the modeling difficult.⁸

An alternative method, which involves convolving transient $I-E$ data,⁹ has been successfully employed to determine the diffusivity of the cobaltocenium cation and iodide in the highly viscous RTIL 1-methyl-3-octylimidazolium hexafluorophosphate.⁸ This convolution method, also known as semiintegral voltammetry, when applied to uncomplicated electron transfer reactions at planar electrodes,¹⁰ gives rise to a function, $M(t)$, which is related to the concentration of electroactive species at the electrode surface:

$$M(t) = \frac{d^{-1/2}I(t)}{dt^{-1/2}} = I(t) * \frac{1}{\sqrt{\pi t}} \quad (3)$$

where the asterisk represents the convolution operation. Transformation of the transient $I-E$ data makes use of the general convolution procedure initially described by Savéant and co-workers,⁹ where semiintegral voltammetry¹¹ is a subset of a range of techniques collectively known as convolution voltammetry. Under purely diffusion-controlled conditions, $M(t)$ reaches its limiting value, M_L :

$$M_L = nFC^bAD^{1/2} \quad (4)$$

This method shares the benefits available with the previously discussed ME and RDE techniques but without the need to record experimental data under near steady-state conditions. Unfortunately, the constraint that mass transport due to nonplanar (radial) diffusion must be negligible limits the use of this technique to relatively large planar electrodes and/or high scan rates and because the charging current is present, background subtraction is essential.^{8,11}

It has been demonstrated¹² that the fully planar diffusion restrictions associated with semiintegral voltammetry can be relaxed by replacing the function $1/(\pi t)^{1/2}$ in eq 3 with the generalized function, $g(t)$, whose form is dependent upon the details of the mechanism and the geometry of the electrode:

$$M(t) = I(t) * g(t) \quad (5)$$

Herein $M(t)$ will be referred to as the semiintegral of the current when calculated based on eq 3 under purely planar diffusion conditions and as the convolved current for other electrode geometries when calculated more generally based on eq 5 taking into account the contribution of radial diffusion to the mass transport. In order to accommodate radial or edge effects, the formalization applied to the inlaid disk geometry¹³ is the bipartite expression which at short times is given by

$$g(t) = \frac{\sqrt{D}}{r} \sum_{j=1}^5 a_j \theta^{(j-2)/2} \quad (6)$$

where θ is the dimensionless time parameter equal to Dt/r^2 with the coefficients a_j listed in Table 1 (available in the Supporting Information). The long-time expression is

$$g(t) = \frac{\sqrt{D}}{r} (b_2 \theta^{-3/2} + \sum_{j=4}^8 b_j \theta^{(3-2j)/2}) \quad (7)$$

with the b_j coefficients also listed in Table 1 in the Supporting Information and the transition from the short to the long time expression occurs when $\theta = 1.304$. The implementation of these equations is based on the application of the convolution algorithm that is described later.

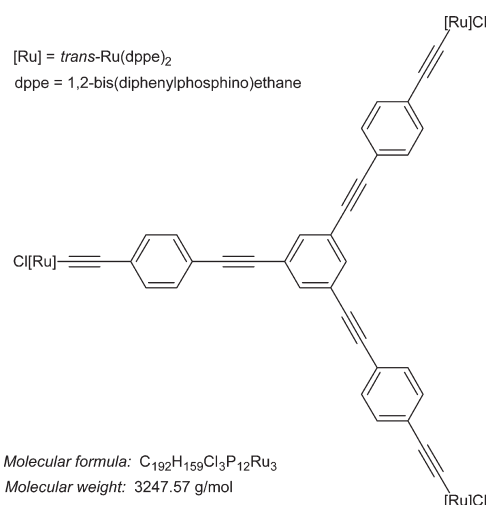
This extension available via eqs 6 and 7 can be applied under conditions where radial diffusion is significant while retaining all of the advantages of the original semiintegration approach. As a result, the enhanced signal-to-background ratio that is attainable with microdisk electrodes at moderate scan rates can be realized, while the need to perform background subtraction is averted. This advantage has been demonstrated with numerical simulations¹⁴ but has yet to be proven directly with experimental data.

In this paper, we demonstrate the robustness of the convolution approach at microdisk electrodes by applying it to the oxidation of ferrocene and iodide, in the molecular solvent acetonitrile and/or the RTIL 1-ethyl-3-methylimidazolium bis(trifluoromethanesulfonyl)imide, in order to establish the conditions under which background subtraction is unnecessary. In addition, an alternative application of the convolution technique, which allows the simultaneous determination of D and nC^b has been explored, using ferrocene, 1,4-dinitro-2,3,5,6-tetramethylbenzene, and an alkynylruthenium trimer as examples.

EXPERIMENTAL SECTION

Reagents. The purification of 1-ethyl-3-methylimidazolium bis-(trifluoromethanesulfonyl)imide ($[C_2mim][NTf_2]$, Io-li-tec GmbH, 99.5%), 1-ethyl-3-methylimidazolium iodide ($[C_2mim]I$, Io-li-tec GmbH, >98%), and tetraethylammonium tetrafluoroborate ($[NEt_4][BF_4]$, Stella Chemifa, 99.9%) and the preparation of 1,4-dinitro-2,3,5,6-tetramethylbenzene (dinitrodurene) is detailed in the Supporting Information. The alkynylruthenium complex (see structure in Chart 1) had previously been prepared at the Research School of Chemistry at The Australian National University¹⁵ and was used as received. Acetone (Merck, EMSURE), acetonitrile (Sigma-

Chart 1. Alkynylruthenium Complex Investigated in This Work.



Aldrich, anhydrous, 99.8%), dichloromethane (Sigma-Aldrich, anhydrous, 99.8%), ferrocene ($[\text{Fe}(\text{Cp})_2]$, where $\text{Cp} = \eta^5\text{-C}_5\text{H}_5$, Fluka, >98%), lithium tetrafluoroborate (LiBF_4 , Stella Chemifa), and tetra-*n*-butylammonium hexafluorophosphate ($[\text{NBu}_4][\text{PF}_6]$, Sigma) were used as supplied by the manufacturer. Acetonitrile, dichloromethane, $[\text{C}_2\text{mim}][\text{NTf}_2]$, $[\text{C}_2\text{mim}]\text{I}$, LiBF_4 , $[\text{NEt}_3][\text{BF}_4]$, and $[\text{NBu}_4][\text{PF}_6]$ were stored and handled under a dry argon atmosphere in a glovebox.

Electrochemical Systems and Procedures. All voltammetric experiments were undertaken under benchtop conditions at ambient temperature (23 ± 1 °C) with a Gamry Reference 600 Potentiostat/Galvanostat/ZRA (Gamry Instruments, Warminster, PA). All solvents were degassed with N_2 prior to experimentation, and a blanket of N_2 was maintained during the course of the voltammetric experiments. A Faraday cage was employed in microdisk electrode experiments. Voltammetric experiments were carried out using a standard three-electrode arrangement. Details on the auxiliary, reference, and working electrodes can be found in the Supporting Information. Experimental uncertainties were estimated by propagation of the standard deviations in the variables of interest.¹⁶

Semiintegral and Convolution Voltammetric Experiments. Semiintegration of the $I-t$ data was performed using an algorithm from de Levie,¹⁷ which was adapted from Oldham and Myland.² A Microsoft Excel macro that includes this algorithm is available free online.¹⁸ The convolved current is readily calculated using an efficient convolution algorithm applicable to data with regularly spaced time intervals:¹⁹

$$\begin{aligned} M(t) &= [I(t)*g(t)]_{t=j\Delta} \\ &= \frac{1}{\Delta} (I_j G_1 + \sum_{j=1}^{J-1} I_{j-j} (G_{j-1} - 2G_j + G_{j+1})) \end{aligned} \quad (8)$$

where Δ is a small increment of the total time, $G(t) = \int_0^t \int_0^t g(t) dt dt$ and the abbreviations I_j and G_j refer to $I(j\Delta)$ and $G(j\Delta)$. The double integral of $g(t)$ at short times for use in the convolution algorithm is obtained from

$$G(t) = \frac{r^3}{D^{3/2}} \sum_{j=1}^5 a_j \theta^{(j+2)/2} \quad (9)$$

and for the long time series:

$$G(t) = \frac{r^3}{D^{3/2}} \left(\sum_{j=1}^3 b_j \theta^{(3-j)/2} + \sum_{j=4}^8 b_j \theta^{(7-2j)/2} \right) \quad (10)$$

with transition occurring when $\theta = 1.368$. The coefficients b_1 and b_3 are integration constants obtained from Aoki et al.²⁰ The double integral of the long-time expression contains eight terms due to the addition of the integration constant for each integration step. The values for the a_j and b_j coefficients are listed in Table 1 in the Supporting Information.

Estimation of D or r and nC^b . The complex time dependence of the diffusion process to a disk electrode is described by eqs 6 and 7, which are defined in terms of θ . It follows that a unique ratio of $\sqrt{D/r}$ will apply to a specific set of experimental conditions and this ratio can be defined as a single parameter, ρ . In order to obtain the convolved current, $M(t)$, it is necessary to input an initial estimate for ρ into the convolution algorithm. If C^b is known and M_L can be obtained from the limiting convolved current plateau, then it is possible

to iteratively refine ρ based on eq 4 for a known value of the electrode radius because

$$\rho = \frac{M_L}{nF\pi r^3 C^b} \quad (11)$$

or if the diffusion coefficient is known:

$$\rho = \frac{nFD^{3/2} C^b}{M_L} \quad (12)$$

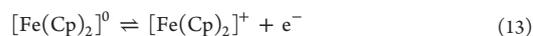
Successive refinements of ρ oscillate and converge on a final value that can then be used to calculate either D or r depending on which is known. In this way it is possible to calibrate the radius of an electrode using a known diffusion coefficient or estimate a diffusion coefficient using a previously calibrated electrode.

If voltammograms are obtained using two different scan rates on the same electrode, then it is possible to calculate both D and nC^b as both voltammograms should result in identical convolved current plateaus even though different time dependencies are involved. If the radius has been calibrated, then the optimized value of ρ provides D and then this can be substituted into eq 4 to estimate the product of n and C^b .

RESULTS AND DISCUSSION

Application of the Semiintegral versus Convulsive Techniques in Voltammetry. Ferrocene in Acetonitrile.

Ferrocene is well-known to undergo an uncomplicated, reversible one-electron oxidation process in a range of molecular solvents:²¹



Assuming that R_u is negligible, under conditions of purely planar diffusion, the peak current (I_p) for a simple, reversible process can be described by the Randles–Sevcik equation:

$$I_p = 0.4463nFA \left(\frac{nFD\nu}{RT} \right)^{1/2} C^b \quad (14)$$

where R is the universal gas constant, ν is the voltammetric scan rate, and T is the temperature. n , A , D , or C^b can therefore be determined using this relationship, assuming all of the other parameters are known. In reality, relatively few electrochemical systems of interest fulfill the above criteria, as even in the case of ferrocene in acetonitrile (see Figure 1a), contributions by radial diffusion, and R_u (210 ± 20 Ω) are not negligible. Consequently, the “unknown parameter” would have to be estimated from the above voltammogram using a “best-fit” approach with numerical simulation.

The M_L plateau of a semiintegrated voltammogram is not sensitive to uncompensated resistance or sluggish heterogeneous kinetics, which makes it applicable to a wide range of electrochemical systems.^{10,11,22–24} The downside to this technique is that the large electrode size and/or fast scan required to ensure that mass-transport by nonplanar diffusion is truly negligible in low viscosity solvents such as acetonitrile makes background subtraction to account for nonfaradaic current mandatory. This problem can be avoided by using the convolution technique, whereby no restriction is applied to the mode of diffusion to the electrode surface, which in turn allows the use of smaller electrodes and moderate scan rates; this principle is demonstrated in Figure 1b. The contribution from radial diffusion at this moderate scan rate (100 mV s⁻¹) causes

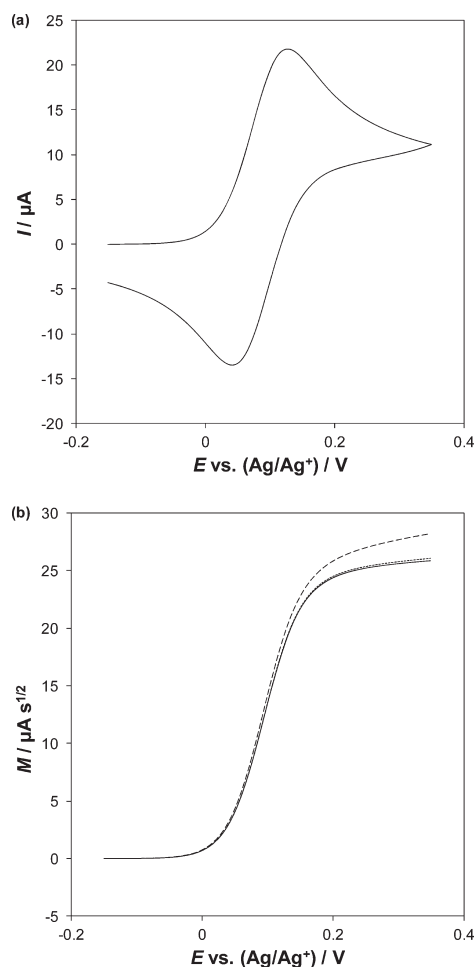


Figure 1. (a) Cyclic voltammogram obtained at a scan rate of 100 mV s^{-1} from $1.7 \text{ mM } [\text{Fe}(\text{Cp})_2]$ in acetonitrile ($0.1 \text{ M } [\text{NBu}_4][\text{PF}_6]$) at a 2.0 mm diameter Pt macrodisk electrode. (b) Semiintegral (---), convolved current (---) and background subtracted convolved current (—) of the voltammogram (forward sweep) in part a.

the M_L plateau of the semiintegral to be sloped, thereby ruling out the simple use of this technique under these conditions. The convolution approach on the other hand does not feature a significant slope, and the parameters D , n , A , or C^b can be calculated using eq 4 (assuming all other parameters are known). As also shown in Figure 1b, the nonfaradaic contribution to the total current at this moderate scan rate is barely detectable, which essentially eliminates the need to perform background subtraction.

Applications of Convolution Voltammetry: Electrode Dimensions and Solvent Properties. Iodide in Acetonitrile. In aprotic solvents such as acetonitrile,^{25,26} it has been well established that iodide undergoes a two step oxidation process to produce molecular iodine:



The following homogeneous equilibrium process complicates the observed reaction mechanism:



Overall, this one-electron per iodide ion reaction is mechanistically more complex than the previously discussed $[\text{Fe}(\text{Cp})_2]^{0/+}$ process. Cyclic voltammograms obtained from the electro-oxidation of $4 \text{ mM } \text{I}^-$ in acetonitrile ($0.2 \text{ M } \text{LiBF}_4$) at a Pt macrodisk electrode with scan rates ranging from 250 to 1000 mV s^{-1} are shown in Figure 2a. The peak to peak

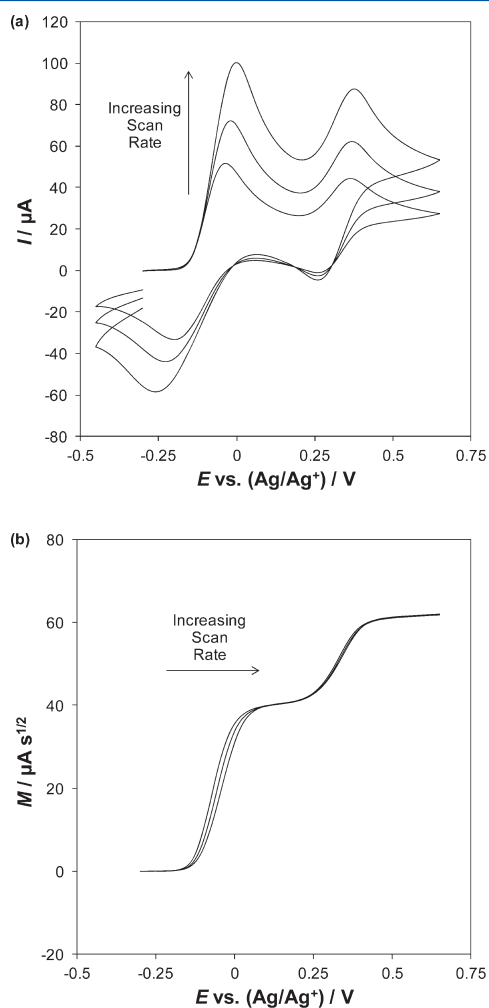


Figure 2. (a) Cyclic voltammograms and (b) linear-sweep convolved current voltammograms obtained from $4.32 \text{ mM } [\text{C}_2\text{mim}]\text{I}$ in acetonitrile ($0.2 \text{ M } \text{LiBF}_4$) at a 2.0 mm diameter Pt macrodisk electrode with scan rates of 250 , 500 , and 1000 mV s^{-1} .

separation (ΔE_p) for the I^-/I_3^- -process described by eq 15 is large and increases significantly over the investigated scan rate range. This indicates sluggish heterogeneous kinetics, which prevents the application of the Randles-Sevcik equation. Additionally, the mechanistic complexity of the iodide electro-oxidation process complicates analysis by numerical

simulation,^{27,28} making it by and large very difficult to calculate the parameters D , n , A , or C^b from the unprocessed transient cyclic voltammetric data.

These parameters would be calculable from the limiting current (I_L) plateau of a steady-state voltammogram obtained using either a RDE or a ME. However, in the present case the recording of an additional data set is unnecessary, as the required information is accessible through convolution; convolved currents of the forward sweep of the above $I-E$ data are shown in Figure 2b. While the sluggish heterogeneous kinetics of the Γ/I_3^- process described by eq 15 clearly affect the overall shape of the convolved-current voltammograms, evident from the shift in this process to increasingly positive potentials with scan rate, the magnitude of M_L is not affected and accordingly the $M-E$ curves feature two well-defined, scan rate independent, diffusion controlled plateaus. As previously noted with the $[\text{Fe}(\text{Cp})_2]^{0/+}$ process in acetonitrile, nonfaradaic current makes a negligible contribution to the total measured current under these conditions and hence background subtraction was not necessary. The diffusion coefficient of iodide was determined to be $1.75 (\pm 0.02) \times 10^{-5} \text{ cm}^2 \text{ s}^{-1}$ by substituting the appropriate values of known parameters in eq 4, which is in excellent agreement with the literature value of $1.68 \times 10^{-5} \text{ cm}^2 \text{ s}^{-1}$.²⁶

Iodide in 1-Ethyl-3-methylimidazolium Bis-(trifluoromethanesulfonyl)imide. In order to investigate how the physicochemical properties of the electrolyte influence the applicability of the convolution technique, further studies on the $\Gamma/I_3^-/I_2$ processes were carried out in the RTIL, $[\text{C}_2\text{mim}][\text{NTf}_2]$. A cyclic voltammogram obtained from 4.31 mM $[\text{C}_2\text{mim}]\text{I}$ in $[\text{C}_2\text{mim}][\text{NTf}_2]$ at a platinum macrodisk electrode is shown in Figure 3a. Iodide electro-oxidation in RTIL media is analogous to that observed in acetonitrile (see Figure 2a); two electron transfer processes are observed, corresponding to the reactions shown in eqs 15 and 16, in agreement with previous reports.^{27–32} In this paper we make no distinction between dissociated and nondissociated forms of iodide.

Once again, because of the kinetic sluggishness of the Γ/I_3^- process and mechanistic complexity of the overall process, it is difficult to extract analytical information (i.e., D , n , A , or C^b) from the unprocessed transient cyclic voltammetric data; the semiintegral of the forward sweep of the above $I-E$ data is shown in Figure 3b. Contrasting the previous example in acetonitrile, nonfaradaic current makes a significant contribution to the total measured current, evident from the severely sloped M_L plateau, making background subtraction a necessity when working with a macrodisk electrode in this RTIL. This is due to the fact that while the faradaic current is orders of magnitude lower in highly viscous RTILs, compared with that in molecular solvent electrolytes (compare Figures 2a and 3a), the values of double layer capacitance (C_{dl}) in the two media are comparable.⁴ The diffusion coefficient of iodide was determined to be $2.74 (\pm 0.03) \times 10^{-7} \text{ cm}^2 \text{ s}^{-1}$ from the background subtracted $M-E$ curve by substituting the appropriate values of known parameters in eq 4, which is in excellent agreement with the literature value of $2.68 \times 10^{-7} \text{ cm}^2 \text{ s}^{-1}$.²⁹

Contributions from nonfaradaic current can be minimized by taking advantage of the enhanced signal-to-background current ratio at a microdisk electrode. A cyclic voltammogram obtained from 4.31 mM $[\text{C}_2\text{mim}]\text{I}$ in $[\text{C}_2\text{mim}][\text{NTf}_2]$ at a platinum microdisk electrode is shown in Figure 4a. The waveshape

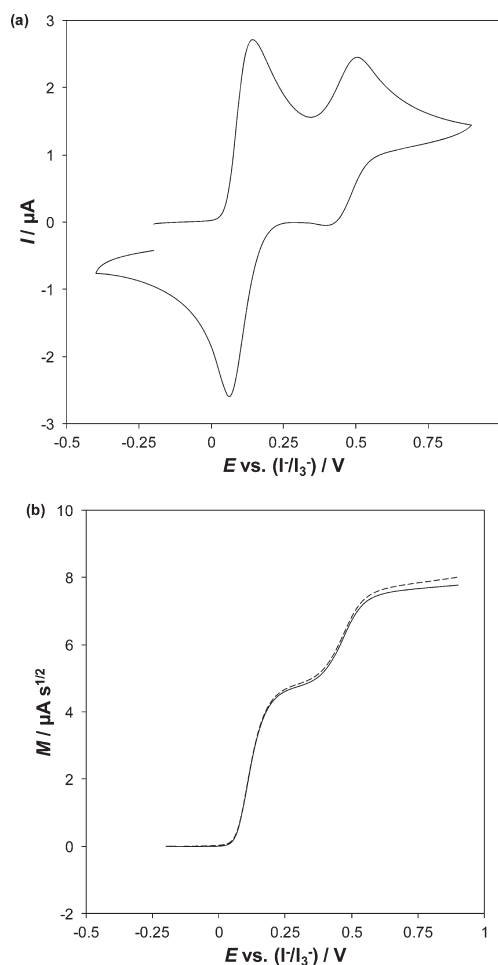


Figure 3. (a) Cyclic voltammogram obtained at a scan rate of 50 mV s^{-1} from 4.31 mM $[\text{C}_2\text{mim}]\text{I}$ in $[\text{C}_2\text{mim}][\text{NTf}_2]$ at a 2.0 mm diameter Pt macrodisk electrode. (b) Semiintegral of the voltammogram (forward sweep) in part a before (—) and after (---) background subtraction.

under these conditions is intermediate between a sigmoidal and a peak-shaped voltammogram, which indicates that radial diffusion contributes significantly to mass-transport. Under these mixed diffusion conditions, steady-state microdisk electrode theory (see eq 1) is not valid and semiintegration is not useful (see eq 3). However, the convolution technique is applicable, as demonstrated in Figure 4b. Evidently, under these conditions nonfaradaic current is negligible and background subtraction is not required. The diffusion coefficient of iodide was determined to be $2.70 (\pm 0.03) \times 10^{-7} \text{ cm}^2 \text{ s}^{-1}$ by substituting the appropriate values of known parameters in eq 4, which is in excellent agreement with the previously determined value from our laboratory²⁷ and that reported in the literature.²⁹

Applications of Convolution Voltammetry: Simultaneous Determination of D and nC^b . In the above discussion, it has been shown how the value of D may be determined from M_L (see eq 4) after convolution of the

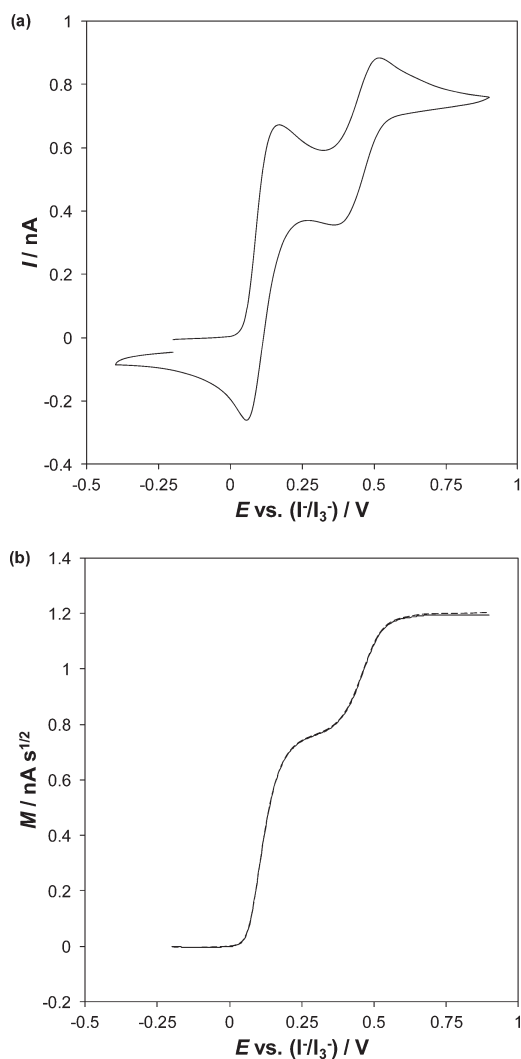


Figure 4. (a) Cyclic voltammogram obtained at a scan rate of 50 mV s^{-1} from $4.31 \text{ mM } [\text{C}_2\text{mim}]\text{I}$ in $[\text{C}_2\text{mim}][\text{NTf}_2]$ at a $25 \text{ }\mu\text{m}$ diameter Pt microdisk electrode. (b) Convolved current of the voltammogram (forward sweep) shown in part a before (—) and after (—) background subtraction.

experimental $I-E$ data when A , n , and C^b are known. An alternative application of the convolution technique allows the constants D and nC^b to be determined simultaneously from two sets of $I-E$ data obtained under conditions with unequal contributions from planar and radial diffusion. The relative contribution of planar and radial diffusion to a disk electrode under a given set of voltammetric conditions can be described by the dimensionless sphericity factor (σ):

$$\sigma = \sqrt{\frac{RTD}{nF\nu r^2}} \quad (18)$$

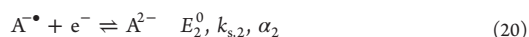
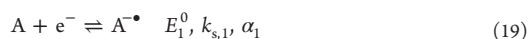
In practice, σ is varied by changing either the electrode dimensions (i.e., r) or the experimental time scale (i.e., ν).³³ This technique is most sensitive when the contributions from

both planar and radial diffusion are significant (i.e., mixed diffusion region, $0.012 < \sigma < 40$) and therefore can be conveniently carried out with disk electrodes of intermediate size (i.e., $20\text{--}200 \text{ }\mu\text{m}$) at moderate scan rates (i.e., $25\text{--}1000 \text{ mV s}^{-1}$).

Ferrocene in 1-Ethyl-3-methylimidazolium Bis-(trifluoromethanesulfonyl)imide. As in acetonitrile (see eq 13), ferrocene undergoes an uncomplicated, electrochemically reversible, one-electron oxidation in a range of RTILs.^{34,35} Despite its moderately high thermodynamic solubility in RTILs ($\sim 62.3 \text{ mM}$ in $[\text{C}_2\text{mim}][\text{NTf}_2]$),³⁶ ferrocene dissolution kinetics in the absence of molecular solvents is extremely slow, making quantitative preparation of solutions problematic and time-consuming.³ Difficulties with this issue can be overcome by using an analytical method which allows D and nC^b to be determined simultaneously (since n is known, the concentration of ferrocene can be determined from the product nC^b), such as double step chronoamperometry,^{28,36,37} or in the present case, convolution voltammetry.

To illustrate the convolution concept, a ferrocene solution of unknown concentration was prepared by bubbling N_2 into $[\text{C}_2\text{mim}][\text{NTf}_2]$ in contact with solid ferrocene for 30 min; the resulting voltammograms obtained at a $25 \text{ }\mu\text{m}$ diameter Pt microdisk electrode are shown in Figure 5a. The waveshape under these conditions is intermediate between a sigmoidal and peak-shaped voltammogram. The $M-E$ curves obtained by convolving the $I-E$ data collected at the two investigated scan rates are shown in Figure 5b. Because of the reversible nature of the $[\text{Fe}(\text{Cp})_2]^{0/+}$ process and the negligible effects of C_{dl} and R_w , the $M-E$ curves almost perfectly coincide, possessing identical M_L plateaus. The values of D and C^b ($n = 1$) were determined to be $4.49 \times 10^{-7} \text{ cm}^2 \text{ s}^{-1}$ and 10.5 mM , respectively. The validity of these parameters was confirmed by comparing simulated and experimental cyclic voltammograms (shown in Figure S1 in the Supporting Information).

Dinitrodurene in Acetonitrile. It has been well established that neutral molecules which contain two identical electroactive groups often gain or lose electrons in two distinct one-electron steps, each step possessing a unique set of electrochemical parameters:



where E^0 , k_s and α are the standard potential, standard heterogeneous electron-transfer rate constant, and transfer coefficient, respectively. On the basis of the principles of electrostatics and focusing on reduction processes (shown above), it is understandable that it is likely to be easier to insert an electron into a neutral species than into a radical anion (i.e., $E_1^0 - E_2^0 > 0$). This situation is called the “normal ordering of potentials” and generally two well-separated waves are observed voltammetrically. However, in some groups of molecules the ordering of potentials is said to be “inverted” (i.e., $E_1^0 - E_2^0 < 0$), owing to a significant structural change associated with the first and/or second electron transfer reaction and a single overall two-electron process is observed voltammetrically.³⁸

Dinitrodurene is well documented to exhibit potential inversion^{38–40} and this should be identifiable by simultaneously determining D and n using the convolutive technique. Cyclic voltammograms obtained from 1.22 mM dinitrodurene in acetonitrile ($0.1 \text{ M } [\text{NEt}_4][\text{BF}_4]$) at a $25 \text{ }\mu\text{m}$ diameter Au

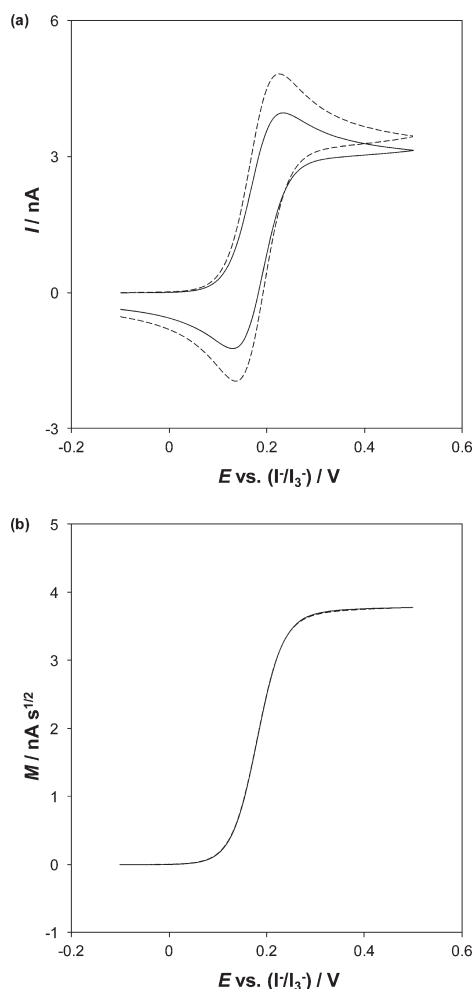


Figure 5. (a) Cyclic voltammograms and (b) linear sweep convoluted current voltammograms obtained from an unknown concentration of $[\text{Fe}(\text{Cp})_2]$ in $[\text{C}_2\text{mim}][\text{NTf}_2]$ at a $25 \mu\text{m}$ diameter Pt microdisk electrode with scan rates of 50 (—) and 100 mV s^{-1} (---).

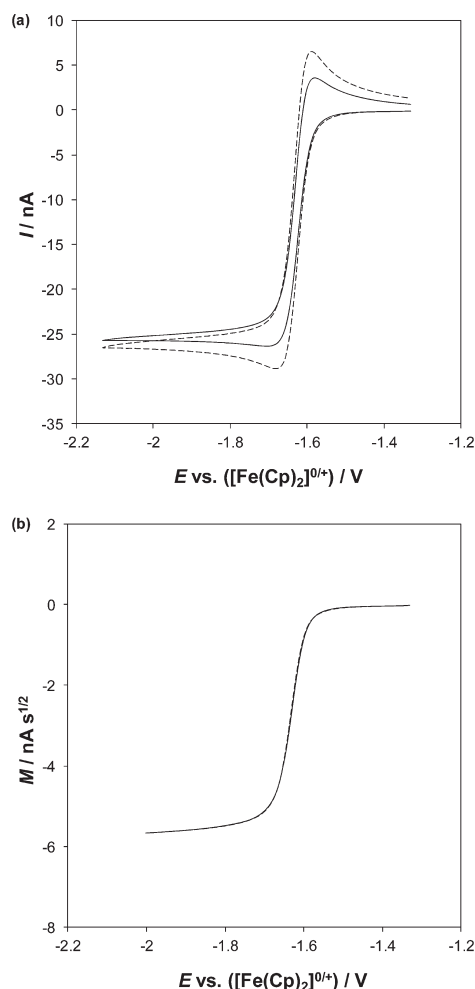


Figure 6. (a) Cyclic voltammograms and (b) linear sweep convoluted current voltammograms obtained from 1.22 mM dinitrodurene in acetonitrile (0.1 M $[\text{NEt}_4][\text{BF}_4]$) at a $25 \mu\text{m}$ diameter Au microdisk electrode with scan rates of 250 (—) and 500 mV s^{-1} (---).

microdisk electrode are shown in Figure 6a. A single, near steady-state reduction wave is observed at reasonably negative potentials (~ -1.65 V vs $[\text{Fe}(\text{Cp})_2]^{0/+}$) at both of the investigated scan rates (250 and 500 mV s^{-1}). The M - E curves obtained by convolving the I - E data collected at the two investigated scan rates are shown in Figure 6b; once again, the M - E curves almost perfectly coincide. The values of D and n ($C^b = 1.22$ mM) were determined to be $1.86 \times 10^{-5} \text{ cm}^2 \text{ s}^{-1}$ and 2.01, respectively. The validity of these parameters was confirmed by comparing simulated and experimental cyclic voltammograms (shown in Figure S2 in the Supporting Information). Additionally, D , E_1^0 , E_2^0 and $E_1^0 - E_2^0$ (determined by simulation) are in excellent agreement with values previously reported.³⁹

Alkynylruthenium Complex in Dichloromethane. The redox state dependent nonlinear optical properties of an alkynylruthenium dendrimer complex (see Chart 1) have been reported.^{41–44} Each of the three identical Ru(II) centers

reportedly undergoes reversible oxidation ($\text{Ru}^{2+/3+}$) in dichloromethane, with an observed ΔE_p value comparable to that of the one electron $[\text{Fe}(\text{Cp})_2]^{0/+}$ process.⁴⁴ This suggests that the three Ru(II) centers are noninteracting and therefore undergo oxidation at very similar potentials. According to the theory derived by Anson and co-workers,⁴⁵ such molecules exhibit voltammetric responses almost indistinguishable from that obtained from the corresponding molecule with a single center (i.e., a reversible one electron transfer) except that there is an enhanced current magnitude. Performing an analysis on the basis of the observed characteristics of the transient voltammetric response of a molecule with multiple non-interacting centers (i.e., $n = 1$) would lead to a gross overestimation of the calculated parameter, whether it be D or C^b .⁴⁶ It is therefore advantageous to perform an analysis that determines D and nC^b simultaneously.

Cyclic voltammograms obtained from a 1.05 mM solution of the alkynylruthenium complex in dichloromethane (0.2 M

$[\text{C}_2\text{mim}][\text{NTf}_2]$) at a $20\ \mu\text{m}$ diameter Pt microdisk electrode are shown in a Figure 7a; a single, near steady-state oxidation

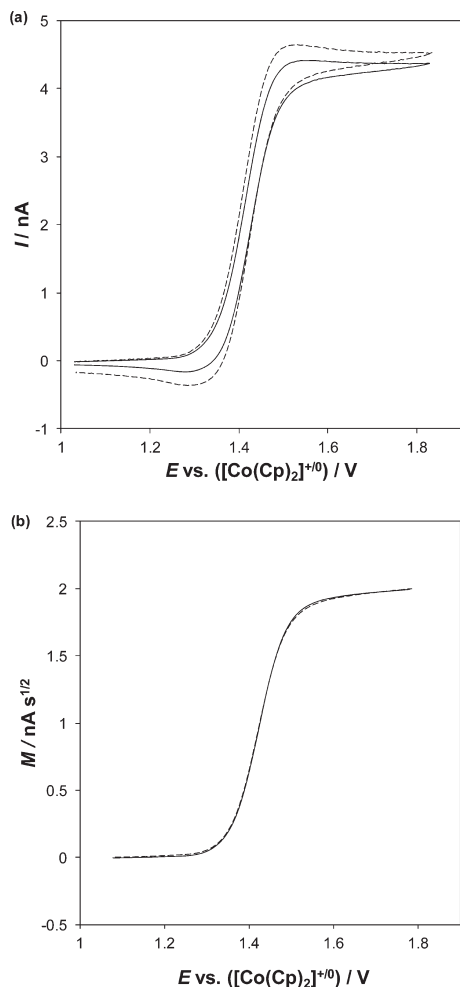


Figure 7. (a) Cyclic voltammograms and (b) linear sweep convolved current voltammograms obtained from a 1.05 mM solution of the alkynylruthenium complex (see Chart 1) in dichloromethane (0.2 M $[\text{C}_2\text{mim}][\text{NTf}_2]$) at a $20\ \mu\text{m}$ diameter Pt microdisk electrode with scan rates of $50\ \text{mV s}^{-1}$ (—) and $100\ \text{mV s}^{-1}$ (---).

wave was observed at all of the investigated scan rates. The transient voltammetric response obtained at a Pt macrodisk electrode (see Figure S3 in the Supporting Information) displays the expected characteristics. Thus, the value of $\Delta E_p \sim 100\ \text{mV}$ at a scan rate of $25\ \text{mV s}^{-1}$ in this highly resistive solvent ($\kappa = 2.03\ \text{mS cm}^{-1}$) is much larger than that expected for a reversible three electron process ($\sim 19\ \text{mV}$) but is comparable to that of the reversible one-electron $[\text{Co}(\text{Cp})_2]^{+0}$ process under these conditions (not shown). The $M-E$ curves obtained by convolving the near steady-state $I-E$ data collected at scan rates of 50 and $100\ \text{mV s}^{-1}$ are shown in Figure 7b; once again, the $M-E$ curves almost perfectly coincide. The values of D and n ($C^b = 1.05\ \text{mM}$) were determined to be $2.96 \times 10^{-6}\ \text{cm}^2\ \text{s}^{-1}$ and 3.02 , respectively. The diffusivity of this

alkynylruthenium complex is much lower than $[\text{Fe}(\text{Cp})_2]^0$ in dichloromethane ($D = 1.67 \times 10^{-5}\ \text{cm}^2\ \text{s}^{-1}$).²¹ However, this is to be expected because of the much larger size of this molecule (D is predicted to be inversely proportional to its hydrodynamic radius, as per the Stokes–Einstein relationship).⁴⁷

Although it is possible to obtain the same information from chronoamperometric experiments, the voltammetric convolution approach avoids instrumental problems arising from the initially large currents that occur in chronoamperometry and the uncertainty as to whether a diffusion limiting current has been obtained due to nonfaradaic current. IR_u effects that greatly affect the initial part of a chronoamperogram are also avoided.

CONCLUSIONS

The robustness of convolution voltammetry has been demonstrated by applying it to a series of electrode processes in both molecular solvents and room temperature ionic liquids. In acetonitrile, the nonfaradaic current is sufficiently small to allow analysis to be carried out on millimolar concentrations of electroactive species without the need for background subtraction, as shown by quantifying the diffusivity of iodide with a platinum macrodisk electrode at scan rates ranging from 250 to $1000\ \text{mV s}^{-1}$. In 1-ethyl-3-methylimidazolium bis-(trifluoromethanesulfonyl)imide, again using iodide as the model system, background subtraction was mandatory when using a macrodisk electrode but could be avoided by using a microdisk electrode, greatly simplifying the analytical procedure. A convolutive procedure used to simultaneously obtain D and nC^b values has also been demonstrated, and three conditions where this capability is valuable have been highlighted, viz. electroactive species that display slow dissolution kinetics, undergo a single multielectron transfer step or contain multiple noninteracting redox centers, as illustrated by the oxidation of ferrocene in an RTIL, the reduction of 1,4-dinitro-2,3,5,6-tetramethylbenzene, and the oxidation of an alkynylruthenium trimer, respectively.

ASSOCIATED CONTENT

Supporting Information

Detailed experimental protocols, simulations of ferrocene oxidation on a platinum microdisk electrode in 1-ethyl-3-methylimidazolium bis(trifluoromethanesulfonyl)imide (Figure S1), simulations of dinitroarene reduction on a gold microdisk electrode in acetonitrile (Figure S2), and cyclic voltammograms obtained from the oxidation of the alkynylruthenium complex on a platinum macrodisk electrode in dichloromethane (Figure S3). This material is available free of charge via the Internet at <http://pubs.acs.org>.

AUTHOR INFORMATION

Corresponding Authors

*E-mail: alan.bond@monash.edu.

*E-mail: pmahon@swin.edu.au.

Notes

The authors declare no competing financial interest.

ACKNOWLEDGMENTS

The authors are pleased to acknowledge the gift of the alkynylruthenium trimer from Professor Mark G. Humphrey of the Research School of Chemistry at The Australian National University.

■ REFERENCES

- (1) Bard, A. J.; Faulkner, L. R. *Electrochemical Methods: Fundamentals and Applications*, 2nd ed.; Wiley: New York, 2001.
- (2) Oldham, K. B.; Myland, J. C. *Fundamentals of Electrochemical Science*; Academic Press: San Diego, CA, 1994.
- (3) Zhang, J.; Bond, A. M. *Analyst* **2005**, *130*, 1132–1147.
- (4) Barrosse-Antle, L. E.; Bond, A. M.; Compton, R. G.; O'Mahony, A. M.; Rogers, E. I.; Silvester, D. S. *Chem.-Asian J.* **2010**, *5*, 202–230.
- (5) Zhao, C.; Burrell, G.; Torriero, A. A. J.; Separovic, F.; Dunlop, N. F.; MacFarlane, D. R.; Bond, A. M. *J. Phys. Chem. B* **2008**, *112*, 6923–6936.
- (6) Armand, M.; Endres, F.; MacFarlane, D. R.; Ohno, H.; Scrosati, B. *Nat. Mater.* **2009**, *8*, 621–629.
- (7) Galinski, M.; Lewandowski, A.; Stepniak, I. *Electrochim. Acta* **2006**, *51*, 5567–5580.
- (8) Bentley, C. L.; Bond, A. M.; Hollenkamp, A. F.; Mahon, P. J.; Zhang, J. *Anal. Chem.* **2012**, *85*, 2239–2245.
- (9) Savéant, J. M. *J. Electroanal. Chem.* **1973**, *44*, 169–187.
- (10) Grenness, M.; Oldham, K. B. *Anal. Chem.* **1972**, *44*, 1121–1129.
- (11) Oldham, K. B. *Anal. Chem.* **1972**, *44*, 196–198.
- (12) Mahon, P. J.; Oldham, K. B. *J. Electroanal. Chem.* **1999**, *464*, 1–13.
- (13) Mahon, P. J. *Electrochim. Acta* **2011**, *56*, 2190–2200.
- (14) Mahon, P. J. *J. Solid State Electrochem.* **2009**, *13*, 573–582.
- (15) McDonagh, A. M.; Powell, C. E.; Morrall, J. P.; Cifuentes, M. P.; Humphrey, M. G. *Organometallics* **2003**, *22*, 1402–1413.
- (16) Skoog, D. A.; West, D. M.; Holler, F. J.; Crouch, S. R. *Fundamentals of Analytical Chemistry*, 8th ed.; Thomson-Brooks/Cole: Belmont, CA, 2004.
- (17) de Levie, R. *How to Use Excel in Analytical Chemistry and in General Scientific Data Analysis*; Cambridge University Press: Cambridge, U.K., 2001.
- (18) de Levie, R. *Excellaneous*. <http://www.bowdoin.edu/~rdelevie/excellaneous/> (accessed September 19, 2013).
- (19) Oldham, K. B. *Anal. Chem.* **1986**, *58*, 2296–2300.
- (20) Aoki, K.; Osteryoung, J. J. *Electroanal. Chem.* **1984**, *160*, 335–339.
- (21) Tsierkezos, N. G. *J. Solution Chem.* **2007**, *36*, 289–302.
- (22) Goto, M.; Oldham, K. B. *Anal. Chem.* **1973**, *45*, 2043–2050.
- (23) Goto, M.; Oldham, K. B. *Anal. Chem.* **1974**, *46*, 1522–1530.
- (24) Oldham, K. B. *J. Electroanal. Chem.* **1976**, *72*, 371–378.
- (25) Hanson, K. J.; Tobias, C. W. *J. Electrochem. Soc.* **1987**, *134*, 2204–2210.
- (26) Macagno, V. A.; Giordano, M. C.; Arvia, A. J. *Electrochim. Acta* **1969**, *14*, 335.
- (27) Bentley, C. L.; Bond, A. M.; Hollenkamp, A. F.; Mahon, P. J.; Zhang, J. *Electrochim. Acta* **2013**, *109*, 554–561.
- (28) Silvester, D. S.; Aldous, L.; Hardacre, C.; Compton, R. G. *J. Phys. Chem. C* **2008**, *112*, 6551–6557.
- (29) Kawano, R.; Watanabe, M. *Chem. Commun.* **2003**, 330–331.
- (30) Kawano, R.; Watanabe, M. *Chem. Commun.* **2005**, 2107–2109.
- (31) Ejigu, A.; Lovelock, K. R. J.; Licence, P.; Walsh, D. A. *Electrochim. Acta* **2011**, *56*, 10313–10320.
- (32) Zhang, Y.; Zheng, J. B. *Electrochim. Acta* **2007**, *52*, 4082–4086.
- (33) Mahon, P. J.; Phillips, W. R. C. *Electrochim. Acta* **2012**, *74*, 16–22.
- (34) De Vreese, P.; Haerens, K.; Matthijs, E.; Binnemans, K. *Electrochim. Acta* **2012**, *76*, 242–248.
- (35) Hultgren, V. M.; Mariotti, A. W. A.; Bond, A. M.; Wedd, A. G. *Anal. Chem.* **2002**, *74*, 3151–3156.
- (36) Rogers, E. I.; Silvester, D. S.; Poole, D. L.; Aldous, L.; Hardacre, C.; Compton, R. G. *J. Phys. Chem. C* **2008**, *112*, 2729–2735.
- (37) Xiong, L.; Aldous, L.; Henstridge, M. C.; Compton, R. G. *Anal. Methods* **2012**, *4*, 371–376.
- (38) Evans, D. H. *Chem. Rev.* **2008**, *108*, 2113–2144.
- (39) Kraiya, C.; Evans, D. H. *J. Electroanal. Chem.* **2004**, *565*, 29–35.
- (40) Evans, D. H.; Hu, K. J. *Chem. Soc., Faraday Trans.* **1996**, *92*, 3983–3990.
- (41) McDonagh, A. M.; Humphrey, M. G.; Samoc, M.; Luther-Davies, B.; Houbrechts, S.; Wada, T.; Sasabe, H.; Persoons, A. *J. Am. Chem. Soc.* **1999**, *121*, 1405–1406.
- (42) Cifuentes, M. P.; Powell, C. E.; Humphrey, M. G.; Heath, G. A.; Samoc, M.; Luther-Davies, B. *J. Phys. Chem. A* **2001**, *105*, 9625–9627.
- (43) Powell, C. E.; Humphrey, M. G.; Cifuentes, M. P.; Morrall, J. P.; Samoc, M.; Luther-Davies, B. *J. Phys. Chem. A* **2003**, *107*, 11264–11266.
- (44) Cifuentes, M. P.; Powell, C. E.; Morrall, J. P.; McDonagh, A. M.; Lucas, N. T.; Humphrey, M. G.; Samoc, M.; Houbrechts, S.; Asselberghs, I.; Clays, K.; Persoons, A.; Isoshima, T. *J. Am. Chem. Soc.* **2006**, *128*, 10819–10832.
- (45) Flanagan, J. B.; Margel, S.; Bard, A. J.; Anson, F. C. *J. Am. Chem. Soc.* **1978**, *100*, 4248–4253.
- (46) Zhang, J.; Bond, A. M.; Belcher, J.; Wallace, K. J.; Steed, J. W. *J. Phys. Chem. B* **2003**, *107*, 5777–5786.
- (47) Atkins, P. W.; De Paula, J. *Atkins' Physical Chemistry*, 9th ed.; Oxford University Press: Oxford, U.K., 2010.

Supporting information for

Applications of convolution voltammetry in electroanalytical chemistry

*Cameron L. Bentley,^{†,‡} Alan M. Bond,[†] Anthony F. Hollenkamp,[‡] Peter J. Mahon[§] and Jie
Zhang[†]*

[†]School of Chemistry, Monash University, Clayton, Vic 3800, Australia

[‡]CSIRO Energy Technology, Box 312, Clayton South, Vic 3169, Australia

[§]Faculty of Life and Social Sciences, Swinburne University of Technology, Hawthorn, Vic
3122, Australia

EXPERIMENTAL SECTION

Preparation of reagents. 1-ethyl-3-methylimidazolium bis(trifluoromethanesulfonyl)imide ($[\text{C}_2\text{mim}][\text{NTf}_2]$, Io-li-tec GmbH, 99.5%) was dried under high vacuum ($\leq 10^{-2}$ mbar) at 45°C for 48 hours and stored under lithium. The residual water was less than 50 ppm by Karl Fischer titration (Metrohm 831 KF Coulometer). 1-ethyl-3-methylimidazolium iodide ($[\text{C}_2\text{mim}]\text{I}$, Io-li-tec GmbH, >98%) was recrystallized twice from a 2:1 mixture of ethyl acetate (Merck, EMSURE) and isopropanol (Merck, EMSURE) then dried under high vacuum for 48 hours. Care was taken during handling and storage of $[\text{C}_2\text{mim}]\text{I}$ to avoid exposure to light. Tetraethylammonium tetrafluoroborate ($[\text{NEt}_4][\text{BF}_4]$, Stella Chemifa, 99.9%) was recrystallised twice from methanol (Merck, EMSURE) and dried at 50°C for 72 hours under vacuum. 1,4-dinitro-2,3,5,6-tetramethylbenzene (dinitrodurene) was prepared by forming a homogeneous slurry of powdered 1,2,4,5-tetramethylbenzene (1.2 g, Sigma-Aldrich, 98%) in 98% H_2SO_4 (7.5 mL, Univar) and adding dropwise a mixture of 70% HNO_3 (Scharlau) and 98% H_2SO_4 (5 mL total, 1:3 v/v) over a period of 2 hours, ensuring the temperature of the reaction mixture remained between 5 and 10°C.¹ The reaction mixture was subsequently quenched in ice water and the crude product was filtered, rinsed and recrystallised from absolute ethanol (Merck, EMSURE). The recrystallised dinitrodurene was finally dried at 65°C for 2 hours (MP = 207-208°C), for a final yield of 49%.

Auxiliary, reference and working electrodes. Platinum mesh was used as the auxiliary electrode. The reference electrode system employed was either Ag/Ag^+ (10 mM AgNO_3 + 0.1 M $[\text{NBu}_4][\text{PF}_6]$ in acetonitrile), I/I_3^- (Pt | 400 mM $[\text{C}_2\text{mim}]\text{I}$ + 100 mM I_2 in $[\text{C}_2\text{mim}][\text{NTf}_2]$) or an Ag wire (in acetonitrile or dichloromethane). When the Ag wire pseudoreference was employed the potential was calibrated against the recommended $[\text{Fe}(\text{Cp})_2]^{0/+}$ or $[\text{Co}(\text{Cp})_2]^{+0}$ process^{2, 3} after the required voltammetric experiments had been performed. The platinum macrodisk working electrode (nominal diameter of 1.6 mm) was purchased from BASi

(Bioanalytical systems, West Lafayette, IN); the platinum macrodisk (nominal diameter of 2.0 mm), platinum microdisk (nominal diameter of 20 μm) and gold microdisk (nominal diameter of 25 μm) working electrodes were purchased from Metrohm (Herisau, SUI). The 25 μm dia. platinum microdisk working electrode was fabricated by sealing a wire of the appropriate dimensions in glass. Macrodisk electrodes were activated by polishing with successively smaller (1 and 0.3 μm) aqueous alumina slurries (Kemet Ltd, Kent, UK) on a clean polishing cloth (Buehler, Lake Bluff, IL). Adherent alumina was removed by sonication in de-ionized water (Milli-Q), before rinsing with acetone. Microdisk electrodes were activated by polishing with an aqueous slurry of 0.05 μm alumina and rinsing thoroughly with de-ionized water then acetone. The active electrode area of each of the electrodes was calibrated voltammetrically using the oxidation of a ferrocene solution of known concentration (1.7 mM in acetonitrile containing 0.1 M $[\text{NBu}_4][\text{PF}_6]$) and adopting a diffusion coefficient of $2.24 \times 10^{-5} \text{ cm}^2 \text{ s}^{-1}$ as published under these conditions.⁴

REFERENCES

- (1) Lind, C. J.; Warren, C. A. Production of 1, 4-dinitro-2, 3, 5, 6-tetraalkylbenzenes. U.S. Patent 3,153,099, October 13, 1964. <http://www.freepatentsonline.com/3153099.pdf> (accessed September 19, 2013).
- (2) Stojanovic, R. S.; Bond, A. M., *Anal. Chem.* **1993**, 65, 56-64.
- (3) Gritzner, G.; Kuta, J., *Pure Appl. Chem.* **1984**, 56, 461-466.
- (4) Rogers, E. I.; Compton, R. G., *J. Electroanal. Chem.* **2010**, 648, 15-19.

Table 1. Values of important polynomial coefficients used in eqs 6, 7, 9 and 10.

j	g(t)		G(t)	
	a _j	b _j	a _j	b _j
1	$\frac{1}{\pi^{1/2}}$	0	$\frac{4}{3\pi^{1/2}}$	$\frac{\pi}{4}$
2	-1	$\frac{1}{4\pi^{1/2}}$	$\frac{-1}{2}$	$\frac{-1}{\pi^{1/2}}$
3	$\frac{3}{2\pi^{1/2}}$	0	$\frac{2}{5\pi^{1/2}}$	0.26180
4	-0.38584	-4.7016x10 ⁻²	-6.4307x10 ⁻²	-6.2688x10 ⁻²
5	7.8535x10 ⁻²	4.7019x10 ⁻³	8.9754x10 ⁻³	1.2538x10 ⁻³
6		1.6079x10 ⁻²		1.8376x10 ⁻³
7		-2.2686x10 ⁻²		-1.4404x10 ⁻³
8		1.2948x10 ⁻²		5.2315x10 ⁻⁴
	$\theta = 1.304$		$\theta = 1.368$	

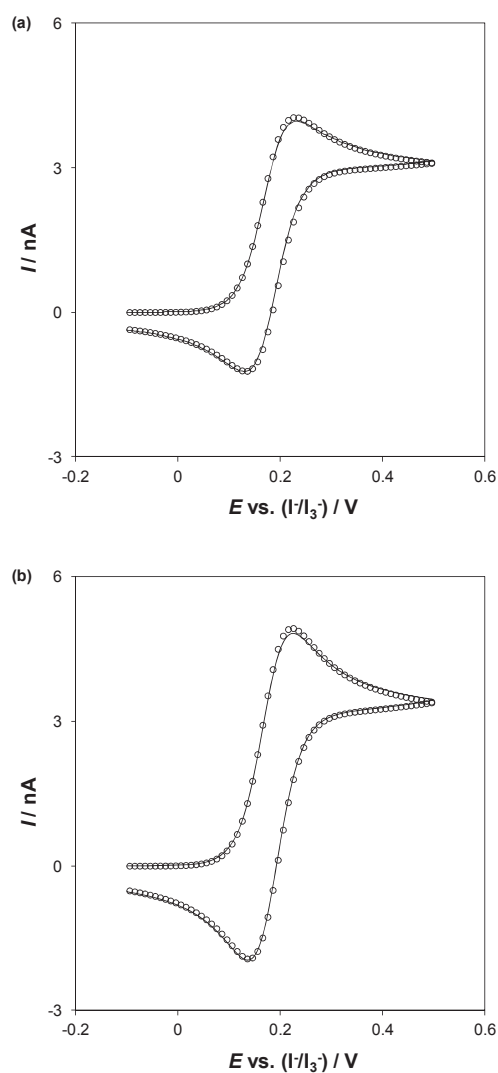


Figure S1. Comparison of simulated (\circ) and experimental cyclic voltammograms ($—$) obtained from $[\text{Fe}(\text{Cp})_2]$ (concentration determined by convolution voltammetry) in $[\text{C}_2\text{mim}][\text{NTf}_2]$ at a $25\ \mu\text{m}$ dia. Pt microdisk electrode with scan rates of (a) 50 and (b) $100\ \text{mV s}^{-1}$. The simulation parameters used were: $D_{\text{red}} = 4.49 \times 10^{-7}\ \text{cm}^2\ \text{s}^{-1}$, $D_{\text{ox}} = 4.20 \times 10^{-7}\ \text{cm}^2\ \text{s}^{-1}$, $C^b = 0.0105\ \text{M}$, $k_s = 10\ \text{cm/s}$, $r = 0.00133\ \text{cm}$, $\alpha = 0.5$, $T = 296\ \text{K}$ and $E^0 = 0.179\ \text{V}$.

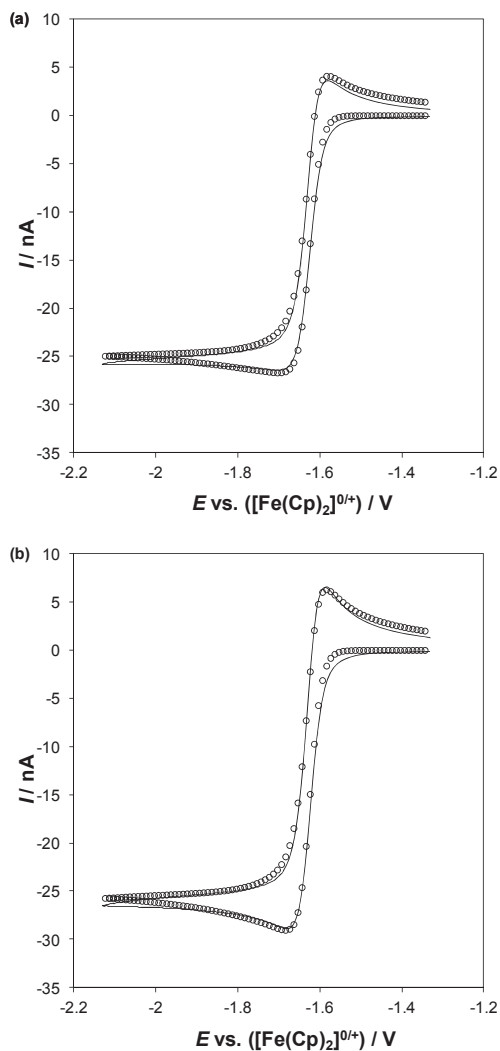


Figure S2. Comparison of simulated (\circ) and experimental cyclic voltammograms ($—$) obtained from 1.22 mM dinitrodurene in acetonitrile (0.1 M $[\text{NEt}_4][\text{BF}_4]$) at a 25 μm dia. Au microdisk electrode with scan rates of (a) 250 and (b) 500 mV s^{-1} . The simulation parameters used were: $D = 1.86 \times 10^{-5} \text{ cm}^2 \text{ s}^{-1}$, $T = 296 \text{ K}$, $E_1^0 = -1.761 \text{ V}$, $E_2^0 = -1.481 \text{ V}$, $r = 0.00133 \text{ cm}$, $\alpha_1 = \alpha_2 = 0.5$, $k_{s,1} = 1.5 \text{ cm s}^{-1}$ and $k_{s,2} = 0.6 \text{ cm s}^{-1}$.

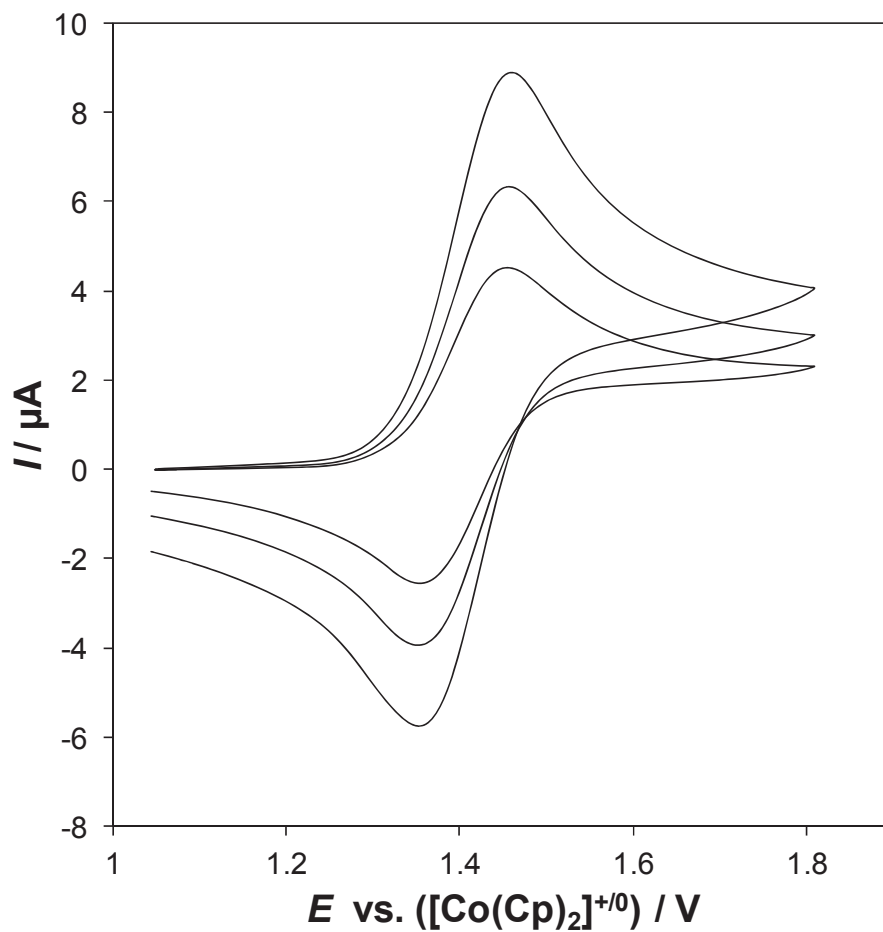


Figure S3. Cyclic voltammograms obtained from a 1.1 mM solution of the alkynylruthenium complex (see Structure 1) in dichloromethane (0.2 M $[\text{C}_2\text{mim}][\text{NTf}_2]$) at a 1.6 mm dia. Pt macrodisk electrode with scan rates (from top to bottom) of 100, 50 and 25 mV s^{-1} .

4. Electrode Reaction and Mass-Transport Mechanisms Associated with the I^-/I_2 Redox Couple in Ionic Liquid Media

The first redox system studied in detail was the I^-/I_2 couple, which has a pivotal role in current DSSC technology. Initial investigations focused on iodide in a single component system (*i.e.*, iodine was absent in the bulk solution), with an emphasis on elucidating the mass-transport behaviour and the electrode material dependence of the heterogeneous charge transfer process using the previously developed electroanalytical methodology (*i.e.*, semiintegration and convolution). Further detail can be found in the following publication:

Bentley, C. L.; Bond, A. M.; Hollenkamp, A. F.; Mahon, P. J.; Zhang, J., *Electrochim. Acta* **2013**, *109*, 554-561.

While investigating the electrode material dependence of the iodide electro-oxidation process, interesting and unexpected behaviour was found when using gold as the electrode material. Further detail can be found in the following publication:

Bentley, C. L.; Bond, A. M.; Hollenkamp, A. F.; Mahon, P. J.; Zhang, J., *Anal. Chem.* **2013**, *85*, 11319–11325.

Finally, iodine was introduced into the bulk solution and its effect on iodide mass-transport was quantified. In addition, the iodide electro-oxidation mechanism was investigated on platinum in greater detail, using a combination of cyclic voltammetry and numerical simulation. Further detail can be found in the following publication:

Bentley, C. L.; Bond, A. M.; Hollenkamp, A. F.; Mahon, P. J.; Zhang, J., *J. Phys. Chem. C* **2014**, *118*, 29663–29673.

Part B: Specific Declaration

Monash University

Declaration for Thesis Chapter 4**Declaration by candidate**

In the case of Chapter 4, the nature and extent of my contribution to the work was the following:

Nature of contribution	Extent of contribution (%)
Experimental work, Manuscript writing/preparation	100%

The following co-authors contributed to the work. If co-authors are students at Monash University, the extent of their contribution in percentage terms must be stated:

Name	Nature of contribution	Extent of contribution (%) for student co-authors only
Cameron L. Bentley	Experimental work, manuscript writing/preparation, editing.	100%
Alan M. Bond	Supervision, proof-reading, editing.	
Anthony F. Hollenkamp	Supervision, proof-reading, editing.	
Peter J. Mahon	Supervision, proof-reading, editing.	
Jie Zhang	Supervision, proof-reading, editing.	

The undersigned hereby certify that the above declaration correctly reflects the nature and extent of the candidate's and co-authors' contributions to this work*.

Candidate's Signature		Date 02/03/2015
Main Supervisor's Signature		Date 02/03/2015



Contents lists available at ScienceDirect

Electrochimica Acta

journal homepage: www.elsevier.com/locate/electacta

Concentration and electrode material dependence of the voltammetric response of iodide on platinum, glassy carbon and boron-doped diamond in the room temperature ionic liquid 1-ethyl-3-methylimidazolium bis(trifluoromethanesulfonyl)imide



Cameron L. Bentley^{a,b}, Alan M. Bond^{a,*,1}, Anthony F. Hollenkamp^b, Peter J. Mahon^c, Jie Zhang^{a,*,*,1}

^a School of Chemistry, Monash University, Clayton, Vic 3800, Australia

^b CSIRO Energy Technology, Box 312, Clayton South, Vic 3169, Australia

^c Faculty of Life and Social Sciences, Swinburne University of Technology, Hawthorn, Vic 3122, Australia

ARTICLE INFO

Article history:

Received 22 May 2013

Received in revised form 11 July 2013

Accepted 11 July 2013

Available online 25 July 2013

Keywords:

Ionic liquid

Dye-sensitized solar cell

Diffusion coefficient

Semi-integration

Nucleation

ABSTRACT

The electro-oxidation of iodide has been investigated as a function of concentration using steady-state microelectrode voltammetry, transient cyclic voltammetry and linear-sweep semi-integral voltammetry on platinum, glassy carbon and boron-doped diamond electrodes in the room temperature ionic liquid 1-ethyl-3-methylimidazolium bis(trifluoromethanesulfonyl)imide. Two oxidation processes are observed on all of the investigated electrode materials, with the first being assigned to the oxidation of iodide to triiodide (confirmed by UV/visible spectroscopy) and the second being attributed to the oxidation of triiodide to iodine. Iodide oxidation is kinetically more facile on platinum compared to glassy carbon or boron-doped diamond. At elevated bulk iodide concentrations, the nucleation and growth of sparingly soluble electrogenerated iodine at the electrode surface was observed and imaged *in situ* using optical microscopy. The diffusion coefficient of iodide was determined to be $2.59 (\pm 0.04) \times 10^{-7} \text{ cm}^2 \text{ s}^{-1}$ and independent of the bulk concentration of iodide. The steady-state iodide oxidation current measured at a platinum microelectrode was found to be a linear function of iodide concentration, as expected if there are no contributions from non-Stokesian mass-transport processes (electron hopping and/or Grothuss-type exchange) under the investigated conditions.

© 2013 Elsevier Ltd. All rights reserved.

1. Introduction

Since the introduction of air/water stable nonhaloaluminate room temperature ionic liquids (RTILs) over two decades ago [1], there has been growing interest in employing these neoteric solvents as replacements for volatile organic compounds in a range of applications. Although the only property common to all RTILs is intrinsic ionic conductivity [2], many of these compounds possess other favourable qualities, such as negligible vapour pressure and high chemical, thermal and electrochemical stability [3]. Indeed, one of the main advantages of RTILs is their versatility; the physicochemical properties of a particular RTIL can be tailored to suit a

specific application by modifying its constituent cation/anion [4]. Several research groups have successfully employed ionic liquids as replacements for 'conventional electrolytes' in a number of electrochemical devices, including dye-sensitized solar cells [5,6], lithium batteries [7], fuel cells [8] and supercapacitors [9].

The dye-sensitized solar cell (DSSC), first reported by O'Regan and Grätzel [10], has been the subject of intensive research over the past two decades. DSSCs are promising candidates to replace traditional (*p-n*) silicon photovoltaics due to their lower manufacturing cost and great versatility in size, shape, flexibility and design. In its most simplistic form, a DSSC has three components: a semi-conductor photoanode (TiO_2) with an adhered photoactive dye, a platinized cathode (counter electrode) and an electrolyte containing a redox shuttle, which is most commonly composed of a volatile organic compound (usually acetonitrile) with dissolved iodide/triiodide (I^-/I_3^-) [6]. There are on-going concerns over the long term stability (solvent evaporation exacerbated by solar heating) and safety (solvent flammability) of electrolyte solutions which contain volatile organic compounds. While these

E-mail addresses: alan.bond@monash.edu (A.M. Bond), jie.zhang@monash.edu (J. Zhang).

¹ ISE Member.

0013-4686/\$ – see front matter © 2013 Elsevier Ltd. All rights reserved.

<http://dx.doi.org/10.1016/j.electacta.2013.07.101>

concerns can be resolved by employing an RTIL as the electrolyte, such systems are yet to achieve the highest levels of photo-voltaic performance [5,6,11]. This implies that some aspects of the electrochemistry of the iodide–iodine couple are not fully understood, thereby offering the prospect of improving the operation of RTIL electrolyte solutions in DSSCs. Kawano and Watanabe reported that a mixture of 1-ethyl-3-methyl-imidazolium bis(trifluoromethanesulfonyl)imide and the corresponding iodide exhibited greatly enhanced diffusion of iodide when iodine was added to the bulk mixture [12,13]. More recently, other groups have shown that enhancements of diffusion of similar order can even occur in much more viscous media such as 1-propyl-3-methyl-imidazolium iodide [14]. While explanations of this behaviour have quite reasonably suggested that rapid exchange processes establish a Grotthus-like extension of diffusion, critical detail on the actual species involved and their interaction with different electrode materials remain unknown. These issues will be important in any optimization of electrolyte function in DSSCs.

The $I^-/I_3^-/I_2$ redox processes have been studied extensively in a range of conventional solvents, most notably water [15] and acetonitrile [16] and to a much lesser extent in RTILs, with a few key studies available in a limited range of electrolytes [12,13,17–19]. Regardless of the solvent, platinum is by far the most widely studied electrode material, on which it is well known that halides chemisorb [20,21]. However, unlike F^- , Cl^- and Br^- which adsorb in anionic form, I^- reacts at the platinum surface to form an uncharged adsorbed species (I_{ads}), which may have a profound effect on electron transfer reactions occurring at the electrode/electrolyte interface [20,22,23].

In aqueous media, iodide has been shown to be oxidized to molecular iodine on platinum in one step, giving rise to a single voltammetric wave [24,25]:



By contrast, in aprotic solvents such as acetonitrile, and analogously in RTILs, iodide has been shown to be oxidized to molecular iodine on platinum in two steps, giving rise to two voltammetric waves [24,25]:



The iodide oxidation process is therefore governed to a significant degree by the homogeneous equilibrium process:



The stability constant of this reaction strongly influences the observed iodide oxidation mechanism [25] and is highly solvent dependent, ranging from *ca.* $10^3 M^{-1}$ in water [26] to *ca.* $10^7 M^{-1}$ in acetonitrile [25,27]. Compton et al. [19] estimated the stability constant of I_3^- to be *ca.* $10^4 M^{-1}$ in 1-butyl-3-methylimidazolium bis(trifluoromethanesulfonyl)imide ($[C_4mim][NTf_2]$) via simulation of voltammetric data.

The heterogeneous electron transfer kinetics of the $I^-/I_3^-/I_2$ redox processes are strongly dependent upon the identity and state (*i.e.* cleanliness, microstructure and surface chemistry) of the electrode material. As previously noted, platinum is the most commonly employed cathode material in current DSSC technology, where it acts as an electrocatalyst for the redox shuttle reaction given in Eq. (2). Obviously the high-cost of noble metals such as platinum is a significant driving force for the development of cheaper cathode materials, notably carbon-based materials [6,28,29]. In comparison to platinum, the $I^-/I_3^-/I_2$ redox system has not been extensively explored on carbon electrodes, with a few studies available with pyrolytic carbon electrodes in water [30,31]

and acetonitrile [32]. Iodide oxidation on pyrolytic carbon is qualitatively similar to that seen on platinum: one wave is observed in aqueous media corresponding to the I^-/I_2 process described by Eq. (1) and two waves are observed in acetonitrile corresponding to the I^-/I_3^- and I_3^-/I_2 processes described by Eqs. (2) and (3) [32]. Analogous studies on the oxidation of iodide on carbon electrode materials in RTIL electrolytes are not available.

In this paper, we present a deeper investigation into the electrochemical behaviour of iodide-containing ionic liquid electrolytes with a view to improving their use in DSSCs. To this end, we report the concentration and electrode material dependence of the voltammetric response of iodide in the room temperature ionic liquid 1-ethyl-3-methylimidazolium bis(trifluoromethanesulfonyl)imide. A variety of voltammetric techniques, including steady-state microelectrode voltammetry, transient cyclic voltammetry and linear sweep semi-integral voltammetry have been employed over a large range of bulk iodide concentrations (10–500 mM) on three distinctly different electrode materials: platinum, glassy carbon (GC) and boron-doped diamond (BDD).

2. Experimental

2.1. Reagents

1-Ethyl-3-methylimidazolium bis(trifluoromethanesulfonyl)imide ($[C_2mim][NTf_2]$, Io-li-tec GmbH, 99.5%) was dried under high vacuum ($\leq 10^{-2}$ mbar) at 45 °C for 48 h and stored under lithium. The residual water was less than 50 ppm by Karl Fischer titration (Metrohm 831 KF Coulometer). 1-Ethyl-3-methylimidazolium iodide ($[C_2mim]I$, Io-li-tec GmbH, >98%) was recrystallized twice from a 2:1 mixture of ethyl acetate (Merck, EMSURE) and isopropanol (Merck, EMSURE) then dried under high vacuum for 48 h. Care was taken during handling and storage of $[C_2mim]I$ to avoid exposure to light. Iodine (Sigma-Aldrich, 99.8%), ferrocene (Fluka, >98%), acetonitrile (Sigma-Aldrich, 99.8%) and acetone (Merck, EMSURE) were used as supplied by the manufacturer. $[C_2mim][NTf_2]$, $[C_2mim]I$ and I_2 were stored and handled under a dry argon atmosphere in a glovebox.

2.2. Electrochemical systems and procedures

Voltammetric experiments at high scan rates ($\geq 10 V s^{-1}$) were carried out with a CH Instruments 760D Potentiostat (CH Instruments, Austin, TX). All other voltammetric experiments were undertaken with a Gamry Reference 600™ Potentiostat/Galvanostat/ZRA (Gamry Instruments, Warminster, PA). All experiments were carried out under benchtop conditions at ambient temperature (21 ± 1 °C). All electrolytes were degassed with N_2 prior to experimentation and a blanket of N_2 was maintained over the electrolytes during the respective experiments. A faraday cage was employed in microelectrode experiments. All voltammetric experiments were carried out using a standard 3-electrode arrangement with a platinum mesh auxiliary electrode and an I^-/I_3^- reference electrode [33] (Pt | 400 mM $[C_2mim]I$ + 100 mM I_2 in $[C_2mim][NTf_2]$). An electrochemical cell with an optically transparent base was used to image the working electrode surface *in situ* using a Nikon Epiphot bright/dark field inverted optical microscope (Nikon Instruments, JP). UV/Visible spectroscopy was performed *in situ* with a Varian Cary 50 Bio UV/Visible Spectrophotometer (Agilent, Santa Clara, CA) in a quartz optically transparent thin layer electrochemical (OTTLE) cell with a platinum mesh working electrode.

The platinum macrodisk (nominal diameter = 1.6 mm), glassy carbon macrodisk (nominal diameter = 3.0 mm) and glassy carbon

microdisk (nominal diameter = 11 μm) were purchased from BASi (Bioanalytical systems, West Lafayette, IN); the platinum microdisk (nominal diameter = 100 μm) was purchased from Metrohm (Herisau, Switzerland); the boron-doped diamond macrodisk (nominal diameter = 3.0 mm) was purchased from Windsor Scientific (Berkshire, UK). The 2 μm diameter platinum microelectrode was fabricated by sealing a Wollaston wire of the appropriate dimensions in a glass capillary [34]. Macroelectrodes were activated by polishing with successively smaller (1, 0.3 and 0.05 μm) aqueous alumina slurries (Kemet, Kent, UK) on a clean polishing cloth (Buehler, Lake Bluff, IL). Adherent alumina was removed by sonication in de-ionized water (Milli-Q), before rinsing with acetone. Microelectrodes were activated by polishing in aqueous 0.05 μm alumina slurry and rinsing thoroughly with de-ionized water then acetone. The active electrode area of each of the electrodes was calibrated voltammetrically using the oxidation of a ferrocene solution of known concentration (1.7 mM in acetonitrile containing 0.1 M $[\text{NBu}_4][\text{PF}_6]$) and adopting a diffusion coefficient of $2.24 \times 10^{-5} \text{ cm}^2 \text{ s}^{-1}$ as published under these conditions [35].

Semi-integration of the $I-t$ data was performed using an algorithm from de Levie [36], which was adapted from Oldham and Myland [37]. A Microsoft Excel macro that includes this algorithm is available free online [38]. Experimental uncertainties were estimated by propagation of the standard deviations in the variables of interest [39].

3. Results and discussion

3.1. Steady-state voltammetric studies on Pt and GC electrodes

Steady-state microelectrode (ME) studies were carried out with a 2 μm dia. Pt microdisk electrode at iodide concentrations ranging from 10 to 500 mM; representative voltammograms are shown in Fig. 1. The voltammetric response in $[\text{C}_2\text{mim}][\text{NTf}_2]$ is strongly dependent on the bulk concentration of iodide. At low bulk iodide concentrations (10 mM, see Fig. 1a), there are two well-defined limiting current plateaus on the steady-state voltammogram, corresponding to the processes given in Eqs. (2) and (3) respectively. The magnitude of the plateaus relative to each other (*i.e.* 2:1) is proportional to the number of electrons involved in each process. The product of the first oxidation reaction was confirmed to be I_3^- by spectroelectrochemistry at a Pt mesh working electrode (see Fig. S1a) upon comparison with an authentic sample (see Fig. S1b). Unfortunately, the product of the second reaction could not be confirmed by the UV/Visible spectroscopic method due to the relatively low molar absorptivity of I_2 compared to I_3^- [40].

At high iodide concentrations (≥ 300 mM, see Fig. 1b), a well-defined voltammetric plateau is still observed for the I^-/I_3^- process, but not for the I_3^-/I_2 process, where a loop is observed upon reversing the direction of the potential sweep. This loop is attributable to the nucleation and growth of sparingly soluble iodine on the surface of the electrode, which was confirmed by optical microscopy (see Section 3.5). Similar observations were made by Compton et al. [19] in their investigation of the electrochemistry of a range of iodide salts in $[\text{C}_4\text{mim}][\text{NTf}_2]$. Considering the high ionic strength of RTILs, it is unsurprising that the charged I^-/I_3^- species are readily soluble, whereas uncharged I_2 is sparingly soluble; analogous issues are encountered when attempting to dissolve uncharged electroactive species such as ferrocene in various RTILs [41].

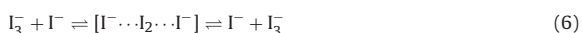
Voltammograms obtained under near steady state conditions at a GC microelectrode resemble those discussed in detail at Pt. However, at low iodide concentration the two processes are less well resolved in the GC case (compare Figs. S2 and 1a). Predominantly this is a result of the initial process being more drawn out

and hence assumed to be less reversible than at the Pt surface, a conclusion that will be supported by data presented in Sections 3.2 and 3.3 when comparing results obtained at Pt and GC macrodisk electrodes under transient conditions.

The diffusion coefficient (D) of an electroactive species can be calculated from the steady-state limiting current (I_L) measured at a ME using the expression [42]:

$$I_L = 4nFC^*aD \quad (5)$$

where n is the number of electrons involved in the charge transfer, F is Faraday's constant, C^* is the bulk concentration of electroactive species, and a is the electrode radius. A number of research groups [5,13,14,43,44] have observed non-Stokesian mass transport in RTILs containing I^-/I_3^- , whereby apparent diffusion coefficients increase with the total concentration of iodine-species present to values which are much higher than can be explained by physical diffusion alone. This phenomenon is thought to be due to a Grotthuss-type homogeneous exchange mechanism, facilitated by the high-ionic strength environment of RTILs:



Given that I_3^- is produced in the vicinity of the electrode surface during oxidation of I^- , it is feasible that this process could occur during I^- oxidation.

Considering the complications associated with the I_3^-/I_2 process at high iodide concentrations, the limiting current for only the I^-/I_3^- process ($n=2/3$) was measured at Pt and plotted against concentration as shown in Fig. 1c. The oxidative limiting current is proportional to the bulk concentration of iodide ($R^2 = 0.9999$), as predicted by Eq. (5) when it is assumed that the diffusion coefficient is independent of concentration. There is no evidence of non-Stokesian mass transport (electron hopping and/or Grotthuss-type exchange) in this $[\text{C}_2\text{mim}][\text{NTf}_2]$ electrolyte, which is in agreement with the work by Kawano and Watanabe [12,13] and Kawano et al. [45], where the authors only observed exchange-reaction enhanced diffusion when both I^- and I_3^- were present in the bulk electrolyte in comparable amounts. The diffusion coefficient of iodide was determined to be $2.59 (\pm 0.04) \times 10^{-7} \text{ cm}^2 \text{ s}^{-1}$ from the slope of the I_L vs. C curve, obtained by linear regression of the experimental data, by substituting the appropriate values of known parameters into Eq. (5). This value is in good agreement with $2.68 \times 10^{-7} \text{ cm}^2 \text{ s}^{-1}$ as reported by Kawano and Watanabe [13] in $[\text{C}_2\text{mim}][\text{NTf}_2]$. This value is also orders of magnitude lower than that reported in acetonitrile, $1.68 \times 10^{-5} \text{ cm}^2 \text{ s}^{-1}$ [46] but is in accordance with the relative viscosities of the electrolytes [47] as predicted by the Stokes–Einstein relation [48].

3.2. Transient voltammetric studies on a Pt electrode

Initial transient voltammetric studies on Pt were carried out with a 1.6 mm dia. macroelectrode at an iodide concentration of 10 mM; cyclic voltammograms obtained at scan rates ranging from 50 mV s^{-1} to 1000 mV s^{-1} are shown in Fig. 2. At all scan rates there are two sets of peaks corresponding to the I^-/I_3^- and I_3^-/I_2 processes described by Eq. (2) and (3) respectively. The oxidation peak ($E_{p,\text{ox}}$) and reduction peak ($E_{p,\text{red}}$) potentials for the I^-/I_3^- processes vary with scan rate, giving rise to peak separations (ΔE_p) of 80 mV, 90 mV, 115 mV, 155 mV, and 200 mV at 50 mV s^{-1} , 100 mV s^{-1} , 250 mV s^{-1} , 500 mV s^{-1} , and 1000 mV s^{-1} respectively. Although the uncompensated resistance (R_u) is significant ($230 \pm 20 \Omega$), the shift in peak potentials are too large to be wholly attributed to ohmic (iR_u) drop. This conclusion is supported by noting that the oxidation/reduction peaks associated with the I_3^-/I_2 process do not shift significantly with scan rate, with average values of $520 \pm 2 \text{ mV}$, $397 \pm 8 \text{ mV}$ and $124 \pm 7 \text{ mV}$ for $E_{p,\text{ox}}$, $E_{p,\text{red}}$ and ΔE_p respectively.

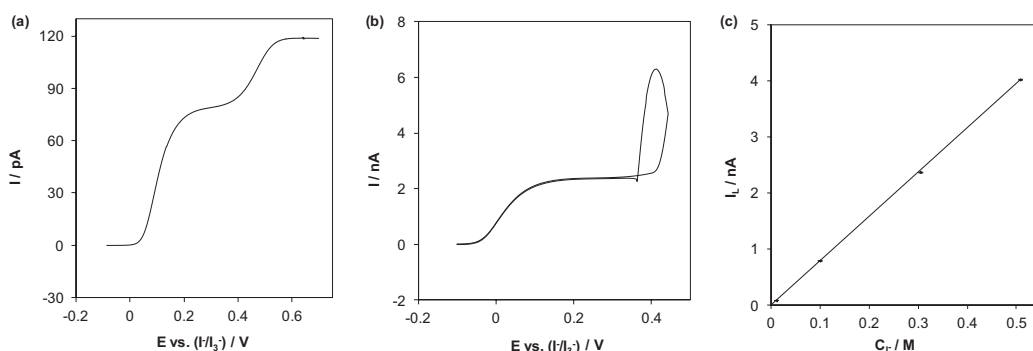


Fig. 1. Steady-state voltammograms obtained from (a) 10 mM [C₂mim]I and (b) 300 mM [C₂mim]I in [C₂mim][NTf₂] using a 2 μm dia. Pt ME with a scan rate of 5 mV s⁻¹. (c) Linear plot of the steady-state limiting current vs. the bulk concentration of iodide ($R^2 = 0.9999$) for the I^-/I_3^- process ($n = 2/3$) at a 2 μm dia. Pt ME. Error bars represent the standard deviation in triplicate measurements.

The scan rate dependence of the voltammetric response of iodide was further investigated using a 100 μm dia. Pt microelectrode; cyclic voltammograms obtained at scan rates ranging from 10 V s⁻¹ to 100 V s⁻¹ are shown in Fig. 3. A microelectrode was employed to minimize the effect of ohmic drop at these high scan rates. At scan rates ≥ 10 V s⁻¹, the significant contribution of non Faradaic charging current to the total current distorts the resulting I - E curve making quantitative treatment of the data difficult. Nevertheless, once again, the oxidation and reduction peak potentials associated with the I^-/I_3^- process shift significantly with scan rate, giving rise to increasingly large ΔE_p values. By contrast, the oxidation peak associated with the I_3^-/I_2^- process is almost independent of scan rate and the related reduction peak shifts by only a small extent (relative to the I^-/I_3^- process).

Based on these observations, it is apparent that on platinum the heterogeneous electron transfer kinetics for the I^-/I_3^- process are significantly more sluggish compared to the I_3^-/I_2^- process which is in agreement with results reported in other media [17–19]. This

reaction involves complicated adsorption/desorption processes and coupled homogeneous reactions and therefore the conventional theories [42], which only take the contributions from mass transport and heterogeneous electron transfer in account are not applicable. Furthermore, since the detailed mechanism of this reaction is yet to be fully understood, it is not possible to obtain any meaningful kinetic information through numerical simulation. Compton et al. [49] have simulated some aspects of the related $Br^-/Br_3^-/Br_2$ system in acetonitrile and [C₄mim][NTf₂], but had to introduce a range of assumptions in their exercise.

3.3. Transient voltammetric studies on GC and BDD electrodes

Transient voltammetric studies on GC were carried out with a 3.0 mm dia. macroelectrode at an iodide concentration of 10 mM; cyclic voltammograms obtained at scan rates ranging from 50 mV s⁻¹ to 1000 mV s⁻¹ are shown in Fig. 4. These cyclic

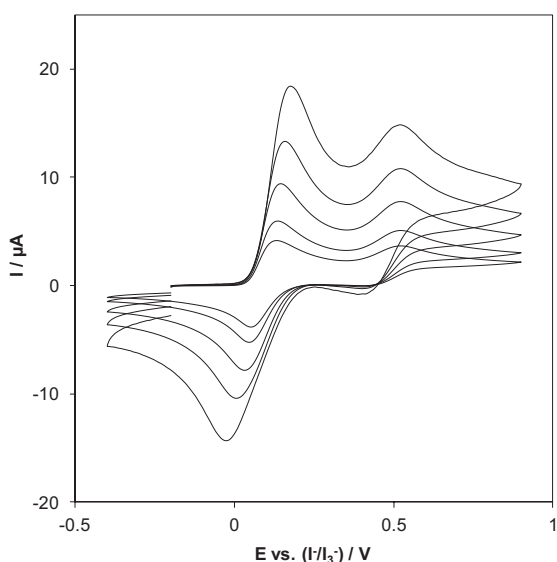


Fig. 2. Cyclic voltammograms obtained from 10 mM [C₂mim]I in [C₂mim][NTf₂] at a 1.6 mm dia. Pt macroelectrode with slow scan rates (from top to bottom) of 1000 mV s⁻¹, 500 mV s⁻¹, 250 mV s⁻¹, 100 mV s⁻¹, and 50 mV s⁻¹.

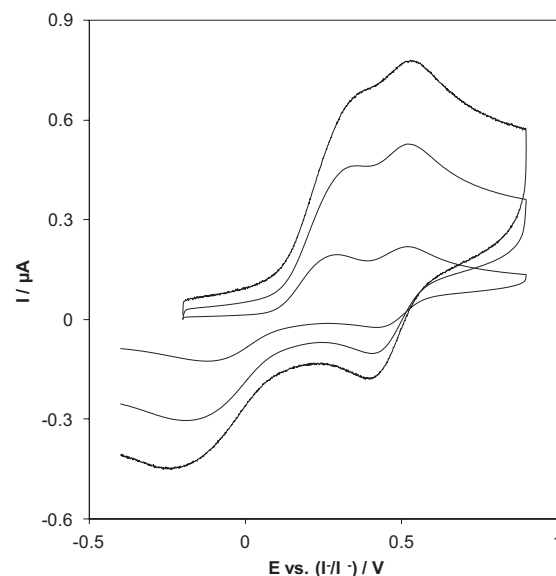


Fig. 3. Cyclic voltammograms obtained from 10 mM [C₂mim]I in [C₂mim][NTf₂] at a 100 μm dia. Pt electrode with fast scan rates (from top to bottom) of 100 V s⁻¹, 50 V s⁻¹, and 10 V s⁻¹.

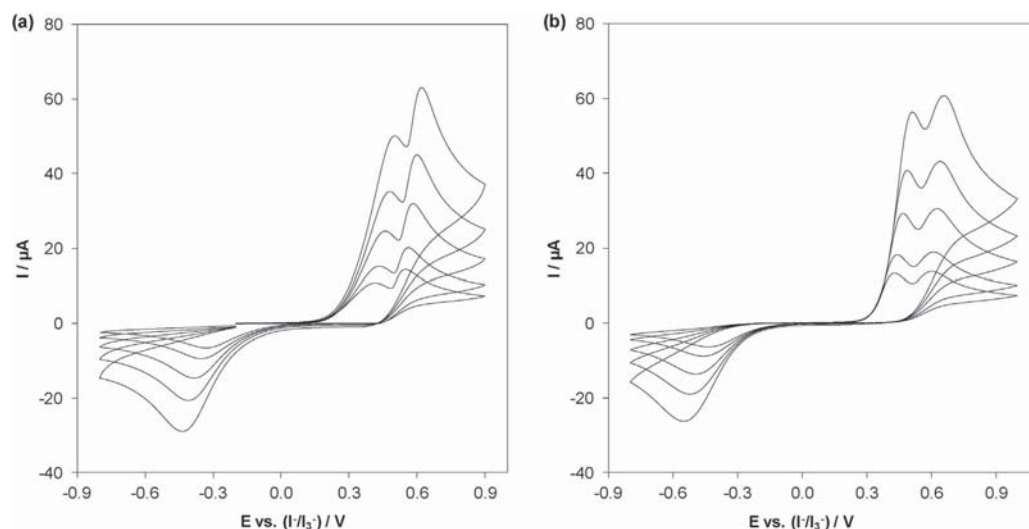


Fig. 4. Cyclic voltammograms obtained from 10 mM $[C_2mim]I$ in $[C_2mim][NTf_2]$ at (a) 3.0 mm dia. GC and (b) a 3.0 mm dia. BDD macroelectrode with scan rates (from top to bottom) of 1000 mV s^{-1} , 500 mV s^{-1} , 250 mV s^{-1} , 100 mV s^{-1} , and 50 mV s^{-1} .

voltammograms look qualitatively similar to those obtained on platinum. Compared to platinum, heterogeneous electron transfer kinetics for the I^-/I_3^- process are considerably more sluggish. This is evident from both the peak potentials (E_p) and the magnitude of ΔE_p for the I^-/I_3^- process, with values of 745 mV, 785 mV, 844 mV, 889 mV, and 940 mV at 50 mV s^{-1} , 100 mV s^{-1} , 250 mV s^{-1} , 500 mV s^{-1} , and 1000 mV s^{-1} respectively. The reduction peak for the I_2/I_3^- process is not well defined on glassy carbon, and unlike on platinum, the oxidation peak shifts with scan rate, with values of 550 mV, 560 mV, 585 mV, 599 mV, and 620 mV (all vs. I^-/I_3^-) at 50 mV s^{-1} , 100 mV s^{-1} , 250 mV s^{-1} , 500 mV s^{-1} , and 1000 mV s^{-1} respectively. Similarly sluggish kinetics are also found with boron-doped diamond as the working electrode (see Fig. 4b). The comparatively facile kinetics on platinum relative to carbon is most likely as a result of the specific interactions (*i.e.* adsorption and/or chemisorption) of halogens/halides with the surface of noble metals [20–23], which is beneficial for inner sphere electron transfer processes [42].

3.4. Semi-integral analysis on Pt and GC electrodes

Through suitable data processing, transient peak-shaped $I-E$ curves can be transformed into forms which closely resemble steady-state voltammograms, which is advantageous for further data processing [42]. Transformation of transient voltammetric data makes use of the general convolution procedure initially described by Savéant et al. [50]. When applied under conditions whereby mass transport occurs by semi-infinite planar diffusion, the technique is known as semi-integration as described by Grenness and Oldham [51] and gives rise to a function, $M(t)$, which is related to the concentration of electroactive species at the electrode surface. Semi-integration has previously been shown to be applicable in high-viscosity RTIL electrolytes [52]; accordingly the forward sweep of the $I-E$ data on platinum and glassy carbon electrodes were semi-integrated, following background subtraction to remove capacitive current (shown in Fig. 5).

The semi-integrated curves resemble steady-state voltammograms at all electrode materials examined (Pt: Fig. 1a, GC: Fig. S2). Thus, there are two limiting current plateaus corresponding to the I^-/I_3^- and I_3^-/I_2 oxidation processes described by Eqs. (2)

and (3) respectively. On platinum, the relative limiting current magnitudes are proportional to the number of electrons involved in each process (*i.e.* 2:1); on glassy carbon, the I^-/I_3^- plateau is not as well defined, but the two processes still convincingly exhibit a 2:1 ratio, strongly suggesting that the overall I^- oxidation processes are analogous on both electrode materials. The distinctive shapes of the semi-integral plots further reinforces the fact that the heterogeneous electron transfer kinetics of the $I^-/I_3^-/I_2$ processes are significantly more sluggish on carbon than on platinum, leading to the requirement of higher overpotentials to drive iodide oxidation on glassy carbon. Furthermore, based

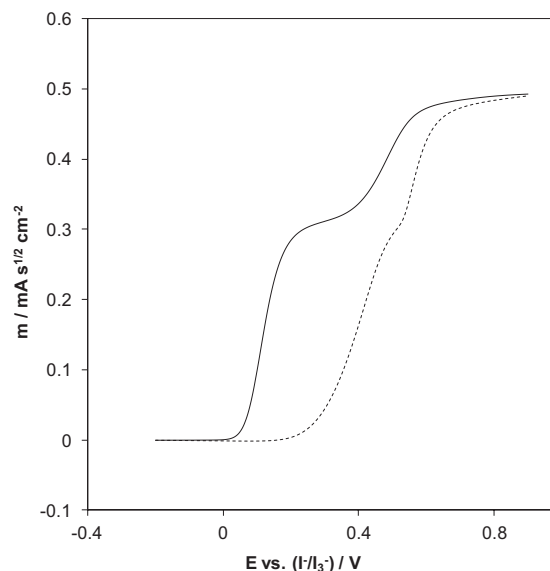


Fig. 5. Comparison of the semi-integrals obtained from 10 mM $[C_2mim]I$ in $[C_2mim][NTf_2]$ at a scan rate of 250 mV s^{-1} on platinum (—) and glassy carbon (---) macrodisk electrodes.

on this and previous observations with cyclic voltammetry, it is apparent that an unmodified glassy carbon electrode is not a viable alternative for platinum as the counter electrode in DSSCs, since significant energetic losses would result from the increased overpotentials required to drive the I^-/I_3^- process.

Under purely diffusion controlled conditions, $M(t)$ reaches its limiting or maximum value, M_L [37,42]:

$$M_L = nFC^*AD^{1/2} \quad (7)$$

where A is the area of the electrode. By transposing Eq. (7) and substituting the appropriate values of known parameters, the diffusion coefficient of iodide was determined to be $2.68 \times 10^{-7} \text{ cm}^2 \text{ s}^{-1}$ and $2.61 \times 10^{-7} \text{ cm}^2 \text{ s}^{-1}$ on platinum and glassy carbon macrodisk electrodes respectively. These values, as required on the basis of the mechanisms proposed on each surface, are in excellent agreement with each other and the value determined at Pt by steady-state ME voltammetry.

3.5. Nucleation and growth of iodine on a Pt electrode

The formation of films of electrogenerated iodine on the surface of platinum electrodes accompanying iodide oxidation has been widely reported in aqueous electrolyte media [53–55]. This phenomenon occurs when the concentration of iodine formed at the electrode surface exceeds its solubility limit (*i.e.* supersaturation at the electrolyte/electrode interface) and reportedly occurs in aqueous electrolytes when the bulk iodide concentration being oxidized exceeds approximately 5 mM [54,55]. Since the solubility of I_2 in a related ionic liquid, $[C_4\text{mim}][\text{NTf}_2]$ is *ca.* 1.70 mM [56] (*cf.* 1.20 mM in water [54]), it is unsurprising that similar complications can arise at high I^- concentrations in $[C_2\text{mim}][\text{NTf}_2]$. A cyclic voltammogram obtained from a 100 mM solution of $[C_2\text{mim}][\text{NTf}_2]$ at a 1.6 mm dia. Pt macroelectrode at a scan rate of 50 mV s^{-1} is shown in Fig. 6. In this figure, the characteristics of the initial I^-/I_3^- process continues to scale with concentration, as previously observed when using the steady-state ME technique. In contrast at this high I^- concentration the I_3^-/I_2 process is much more complicated, owing to the formation of a solid product on the electrode surface. Similar voltammetric behaviour was observed at scan rates ranging from 50 to 500 mV s^{-1} (see Fig. S3).

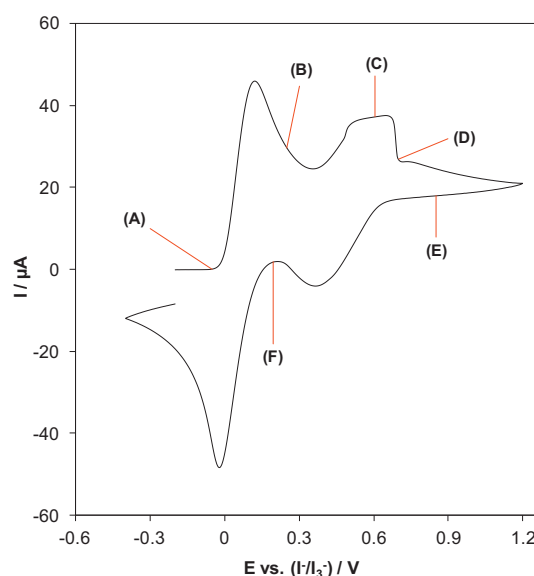


Fig. 6. Cyclic voltammogram obtained from 100 mM $[C_2\text{mim}][\text{NTf}_2]$ in $[C_2\text{mim}][\text{NTf}_2]$ at a 1.6 mm dia. Pt macroelectrode at a scan rate of 50 mV s^{-1} . The letters designated correspond to the labels on the optical micrographs shown in Fig. 7.

The platinum working electrode surface was imaged by *in situ* using optical microscopy; the letters on the voltammogram in Fig. 6 correspond to the optical micrographs displayed in Fig. 7. Prior to the onset of faradaic current and up to (A) (starting from the initial potential), the electrode surface remains unchanged. Upon scanning the potential from (A) to (B), a brown colour gradually develops at the electrode surface, indicating the generation of I_3^- . As the potential progresses from (B), the current initially increases as the oxidation of I_3^- to I_2 commences, but does not reach a maximum as expected with a diffusion controlled, solution based process. Rather, a distinct 'plateau-region' is detected when it is postulated that the concentration of electrogenerated iodine in the

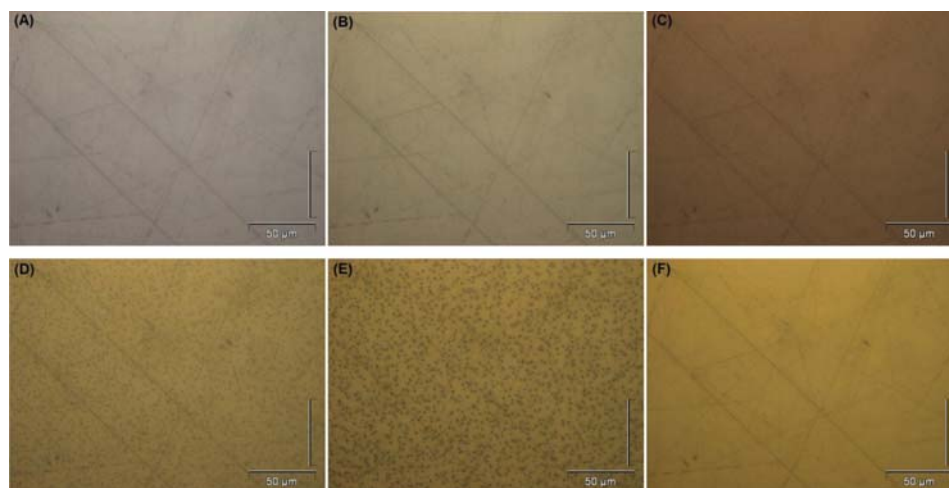


Fig. 7. Optical micrographs (mag. = $500\times$) of the surface of a 1.6 mm Pt dia. macroelectrode in a solution of 100 mM $[C_2\text{mim}][\text{NTf}_2]$ during a cyclic voltammetric experiment at a scan rate of 50 mV s^{-1} . The designated letters correspond to the potentials (all vs. I^-/I_3^-), as shown on the cyclic voltammogram in Fig. 6: (A) -0.050 V , (B) 0.250 V , (C) 0.605 V , (D) 0.700 V , (E) 0.850 V , and (F) 0.195 V .

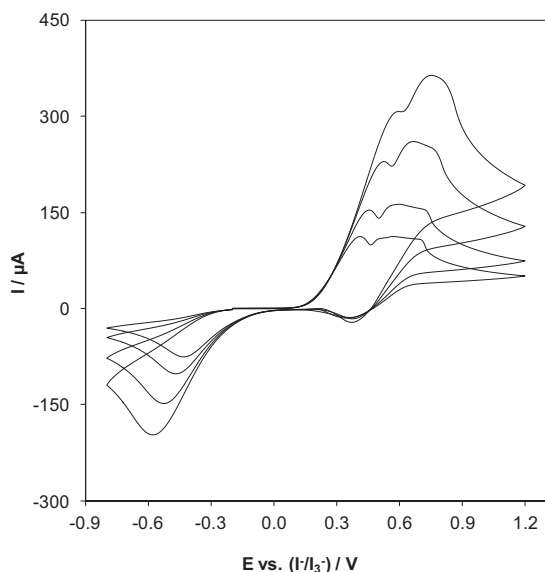


Fig. 8. Cyclic voltammograms obtained from 100 mM [C₂mim]⁺ in [C₂mim][NTf₂] at a 3.0 mm dia. GC macroelectrode with scan rates (from top to bottom) of 500 mV s⁻¹, 250 mV s⁻¹, 100 mV s⁻¹, and 50 mV s⁻¹.

vicinity of the electrode surface exceeds the solubility limit and nucleation of microcrystalline iodine occurs to produce a dark 'film' covering the electrode surface, as seen at (C). The adherence of insoluble, electrically insulating I₂ partially blocks the electrode surface and hence the only feasible site where the electrochemical reaction can proceed is at the three phase (Pt-electrolyte-I₂) junction [57]. When the potential reaches (C), the current suddenly decreases, which is thought to coincide with growth of substantial I₂ solid, so that the dark 'film' is replaced by crystals of I₂ on the electrode surface, as seen at (D). Upon sweeping the potential past (D), the current exhibits a typical mass-transport controlled decay (Cottrellian $t^{-1/2}$ decay), indicating that growth of the I₂ nuclei is governed by one-dimensional (planar) diffusion of I⁻ to the electrode surface, as seen at (E) [58]. After reversing the scan direction and when reverting towards more negative potentials, the surface deposit eventually disappears as a result of the reduction of insoluble I₂ to soluble I₃⁻ (and eventually to soluble I⁻), as seen at (F). Alternatively, if the potential sweep is concluded at (E) and the working electrode potential is allowed to return to open circuit value, the I₂ crystals on the electrode surface rapidly dissolve, which is predominantly due to the reaction with the influx of I⁻ from bulk solution (I₃⁻ is highly soluble) and to a small extent due to dissolution (I₂ is sparingly soluble) [55].

3.6. Nucleation and growth of iodine on a GC electrode

Nucleation and growth of I₂ on a GC electrode also was detected with a 3.0 mm dia. macroelectrode using an iodide concentration of 100 mM; cyclic voltammograms obtained at scan rates ranging from 50 mV s⁻¹ to 500 mV s⁻¹ are shown in Fig. 8. Again, the I⁻/I₃⁻ process remains diffusion controlled at higher concentrations, whereas the I₃⁻/I₂ process becomes influenced by the nucleation and growth of iodine on the electrode surface. Despite the disparity in the heterogeneous kinetics of the I⁻/I₃⁻/I₂ processes on GC and Pt, a very similar set of observations are found regarding the nucleation and growth of I₂ (see optical microscopy images in Figs. S4 and S5).

4. Conclusions

The voltammetric oxidation of iodide in the room temperature ionic liquid 1-ethyl-3-methylimidazolium bis(trifluoromethanesulfonyl)imide has been investigated in detail using a variety of techniques. As observed in the molecular solvent acetonitrile, two processes are observed on platinum, glassy carbon and boron-doped diamond, which are assigned to the initial formation of triiodide (confirmed by UV/Visible spectroscopy), followed by the oxidation of triiodide to iodine. In combination, the two processes represent an overall one electron per iodide ion process. Using steady-state microelectrode voltammetry, the diffusion coefficient of iodide was found to be independent of concentration, indicating that there are no contributions from non-Stokesian mass-transport processes (electron hopping and/or Grotthuss-type exchange) under the investigated conditions. The nucleation and growth of sparingly soluble iodine generated during iodide oxidation at elevated concentrations on platinum and glassy carbon was observed and imaged *in situ* using optical microscopy. Linear sweep semi-integral and transient cyclic voltammetry revealed that the iodide oxidation process is kinetically more facile on platinum than on glassy carbon or boron-doped diamond, with substantial overpotentials present at the carbon electrodes.

Supplementary materials

Supplementary materials associated with this article are available with the on-line version only.

References

- [1] J.S. Wilkes, A short history of ionic liquids—from molten salts to neoteric solvents, *Green Chemistry* 4 (2) (2002) 73–80.
- [2] D.R. MacFarlane, K.R. Seddon, Ionic liquids—progress on the fundamental issues, *Australian Journal of Chemistry* 60 (1) (2007) 3–5.
- [3] M. Armand, F. Endres, D.R. MacFarlane, H. Ohno, B. Scrosati, Ionic-liquid materials for the electrochemical challenges of the future, *Nature Materials* 8 (8) (2009) 621–629.
- [4] P.M. Dean, J.M. Pringle, D.R. MacFarlane, Structural analysis of low melting organic salts: perspectives on ionic liquids, *Physical Chemistry Chemical Physics* 12 (32) (2010) 9144–9153.
- [5] N. Papageorgiou, Y. Athanassov, M. Armand, P. Bonhote, H. Pettersson, A. Azam, M. Gratzel, The performance and stability of ambient temperature molten salts for solar cell applications, *Journal of the Electrochemical Society* 143 (10) (1996) 3099–3108.
- [6] A. Hagfeldt, G. Boschloo, L.C. Sun, L. Kloo, H. Pettersson, Dye-sensitized solar cells, *Chemical Reviews* 110 (11) (2010) 6595–6663.
- [7] P.C. Howlett, D.R. MacFarlane, A.F. Hollenkamp, High lithium metal cycling efficiency in a room-temperature ionic liquid, *Electrochemical and Solid-State Letters* 7 (5) (2004) A97–A101.
- [8] R.F. de Souza, J.C. Padilha, R.S. Goncalves, J. Dupont, Room temperature dialkylimidazolium ionic liquid-based fuel cells, *Electrochemistry Communications* 5 (8) (2003) 728–731.
- [9] A. Balducci, R. Dugas, P.L. Taberna, P. Simon, D. Plee, M. Mastragostino, S. Passerini, High temperature carbon-carbon supercapacitor using ionic liquid as electrolyte, *Journal of Power Sources* 165 (2) (2007) 922–927.
- [10] B. O'Regan, M. Gratzel, A low-cost, high-efficiency solar cell based on dye-sensitized colloidal TiO₂ films, *Nature* 353 (6346) (1991) 737–740.
- [11] P. Wang, S.M. Zakeeruddin, J.E. Moser, R. Humphry-Baker, M. Gratzel, A solvent-free, SeCN⁻/[SeCN]₃⁻ based ionic liquid electrolyte for high-efficiency dye-sensitized nanocrystalline solar cells, *Journal of the American Chemical Society* 126 (23) (2004) 7164–7165.
- [12] R. Kawano, M. Watanabe, Anomaly of charge transport of an iodide/tri-iodide redox couple in an ionic liquid and its importance in dye-sensitized solar cells, *Chemical Communications* (16) (2005) 2107–2109.
- [13] R. Kawano, M. Watanabe, Equilibrium potentials and charge transport of an I⁻/I₃⁻ redox couple in an ionic liquid, *Chemical Communications* (3) (2003) 330–331.
- [14] V.K. Thorsmolle, G. Rothenberger, D. Topgaard, J.C. Brauer, D.B. Kuang, S.M. Zakeeruddin, B. Lindman, M. Gratzel, J.E. Moser, Extraordinarily efficient conduction in a redox-active ionic liquid, *ChemPhysChem* 12 (1) (2011) 145–149.
- [15] L.M. Dane, L.J.J. Janssen, J.G. Hoogland, Iodine/iodide redox couple at a platinum electrode, *Electrochimica Acta* 13 (3) (1968) 507.
- [16] A.I. Popov, D.H. Geske, Studies on the chemistry of halogen and of polyhalides. 13. voltammetry of iodine species in acetonitrile, *Journal of the American Chemical Society* 80 (6) (1958) 1340–1352.

- [17] A. Ejigu, K.R.J. Lovelock, P. Licence, D.A. Walsh, Iodide/triiodide electrochemistry in ionic liquids: effect of viscosity on mass transport, voltammetry and scanning electrochemical microscopy, *Electrochimica Acta* 56 (28) (2011) 10313–10320.
- [18] Y. Zhang, J.B. Zheng, Investigation on the electro-oxidation of iodide in the room temperature ionic liquid, 1-butyl-3-methylimidazolium tetrafluoroborate at platinum electrode, *Electrochimica Acta* 52 (12) (2007) 4082–4086.
- [19] D.S. Silvester, L. Aldous, C. Hardacre, R.G. Compton, Electrooxidation of the iodides [C₄mim][I], [Li], [Na], [K], [Rb], and [Cs] in the room temperature ionic liquid [C₄mim][NTf₂], *Journal of Physical Chemistry C* 112 (16) (2008) 6551–6557.
- [20] A.T. Hubbard, Electrochemistry of chemisorbed molecules. III. determination of the oxidation state of halides chemisorbed on platinum. reactivity and catalytic properties of adsorbed species, *Journal of Physics and Chemistry* 79 (8) (1975) 808–815.
- [21] G.M. Swain, 5 – Solid electrode materials: pretreatment and activation, in: C.G. Zoski (Ed.), *Handbook of Electrochemistry*, 1st ed., Elsevier, Amsterdam, 2007, pp. 111–153.
- [22] T. Mebrahtu, J.F. Rodriguez, B.G. Bravo, M.P. Soriaga, Hydrogenative/cathodic stripping of iodine chemisorbed on smooth polycrystalline platinum electrodes, *Journal of Electroanalytical Chemistry* 219 (1–2) (1987) 327–333.
- [23] B.G. Bravo, T. Mebrahtu, J.F. Rodriguez, M.P. Soriaga, Electroactivity of strongly-adsorbed redox centers: reduction of iodine chemisorbed on platinum in aprotic solvent, *Journal of Electroanalytical Chemistry* 221 (1–2) (1987) 281–287.
- [24] R.T. Iwamoto, Solvent Effects on the Electro-oxidation of Iodide Ion, *Analytical Chemistry* 31 (5) (1959) 955.
- [25] R. Guidelli, G. Piccardi, The dissociation constant of I₃⁻ in the voltammetric behaviour of the iodine-iodide couple, *Electrochimica Acta* 12 (8) (1967), 1085–8.
- [26] E. Gebert, Solvent effects in the iodide-iodine-triiodide complex equilibrium, *Journal of the American Chemical Society* 76 (8) (1954) 2049–2054.
- [27] A.I. Popov, R.H. Rygg, N.E. Skelly, Studies on the chemistry of halogens and of polyhalides.9. electrical conductance study of higher polyiodide complex ions in acetonitrile solutions, *Journal of the American Chemical Society* 78 (22) (1956) 5740–5744.
- [28] A. Kay, M. Gratzel, Low cost photovoltaic modules based on dye sensitized nanocrystalline titanium dioxide and carbon powder, *Solar Energy Materials and Solar Cells* 44 (1) (1996) 99–117.
- [29] T.N. Murakami, S. Ito, Q. Wang, M.K. Nazeeruddin, T. Bessho, Highly efficient dye-sensitized solar cells based on carbon black counter electrodes, *Journal of the Electrochemical Society* 153 (12) (2006) A2255–A2261.
- [30] H.E. Zittel, Voltammetry of the iodine system in aqueous medium at the pyrolytic graphite electrode, *Journal of Electroanalytical Chemistry* 11 (2) (1966) 85–93.
- [31] G. Dryhurst, P.J. Elving, Voltammetric determination of iodide and bromide at rotating pyrolytic graphite electrode, *Journal of Electroanalytical Chemistry* 12 (5–6) (1966), 416–8.
- [32] P.J. Elving, Electrooxidation of halides at pyrolytic graphite electrode in aqueous and acetonitrile solutions, *Analytical Chemistry* 39 (6) (1967) 606–615.
- [33] A.P. Dias, N. Papageorgiou, K. Kalyanasundaram, M. Gratzel, Hydrophobic, highly conductive ambient-temperature molten salts, *Inorganic Chemistry* 35 (5) (1996) 1168–1178.
- [34] B. Liu, 6.3.2 – Platinum and gold inlaid disks $\leq 5\ \mu\text{m}$ diameter, in: C.G. Zoski (Ed.), *Handbook of Electrochemistry*, 1st ed., Elsevier, Amsterdam, 2007, pp. 197–199.
- [35] E.I. Rogers, D.S. Silvester, D.L. Poole, L. Aldous, C. Hardacre, R.G. Compton, Voltammetric characterization of the ferrocene vertical bar ferrocenium and cobaltocenium vertical bar cobaltocene redox couples in RTILs, *Journal of Physical Chemistry C* 112 (7) (2008) 2729–2735.
- [36] R. de Levie, *How to Use Excel® in Analytical Chemistry and in General Scientific Data Analysis*, Cambridge University Press, Cambridge, 2001.
- [37] K.B. Oldham, J.C. Myland, *Fundamentals of Electrochemical Science*, Academic Press, San Diego, 1994.
- [38] R. de Levie, *Excellaneous*, <http://www.bowdoin.edu/~rdelevie/excellaneous/> (accessed 21.05.13).
- [39] D.A. Skoog, D.M. West, F.J. Holler, S.R. Crouch, *Fundamentals of Analytical Chemistry*, 8th ed., Thomson-Brooks/Cole, Belmont, CA, 2004.
- [40] K.J. Hanson, C.W. Tobias, Electrochemistry of iodide in propylene carbonate.1. cyclic voltammetry monitored by optical spectroscopy, *Journal of the Electrochemical Society* 134 (9) (1987) 2204–2210.
- [41] V.M. Hultgren, A.W.A. Mariotti, A.M. Bond, A.G. Wedd, Reference potential calibration and voltammetry at macrodisk electrodes of metallocene derivatives in the ionic liquid [bmim][PF₆], *Analytical Chemistry* 74 (13) (2002) 3151–3156.
- [42] A.J. Bard, L.R. Faulkner, *Electrochemical Methods: Fundamentals and Applications*, 2nd ed., Wiley, New York, 2001.
- [43] M. Zistler, P. Wachter, P. Wasserscheid, D. Gerhard, A. Hinsch, R. Sastrawan, H.J. Gores, Comparison of electrochemical methods for triiodide diffusion coefficient measurements and observation of non-stokesian diffusion behaviour in binary mixtures of two ionic liquids, *Electrochimica Acta* 52 (1) (2006) 161–169.
- [44] F. Hao, H. Lin, J. Zhang, J.B. Li, Balance between the physical diffusion and the exchange reaction on binary ionic liquid electrolyte for dye-sensitized solar cells, *Journal of Power Sources* 196 (3) (2011) 1645–1650.
- [45] R. Kawano, H. Matsui, C. Matsuyama, A. Sato, M. Susan, N. Tanabe, M. Watanabe, High performance dye-sensitized solar cells using ionic liquids as their electrolytes, *Journal of Photochemistry and Photobiology A: Chemistry* 164 (1–3) (2004) 87–92.
- [46] V.A. Macagno, M.C. Giordano, A.J. Arvia, Kinetics and mechanisms of electrochemical reactions on platinum with solutions of iodine-sodium iodide in acetonitrile, *Electrochimica Acta* 14 (4) (1969) 335.
- [47] L.E. Barrosse-Antle, A.M. Bond, R.G. Compton, A.M. O'Mahony, E.I. Rogers, D.S. Silvester, Voltammetry in room temperature ionic liquids: comparisons and contrasts with conventional electrochemical solvents, *Chemistry-an Asian Journal* 5 (2) (2010) 202–230.
- [48] H. Tokuda, K. Hayamizu, K. Ishii, M.A.B.H. Susan, M. Watanabe, Physicochemical properties and structures of room temperature ionic liquids. 1. variation of anionic species, *The Journal of Physical Chemistry B* 108 (42) (2004) 16593–16600.
- [49] G.D. Allen, M.C. Buzzeo, C. Villagran, C. Hardacre, R.G. Compton, A mechanistic study of the electro-oxidation of bromide in acetonitrile and the room temperature ionic liquid, 1-butyl-3-methylimidazolium bis(trifluoromethylsulfonyl)imide at platinum electrodes, *Journal of Electroanalytical Chemistry* 575 (2) (2005) 311–320.
- [50] J.M. Saveant, Convolutional potential sweep voltammetry.1. introduction, *Journal of Electroanalytical Chemistry* 44 (2) (1973) 169–187.
- [51] M. Grenness, K.B. Oldham, Semi-integral electroanalysis - theory and verification, *Analytical Chemistry* 44 (7) (1972) 1121–1129.
- [52] C.L. Bentley, A.M. Bond, A.F. Hollenkamp, P.J. Mahon, J. Zhang, Advantages available in the application of the semi-integral electroanalysis technique for the determination of diffusion coefficients in the highly viscous ionic liquid 1-methyl-3-octylimidazolium hexafluorophosphate, *Analytical Chemistry* 85 (4) (2012) 2239–2245.
- [53] E.C. Toren, C.P. Driscoll, Polarographic study of the iodine-iodide couple at the rotating platinum electrode, *Analytical Chemistry* 38 (7) (1966), 872–8.
- [54] S. Swathirajan, S. Bruckenstein, Ring-disk electrode studies of the formation, growth and transformation of iodine films formed during the anodic-oxidation of iodide on platinum, *Journal of Electroanalytical Chemistry* 112 (1) (1980) 25–38.
- [55] S. Bruckenstein, Ring-disk electrode studies of the open-circuit dissolution of iodine films formed during the anodic oxidation of iodide on platinum, *Journal of Electroanalytical Chemistry* 125 (1) (1981) 63–71.
- [56] E.I. Rogers, I. Streeter, L. Aldous, C. Hardacre, R.G. Compton, Electrode kinetics and mechanism of iodine reduction in the room-temperature ionic liquid [C₄mim][NTf₂], *Journal of Physical Chemistry C* 112 (29) (2008) 10976–10981.
- [57] K.B. Oldham, Voltammetry at a three-phase junction, *Journal of Solid State Electrochemistry* 2 (6) (1998) 367–377.
- [58] D. Grujicic, B. Pestic, Electrodeposition of copper: the nucleation mechanisms, *Electrochimica Acta* 47 (18) (2002) 2901–2912.

Supplementary data for

Concentration and electrode material dependence of the
voltammetric response of iodide on platinum, glassy
carbon and boron-doped diamond in the room
temperature ionic liquid 1-ethyl-3-methylimidazolium
bis(trifluoromethanesulfonyl)imide

Cameron L. Bentley^{a,b}, Alan M. Bond^a, Anthony F. Hollenkamp^b, Peter J. Mahon^c and Jie
Zhang^a

^aSchool of Chemistry, Monash University, Clayton, Vic 3800, Australia

^bCSIRO Energy Technology, Box 312, Clayton South, Vic 3169, Australia

^cFaculty of Life and Social Sciences, Swinburne University of Technology, Hawthorn, Vic 3122,
Australia

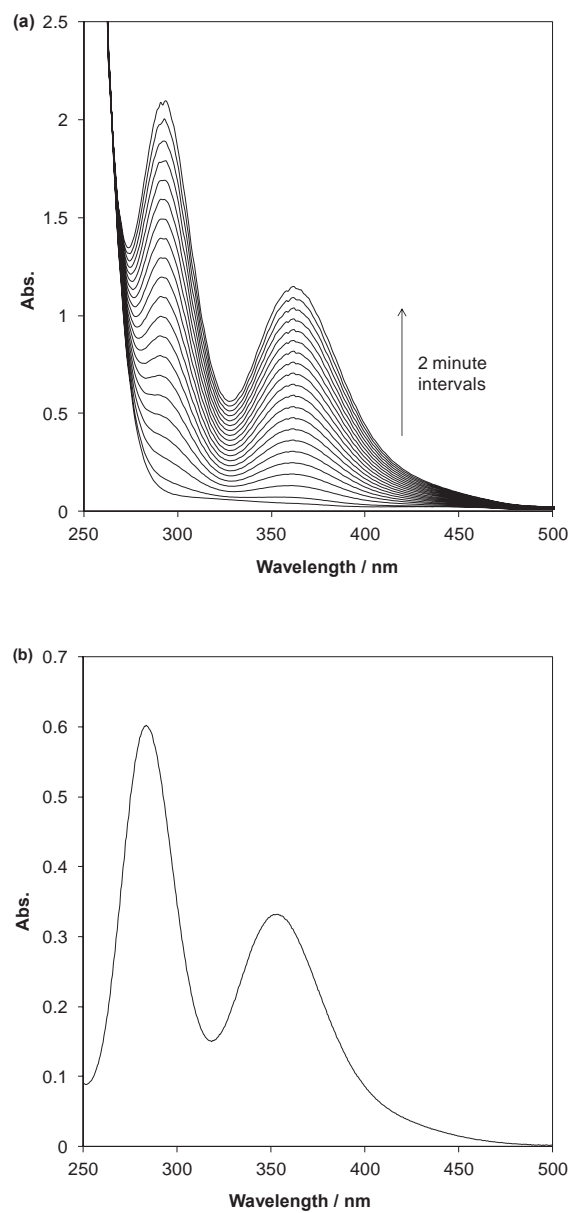


Fig. S1. (a) UV/Visible spectra recorded when the potential was stepped to 0.35 V vs. I⁻/I₃⁻ in a quartz OTTLE cell containing 10 mM [C₂mim]I in [C₂mim][NTf₂] and a platinum mesh working electrode. (b) UV/Visible spectrum obtained from 0.14 mM I⁻:I₃⁻ (1:1) in [C₂mim][NTf₂].

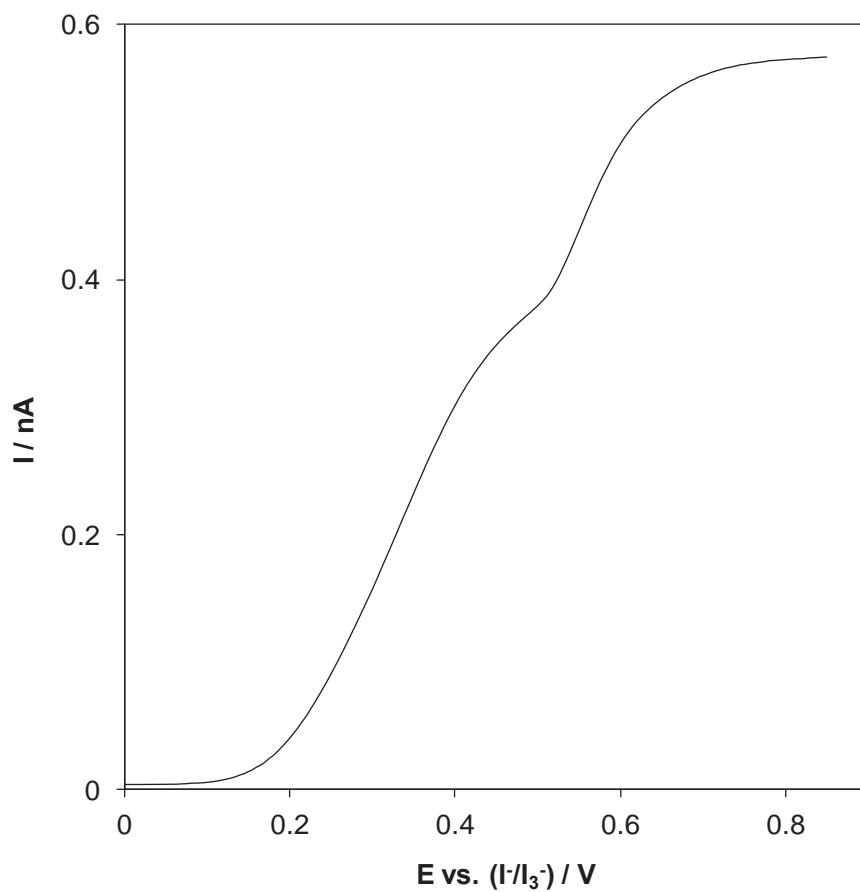


Fig. S2. Near steady-state voltammogram obtained from 10 mM $[C_2mim]I$ in $[C_2mim][NTf_2]$ at an 11 μm dia. glassy carbon microelectrode with a scan rate of 5 mV s^{-1} .

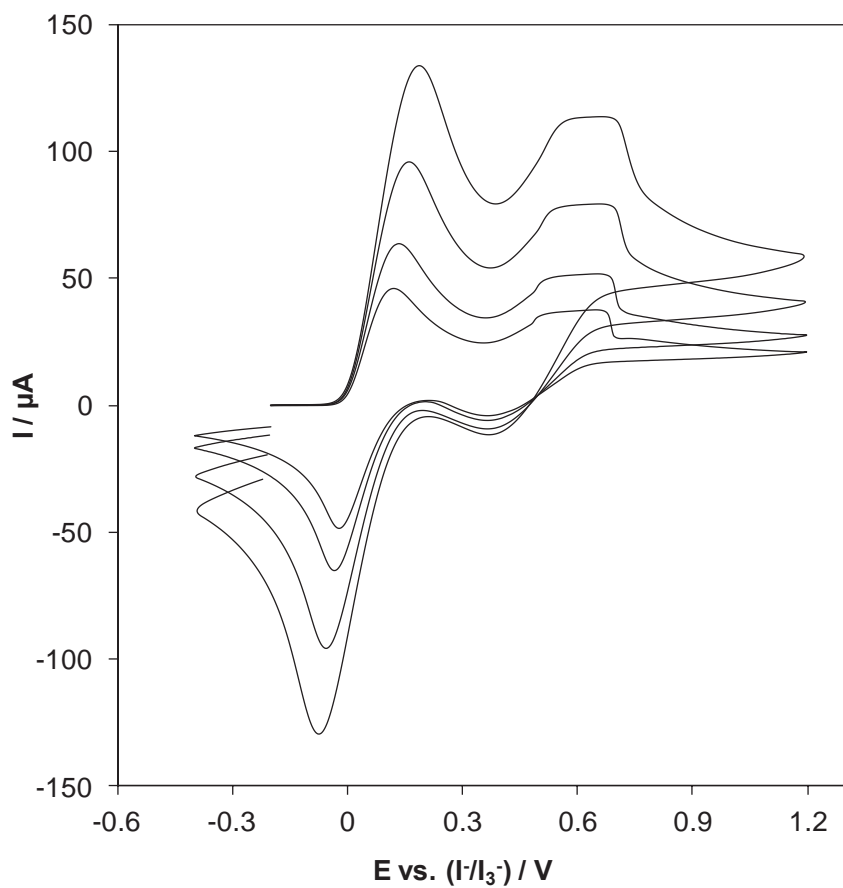


Fig. S3. Cyclic voltammograms obtained from 100 mM [C₂mim]I in [C₂mim][NTf₂] at a 1.6 mm dia. Pt macroelectrode with scan rates (from top to bottom) of 500 $mV s^{-1}$, 250 $mV s^{-1}$, 100 $mV s^{-1}$ and 50 $mV s^{-1}$.

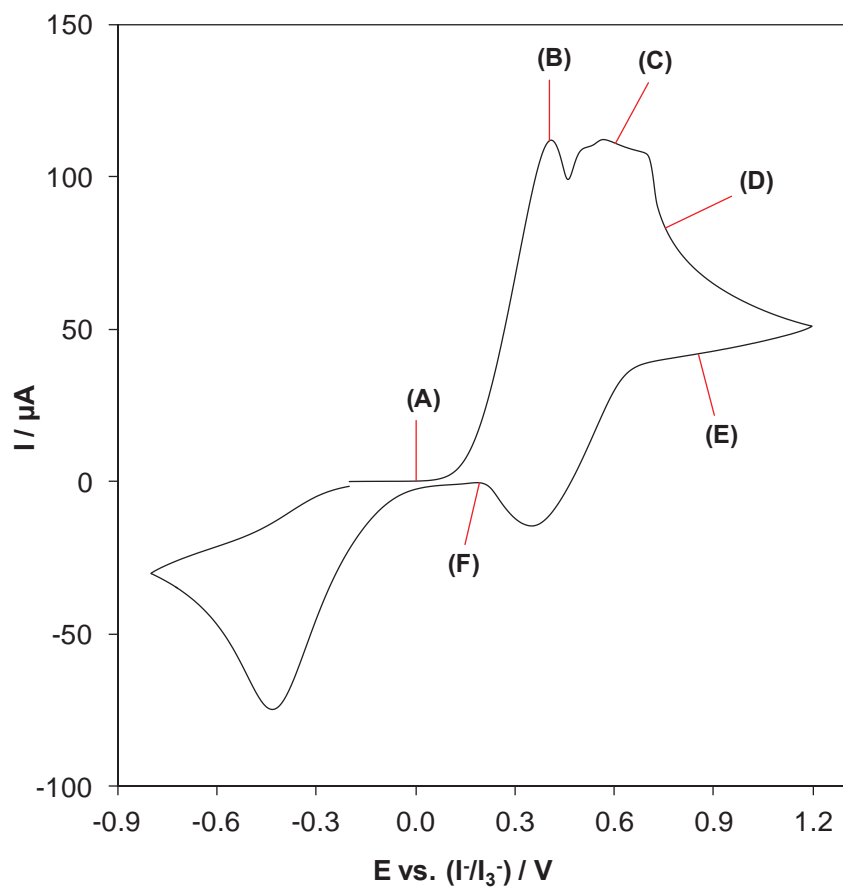


Fig. S4. Cyclic voltammogram obtained from 100 mM [C₂mim]I in [C₂mim][NTf₂] at a 3.0 mm dia. glassy carbon macroelectrode at a scan rate of 50 mV s⁻¹. The letters designated correspond to the labels on the optical micrographs shown in Fig. S5.

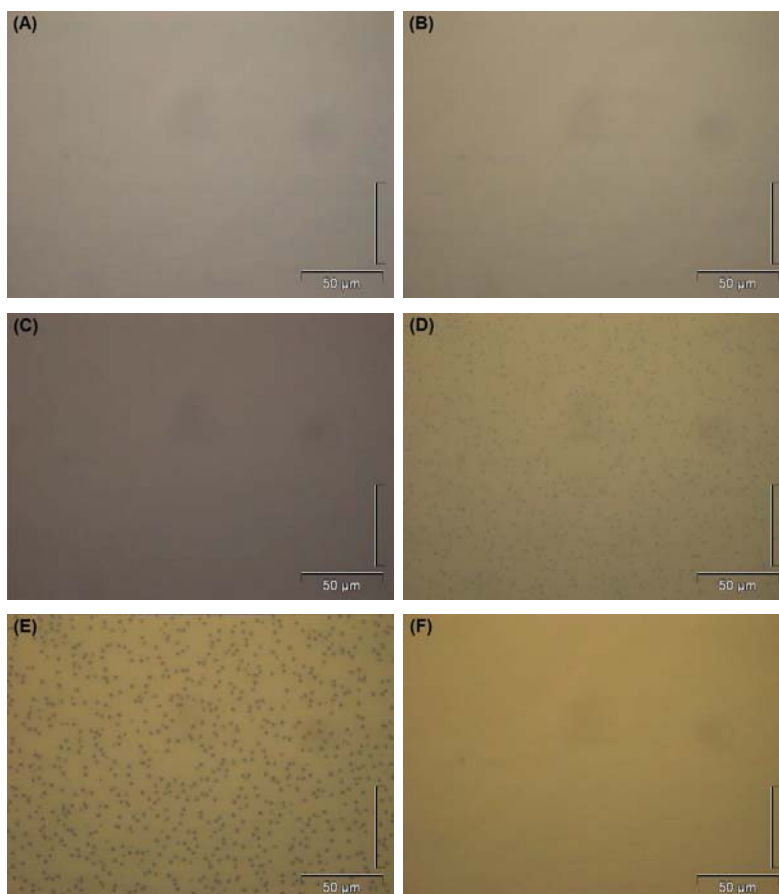


Fig. S5. Optical micrographs (*mag.* = 500 \times) of the surface of a 3.0 mm dia. glassy carbon macroelectrode in a solution of 100 mM [C₂mim]I in [C₂mim][NTf₂] during a cyclic voltammetric experiment at a scan rate of 50 mV s⁻¹. The designated letters correspond to the potentials (all vs. I⁻/I₃⁻), as shown on the cyclic voltammogram in Fig. S4: (A) 0 V, (B) 0.405 V, (C) 0.605 V, (D) 0.755 V, (E) 0.855 V and (F) 0.195 V.

Unexpected Complexity in the Electro-Oxidation of Iodide on Gold in the Ionic Liquid 1-Ethyl-3-methylimidazolium bis(trifluoromethanesulfonyl)imide

Cameron L. Bentley,^{†,‡} Alan M. Bond,^{*,†} Anthony F. Hollenkamp,^{*,‡} Peter J. Mahon,[§] and Jie Zhang^{*,†}

[†]School of Chemistry, Monash University, Clayton, Vic 3800, Australia

[‡]CSIRO Energy Technology, Box 312, Clayton South, Vic 3169, Australia

[§]Faculty of Life and Social Sciences, Swinburne University of Technology, Hawthorn, Vic 3122, Australia

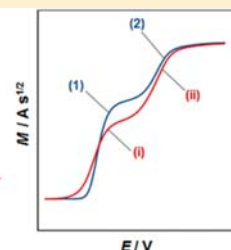
Supporting Information

ABSTRACT: The electro-oxidation of iodide on a gold electrode in the room temperature ionic liquid 1-ethyl-3-methylimidazolium bis(trifluoromethanesulfonyl)imide has been investigated using transient cyclic voltammetry, linear-sweep semi-integral voltammetry, an electrochemical quartz crystal microbalance technique, and coulometry/electrogravimetry. Two oxidation processes are observed, with an electron stoichiometry of 1:1, compared with the well-known 2:1 electron stoichiometry observed on other commonly used electrode materials, such as platinum, glassy carbon, and boron-doped diamond, under identical conditions. Detailed mechanistic information, obtained in situ using an electrochemical quartz crystal microbalance, reveals that this unusual observation can be attributed to the dissolution of the gold electrode in the presence of iodide. Coulometric/electrogravimetric analysis suggests that the oxidation state of the soluble gold species is +1 and that diiodoaurate, $[\text{AuI}_2]^-$, is the likely intermediate. A proportionally smaller amount of triiodide intermediate is also detected by means of UV-vis spectroscopy. On this basis, it is proposed that iodide oxidation on gold occurs via two parallel pathways: predominantly via a diiodoaurate intermediate $2\text{I}^- + \text{Au} \rightleftharpoons [\text{AuI}_2]^- + \text{e}^-$ and $[\text{AuI}_2]^- \rightleftharpoons \text{I}_2 + \text{Au} + \text{e}^-$ and to a lesser extent via a triiodide intermediate $3\text{I}^- \rightleftharpoons \text{I}_3^- + 2\text{e}^-$ and $\text{I}_3^- \rightleftharpoons 3/2\text{I}_2 + \text{e}^-$. This proposed mechanism was further supported by voltammetric investigations with an authentic sample of the anionic $[\text{AuI}_2]^-$ complex.

Platinum:



Gold:



Since their introduction over two decades ago, air/water stable nonhaloaluminate room temperature ionic liquids (RTILs) have been employed as replacements for volatile organic solvents in a range of applications.¹ RTILs are intrinsic ionic conductors,² and many possess favorable properties such as negligible vapor pressure and high chemical, thermal, and electrochemical stability.³ Indeed, the distinctive physicochemical properties possessed by a particular RTIL are determined by its constituent cation/anion and therefore can be tailored to suit specific applications.⁴ The versatile nature of RTILs has allowed them to be successfully employed as replacements for “conventional electrolytes” in a range of electrochemical devices, including dye-sensitized solar cells,^{5,6} lithium batteries,⁷ fuel cells,⁸ and supercapacitors.⁹

The dye-sensitized solar cell (DSSC), as reported by O'Regan and Grätzel,¹⁰ has been the subject of intensive research over the past two decades. Lower manufacturing costs and great versatility in design (size, shape, flexibility, etc.) mean that DSSCs are possible replacements for traditional (*p*-/*n*-) silicon photovoltaics in a range of applications. The DSSC has three fundamental components: (1) a TiO_2 semiconductor photoanode with an adhered photoactive dye; (2) a platinized counter electrode (cathode); (3) an electrolyte solution in

which the oxidized and reduced forms of a suitable redox couple are present so as to establish a redox shuttle system that regenerates the reduced form of the dye. According to the original work, solutions of tetra-alkyl ammonium salts of iodide/triiodide (I^-/I_3^-) in acetonitrile meet the dual requirements for an appropriate electrode potential combined with sufficient transport properties of the redox-active species.⁶ However, these electrolyte solutions impose severe restrictions on device performance due to poor stability (high solvent volatility and corrosivity of trace iodine) and limited safety (solvent flammability) of DSSCs under light soaking conditions. These issues can be averted by employing an electrolyte solution that is based on an appropriate RTIL.^{5,6,11}

Another issue that is embedded in DSSC technology is the high cost of platinum, which is a significant driving force for the development of alternative cathode materials.⁶ While obviously sensible, this endeavor runs counter to the well-known kinetic facility of the I^-/I_3^- redox process¹² at noble-metal electrode materials.^{13–17} Platinum, in particular, has been a widely

Received: July 15, 2013

Accepted: October 21, 2013

Published: October 21, 2013

studied electrode material for the $I^-/I_3^-/I_2$ redox processes in a range of solvents, including water,¹⁸ acetonitrile,¹⁹ and ionic liquids.^{17,20–24} It is well-known that iodide is oxidized to molecular iodine in an overall one electron per iodide ion process:



It has also been well-established that iodide and iodine combine homogeneously to form the polyhalogen complex anion, triiodide:



The stability constant of this reaction is highly solvent dependent, ranging from $\approx 10^3 \text{ M}^{-1}$ in water²⁵ to $\approx 10^7 \text{ M}^{-1}$ in acetonitrile,^{26,27} and has a strong bearing on the observed iodide oxidation mechanism.²⁶ On platinum, the overall oxidation process shown in eq 1 may occur in one step, giving rise to a single voltammetric process (as observed in aqueous media^{26,28–30}) or in two steps (via an I_3^- intermediate), giving rise to two voltammetric processes (as observed in acetonitrile^{26,28,31} and ionic liquids^{17,20–24}):



Analogous voltammetric behavior is observed on glassy carbon and boron-doped diamond electrodes, albeit with significant overpotentials when compared with the behavior at platinum.¹⁷

In contrast, iodide electro-oxidation has not been studied extensively on gold electrodes. Only a few studies have been reported so far, and all were undertaken in conventional organic/aqueous electrolyte media. Loo et al.³² investigated the surface adsorbed complexes formed on a gold electrode during oxidative polarization in aqueous halide media in situ using surface-enhanced Raman spectroscopy; Au(I) and Au(III) species of the type $[AuX_2]^-$ and $[AuX_4]^-$, respectively, were detected at the electrode surface at increasingly positive potentials for all of the investigated halides ($X^- = Cl^-, Br^-,$ and I^-). A study by Qi et al.³³ on the voltammetric response of iodide on a gold electrode in aqueous media revealed a complex reaction pathway, with a myriad of reactions being possible due to significant overlap between the standard potentials for iodide and gold oxidation. Guo et al.³⁴ characterized the soluble species formed upon oxidative polarization of a gold electrode in acetonitrile containing dissolved iodide in situ using electrochemical/electrospray mass spectrometry; two diffusion-controlled voltammetric processes were observed, and the products associated with each (at increasingly positive potential) were $[AuI_2]^-$ and I_3^- , respectively. Even this limited number of studies suggest that the electrochemical behavior of the I^-/I_3^- couple at gold electrodes is likely to be appreciably more complicated than that observed at platinum and carbon electrodes.

In this paper, we report the electrochemical behavior of iodide on a gold electrode in the room temperature ionic liquid 1-ethyl-3-methylimidazolium bis(trifluoromethanesulfonyl)imide. A variety of techniques, including transient cyclic voltammetry, linear sweep semi-integral voltammetry, EQCM, UV-vis spectroscopy, and coulometry/electrogravimetry are employed to elucidate the redox mechanism and characterize the electrogenerated intermediate species. In the course of this investigation, we confirm that when gold is the electrode

material, it is far from “noble” in its behavior and actually becomes intimately involved in the course of iodide electro-oxidation. This in turn presents new insights into the operation of the I^-/I_3^- electrode in DSSCs.

EXPERIMENTAL SECTION

Reagents. The compound 1-ethyl-3-methylimidazolium bis(trifluoromethanesulfonyl)imide ($[C_2mim][NTf_2]$, Io-li-tec GmbH, 99.5%) was dried under high vacuum ($\leq 10^{-2}$ mbar) at 45 °C for 48 h and stored under lithium. The residual water was less than 50 ppm, as determined by Karl Fischer titration (Metrohm 831 KF Coulometer). Additionally, 1-ethyl-3-methylimidazolium iodide ($[C_2mim]I$, Io-li-tec GmbH, >98%) was recrystallized twice from a 2:1 mixture of ethyl acetate (Merck, EMSURE) and isopropanol (Merck, EMSURE) and then dried under high vacuum for 48 h. Care was taken during handling and storage of $[C_2mim]I$ to avoid exposure to light. Tetra-*n*-butylammonium diiodoaurate ($[NBu_4][AuI_2]$) was prepared by suspending gold foil (0.53 g, Sigma-Aldrich, $\geq 99.9\%$), iodine (0.39 g, Sigma-Aldrich, 99.8%), and tetra-*n*-butylammonium iodide (1.08 g, $[NBu_4]I$, Sigma-Aldrich, $\geq 99\%$) in absolute ethanol (8 cm³, Merck, EMSURE) and refluxing for 72 h ($2Au + I_3^- + I^- \rightleftharpoons 2[AuI_2]^-$).³⁵ The crude product, $[NBu_4][AuI_2]$ (confirmed by electrospray ionization mass spectrometry) was recrystallized twice from dry ethyl acetate,³⁶ washed with diethyl ether (Merck, EMSURE), and dried under vacuum, for a final yield of 77%. To avoid excessive moisture pickup, this procedure was carried out under an atmosphere of dry N₂ using standard Schlenk techniques. Tetra-*n*-butylammonium hexafluorophosphate ($[NBu_4][PF_6]$, Sigma-Aldrich) was dried under vacuum at 80 °C for 24 h. Ferrocene (Fluka, >98%), acetonitrile (Sigma-Aldrich, 99.8%), and acetone (Merck, EMSURE) were used as supplied by the manufacturer; $[C_2mim][NTf_2]$, $[C_2mim]I$, $[NBu_4]I$, $[NBu_4][AuI_2]$, $[NBu_4][PF_6]$, and I₂ were stored and handled under a dry argon atmosphere in a glovebox.

Electrochemical Systems and Procedures. Voltammetric experiments were undertaken with a Gamry Reference 600 Potentiostat/Galvanostat/ZRA (Warminster, PA). The electrochemical quartz crystal microbalance experiments were carried out using an impedance method (passive EQCM) on an Agilent E5061A ENA Series Network Analyzer (Santa Clara, CA) coupled to an Autolab PGSTAT302N potentiostat (Metrohm, Herisau, SUI). All experiments were carried out under benchtop conditions at ambient temperature (21 ± 1 °C). All electrolyte solutions were degassed with N₂ prior to experimentation, and a blanket of N₂ was maintained over the electrolytes while undertaking experiments. All voltammetric experiments were carried out using a standard 3-electrode arrangement with a platinum mesh auxiliary electrode and an I^-/I_3^- reference electrode³⁷ (Pt | 400 mM $[C_2mim]I$ + 100 mM I₂ in $[C_2mim][NTf_2]$). UV-vis spectroscopy was performed with a Varian Cary 50 Bio UV-vis spectrophotometer (Agilent, Santa Clara, CA).

The platinum macrodisk electrode (nominal diameter = 1.6 mm) was purchased from BASi (Bioanalytical Systems, West Lafayette, IN), and the gold macrodisk electrode (nominal diameter = 3.0 mm) was purchased from Metrohm (Herisau, Switzerland). Macroelectrodes were activated by polishing with successively smaller (1, 0.3, and 0.05 μm) aqueous alumina slurries (Kemet, Kent, U.K.) on a clean polishing cloth (Buehler, Lake Bluff, IL). Adherent alumina were removed by

sonication in deionized water (Milli-Q), before rinsing with acetone. The EQCM working electrode was a 13 mm diameter AT-cut α -quartz crystal (Bright Star Crystals, Rowville, AUS), which had gold disks (5.0 mm diameter) vapor deposited on each side; the electrode resonated in air at 10 ± 0.05 MHz. The change in resonant frequency (Δf_0) in the quartz crystal electrode is related to the change in mass (Δm) by the Sauerbrey equation:^{38,39}

$$\begin{aligned}\Delta f_0 &= f_0(m + \Delta m) - f_0(m) = -\left(\frac{f_0(m)}{Ax_q\rho_q}\right)\Delta m \\ &= -S\Delta m\end{aligned}\quad (5)$$

where x_q is the thickness of the quartz crystal, ρ_q is the density of the quartz crystal (2.645 g cm^{-3} at 20°C), A is the active electrode surface area, and S is the Sauerbrey constant. Before each experiment, the EQCM working electrode was cleaned using concentrated nitric acid and rinsed successively with distilled water and acetone. The gold foil electrode (Sigma-Aldrich, $\geq 99.9\%$) used in the coulometry experiments was cleaned in concentrated nitric acid and rinsed successively in distilled water and acetone prior to use.

The active area of the relevant electrodes was calibrated voltammetrically using the oxidation of a ferrocene solution of known concentration (1.7 mM in acetonitrile containing 0.1 M $[\text{NBu}_4][\text{PF}_6]$) and adopting a diffusion coefficient of $2.24 \times 10^{-5} \text{ cm}^2 \text{ s}^{-1}$ as published under these conditions.⁴⁰ Semi-integration of the $I-t$ data was performed using an algorithm from de Levie,⁴¹ which was adapted from Oldham and Myland.⁴² A Microsoft Excel macro that includes this algorithm is available free online.⁴³

RESULTS AND DISCUSSION

Cyclic Voltammetry of Γ^- on Au. Initial investigations on gold were carried out with a 3.0 mm diameter electrode at an iodide concentration of 10 mM; cyclic voltammograms obtained at scan rates ranging from 50 to 1000 mV s^{-1} are shown in Figure 1. For comparison, experiments were also undertaken using a Pt electrode (shown in Figure 2). At all scan rates, there are two sets of oxidation/reduction peaks observed on both Au and Pt electrodes. On the gold electrode, the oxidation peak ($E_{p,\text{ox}}$) and reduction peak ($E_{p,\text{red}}$) potentials for the first process both shift in a positive direction with scan rate, though separation between the peaks (ΔE_p) is constant with scan rate ($\Delta E_p = 189.7 \pm 0.1 \text{ mV}$). This is a stark contrast to the first redox process on platinum (Γ^-/I_3^-), whereby ΔE_p changes significantly with scan rate as a result of sluggish heterogeneous electron-transfer kinetics.^{17,22,24} The voltammetric characteristics of the second process obtained on both gold and platinum are similar; $E_{p,\text{ox}}$, $E_{p,\text{red}}$, and ΔE_p are all relatively constant over the range of scan rates investigated, with values of 533 ± 3 , 393 ± 3 (both vs Γ^-/I_3^-), and $139.9 \pm 0.1 \text{ mV}$ respectively (on Au). Overall, iodide redox chemistry appears to be more complex on a gold compared to platinum or carbon electrodes, with noticeable broadening of the reduction peaks for both of the processes.

Linear Sweep Semi-Integral Voltammetry of Γ^- on Au.

In order to identify the relative number of electrons involved in each step, transient (peak-shaped) potential sweep voltammetric data (Figures 1 and 2) were transformed into forms which closely resemble steady-state voltammetric curves.¹² Transforming the data is achieved using the general

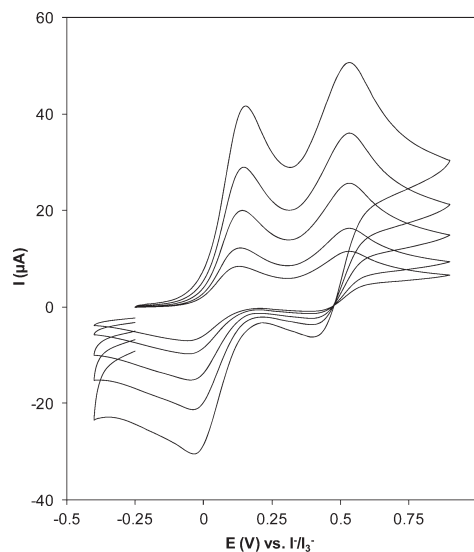


Figure 1. Cyclic voltammograms obtained from 10 mM $[\text{C}_2\text{mim}]\text{I}$ in $[\text{C}_2\text{mim}][\text{NTf}_2]$ at a 3.0 mm diameter Au macroelectrode with scan rates (from top to bottom) of 1000, 500, 250, 100, and 50 mV s^{-1} .

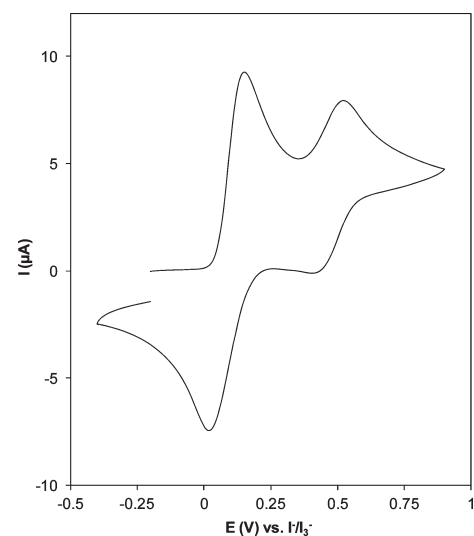


Figure 2. Cyclic voltammogram obtained from 10 mM $[\text{C}_2\text{mim}]\text{I}$ in $[\text{C}_2\text{mim}][\text{NTf}_2]$ at a 1.6 mm diameter Pt macroelectrode at a scan rate of 250 mV s^{-1} .

convolution procedure initially described by Savéant and co-workers,⁴⁴ which, when applied under conditions whereby mass transport occurs by semi-infinite planar diffusion, is known as semi-integration, as described by Oldham.⁴⁵ Semi-integration of $I-E$ data gives rise to a function, $M(t)$, which is related to the concentration of electroactive species at the electrode surface. Semi-integration has previously been shown to be applicable in high-viscosity RTIL electrolytes;⁴⁶ accordingly, the forward sweep of the $I-E$ data on gold and platinum electrodes were semi-integrated, following background subtraction to remove capacitive current (shown in Figure 3).

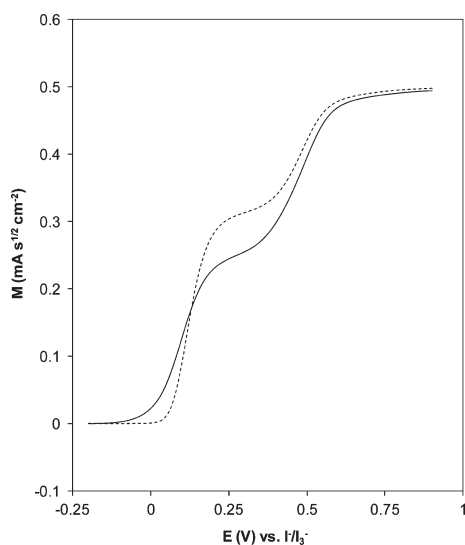


Figure 3. Comparison of the background corrected semi-integrals obtained from 10 mM $[\text{C}_2\text{mim}]\text{I}$ in $[\text{C}_2\text{mim}][\text{NTf}_2]$ at a scan rate of 250 mV s^{-1} on gold (—) and platinum (---) macrodisk electrodes.

The M - E curves resemble near steady-state voltammograms obtained with the respective electrode materials (Au: Figure S1a; Pt: Figure S1b). Intriguingly, the magnitude of the plateaus relative to one another (proportional to the number of electrons involved in each process) is different on gold and platinum electrodes. On platinum, as is well-known, the limiting current magnitudes exhibit a 2:1 ratio, corresponding to the I^-/I_3^- and I_3^-/I_2 oxidation processes described by eqs 3 and 4, respectively. On gold, the relative limiting current magnitudes exhibit a 1:1 ratio, indicative of a different iodide oxidation mechanism. This observation may be linked to the fact that gold is less inert in the presence of iodide compared with platinum- or carbon-based materials. For example, gold is known to be liable to chemical and/or electrochemical dissolution in aqueous^{47,48} and nonaqueous⁴⁹ solutions that contain a mixture of halide (complexant) and halogen (oxidant). Further, gold undergoes reversible dissolution/deposition⁵⁰ in solutions containing mixtures of I^- and I_3^- as per the following reaction:



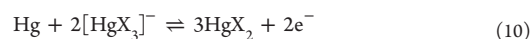
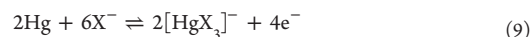
Indeed, iodide has been proposed as a substitute for highly toxic cyanide in the dissolution phase of gold refining.^{47,48,51}

It is well-known that one electron is involved in the overall electro-oxidation of each iodide ion on platinum. The magnitude of the area-normalized M_L plateaus on both Au and Pt are comparable (see Figure 3), suggesting that the number of electrons involved during electro-oxidation of each iodide ion on gold is also one. Therefore, the difference between the iodide oxidation mechanism on gold and platinum must arise from a disparity in the intermediate formed after the initial oxidation process; on platinum it is well-established that this intermediate is triiodide, as shown in the reaction described by eq 3. In accordance with these results, the intermediate formed on the gold electrode may: (a) be a soluble gold-iodide compound/complex and (b) liberate iodine/iodide upon

oxidation/reduction, respectively, with 1:1 electron stoichiometry, as described by the following equations:



This mechanism has been proposed on the basis of the electrochemical behavior of gold in conventional media containing iodide.^{32,33,52} In addition, Compton and co-workers⁵³ have previously suggested that the formation of gold-halide complex intermediates is feasible when investigating the oxidation of chloride on gold in a range of ionic liquids. Interestingly, theoretical calculations (geometric optimization and potential energy surface mapping) by Kloo and co-workers⁵⁴ indicated that $[\text{AuI}_2]^-$ and I_3^- are closely related and should be more-or-less exchangeable in polyiodides and gold(I) compounds containing the former. It is also worth noting that direct participation (dissolution) of the gold electrode during charge transfer parallels the well-known mechanism for mercury oxidation in the presence of halides in nonaqueous media:⁵⁵



where X^- is chloride, bromide, or iodide. When investigated using DC polarography, the iodide ion gives two well-defined oxidation waves on a mercury electrode, the first being assigned to the reversible oxidation of mercury to soluble triiodomercurate and the second to the reversible oxidation of mercury to soluble mercuric iodide.⁵⁶

EQCM Studies on a Au Thin-Film Electrode. If the above-proposed mechanism is valid, a change in mass of the gold electrode can be expected during the voltammetric experiment and thus may be detectable by EQCM. The cyclic voltammogram of the first oxidation process and corresponding Δf_0 - E curve obtained with an Au quartz-crystal electrode at an iodide concentration of 10 mM is shown in Figure 4. Indeed, a decrease in electrode mass was detected during the forward (oxidative) potential sweep, and the lost mass was partially recovered during the reverse (reductive) potential sweep. This observation is consistent with the mechanism described by eq 7. The experiment was repeated at an iodide concentration of 300 mM in order to improve the signal-to-noise ratio; a cyclic voltammogram and corresponding Δf_0 - E curve is shown in Figure 5. The upper potential limit of the potential sweep was limited to 0 V versus I^-/I_3^- , as it was found that the thin film of gold was completely stripped upon further scanning to more positive potentials, exposing the underlying chromium adhesion layer⁵⁷ (shown in Figure S2). The EQCM/voltammetric characteristics of the first process scale with concentration because again the oxidation/reduction processes correspond to a decrease/increase in electrode mass, respectively, which is consistent with a reaction of the type described by eq 7.

Coulometric Studies with a Au Foil Electrode. To confirm that the oxidation state of Au in the dissolved Au-iodide complex is +1, electrogravimetric analysis (bulk electrolysis) at 0.2 V versus I^-/I_3^- was carried out. During the bulk electrolysis experiment, the initially colorless electrolyte changed to a brown color characteristic of I_3^- , the presence of which was confirmed using UV-vis spectroscopy. This observation suggests that two oxidation processes are occurring simultaneously at the investigated hold potential: the oxidation

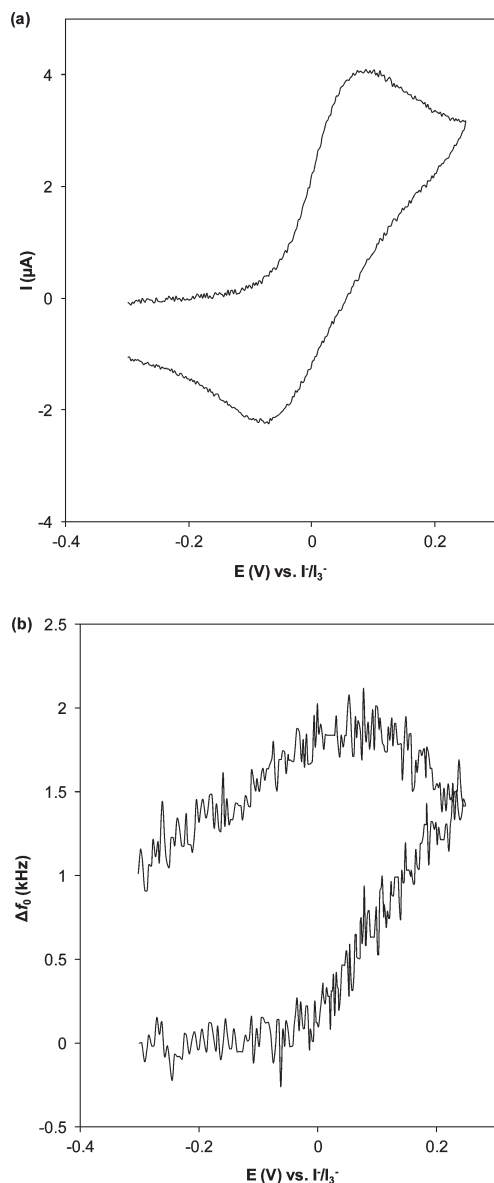


Figure 4. (a) Cyclic voltammogram and (b) corresponding Δf_0 - E curve obtained from 10 mM $[\text{C}_2\text{mim}]\text{I}$ in $[\text{C}_2\text{mim}][\text{NTf}_2]$ at a Au quartz crystal electrode ($A = 0.28 \text{ cm}^2$) at a scan rate of 1 mV s^{-1} .

of gold to diiodoaurate, as shown in the reaction described by eq 7, and the oxidation of iodide to triiodide, as shown in the reaction described by eq 3. The formation of two distinct products during oxidation is consistent with the broad reduction peaks observed during cyclic voltammetry (see Figure 1). The quantity of electricity passed through the cell (Q_{T}) is therefore consumed by the oxidation reactions described by eqs 3 and 7, thus:

$$Q_{\text{T}} = Q_{\text{Au}} + Q_{\text{I}_3^-} \quad (11)$$

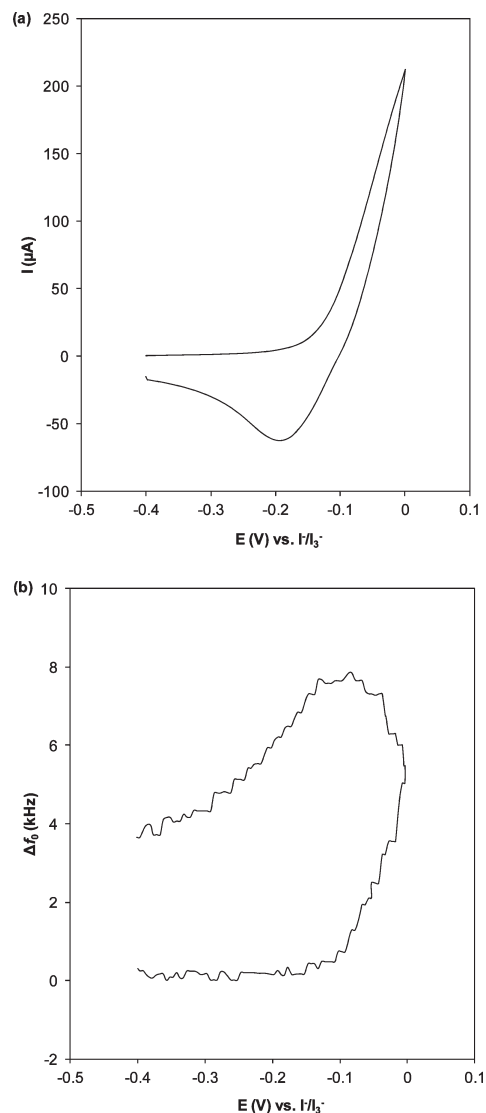


Figure 5. (a) Cyclic voltammogram and (b) corresponding Δf_0 - E curve obtained from 300 mM $[\text{C}_2\text{mim}]\text{I}$ in $[\text{C}_2\text{mim}][\text{NTf}_2]$ at a Au quartz crystal electrode ($A = 0.28 \text{ cm}^2$) at a scan rate of 5 mV s^{-1} .

The amount of electrogenerated triiodide (and hence $Q_{\text{I}_3^-}$) was calculated using UV-vis spectroscopy after preparing a standard curve (shown in Figure S3). The presence of the soluble gold-iodide intermediate had no observable effect on the UV-vis spectrum of triiodide, implying that the dissolved species is colorless; the $[\text{AuI}_2]^-$ anion reportedly possesses no UV-vis spectrophotometric activity.⁴⁸ Thus, Q_{Au} was calculated using eq 11, and the oxidation state of gold was determined using Faraday's laws of electrolysis:

$$z = \frac{Q_{\text{Au}} M}{mF} \quad (12)$$

where m is the difference in the mass of the gold electrode before and after electrolysis, M is the atomic mass of gold, F is

Faraday's constant, and z is the valence number of the oxidized gold species. By substituting the appropriate values of known parameters into eq 12, z was determined to be 1.01, in agreement with the reactions described by eqs 7 and 8. Q_{Au} accounted for roughly 88% of Q_T , indicating that the reaction described by eq 7 is the predominant oxidation pathway, which explains why 1:1 electron stoichiometry is observed voltammetrically (as shown in Figure 3).

Voltammetric Studies of $[AuI_2]^-$ on Au. To further support the proposed mechanism, $[NBu_4][AuI_2]$ was synthesized, and voltammetric experiments were undertaken in $[C_2mim][NTf_2]$ containing 2 mM of $[NBu_4][AuI_2]$ on a gold electrode. A cyclic voltammogram recorded at 25 mV s^{-1} is shown in Figure 6a. As was to be expected based on the reactions described by eqs 7 and 8, starting from open circuit potential, $[AuI_2]^-$ gives rise to two waves of equal magnitude (one oxidative and one reductive). The midpoint potentials (E_{mid}) defined as

$$E_{mid} = \frac{E_{p,ox} + E_{p,red}}{2} \quad (13)$$

are comparable for both processes to those obtained with I^- under identical conditions (see Figure 6b). E_{mid} (all vs I^-/I_3^-) on the second cycle is equal to 10 and 462 mV for the processes occurring at lower and higher potentials, respectively, for $[AuI_2]^-$, compared to 15 and 455 mV for I^- . Similar variation in E_{mid} was observed when changing the direction of the initial sweep and is thought to arise from the nature of the redox mechanism (i.e., adsorption and dissolution/deposition processes at the electrode surface give rise to slight irreproducibility). On the basis of these and previous results, we conclude that iodide oxidation to molecular iodine on a gold electrode occurs predominantly via a diiodoaurate intermediate, as shown in the reactions described by eqs 7 and 8, and to a lesser extent, via a triiodide intermediate, analogous to what is observed on platinum, as shown in the reactions described by eqs 3 and 4.

CONCLUSIONS

The electro-oxidation of iodide on a gold electrode in the room temperature ionic liquid 1-ethyl-3-methylimidazolium bis-(trifluoromethanesulfonyl)imide has been investigated in detail using a variety of techniques. Two oxidation processes with an electron stoichiometry of 1:1 are observed on a gold electrode, compared to the well-known 2:1 electron stoichiometry observed on platinum under identical conditions. Dissolution of the gold electrode, detected in situ using EQCM, was found to coincide with the first iodide oxidation process, and the oxidation state of the soluble gold species was found to be +1 using coulometric/electrogravimetric analysis. Quantitative treatment of the coulometric data suggests that iodide oxidation to molecular iodine on gold occurs predominantly via a diiodoaurate intermediate, and to a lesser extent, via a triiodide intermediate (detected using UV-vis spectroscopy). Diiodoaurate was further confirmed as the intermediate by investigating the voltammetric response of this species at a gold electrode. Uncovering a pathway for oxidation that is clearly distinct from the established one involving triiodide, and with electron transfer kinetics that appear to be superior, offers the prospect for enhancing the performance of the I^-/I_3^- redox couple in dye-sensitized solar cells. While this is unlikely to involve the replacement of platinum-coated electrodes with gold-coated

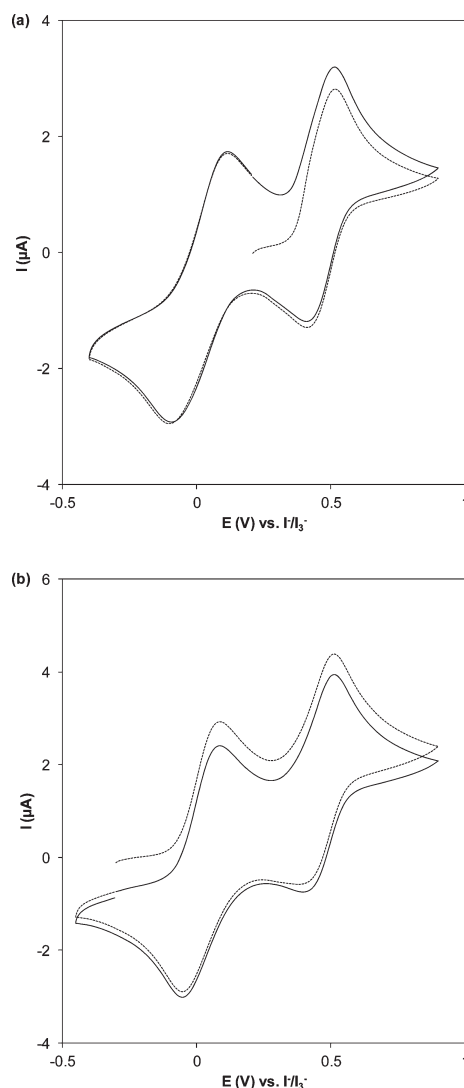


Figure 6. Cyclic voltammogram obtained from (a) 2 mM $[NBu_4][AuI_2]$ and (b) 4 mM $[C_2mim]I$ in $[C_2mim][NTf_2]$ at a 3.0 mm diameter Au macroelectrode at a scan rate of 25 mV s^{-1} . First (---) and second (—) cycles are shown.

equivalents, there may be other conductive substrates where analogous reactions and substrate interactions allow for fast, reversible operation of the iodide–triiodide couple. In support of the feasibility of this approach, it is worth recalling that the rather moderate potential of the latter invites consideration of a large range of possible electrode materials and composites.

ASSOCIATED CONTENT

Supporting Information

Near steady-state voltammograms obtained from the electro-oxidation of iodide on gold and platinum (Figure S1), an EQCM experiment demonstrating the complete stripping of the gold thin film electrode during iodide electro-oxidation (Figure S2), and the standard curve/UV-visible spectrum used

to calculate the amount of triiodide formed during bulk electrolysis (Figure S3). This material is available free of charge via the Internet at <http://pubs.acs.org>.

AUTHOR INFORMATION

Corresponding Authors



Notes

The authors declare no competing financial interest.

ACKNOWLEDGMENTS

We thank Dr. Thomas Ruether for assistance with synthesis of the $[\text{NBu}_4][\text{AuI}_2]$ complex.

REFERENCES

- Wilkes, J. S. *Green Chem.* **2002**, *4*, 73–80.
- MacFarlane, D. R.; Seddon, K. R. *Aust. J. Chem.* **2007**, *60*, 3–5.
- Armand, M.; Endres, F.; MacFarlane, D. R.; Ohno, H.; Scrosati, B. *Nat. Mater.* **2009**, *8*, 621–629.
- Dean, P. M.; Pringle, J. M.; MacFarlane, D. R. *Phys. Chem. Chem. Phys.* **2010**, *12*, 9144–9153.
- Papageorgiou, N.; Athanassov, Y.; Armand, M.; Bonhote, P.; Pettersson, H.; Azam, A.; Grätzel, M. *J. Electrochem. Soc.* **1996**, *143*, 3099–3108.
- Hagfeldt, A.; Boschloo, G.; Sun, L. C.; Kloo, L.; Pettersson, H. *Chem. Rev.* **2010**, *110*, 6595–6663.
- Howlett, P. C.; MacFarlane, D. R.; Hollenkamp, A. F. *Electrochem. Solid State Lett.* **2004**, *7*, A97–A101.
- de Souza, R. F.; Padilha, J. C.; Goncalves, R. S.; Dupont, J. *Electrochem. Commun.* **2003**, *5*, 728–731.
- Balducci, A.; Dugas, R.; Taberna, P. L.; Simon, P.; Plee, D.; Mastragostino, M.; Passerini, S. *J. Power Sources* **2007**, *165*, 922–927.
- O'Regan, B.; Grätzel, M. *Nature* **1991**, *353*, 737–740.
- Wang, P.; Zakeeruddin, S. M.; Moser, J. E.; Humphry-Baker, R.; Grätzel, M. *J. Am. Chem. Soc.* **2004**, *126*, 7164–7165.
- Bard, A. J.; Faulkner, L. R. *Electrochemical Methods: Fundamentals and Applications*, 2nd ed.; Wiley: New York, 2001.
- Swain, G. M. In *Handbook of Electrochemistry*, 1st ed.; Zoski, C. G., Ed.; Elsevier: Amsterdam, 2007; pp 111–153.
- Hubbard, A. T. *J. Phys. Chem.* **1975**, *79*, 808–815.
- Mebrahtu, T.; Rodriguez, J. F.; Bravo, B. G.; Soriaga, M. P. *J. Electroanal. Chem.* **1987**, *219*, 327–333.
- Bravo, B. G.; Mebrahtu, T.; Rodriguez, J. F.; Soriaga, M. P. *J. Electroanal. Chem.* **1987**, *221*, 281–287.
- Bentley, C. L.; Bond, A. M.; Hollenkamp, A. F.; Mahon, P. J.; Zhang, J. *Electrochim. Acta* **2013**, *109*, 554–561.
- Dane, L. M.; Janssen, L. J. J.; Hoogland, J. G. *Electrochim. Acta* **1968**, *13*, 507–513.
- Popov, A. L.; Geske, D. H. *J. Am. Chem. Soc.* **1958**, *80*, 1340–1352.
- Kawano, R.; Watanabe, M. *Chem. Commun.* **2003**, 330–331.
- Kawano, R.; Watanabe, M. *Chem. Commun.* **2005**, 2107–2109.
- Ejigu, A.; Lovelock, K. R. J.; Licence, P.; Walsh, D. A. *Electrochim. Acta* **2011**, *56*, 10313–10320.
- Zhang, Y.; Zheng, J. B. *Electrochim. Acta* **2007**, *52*, 4082–4086.
- Silvester, D. S.; Aldous, L.; Hardacre, C.; Compton, R. G. *J. Phys. Chem. C* **2008**, *112*, 6551–6557.
- Gebert, E. *J. Am. Chem. Soc.* **1954**, *76*, 2049–2054.
- Guidelli, R.; Piccardi, G. *Electrochim. Acta* **1967**, *12*, 1085–1095.
- Popov, A. L.; Rygg, R. H.; Skelly, N. E. *J. Am. Chem. Soc.* **1956**, *78*, 5740–5744.
- Iwamoto, R. T. *Anal. Chem.* **1959**, *31*, 955.
- Zittel, H. E. *J. Electroanal. Chem.* **1966**, *11*, 85–93.
- Dryhurst, G.; Elving, P. J. *J. Electroanal. Chem.* **1966**, *12*, 416.
- Elving, P. J. *Anal. Chem.* **1967**, *39*, 606–615.
- Loo, B. H. *J. Phys. Chem.* **1982**, *86*, 433–437.
- Qi, P. H.; Hiskey, J. B. *Hydrometallurgy* **1993**, *32*, 161–179.
- Zhao, S. F.; Lu, J. X.; Bond, A. M.; Zhang, J. *Chem.—Eur. J.* **2012**, *18*, 5290–5301.
- Baker, L. J.; Bott, R. C.; Bowmaker, G. A.; Healy, P. C.; Skelton, B. W.; Schwerdtfeger, P.; White, A. H. *J. Chem. Soc., Dalton Trans.* **1995**, 1341–1347.
- Ohtsuka, I.; Nakayama, H.; Ishii, K. *J. Raman Spectrosc.* **1989**, *20*, 489–492.
- Dias, A. P.; Papageorgiou, N.; Kalyanasundaram, K.; Grätzel, M. *Inorg. Chem.* **1996**, *35*, 1168–1178.
- Sauerbrey, G. *Zeitschrift Fur Physik* **1959**, *155*, 206–222.
- Snook, G. A.; Bond, A. M.; Fletcher, S. *J. Electroanal. Chem.* **2002**, *526*, 1–9.
- Rogers, E. I.; Silvester, D. S.; Poole, D. L.; Aldous, L.; Hardacre, C.; Compton, R. G. *J. Phys. Chem. C* **2008**, *112*, 2729–2735.
- de Levie, R. *How to Use Excel® in Analytical Chemistry and in General Scientific Data Analysis*; Cambridge University Press: Cambridge, U.K., 2001.
- Oldham, K. B.; Myland, J. C. *Fundamentals of Electrochemical Science*; Academic Press: San Diego, CA, 1994.
- de Levie, R. *Excellaneous*. <http://www.bowdoin.edu/~rdelevie/excellaneous/> (accessed September 19, 2013).
- Saveant, J. M. *J. Electroanal. Chem.* **1973**, *44*, 169–187.
- Grenness, M.; Oldham, K. B. *Anal. Chem.* **1972**, *44*, 1121–1129.
- Bentley, C. L.; Bond, A. M.; Hollenkamp, A. F.; Mahon, P. J.; Zhang, J. *Anal. Chem.* **2012**, *85*, 2239–2245.
- Issaev, N.; Osteryoung, J. G. *J. Electrochem. Soc.* **1998**, *145*, 974–981.
- Issaev, N.; Osteryoung, J. G. *J. Electrochem. Soc.* **1996**, *143*, 3477–3482.
- Nakao, Y. *J. Chem. Soc., Chem. Commun.* **1992**, 426–427.
- Nakao, Y.; Sone, K. *Chem. Commun.* **1996**, 897–898.
- Hu, Z.; Ritzdorf, T. *J. Electrochem. Soc.* **2007**, *154*, D543–D549.
- Guo, T.; Li, L. D.; Cammarata, V.; Illies, A. *J. Phys. Chem. B* **2005**, *109*, 7821–7825.
- Villagran, C.; Banks, C. E.; Hardacre, C.; Compton, R. G. *Anal. Chem.* **2004**, *76*, 1998–2003.
- Svensson, P. H.; Rosdahl, J.; Kloo, L. *Chem.—Eur. J.* **1999**, *5*, 305–311.
- Bond, A. M. *Modern Polarographic Methods in Analytical Chemistry*; Marcel Dekker: New York, 1980.
- Matsui, Y.; Kurosaki, Y.; Date, Y. *Bull. Chem. Soc. Jpn.* **1970**, *43*, 1707.
- Deakin, M. R.; Buttry, D. A. *Anal. Chem.* **1989**, *61*, 1147A–1154A.

Supporting information for

Unexpected complexity in the electro-oxidation of
iodide on gold in the ionic liquid 1-ethyl-3-
methylimidazolium
bis(trifluoromethanesulfonyl)imide

*Cameron L. Bentley,^{†,‡} Alan M. Bond,[†] Anthony F. Hollenkamp,[‡] Peter J. Mahon[§] and Jie
Zhang[†]*

[†]School of Chemistry, Monash University, Clayton, Vic 3800, Australia

[‡]CSIRO Energy Technology, Box 312, Clayton South, Vic 3169, Australia

[§]Faculty of Life and Social Sciences, Swinburne University of Technology, Hawthorn, Vic 3122,
Australia

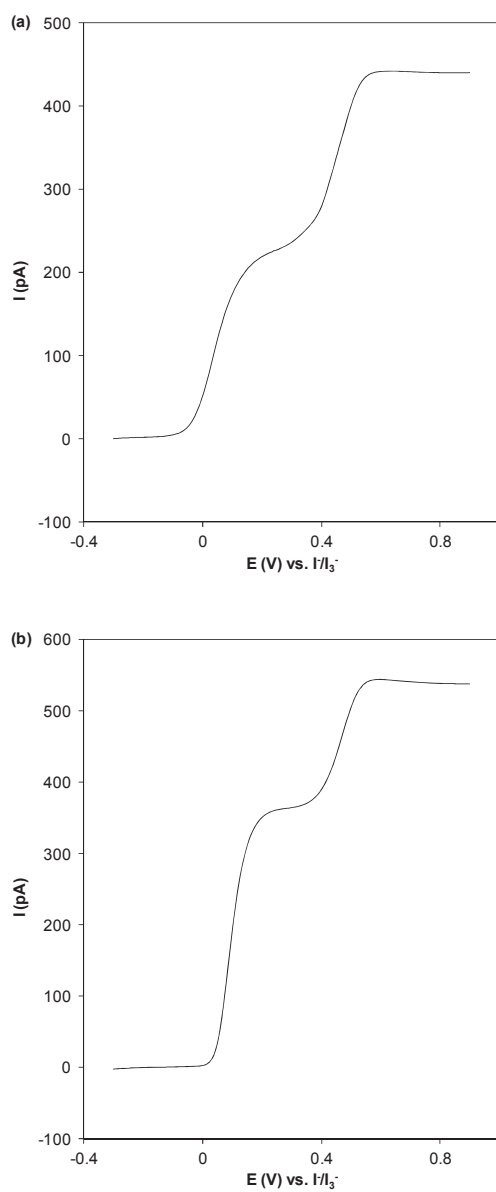


Figure S1. Near steady-state voltammograms obtained from 10 mM $[\text{C}_2\text{mim}]\text{I}$ in $[\text{C}_2\text{mim}][\text{NTf}_2]$ using a 10 μm dia. Au microelectrode (a) and 10 μm dia. Pt microelectrode (b) with a scan rate of 5 mV s^{-1} .

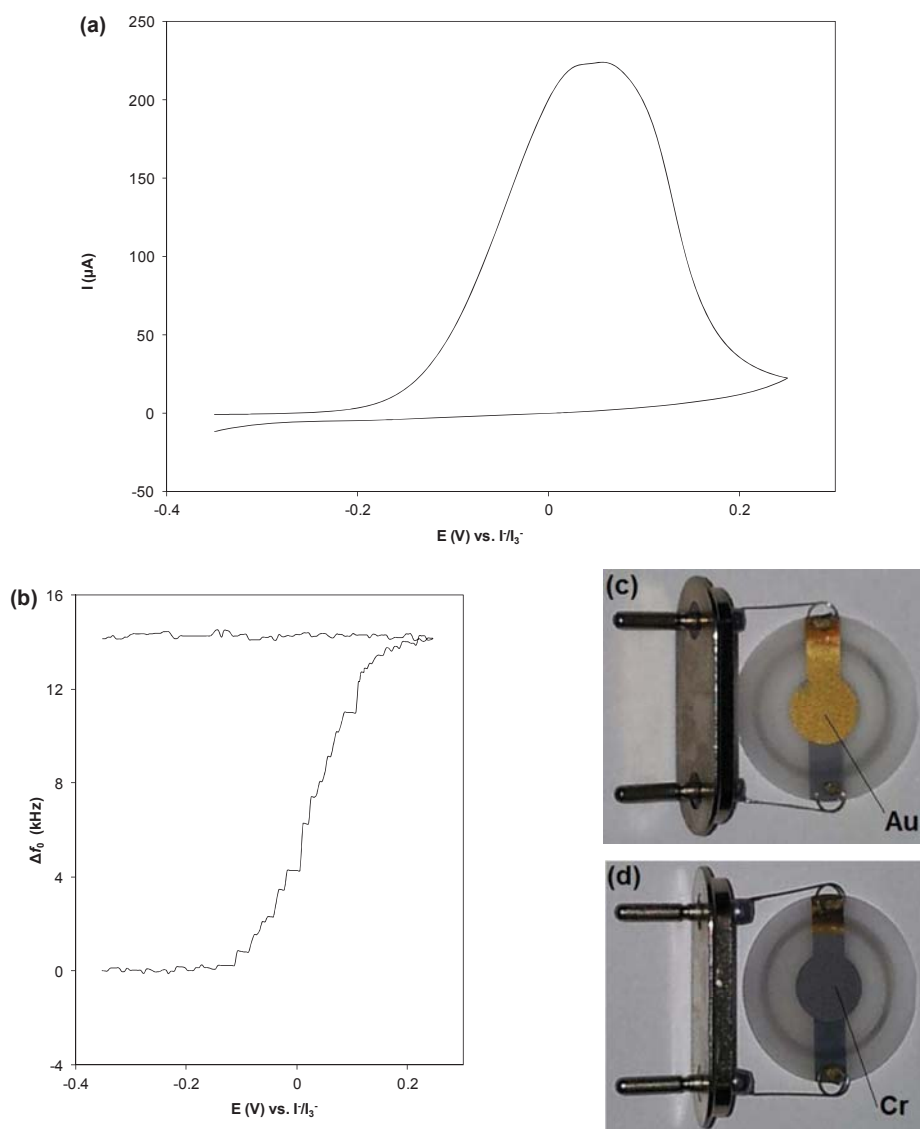


Figure S2. (a) A cyclic voltammogram and (b) corresponding Δf_0 -E curve obtained from 300 mM $[\text{C}_2\text{mim}]\text{I}$ in $[\text{C}_2\text{mim}][\text{NTf}_2]$ at an Au quartz crystal electrode ($A = 0.28 \text{ cm}^2$) at a scan rate of 5 mV s^{-1} . Accompanying are images of the Au quartz crystal electrode (c) before and (d) after the cyclic voltammetry experiment.

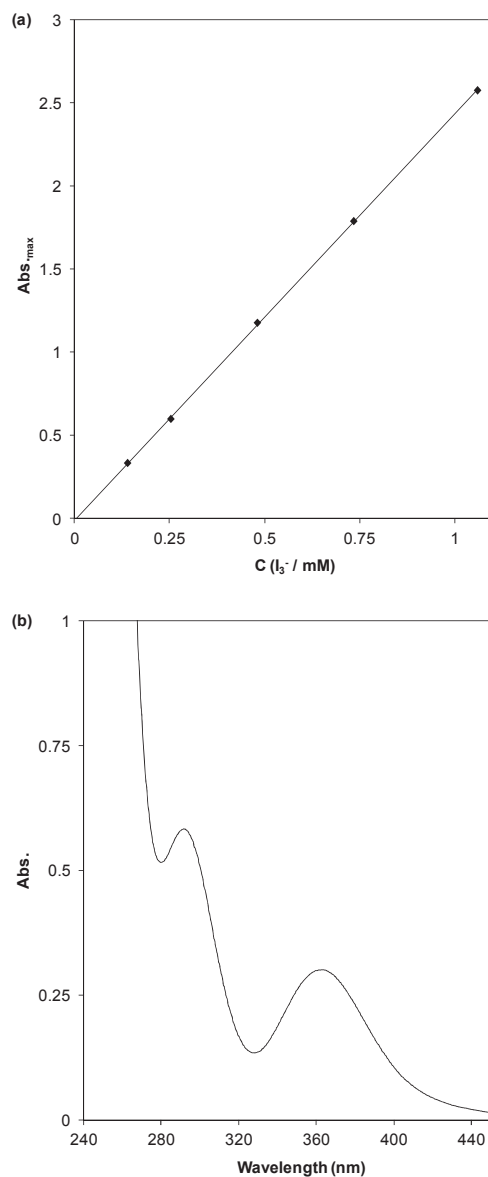


Figure S3. (a) Linear plot of the absorbance maxima (*ca.* 360 nm) vs. the bulk concentration of triiodide (1:1 with iodide) in $[C_2mim][NTf_2]$ ($R^2 = 0.99992$). (b) UV/Visible spectrum of the solution obtained after an Au foil electrode held at 0.2 V vs. I/I_3^- for 6.5 hours in 10 mM $[C_2mim]I$ in $[C_2mim][NTf_2]$.

Electrode Reaction and Mass-Transport Mechanisms Associated with the Iodide/Triiodide Couple in the Ionic Liquid 1-Ethyl-3-methylimidazolium Bis(trifluoromethanesulfonyl)imide

Cameron L. Bentley,^{†,‡} Alan M. Bond,[†] Anthony F. Hollenkamp,^{*,‡} Peter J. Mahon,[§] and Jie Zhang^{*,†}

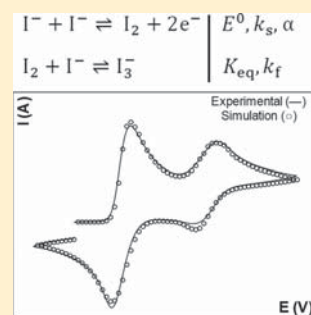
[†]School of Chemistry, Monash University, Clayton, Vic 3800, Australia

[‡]CSIRO Energy Flagship, Box 312, Clayton South, Vic 3169, Australia

[§]Faculty of Science, Engineering and Technology, Swinburne University of Technology, Hawthorn, Vic 3122, Australia

Supporting Information

ABSTRACT: The oxidation and reduction processes associated with the iodide/triiodide (I^-/I_3^-) couple have been investigated in the room temperature ionic liquid 1-ethyl-3-methylimidazolium bis(trifluoromethanesulfonyl)imide using cyclic voltammetry, convolution voltammetry, and chronoamperometry. Analogous to the case in acetonitrile, two processes with a relative electron stoichiometry of 2:1 are observed at a platinum electrode and are assigned to the I^-/I_3^- and I_3^-/I_2 processes at lower and higher potentials, respectively. The electro-oxidation of I^- has been simulated using a termolecular charge transfer mechanism: $I_2 + 2e^- \rightleftharpoons I^- + I^-$ (E^0, k_s, α), $I_2 + I^- \rightleftharpoons I_3^-$ (K_{eq}, k_f), where E^0 , k_s , α , K_{eq} , and k_f are the standard potential, standard heterogeneous electron-transfer rate constant, charge transfer coefficient, equilibrium (stability) constant, and bimolecular (forward) rate constant, respectively. The stability constant of I_3^- in this ionic liquid ($K_{eq} = 2.3 \times 10^6$, estimated by simulation) is comparable to that reported in acetonitrile ($K_{eq} \approx 10^7$). The reduction of I_3^- to I^- has also been modeled in the ionic liquid using a kinetically controlled CE mechanism. For this process, the delicate balance between kinetic and diffusion control is sensitive to the voltammetric scan rate, electrode geometry, and total concentration/ratio of I^-/I_2 , thereby making it difficult to estimate the diffusion coefficient of I_3^- . In contrast, the oxidation of I^- to I_3^- proceeds via a diffusion-controlled EC mechanism and the diffusivity of I^- is directly proportional to the bulk concentration of I_3^- , showing an enhancement of $\approx 50\%$ when the bulk concentration of I_3^- is increased from 0 to 500 mM. This enhancement cannot be explained by a decrease in solution viscosity and has been attributed to electron hopping and/or a Grothuss-type bond-exchange reaction between I^- and I_3^- , in agreement with previous reports.



INTRODUCTION

Since the introduction of air/water stable nonhaloaluminate room temperature ionic liquids (RTILs) more than two decades ago, there has been ongoing interest in using these neoteric solvents as replacements for volatile molecular solvents in a range of applications.¹ RTILs are composed entirely of ions and often tend to be nonvolatile with high chemical, electrochemical, and thermal stability.² Being intrinsic ionic conductors, RTILs can readily be employed in electrochemistry as nonflammable and relatively inert electrolytes. Unfortunately, due to the relatively strong cohesive (electrostatic) forces operating within an RTIL, they are typically 10 to 10⁴ times more viscous than “conventional” molecular solvents, resulting in sluggish physical mass transport.³ Despite this limitation, many research groups have managed to successfully employ RTILs as “alternative electrolytes” in a range of electrochemical devices, including dye-sensitized solar cells,^{4,5} lithium batteries,⁶ fuel cells,⁷ and supercapacitors.⁸

Since first reported by O'Regan and Grätzel⁹ over 20 years ago, intensive research efforts have focused on improving and optimizing the performance of the dye-sensitized solar cell

(DSSC). Owing to the low manufacturing cost and design versatility (i.e., size, shape, and flexibility) of DSSCs, they are considered to be promising candidates to replace traditional (*p-n*) silicon photovoltaics in a range of applications. In essence, a prototypical DSSC has three fundamental components: (1) a TiO₂ semiconductor photoanode with an adsorbed photoactive dye; (2) a platinumized counter electrode (cathode); and (3) an electrolyte solution containing the oxidized and reduced forms of a suitable redox couple so as to establish a redox shuttle system that regenerates the reduced form of the dye. As in the original paper, iodide/triiodide (I^-/I_3^-) dissolved in acetonitrile is still the most commonly employed electrolyte formulation, meeting the dual requirements for an appropriate electrode potential combined with sufficient charge transport properties.⁵ Nevertheless, acetonitrile imposes restrictions on device performance due to the poor long-term stability (relatively high solvent volatility) and

Received: July 14, 2014

Revised: August 24, 2014

Published: August 26, 2014

safety (solvent flammability) under light soaking conditions. These issues can be minimized by employing an electrolyte solution that is based on an appropriate RTIL.^{4,5,10}

The voltammetric behavior of the iodide/iodine (Γ^-/I_2) redox couple is largely dependent upon the electrode material employed and the properties of the solvent (electrolyte). Although unique interactions are known to occur between Γ^-/I_2 and electrode materials such as gold^{11,12} and mercury,^{13,14} it is well established that the following overall process occurs at inert electrode materials such as platinum and carbon:



The heterogeneous electron-transfer kinetics of this inner sphere process¹⁵ are facile at noble metal electrode materials.¹⁶ However, Γ^- oxidation/ I_2 reduction is complicated by the homogeneous equilibrium process:

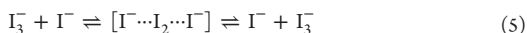


As a result, Γ^- oxidation/ I_2 reduction often occurs in two well resolved steps (i.e., via a I_3^- intermediate), giving rise to two voltammetric processes:



The potential gap separating the two voltammetric processes is proportional to the magnitude of K_{eq} for the reaction shown in eq 2,^{17,18} with only a single process observable in water ($K_{eq} \approx 10^3$),¹⁹ but two well resolved ones observable in acetonitrile ($K_{eq} \approx 10^7$).^{17,20} The limited number of studies available in RTILs^{16,21–26} have revealed Γ^-/I_2 electrochemistry analogous to that observed in aprotic molecular solvents such as acetonitrile.

Despite the clear safety and stability benefits achieved from employing an RTIL as the electrolyte in DSSCs, practical application remains a challenge due to the physical mass-transport limitations associated with the intrinsically high viscosity of these electrolytes. Nevertheless, several research groups^{21,22,27–30} have reported significantly greater mass transport of the Γ^-/I_3^- redox couple in RTIL electrolytes than expected, which is often attributed to a rapid exchange process establishing a Grotthuss-like extension of diffusion:



where I_2 is exchanged between Γ^- and I_3^- , displacing them without physical mass transfer. Indeed, collision of ions of like charge (i.e., Γ^-/I_3^-) is more favored under conditions of high ionic strength due to a phenomenon known as the “kinetic salt effect”,³¹ making the process shown in eq 5 more feasible in RTILs^{27,28,30,32} and concentrated aqueous electrolyte solutions.^{33,34} Understanding this mass transfer phenomenon is obviously an important step in the optimization of any RTIL electrolyte function in DSSCs.

Studies by Kawano and Watanabe^{21,22} on the steady-state voltammetric behavior of the Γ^-/I_3^- redox system in 1-ethyl-3-methylimidazolium bis(trifluoromethanesulfonyl)imide ($[C_2mim][NTf_2]$) at a Pt microelectrode revealed exceptionally fast charge transport. The apparent diffusivity (D_{app}) of the two species (based on the assumption that $D_{\Gamma^-} = D_{I_3^-} = D_{app}$) was divided into contributions from simple physical diffusion (D_{phys}) and exchange-reaction-based diffusion (D_{ex}) as per the Dahms–Ruff equation:^{12,14}

$$D_{app} = D_{phys} + D_{ex} = D_{phys} + \frac{1}{6}k_{ex}\delta^2c \quad (6)$$

where k_{ex} is the bimolecular exchange-reaction rate constant, δ is the center-to-center intersite distance at the time of the exchange reaction, and c is the total concentration of the electroactive species involved (i.e., $[\Gamma^-] + [I_3^-]$). On this basis, it was concluded that D_{ex} makes a dominant contribution to D_{app} when the concentration of redox species is high and the molar ratio of Γ^- and I_3^- is comparable. Furthermore, in another study,³⁵ the authors reported DSSCs containing RTIL electrolytes with short-circuit currents greater than 80% of that achievable in cells employing conventional organic electrolytes, despite the viscosity of the former being >10-fold higher than the latter.

More recently, Gores and co-workers^{27,28,30,32} have investigated the unusual mass-transport phenomenon in a variety of imidazolium-based ionic liquids, typically at a fixed concentration of I_3^- (≈ 0.05 M) and an extended range of Γ^- concentrations, achieved by adding a variable mole fraction of the highly viscous RTIL 1-propyl-3-methylimidazolium iodide ($[C_3mim]I$). Using steady-state ultramicroelectrode voltammetry or polarization measurements in thin layer cells to quantify $D_{I_3^-}$, these authors provided strong evidence for an exchange-reaction-mediated enhancement in mass transport, with the increase in viscosity as a result of increasing the mole fraction of $[C_3mim]I$ being several times larger than the observed decrease in $D_{I_3^-}$, contrary to what is predicted based on the Stokes–Einstein relationship ($D \propto 1/\eta$).³¹ A recent study by Grätzel and co-workers³⁶ also demonstrated that the conductivity of $[C_3mim]I$ increases significantly upon adding molecular iodine to values beyond which can be explained by a simple decrease in solution viscosity. The order-of-magnitude increase in ionic conductivity was attributed to the enhancement of the mobility of Γ^-/I_3^- as a result of a Grotthuss-like bond-exchange process.

In this paper, we present a detailed investigation into the voltammetric behavior of the Γ^-/I_3^- couple in $[C_2mim][NTf_2]$, with a strong focus on electrode reaction and mass-transport mechanisms. The electro-oxidation of iodide has been investigated by cyclic voltammetry at platinum macro- and microdisk electrodes, with mechanistic information determined by modeling based on the use of the DigiElch digital simulation software package. The redox behavior of triiodide in the absence and presence of excess iodide has also been examined at platinum disk electrodes using cyclic and convolution voltammetry. Finally, the Grotthuss-like extension of diffusion has been studied by quantifying the diffusivity of iodide over a large concentration range in the presence of variable concentrations of triiodide using a chronoamperometric technique.

EXPERIMENTAL SECTION

Reagents. 1-Ethyl-3-methylimidazolium bis(trifluoromethanesulfonyl)imide ($[C_2mim][NTf_2]$, Iolitec, 99.5%) was dried under high vacuum ($\leq 10^{-2}$ mbar) at 45 °C for 48 h and stored under lithium. The residual water content was less than 50 ppm by Karl Fischer titration (Metrohm 831 KF Coulometer). 1-Ethyl-3-methylimidazolium iodide ($[C_2mim]I$, Iolitec, >98%) was recrystallized twice from a 2:1 mixture of ethyl acetate (Merck, EMSURE) and isopropanol (Merck, EMSURE) and then dried under high vacuum for 48 h. Care was taken during handling and storage of $[C_2mim]I$ to avoid exposure to light. Iodine (Sigma-Aldrich,

99.8%), ferrocene (Fluka, >98%), acetonitrile (Sigma-Aldrich, 99.8%), lithium tetrafluoroborate (LiBF₄, Stella Chemifa), sulfuric acid (Univar), silver nitrate (AgNO₃, BDH, 99.9%), tetra-*n*-butylammonium hexafluorophosphate ([NBu₄][PF₆], Sigma-Aldrich), and acetone (Merck, EMSURE) were used as supplied by the manufacturer. [C₂mim][NTf₂], [C₂mim]I, and I₂ were stored and handled under a dry argon atmosphere in a glovebox.

Electrochemical Systems and Procedures. All voltammetric experiments were carried out under benchtop conditions at ambient temperature (24 ± 1 °C) with a Gamry Reference 600 Potentiostat/Galvanostat/ZRA (Gamry Instruments, USA). All solvents were degassed with N₂ prior to experimentation, and a blanket of N₂ was maintained during the course of the voltammetric experiments. A Faraday cage was employed to minimize noise in all microelectrode experiments. All voltammetric experiments in [C₂mim][NTf₂] were carried out using a standard three-electrode arrangement with a working electrode as described below, a Pt wire auxiliary electrode and an I⁻/I₃⁻ reference electrode (Pt | 400 mM [C₂mim]I + 100 mM I₂ in [C₂mim][NTf₂]). It was assumed that I⁻ and I₂ immediately formed I₃⁻ (eq 2) upon mixing. All voltammetric experiments in acetonitrile were carried out using a standard three-electrode arrangement with a working electrode as described below, a Pt wire auxiliary electrode and an Ag/Ag⁺ reference electrode (10 mM AgNO₃ + 0.1 M [NBu₄][PF₆] in acetonitrile). Viscosity was measured using the falling ball method with an Anton Paar Automated Microviscometer (AMVn). Density was measured with an Anton Paar DMA 4500 M Density Meter.

The Pt macrodisk with a nominal diameter of 1.6 mm was purchased from BASi (Bioanalytical Systems, USA). The Pt macrodisk with a nominal diameter of 2.0 mm and the Pt microdisk with a nominal diameter of 20 μm were purchased from Metrohm (Switzerland). Macrodisk electrodes were activated by polishing with successively smaller (1 and 0.3 μm) aqueous alumina slurries (Kemet, U.K.) on a clean polishing cloth (Buehler, USA). Adherent alumina was removed by sonication in deionized water (Milli-Q). Microdisk electrodes were activated by polishing with an aqueous slurry of 0.05 μm alumina and rinsing thoroughly with deionized water. Prior to experimentation, the relevant electrodes were preconditioned in 0.1 M sulfuric acid by scanning between the oxygen and hydrogen evolution reactions³⁷ with subsequent rinsing in deionized water and acetone. The active electrode area (*A*) of each of the electrodes was calibrated voltammetrically using the oxidation of a ferrocene solution of known concentration (2.0 mM in acetonitrile containing 0.10 M [NBu₄][PF₆]) and adopting a diffusion coefficient of 2.4 × 10⁻⁵ cm² s⁻¹, as published under these conditions, along with Randles–Sevcik equation for the peak current.¹⁵

Data Treatment and Processing. The algorithm used to calculate the convolved currents has been reported previously.³⁸ The chronoamperometric (*I*–*t*) decay curves were analyzed using the following equations, as proposed by Shoup and Szabo,³⁹ which sufficiently describe the current response at a microdisk electrode over the entire time domain, with a maximum error of less than 0.6%:

$$I = -4nFDC^b r_0 f(t) \quad (7)$$

$$f(t) = 0.7854 + 0.8862\tau^{-1/2} + 0.2146 \exp(-0.7823\tau^{-1/2}) \quad (8)$$

where *D* is the diffusion coefficient, *n* is the stoichiometric number of electrons, *r*₀ is the radius of the microdisk, *C*^b is the bulk concentration of electroactive species, *F* is Faraday's constant, and the dimensionless time parameter, *τ*, is given by

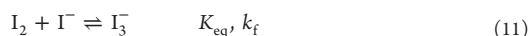
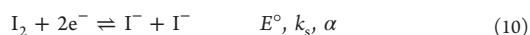
$$\tau = \frac{4Dt}{r_0^2} \quad (9)$$

Diffusion coefficients were extracted by fitting the experimental data with the theoretical transients described by eqs 7 and 8 (*C*^b, *n* and *r*₀ known) using the nonlinear curve fitting function available in OriginPro 9.0 software (OriginLab, USA). The chronoamperometric data was fitted between the limits of 0.2 to 1.5 s, and the sample time used in all experiments was 0.02 s. Voltammetric simulations were undertaken using the DigiElch software package (v. 7F, Elchsoft, Germany).

RESULTS AND DISCUSSION

Voltammetric Oxidation of I⁻ in [C₂mim][NTf₂]. The electro-oxidation of I⁻ at a Pt macrodisk electrode was investigated using a range of scan rates and concentrations; representative cyclic voltammograms are shown in Figure 1. In agreement with our previous work,¹⁶ there are two couples corresponding to the I⁻/I₃⁻ and I₃⁻/I₂ processes (at increasingly positive potentials) described by eqs 3 and 4, respectively. The potential gap between the two processes becomes larger with concentration as a result of the I⁻/I₃⁻ process shifting negatively and the I₃⁻/I₂ process shifting toward more positive potentials. Very high concentrations of I⁻ were not investigated due to the complications caused by the nucleation and growth of sparingly soluble I₂ on the electrode surface.^{16,25}

Figure 1 also contains simulations of the voltammetry; the following termolecular charge transfer mechanism was found to give good agreement with the experimental data:



where *E*[°], *k*_s, *α*, *K*_{eq}, and *k*_f are the standard potential, standard heterogeneous electron-transfer rate constant, charge transfer coefficient, equilibrium (stability) constant, and bimolecular (forward) rate constant, respectively. A reaction mechanism of this type has previously been considered by Macagno and Giordano⁴⁰ when investigating the voltammetry of the I⁻/I₂ couple at Pt in acetonitrile. Excellent fits between the experimental and simulated voltammograms are achieved over a range of scan rates and I⁻ concentrations when using the simulation parameters outlined in Table 1. In all simulations uncompensated resistance (*R*_u) and double layer capacitance (*C*_{dl}) were taken to be equal to 0 Ω and 0 F, respectively. The diffusion coefficients of I₃⁻, I⁻, and I₂ were all measured experimentally using convolution voltammetry, shown in Figures 3b, 6b, and S1, respectively. Interestingly, the stability constant of I₃⁻ in this media (*K*_{eq} = 2.3 × 10⁶) is comparable to that reported in acetonitrile (*K*_{stab} ≈ 10⁷),^{17,20} which may explain why analogous voltammetry is observed in these two physicochemically disparate solvents.

It is important to note that the major apparent limitation of this model is the unrealistically high value for the bimolecular

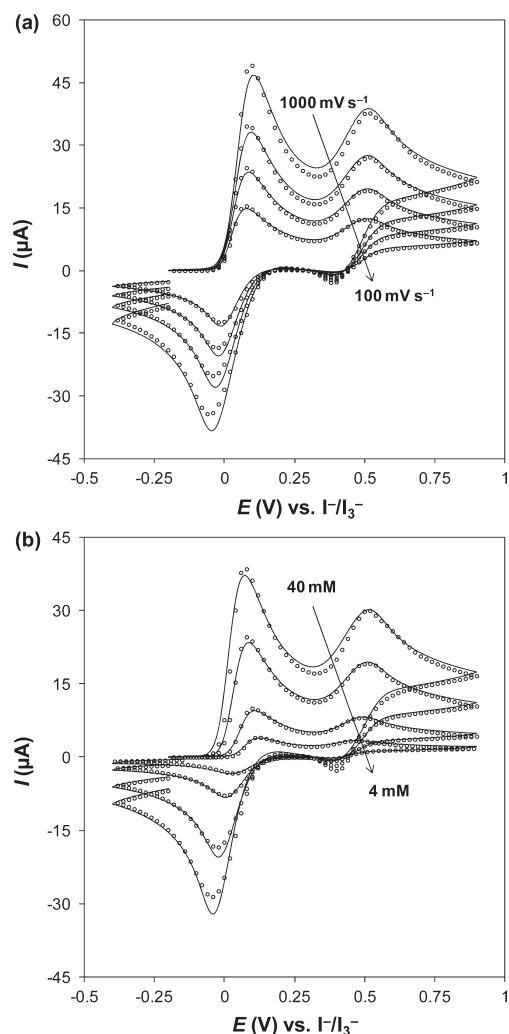


Figure 1. Comparison of the simulated (○) and experimental (—) cyclic voltammograms for the oxidation of $[\text{C}_2\text{mim}]\text{I}$ in $[\text{C}_2\text{mim}][\text{NTf}_2]$ at a 1.6 mm diameter Pt macrodisk electrode with (a) an I^- concentration of 25 mM and scan rates of (from top to bottom) 1000, 500, 250, and 100 mV s^{-1} and (b) a scan rate of 250 mV s^{-1} and I^- concentrations of (from top to bottom) 40 mM, 25 mM, 10 mM, and 4 mM. Simulation parameters are available in Table 1.

rate constant ($k_f = 5 \times 10^{14} \text{ M}^{-1} \text{ s}^{-1}$), which is orders of magnitude higher than the normal diffusion-controlled limit for a bimolecular reaction in this viscous media (10^8 to $10^9 \text{ M}^{-1} \text{ s}^{-1}$). For this reason, the K_{eq} and k_f values given in Table 1 hereafter will be referred to as “apparent” constants. If a more realistic value for $k_{f,\text{app}}$ is used in the simulation, $k_{b,\text{app}}$ becomes negligibly small and the equilibrium shown in eq 11 becomes effectively irreversible on the time scale of the voltammetric experiment; consequently, two “reversible” electron-transfer processes are not observed, as demonstrated in Figure S2. If $K_{\text{eq,app}}$ is decreased in order to increase $k_{b,\text{app}}$ (at a fixed $k_{f,\text{app}}$ value), the potential gap between the I^-/I_3^- and I_3^-/I_2 processes decreases¹⁷ and eventually only a single voltammetric process is observed, as demonstrated in Figure S3. In order to

Table 1. Simulation Parameters Used in Figure 1 To Model the Electro-Oxidation of I^- (from $[\text{C}_2\text{mim}]\text{I}$) in $[\text{C}_2\text{mim}][\text{NTf}_2]$ at a 1.6 mm Diameter Pt Macrodisk Electrode

Parameter	Value
E° (V)	0.135
k_s (cm s^{-1})	1.8
α	0.35
$K_{\text{eq,app}}$	2.3×10^6
$k_{f,\text{app}}$ ($\text{M}^{-1} \text{ s}^{-1}$)	5×10^{14}
D_{I^-} ($\times 10^{-7} \text{ cm}^2 \text{ s}^{-1}$)	2.65
D_{I_2} ($\times 10^{-7} \text{ cm}^2 \text{ s}^{-1}$)	4.3
D_{I_3} ($\times 10^{-7} \text{ cm}^2 \text{ s}^{-1}$)	7.8
T (K)	298.2

achieve the reversible voltammograms observed experimentally, the reaction shown in eq 11 must be rapid enough to attain equilibrium. This deficiency in the model is not specific to the RTIL solvent employed, as a similarly unrealistic $k_{f,\text{app}}$ value was required to simulate the electro-oxidation of I^- in acetonitrile using this model, as shown in Figure S4.

The unacceptably large $k_{f,\text{app}}$ value shown in Table 1 is likely to be an artifact of the overly simple mechanism employed in the simulations (eqs 10 and 11). Consequently, parameters deduced on the basis of this modeling are unlikely to have any “real” physical significance. The large $k_{f,\text{app}}$ value is required in the simulations so that the reaction shown in eq 11 remains close to equilibrium. If this condition is met, the reaction scheme shown in eqs 10 and 11 is identical to the scheme described in eqs 12–14, since a combination of eqs 12 and 13 gives eq 10 and a combination of eqs 12 and 14 gives eq 11:



This latter reaction scheme does not require the use of any physically unacceptable $k_{f,\text{app}}$ parameter and in this respect is superior for simulating the voltammetric data. However, it becomes increasingly difficult to obtain unique parameters from the simulations when a large number of “unknowns” have to be included in the model, and therefore, the “simplest” version of the theory (eqs 10 and 11) has been employed in this paper. It should be noted that adsorption has been omitted in both schemes, despite the propensity of halides to chemisorb on platinum^{41–43} and despite the inner sphere nature of the $\text{I}^-/\text{I}_3^-/\text{I}_2$ charge transfer processes.^{11,16}

Despite the shortcomings, simulations based on the “simplified” scheme shown in eqs 10 and 11 successfully predict the dependence of the peak potentials on scan rate (100–1000 mV s^{-1}) and I^- concentration (4–40 mM). Fits of simulated and experimental data at I^- concentrations of 4 mM, 10 mM, and 40 mM for both processes are shown in Figures S5, S6, and S7, respectively and for the I^-/I_3^- process alone at 25 mM in Figure S8.

Voltammetric Response of I_3^- in $[\text{C}_2\text{mim}][\text{NTf}_2]$. A solution of I_3^- was prepared in $[\text{C}_2\text{mim}][\text{NTf}_2]$ by mixing an equimolar amount of $[\text{C}_2\text{mim}]\text{I}$ with I_2 ; the cyclic voltammetric response of such a mixture on platinum is shown in Figure 2. As expected on the basis of the accepted mechanism (see eqs 3 and 4), starting from open circuit potential (OCP), I_3^- gives

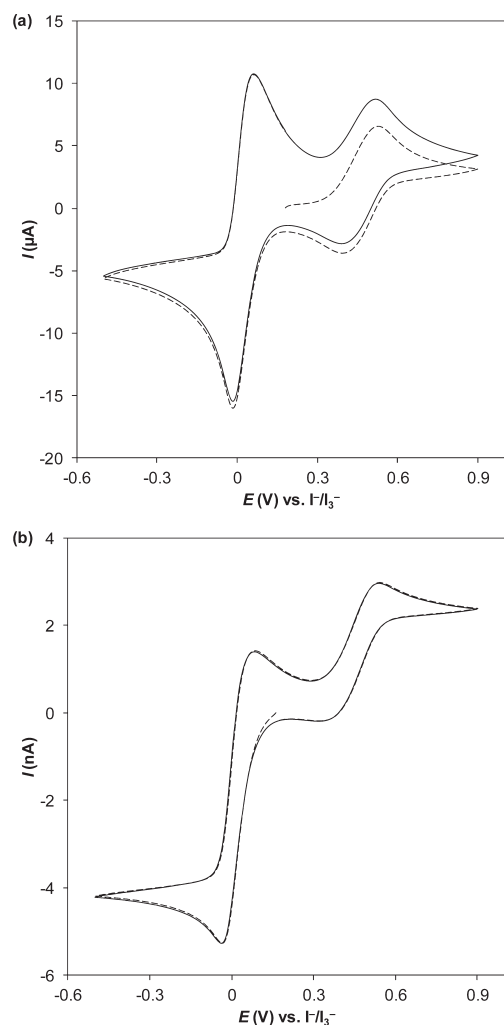


Figure 2. Cyclic voltammograms obtained from 10 mM $[\text{C}_2\text{mim}]\text{I}$ + 10 mM I_2 ($[\text{I}_3^-] = 10$ mM) in $[\text{C}_2\text{mim}][\text{NTf}_2]$ at a (a) 1.6 mm diameter Pt microdisk electrode and a (b) 20 μm diameter Pt microdisk electrode with a scan rate of 50 mV s^{-1} . First (---) and second (—) cycles are shown.

rise to two voltammetric waves: one oxidative and one reductive. The 2:1 reductive to oxidative current ratio of these processes (proportional to n) is evident from the cyclic voltammogram obtained at a Pt microdisk electrode, shown in Figure 2b. It is difficult to approach true steady-state conditions in this viscous electrolyte, and as a result, the contribution from both radial and planar diffusion is significant under the investigated conditions.³⁸ Only the reductive wave was investigated at elevated I_3^- concentrations because of the complications associated with the nucleation and growth of sparingly soluble I_2 on the electrode surface.^{16,25}

Cyclic voltammograms obtained from the reduction of 100 mM I_3^- at a Pt microdisk electrode with scan rates ranging from 10 to 750 mV s^{-1} are shown in Figure 3. As expected, the waveshape becomes less sigmoidal (near steady-state) and more peak-shaped (transient) at increasing scan rates. Also

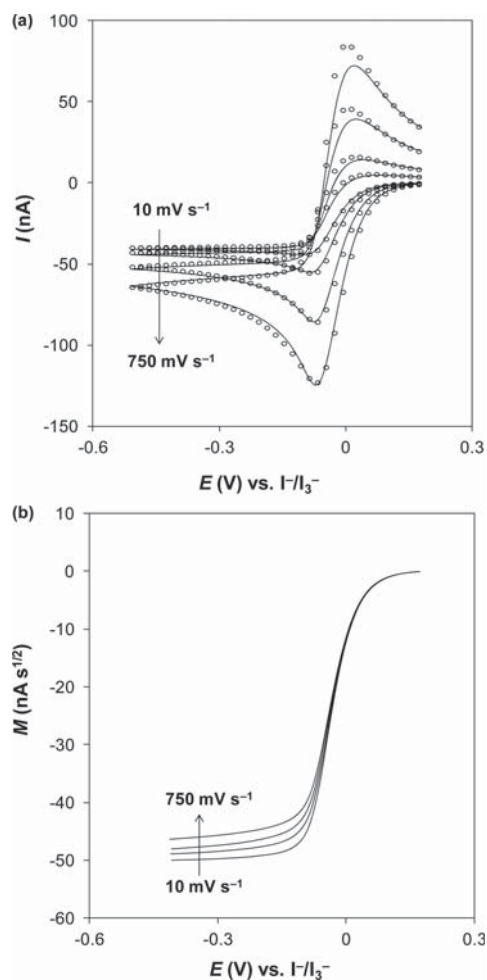


Figure 3. (a) Comparison of the simulated (O) and experimental (—) cyclic voltammograms for 100 mM $[\text{C}_2\text{mim}]\text{I}$ + 100 mM I_2 ($[\text{I}_3^-] = 100$ mM) in $[\text{C}_2\text{mim}][\text{NTf}_2]$ at a 20 μm diameter Pt microdisk electrode with scan rates of 750, 250, 50, and 10 mV s^{-1} . (b) Linear-sweep convolved current voltammograms obtained from the experimental data (negative potential scan) shown in part a. Simulation parameters are as provided in Table 1, except $k_s = 30$ cm s^{-1} and $D_{\Gamma} = 2.85 \times 10^{-7}$ $\text{cm}^2 \text{s}^{-1}$.

shown in the figure are simulations performed using the previously discussed termolecular mechanism; once again, there is good agreement between the experimental and simulated data, adding further confidence that the proposed model is valid in at least the phenomenological sense. The parameters used in the simulation were the same as those outlined in Table 1, except D_{Γ} was adjusted to 2.85×10^{-7} $\text{cm}^2 \text{s}^{-1}$, the value obtained in the presence of 100 mM I_3^- (*vide infra*). k_s also was increased to 30 cm s^{-1} , which can be justified on the basis that the $\Gamma/\text{I}_3^-/\text{I}_2$ processes are inner-sphere reactions,¹⁶ meaning that the heterogeneous electron-transfer kinetics are sensitive to the identity, purity, and surface-state (i.e., cleanliness, microstructure, and surface chemistry) of the electrode material.⁴⁴ Indeed, it was observed experimentally that the electron-transfer kinetics of the $\Gamma/\text{I}_3^-/\text{I}_2$ processes are strongly

influenced by the electrode preparation protocol, being most facile after polishing and electrochemical cleaning in aqueous sulfuric acid (Figure S9), and by the history of the electrode, with the kinetics becoming fastest in the first few voltammetric cycles performed after electrode preparation (Figure S10). Although the macrodisk electrode used in Figure 1 and the microdisk electrode used in Figure 3 are both made from platinum, their surface states may not be identical, as differences could readily arise during preparation (compare macrodisk vs microdisk protocols in the Experimental Section), accounting for the disparity in k_s . Additional simulations are included in the Supporting Information (see Figure S11) which demonstrate how varying k_s influences the shape of the resulting voltammogram.

In order to quantify the diffusivity of I_3^- , the voltammograms (I - E data) shown in Figure 3a were transformed using a convolutive technique;³⁸ the resulting convoluted current voltammograms (M - E data) are shown Figure 3b. Under purely diffusion-controlled conditions, the convoluted current (M) reaches its maximum or limiting value, M_L , which is independent of the voltammetric scan rate:

$$M_L = nAFC^b\sqrt{D} \quad (15)$$

At a scan rate of 10 mV s^{-1} , the M - E curve resembles a steady-state voltammogram, with a well-defined and flat M_L plateau. By substituting the appropriate values into eq 15, the diffusion coefficient of I_3^- was determined to be $4.3 \times 10^{-7} \text{ cm}^2 \text{ s}^{-1}$. Interestingly, despite the larger size of I_3^- compared to I^- , $D_{I_3^-}$ in this media is $\approx 60\%$ larger than D_{I^-} ; it is thought that this is the case because I_3^- possesses a more diffuse charge density than I^- , resulting in weaker interactions with the high ionic strength environment and therefore less hindered mass transport. Also shown in Figure 3b with an I_3^- concentration of $\approx 100 \text{ mM}$, the M_L plateau of the convoluted current voltammograms begins to decrease in size and become noticeably sloped at scan rates above 10 mV s^{-1} , suggesting that the I_3^- reduction process is subject to kinetic-control. This phenomenon can be explained by considering that the heterogeneous electron-transfer step is preceded by a chemical step; hence, I_3^- reduction is described by a CE mechanism:

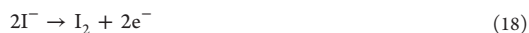


As the time scale of the experiment is decreased (achieved experimentally by increasing the voltammetric sweep rate), the kinetics of the chemical prestep shown in eq 16 become limiting and hence diffusion control can no longer be attained. It is also worth noting that this trend is predicted in the previously discussed model (mechanism shown in eqs 10 and 11); simulated convoluted-current voltammograms obtained at scan rates ranging from 1 mV s^{-1} to 100 V s^{-1} are shown in Figure S12.

In addition to the experimental time scale (i.e., the scan rate, ν), the delicate balance between kinetic and diffusion control is also dictated by the composition of the mixture (i.e., the total concentration and ratio of I^-/I_2) and the electrode geometry, as the enhanced mass transport to microdisk electrodes favors kinetic control. Achieving near steady-state conditions in even the most fluid RTILs imposes severe limitations on the voltammetric scan rate ($\nu \leq 5 \text{ mV s}^{-1}$) and electrode geometry ($r_0 \leq 5 \text{ }\mu\text{m}$) that can be used, as demonstrated in previous studies.^{16,21,22} Convolutive voltammetry on the other hand has

no such limitations, allowing the experimental time scale and mass-transport rate to the electrode to be easily controlled by changing ν and r_0 , respectively. In order to quantify the true diffusion coefficient of I_3^- , it is clear that diffusion control must be attained, and this can only be assured by performing a series of experiments over a range of scan rates. In light of this difficulty, we will not attempt to quantify $D_{I_3^-}$ over a range of experimental conditions, but investigate how D_{I^-} changes with solution composition in order to probe the enhanced mass-transport phenomenon reported in the literature (addressed below).

Voltammetry of Mixtures of I^- and I_3^- in $[C_2\text{mim}][\text{NTf}_2]$. Mixtures containing an excess of I^- over I_2 were prepared in $[C_2\text{mim}][\text{NTf}_2]$; I^- and I_3^- are assumed to be the two predominant species in solution. Cyclic voltammograms obtained from a 1:1 mixture of I^- and I_3^- at a Pt macrodisk electrode are shown in Figure 4. Starting from the OCP, and initially sweeping toward negative potentials (Figure 4a) results in the reduction of I_3^- to I^- , a CE mechanism (see eqs 13 and 14). Sweeping positively (Figure 4b) toward approximately $+0.3 \text{ V vs } I^-/I_3^-$ (i.e., between the two oxidative peaks) results in the oxidation of I^- to I_3^- , via an EC mechanism:



Sweeping toward more positive potentials past $+0.3 \text{ V vs } I^-/I_3^-$ results in the oxidation of I_3^- to I_2 , via another CE mechanism:



where I_3^- originates from both the bulk solution and the precursor I^- oxidation step (electrogenerated I_3^-). As shown in the second cycle of potential (Figure 4), two sets of peaks are observed overall, and the total current is proportional to $[I_3^-] + 1/3[I^-]$, in accordance with the electron stoichiometry of these two species.

Again, only the I^-/I_3^- process was able to be studied at elevated concentrations, due to complications with the nucleation and growth of sparingly soluble I_2 on the electrode surface. Cyclic voltammograms demonstrating the reduction of $\approx 20 \text{ mM } I_3^-$ in the presence of variable concentrations of I^- at a Pt microdisk electrode are shown in Figure 5. Increasing the concentration of I^- shifts the I_3^-/I^- reduction process toward more negative potentials, as previously observed for the oxidation of I^- (Figure 1b). This result is predicted from the model (given in eqs 10 and 11) and arises because increasing $[I^-]$ at a fixed $[I_2]$ (or vice versa) shifts the equilibrium reaction shown in eq 11 to the right (i.e., toward I_3^- formation), making it more difficult to reduce I_3^- , and thus the reductive process undergoes a shift toward more negative potentials.

Mass Transport of I^- in $[C_2\text{mim}][\text{NTf}_2]$. In a previous study,¹⁶ we reported that, in the absence of I_3^- , the diffusivity of I^- is constant up to a bulk concentration of at least 500 mM in $[C_2\text{mim}][\text{NTf}_2]$; using a steady-state technique, with a scan rate of 5 mV s^{-1} at a $2 \text{ }\mu\text{m}$ diameter Pt microdisk electrode, the diffusivity of I^- was found to be $2.59 (\pm 0.04) \times 10^{-7} \text{ cm}^2 \text{ s}^{-1}$. That study is expanded upon here with near steady-state voltammograms obtained from the electro-oxidation of I^- on a Pt microdisk electrode at a range of scan rates shown in Figure 6a. As expected, at increasingly positive potentials, there are two near-sigmoidal shaped waves exhibiting a 2:1 current ratio,

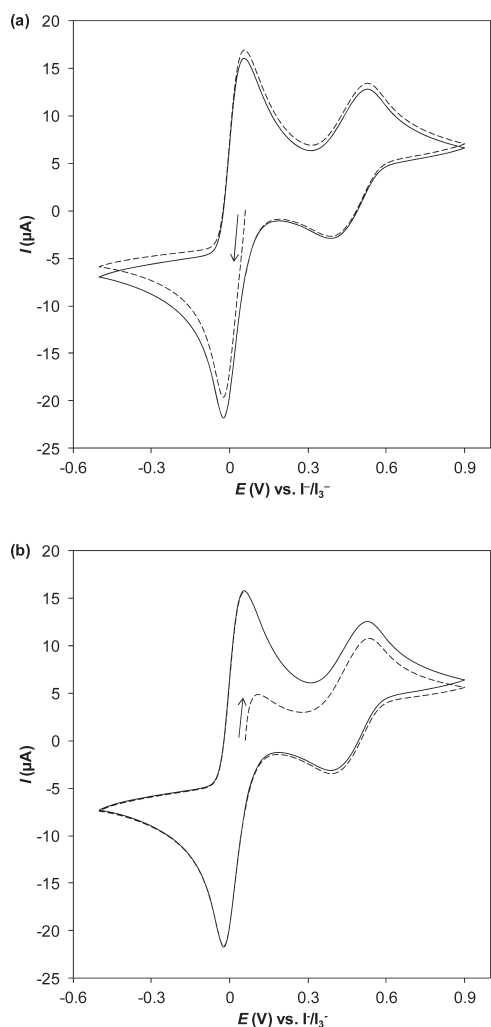


Figure 4. Cyclic voltammograms obtained from 22 mM $[\text{C}_2\text{mim}]\text{I}$ + 11 mM I_3^- (i.e., $[\text{I}^-] = 11$ mM and $[\text{I}_3^-] = 11$ mM) in $[\text{C}_2\text{mim}][\text{NTf}_2]$ at a 1.6 mm diameter Pt macrodisk electrode with a scan rate of 50 mV s^{-1} . The sweep direction was initially toward (a) negative and (b) positive potentials starting from the open circuit potential. First (---) and second (—) cycles are shown.

corresponding to the I^-/I_3^- and I_3^-/I_2 processes described by eqs 3 and 4, respectively. Also depicted are results of simulations obtained using the mechanism given in eqs 10 and 11 and the simulation parameters summarized in Table 1, with k_s adjusted as per the previous discussion. Once again, there is excellent agreement between the experimental and simulated data. $M-E$ curves obtained by convolutive transformation of the $I-E$ data are shown in Figure 6b; the M_L plateaux of these curves are independent of scan rate, indicating that the process is diffusion-controlled. The diffusion coefficient of I^- is readily calculable from the I^-/I_3^- ($n = 2/3$) or the I_3^-/I_2 plateau ($n = 1$). In either case, D_{I^-} was determined to be $2.62 \times 10^{-7} \text{ cm}^2 \text{ s}^{-1}$ by substituting the appropriate values into eq 15, in excellent agreement with our previous study.¹⁶ Unlike I_3^- oxidation or reduction (both CE processes), the I^- oxidation

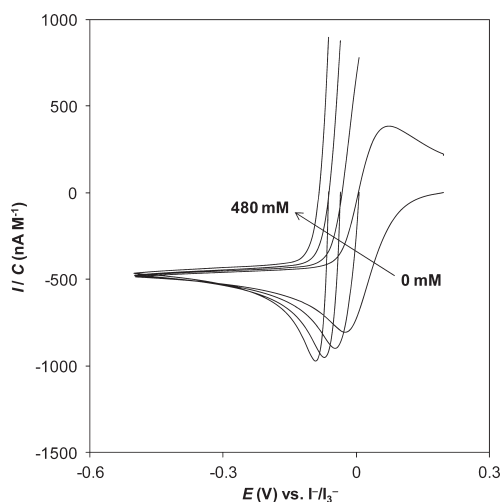


Figure 5. Concentration-normalized cyclic voltammograms obtained at a 20 μm diameter Pt microdisk electrode with a scan rate of 250 mV s^{-1} from the reduction of ≈ 20 mM I_3^- in the presence of (from right to left) 0, 80, 230, and 480 mM $[\text{C}_2\text{mim}]\text{I}$ in $[\text{C}_2\text{mim}][\text{NTf}_2]$.

process is not preceded by a chemical step and therefore is not subject to kinetic limitations. Accordingly, I^- is the ideal species to investigate the Grotthuss-like extension of diffusion in this system.

A series of solutions containing 10–500 mM I^-/I_3^- with $[\text{I}^-]:[\text{I}_3^-]$ ratios ranging from 5:1 to 1:2 were prepared and characterized voltammetrically (see Figures 4 and 5 as examples). The diffusivity of I^- in each of the mixtures was quantified using a chronoamperometric technique: the potential was stepped from the OCP to a value ≈ 120 mV positive of the I^-/I_3^- oxidation peak ($n = 2/3$) and the resulting diffusion-controlled $I-t$ curve was fitted using the Shoup–Szabo approximation (eqs 7–9).³⁹ Chronoamperograms obtained from 1:1 $[\text{I}^-]:[\text{I}_3^-]$ mixtures in $[\text{C}_2\text{mim}][\text{NTf}_2]$ at a Pt microdisk electrode are shown in Figure 7a. As can be seen in the figure, the Shoup–Szabo fits are excellent at all of the investigated concentrations ($R^2 > 0.999$). The diffusivity of I^- increased with the total concentration (i.e., $[\text{I}^-] + [\text{I}_3^-]$), evident from the trend in the concentration-normalized chronoamperograms shown in Figure 7b. The enhancement in the concentration-normalized current with total concentration was not observed in the simulated data (Figure S13), meaning it is not inherent to the iodide oxidation mechanism and therefore results from a genuine increase in the diffusivity of I^- . Although a similar enhancement in the I_3^- reduction current was observed experimentally (shown in Figure S14), no attempt was made to quantify the increase in $D_{\text{I}_3^-}$, due to the previously discussed difficulties in ensuring diffusion-controlled conditions.

Shown in Figure 8a is a plot of D_{I^-} vs $[\text{I}^-]$. In all instances, except when I_3^- is absent from the bulk solution (i.e., the 1:0 ratio), D_{I^-} was found to increase with concentration. All curves are approximately linear and intercept the D -axis at $\approx 2.6 \times 10^{-7} \text{ cm}^2 \text{ s}^{-1}$, the diffusion coefficient of I^- in the absence of I_3^- . The slopes of the D_{I^-} vs $[\text{I}^-]$ plots depend on the ratio of $[\text{I}^-]:[\text{I}_3^-]$, with greater enhancements occurring at high concentrations when $[\text{I}^-]$ and $[\text{I}_3^-]$ are comparable, in qualitative agreement

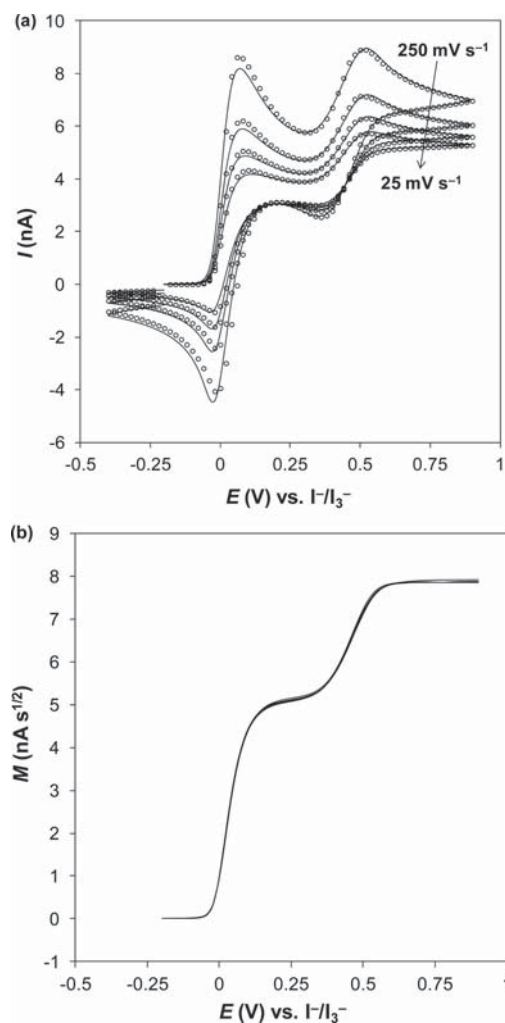


Figure 6. (a) Comparison of simulated (○) and experimental (—) cyclic voltammograms obtained from 40 mM $[\text{C}_2\text{mim}]\text{I}$ in $[\text{C}_2\text{mim}][\text{NTf}_2]$ at a $20\ \mu\text{m}$ diameter Pt microdisk electrode with scan rates of (from top to bottom) 250, 100, 50, and $25\ \text{mV s}^{-1}$. (b) Linear-sweep convolved current voltammograms obtained from the experimental data (positive potential scan) shown in part a. Simulation parameters are the same as in Table 1, except $k_s = 8\ \text{cm s}^{-1}$.

with the studies by Kawano and Watanabe.^{21,22} Intriguingly, when D_{I^-} is plotted against $[\text{I}_3^-]$, all curves possess a similar gradient and intercept (shown in Figure 8b); these results indicate that the diffusion coefficient of I^- is directly proportional to the concentration of I_3^- present, regardless of the ratio. The largest value for D_{I^-} , $3.92 \times 10^{-7}\ \text{cm}^2\ \text{s}^{-1}$, derived from a mixture containing $\approx 250\ \text{mM}\ \text{I}^-$ and $\approx 500\ \text{mM}\ \text{I}_3^-$, is significantly larger than that obtained in the absence of I_3^- , $2.62 \times 10^{-7}\ \text{cm}^2\ \text{s}^{-1}$ (see Figure 8a), corresponding to a $\approx 50\%$ enhancement in diffusivity. The enhancement in diffusivity is not attributable to a decrease in the viscosity, demonstrated by the fact that the $\approx 250\ \text{mM}\ \text{I}^-$ and $\approx 500\ \text{mM}\ \text{I}_3^-$ mixture discussed above possesses a viscosity of (35.0 mPa·s) comparable to that of the neat RTIL (31.6 mPa·s) at $25\ ^\circ\text{C}$.

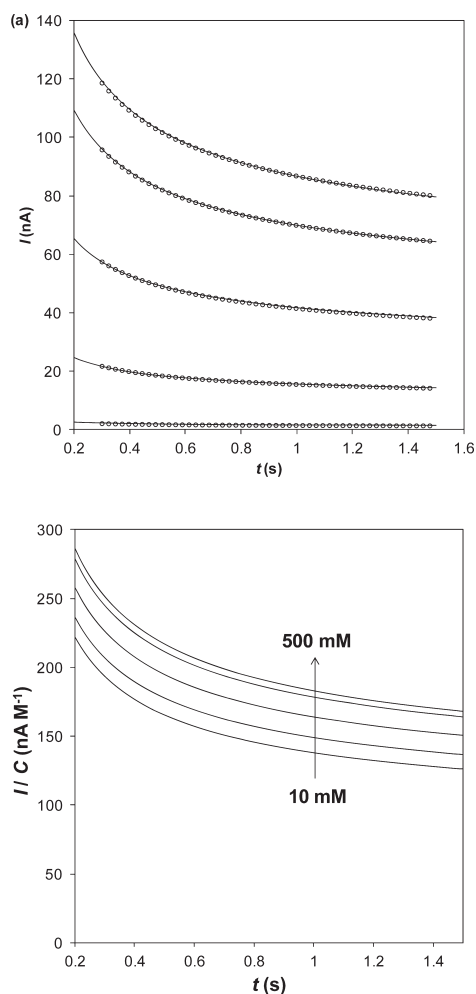


Figure 7. (a) Experimental (—) and Shoup–Szabo theoretical chronoamperograms (○) and (b) concentration-normalized chronoamperograms obtained from the diffusion-controlled oxidation of I^- to I_3^- as per eq 3 ($n = 2/3$), in a 1:1 mixture of I^- and I_3^- in $[\text{C}_2\text{mim}][\text{NTf}_2]$ at a $20\ \mu\text{m}$ diameter Pt microdisk electrode. The bulk concentrations of I^- and I_3^- are (from top to bottom) 500, 375, 250, 100, and 10 mM.

The accelerated mass transport is therefore non-Stokesian (i.e., does not obey the Stokes–Einstein equation) in origin and is attributable to electron-hopping and/or Grotthuss-type exchange between I^- and I_3^- , facilitated by the high ionic strength environment of RTILs.^{21,22,27–30}

Deviation from the Stokes–Einstein equation was first reported by Grotthuss⁴⁵ to explain the high mobility of protons in water and is thought to be facilitated by a bimolecular exchange reaction of the type:



where X is an atom, radical, ion, molecule, or electron that can be exchanged between A/A* and the asterisks serve only to distinguish between the two molecules.⁴⁶ In the above reaction scheme, AX (i.e., I_3^-) and A* (i.e., I^-) are transported

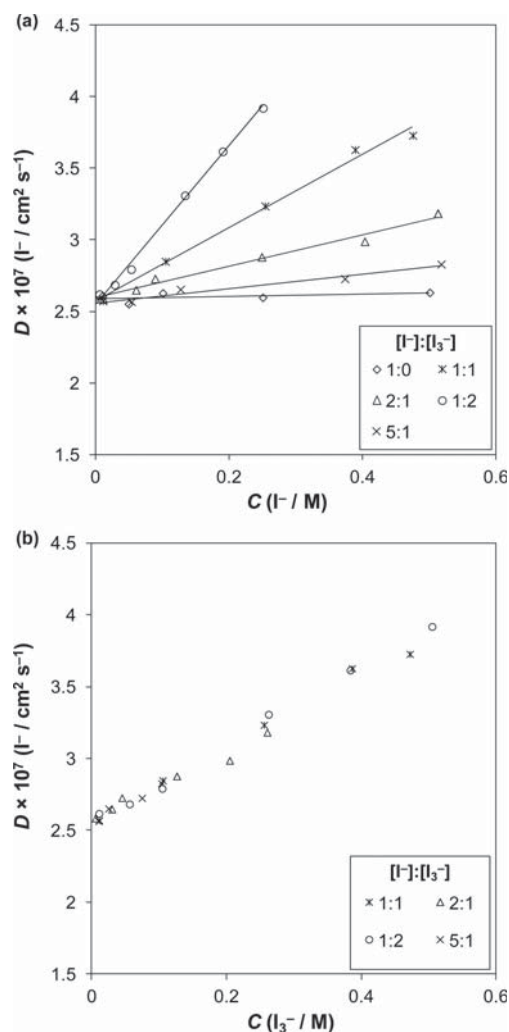


Figure 8. Plots of the diffusion coefficient of I^- calculated by fitting of chronoamperometric transients with the Shoup–Szabo equation vs (a) the bulk concentration of I^- and (b) the bulk concentration of I_3^- . Trend lines are included in part a to guide the reader's eye.

(displaced) a well-defined distance, governed by the physical size of A and AX, and because the exchange process is favored in the direction of any existing chemical potential gradients, this additional transport mechanism is additive with physical mass-transport processes, enhancing the flux of the species involved.⁴⁶ Enhanced mass-transfer via an electron hopping or bond-exchange mechanism is predicted to occur in media containing both the reduced and oxidized forms of an electroactive species (i.e., $\text{Fe}^{2+}/\text{Fe}^{3+}$ or I^-/I_3^-), as described in the original work by Dahms⁴⁷ and Ruff et al.^{46,48}

If the reaction shown in eq 11 is not limiting so the process is at equilibrium on the voltammetric time scale, the relationship in eq 23 is expected to hold (as per the Dahms–Ruff equation; see eq 6):^{46,47,49}

$$D_{\text{I}^-} \propto k_{\text{ex}}([\text{I}^-] + [\text{I}_3^-]) \quad (23)$$

On this basis, it is expected that the diffusivity of iodide is proportional to the sum of the concentrations of the redox species participating in the exchange reaction (see eq 5): I^- and I_3^- . One consequence of this relationship is that the exchange reaction mediated enhancement in diffusion would be possible in a system which only contains a single component dissolved in the bulk solution (i.e., I^- in the absence of I_3^- or vice versa), where the other component is electrogenerated during the voltammetric perturbation, leading to a concentration dependent diffusion coefficient (i.e. $D_{\text{I}^-} \propto [\text{I}^-]$). On the other hand, if the reaction in eq 11 is limiting, a pseudo-first-order condition may be assumed to give the following relationship:^{36,46,47}

$$D_{\text{I}^-} \propto k_{\text{ex}}[\text{I}_3^-] \quad (24)$$

In other words, the diffusivity of iodide is proportional to only the concentration of the other redox species participating in the exchange reaction, I_3^- , and no enhancement is possible when only a single component is present prior to the voltammetric perturbation, as observed experimentally. Although it has been established that the equilibrium reaction shown in eq 11 is rapid, at all potentials apart from those in the vicinity of $E^{\circ'}$, the concentration of one of I^- or I_2 will be orders-of-magnitude higher than that of the other (i.e., during I^- oxidation, $[\text{I}^-]_{\text{surface}} \approx 0 \text{ M}$, so $[\text{I}_2]_{\text{surface}} \gg [\text{I}^-]_{\text{surface}}$), which limits the rate of I_3^- formation, despite the large value of k_{f} . As a result, any I_3^- generated at the electrode surface during I^- oxidation in a single component system (i.e., only I^- present) is insufficient to facilitate the exchange reaction to any appreciable extent (therefore, D_{I^-} is independent of $[\text{I}^-]_{\text{bulk}}$) and in a dual component system (i.e., both I^- and I_3^- present) is insignificant compared to the concentration present in bulk solution (therefore, D_{I^-} is only dependent upon $[\text{I}_3^-]_{\text{bulk}}$). An equivalent situation is expected for the diffusivity of I_3^- (i.e., $D_{\text{I}_3^-} \propto [\text{I}^-]_{\text{bulk}}$), although, in this case it is difficult to confirm this experimentally for the previously discussed reasons.

If a pseudo-first-order condition is assumed (previously addressed), from the Dahms–Ruff equation^{12,14} (shown in eq 6), a plot of D_{I^-} vs $[\text{I}_3^-]$ is predicted to be linear:

$$D_{\text{I}^-} = D_{\text{phys}} + \frac{k_{\text{ex}}\delta^2}{6}[\text{I}_3^-] \quad (25)$$

The physical diffusion coefficient of iodide (D_{phys}) can therefore be determined from the D -intercept (see above) and the bimolecular exchange rate constant, k_{ex} , can be estimated from the slope if the center-to-center intersite distance at the time of the exchange reaction, δ , is known. From the mean slope of the curves shown in Figure 8b, $2.5 \times 10^{-7} \text{ cm}^2 \text{ s}^{-1} \text{ M}^{-1}$, and assuming $\delta = 9.3 \times 10^{-8} \text{ cm}$,³⁶ k_{ex} is estimated to be $\approx 2 \times 10^8 \text{ M}^{-1} \text{ s}^{-1}$. If we assume that the diffusion-controlled rate constant for the exchange reaction between I^- and I_3^- is described by the steady-state Smoluchowski equation,³⁶ $k_{\text{ex,lim}}$ can be calculated using the following expression:⁵⁰

$$k_{\text{ex,lim}} = \frac{4\pi(D_{\text{I}^-} + D_{\text{I}_3^-})\delta N_{\text{A}}}{1000} \quad (26)$$

where N_{A} is the Avogadro constant. Substituting the following into eq 26, $D_{\text{I}^-} = 2.6 \times 10^{-7} \text{ cm}^2 \text{ s}^{-1}$, $D_{\text{I}_3^-} = 4.3 \times 10^{-7} \text{ cm}^2 \text{ s}^{-1}$, and $\delta = 9.3 \times 10^{-8} \text{ cm}$, $k_{\text{ex,lim}}$ is estimated to be $\approx 5 \times 10^8 \text{ M}^{-1} \text{ s}^{-1}$, the same order of magnitude as the value of k_{ex} estimated from the experimental data, suggesting the at the exchange reaction between I^- and I_3^- is diffusion controlled.

When the Γ^-/I_3^- couple is employed as the redox shuttle in a DSSC electrolyte, Γ^- is always present in a large excess, because I_3^- is (a) corrosive; (b) a strong chromophore and; (c) an electron acceptor (recombination with electrons in the TiO_2 photoanode decreases efficiency). Under these circumstances, it follows that I_3^- is the diffusion limiting species in an operational DSSC and, therefore, the value of $D_{I_3^-}$ is of the utmost importance in any electrolyte formulation. Unfortunately, $D_{I_3^-}$ has not been quantified due to the difficulties highlighted above. However, it is likely that I_3^- undergoes a similar diffusivity enhancement in the presence of excess Γ^- due to the nature of the exchange reaction shown in eq 5. Thus, one might expect that maximizing the concentration of Γ^- in an RTIL electrolyte would translate to the largest $D_{I_3^-}$ value (and thus the best DSSC performance). In reality it is not this simple, as increasing the concentration of Γ^- also increases the viscosity of the electrolyte, thereby hindering physical mass transport. Varying the ratio between the redox active (i.e., $[C_2mim]I$) and redox inactive (i.e., $[C_2mim][NTf_2]$) components of a RTIL mixture to maximize the contributions from both exchange-reaction-based mass transport and physical mass transport is therefore a key factor in achieving optimum electrolyte performance in a DSSC.

CONCLUSIONS

The voltammetric behavior of the iodide/triiodide couple has been investigated in detail in the room temperature ionic liquid 1-ethyl-3-methylimidazolium bis(trifluoromethanesulfonyl)imide. As observed in the molecular solvent acetonitrile, two processes with a relative electron stoichiometry of 2:1 are observed at a platinum electrode, which are assigned to the Γ^-/I_3^- and I_3^-/I_2 processes at lower and higher potentials, respectively. The electro-oxidation of iodide on a platinum macro- and microdisk electrode was simulated, and the apparent stability constant of triiodide in this ionic liquid medium, estimated from experiment–simulation comparisons, was found to be comparable to that previously reported in acetonitrile. The electroreduction of triiodide to iodide, a CE mechanism, was successfully modeled using the proposed mechanism and was found to be kinetically controlled at typical voltammetric time scales, thereby making it difficult to quantify the diffusivity of triiodide in this ionic liquid medium. The electro-oxidation of iodide to triiodide, an EC mechanism, was found to be diffusion controlled at sufficiently positive potentials, and the diffusivity of iodide was quantified in the presence of variable mole ratios of triiodide over a large concentration range using a chronoamperometric technique. The diffusivity of iodide was found to be directly proportional to the concentration of triiodide present, showing up to a $\approx 50\%$ enhancement under the conditions investigated. This (non-Stokesian) enhancement in mass transport was attributed to electron-hopping and/or a Grotthus-type exchange reaction between iodide and triiodide.

ASSOCIATED CONTENT

Supporting Information

Near steady-state voltammogram of iodine (Figure S1), simulated cyclic voltammograms demonstrating the influence of k_f (Figure S2) and K_{eq} (Figure S3), simulation–experiment comparison for the electro-oxidation of iodide in acetonitrile (Figure S4 and Table S1), additional simulation–experiment comparisons at iodide concentrations ranging from 4 to 40 mM

in $[C_2mim][NTf_2]$ (Figures S5–S8), cyclic voltammograms highlighting the importance of the electrode preparation protocol (Figures S9 and S11), simulated convoluted current voltammograms carried out for the electroreduction of triiodide at scan rates ranging from 1 mV s^{-1} to 100 V s^{-1} (Figure S12), simulated chronoamperograms carried out for the diffusion controlled oxidation of iodide in the presence of 5–500 mM triiodide (Figure S13), and experimental chronoamperograms obtained from the reduction of triiodide (Figure S14). This material is available free of charge via the Internet at <http://pubs.acs.org>.

AUTHOR INFORMATION

Corresponding Authors

[REDACTED]

Notes

The authors declare no competing financial interest.

REFERENCES

- Wilkes, J. S. A Short History of Ionic Liquids—From Molten Salts to Neoteric Solvents. *Green Chem.* **2002**, *4*, 73–80.
- Armand, M.; Endres, F.; MacFarlane, D. R.; Ohno, H.; Scrosati, B. Ionic-Liquid Materials for the Electrochemical Challenges of the Future. *Nat. Mater.* **2009**, *8*, 621–629.
- Galinski, M.; Lewandowski, A.; Stepniak, I. Ionic Liquids as Electrolytes. *Electrochim. Acta* **2006**, *51*, 5567–5580.
- Papageorgiou, N.; Athanassov, Y.; Armand, M.; Bonhote, P.; Pettersson, H.; Azam, A.; Grätzel, M. The Performance and Stability of Ambient Temperature Molten Salts for Solar Cell Applications. *J. Electrochem. Soc.* **1996**, *143*, 3099–3108.
- Hagfeldt, A.; Boschloo, G.; Sun, L. C.; Kloo, L.; Pettersson, H. Dye-Sensitized Solar Cells. *Chem. Rev.* **2010**, *110*, 6595–6663.
- Howlett, P. C.; MacFarlane, D. R.; Hollenkamp, A. F. High Lithium Metal Cycling Efficiency in a Room-Temperature Ionic Liquid. *Electrochem. Solid State Lett.* **2004**, *7*, A97–A101.
- de Souza, R. F.; Padilha, J. C.; Goncalves, R. S.; Dupont, J. Room Temperature Dialkylimidazolium Ionic Liquid-based Fuel Cells. *Electrochem. Commun.* **2003**, *5*, 728–731.
- Balducci, A.; Dugas, R.; Taberna, P. L.; Simon, P.; Plee, D.; Mastragostino, M.; Passerini, S. High Temperature Carbon-carbon Supercapacitor using Ionic Liquid as Electrolyte. *J. Power Sources* **2007**, *165*, 922–927.
- O'Regan, B.; Grätzel, M. A Low-cost, High-efficiency Solar-cell Based on Dye-sensitized Colloidal TiO_2 Films. *Nature* **1991**, *353*, 737–740.
- Wang, P.; Zakeeruddin, S. M.; Moser, J. E.; Humphry-Baker, R.; Grätzel, M. A Solvent-free, $SeCN^-(SeCN)(3)^{-}$ Based Ionic Liquid Electrolyte for High-efficiency Dye-sensitized Nanocrystalline Solar Cells. *J. Am. Chem. Soc.* **2004**, *126*, 7164–7165.
- Bentley, C. L.; Bond, A. M.; Hollenkamp, A. F.; Mahon, P. J.; Zhang, J. Unexpected Complexity in the Electro-Oxidation of Iodide on Gold in the Ionic Liquid 1-ethyl-3-methylimidazolium Bis-(trifluoromethanesulfonyl)imide. *Anal. Chem.* **2013**, *85*, 11319–11325.
- Guo, T.; Li, L. D.; Cammarata, V.; Illies, A. Electrochemical/electrospray Mass Spectrometric Studies of I- and SCN^- at Gold and Platinum Electrodes: Direct Detection of $(SCN)(3)^{-}$. *J. Phys. Chem. B* **2005**, *109*, 7821–7825.
- Bond, A. M. *Modern Polarographic Methods in Analytical Chemistry*; M. Dekker: New York, 1980.
- Matsui, Y.; Kurosaki, Y.; Date, Y. Polarography of Halides in Dimethylformamide 0.2. Iodide Ion, Triiodomercurate Ion, and Mercuric Iodide. *Bull. Chem. Soc. Jpn.* **1970**, *43*, 1707–1714.
- Bard, A. J.; Faulkner, L. R. *Electrochemical methods: Fundamentals and Applications*, 2nd ed.; Wiley: New York, 2001.
- Bentley, C. L.; Bond, A. M.; Hollenkamp, A. F.; Mahon, P. J.; Zhang, J. Concentration and Electrode Material Dependence of the

Voltammetric Response of Iodide on Platinum, Glassy Carbon and Boron-doped Diamond in the Room Temperature Ionic Liquid 1-ethyl-3-methylimidazolium Bis(Trifluoromethanesulfonyl)Imide. *Electrochim. Acta* **2013**, *109*, 554–561.

(17) Guidelli, R.; Piccardi, G. The Dissociation Constant of I_3^- in the Voltammetric Behaviour of the Iodine-iodide Couple. *Electrochim. Acta* **1967**, *12*, 1085–1095.

(18) Iwamoto, R. T. Solvent Effects on the Electro-oxidation of Iodide Ion. *Anal. Chem.* **1959**, *31*, 955–955.

(19) Gebert, E. Solvent Effects in the Iodide Iodine Triiodide Complex Equilibrium. *J. Am. Chem. Soc.* **1954**, *76*, 2049–2054.

(20) Popov, A. I.; Rygg, R. H.; Skelly, N. E. Studies on the Chemistry of Halogens and of Polyhalides 0.9. Electrical Conductance Study of Higher Polyiodide Complex Ions in Acetonitrile Solutions. *J. Am. Chem. Soc.* **1956**, *78*, 5740–5744.

(21) Kawano, R.; Watanabe, M. Equilibrium Potentials and Charge Transport of an I⁻/I₃⁻ Redox Couple in an Ionic Liquid. *Chem. Commun.* **2003**, 330–331.

(22) Kawano, R.; Watanabe, M. Anomaly of Charge Transport of an Iodide/tri-iodide Redox Couple in an Ionic Liquid and Its Importance in Dye-sensitized Solar Cells. *Chem. Commun.* **2005**, 2107–2109.

(23) Ejigu, A.; Lovelock, K. R. J.; Licence, P.; Walsh, D. A. Iodide/triiodide Electrochemistry in Ionic Liquids: Effect of Viscosity on Mass Transport, Voltammetry and Scanning Electrochemical Microscopy. *Electrochim. Acta* **2011**, *56*, 10313–10320.

(24) Zhang, Y.; Zheng, J. B. Investigation on the Electro-oxidation of Iodide in the Room Temperature Ionic Liquid, 1-butyl-3-methylimidazolium Tetrafluoroborate at Platinum Electrode. *Electrochim. Acta* **2007**, *52*, 4082–4086.

(25) Silvester, D. S.; Aldous, L.; Hardacre, C.; Compton, R. G. Electrooxidation of the Iodides [C₄mim]I, LiI, NaI, KI, RbI, and CsI in the Room Temperature Ionic Liquid [C₄mim][NTf₂]. *J. Phys. Chem. C* **2008**, *112*, 6551–6557.

(26) Rogers, E. I.; Streeter, I.; Aldous, L.; Hardacre, C.; Compton, R. G. Electrode Kinetics and Mechanism of Iodine Reduction in the Room-temperature Ionic Liquid C(4)mim NTf₂. *J. Phys. Chem. C* **2008**, *112*, 10976–10981.

(27) Wachter, P.; Schreiner, C.; Zistler, M.; Gerhard, D.; Wasserscheid, P.; Gores, H. J. A Microelectrode Study of Triiodide Diffusion Coefficients in Mixtures of Room Temperature Ionic Liquids, Useful for Dye-sensitized Solar Cells. *Microchim. Acta* **2008**, *160*, 125–133.

(28) Wachter, P.; Zistler, M.; Schreiner, C.; Fleischmann, M.; Gerhard, D.; Wasserscheid, P.; Barthel, J.; Gores, H. J. Temperature Dependence of the Non-Stokesian Charge Transport in Binary Blends of Ionic Liquids. *J. Chem. Eng. Data* **2009**, *54*, 491–497.

(29) Zistler, M.; Schreiner, C.; Wachter, P.; Wasserscheid, P.; Gerhard, D.; Gores, H. J. Electrochemical Characterization of 1-ethyl-3-methylimidazolium Thiocyanate and Measurement of Triiodide Diffusion Coefficients in Blends of Two Ionic Liquids. *Int. J. Electrochem. Sci.* **2008**, *3*, 236–245.

(30) Zistler, M.; Wachter, P.; Schreiner, C.; Gores, H. J. Electrochemical Measurement of Triiodide Diffusion Coefficients in Blends of Ionic Liquids Results for Improving a Critical Parameter of Dye-sensitized Solar Cells. *J. Mol. Liq.* **2010**, *156*, 52–57.

(31) Atkins, P. W.; De Paula, J. *Atkins' Physical chemistry*, 9th ed.; Oxford University Press: Oxford, 2010.

(32) Zistler, M.; Wachter, P.; Wasserscheid, P.; Gerhard, D.; Hinsch, A.; Sastrawan, R.; Gores, H. J. Comparison of Electrochemical Methods for Triiodide Diffusion Coefficient Measurements and Observation of Non-Stokesian Diffusion Behaviour in Binary Mixtures of Two Ionic Liquids. *Electrochim. Acta* **2006**, *52*, 161–169.

(33) Genser, E. E.; Connick, R. E. Exchange of Iodide Ion with Triiodide Ion Studied by Nuclear Magnetic Resonance. *J. Chem. Phys.* **1973**, *58*, 990–996.

(34) Ruff, I.; Friedrich, J.; Csillag, K. Transfer Diffusion. III. Kinetics and Mechanism of Triiodide-Iodide Exchange-Reaction. *J. Phys. Chem.* **1972**, *76*, 162–165.

(35) Kawano, R.; Matsui, H.; Matsuyama, C.; Sato, A.; Susan, M.; Tanabe, N.; Watanabe, M. High Performance Dye-Sensitized Solar Cells Using Ionic Liquids as Their Electrolytes. *J. Photochem. Photobiol., A: Chem.* **2004**, *164*, 87–92.

(36) Thorsmolle, V. K.; Rothenberger, G.; Topgaard, D.; Brauer, J. C.; Kuang, D. B.; Zakeeruddin, S. M.; Lindman, B.; Grätzel, M.; Moser, J. E. Extraordinarily Efficient Conduction in a Redox-Active Ionic Liquid. *ChemPhysChem* **2011**, *12*, 145–149.

(37) Swain, G. M., Solid Electrode Materials: Pretreatment and Activation. In *Handbook of Electrochemistry*, 1st ed.; Zoski, C. G., Ed.; Elsevier: Amsterdam, 2007; Chapter 5, pp 111–153.

(38) Bentley, C. L.; Bond, A. M.; Hollenkamp, A. F.; Mahon, P. J.; Zhang, J. Applications of Convolution Voltammetry in Electro-analytical Chemistry. *Anal. Chem.* **2014**, *86*, 2073–2081.

(39) Shoup, D.; Szabo, A. Chronoamperometric Current at Finite Disk Electrodes. *J. Electroanal. Chem.* **1982**, *140*, 237–245.

(40) Macagno, V. A.; Giordano, M. C.; Arvia, A. J. Kinetics and Mechanisms of Electrochemical Reactions on Platinum with Solutions of Iodine-Sodium Iodide in Acetonitrile. *Electrochim. Acta* **1969**, *14*, 335–357.

(41) Hubbard, A. T. Electrochemistry of Chemisorbed Molecules. III. Determination of the Oxidation State of Halides Chemisorbed on Platinum. Reactivity and Catalytic Properties of Adsorbed Species. *J. Phys. Chem.* **1975**, *79*, 808–815.

(42) Mebrahtu, T.; Rodriguez, J. F.; Bravo, B. G.; Soriaga, M. P. Hydrogenative/Cathodic Stripping of Iodine Chemisorbed on Smooth Polycrystalline Platinum Electrodes. *J. Electroanal. Chem.* **1987**, *219*, 327–333.

(43) Bravo, B. G.; Mebrahtu, T.; Rodriguez, J. F.; Soriaga, M. P. Electroactivity of Strongly-Absorbed Redox Centers: Reduction of Iodine Chemisorbed on Platinum in Aprotic Solvent. *J. Electroanal. Chem.* **1987**, *221*, 281–287.

(44) Zhang, J.; Zhang, L.; Liu, H.; Sun, A.; Liu, R.-S. *Electrochemical Technologies for Energy Storage and Conversion*, 1st ed.; Wiley-VCH: Weinheim, 2011.

(45) Grotthus, C. J. T. Sur la décomposition de l'eau et des corps qu'elle tient en dissolution à l'aide de l'électricité galvanique. *Ann. Chim.* **1806**, *58*, 54–54.

(46) Ruff, I.; Friedrich, V. J. Transfer Diffusion. I. Theoretical. *J. Phys. Chem.* **1971**, *75*, 3297–3302.

(47) Dahms, H. Electronic Conduction in Aqueous Solution. *J. Phys. Chem.* **1968**, *72*, 362–364.

(48) Ruff, I. Transfer Diffusion. II. Kinetics of Electron Exchange Reaction Between Ferrocene and Ferricinium Ion in Alcohols. *J. Phys. Chem.* **1971**, *75*, 3303–3309.

(49) Andrieux, C. P.; Savéant, J. M. Electron-Transfer Through Redox Polymer-Films. *J. Electroanal. Chem.* **1980**, *111*, 377–381.

(50) Solangi, A.; Bond, A. M.; Bugar, I.; Hollenkamp, A. F.; Horne, M. D.; Rütger, T.; Zhao, C. Comparison of Diffusivity Data Derived from Electrochemical and NMR Investigations of the SeCN(−)/(SeCN)(2)/(SeCN)(3)(−) System in Ionic Liquids. *J. Phys. Chem. B* **2011**, *115*, 6843–6852.

Supporting information for

Electrode reaction and mass transport mechanisms
associated with the iodide/triiodide couple in the
ionic liquid 1-ethyl-3-methylimidazolium
bis(trifluoromethanesulfonyl)imide

*Cameron L. Bentley,^{†,‡} Alan M. Bond,[†] Anthony F. Hollenkamp,[‡] Peter J. Mahon[§] and Jie
Zhang[†]*

[†]School of Chemistry, Monash University, Clayton, Vic 3800, Australia

[‡]CSIRO Energy Flagship, Box 312, Clayton South, Vic 3169, Australia

[§]Faculty of Science, Engineering and Technology, Swinburne University of Technology,
Hawthorn, Vic 3122, Australia

Keywords: Γ/I_3^- process; convolution voltammetry; cyclic voltammetry; chronoamperometry;
non-Stokesian mass transport

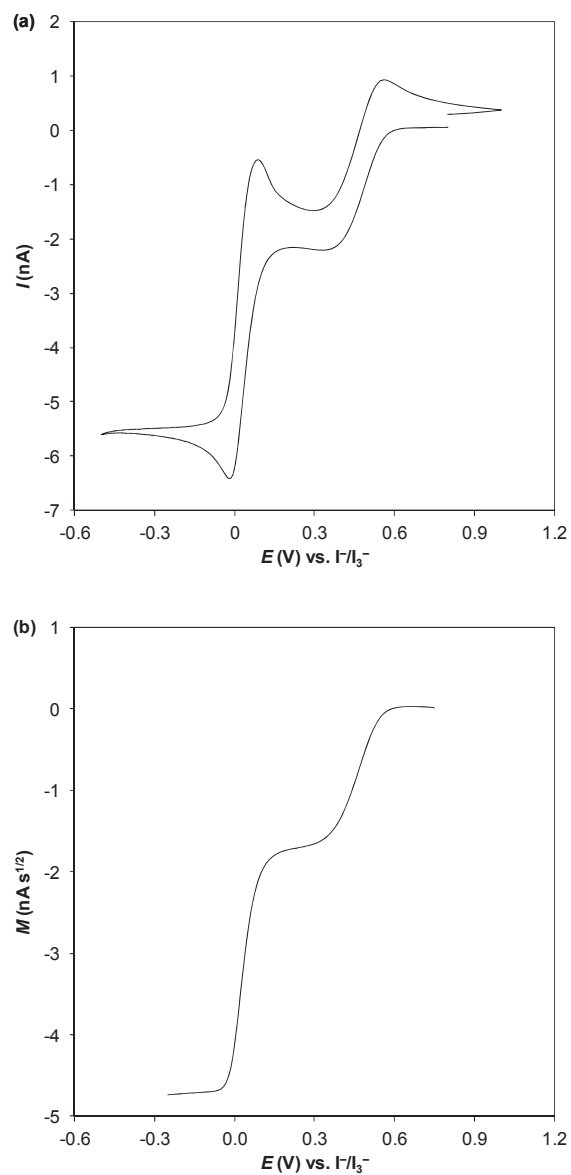


Figure S1. Cyclic (a) and linear sweep convolved current (b) voltammogram obtained from 7.3 mM I_2 in $[\text{C}_2\text{mim}][\text{NTf}_2]$ at a 20 μm dia. Pt microdisk electrode with a scan rate of 50 mV s^{-1} .

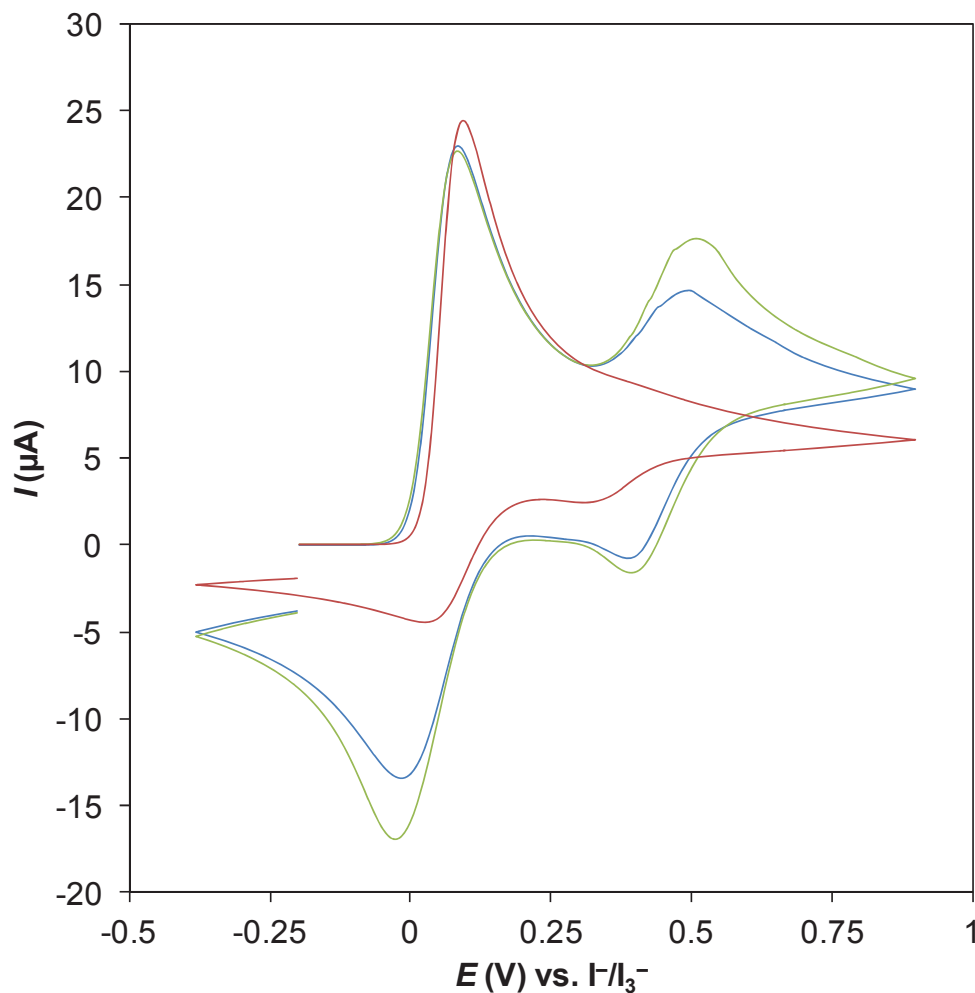


Figure S2. Cyclic voltammograms simulated on the basis of the mechanism given in Eqs. 10 and 11, used to mimic the oxidation of 25 mM [C₂mim]I in [C₂mim][NTf₂] at a 1.6 mm dia. Pt macrodisk electrode with a scan rate of 250 mV s⁻¹. Simulation parameters are as in Table 1, except k_f ($\text{M}^{-1} \text{s}^{-1}$) is 5×10^9 (red trace), 1×10^{12} (blue trace) or 5×10^{14} (green trace).

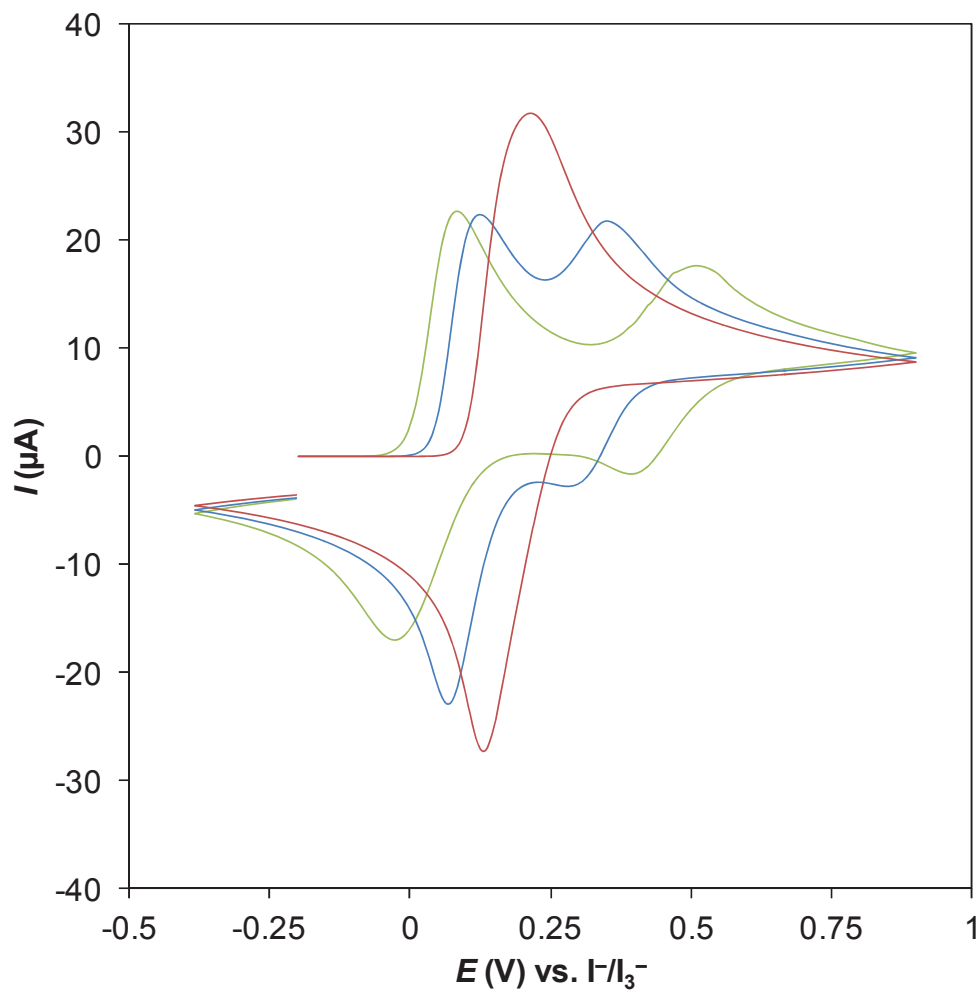


Figure S3. Cyclic voltammograms simulated on the basis of the mechanism given in Eqs. 10 and 11, used to mimic the oxidation of 25 mM $[\text{C}_2\text{mim}]\text{I}$ in $[\text{C}_2\text{mim}][\text{NTf}_2]$ at a 1.6 mm dia. Pt macrodisk electrode with a scan rate of 250 mV s^{-1} . Simulation parameters are as in Table 1, except K_{eq} is 2.3×10^2 (red trace), 2.3×10^4 (blue trace) or 2.3×10^6 (green trace).

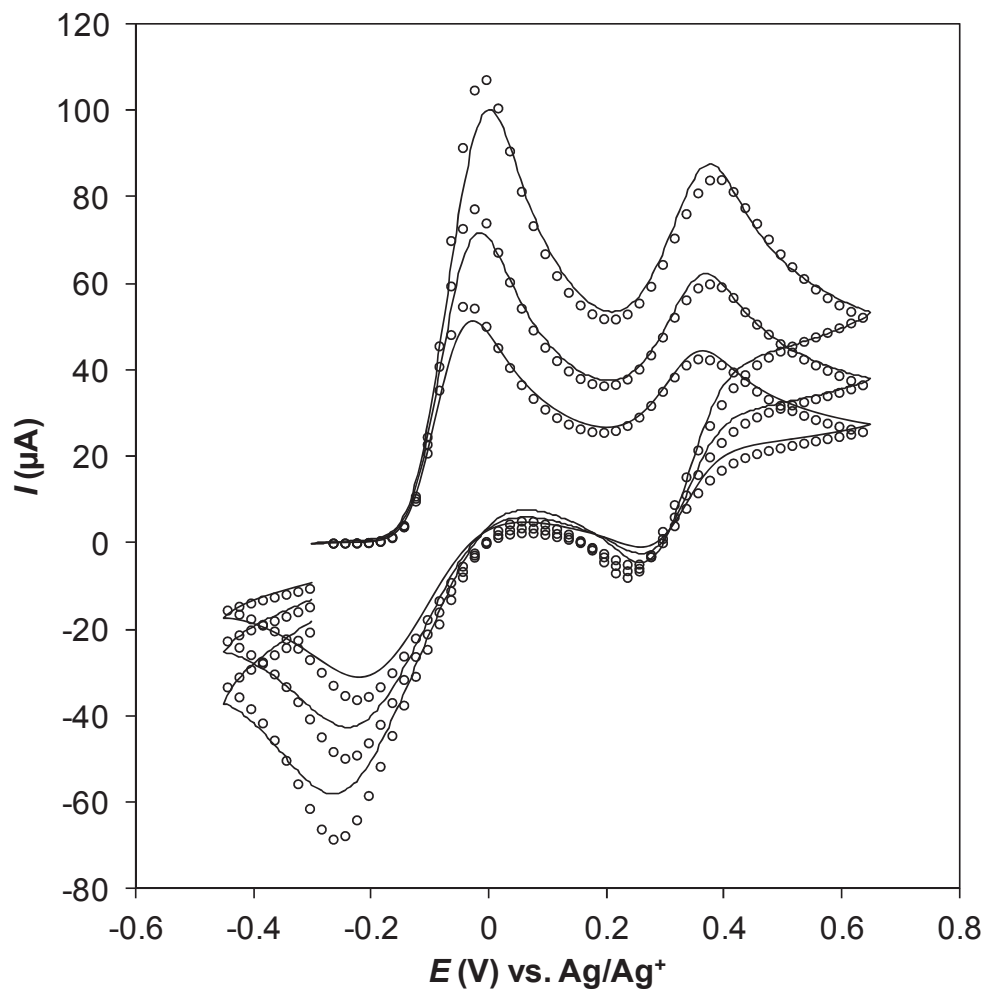


Figure S4. Comparison of experimental (—) and simulated (○) cyclic voltammograms obtained from the oxidation of 4 mM [C₂mim]I in acetonitrile (0.2 M LiBF₄) at a 2.0 mm dia. Pt macrodisk electrode with scan rates of (from top to bottom) 1000, 500 and 250 mV s⁻¹. The simulation parameters are given in Table S1.

Table S1. Simulation parameters used in Figure S4 to model the electro-oxidation of 4 mM [C₂mim]I in acetonitrile (0.2 M LiBF₄) at a 2.0 mm dia. Pt macrodisk electrode.

Parameter	Value
E^0 (V)	-0.04
k_s (cm s ⁻¹)	10
α	0.32
$K_{\text{eq,app}}$ (M ⁻¹)	1×10^7
$k_{\text{f,app}}$ (M ⁻¹ s ⁻¹)	10^{16}
D_{I^-} ($\times 10^{-7}$ cm ² s ⁻¹)	1.8
$D_{\text{I}_3^-}$ ($\times 10^{-7}$ cm ² s ⁻¹)	2.3
D_{I_2} ($\times 10^{-7}$ cm ² s ⁻¹)	2.5
C_{dl} (F)	0
R_u (Ω)	200
T (K)	298.2

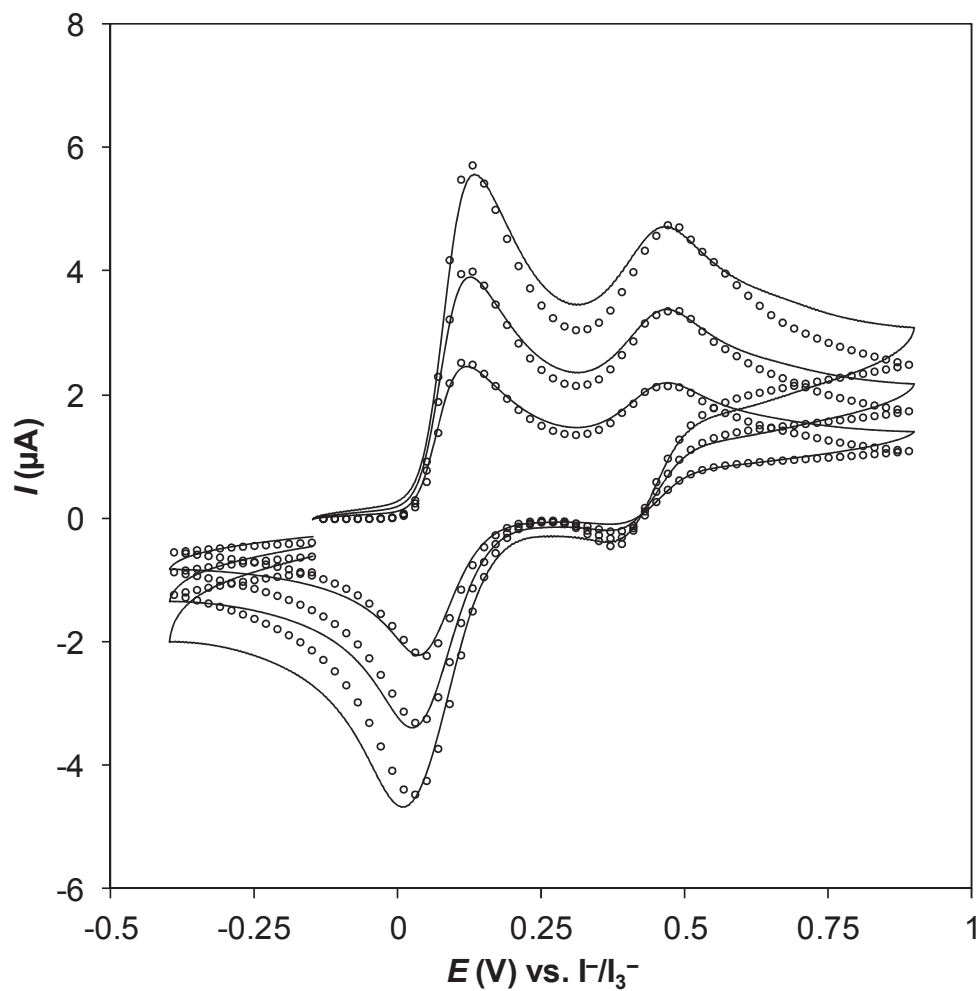


Figure S5. Comparison of the simulated (\circ) and experimental (—) cyclic voltammograms for the oxidation of 4 mM $[\text{C}_2\text{mim}]\text{I}$ in $[\text{C}_2\text{mim}][\text{NTf}_2]$ at a 1.6 mm dia. Pt macrodisk electrode with scan rates of (from top to bottom) 500, 250 and 100 mV s^{-1} . Simulation parameters are as given in Table 1.

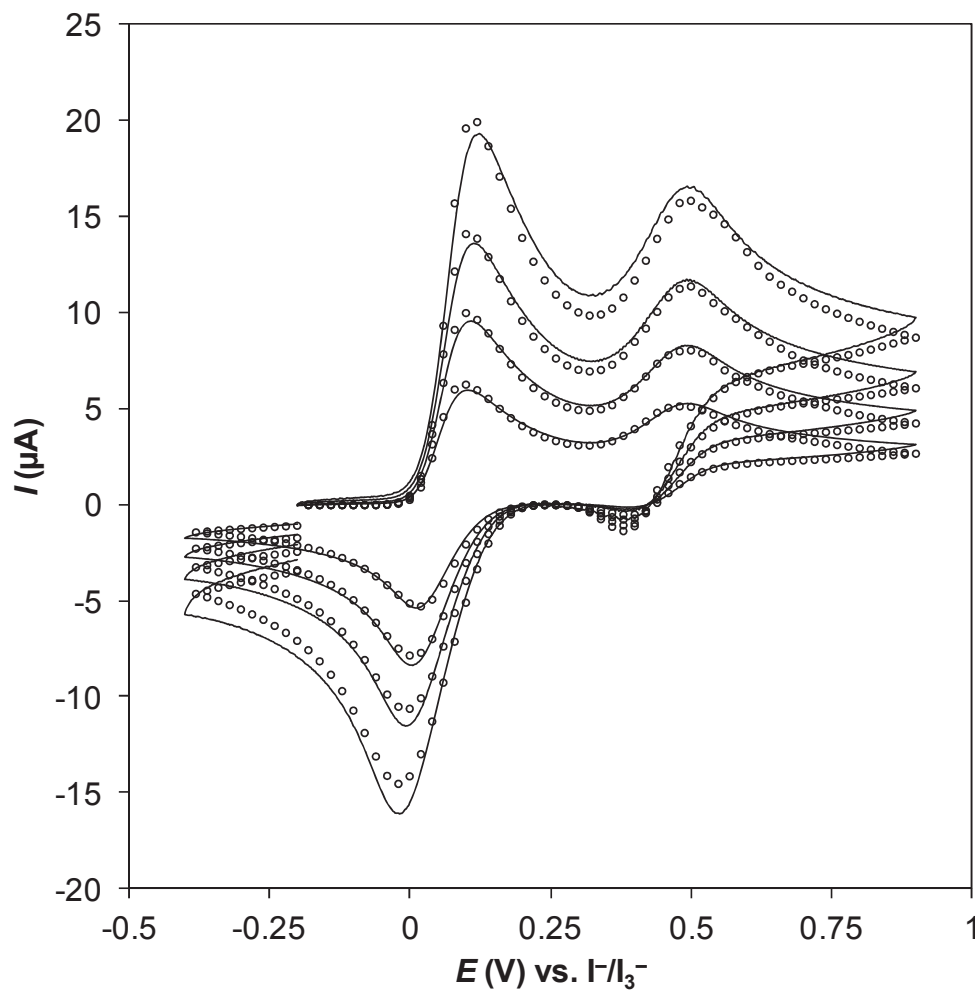


Figure S6. Comparison of the simulated (\circ) and experimental ($—$) cyclic voltammograms for the oxidation of 10 mM $[\text{C}_2\text{mim}]\text{I}$ in $[\text{C}_2\text{mim}][\text{NTf}_2]$ at a 1.6 mm dia. Pt macrodisk electrode with scan rates of (from top to bottom) 1000, 500, 250 and 100 mV s^{-1} . Simulation parameters are as given in Table 1.

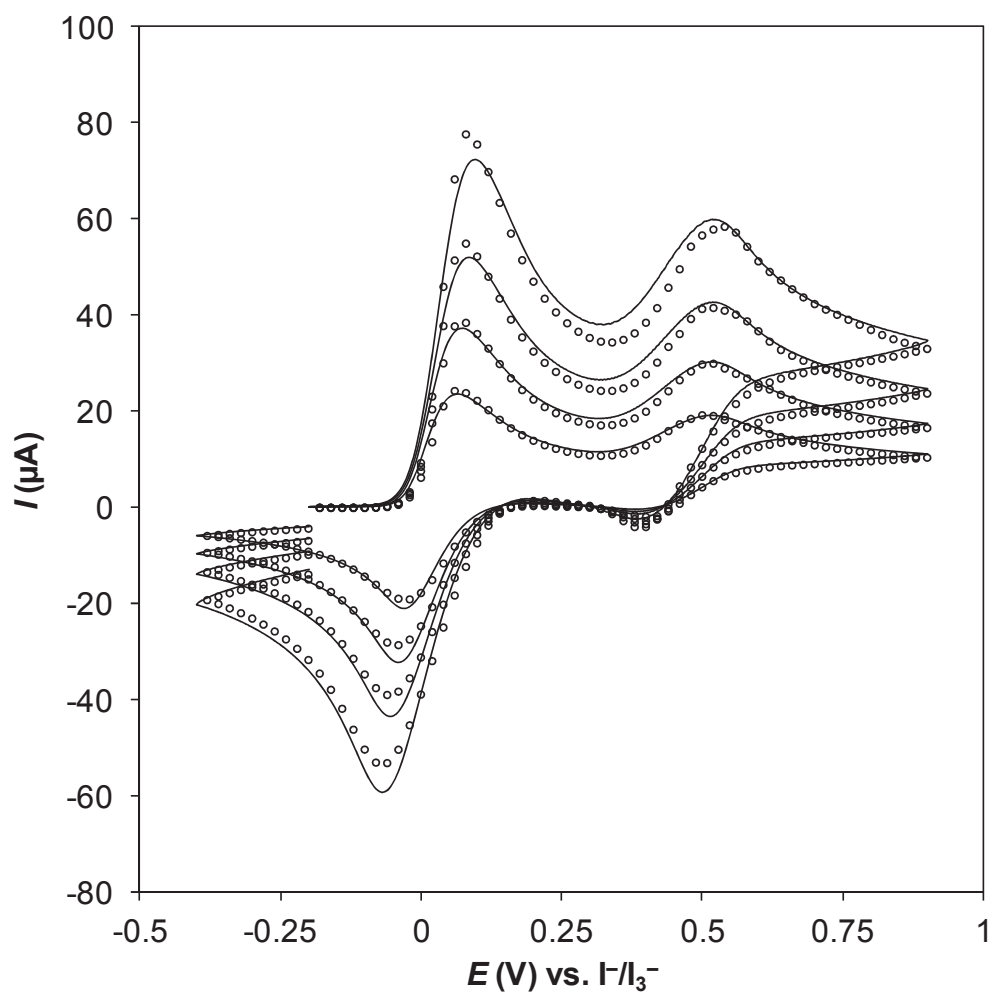


Figure S7. Comparison of the simulated (\circ) and experimental ($—$) cyclic voltammograms for the oxidation of 40 mM $[\text{C}_2\text{mim}]\text{I}$ in $[\text{C}_2\text{mim}][\text{NTf}_2]$ at a 1.6 mm dia. Pt macrodisk electrode with scan rates of (from top to bottom) 1000, 500, 250 and 100 mV s^{-1} . Simulation parameters are as given in Table 1.

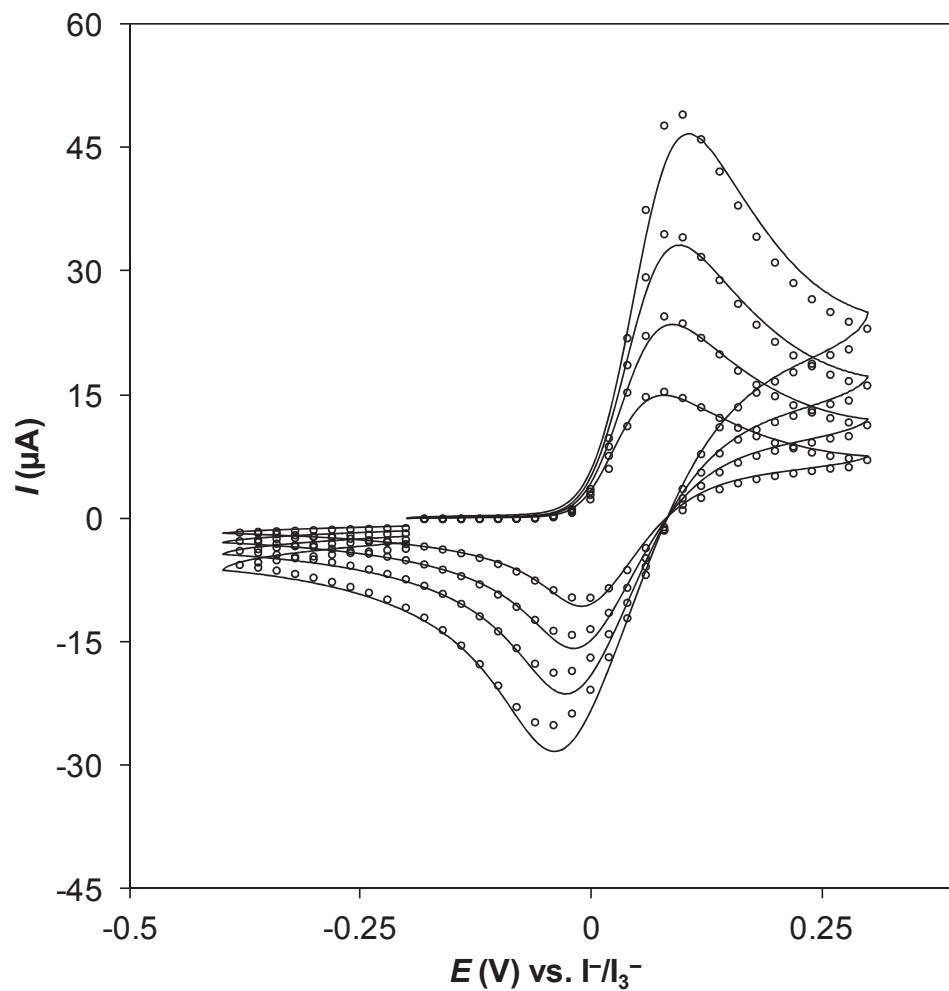


Figure S8. Comparison of the simulated (\circ) and experimental ($—$) cyclic voltammograms for the oxidation of 25 mM $[\text{C}_2\text{mim}]\text{I}$ in $[\text{C}_2\text{mim}][\text{NTf}_2]$ (I^-/I_3^- process only) at a 1.6 mm dia. Pt macrodisk electrode with scan rates of (from top to bottom) 1000, 500, 250 and 100 mV s^{-1} . Simulation parameters are as given in Table 1.

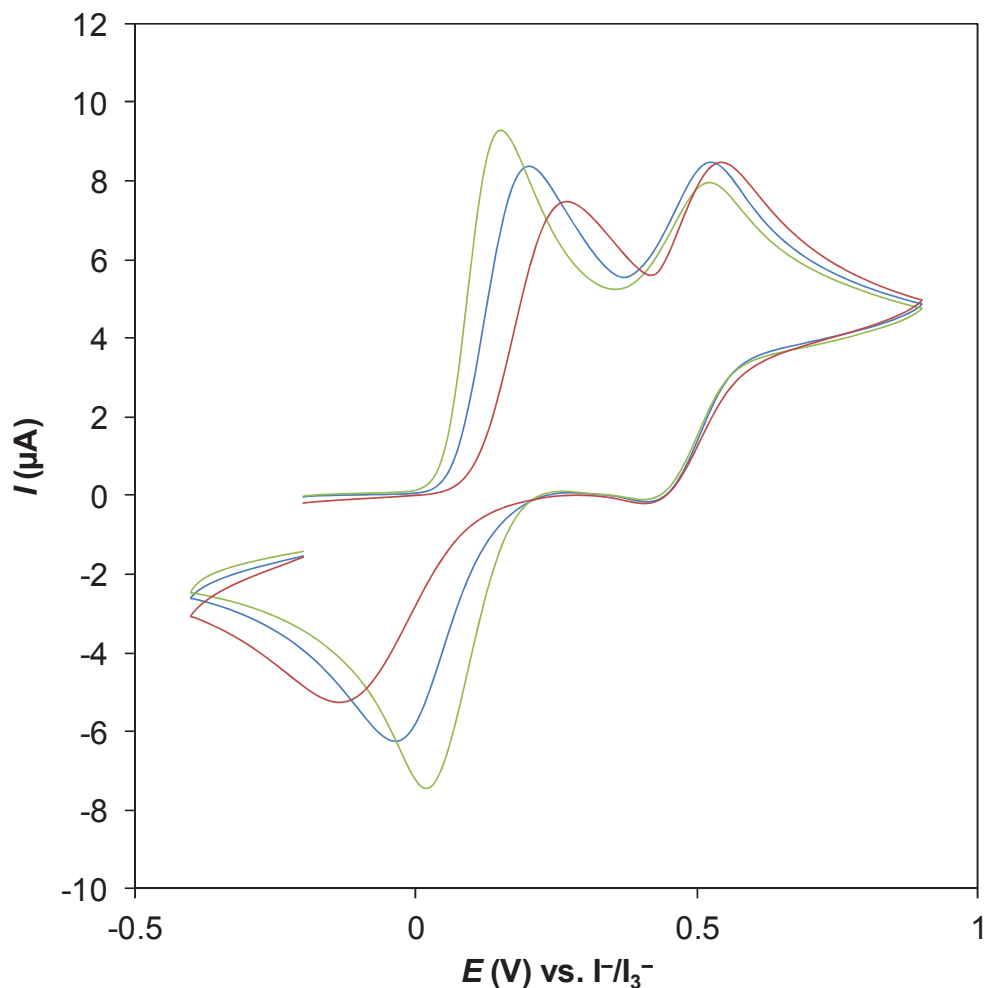


Figure S9. Cyclic voltammograms obtained from the oxidation of 10 mM $[\text{C}_2\text{mim}]\text{I}$ in $[\text{C}_2\text{mim}][\text{NTf}_2]$ at a 1.6 mm dia. Pt macrodisk electrode with a scan rate of 250 mV s^{-1} . Prior to the relevant sweep, the working electrode was either not activated (red trace), activated by polishing (blue trace), or activated by polishing and electrochemically cleaning in aqueous sulphuric acid (green trace). The polishing and electrochemical cleaning protocols are described in the Experimental Section.

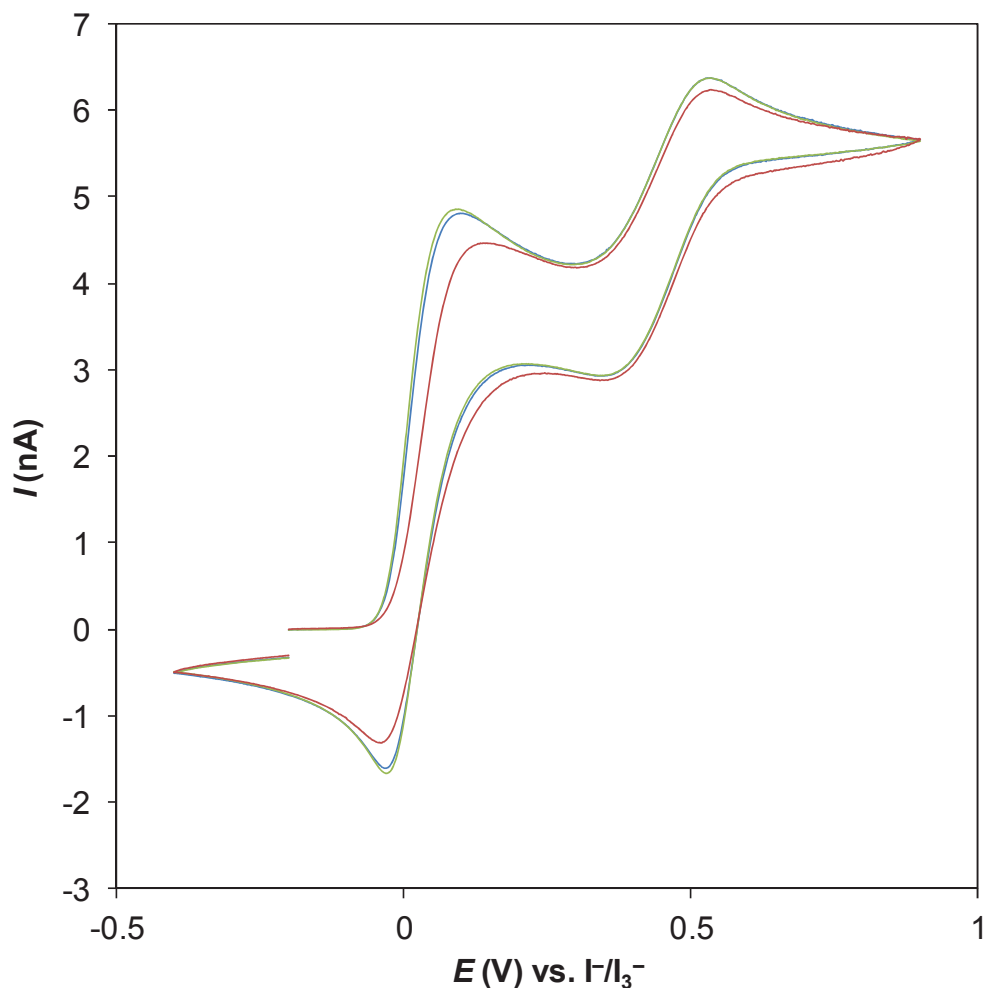


Figure S10. Cyclic voltammograms obtained from the oxidation of 40 mM $[C_2mim]I$ in $[C_2mim][NTf_2]$ at a 20 μm dia. Pt microdisk electrode with a scan rate of 50 mV s^{-1} . The voltammograms represent the first (red trace), second (blue trace) and third (green trace) sweeps taken immediately after the electrode was activated by polishing and electrochemically cleaned as detailed in the Experimental Section.

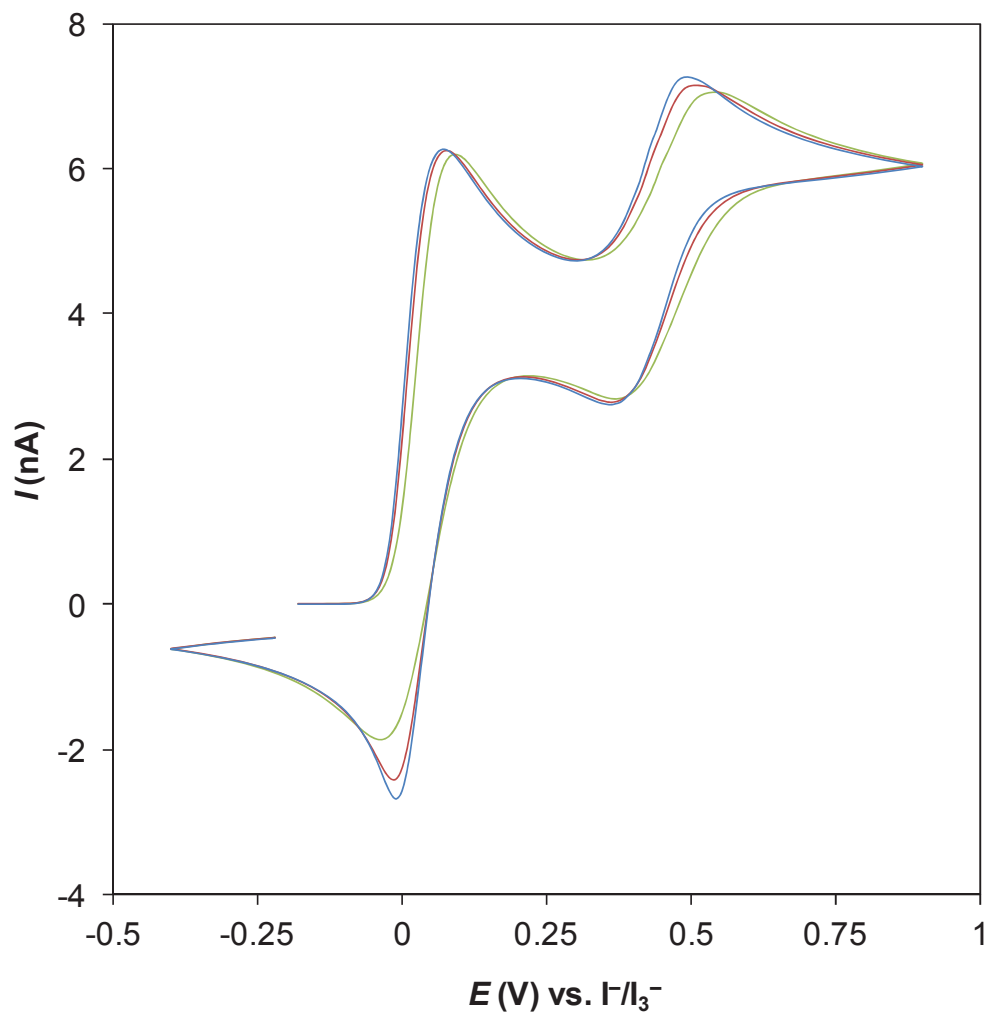


Figure S11. Cyclic voltammograms simulated on the basis of the mechanism given in Eqs. 10 and 11, used to mimic the oxidation of 40 mM $[\text{C}_2\text{mim}]\text{I}$ in $[\text{C}_2\text{mim}][\text{NTf}_2]$ at a 20 μm dia. Pt microdisk electrode with a scan rate of 100 mV s^{-1} . Simulation parameters are as in Table 1, except k_s (cm/s) is 1.8 (green trace), 8 (red trace) or 30 (blue trace).

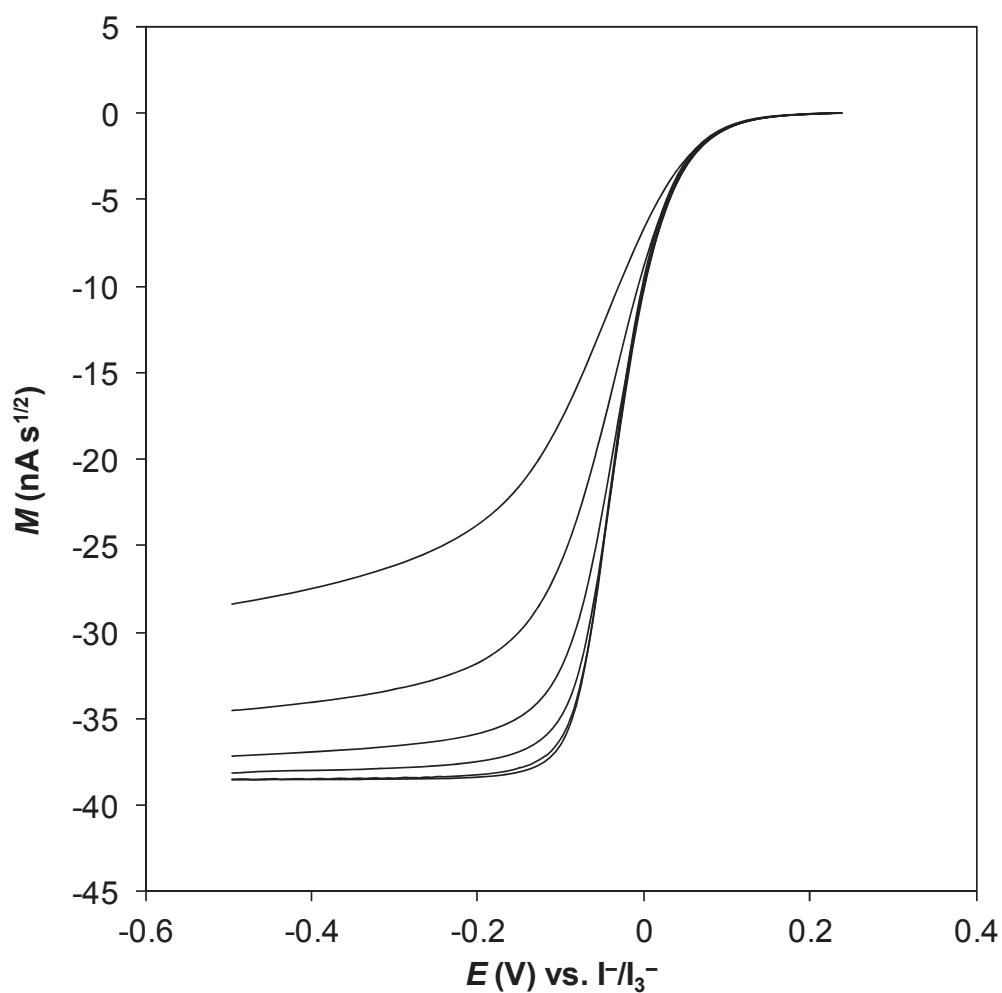


Figure S12. Simulated linear sweep convolved current voltammograms obtained using the mechanism given in Eqs. 10 and 11, in order to mimic the reduction of 100 mM [C₂mim]I + 100 mM I₂ ([I₃⁻] = 100 mM) in [C₂mim][NTf₂] at a 20 μm dia. Pt microdisk electrode with scan rates of (from top to bottom) 100000, 10000, 1000, 100, 10 and 1 mV s⁻¹. Simulation parameters are as given in Table 1, except $k_s = 30 \text{ cm s}^{-1}$ and $D_{I^-} = 2.85 \times 10^{-7} \text{ cm}^2 \text{ s}^{-1}$.

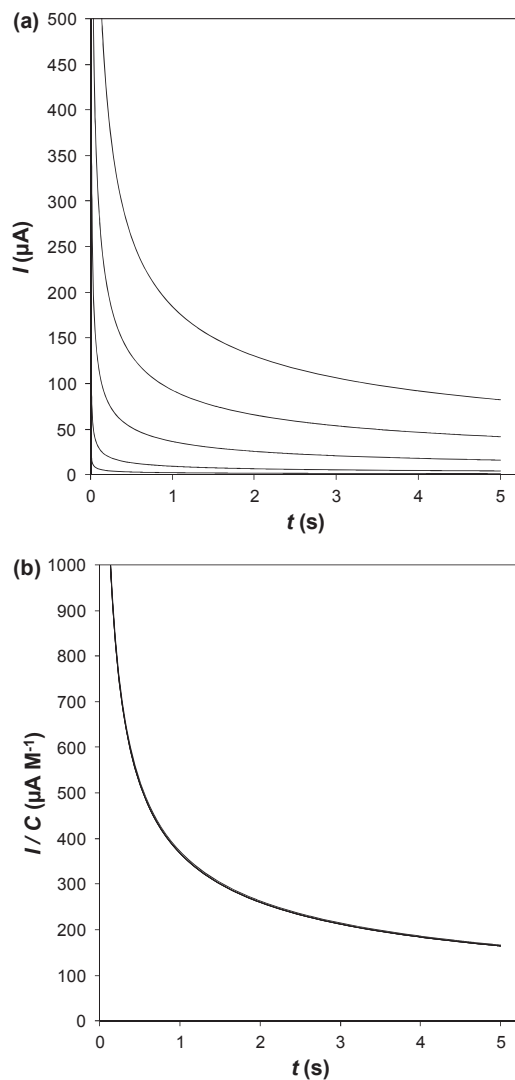


Figure S13. (a) Simulated and (b) concentration-normalized simulated chronoamperograms obtained using the mechanism given in Eqs. 10 and 11, in order to mimic the diffusion controlled oxidation of I^- to I_3^- as per Eq. 3 ($n = 2/3$), in a 1:1 mixture of I^- and I_3^- in $[\text{C}_2\text{mim}][\text{NTf}_2]$ at a 1.6 mm dia. Pt macrodisk electrode. The bulk concentrations of I^- and I_3^- are (from top to bottom) 500, 250, 100, 25 and 5 mM. Simulation parameters are as given in Table 1.

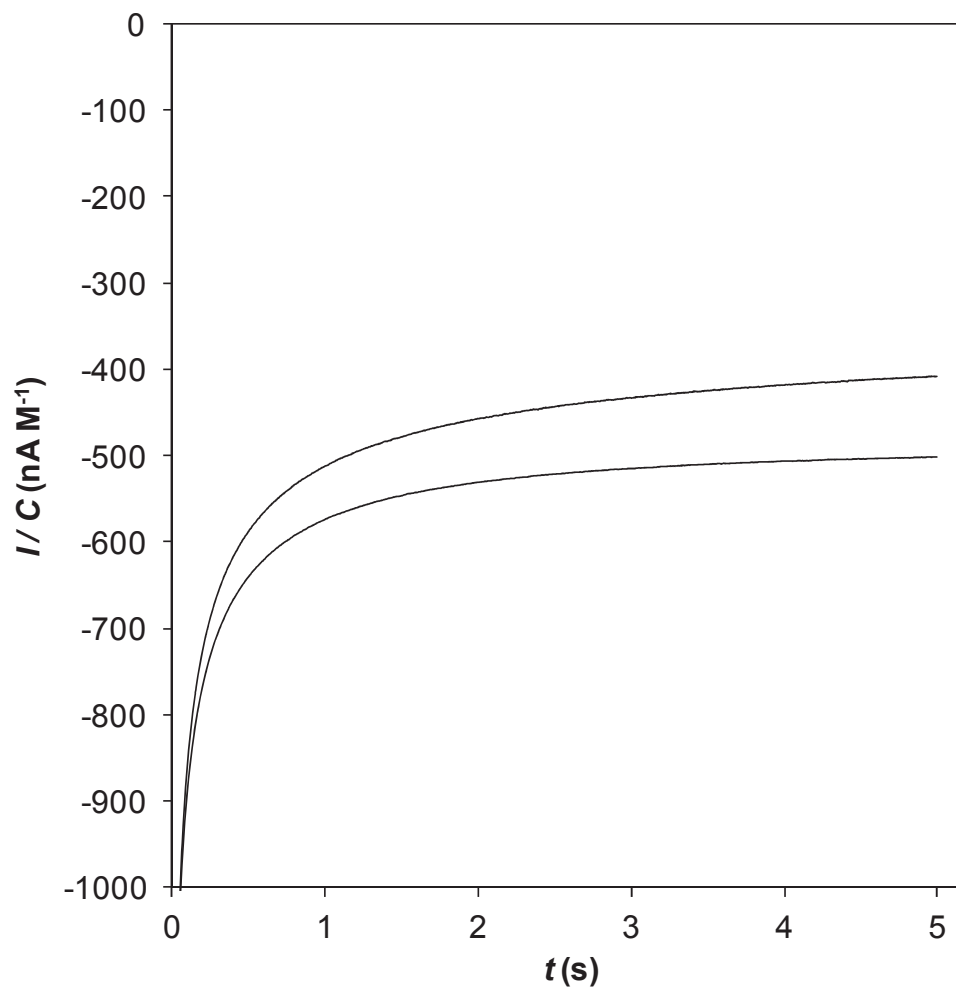


Figure S14. Concentration-normalized chronoamperograms obtained from the reduction of I_3^- to I^- as per Eq. 3 ($n = 2$), in a 1:2 mixture of I^- and I_3^- in $[C_2mim][NTf_2]$ at a 20 μm dia. Pt microdisk electrode. The bulk concentration of I_3^- is 10 (top) and 250 mM (bottom).

5. Proton Transport, Hydrogen Evolution and Equilibrium Acidity (pK_a) in Ionic Liquid Media

The second redox system studied in detail was the H^+/H_2 couple, which plays a pivotal role in a number of technologically important reactions, including water splitting and PEMFC operation. In addition, proton transfer is an important step in a myriad of (electro)chemical reactions, including photosynthesis and electrochemical CO_2 reduction. Initially, hydrogen evolution and proton transport in bis(trifluoromethanesulfonyl)imide ionic liquids was investigated, with the conjugate acid of this anion (*i.e.*, $H[NTf_2]$) as the proton source. Further detail can be found in the following publication:

Bentley, C. L.; Bond, A. M.; Hollenkamp, A. F.; Mahon, P. J.; Zhang, J., *J. Phys. Chem. C* **2014**, *118*, 22439–22449.

After characterising the $H[NTf_2]/H_2$ process, proton reduction from a range of weak acids (*i.e.*, the HA/H_2 or BH^+/H_2 process) was investigated in 1-ethyl-3-methylimidazolium bis(trifluoromethanesulfonyl)imide. During this study, a straightforward voltammetric method for estimating the pK_a of weak acids was devised, and an equilibrium acidity scale featuring 20 acids (*i.e.*, protonated amines, sulfonamides, phenols, carboxylic acids or sulfonic acids) spanning 18 orders of magnitude in acid strength ($2.0 \leq pK_a \leq 19.5$) was established in this media. At the time of writing this thesis, two manuscripts were being prepared from this work, titled: “*Electrochemical Proton Reduction and Equilibrium Acidity (pK_a) in Aprotic Ionic Liquids: Protonated Amines and Sulfonamide Acids*” and “*Electrochemical Proton Reduction and Equilibrium Acidity (pK_a) in Aprotic Ionic Liquids: Phenols, Carboxylic Acids and Sulfonic Acids*”. These manuscripts have been included in this chapter and will be submitted as research articles to a reputable journal in the period following thesis submission.

Part B: Specific Declaration

Monash University

Declaration for Thesis Chapter 5**Declaration by candidate**

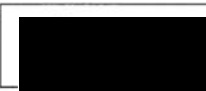
In the case of Chapter 5, the nature and extent of my contribution to the work was the following:

Nature of contribution	Extent of contribution (%)
Experimental work, Manuscript writing/preparation	100%

The following co-authors contributed to the work. If co-authors are students at Monash University, the extent of their contribution in percentage terms must be stated:

Name	Nature of contribution	Extent of contribution (%) for student co-authors only
Cameron L. Bentley	Experimental work, manuscript writing/preparation, editing.	100%
Alan M. Bond	Supervision, proof-reading, editing.	
Anthony F. Hollenkamp	Supervision, proof-reading, editing.	
Peter J. Mahon	Supervision, proof-reading, editing.	
Jie Zhang	Supervision, proof-reading, editing.	

The undersigned hereby certify that the above declaration correctly reflects the nature and extent of the candidate's and co-authors' contributions to this work*.

Candidate's Signature		Date 02/03/2015
Main Supervisor's Signature		Date 02/03/2015

Mass Transport Studies and Hydrogen Evolution at a Platinum Electrode Using Bis(trifluoromethanesulfonyl)imide as the Proton Source in Ionic Liquids and Conventional Solvents

Cameron L. Bentley,^{†,‡} Alan M. Bond,[†] Anthony F. Hollenkamp,^{*,‡} Peter J. Mahon,^{*,§} and Jie Zhang^{*,†}

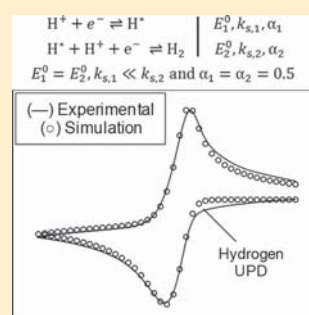
[†]School of Chemistry, Monash University, Clayton, Vic 3800, Australia

[‡]CSIRO Energy Flagship, Box 312, Clayton South, Vic 3169, Australia

[§]Faculty of Science, Engineering and Technology, Swinburne University of Technology, Hawthorn, Vic 3122, Australia

Supporting Information

ABSTRACT: The hydrogen evolution reaction at a platinum electrode and proton transport using bis(trifluoromethanesulfonyl)imide (H[NTf₂]) as the proton source has been investigated in six aprotic [NTf₂]⁻ ionic liquids (ILs), a protic [NTf₂]⁻ IL, propylene carbonate, and water. Proton reduction to form hydrogen in ILs is highly sensitive to the surface state of the platinum electrode, requiring oxidative preconditioning at ~2 V versus Fc/Fc⁺ (Fc = ferrocene) to “activate” the electrode and achieve reproducible voltammetry. The hydrogen evolution reaction at a preconditioned electrode in ILs has been simulated by combining the classical Volmer, H⁺ + e⁻ ⇌ H* (E₁⁰, k_{s,1}, α₁), and Heyrovsky reactions, H⁺ + H* + e⁻ ⇌ H₂ (E₂⁰, k_{s,2}, α₂), where E⁰, k_s, and α are the standard potential, standard heterogeneous electron-transfer rate constant, and charge transfer coefficient, respectively. The Volmer reaction is the rate-determining step on platinum in IL media and the formal potential of the H⁺/H₂ process is insensitive to the identity of the IL cation, lying at approximately -30 mV with respect to the Fc/Fc⁺ process. Proton transport in the ILs investigated obeys the Stokes–Einstein equation. Furthermore, the proton diffusion coefficient (measured electrochemically) is essentially identical to the self-diffusion coefficient of [NTf₂]⁻ (measured with pulsed field gradient spin–echo NMR), indicating that the protons are transported as undissociated H[NTf₂]. The Stokes radius of H[NTf₂] is estimated to be 3.24 Å from the slope of a Stokes–Einstein plot, in agreement with the literature. Proton transport in propylene carbonate follows the same Stokesian relationship, implying that H[NTf₂] also is not dissociated in this molecular solvent. Finally, proton transport in water follows the well-established Grotthuss mechanism, as expected. Although we have shown that there is no Grotthuss-like proton conduction mechanism operating in the investigated ILs, this work lays the foundation for further studies on proton reduction, activity, and transport in this class of solvent. Ultimately, the goal is to develop an IL formulation which facilitates facile anhydrous proton conduction over a wide temperature range.



INTRODUCTION

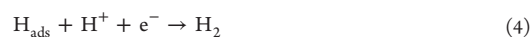
Proton (H⁺) transfer is involved with some of the most important and common reactions in biology and chemistry.^{1,2} For example, proton transfer and conduction play an important role in a range of “green” energy conversion technologies, including electrochemical CO₂ fixation,³ methanol oxidation,⁴ and water (photo)electrolysis.⁵ The proton reduction reaction (or hydrogen evolution reaction, HER) is of wide technological importance and has therefore been studied extensively at many electrode surfaces in a range of media,^{6–8} predominantly aqueous:^{9–11}



This H⁺/H₂ couple (eq 1) also forms the basis of the fundamental reference potential scale in aqueous electrochemistry, the normal (NHE) or standard (SHE) hydrogen electrode.¹²

Although eq 1 is conceptually simple, involving the transfer of one electron per proton, it is subject to significant kinetic

barriers and therefore requires a suitable electrode (electrocatalyst) to proceed at an economically viable rate. Indeed, it has been well-established that different metals display vastly different catalytic activities toward proton reduction/hydrogen oxidation, with exchange current densities ranging from approximately 10⁻⁹ A m⁻² on Pb, a “poor” electrocatalyst, to 10 A m⁻² on Pt, a “good” electrocatalyst.¹³ In acidic aqueous media, the HER is postulated to proceed via a combination of the following three elementary reactions:^{7,9,13}



Received: October 27, 2014

Revised: November 13, 2014

Published: November 14, 2014

where H_{ads} is a chemisorbed hydrogen atom and eqs 2–4 are known as the Volmer (or discharge), Tafel (or combination), and Heyrovsky (or ion + atom) reactions, respectively. Thus, the formation of H_{ads} on the electrode surface (eq 2) by electron transfer (reduction) is followed either by surface migration and dimerization of H_{ads} (eq 3) to form H_2 or the direct formation of H_2 from H_{ads} upon electron transfer to H^+ in solution (eq 4). The preferred reaction pathway depends on the identity of the metallic electrode and is thought to be governed by whether eq 2 is sluggish or facile relative to H_{ads} migration across the electrode surface.⁷

Proton conduction and hydrogen evolution plays an important role in the efficient operation of proton-exchange membrane fuel cells (PEMFCs).¹⁴ These intensively studied cells possess favorable properties that include high power density and high efficiency. In essence, a PEMFC consists of two electrodes, one where H_2 oxidation to H^+ occurs, and one where O_2 reduction to H_2O occurs, separated by a proton-exchange membrane (PEM). Traditionally, the PEM is composed of a hydrated polyelectrolyte (the archetype being a perfluorosulfonic acid such as Nafion), which is a mechanically stable proton conductor only in the presence of water, limiting operation to temperatures below 100 °C (typically ≤ 80 °C).¹⁵ Increasing the operating temperature of PEMFCs above 100 °C would be beneficial, as the elevated temperatures would reduce activation overpotentials (i.e., improved heterogeneous kinetics), improve gas diffusion, and increase the tolerance of Pt catalysts to CO poisoning, allowing the use of less-pure H_2 feed stocks. As a result, there is ongoing interest in replacing traditional PEMs with proton conducting materials which are able to operate at temperatures in excess of 100 °C.^{16,17}

Air/water stable nonhaloaluminate ionic liquids (ILs) have been identified as potential ‘anhydrous proton conductors’, which could be employed at temperatures well above 100 °C.^{15,17} ILs are made up entirely of ions, meaning they are intrinsic ionic conductors and have therefore been employed extensively in the field of electrochemistry as electrolytes.² The strong cohesive forces operating in an IL means they often possess negligible vapor pressures but also, unfortunately, high viscosities, often in the range of 20 to 1000 mPa s.¹⁸ ILs are commonly aprotic, meaning they contain no dissociable protons in their structures; these compounds are referred to herein as aprotic ionic liquids (AILs). A subset of ILs, known generally as protic ionic liquids (PILs), formed through the transfer of a proton from a Bronsted acid to a Bronsted base, are particularly promising candidates as ‘anhydrous proton conductors’.^{19,20} Although IL formulations which exhibit fast proton transport and facile hydrogen oxidation/oxygen reduction kinetics have been reported,²¹ only a few supporting mechanistic studies on the H^+/H_2 electrode reaction^{8,20,22} and proton conduction^{23,24} have appeared. It is thought that through the selection of suitable IL formulations, proton conduction via a Grotthuss-type mechanism may be possible, which would serve to offset the limited physical mass transport in these electrolytes, imposed by their intrinsically high viscosity.^{15,23} Although PEMFCs have been the focus of much of the discussion thus far, there are applications in areas such as synthetic chemistry (i.e., hydrogenation/dehydrogenation), separations chemistry, and electrochemistry (i.e., electrochemical hydrogenation and gas sensors) which also would benefit from high temperature, anhydrous proton conduction.

In this study, we have investigated the proton reduction reaction using protons from bis(trifluoromethanesulfonyl)imide, $H[NTf_2]$, in a range of AILs which possess the common $[NTf_2]^-$ anion using cyclic voltammetry at a platinum electrode with computational simulations. Proton transport has been quantified electrochemically using chronoamperometry and convolution voltammetry, and correlated with the self-diffusion coefficient of $[NTf_2]^-$, measured using pulsed field gradient spin-echo NMR. Parallel investigations have been carried out in triethylammonium bis(trifluoromethanesulfonyl)imide (a PIL), propylene carbonate (an aprotic molecular solvent), and water (a protic solvent) to highlight the similarities and differences between these different classes of solvent.

EXPERIMENTAL SECTION

Reagents. 1-Ethyl-3-methylimidazolium bis-(trifluoromethanesulfonyl)imide ($[C_2mim][NTf_2]$, Iolitec), triethylsulfonium bis(trifluoromethanesulfonyl)imide ($[S_{2,2,2}][NTf_2]$, Solvent Innovation), 1-methyl-1-butylpyrrolidinium bis(trifluoromethanesulfonyl)imide ($[C_4mpyr][NTf_2]$, Merck), 1-butyl-2,3-dimethylimidazolium bis-(trifluoromethanesulfonyl)imide ($[C_4dmim][NTf_2]$, Solvent Innovation), and dimethylethylpropylammonium bis-(trifluoromethanesulfonyl)imide ($[N_{1,1,2,3}][NTf_2]$, Merck) were commercial samples. Tributylmethylammonium bis-(trifluoromethanesulfonyl)imide ($[N_{1,4,4,4}][NTf_2]$) was prepared by a metathesis reaction between lithium bis-(trifluoromethanesulfonyl)imide ($Li[NTf_2]$, 3 M Fluorad) and tributylmethylammonium methylsulfate ($[N_{1,4,4,4}][CH_3OSO_3]$, Sigma-Aldrich) in deionized water (Millipore Milli-Q Plus 185). Following preparation, $[N_{1,4,4,4}][NTf_2]$ was taken up in dichloromethane (Merck, EMSURE) and rinsed repeatedly with water to extract residual $Li[CH_3OSO_3]$. Triethylammonium bis(trifluoromethanesulfonyl)imide ($[N_{H,2,2,2}][NTf_2]$) was prepared by a metathesis reaction between $Li[NTf_2]$ and triethylammonium chloride ($[N_{H,2,2,2}]Cl$, Sigma-Aldrich, recrystallized from ethanol) in deionized water. Following preparation, $[N_{H,2,2,2}][NTf_2]$ was taken up in dichloromethane (Merck, EMSURE) and rinsed repeatedly with water to extract residual $LiCl$ until the aqueous phase passed the $AgNO_3$ test. Before use, each of the ILs was dried under high vacuum ($\leq 10^{-1}$ mbar) at 45 °C for 48 h. The residual water content was less than 100 ppm by Karl Fischer titration (Metrohm 831 KF Coulometer).

Bis(trifluoromethanesulfonyl)imide ($H[NTf_2]$, Sigma-Aldrich, 95%) was purified by sublimation under high vacuum. Ferrocene (Fc, Fluka, >98%) was recrystallized from *n*-pentane (Merck, EMSURE). Propylene carbonate (Sigma-Aldrich, anhydrous, 99.7%), acetonitrile (Alfa-Aesar, anhydrous, 99.7%), tetra-*n*-butylammonium hexafluorophosphate ($[NBu_4][PF_6]$, Sigma-Aldrich), and silver nitrate ($AgNO_3$, BDH, 99.9%) were used as supplied by the manufacturer. All water-sensitive reagents were stored and handled under a dry argon atmosphere in a glovebox.

Electrochemical Systems and Procedures. All voltammetric experiments were carried out under benchtop conditions at ambient temperature (24 ± 1 °C) with a Gamry Reference 600 Potentiostat/Galvanostat/ZRA (Gamry Instruments). All solvents were degassed with N_2 prior to experimentation, and a blanket of N_2 was maintained during the course of the voltammetric experiments. A faraday cage was employed to minimize noise in all microelectrode experiments. Positive feedback iR_u compensation (R_u = uncompensated resistance)

was employed in macroelectrode experiments (R_u was estimated by electrochemical impedance). All voltammetric experiments were carried out using a standard 3-electrode arrangement with a working and reference electrode as described below and a Pt wire auxiliary electrode. In IL media, an Ag wire which had been immersed in the IL under investigation (neat) and sealed in a fritted (Vycor glass frit) glass tube served as the pseudo reference electrode. In propylene carbonate, an analogous pseudo reference electrode was employed, except the wire was immersed in 0.85 M $[\text{C}_2\text{mim}][\text{NTf}_2]$ in PC. The pseudo reference electrode potential was calibrated against the formal potential of the IUPAC recommended Fc/Fc^+ process²⁵ in the electrolyte of interest, taking into careful consideration the difference in the diffusion coefficients of Fc and Fc^+ .^{7,26} A Metrohm double junction Ag/AgCl (3 M KCl) reference electrode was employed in experiments in aqueous media.

The Pt macrodisk with a nominal diameter of 1.6 mm, Au macrodisk with a nominal diameter of 1.6 mm, and glassy carbon macrodisk with a nominal diameter of 3.0 mm were purchased from BASi (Bioanalytical Systems), the boron-doped diamond electrode with a nominal diameter of 3.0 mm was purchased from Windsor Scientific (Berkshire, U.K.), and the Pt microdisk with a nominal diameter of 20 μm was purchased from Metrohm. The macrodisk electrodes were activated by polishing with successively smaller (1 and 0.3 μm) aqueous alumina slurries (Kemet, U.K.) on a clean polishing cloth (Buehler). Adherent alumina was removed by sonication in deionized water. The Pt microdisk electrode was activated by polishing with an aqueous slurry of 0.3 μm alumina and rinsing thoroughly with deionized water. The working electrode was preconditioned prior to sweeping by anodic polarization at ~ 2 V versus Fc/Fc^+ for ≤ 1 ms (described below). The active electrode area (A) of each of the electrodes was calibrated with convolution voltammetry,^{27–29} using the oxidation of a Fc solution of known concentration (2.0 mM in acetonitrile containing 0.10 M $[\text{NBu}_4][\text{PF}_6]$) and adopting a diffusion coefficient of 2.4×10^{-5} $\text{cm}^2 \text{s}^{-1}$, as published under these conditions.¹²

Viscosity was measured using the falling ball method with an Anton Paar automated microviscometer (AMVn). Density was measured with an Anton Paar DMA 4500 M density meter. NMR self-diffusion coefficients were determined using the pulsed field gradients spin echo (PGSE) method utilizing a Bruker Av500 NMR spectrometer equipped with a 5 mm Bruker CryoProbe Prodigy H/F-C/N-D probe operating at 500.13 MHz for ^1H and 470.55 MHz for ^{19}F with a 6.6 G/mm z gradient. Samples were maintained at 25 $^\circ\text{C}$, and at least 30 min was allowed for each sample to thermally equilibrate before any measurements were made. The self diffusion coefficients were measured with a stimulated echo sequence with one spoil gradient. The diffusion time (Δ) and the gradient pulse length (δ) were optimized for each sample; Δ was either 50 or 100 ms, while δ was between 1 and 10 ms. Gradient pulses were smoothed square chirp shape. Experiments were performed as Pseudo-2D with a linear variation of the gradient from 2 to 95% of maximum intensity in 32 steps.

Data Treatment and Processing. The algorithm used to calculate the convolved currents has been reported previously.³⁸ The chronoamperometric ($I-t$) decay curves were analyzed using the following equations, as proposed by Shoup and Szabo,³⁹ which sufficiently describe the current response at

a microdisk electrode over the entire time domain, with a maximum error of 0.6%:

$$I = -4nFDC^b r_0 f(t) \quad (5)$$

$$f(t) = 0.7854 + 0.8862\tau^{-1/2} + 0.2146 \exp(-0.7823\tau^{-1/2}) \quad (6)$$

where n is the stoichiometric number of electrons, r_0 is the radius of the microdisk, C^b is the bulk concentration of electroactive species, F is Faraday's constant, and the dimensionless time parameter, τ , is given by

$$\tau = \frac{4Dt}{r_0^2} \quad (7)$$

Electrochemical diffusion coefficients (D) were extracted by fitting the experimental data with the theoretical transients described by eqs 5 and 6 (C^b , n , and r_0 known) using the nonlinear curve fitting function available in OriginPro 9.0 (OriginLab). The sample time used in all chronoamperometric experiments was 0.02 s. Voltammetric simulations were undertaken using the DigiElch software package (v. 7F, Elchsoft, Germany).

The PGSE-NMR data were processed, and the peak areas (integrals) were used to fit the following equation to determine the diffusion coefficient:

$$I = I_0 \exp\left(-D(2\pi\gamma G\delta)^2 \left(\frac{\Delta - \delta}{3}\right)\right) \quad (8)$$

where I is the signal intensity, I_0 is the initial intensity, γ is the gyromagnetic ratio (4258 $\text{s}^{-1} \text{G}^{-1}$ for ^1H and 4005 $\text{s}^{-1} \text{G}^{-1}$ for ^{19}F), and G is the gradient strength. Experimental uncertainties were estimated by propagation of the standard deviations in the variables of interest.³⁰

RESULTS AND DISCUSSION

Electrode Preconditioning. The electro-reduction of $\text{H}[\text{NTf}_2]$ was initially investigated at Pt electrodes in $[\text{C}_2\text{mim}][\text{NTf}_2]$. Platinum was chosen as the electrode material because chemically reversible H^+ reduction is readily achievable, with the oxidation of H_2 clearly visible on the reverse sweep at a macrodisk Pt electrode (see below). In comparison, H^+ reduction was found to be chemically irreversible on gold (i.e., no oxidative wave) and barely detectable on glassy carbon or boron-doped diamond due to their low catalytic activity (data not shown). These observations are consistent with previous studies on proton reduction/hydrogen oxidation in conventional solvents^{6,9} and ionic liquids.⁷

During the course of the preliminary investigations on platinum, it was found that the voltammetric response detected was very sensitive to the "history" of the electrode (i.e., cleanliness/surface state). This is clearly demonstrated in the microelectrode voltammogram shown in Figure 1a. After the electrode has been freshly polished (cycle 1), a well-defined voltammetric reductive response is obtained, which noticeably degrades on subsequent cycles of potential, becoming flattened and less peak-shaped. It is likely that the number of "active sites" on the electrode surface progressively decreases with potential cycling, resulting in more sluggish heterogeneous electron-transfer kinetics (i.e., the electrode becomes "deactivated"). This electrode "deactivation" phenomenon is both potential and time dependent, as leaving the electrode

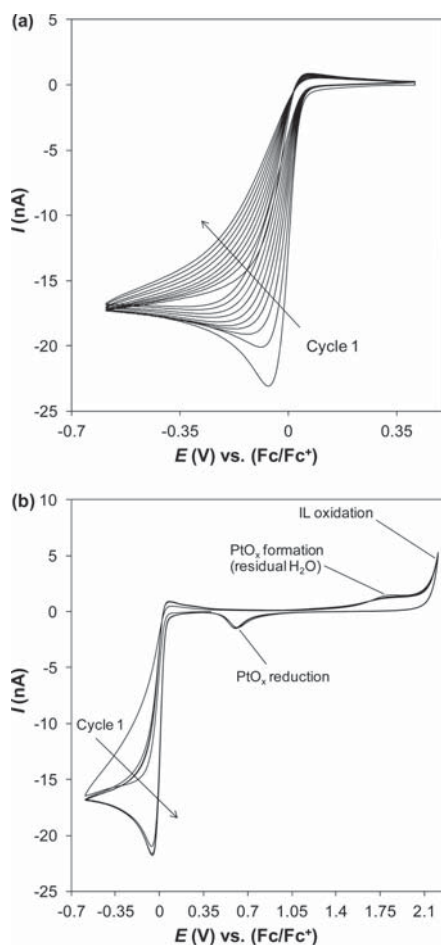


Figure 1. Cyclic voltammograms obtained from the reduction of 100.9 mM H[NTf₂] in [C₂mim][NTf₂] at a 20 μm diameter Pt microdisk electrode with a scan rate of 100 mV s⁻¹. Ten cycles in the potential range 0.41 to -0.59 V (vs Fc/Fc⁺) are shown in (a) and 4 cycles in the potential range from 2.21 to -0.59 V (vs Fc/Fc⁺) are shown in (b).

submerged in the IL at open circuit for prolonged periods causes a similar degradation in the voltammetric response.

The initial voltammetric response can be recovered by mechanically polishing the electrode (see Experimental Section) or by electrochemical conditioning at oxidative potentials (“anodic polarization”), as is demonstrated in Figure 1b. When the oxidative limit is extended from 0.4 to 2.2 V (vs Fc/Fc⁺), the initially degraded response improves with cycling (see Figure 1b), indicating that the electrode is “activated” at oxidative potentials. The broad peak starting at 1.4 V in Figure 1b has been attributed to the formation of platinum oxides (PtO_x) on the electrode surface from the oxidation of residual water in the IL, and the symmetric peak centered at 0.7 V on the reverse sweep has been assigned to the reduction of the PtO_x species.³¹ Activation of the electrode for proton reduction/hydrogen oxidation by “anodic polarization” has previously been reported in both conventional solvents⁶ and ionic liquids.³² Barrette and Sawyer⁶ postulated that deactivation occurred due to the specific adsorption of solvent

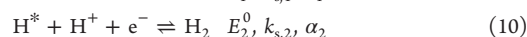
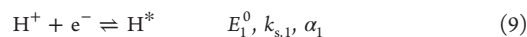
molecules and/or impurities on the electrode surface and that “preanodization” converts the blocked Pt surface to PtO_x, which, when subsequently reduced prior to voltammetric sweeping, results in a pristine, electrocatalytically active Pt surface. Whatever the cause, in these studies it was found that reproducible “activation” of the electrode could be achieved by stepping the potential to ~2 V versus Fc/Fc⁺ for ≤1 ms, stirring the solution and then allowing the system to equilibrate for ~10 s before beginning the sweep.

Hydrogen Evolution Reaction in Aprotic Ionic Liquids.

Further studies on the electro-reduction of H[NTf₂] were carried out in a range of AILs; representative cyclic voltammograms obtained in [C₂mim][NTf₂] at Pt macro- and microdisk electrodes are shown in Figure 2. The peak-to-peak separation (ΔE_p) at a Pt macrodisk electrode (see Figure 2a) increases with increasing scan rate, with values of 72.1, 82.2, and 92.3 mV at 100, 250, and 500 mV s⁻¹, respectively, indicating that the proton reduction process is quasi-reversible, in agreement with previous reports.^{7,8,32,33} At a Pt microdisk electrode (see Figure 2, panels b and c), the reduction process is peak-shaped (transient response) and the corresponding oxidation process is sigmoidal (near steady-state response), reflecting the 100-fold difference between D_{H⁺} (ca. 10⁻⁷ cm² s⁻¹) and D_{H₂} (ca. 10⁻⁵ cm² s⁻¹) in this medium.^{7,22,34} D_{H⁺} is used herein to refer to the electrochemically measured proton diffusion coefficient, regardless of the identity of the diffusing species (addressed in detail below). The large difference in D_{H⁺} and D_{H₂} highlights the need to perform numerical simulations to accurately assign the formal potential (E⁰) when the voltammogram is obtained in the mixed diffusion region (see Figure 2b), where the contributions of both planar and radial diffusion to mass transport are significant, as addressed below.

At both the Pt macro- and microdisk electrodes, prior to the main reduction process is a region which corresponds to the underpotential deposition (UPD) of adsorbed hydrogen on the electrode (labeled in Figure 2, panels a and b), which is well-known to occur at potentials positive of the equilibrium potential on platinum and palladium surfaces.⁹ The current from this surface-confined process is more prominent in highly viscous ILs (i.e., [N_{1,4,4,4}][NTf₂]) at low H[NTf₂] concentrations (≤25 mM) and high scan rates (ν ≥ 250 mV s⁻¹). Interestingly, although the thermodynamic solubility of H₂ is typically less than 5 mM in the investigated ILs,³² no complications from bubble formation/growth were encountered at H[NTf₂] concentrations ≤100 mM on the timescale of the voltammetric experiments. This indicates that bubble nucleation and growth are sluggish in this media, although H₂ bubbles were observable on the Pt electrode surface in situ with an optical microscope during H[NTf₂] reduction at concentrations above 100 mM, as is shown in Figure S1 of the Supporting Information.

Also shown in Figure 2 are simulations of the voltammetry. A number of mechanisms were considered (examples shown in Figures S2 and S3 of the Supporting Information) and the following was found to be consistent with the experimental data under a wide range of conditions:



where E⁰, k_s, and α are the standard potential, standard heterogeneous electron-transfer rate constant, and charge

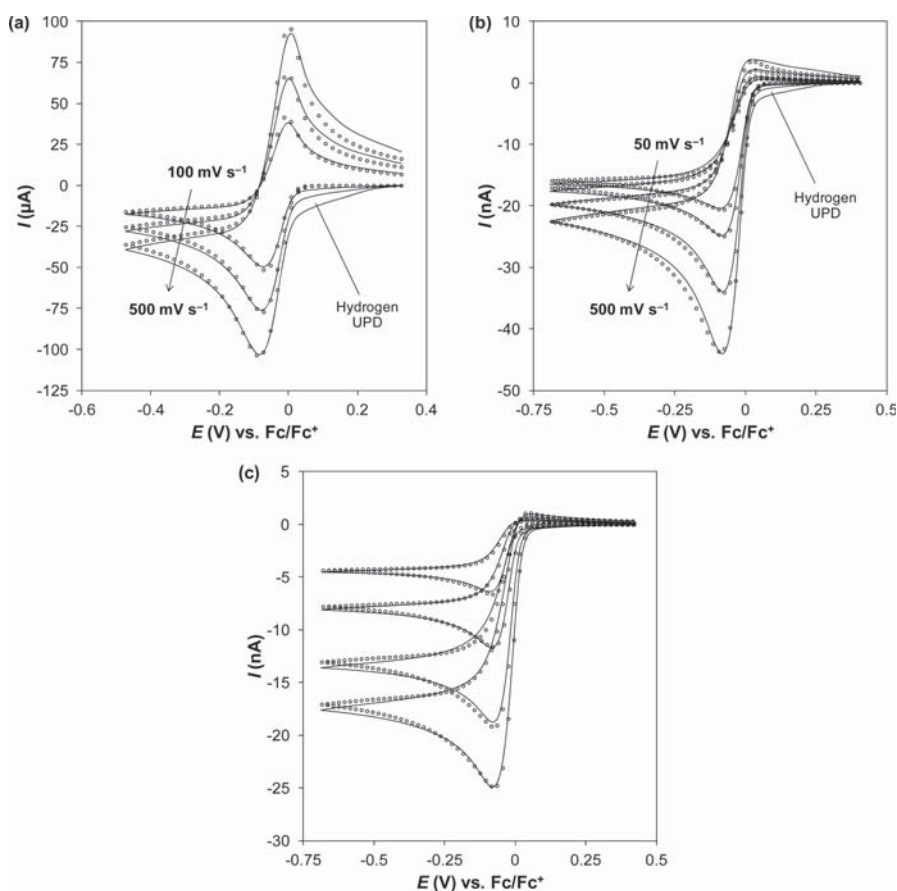


Figure 2. Comparison of the simulated (O) and experimental (—) cyclic voltammograms obtained for the reduction of H[NTf₂] in [C₂mim][NTf₂] at a (a) 1.6 mm diameter Pt macrodisk electrode ($C^b = 49.8$ mM, $\nu = 500, 250,$ and 100 mV s⁻¹), (b) 20 μ m diameter Pt microdisk electrode ($C^b = 99.2$ mM, $\nu = 500, 250, 100,$ and 50 mV s⁻¹), and (c) 20 μ m diameter Pt microdisk electrode ($C^b = 99.2, 75.8, 44.5,$ and 25.4 mM, $\nu = 100$ mV s⁻¹). Simulation parameters are available in Table 1.

Table 1. Data Extracted from the Comparison of Experimental and Simulated Cyclic Voltammetric Data Obtained Based on the Mechanism Described by Eqs 9 and 10

AIL	E^0 (V vs Fc/Fc ⁺)	$k_{s,1}$ (10 ⁻⁴ cm s ⁻¹)	D_{H^+} (10 ⁻⁷ cm ² s ⁻¹)	D_{H_2} (10 ⁻⁵ cm ² s ⁻¹)
[C ₂ mim][NTf ₂]	-0.030	7 (± 1)	3.1 (± 0.05)	2.2 (± 0.2)
[C ₄ mpyr][NTf ₂]	-0.036	3.5 (± 0.5)	1.46 (± 0.03)	1.4 (± 0.2)
[S _{2,2,2}][NTf ₂]	-0.037	5.5 (± 0.5)	2.96 (± 0.04)	2.2 (± 0.2)
[C ₄ dmim][NTf ₂]	-0.030	4 (± 0.5)	1.16 (± 0.02)	1.2 (± 0.2)
[N _{1,1,2,3}][NTf ₂]	-0.015	5 (± 0.5)	1.35 (± 0.02)	1.3 (± 0.2)
[N _{1,4,4,4}][NTf ₂]	-0.012	0.75 (± 0.05)	0.22 (± 0.004)	0.3 (± 0.05)

transfer coefficient, respectively. The reactions given in eqs 0 and 10 correspond to the Volmer and Heyrovsky equations, respectively (see eqs 2 and 4). Excellent fits between the experimental and simulated voltammograms are achieved over a wide range of scan rates and H[NTf₂] concentrations when using the simulation parameters outlined in Table 1. In all simulations, it was taken that $E_2^0 = E_1^0$, $\alpha_1 = \alpha_2 = 0.5$, $k_{s,2} = 10000$ cm s⁻¹ (reversible), $D_{H^+} = 10^{-15}$ cm² s⁻¹ (explained below), $R_u = 0$ Ω , and double layer capacitance (C_{dl}) = 0 F. D_{H^+} was measured experimentally using convolution voltammetry or chronoamperometry (discussed in detail below) and D_{H_2} was

estimated using double step chronoamperometry at a microdisk electrode (example shown in Figure S4 of the Supporting Information).³⁵ Fits of simulated and experimental data in each of the ILs are included in Figures S5–S9 of the Supporting Information.

The identity of the cation has very little influence on the formal potential of the H⁺/H₂ couple, as it is nearly constant in all of the ILs, approximately 30 mV negative of the Fc/Fc⁺ couple, in agreement with the findings by Compton and co-workers.⁸ $k_{s,1}$ is comparable in all of the ILs (ca. 10⁻⁴ cm s⁻¹) except for the highly viscous [N_{1,4,4,4}][NTf₂] (ca. 10⁻⁵ cm s⁻¹).

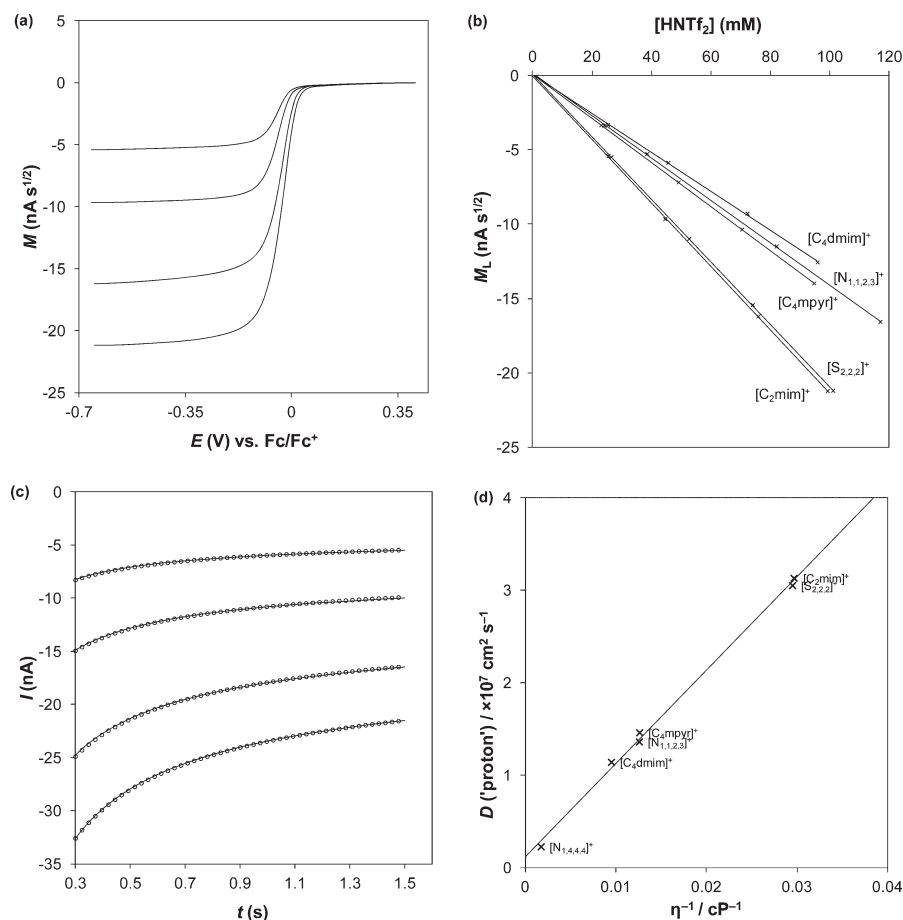


Figure 3. (a) Linear-sweep convolved current voltammograms obtained from the reduction of (from top to bottom) 25.4, 44.5, 75.8, and 99.2 mM H[NTf₂] in [C₂mim][NTf₂] at a 20 μm diameter Pt microdisk electrode with a scan rate of 100 mV s⁻¹. (b) Linear plots of the limiting convolved current (M_L) versus the concentration of H[NTf₂] in various ILs ($R^2 > 0.9995$). (c) Experimental (—) and Shoup-Szabo theoretical chronoamperograms (○) obtained from H[NTf₂] solutions outlined in (a) at a step potential of -0.54 V vs Fc/Fc⁺. (d) Linear plot of the “proton” diffusion coefficient vs the fluidity ($1/\eta$) of the medium ($R^2 = 0.998$).

The Volmer reaction (eq 9) was found to be the rate-determining step for the HER on Pt, also in agreement with the work by Compton and co-workers.^{7,8} Despite the fact that it has been well-established that the chemisorption of hydrogen atoms during the Volmer reaction (see eq 2) is an integral step during reductive H₂ evolution on Pt,^{9,11} adsorption was omitted in the simulations for the sake of simplicity, as it is difficult to obtain unique parameters when a large number of “unknowns” have to be included in the model (including adsorption would require assumptions about the adsorption isotherm). Consequently, the main discrepancy between the experimental and simulated data is in the hydrogen UPD region (explained above), as is evident in Figure 2. Although we have treated H* as a solution based (diffusing) species in the simulations, the diffusion coefficient employed (10^{-15} cm² s⁻¹) ensures that the diffusion layer thickness (for H*) is less than 5 nm on the timescale of a voltammetric experiment, so this species is essentially “surface confined”. In practice, the simulations were found to be insensitive to D_{H^*} when the value was set to below 10^{-10} cm² s⁻¹.

Finally, it is worth noting that although the mechanism represented by eqs 9 and 10 is in excellent agreement with the experimental data, the following alternative mechanism cannot be ruled out:



where the reactions given in eqs 11 and 12 correspond to the Volmer and Tafel equations, respectively (see eqs 2 and 3). This is because the proton reduction process is controlled by the first electron transfer step (i.e., $k_{s,1} \ll k_{s,2}$), which means that the second step is simply required to fulfill the stoichiometry requirements of the overall process (see eq 1), with no kinetic limitations. Indeed, the above mechanism was also found to be consistent with the experimental data over a wide range of conditions when eq 12 is treated as a homogeneous process with arbitrarily defined K_{eq} and k_f values (adsorption was omitted in the simulations as discussed above), as is shown in Figure S2 of the Supporting Information.

Table 2. Summary of D_{H^+} Measured Electrochemically Using Convolution Voltammetry (ConV) or Chronoamperometry with Shoup-Szabo Fitting (CA_{SS}) over a Bulk $H[NTf_2]$ Concentration Range of 25 to 100 mM, $D_{[NTf_2]^-}$ Measured Using PGSE-NMR and IL Viscosities

AIL	ConV/ D_{H^+} (10^{-7} cm ² s ⁻¹)	CA_{SS}/D_{H^+} (10^{-7} cm ² s ⁻¹)	$D_{[NTf_2]^-}$ (10^{-7} cm ² s ⁻¹)	$D_{H^+}/D_{[NTf_2]^-}$	η (mPa s)
[C ₂ mim][NTf ₂]	3.13 (± 0.07)	3.09 (± 0.06)	3.10	1.00	33.7
[S _{2,2,2}][NTf ₂]	3.06 (± 0.07)	2.96 (± 0.05)	2.99	0.99	33.9
[C ₄ mpyr][NTf ₂]	1.52 (± 0.03)	1.46 (± 0.08)	1.43	1.02	79.2
[N _{1,1,2,3}][NTf ₂]	1.41 (± 0.03)	1.36 (± 0.06)	1.38	0.99	79.4
[C ₄ dmim][NTf ₂]	1.19 (± 0.03)	1.14 (± 0.04)	1.08	1.06	105.2
[N _{1,4,4,4}][NTf ₂]	0.234 (± 0.005) [†]	0.226 (± 0.006)	0.225	1.00	572.7

[†]Estimated from 100 mM data set only.

Ultimately, the mechanism represented by eqs 9 and 10 was chosen as it avoids the inclusion of a physically insignificant homogeneous process (i.e., eq 12).

Proton Transport in Aprotic Ionic Liquids. D_{H^+} was quantified in each of the ILs using convolution voltammetry and chronoamperometry over a $H[NTf_2]$ concentration range of 25 to 100 mM. Linear sweep convoluted-current voltammograms obtained from $H[NTf_2]$ at a Pt microdisk electrode in [C₂mim][NTf₂] are shown in Figure 3a. The convoluted-current voltammograms superficially resemble steady-state voltammograms, being sigmoidal in shape with a well-defined mass transport limited plateau (M_L). Under purely diffusion-controlled conditions, M_L can be calculated as follows:

$$M_L = nAFC^b\sqrt{D} \quad (13)$$

On this basis, a plot of M_L versus C^b is expected to be linear, as is shown in Figure 3b. D_{H^+} was calculated from the slope of the M_L versus C^b plots, obtained by linear regression of the experimental data (in all cases, $R^2 \geq 0.9995$). D_{H^+} was also calculated using a chronoamperometric technique by fitting diffusion controlled $I-t$ curves obtained at a Pt microdisk electrode using the Shoup-Szabo approximation (see Figure 3c). The self-diffusion coefficient of the $[NTf_2]^-$ anion was also quantified in each of the 100 mM IL solutions using ¹⁹F PGSE-NMR. Mass transport data are summarized in Table 2. Unfortunately, in the investigated concentration range, the acidic proton did not give a well-defined ¹H resonance and thus no attempt was made to directly quantify D_{H^+} using PGSE-NMR.

D_{H^+} was found to be independent of the concentration of $H[NTf_2]$ in all of the investigated ILs. Additionally, the D_{H^+} value calculated using the two electrochemical methods are in excellent agreement, highlighting the value of the convolution method^{27–29} as an alternative to the well-established chronoamperometric method²⁶ for quantitation of D and/or nC^b in ILs. Furthermore, the electrochemically derived D_{H^+} values are almost identical to $D_{[NTf_2]^-}$ values measured using PGSE-NMR, evidenced by the $D_{H^+}/D_{[NTf_2]^-}$ ratio, which is close to unity in all of the investigated ILs. D_{H^+} , measured electrochemically, corresponds to the chemical species (i.e., the acid, HA), which diffuses to the electrode surface during the voltammetric perturbation and gives up a proton for reduction. During this measurement, the system is not at equilibrium, as diffusion occurs down a concentration gradient (induced by the voltammetric perturbation) within the diffusion layer adjacent to the electrode surface. On the other hand, $D_{[NTf_2]^-}$, measured by PGSE-NMR, corresponds to the average of all $[NTf_2]^-$ species in solution contributing to the ¹⁹F resonance ($H[NTf_2]$

and $[NTf_2]^-$ are not distinguishable by NMR). During this measurement, the system is at equilibrium, as diffusion is occurring in the absence of a concentration (or chemical potential) gradient. The coincidence between D_{H^+} and $D_{[NTf_2]^-}$ indicates that the electrochemically active protonated species (i.e., "HA") must be $H[NTf_2]$. Therefore, the hydrogen evolution reaction in this media is thought to be a CE process:



where proton reduction (eq 14) is preceded by a chemical dissociation step (eq 15). The diffusion-controlled responses obtained with convolution voltammetry and chronoamperometry indicates that the dissociation step is not limiting on the voltammetric timescale. Although $H[NTf_2]$ is a superacid and would therefore readily dissociate in an aqueous environment (to form $[NTf_2]^-$ and H_3O^+), no such reaction is possible in a dry AIL. There has so far been no evidence to indicate the existence of "solvated protons" in IL media (i.e., an IL- H^+ species comparable to H_3O^+).³⁶ As a result, the protons remain associated with the anion part of the IL, and the strongest acid that can possibly exist in a $[NTf_2]^-$ IL is therefore $H[NTf_2]$.³⁷

The diffusivity of a solute in solution is inversely proportional to the frictional force acting upon it:

$$D = \frac{k_B T}{f} \quad (16)$$

This is a form of the Einstein-relation, where k_B is the Boltzmann constant, T is the absolute temperature, and f is a friction coefficient.³⁸ By likening the dissolved solute to a rigid solid sphere with a radius, r_H , diffusing in a continuum of solvent with a viscosity, η , f can be calculated using Stokes-Law:^{39,40}

$$f = 4\pi\eta r_H + 2\pi\eta r_H = 6\pi\eta r_H \quad (17)$$

The first term represents a force due to pressure built up in front of a diffusing solute, and the second term is a frictional force parallel to its surface.^{39,41,42} Combining eqs 16 and 17 gives the Stokes–Einstein equation:³⁸

$$D = \frac{k_B T}{6\pi\eta r_H} \quad (18)$$

The Stokes–Einstein equation, as written in eq 18, is strictly only valid when the size of the solute is large compared to the size of the solvent (i.e., when $r_{\text{solute}}/r_{\text{solvent}} > 5$). To accommodate this fact, the Stokes–Einstein equation is often written in the form:

$$D = \frac{k_B T}{c \pi \eta r_H} \quad (19)$$

where c is a constant with a value of 4 (“perfect slip”) or 6 (“perfect stick”).³⁹ The value of 4 arises because the second term of eq 17 (arising from frictional force parallel to the solute surface) disappears when the solvent is able to “slip past” the surface of a small solute particle (typically when $r_{\text{solute}} < 0.5$ nm).^{39,43} In practice, an empirical constant with a value between 4 and 6 is often used for small solutes in conventional solvents^{39,41,42} and ionic liquids.^{44,45}

In any case, if it is assumed that the constant, c , and the Stokes radius of $\text{H}[\text{NTf}_2]$, r_H , does not vary between ILs, a plot of D versus $1/\eta$ is predicted to be linear, as is shown in Figure 3d. Evidently, the D versus $1/\eta$ plot is linear and probably passes through the origin, within experimental error. The adherence of proton transport to the Stokes–Einstein equation and the fact that D_{H^+} is independent of $\text{H}[\text{NTf}_2]$ concentration indicates that a Grotthuss-type mechanism (discussed below) is not operating in the investigated ILs. The value of r_H , calculated from the slope of the D versus $1/\eta$ curve (obtained by linear regression of the experimental data) with $c = 6$ is 2.16 Å and with $c = 4$ is 3.24 Å. Ue³⁹ estimated the ionic radii of $[\text{NTf}_2]^-$ to be ~ 3.25 Å with molecular modeling and crystallographic data, which is in excellent agreement with the value calculated from our data, assuming $c = 4$. Interestingly, Ue also concluded that $[\text{NTf}_2]^-$ and a range of other similarly sized anions approached behavior for perfect slip ($c = 4$) in propylene carbonate (PC), a solvent which is of a comparable size ($r = 2.76$ Å) to the $[\text{NTf}_2]^-$ anion; our data are also consistent with this finding.

As shown in Table 1, the diffusivity of H_2 in these AILs also qualitatively follows the D versus $1/\eta$ trend predicted by the Stokes–Einstein equation (D_{H_2} is consistently ~ 100 -fold higher than D_{H^+} in all of the AILs). This data has not been treated quantitatively because D_{H_2} was measured indirectly by double-step chronoamperometry, and there is significantly more uncertainty associated with the outcome of the fitting of the data. Interestingly, although the D versus $1/\eta$ trend is followed within this group of AILs, the relationship breaks down when comparing these data to conventional solvents, as the reported⁴³ diffusion coefficient of H_2 in water ($\eta = 0.89$ mPa s at 25 °C) is 4.50×10^{-5} cm² s⁻¹.

Hydrogen Evolution Reaction in a Protic Ionic Liquid.

Further investigations on the electro-reduction of $\text{H}[\text{NTf}_2]$ were carried out in the protic ionic liquid $[\text{N}_{\text{H},2,2,2}][\text{NTf}_2]$. As discussed above, PILs are formed through the transfer of a proton from a Brønsted acid (i.e., $\text{H}[\text{NTf}_2]$) to a Brønsted base (i.e., $[\text{N}_{2,2,2}]$) and, therefore, unlike AILs, have a proton available for hydrogen bonding.¹⁵ Cyclic voltammograms obtained from the electro-reduction of $\text{H}[\text{NTf}_2]$ at a Pt microdisk electrode in $[\text{N}_{\text{H},2,2,2}][\text{NTf}_2]$ are shown in Figure 4. The voltammetric response is analogous to that obtained in the previously investigated AILs, with a transient (peak-shaped) reduction process and a near steady-state (sigmoidal) oxidation one. Once again, there is an obvious hydrogen UPD region and the simulations revealed a H^+/H_2 formal potential approximately 30 mV negative of the Fc/Fc^+ process. D_{H^+} , measured by electrochemical methods, is equal to 2.28×10^{-7} cm² s⁻¹, which is as expected from the previously discussed D versus $1/\eta$ plot ($\eta = 54.1$ mPa s, see Figure 3d) and is once again,

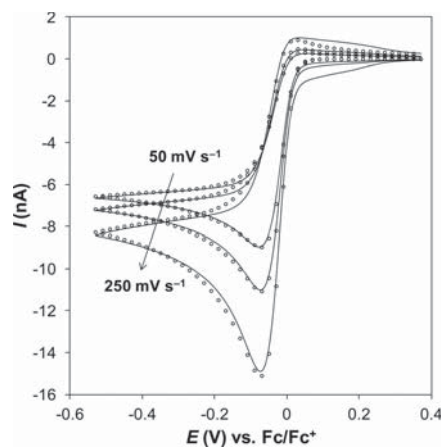


Figure 4. Comparison of simulated (○) and experimental (—) cyclic voltammograms obtained from the reduction of 51.2 mM $\text{H}[\text{NTf}_2]$ in $[\text{N}_{\text{H},2,2,2}][\text{NTf}_2]$ at a 20 μm diameter Pt microdisk electrode with scan rates of 250, 100, and 50 mV s^{-1} . Simulations were carried out using the mechanism shown in eqs 9 and 10 with the following parameters: $E_2^0 = E_1^0 = -0.032$ V, $\alpha_1 = \alpha_2 = 0.5$, $k_{s,1} = 0.0008$ cm s⁻¹, $k_{s,2} = 10000$ cm s⁻¹, $D(\text{H}^+) = 2.3 \times 10^{-7}$ cm² s⁻¹, $D(\text{H}_2) = 2.1 \times 10^{-5}$ cm² s⁻¹.

comparable to $D_{[\text{NTf}_2]^-}$, 2.19×10^{-7} cm² s⁻¹, measured using PGSE-NMR.

With respect to the $\text{H}[\text{NTf}_2]$ reduction mechanism and proton transport, there appears to be no difference between this PIL and the previously investigated AILs. This is unsurprising, considering $\text{H}[\text{NTf}_2]$ is a superacid, and therefore, complete proton transfer to $[\text{N}_{2,2,2}]$ would be expected.¹⁵ As a result, in a stoichiometric mixture of $\text{H}[\text{NTf}_2]$ and $[\text{N}_{2,2,2}]$, there are no free basic sites (i.e., unprotonated amine), which would potentially be required to facilitate proton hopping.^{23,24} It should be noted that the proton reduction response shown in Figure 4 is solely due to the $\text{H}[\text{NTf}_2]$ introduced into the neat $[\text{N}_{\text{H},2,2,2}][\text{NTf}_2]$. The proton on the amine, $[\text{N}_{\text{H},2,2,2}]^+$, can also be reduced; however, this species is a significantly weaker acid than $\text{H}[\text{NTf}_2]$ and therefore much more negative potentials (ca. -0.9 V vs Fc/Fc^+) must be reached before bulk proton reduction is observed (data not shown).

Hydrogen Evolution Reaction in Conventional Solvents. The electro-reduction of $\text{H}[\text{NTf}_2]$ was investigated in two conventional solvents: propylene carbonate (PC, cyclic voltammograms shown in Figure 5) and water (cyclic voltammograms shown in Figure 6). In both media, the supporting electrolyte contained the $[\text{NTf}_2]^-$ anion (0.85 M $[\text{C}_2\text{mim}][\text{NTf}_2]$ in PC and 0.5 M $\text{Li}[\text{NTf}_2]$ in water), the employed acid concentration was above 5 mM in order to minimize the obtrusiveness of the hydrogen UPD region, and the electrode was oxidatively preconditioned as previously discussed.

In PC, ΔE_p increases with an increasing scan rate, with values of 63.9, 69.8, 73.7, 85.7, and 94.0 mV at 50, 100, 250, 500, and 1000 mV s^{-1} , indicating the proton reduction process is quasi-reversible, analogous to what was obtained in the IL media. Assuming the formal potential of the Fc/Fc^+ process is solvent-independent,^{46,47} the proton reduction wave is shifted to more negative potentials in PC compared to the ILs. This is unsurprising, since the strength of an acid is strongly dependent upon the properties of the solvent (i.e., donor number and

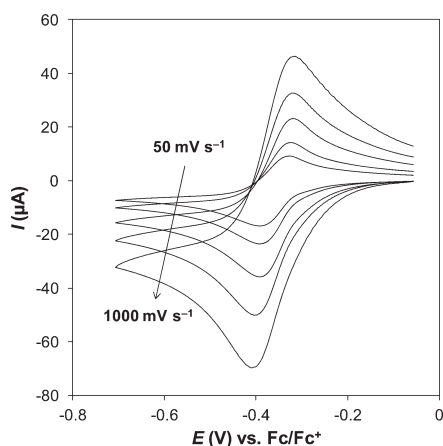


Figure 5. Cyclic voltammograms obtained from the reduction of 9.28 mM H[NTf₂] in propylene carbonate (+0.85 M [C₂mim][NTf₂]) at a 1.6 mm diameter Pt macrodisk electrode with scan rates of 1000, 500, 250, 100, and 50 mV s⁻¹.

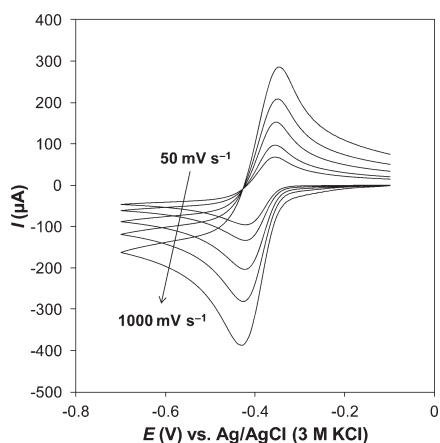


Figure 6. Cyclic voltammograms obtained from the reduction of 8.56 mM H[NTf₂] in water (+0.5 M Li[NTf₂]) at a 1.6 mm diameter Pt macrodisk electrode with scan rates of 1000, 500, 250, 100, and 50 mV s⁻¹.

dielectric constant),³⁷ which are likely to be quite different in these physicochemically disparate solvents. D_{H^+} , measured with

electrochemistry, is equal to $2.56 \times 10^{-6} \text{ cm}^2 \text{ s}^{-1}$, an order of magnitude higher than that recorded in the ILs (see Table 2). Extrapolating the previous D versus $1/\eta$ plot (see Figure 3d) to the viscosity of this medium ($\eta = 3.8 \text{ mPa s}$) gives a diffusion coefficient of $\sim 2.7 \times 10^{-6} \text{ cm}^2 \text{ s}^{-1}$, in good agreement with the experimentally determined value. In addition, D_{H^+} is comparable to $D_{[\text{NTf}_2]^-}$, $2.82 \times 10^{-7} \text{ cm}^2 \text{ s}^{-1}$, measured using PGSE-NMR. These results suggest that the acid, H[NTf₂], remains undissociated when dissolved in PC (i.e., the proton is not “solvated”).

In water, ΔE_p also increases with an increasing scan rate, with values of 65.9, 65.8, 71.8, 75.7, and 85.7 mV at 50, 100, 250, 500, and 1000 mV s⁻¹. The measured currents are an order of magnitude higher than those in PC, reflecting the exceptionally high value for D_{H^+} , $6.47 \times 10^{-5} \text{ cm}^2 \text{ s}^{-1}$, which is comparable to the reported value of $8.0 \times 10^{-5} \text{ cm}^2 \text{ s}^{-1}$.⁴⁸ D_{H^+} is much higher than that predicted by extrapolating the D versus $1/\eta$ plot to a viscosity of 1.05 mPa s, $\sim 9.6 \times 10^{-6} \text{ cm}^2 \text{ s}^{-1}$ (which is comparable to $D_{[\text{NTf}_2]^-}$ in this medium, $1.08 \times 10^{-5} \text{ cm}^2 \text{ s}^{-1}$, measured using PGSE-NMR). This is not surprising, since H[NTf₂] is a superacid, it readily dissociates in aqueous media, and therefore the diffusing species is H₃O⁺ not H[NTf₂]. In addition, it is thought that proton conduction in aqueous solution occurs by a combination of a vehicle mechanism (i.e., viscous drift of H₃O⁺) and the Grotthuss mechanism (homogeneous exchange between H₃O⁺ and H₂O), leading to enhanced mass transfer.²

All of the mass transport data discussed in this work are summarized in Table 3. If it is assumed that the constant, c , and Stokes radius, r_{H^+} are the same in all of the investigated electrolyte media, the Stokes–Einstein equation (see eq 19) predicts that the product of the diffusion coefficient and medium viscosity ($D \cdot \eta$, see Table 3) should be solvent independent. $D_{[\text{NTf}_2]^-} \cdot \eta$ is relatively constant (within experimental error) in all of the investigated media, with an average value of $\sim 1.12 \times 10^{-12} \text{ N}$. This implies that the Stokes radius of [NTf₂]⁻ is constant, and is therefore unaffected by the high ionic strength environment of ILs or the solvating properties of PC and H₂O. $D_{\text{H}^+} \cdot \eta$ is relatively constant in all of the ILs and the PC-based electrolyte, with an average value of $\sim 1.13 \times 10^{-12} \text{ N}$, reflecting that the diffusing protonated species (i.e., H[NTf₂]) is the same in all of the aforementioned electrolytes. The unusually high diffusion coefficient of protons in water (reflected by the unusually high $D_{\text{H}^+} \cdot \eta$ value, $6.80 \times 10^{-12} \text{ N}$) can be explained by proton hopping between H₃O⁺ and H₂O via the well-known Grotthuss mechanism,^{2,49} which is facilitated by the strong hydrogen-bonding network present

Table 3. Summary of Solvent (Electrolyte) Viscosities, D_{H^+} (Determined with Electrochemistry) and $D_{[\text{NTf}_2]^-}$ (Determined with PGSE-NMR)

solvent	supporting electrolyte	η (mPa s)	D_{H^+} ($10^{-7} \text{ cm}^2 \text{ s}^{-1}$)	$D_{\text{H}^+} \cdot \eta$ (10^{-12} N)	$D_{[\text{NTf}_2]^-}$ ($10^{-7} \text{ cm}^2 \text{ s}^{-1}$)	$D_{[\text{NTf}_2]^-} \cdot \eta$ (10^{-12} N)
[C ₂ mim][NTf ₂]	–	33.7	3.13	1.05	3.10	1.04
[S _{2,2,2}][NTf ₂]	–	33.9	3.05	1.03	2.99	1.01
[C ₄ mpyr][NTf ₂]	–	79.2	1.46	1.16	1.43	1.13
[N _{1,1,2,3}][NTf ₂]	–	79.4	1.36	1.08	1.38	1.10
[C ₄ dmim][NTf ₂]	–	105.2	1.14	1.19	1.08	1.14
[N _{1,4,4,4}][NTf ₂]	–	572.7	0.226	1.29	0.225	1.29
[N _{4,2,2,2}][NTf ₂]	–	54.1	2.28	1.23	2.19	1.18
propylene carbonate	0.85 M [C ₂ mim][NTf ₂]	3.8	25.6	0.97	28.2	1.07
water	0.5 M Li[NTf ₂]	1.05	647	6.80	108	1.13

in this type of media. Evidently, an analogous mechanism is not operating in any of the investigated ILs or PC.

Increasing the rate of proton conduction would be beneficial in terms of the performance of any electrochemical devices (i.e., PEMFCs). Evidently, the ILs investigated in this study are a long way from reaching the performance of aqueous electrolytes, with proton diffusivity being >100 faster in the latter compared to the former. Nonetheless, this study provides the groundwork for further investigations on the proton reduction mechanism, proton activity (pK_a), and proton conduction in ILs, which will be addressed in future publications. It is worth noting that a positive deviation from the D versus $1/\eta$ plot (see Figure 3d) will be particularly useful in identifying additional contributions to proton transport (i.e., Grotthuss-type proton hopping) or “enhanced mass transport”, possibly achieved through the inclusion of molecular additives such as water in the acid/IL mixture.

CONCLUSIONS

Electrochemical proton reduction and proton transport have been investigated in six aprotic ionic liquids, $[C_2mim][NTf_2]$, $[C_4mpyr][NTf_2]$, $[C_4dmim][NTf_2]$, $[S_{2,2,2}][NTf_2]$, $[N_{1,1,2,3}][NTf_2]$, and $[N_{1,4,4,4}][NTf_2]$; a protic ionic liquid, $[N_{H,2,2,2}][NTf_2]$; an aprotic solvent, propylene carbonate; and a protic solvent, water. Using $H[NTf_2]$ as the proton source, it was found that proton reduction is very sensitive to the surface-state of the platinum electrode, requiring preconditioning at oxidative potentials to achieve a well-defined and reproducible cyclic voltammetric response. Computational simulations revealed that the Volmer reaction is the rate-determining step for the hydrogen evolution reaction in AIL media and that the formal potential of the H^+/H_2 couple is essentially insensitive to the identity of the AIL cation. The electrode reaction mechanism and H^+/H_2 formal potential were found to be analogous in the PIL, $[N_{H,2,2,2}][NTf_2]$.

Proton transport in the investigated ILs was found to obey the Stokes–Einstein equation, with the constant, ζ , taking the value of 4 due to the comparable size of the “solute” and “solvent” (i.e., perfect “slip” behavior) and correlation with $[NTf_2]^-$ self-diffusion data collected with PGSE-NMR indicated that $H[NTf_2]$ is not dissociated in this environment (i.e., the protons diffuse as $H[NTf_2]$). Proton transport in propylene carbonate was also found to closely follow the same Stokes–Einstein relationship, indicating that $H[NTf_2]$ is not dissociated or solvated in this environment. Proton transport in water on the other hand did not obey the same Stokes–Einstein relationship, being much faster than predicted based on the viscosity of this medium due to the well-established Grotthuss mechanism. Although our results have revealed that in terms of proton transport, ILs are a long way from reaching the performance of water-based electrolytes, this work has laid the foundation for further studies on proton reduction, activity, and transport in ILs; the ultimate goal would be to develop an IL formulation which facilitates facile anhydrous proton conduction over a large temperature range.

ASSOCIATED CONTENT

Supporting Information

In situ optical micrograph of a H_2 bubble formed on a Pt surface during H^+ reduction at elevated $H[NTf_2]$ concentrations (Figure S1), cyclic voltammetric experiment/simulation comparisons for alternative proton reduction mechanisms in $[C_2mim][NTf_2]$ (Figures S2 and S3), double-step

chronoamperogram used to estimate the diffusivity of H_2 in $[C_2mim][NTf_2]$ (Figure S4), and cyclic voltammetric experiment/simulation comparisons carried out for $H[NTf_2]$ reduction in $[C_4mpyr][NTf_2]$ (Figure S5), $[S_{2,2,2}][NTf_2]$ (Figure S6), $[C_4dmim][NTf_2]$ (Figure S7), $[N_{1,1,2,3}][NTf_2]$ (Figure S8), and $[N_{1,4,4,4}][NTf_2]$ (Figure S9). This material is available free of charge via the Internet at <http://pubs.acs.org>.

AUTHOR INFORMATION

Corresponding Authors



Notes

The authors declare no competing financial interest.

ACKNOWLEDGMENTS

The authors thank Dr. Thomas R  ther for assistance in preparing $[N_{1,4,4,4}][NTf_2]$ and $[N_{H,2,2,2}][NTf_2]$ and Dr. Roger Mulder for performing the PGSE-NMR experiments.

REFERENCES

- Migliore, A.; Polizzi, N. F.; Therien, M. J.; Beratan, D. N. Biochemistry and Theory of Proton-Coupled Electron Transfer. *Chem. Rev.* **2014**, *114*, 3381–3465.
- Kreuer, K. D. Proton Conductivity: Materials and Applications. *Chem. Mater.* **1996**, *8*, 610–641.
- Mikkelsen, M.; Jorgensen, M.; Krebs, F. C. The Teraton Challenge. A Review of Fixation and Transformation of Carbon Dioxide. *Energy Environ. Sci.* **2010**, *3*, 43–81.
- Arico, A. S.; Srinivasan, S.; Antonucci, V. DMFCs: From Fundamental Aspects to Technology Development. *Fuel Cells* **2001**, *1*, 133–161.
- Bard, A. J.; Fox, M. A. Artificial Photosynthesis: Solar Splitting of Water to Hydrogen and Oxygen. *Acc. Chem. Res.* **1995**, *28*, 141–145.
- Barrette, W. C.; Sawyer, D. T. Determination of Dissolved Hydrogen and Effects of Media and Electrode Materials on the Electrochemical Oxidation of Molecular-Hydrogen. *Anal. Chem.* **1984**, *56*, 653–657.
- Meng, Y.; Aldous, L.; Belding, S. R.; Compton, R. G. The Hydrogen Evolution Reaction in a Room Temperature Ionic Liquid: Mechanism and Electrocatalyst Trends. *Phys. Chem. Chem. Phys.* **2012**, *14*, 5222–5228.
- Meng, Y.; Aldous, L.; Belding, S. R.; Compton, R. G. The Formal Potentials and Electrode Kinetics of the Proton/Hydrogen Couple in Various Room Temperature Ionic Liquids. *Chem. Commun.* **2012**, *48*, 5572–5574.
- Kibler, L. A. Hydrogen Electrocatalysis. *ChemPhysChem* **2006**, *7*, 985–991.
- Jaworski, A.; Donten, M.; Stojek, Z.; Osteryoung, J. G. Conditions of Strict Voltammetric Reversibility of the H^+/H_2 Couple at Platinum Electrodes. *Anal. Chem.* **1999**, *71*, 243–246.
- Conway, B. E.; Tilak, B. V. Interfacial Processes Involving Electrocatalytic Evolution and Oxidation of H_2 , and the Role of Chemisorbed H. *Electrochim. Acta* **2002**, *47*, 3571–3594.
- Bard, A. J.; Faulkner, L. R. *Electrochemical Methods: Fundamentals and Applications*, 2nd ed.; Wiley: New York, 2001.
- Rieger, P. H. *Electrochemistry*, 2nd ed.; Chapman & Hall: New York, 1994.
- Litster, S.; McLean, G. PEM Fuel Cell Electrodes. *J. Power Sources* **2004**, *130*, 61–76.
- Greaves, T. L.; Drummond, C. J. Protic Ionic Liquids: Properties and Applications. *Chem. Rev.* **2008**, *108*, 206–237.
- Zhang, J. L.; Xie, Z.; Zhang, J. J.; Tanga, Y. H.; Song, C. J.; Navessin, T.; Shi, Z. Q.; Song, D. T.; Wang, H. J.; Wilkinson, D. P.;

Liu, Z. S.; Holdcroft, S. High Temperature PEM Fuel Cells. *J. Power Sources* **2006**, *160*, 872–891.

(17) Lee, S. Y.; Ogawa, A.; Kanno, M.; Nakamoto, H.; Yasuda, T.; Watanabe, M. Nonhumidified Intermediate Temperature Fuel Cells Using Protic Ionic Liquids. *J. Am. Chem. Soc.* **2010**, *132*, 9764–9773.

(18) Galinski, M.; Lewandowski, A.; Stepniak, I. Ionic Liquids as Electrolytes. *Electrochim. Acta* **2006**, *51*, 5567–5580.

(19) Belieres, J.-P.; Angell, C. A. Protic Ionic Liquids: Preparation, Characterization, and Proton Free Energy Level Representation. *J. Phys. Chem. B* **2007**, *111*, 4926–4937.

(20) Bautista-Martinez, J. A.; Tang, L.; Belieres, J. P.; Zeller, R.; Angell, C. A.; Friesen, C. Hydrogen Redox in Protic Ionic Liquids and a Direct Measurement of Proton Thermodynamics. *J. Phys. Chem. C* **2009**, *113*, 12586–12593.

(21) Nakamoto, H.; Watanabe, M. Bronsted Acid-Base Ionic Liquids for Fuel Cell Electrolytes. *Chem. Commun.* **2007**, 2539–2541.

(22) Silvester, D. S.; Aldous, L.; Hardacre, C.; Compton, R. G. An Electrochemical Study of the Oxidation of Hydrogen at Platinum Electrodes in Several Room Temperature Ionic Liquids. *J. Phys. Chem. B* **2007**, *111*, 5000–5007.

(23) Noda, A.; Susan, A. B.; Kudo, K.; Mitsushima, S.; Hayamizu, K.; Watanabe, M. Bronsted Acid-Base Ionic Liquids as Proton-conducting Nonaqueous Electrolytes. *J. Phys. Chem. B* **2003**, *107*, 4024–4033.

(24) Susan, M.; Noda, A.; Mitsushima, S.; Watanabe, M. Bronsted Acid-Base Ionic Liquids and Their Use as New Materials for Anhydrous Proton Conductors. *Chem. Commun.* **2003**, 938–939.

(25) Gritzner, G.; Kuta, J. Recommendations on Reporting Electrode-Potentials in Nonaqueous Solvents. *Pure Appl. Chem.* **1984**, *56*, 461–466.

(26) Rogers, E. I.; Silvester, D. S.; Poole, D. L.; Aldous, L.; Hardacre, C.; Compton, R. G. Voltammetric Characterization of the Ferrocenyl Ferrocenium and Cobaltocenium/Cobaltocene Redox Couples in RTILs. *J. Phys. Chem. C* **2008**, *112*, 2729–2735.

(27) Mahon, P. J.; Oldham, K. B. Convolution Modelling of Electrochemical Processes Based on the Relationship Between the Current and the Surface Concentration. *J. Electroanal. Chem.* **1999**, *464*, 1–13.

(28) Bentley, C. L.; Bond, A. M.; Hollenkamp, A. F.; Mahon, P. J.; Zhang, J. Applications of Convolution Voltammetry in Electroanalytical Chemistry. *Anal. Chem.* **2014**, *86*, 2073–2081.

(29) Bentley, C. L.; Bond, A. M.; Hollenkamp, A. F.; Mahon, P. J.; Zhang, J. Electrode Reaction and Mass-Transport Mechanisms Associated with the Iodide/Triiodide Couple in the Ionic Liquid 1-Ethyl-3-methylimidazolium Bis(trifluoromethanesulfonyl)imide. *J. Phys. Chem. C* **2014**, *118*, 22439–22449.

(30) Skoog, D. A.; West, D. M.; Holler, F. J.; Crouch, S. R. *Fundamentals of Analytical Chemistry*, 8th ed.; Thomson-Brooks/Cole: Belmont, CA, 2004.

(31) Zhao, C.; Bond, A. M.; Lu, X. Y. Determination of Water in Room Temperature Ionic Liquids by Cathodic Stripping Voltammetry at a Gold Electrode. *Anal. Chem.* **2012**, *84*, 2784–2791.

(32) Silvester, D. S.; Ward, K. R.; Aldous, L.; Hardacre, C.; Compton, R. G. The Electrochemical Oxidation of Hydrogen at Activated Platinum Electrodes in Room Temperature Ionic Liquids as Solvents. *J. Electroanal. Chem.* **2008**, *618*, 53–60.

(33) Meng, Y.; Aldous, L.; Compton, R. G. Electrochemistry of Hydrogen in the Room Temperature Ionic Liquid 1-Butyl-3-methylimidazolium Bis(trifluoromethylsulfonyl)imide: Dissolved Hydrogen “Lubricates” Diffusional Transport. *J. Phys. Chem. C* **2011**, *115*, 14334–14340.

(34) Klymenko, O. V.; Wadhawan, J. D.; Hardacre, C.; Seddon, K. R. Voltammetry of Oxygen in the Room-Temperature Ionic Liquids 1-Ethyl-3-methylimidazolium Bis((trifluoromethyl)sulfonyl)imide and Hexyltriethylammonium Bis((trifluoromethyl)sulfonyl)imide: One-Electron Reduction To Form Superoxide. Steady-State and Transient Behavior in the Same Cyclic Voltammogram Resulting from Widely Different Diffusion Coefficients of Oxygen and Superoxide. *J. Phys. Chem. A* **2003**, *107*, 8872–8878.

(35) Klymenko, O. V.; Evans, R. G.; Hardacre, C.; Svir, I. B.; Compton, R. G. Double Potential Step Chronoamperometry at Microdisk Electrodes: Simulating the Case of Unequal Diffusion Coefficients. *J. Electroanal. Chem.* **2004**, *571*, 211–221.

(36) MacFarlane, D. R.; Pringle, J. M.; Johansson, K. M.; Forsyth, S. A.; Forsyth, M. Lewis Base Ionic Liquids. *Chem. Commun.* **2006**, 1905–1917.

(37) Barhdadi, R.; Troupel, M.; Comminges, C.; Laurent, M.; Doherty, A. Electrochemical Determination of pK(a) of N-Bases in Ionic Liquid Media. *J. Phys. Chem. B* **2012**, *116*, 277–282.

(38) Atkins, P. W.; De Paula, J. *Atkins' Physical Chemistry*, 9th ed.; Oxford University Press: Oxford, 2010.

(39) Ue, M. Mobility and Ionic Association of Lithium and Quaternary Ammonium Salts in Propylene Carbonate and γ -Butyrolactone. *J. Electrochem. Soc.* **1994**, *141*, 3336–3342.

(40) Robinson, R. A.; Stokes, R. H. *Electrolyte Solutions. The Measurement and Interpretation of Conductance, Chemical Potential and Diffusion in Solutions of Simple Electrolytes*, 2nd ed.; Butterworths Scientific Publications: London, 1959.

(41) Matsuura, N.; Umamoto, K.; Takeda, Y. Formulation of Stokes Radii in DMF, DMSO and Propylene Carbonate with Solvent Structure Cavity Size as Parameter. *Bull. Chem. Soc. Jpn.* **1975**, *48*, 2253–2257.

(42) Edward, J. T. Molecular Volumes and Stokes-Einstein Equation. *J. Chem. Educ.* **1970**, *47*, 261–270.

(43) Cussler, E. L. *Diffusion: Mass Transfer in Fluid Systems*, 3rd ed.; Cambridge University Press: New York, 2009.

(44) Tokuda, H.; Hayamizu, K.; Ishii, K.; Susan, M. A. B. H.; Watanabe, M. Physicochemical Properties and Structures of Room Temperature Ionic Liquids. 2. Variation of Alkyl Chain Length in Imidazolium Cation. *J. Phys. Chem. B* **2005**, *109*, 6103–6110.

(45) Hapiot, P.; Lagrost, C. Electrochemical Reactivity in Room-Temperature Ionic Liquids. *Chem. Rev.* **2008**, *108*, 2238–2264.

(46) Stojanovic, R. S.; Bond, A. M. Examination of Conditions under Which the Reduction of the Cobaltocenium Cation Can Be Used as a Standard Voltammetric Reference Process in Organic and Aqueous Solvents. *Anal. Chem.* **1993**, *65*, 56–64.

(47) Hultgren, V. M.; Mariotti, A. W. A.; Bond, A. M.; Wedd, A. G. Reference Potential Calibration and Voltammetry at Macrodisk Electrodes of Metallocene Derivatives in the Ionic Liquid BMIM PF₆. *Anal. Chem.* **2002**, *74*, 3151–3156.

(48) Slevin, C. J.; Unwin, P. R. Lateral Proton Diffusion Rates along Stearic Acid Monolayers. *J. Am. Chem. Soc.* **2000**, *122*, 2597–2602.

(49) Grothuss, C. J. T. Sur la Décomposition de L'Eau et Des Corps qu'elle Tient en Dissolution à L'Aide de L'Électricité Galvanique. *Ann. Chim.* **1806**, *58*, 54–54.

Supporting information for

Mass Transport Studies and Hydrogen Evolution
at a Platinum Electrode Using
Bis(trifluoromethanesulfonyl)imide as the Proton
Source in Ionic Liquids and Conventional Solvents

*Cameron L. Bentley,^{†,‡} Alan M. Bond,[†] Anthony F. Hollenkamp,[‡] Peter J. Mahon[§] and Jie
Zhang[†]*

[†]School of Chemistry, Monash University, Clayton, Vic 3800, Australia

[‡]CSIRO Energy Flagship, Box 312, Clayton South, Vic 3169, Australia

[§]Faculty of Science, Engineering and Technology, Swinburne University of Technology,
Hawthorn, Vic 3122, Australia

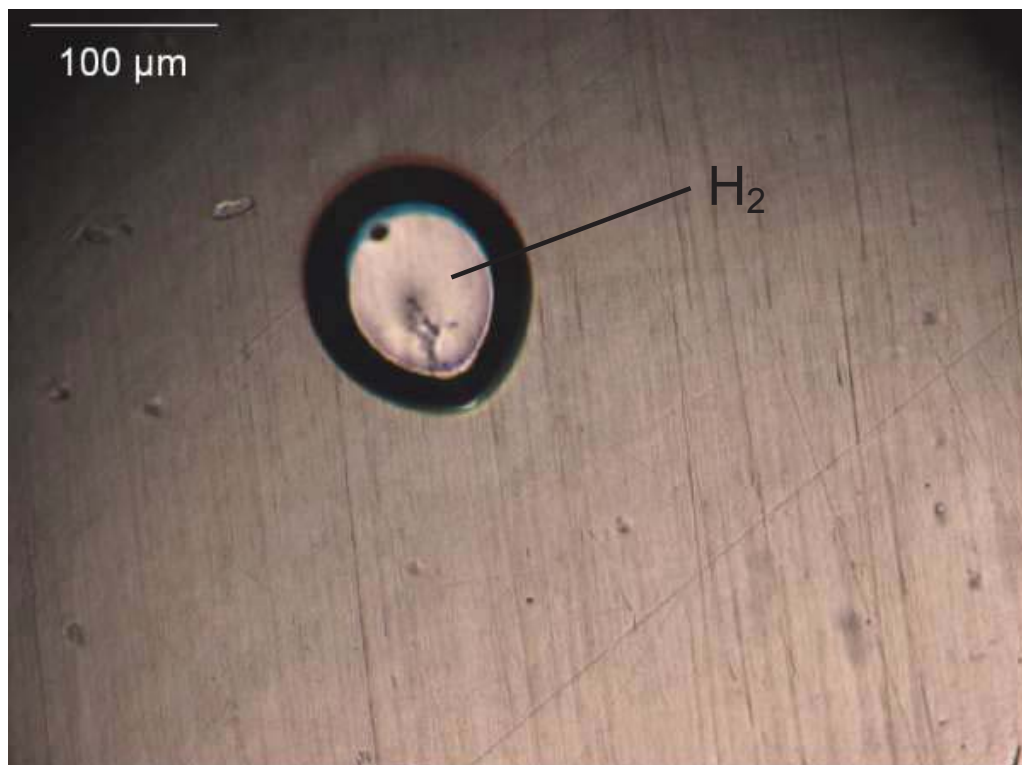


Figure S1. Optical micrograph (magnification = 100×) of the surface of a 1.6 mm dia. Pt macrodisk electrode taken *in situ* during the diffusion-controlled electro-reduction of 500 mM H[NTf₂] in [C₂mim][NTf₂].

Simulations: Alternative Mechanism 1



- 1st order in H⁺
- Homogeneous reaction (Eq. S2) has no physical significance
- Fictitiously large k_f required for reversible voltammetry

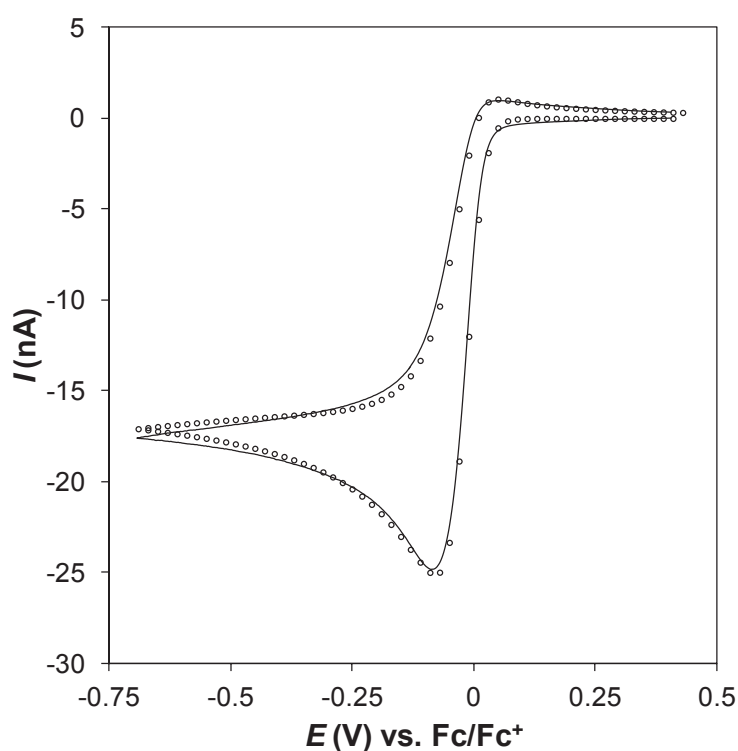


Figure S2. Comparison of a simulated (○) and experimental (—) cyclic voltammogram obtained for the reduction of 99.2 mM H[NTf₂] in [C₂mim][NTf₂] at a 20 μm dia. Pt microdisk electrode with a scan rate of 100 mV s⁻¹. The simulation was performed using the mechanism outlined by Eqs. S1 and S2, with the following parameters: $E^0 = -0.148$ V, $k_s = 0.02$ cm s⁻¹, $\alpha = 0.5$, $K_{\text{eq}} = 10^4$, $k_f = 10^{14}$ M⁻¹ s⁻¹. Diffusion coefficients are outlined in Table 1.

S3

Simulations: Alternative Mechanism 2



- 2nd order in H⁺
- Poor fit at different concentrations
- Poor fit at high scan rates

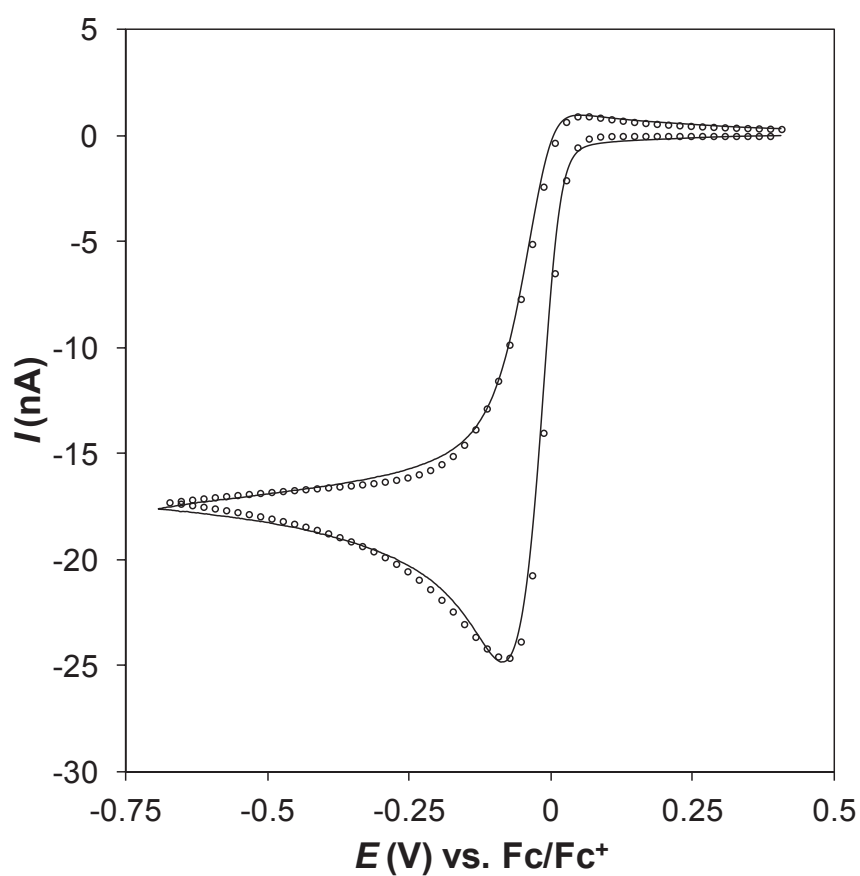


Figure S3. Comparison of a simulated (○) and experimental (—) cyclic voltammogram obtained for the reduction of 99.2 mM H[NTf₂] in [C₂mim][NTf₂] at a 20 μm dia. Pt microdisk electrode with a scan rate of 100 mV s⁻¹. The simulation was performed using the mechanism outlined by Eq. S3, with the following parameters: $E^0 = -0.03$ V, $k_s = 0.012$ cm s⁻¹, $\alpha = 0.5$. Diffusion coefficients are outlined in Table 1.

S4

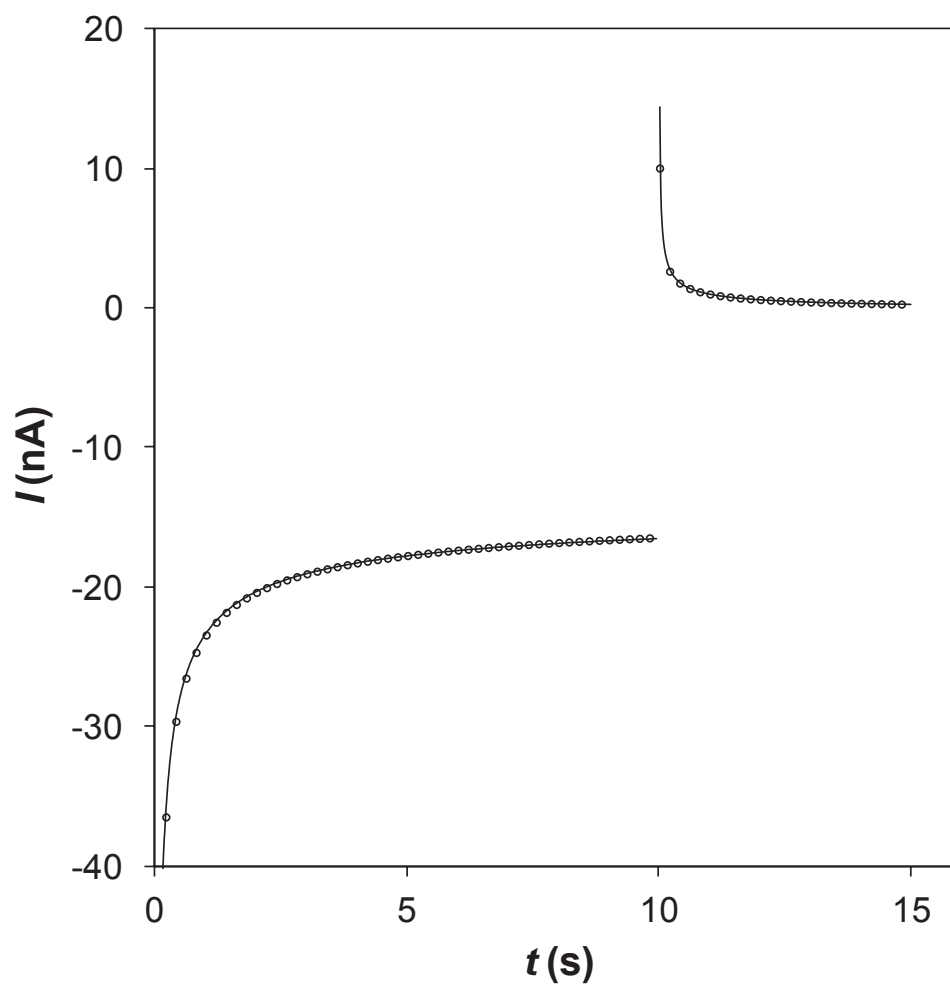


Figure S4. Comparison of the simulated (\circ) and experimental ($—$) chronoamperograms for the reduction of 99.2 mM H[NTf₂] in [C₂mim][NTf₂] at a 20 μ m dia. Pt microdisk electrode with step potentials of -0.54 V vs. Fc/Fc⁺ (10 sec) and 0.41 V vs. Fc/Fc⁺ (5 sec). The simulation was performed using the mechanism outlined by Eqs. 9 and 10 and the parameters in Table 1.

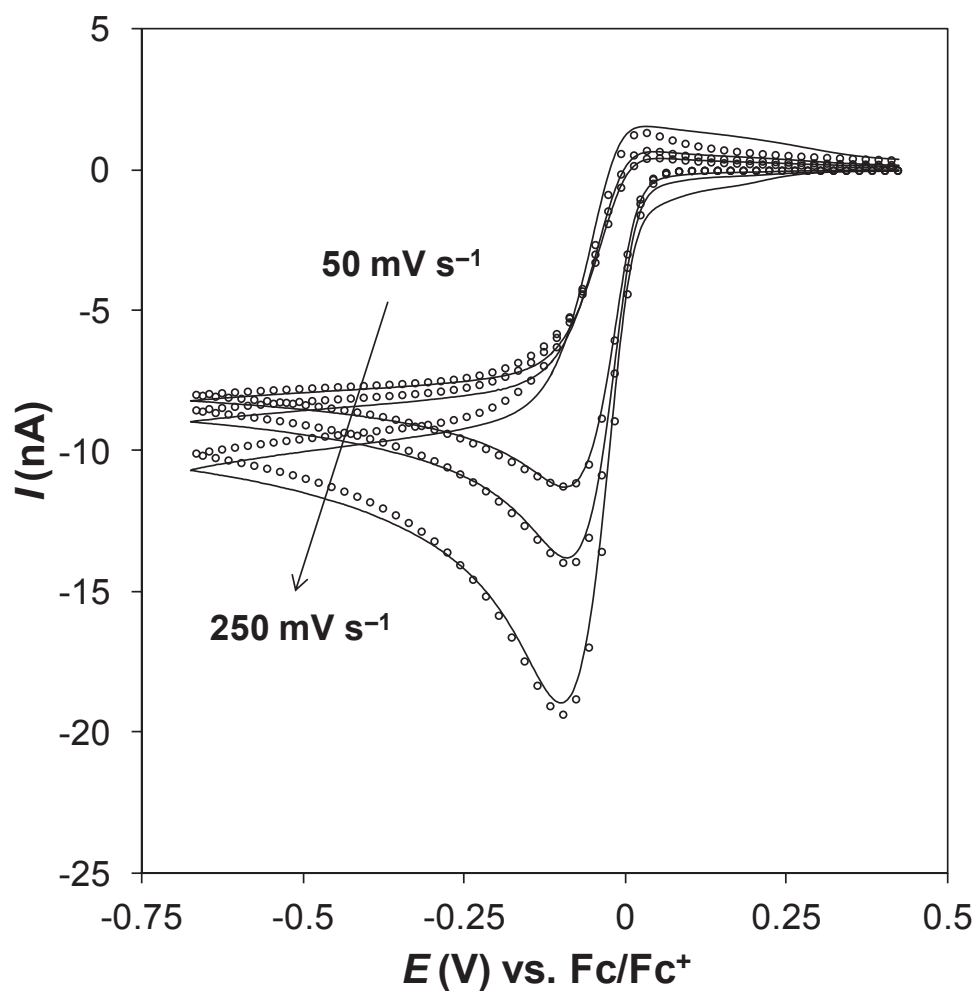


Figure S5. Comparison of simulated (\circ) and experimental (—) cyclic voltammograms obtained from the reduction of 94.6 mM $\text{H}[\text{NTf}_2]$ in $[\text{C}_4\text{mpyr}][\text{NTf}_2]$ at a 20 μm dia. Pt microdisk electrode with scan rates of 250, 100 and 50 mV s^{-1} . The simulation was performed using the mechanism outlined by Eqs. 9 and 10 and the parameters in Table 1.

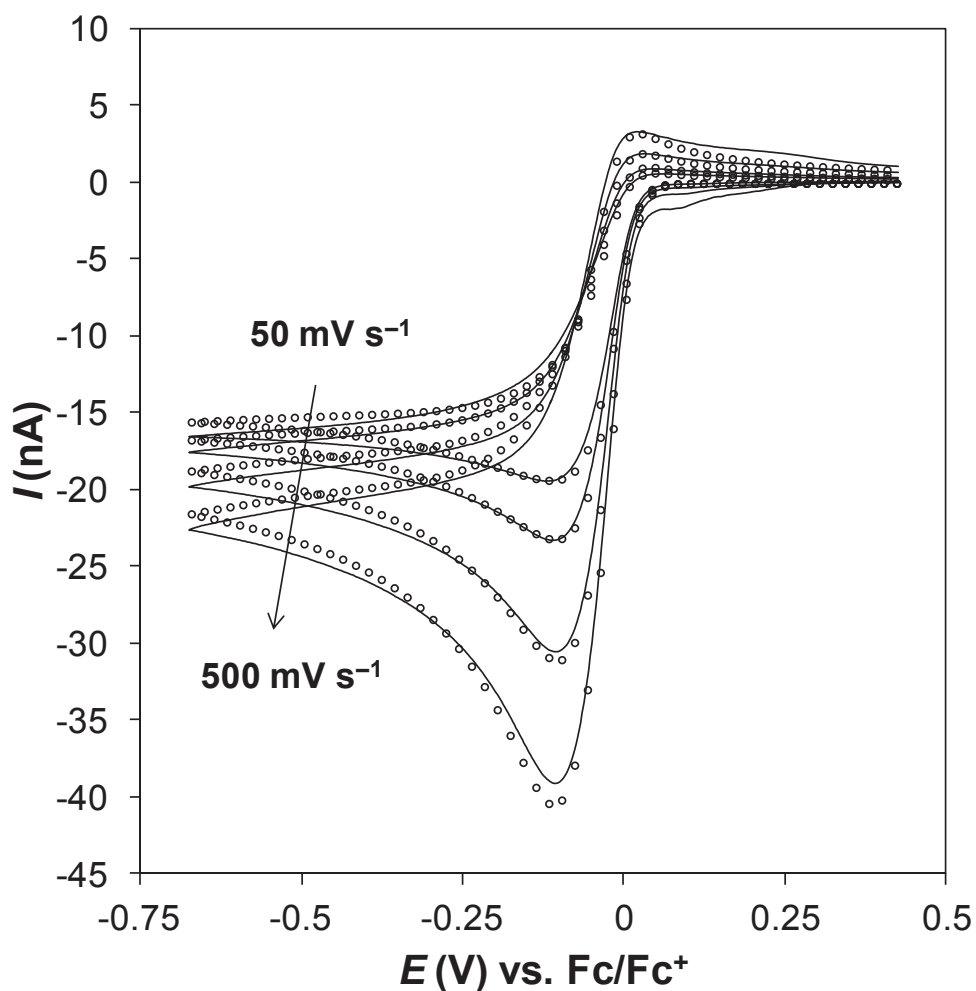


Figure S6. Comparison of simulated (\circ) and experimental ($—$) cyclic voltammograms obtained from the reduction of 100.2 mM $\text{H}[\text{NTf}_2]$ in $[\text{S}_{2,2,2}][\text{NTf}_2]$ at a 20 μm dia. Pt microdisk electrode with scan rates of 500, 250, 100 and 50 mV s^{-1} . The simulation was performed using the mechanism outlined by Eqs. 9 and 10 and the parameters in Table 1.

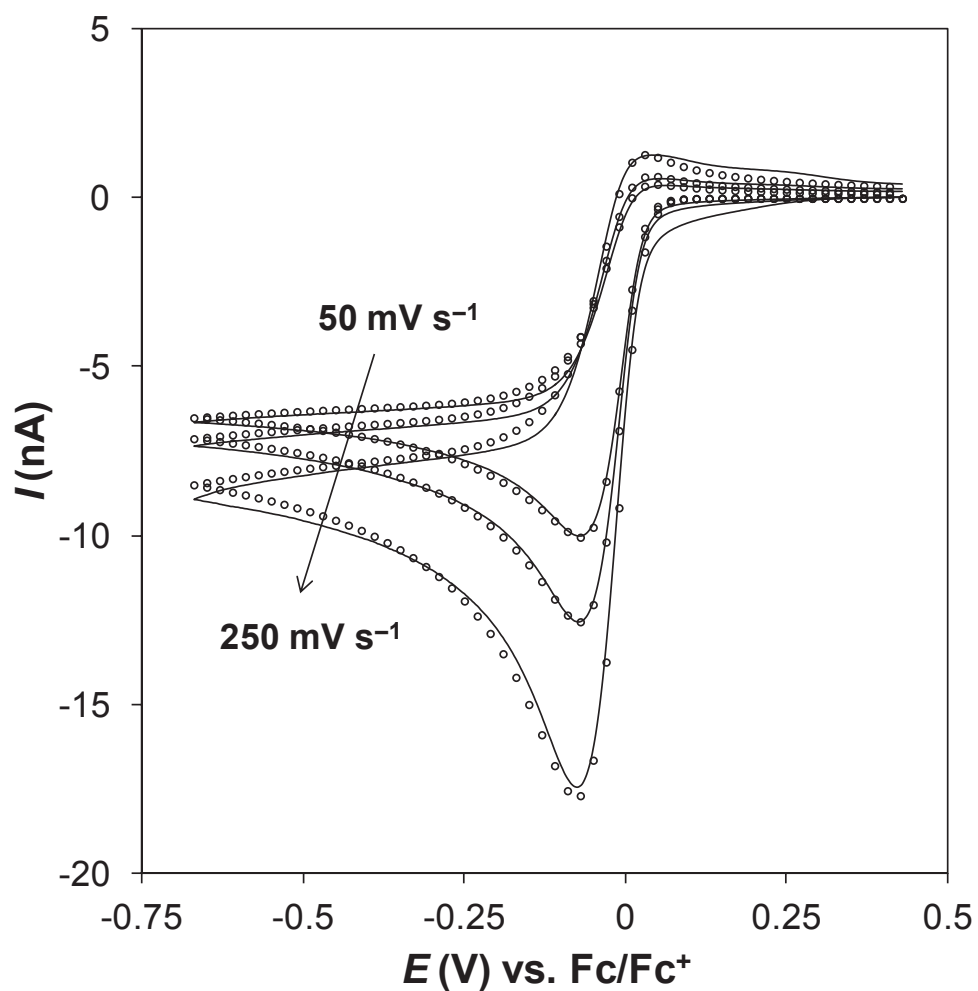


Figure S7. Comparison of simulated (\circ) and experimental ($—$) cyclic voltammograms obtained from the reduction of 95.8 mM H[NTf₂] in [C₄dmim][NTf₂] at a 20 μ m dia. Pt microdisk electrode with scan rates of 250, 100 and 50 mV s^{-1} . The simulation was performed using the mechanism outlined by Eqs. 9 and 10 and the parameters in Table 1.

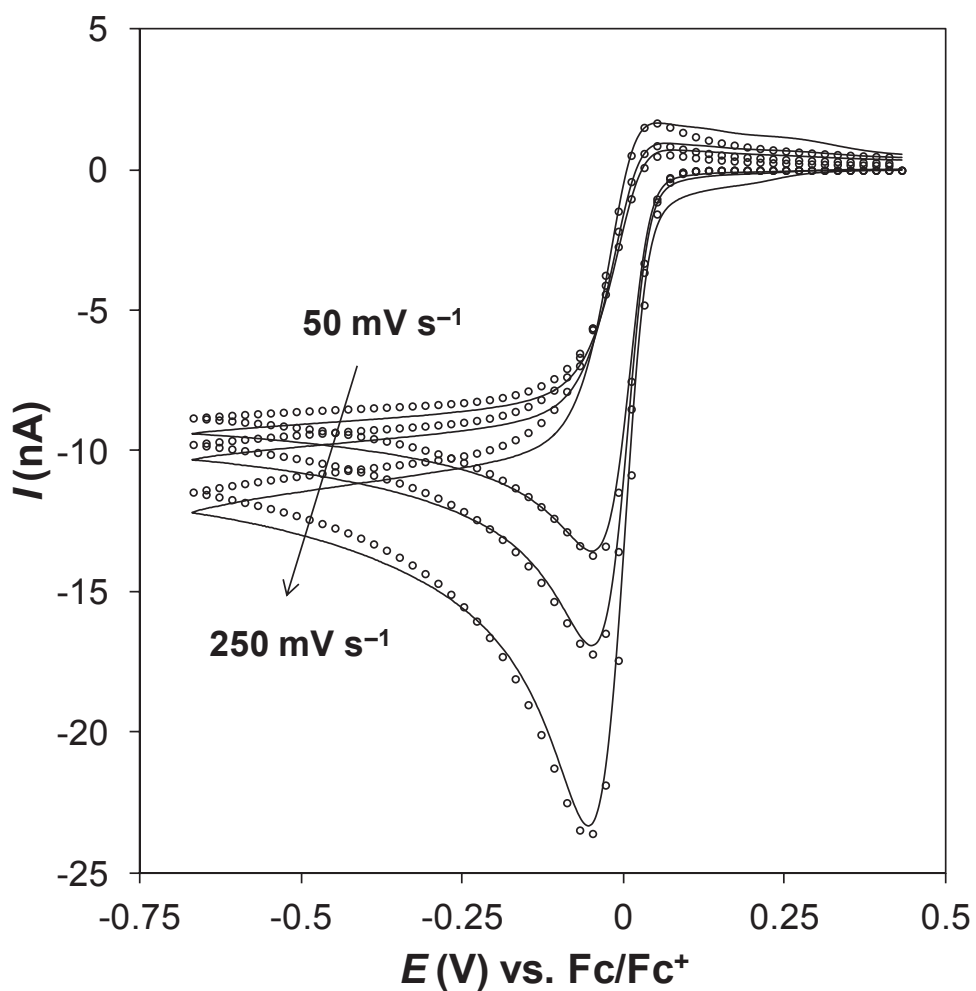


Figure S8. Comparison of simulated (\circ) and experimental ($—$) cyclic voltammograms obtained from the reduction of 116.9 mM H[NTf₂] in [N_{1,1,2,3}][NTf₂] at a 20 μ m dia. Pt microdisk electrode with scan rates of 250, 100 and 50 mV s^{-1} . The simulation was performed using the mechanism outlined by Eqs. 9 and 10 and the parameters in Table 1.

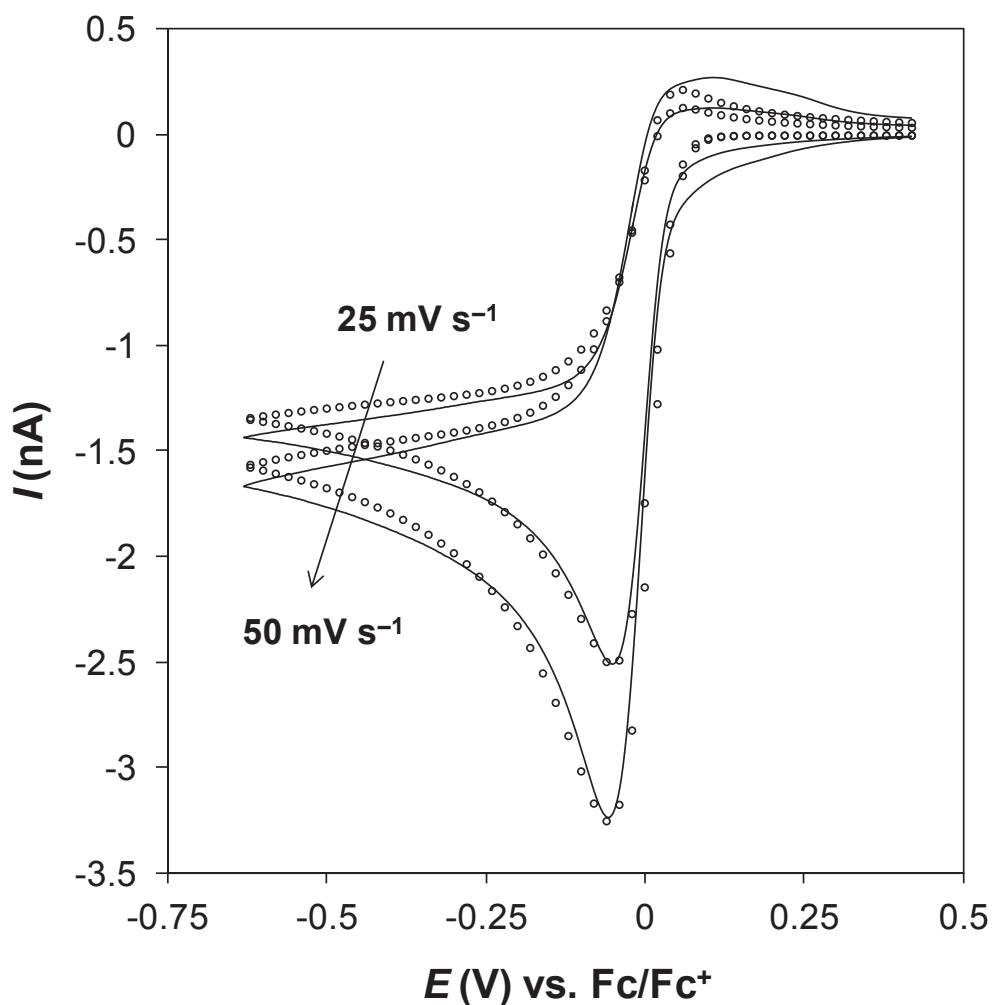


Figure S9. Comparison of simulated (\circ) and experimental ($—$) cyclic voltammograms obtained from the reduction of 91.1 mM $H[NTf_2]$ in $[N_{1,4,4,4}][NTf_2]$ at a 20 μm dia. Pt microdisk electrode with scan rates of 50 and 25 $mV s^{-1}$. The simulation was performed using the mechanism outlined by Eqs. 9 and 10 and the parameters in Table 1.

Electrochemical Proton Reduction and
Equilibrium Acidity (pK_a) in Aprotic Ionic
Liquids: Protonated Amines and Sulfonamide
Acids

*Cameron L. Bentley,^{†,‡} Alan M. Bond,[†] Anthony F. Hollenkamp,[‡] Peter J. Mahon[§] and Jie
Zhang[†]*

[†]School of Chemistry, Monash University, Clayton, Vic 3800, Australia

[‡]CSIRO Energy, Box 312, Clayton South, Vic 3169, Australia

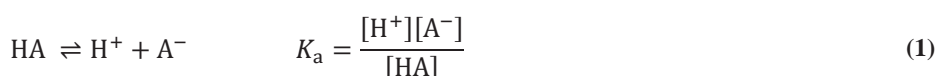
[§]Faculty of Science, Engineering and Technology, Swinburne University of Technology,
Hawthorn, Vic 3122, Australia

Abstract. Many organic compounds contain acidic and/or basic groups that dictate their physical, chemical and biological properties. For this reason, the acid dissociation constant, K_a , a quantitative measure of acid strength in solution, is a fundamentally important parameter in organic (synthetic) chemistry and related fields. In this study, the thermodynamics, kinetics and mechanisms of the proton reduction (hydrogen evolution) reaction at a platinum electrode have been investigated in the room temperature ionic liquid (IL) 1-ethyl-3-methylimidazolium bis(trifluoromethanesulfonyl)imide, [C₂mim][NTf₂], using a range of nitrogen (R_xNH) acids as the proton source. The formal potential of the H⁺/H₂ process (where H⁺ signifies a ‘solvated’ proton, *e.g.* H[NTf₂] in [C₂mim][NTf₂]) has been shown to be strongly dependent on the identity of the IL anion, making direct comparison of p*K*_a data between ILs with different constituent anions impossible. The H⁺/H₂ process has been simulated by combining the classical Volmer, H⁺ + e⁻ ⇌ H* and Tafel reactions, H* + H* ⇌ H₂, to give the overall reaction, H⁺ + e⁻ ⇌ ½H₂. Proton reduction (hydrogen evolution) from weak nitrogen acids (protonated amines, BH⁺, or neutral sulfonamides, HA) is a diffusion controlled process which occurs in the potential region negative of the H⁺/H₂ process. Simulations reveal that weak acid dissociation, HA (or BH⁺) ⇌ H⁺ + A⁻ (or B), is limiting on the voltammetric timescale when p*K*_a > 4, meaning proton reduction *via* a CE mechanism (where C is the acid dissociation step) cannot account for the experimentally observed mass-transport limited currents. Under these conditions, proton reduction must proceed *via* an alternate pathway, where the weak acid undergoes direct reduction at the platinum electrode surface, HA (or BH⁺) + e⁻ ⇌ ½H₂ + A⁻ (or B). Finally, the p*K*_a values for ten weak nitrogen acids have been calculated (5.2 < p*K*_a < 19.5) from voltammetrically derived reversible half wave potentials ($E_{1/2}$) and diffusion coefficients (D), highlighting the utility of voltammetry as a convenient and relatively straightforward method for quantifying equilibrium acidity.

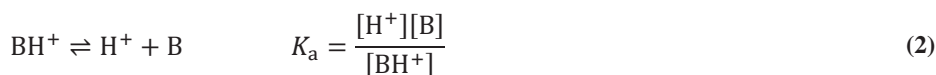
Keywords: hydrogen evolution reaction, voltammetry, acid dissociation constant, Brønsted acid/base

Introduction

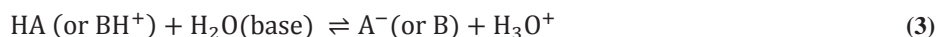
Some of the most important reactions in biology and chemistry involve one or more proton (H^+) transfer steps.¹⁻⁵ The acid dissociation constant (K_a) of a Brønsted acid, HA, formally defined as follows, is a quantitative measure of acid strength:



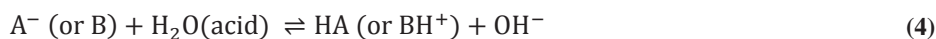
Although the acid is taken to be a neutral species (HA) in Eq. 1, the following equation is equally valid for a cationic acid species, BH^+ (*i.e.*, a protonated neutral base, B):



The concept of Brønsted acidity/basicity is well established in aqueous media⁶, where water, an amphoteric species, can act as a Brønsted base and accept a proton:



or as a Brønsted acid and donate a proton:



From Eq. 3, it is clear that the hydronium ion (also known as a hydrated/solvated proton), H_3O^+ , which has a pK_a of -1.74 (where $pK_a = -\log_{10}K_a$), is the strongest acid that can exist in aqueous solution. The process shown in Eq. 3 effectively ‘levels’ the acidity of all strong acids ($pK_a < -1.74$) in aqueous media and is the origin of the aqueous pK_a scale.^{7, 8}

Many organic compounds contain acidic and/or basic groups that dictate their physical, chemical and biological properties. Indeed, bond transformations in solution

frequently involve the cleavage or formation of 'R-H' bonds. As described above, pK_a describes the Gibbs energy of 'R-H' bond heterolysis, making it a critically important thermodynamic parameter in synthetic chemistry and related fields.⁹⁻¹¹ The equilibrium acidity (pK_a) is a solvent dependent parameter, being influenced by the ability of the solvent to solvate each of the species outlined in Eqs. 1 (HA, H⁺ and A⁻) or 2 (BH⁺, H⁺ and B). It follows that solvent acidity/basicity, dielectric properties and ability to donate/accept hydrogen bonds can all influence the pK_a of an acid in solution.^{11, 12} Although pK_a data is most readily available in water^{13, 14}, pK_a scales have been established in a range of non-aqueous solvents, including acetonitrile¹⁵, dimethylsulfoxide^{11, 16, 17} and 1,2-dichloroethane¹⁵. A variety of methods¹⁸ have been employed to quantify equilibrium acidities in conventional media, including potentiometry¹⁹, spectrophotometry^{11, 20} and voltammetry^{12, 16, 17}.

Air/water stable non-haloaluminate room temperature ionic liquids (ILs) have shown promise as replacements for volatile molecular solvents (such as those listed above) in a range of applications.²¹ ILs are typically composed of a bulky organic cation and an inorganic anion with extensive charge delocalization. They are often referred to as 'designer solvents' because their physicochemical properties can be 'tuned' to an extent by changing their constituent cation and/or anion.^{22, 23} Relatively strong electrostatic (cohesive) forces operate within ILs, which means they often tend to be highly viscous and non-volatile.²⁴ Protons released from the dissociation of a Brønsted acid in an IL must associate with (or be 'solvated' by) the most basic component of the IL, most commonly the anion (A_{IL}⁻):



where HA_{IL} is the strongest acid that may exist in a given IL. HA_{IL} effectively levels the acidity of strong acids in IL media, comparable to H₃O⁺ in aqueous media. In other words, HA_{IL} is origin of the pK_a scale in IL media and for this reason pK_a data are not directly

comparable between ILs with different constituent anions.^{7,9,10} From this point forward, ‘H⁺’ refers to the ‘solvated’ proton species and is equivalent to HA_{IL} in the context of ILs. Unfortunately, absolute p*K*_a data for weak acids in ILs are scarcely available.^{7,9,10}

It can be shown^{7,12,25} that the difference in the formal potential (E^0) of the HA/H₂ or BH⁺/H₂ couple and the H⁺/H₂ couple is proportional to the equilibrium acidity of HA or BH⁺ (*i.e.*, $\Delta E^0 \propto \text{p}K_a$). Therefore, in this study, we will employ electrochemical methods such as cyclic voltammetry²⁵ to probe the thermodynamics, kinetics and mechanisms of the H⁺/H₂ and HA/H₂ (or BH⁺/H₂) processes. The proton overall reduction reaction (or hydrogen evolution reaction, HER) is a conceptually simple process, involving the transfer of one electron per proton²⁶⁻³¹:



However, this reaction is subject to significant kinetic barriers, requiring an electrocatalyst to proceed at an economically viable rate.³² The HER has been most extensively studied in acidic aqueous media, where it is postulated to proceed *via* a combination of the following three elementary reactions^{27,29,32}:



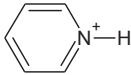
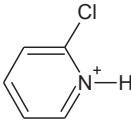
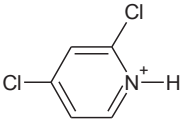
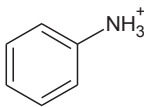
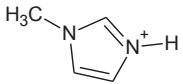
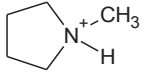
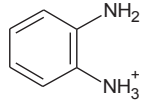
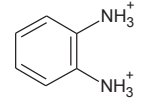
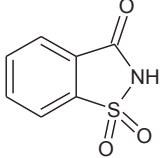
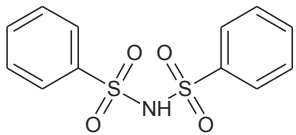
where H_{ads} is a chemisorbed hydrogen atom and Eqs. 7, 8 and 9 are known as the Volmer, Tafel and Heyrovsky reactions, respectively.²⁷ In a previous publication³³, we investigated the proton reduction reaction at a platinum electrode in a range of bis(trifluoromethanesulfonyl)imide ILs using H[NTf₂] as the proton source (*i.e.*, the H⁺/H₂ process). Our results indicated that the Volmer reaction (Eq. 7) is the rate determining step

for the HER in the IL media and that $E^0(\text{H}^+/\text{H}_2)$ is essentially insensitive to the identity of the IL cation.

Surprisingly, detailed studies available on the proton reduction process from weak acids in IL media are scarce. Doherty *et al.*⁷ have investigated the proton reduction process from five protonated amines (*i.e.*, the BH^+/H_2 couple) at a platinum electrode in a range of ILs. The BH^+/H_2 process is quasi-reversible and occurs at potentials negative of the H^+/H_2 process. By assuming $\Delta E^0 \approx \Delta E_{1/2}$ (where $E_{1/2}$ is the reversible half-wave potential), an approximation which introduces considerable systematic error into the determination of $\text{p}K_{\text{a}}$ (*vide infra*), the authors estimated the $\text{p}K_{\text{a}}$ value directly from a transient cyclic voltammogram and found that the strength of a given acid depends strongly on the constituent anion of the IL.

In this paper, the thermodynamics, kinetics and mechanisms of the proton reduction (hydrogen evolution) reaction at a platinum electrode have been investigated in the room temperature ionic liquid 1-ethyl-3-methylimidazolium bis(trifluoromethanesulfonyl)imide using ten nitrogen acids (protonated amines or sulfonamides, structures shown in Table 1) that cover a wide range of acidities as the proton source. The proton reduction process has been characterized predominantly using cyclic voltammetry with computational simulation. We also present a relatively straightforward method for calculating the $\text{p}K_{\text{a}}$ of weak acids in IL media, based on a combination of cyclic voltammetry and chronoamperometry. A companion study has also been undertaken using a range of oxyacids (phenols, carboxylic acids or sulfonic acids), which will be presented elsewhere.³⁴

Table 1. Names and structures of the protonated amines and sulfonamide acids (known collectively as nitrogen acids) investigated in this work.

Name of the parent compound	Acid structure	Abbreviation
Pyridine		[Pyr-H][NTf ₂]
2-chloropyridine		[ClPyr-H][NTf ₂]
2,4-dichloropyridine		[dClPyr-H][NTf ₂]
Aniline		[An-H][NTf ₂]
<i>N</i> -methylimidazole		[MeIm-H][NTf ₂]
<i>N</i> -methylpyrrolidine		[MePyrd-H][NTf ₂]
<i>o</i> -phenylenediamine		[oPD-H][NTf ₂]
<i>o</i> -phenylenediamine		[oPD-H ₂][NTf ₂] ₂
Saccharin		SACC
Di(benzenesulfonyl)amide		DBSA

7

Experimental Section

Reagents. 1-ethyl-3-methylimidazolium bis(trifluoromethanesulfonyl)imide ([C₂mim][NTf₂], Io-li-tec, $\eta = 33.7$ mPa s, $\rho = 1.52$ g cm⁻³) and 1-ethyl-3-methylimidazolium trifluoromethanesulfonate ([C₂mim][OTf], Merck, $\eta = 50.5$ mPa s, $\rho = 1.39$ g cm⁻³) were dried under high vacuum ($\leq 10^{-2}$ mbar) at 45°C for 48 hours prior to use. The residual water content was less than 100 ppm as determined by Karl Fischer titration (Metrohm 831 KF Coulometer). Bis(trifluoromethanesulfonyl)imide (H[NTf₂], Sigma-Aldrich, 95%) was purified by sublimation under high vacuum. Ferrocene (Fc, Fluka, >98%) was recrystallized from *n*-pentane (Merck, EMSURE). N-methylimidazole (Sigma-Aldrich) was purified by vacuum distillation over lithium. Aniline (Sigma-Aldrich) was purified by vacuum distillation over potassium hydroxide (Merck). Trifluoromethanesulfonic (triflic) acid (H[OTf], Sigma-Aldrich, 98%), N-methylpyrrolidine (Sigma-Aldrich, 99%), pyridine (BDH, 99.8%), saccharin (Fluka, >99%), di(benzenesulfonyl)amide (TCI, 97%), 2-chloropyridine (Sigma-Aldrich, 99%), 2,4-dichloropyridine (Combi-Blocks, 98%), *o*-phenylenediamine (Sigma-Aldrich, 99.5%), acetonitrile (Alfa-Aesar, anhydrous, 99.7%) and tetra-*n*-butylammonium hexafluorophosphate ([NBu₄][PF₆], Sigma-Aldrich) were used as supplied by the manufacturer. The protonated amine salts were prepared in methanol (Merck, >99.9%) by adding a stoichiometric amount of H[NTf₂] and stirring for several hours. Methanol was subsequently removed on a rotary evaporator and the remaining salt was dried under high vacuum at 45°C for at least 12 hours before use. All water-sensitive reagents were stored and handled under a dry argon atmosphere in a glovebox.

Electrochemical systems and procedures. All voltammetric experiments were carried out under benchtop conditions at ambient temperature ($24 \pm 1^\circ\text{C}$) with a Gamry Reference 600 Potentiostat/Galvanostat/ZRA (Gamry Instruments, USA). All solvents were degassed with N₂ prior to experimentation and a blanket of N₂ was maintained during the course of the

voltammetric experiments. A faraday cage was employed to minimize noise in all microelectrode experiments. Positive feedback iR_u compensation (R_u = uncompensated resistance) was employed in macroelectrode experiments (R_u was estimated by electrochemical impedance spectroscopy). All voltammetric experiments were carried out using a standard 3-electrode arrangement with a working and reference electrode as described below and a Pt wire auxiliary electrode. An Ag wire which had been immersed in the IL under investigation (neat) and sealed in a fritted (Vycor glass frit) glass tube served as the pseudo reference electrode. The pseudo reference electrode potential was calibrated against the formal potential of the IUPAC recommended Fc/Fc⁺ process³⁵ in the electrolyte of interest, taking into careful consideration the difference in the diffusion coefficients of Fc and Fc⁺.^{27, 36}

The Pt macrodisk with a nominal diameter of 1.6 mm was purchased from BASi (Bioanalytical Systems, USA) and the Pt microdisk with a nominal diameter of 20 μm was purchased from Metrohm (Switzerland). The Pt macrodisk electrode was activated by polishing with successively smaller (1 and 0.3 μm) aqueous alumina slurries (Kemet, UK) on a clean polishing cloth (Buehler, USA). Adherent alumina was removed by sonication in de-ionized water. The Pt microdisk electrode was activated by polishing with an aqueous slurry of 0.3 μm alumina and rinsed thoroughly with de-ionized water. The working electrode was preconditioned prior to sweeping by anodic polarization at 1.5 to 2.2 V vs. Fc/Fc⁺ for ≤ 10 ms as has been previously reported.³³ The active electrode area (A) of each of the electrodes was calibrated with convolution voltammetry³⁷⁻³⁹, using the oxidation of a Fc solution of known concentration (2.0 mM in acetonitrile containing 0.10 M [NBu₄][PF₆]) and adopting a diffusion coefficient of $2.4 \times 10^{-5} \text{ cm}^2 \text{ s}^{-1}$, as published under these conditions.²⁵

Viscosity was measured using the falling ball method with an Anton Paar Automated Microviscometer (AMVn). Density was measured with an Anton Paar DMA 4500M Density Meter.

Data treatment and processing. The algorithm used to calculate the convolved currents is the same as used previously.³⁸ Derivative cyclic voltammograms (*i.e.*, 1st order derivative of current or 2nd order derivative of charge) were constructed by differentiating experimental current data with respect to time using the differentiate function available in OriginPro 9.0 software. Savitzky-Golay data smoothing (polynomial order 2) was performed prior to estimating the derivative peak potentials. The diffusion coefficients (D) of H^+ , BH^+ and HA were estimated from chronoamperometric ($I-t$) decay curves obtained at a microdisk electrode using the Shoup and Szabo⁴⁰ method, as reported elsewhere.^{33, 36} The diffusion coefficient (D) of H_2 was estimated from the second (oxidative) step of a double-step chronoamperogram using numerical simulation as has been previously described.⁴¹ The sample time used in all chronoamperometric experiments was 0.01 s. Voltammetric simulations were undertaken using the DigiElch software package (v. 7F, Elchsoft, Germany). The pK_a of 2,4-dichloropyridine was estimated using the MarvinSketch software package (v. 14.12.15.0, Chemaxon).

Results and Discussion

Electroreduction of ‘solvated’ H^+ in $[C_2mim][NTf_2]$ and $[C_2mim][OTf]$. Initial investigations focused on establishing the proton reduction process from ‘solvated’ H^+ in $[C_2mim][NTf_2]$ and $[C_2mim][OTf]$. Prior to voltammetric cycling of the potential, the platinum electrode was preconditioned by ‘anodic polarization’ at oxidative potentials (typically > 1.5 V vs. Fc/Fc^+), as was highlighted in a previous publication.³³ Shown in Figure 1a is a cyclic voltammogram obtained from the reduction of $H[NTf_2]$ at a platinum macrodisk electrode in $[C_2mim][NTf_2]$. This is a one electron per proton process, which occurs in the potential region just negative of the Fc/Fc^+ process, producing molecular hydrogen (H_2) as per Eq. 6.^{27, 28, 33} The voltammetric peak-to-peak separation (ΔE_p) increases with increasing scan rate, with values of 72.2, 82.2 and 92.3 mV at 100, 250 and 500 $mV s^{-1}$, respectively (see Figure S1), indicating that the $H[NTf_2]/H_2$ process is quasi-reversible (R_u is expected to be negligible, see Experimental Section). In a previous publication³³, we demonstrated that $H[NTf_2]$ is not dissociated when dissolved in ILs containing the $[NTf_2]^-$ anion (*i.e.*, the protons diffuse as $H[NTf_2]$). In other words, $H[NTf_2]$ is the ‘solvated proton’ species in $[C_2mim][NTf_2]$, comparable to H_3O^+ in aqueous media. Since $H[NTf_2]$ is the strongest acid that can exist in $[C_2mim][NTf_2]$, the $H[NTf_2]/H_2$ process shown in Figure 1a will serve as the equilibrium acidity scale reference point in this medium. We have shown in the Supporting Information that $H[NTf_2]$ has a pK_a of -0.59 in $[C_2mim][NTf_2]$.⁸

Shown in Figure 1b is a cyclic voltammogram obtained from the reduction of $H[OTf]$ in $[C_2mim][OTf]$ at a platinum macrodisk electrode. Once again, ΔE_p increases with increasing scan rate, albeit to a greater extent than in $[C_2mim][NTf_2]$, with values of 105.4, 113.4 and 125.4 mV at 100, 250 and 500 $mV s^{-1}$, respectively (see Figure S2), indicating that the $H[OTf]/H_2$ process is quasi-reversible. Assuming that $E^0(Fc/Fc^+)$ is solvent independent^{42, 43}, the $H[OTf]/H_2$ process in $[C_2mim][OTf]$ occurs at potentials approximately

11

300 mV more negative than the H[NTf₂]/H₂ process in [C₂mim][NTf₂]. Since H[OTf] is the ‘solvated proton’ species in [C₂mim][OTf] (comparable to H[NTf₂] in [C₂mim][NTf₂] or H₃O⁺ in H₂O), it is clear that the equilibrium acidity scale reference point is considerably different in [C₂mim][OTf] and [C₂mim][NTf₂], making direct comparison of pK_a data between these media impossible. Using the same procedure outlined in the Supporting Information, H[OTf] has a pK_a of -0.73 in [C₂mim][OTf].

Shown in Figure 1c is the proton reduction process obtained at a platinum macrodisk electrode when H[NTf₂] is dissolved in [C₂mim][OTf]. Again, ΔE_p increases with increasing scan rate, with values of 107.4, 121.4 and 137.4 mV at 100, 250 and 500 mV s⁻¹, respectively (see Figure S3), indicating that this proton reduction process is quasi-reversible. The ‘H[NTf₂]/H₂ process’ appears to be very similar to the H[OTf]/H₂ process in [C₂mim][OTf], being a quasi-reversible, one electron per proton process, which occurs in the potential region approximately 350 mV negative of the Fc/Fc⁺ process. The close coincidence between the ‘H[NTf₂]/H₂’ and H[OTf]/H₂ processes indicates that the following equilibrium lies to the right in [C₂mim][OTf]:



In other words, H[NTf₂] behaves as a ‘strong acid’ in [C₂mim][OTf] (pK_a < -0.73), undergoing complete dissociation to form H[OTf] and [NTf₂]⁻. Consequently, the H[OTf]/H₂ couple is responsible for the proton reduction process observed in Figure 1c. The higher proton affinity of [OTf]⁻ compared to [NTf₂]⁻ is thought to be due to the smaller size and more localized negative charge density of the former.^{9, 10} Conversely, it would be expected that H[OTf] behaves as a ‘weak acid’ in [NTf₂]⁻ ILs, which was found to be the case in our companion study.³⁴

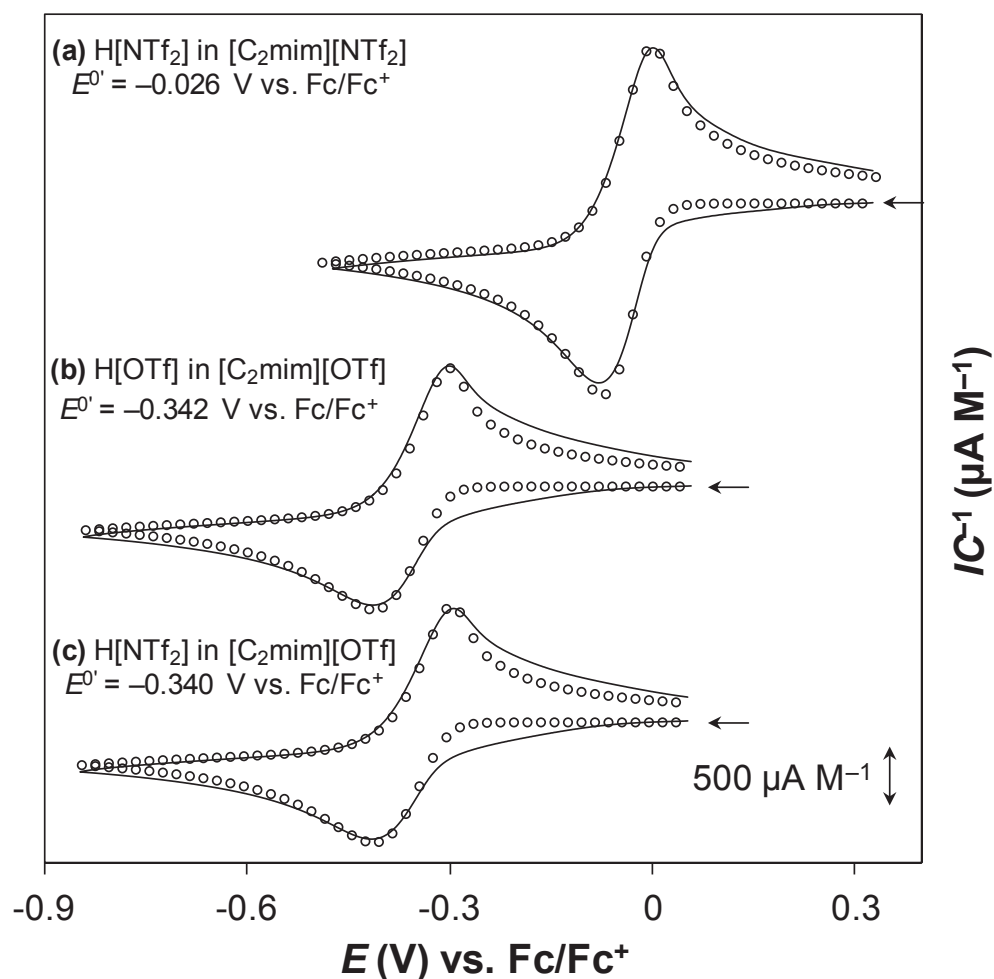
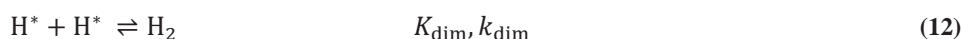
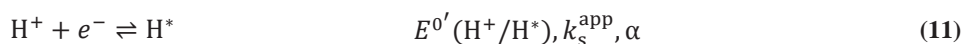


Figure 1. Comparison of the simulated (\circ) and experimental ($—$) concentration-normalized cyclic voltammograms showing the proton reduction process obtained from (a) 49.8 mM $\text{H}[\text{NTf}_2]$ in $[\text{C}_2\text{mim}][\text{NTf}_2]$, (b) 41.1 mM $\text{H}[\text{OTf}]$ in $[\text{C}_2\text{mim}][\text{OTf}]$ and, (c) 42.0 mM $\text{H}[\text{NTf}_2]$ in $[\text{C}_2\text{mim}][\text{OTf}]$ at a 1.6 mm dia. Pt macrodisk electrode with a scan rate of 250 mV s^{-1} . The arrows indicate zero current for each of the voltammograms. Simulation parameters are available in Table 2.

Simulation of the electroreduction of ‘solvated’ H^+ in $[C_2mim][NTf_2]$ and $[C_2mim][OTf]$. Also shown in Figure 1 are simulations of the cyclic voltammograms. A number of mechanisms were considered³³ and the following was found to be consistent with the experimental data under a wide range of experimental conditions:



where $E^{0'}(H^+/H^*)$, k_s^{app} and α are the formal potential of the H^+/H^* couple, apparent standard heterogeneous electron-transfer rate constant (*vide infra*) and charge transfer coefficient respectively. Additionally, Eq. 12 has been treated as a homogeneous process with arbitrarily defined dimerization equilibrium constant (K_{dim}) and dimerization rate constant (k_{dim}) values. Here, H^+ denotes a ‘solvated’ proton, referring to the strongest acid which can exist in a given medium, which in the current context is equivalent to HA_{IL} . The reactions given in Eqs. 11 and 12 correspond to the Volmer and Tafel equations respectively (see Eqs. 7 and 8). Although in reality H^* is likely to be a surface confined species^{29, 31}, it has been treated as solution based (diffusing) species in the simulations, as justified in a previous publication.³³ One consequence of treatment of the mechanism in this manner is that the process shown in Eq. 12 has no physical significance and the following parameters: k_s^{app} , K_{dim} , k_{dim} and D_{H^*} are not quantitatively meaningful.¹⁶ For this reason, k_s has been given the superscript ‘app’ to signify that it is the ‘apparent’ heterogeneous rate constant used in the simulations.

In all simulations, it was taken that $D_{H^*} = 10^{-10} \text{ cm}^2 \text{ s}^{-1}$, $K_{dim} = 10^4$, $k_{dim} = 10^{16} \text{ M}^{-1} \text{ s}^{-1}$, uncompensated resistance (R_u) = 0 Ω and double layer capacitance (C_{dl}) = 0 F. The $E^{0'}$ value used in the simulations corresponds to the fictitious H^+/H^* couple and is related to $E^{0'}(H^+/H_2)$ as follows:

$$E^{0'}(\text{H}^+/\text{H}^*) = E^{0'}(\text{H}^+/\text{H}_2) - \frac{RT}{2F} \ln(K_{\text{dim}}) = E^{0'}(\text{H}^+/\text{H}_2) - 0.118 \text{ V} \quad (13)$$

where R is the gas constant, F is Faraday's constant and T is temperature. The parameters derived by simulation of the experimental data are outlined in Table 2. The experiment-simulation comparison for the reduction of H[NTf₂] in [C₂mim][NTf₂], H[OTf] in [C₂mim][OTf] and H[NTf₂] in [C₂mim][OTf] at multiple scan rates are provided in the Supporting Information (Figures S1 to S3). The mechanism shown in Eqs. 11 and 12 has been expanded upon below to simulate the reduction of protonated amines or sulfonamide acids in [C₂mim][NTf₂].

As shown in Figures S1 to S3, excellent fits between the experimental and simulated voltammograms are achieved over a wide range of scan rates when using the simulation parameters outlined in Table 2. As was highlighted in a previous publication³³, the main discrepancy between the experimental and simulated data is in the hydrogen underpotential deposition (UPD) region, prior to the main (solution based) reduction process.⁹ The formal potential of the H⁺/H₂ process in [C₂mim][NTf₂] is -0.026 V vs. Fc/Fc⁺, compared to -0.342 V vs. Fc/Fc⁺ in [C₂mim][OTf]. In addition, $E^{0'}(\text{H}^+/\text{H}_2)$ obtained from H[NTf₂] in [C₂mim][OTf], -0.340 V vs. Fc/Fc⁺, is nearly identical to that obtained from H[OTf] in [C₂mim][OTf], supporting our previous conclusion that H[NTf₂] acts as a strong acid in this media. Also highlighted in a previous publication³³, the Volmer reaction (Eq. 11) is the rate determining step for the HER on Pt in the investigated ILs, where the second step (Eq. 12) is simply required to fulfill the stoichiometry requirements of the overall process (see Eq. 6). Although the k_s^{app} values derived from the simulations are not quantitatively meaningful in an absolute sense, the relative magnitude of the values indicates that the hydrogen evolution reaction is more kinetically facile in [C₂mim][NTf₂] ($k_s^{\text{app}} \approx 0.02 \text{ cm s}^{-1}$) than in [C₂mim][OTf] ($k_s^{\text{app}} \approx 0.004 \text{ cm s}^{-1}$), in agreement with the previously noted ΔE_p vs. scan rate

trends. It is also worth noting that degradation of the voltammetric response caused by slowing heterogeneous electron transfer kinetics with potential cycling³³, occurred more rapidly in [C₂mim][OTf] than in [C₂mim][NTf₂] suggesting that that electrode ‘deactivation’ is intrinsically linked to the IL anion.

Table 2. Parameters extracted from the comparison of experimental cyclic voltammetric data for the electroreduction of ‘solvated’ H⁺ in [C₂mim][NTf₂] or [C₂mim][OTf] and simulated data, based on the mechanism described by Eqs. 11 and 12.

IL	Acid	$E^0(\text{H}^+/\text{H}_2)$ / V	α	$k_s^{\text{app}} /$ cm s ⁻¹	$D(\text{H}^+) / 10^{-7}$ cm ² s ⁻¹	$D(\text{H}_2) / 10^{-5}$ cm ² s ⁻¹
[C ₂ mim][NTf ₂]	H[NTf ₂]	-0.026	0.50	0.022	3.1	2.2
[C ₂ mim][OTf]	H[OTf]	-0.342	0.40	0.0043	1.8	1.2
[C ₂ mim][OTf]	H[NTf ₂]	-0.340	0.40	0.0040	1.7	1.2

Proton reduction from weak nitrogen acids in [C₂mim][NTf₂]. Further studies were focused on the proton reduction process from a range of weak nitrogen acids (*i.e.*, BH⁺/H₂ or HA/H₂ couple) in [C₂mim][NTf₂]. The name and structure of all of the nitrogen acids investigated were previously shown in Table 1. The electrode was activated prior to sweeping by oxidative pretreatment as discussed above. Representative cyclic voltammograms obtained from a typical monoprotonated amine, [Pyr-H][NTf₂], are shown in Figure 2a. Proton reduction from [Pyr-H]⁺ gives rise to a one-electron per proton process at potentials approximately 700 mV negative of the H[NTf₂]/H₂ process (see Figure 1a). ΔE_p increases with increasing scan rate, with values of 114, 120, 136 and 156 mV at 50, 100, 250 and 500 mV s⁻¹, respectively, indicating that proton reduction from this weak acid is a quasi-reversible process.

A diprotonated amine, [oPD-H₂][NTf₂]₂, was also investigated; representative cyclic voltammograms are shown in Figure 2b. Proton reduction from [oPD-H₂][NTf₂]₂ gives rise to two one-electron per proton processes in the potential regions approximately 200 mV and 550 mV negative of the H[NTf₂]/H₂ process (see Figure 1a), corresponding to the first and second deprotonation, respectively. Hydrogen UPD can be seen prior to the first proton reduction process at high scan rates; this was found to be the case with all of the acids investigated in this work. ΔE_p for the process corresponding to the first deprotonation increases substantially with scan rate, with values of 142, 170 and 250 mV at 50, 100 and 250 mV s⁻¹, respectively. By contrast, ΔE_p for the process corresponding to the second deprotonation increases to a lesser extent with scan rate, with values of 87.9, 93.8 and 108 mV at 50, 100 and 250 mV s⁻¹, respectively. These results qualitatively indicate that hydrogen evolution from monoprotonated [oPD-H]⁺ is more kinetically facile than from diprotonated [oPD-H₂]²⁺ in this media, suggesting that the charge of the weak acid may influence the heterogeneous electron transfer kinetics of the proton reduction process.

Cyclic voltammograms obtained from two neutral sulfonamide acids, SACC and DBSA, are shown in Figure 3a and b, respectively. Proton reduction from SACC (see Figure 3a) occurs in the same potential region as [Pyr-H][NTf₂], approximately 700 mV negative of the H[NTf₂]/H₂ process. Hydrogen evolution from SACC is a quasi-reversible process, featuring large ΔE_p values of 254, 284, 334 and 382 mV at 50, 100, 250 and 500 mV s⁻¹, respectively. Proton reduction from DBSA occurs in the same potential region as [oPD-H][NTf₂], approximately 550 mV negative of the H[NTf₂]/H₂ process. Once again, hydrogen evolution from DBSA is a quasi-reversible process, featuring large ΔE_p values of 232, 278, 348 and 406 mV at 50, 100, 250 and 500 mV s⁻¹, respectively. The magnitude of these ΔE_p values qualitatively indicate that hydrogen evolution from the sulfonamide acids is kinetically more sluggish than from monoprotonated amines of similar strength (*i.e.*, [Pyr-H][NTf₂] or [oPD-H][NTf₂]). In the present case, it is unlikely this trend in heterogeneous kinetics (*i.e.*, electrochemical reversibility) is solely attributable to the difference in the charge of the weak nitrogen acids, since amines and sulfonamides are structurally and chemically disparate species (explored in greater detail below). Cyclic voltammograms obtained from all of the weak acids outlined in Table 1 are included in the Supporting Information (Figures S4 to S13).

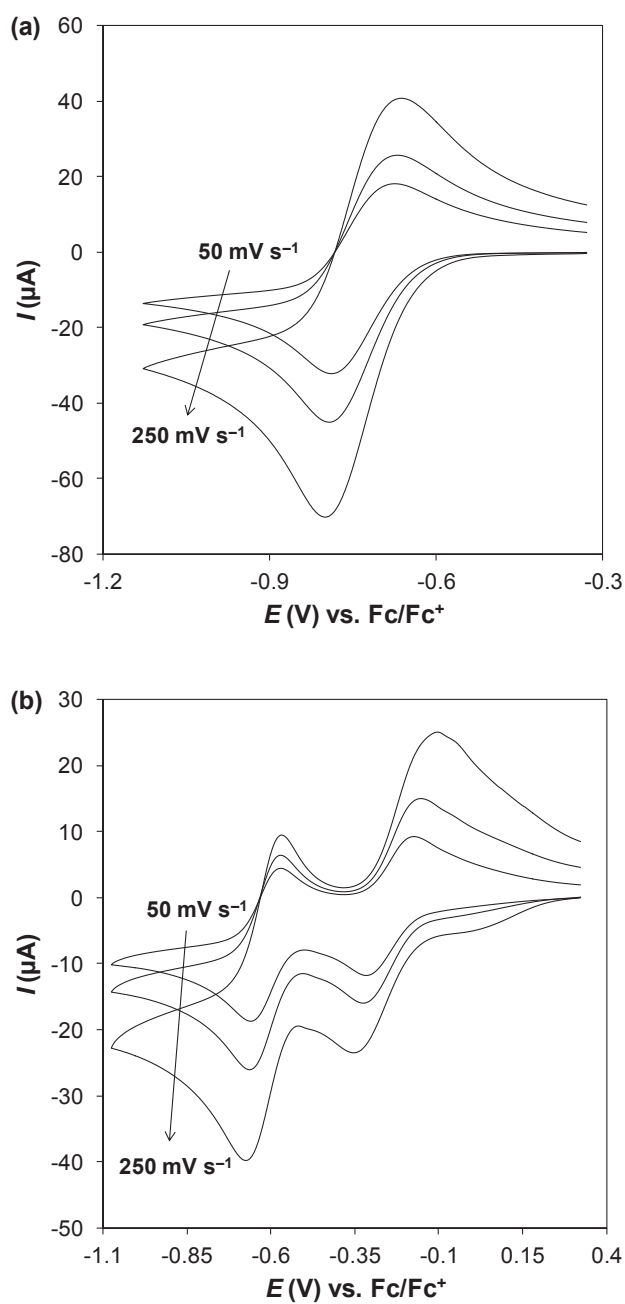


Figure 2. Cyclic voltammograms showing the proton reduction process obtained from (a) 50.2 mM [Pyr-H][NTf₂] and (b) 33.0 mM [oPD-H₂][NTf₂]₂ in [C₂mim][NTf₂] at a 1.6 mm dia. Pt macrodisk electrode with scan rates of 50, 100 and 250 mV s⁻¹.

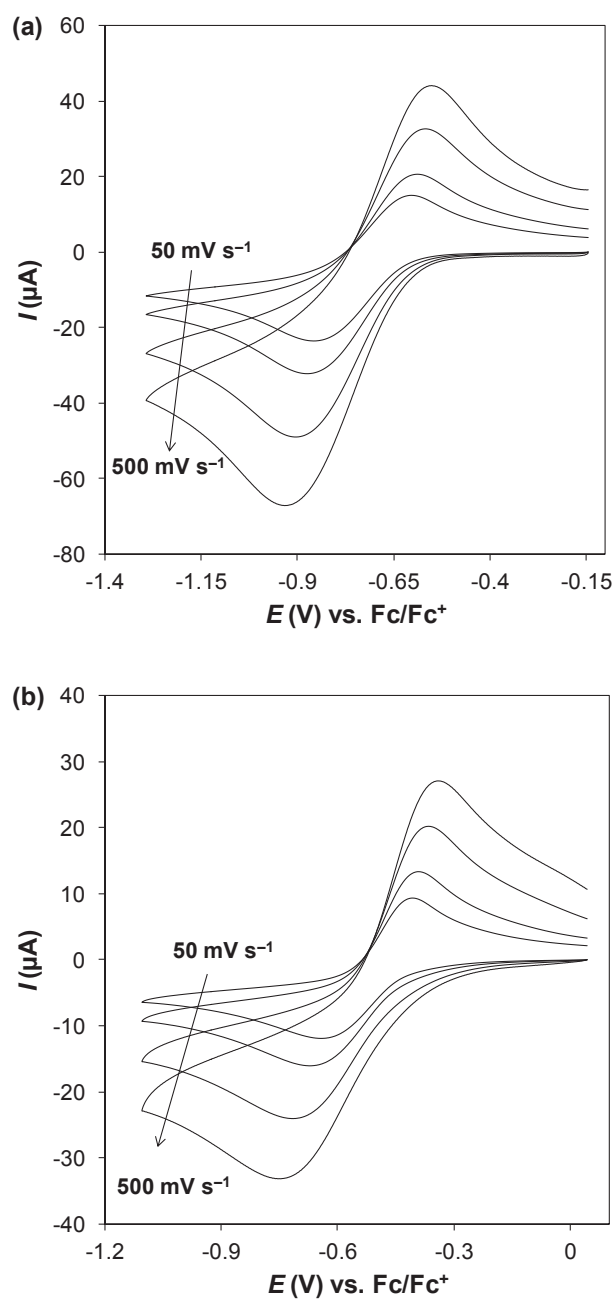


Figure 3. Cyclic voltammograms showing the proton reduction process obtained from (a) 58.3 mM SACC and (b) 37.6 mM DBSA in $[\text{C}_2\text{mim}][\text{NTf}_2]$ at a 1.6 mm dia. Pt macrodisk electrode with scan rates of 50, 100, 250 and 500 mV s^{-1} .

Simulation of the proton reduction process from weak nitrogen acids in [C₂mim][NTf₂]. The overall proton reduction process from a weak acid is:



where B/BH⁺ correspond to a neutral base/conjugate cation acid and HA/A⁻ correspond to a neutral acid/conjugate anion base. The two reactions described above are stoichiometrically equivalent and although the following discussion refers to the BH⁺/H₂ couple, it is equally applicable to the HA/H₂ couple. In order to simulate the BH⁺/H₂ process, a *CE* mechanism was considered, whereby proton reduction *via* the mechanism described by Eqs. 11 and 12 is preceded by dissociation of BH⁺:



where k_{dissoc} is the dissociation rate constant and k_{assoc} is the association rate constant. In all simulations, k_{assoc} was set to be $5 \times 10^8 \text{ M}^{-1} \text{ s}^{-1}$ which is thought to approximate the diffusion controlled limit for a bimolecular reaction in this viscous electrolyte.³⁹ Additionally, in all simulations it was assumed that $D_{\text{B}} = D_{\text{BH}^+}$ and the parameters for Eqs. 11 and 12 were taken from Table 2. Simulations were carried out for [dCIPyr-H][NTf₂] using the diffusivity and pK_a values outlined in Table 3; the results are shown in Figure 4. Evidently, BH⁺ reduction solely *via* the *CE* pathway cannot support a mass-transport controlled current, even at 50 mV s^{-1} . This is because $k_{\text{dissoc}} = K_a k_{\text{assoc}}$ and k_{assoc} cannot exceed the diffusion controlled limit, which, in the present case means $k_{\text{dissoc}} \approx 300 \text{ s}^{-1}$, making the reaction shown in Eq. 16 limiting on the voltammetric timescale.

Clearly, a parallel reaction pathway must be available to support the diffusion controlled currents observed experimentally. One possibility is that BH⁺ undergoes direct

reduction (*DR* mechanism) at the electrode surface without prior dissociation, giving rise to surface adsorbed H^* as previously discussed:



This reaction is conceptually analogous to the direct reduction of water at platinum in neutral or basic aqueous solution.¹⁷ Simulations were carried out by combining Eqs. 11, 12, 16 and 17; the result is also shown in Figure 4. There is excellent agreement between the simulations and experimental data when the *DR* pathway (Eq. 17) also is considered. Simulation-experiment comparisons for all of the investigated weak acids are included in the Supporting Information (Figures S3 to S13). The parameters derived by simulation of the experimental data are outlined in Table 3.

Table 3. Parameters extracted from the comparison of experimental cyclic voltammetric data for the proton reduction process from ten weak nitrogen acids in $[C_2mim][NTf_2]$ and simulated data, based on the mechanism described by Eqs. 11, 12, 16 and 17.

Nitrogen Acid	$E^{0'}(BH^+/H_2)$ or $(HA/H_2) / V$	α_{DR}	$k_s^{app}(DR) /$ $cm\ s^{-1}$	pK_a	$D(\text{acid}) / 10^{-7}\ cm^2$ s^{-1}
[MePyr _d -H][NTf ₂]	-1.18	0.53	0.0080	19.5	4.0
[MeIm-H][NTf ₂]	-0.977	0.50	0.018	16.1	3.2
[Pyr-H][NTf ₂]	-0.810	0.50	0.045	13.2	3.5
[oPD-H][NTf ₂]	-0.695	0.50	0.057	11.3	1.7
[An-H][NTf ₂]	-0.664	0.50	0.053	10.8	2.0
[ClPyr-H][NTf ₂]	-0.474	0.50	0.058	7.6	3.2
[dClPyr-H][NTf ₂]	-0.395	0.50	0.055	6.2	2.4
[oPD-H ₂][NTf ₂] ₂	-0.337	0.50	0.015	5.3	1.2
SACC	-0.797	0.42	0.0025	13.0	2.0
DBSA	-0.587	0.32	0.0014	9.5	1.5

As shown in Figures S3 to S13, excellent fits between the experimental and simulated voltammograms are achieved over a wide range of scan rates when using the simulation parameters outlined in Table 3. Once again, the main discrepancy between the experimental and simulated data is in the hydrogen UPD region.¹⁶ Fourteen orders of magnitude in acid strength (K_a) have been covered in this study, ranging from $pK_a = 5.3$ for $[\text{oPD-H}_2][\text{NTf}_2]_2$ to $pK_a = 19.5$ for $[\text{MePyrd-H}][\text{NTf}_2]$. The diffusion coefficients used in the simulations were initially estimated by double step chronoamperometry (see Experimental Section). D_{BH^+} follows the expected trend, decreasing with increasing substituent size ($D_{[\text{Pyr-H}]^+} > D_{[\text{ClPyr-H}]^+} > D_{[\text{dClPyr-H}]^+}$), substituent number ($D_{[\text{An-H}]^+} > D_{[\text{oPD-H}]^+}$) and charge ($D_{[\text{oPD-H}]^+} > D_{[\text{oPD-H}_2]^{2+}}$).

As shown in Table 3, the k_s^{app} among the monocationic protonated amine acids is comparable for $[\text{dClPyr-H}]^+$, $[\text{ClPyr-H}]^+$, $[\text{An-H}]^+$ and $[\text{oPD-H}]^+$ ($6.2 \leq pK_a \leq 11.3$) and then decreases with increasing pK_a for $[\text{Pyr-H}]^+$ ($pK_a = 13.2$), $[\text{MeIm-H}]^+$ ($pK_a = 16.1$) and $[\text{MePyrd-H}]^+$ ($pK_a = 19.5$). This trend is not likely to be the result of a double layer effect²⁵, which would predict that the apparent k_s increases at increasingly negative potentials for cationic species (assuming all of the processes are negative of the point of zero charge). Since Eq. 17 is the rate determining step, one possible explanation for this trend is that activation energy (overpotential) required to break the N-H bond is related to the heterolytic bond dissociation energy, which is larger for the weaker acids (proportional to pK_a).^{16, 17} Also evident from the data in Table 3, the proton reduction process from monocationic nitrogen acids is more kinetically facile (electrochemically reversible) than from dicationic or neutral nitrogen acids of comparable strength. Since $[\text{oPD-H}]^+$ and $[\text{oPD-H}_2]^{2+}$ are structurally identical, the trend in k_s^{app} is most likely related to the charge of the respective acids. A similar comparison cannot be made between the monocationic protonated amine acids and

neutral sulfonamide acids, because structural variations in the vicinity of the acidic proton on the parent acid may affect the kinetics of the Volmer-type reaction shown in Eq. 17.

Further simulations carried using the *CE* (see Eqs. 11, 12 and 16), *DR* (see Eqs. 12 and 17) or *CE + DR* pathways are included in the Supporting Information (Figures S14 to S18). Setting k_{assoc} to be the diffusion controlled value ($5 \times 10^8 \text{ M}^{-1} \text{ s}^{-1}$) and using a ‘typical’ set of simulation parameters for proton reduction in [C₂mim][NTf₂] (outlined in Table S1), it was found that proton reduction through the *CE* pathway could only attain a diffusion controlled current when $\text{p}K_{\text{a}} < 4$. It was also found that proton reduction through the *DR* pathway becomes insignificant when $\text{p}K_{\text{a}} < 2$. Although these are generalizations, as they strictly only apply under the conditions investigated ($r_0 = 0.0825 \text{ cm}$, $v = 500 \text{ mV s}^{-1}$), they do provide valuable insight into how the preferred proton reduction pathway relates to the strength of the weak acid. In line with the simulations, we have shown in our companion study³⁴ that H[OTf] has a $\text{p}K_{\text{a}}$ of approximately 2 in [C₂mim][NTf₂], allowing proton reduction to proceed *via* the *CE* pathway. These simulations are in qualitative agreement with the studies by Evans *et al.*^{16, 17} on the reduction of weak acids in dimethylsulfoxide ($k_{\text{assoc}} \approx 1 \times 10^{10} \text{ M}^{-1} \text{ s}^{-1}$), where the authors postulated that there is a transition from the *CE* pathway to the *DR* pathway when $\text{p}K_{\text{a}} > 6$.

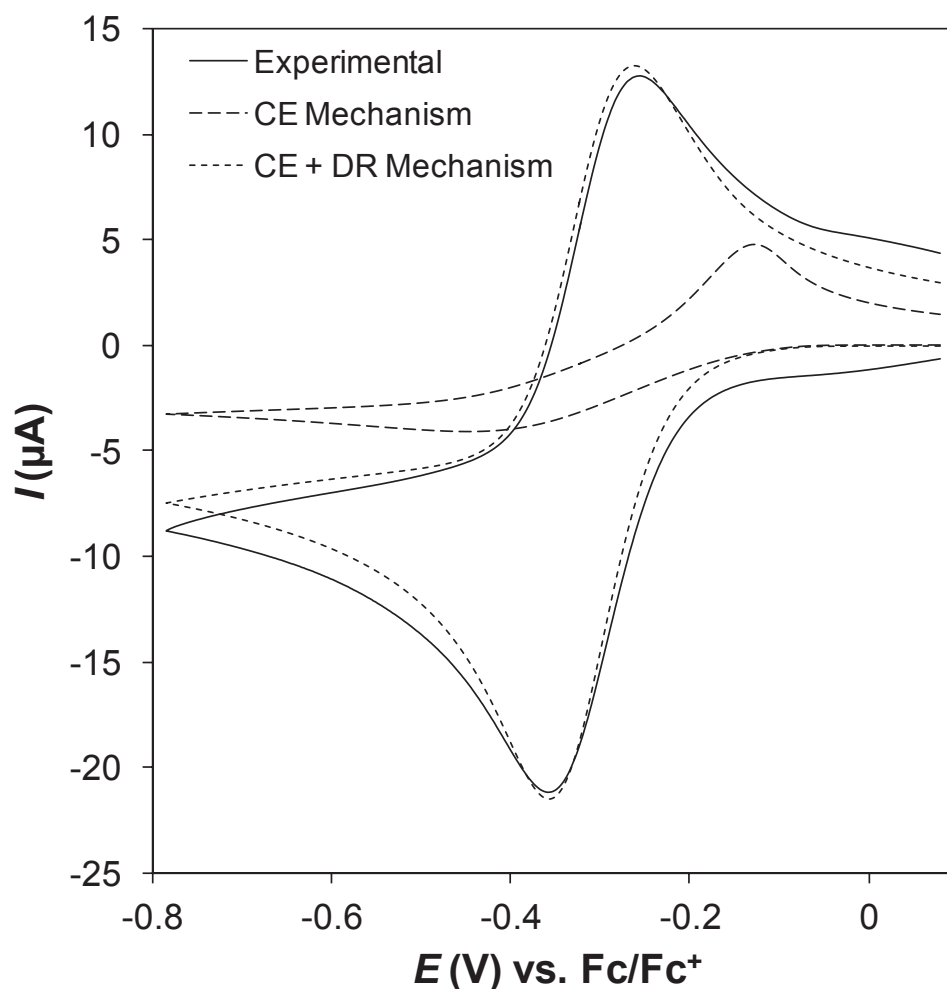


Figure 4. Comparison of simulated and experimental (solid line) cyclic voltammograms showing the proton reduction process obtained from 38.7 mM [dClPyr-H][NTf₂] in [C₂mim][NTf₂] at a 1.6 mm dia. Pt macrodisk electrode with a scan rate of 100 mV s⁻¹. The simulations were carried out using the *CE* mechanism only (dashed line, see Eqs. 11, 12 and 16) or the *CE* + *DR* mechanism (dotted line, see Eqs. 11, 12, 16 and 17). Simulation parameters are available in Table 2 (*CE*) or Table 3 (*CE* + *DR*).

Calculating the pK_a of weak nitrogen acids in $[C_2mim][NTf_2]$. The hydrogen evolution reaction is given in Eq. 6, where H^+ is the strongest acid which can exist in a given medium (*i.e.*, a ‘solvated proton’), which in the current context is equivalent to $H[NTf_2]$. If it is assumed that activities are equal to molar concentrations, as justified by Doherty and co-workers⁷, the Nernst Equation for the H^+/H_2 couple is as follows:

$$E = E^{0'}(H^+/H_2) + \frac{RT}{2F} \ln \frac{[H^+]^2}{[H_2]} \quad (18)$$

Here, the concentration rather than pressure-based standard state of H_2 has been used. Proton reduction from a weak acid can be described by the process given in Eq. 14. Once again, if it is assumed that activities are equal to molar concentrations, the Nernst Equation for the BH^+/H_2 couple is as follows:

$$E = E^{0'}(BH^+/H_2) + \frac{RT}{2F} \ln \frac{[BH^+]^2}{[B]^2[H_2]} \quad (19)$$

If Eq. 18 is subtracted from Eq. 19, we get:

$$E^{0'}(BH^+/H_2) - E^{0'}(H^+/H_2) = \frac{RT}{F} \ln \frac{[B][H^+]}{[BH^+]} = -\frac{2.303RT}{F} pK_a \quad (20)$$

so the pK_a of an acid can be estimated if $E^{0'}(H^+/H_2)$ and $E^{0'}(BH^+/H_2)$ are known. Although $E^{0'}(H^+/H_2)$ was previously estimated to be -0.026 V using numerical simulation (see Table 2), it can be more conveniently calculated directly from a transient cyclic voltammogram (see Figure 1a) as follows. Under conditions where mass transport is governed solely by semi-infinite planar diffusion and H^+ is the only species initially present in solution, the following relationship between $E^{0'}(H^+/H_2)$ and the reversible half wave potential, $E_{1/2}$, can be derived from Eq. 18 using the diffusion layer method^{17, 25, 30, 44}:

$$E^{0'}(H^+/H_2) = E_{1/2}(H^+/H_2) - \frac{RT}{2F} \ln \left(\frac{\sqrt{D_{H_2}}}{\sqrt{D_{H^+}}} \right) - \frac{RT}{2F} \ln [H^+]_b \quad (21)$$

where the subscript 'b' signifies 'bulk concentration'. $E_{1/2}$ can be estimated from a transient cyclic voltammogram as follows:

$$E_{1/2} \cong \frac{E_{p,ox} + E_{p,red}}{2} = E_{mid} \quad (22)$$

where $E_{p,ox}$ and $E_{p,red}$ are the oxidation and reduction peak potentials respectively.¹⁷ D_{H^+} and D_{H_2} can be estimated experimentally using double step chronoamperometry, as outlined in the Experimental Section. D_{H_2}/D_{H^+} is approximately equal to 100 (in a range of ILs³³) and $[H^+]_b$ is typically 0.02 to 0.05 M, meaning both of the logarithmic terms in Eq. 21 are significant. The $E^{0'}(H^+/H_2)$ values estimated using Eq. 21 are -0.027 V and -0.345 V in $[C_2mim][NTf_2]$ and $[C_2mim][OTf]$, respectively and are in excellent agreement with the values previously determined with numerical simulation (see Table 2). Likewise, $E^{0'}(BH^+/H_2)$ can be estimated using numerical simulation (see Table 3) or directly from a transient cyclic voltammogram using the following equation, derived from Eq. 19 using the diffusion layer method^{17, 25}:

$$E^{0'}(BH^+/H_2) = E_{1/2}(BH^+/H_2) - \frac{RT}{2F} \ln \left(\frac{4\sqrt{D_{H_2}D_B}}{\sqrt{D_{BH^+}^3}} \right) + \frac{RT}{2F} \ln[BH^+]_b \quad (23)$$

Once again, the derivation of Eq. 23 assumes mass transport to the electrode surface is governed solely by semi-infinite planar diffusion and BH^+ is the only species initially present in solution. Although D_{BH^+} and D_{H_2} can be estimated using double step chronoamperometry, D_B cannot be readily estimated by electrochemical methods. If it is assumed that $D_B = D_{BH^+}$, Eq. 23 reduces to:

$$E^{0'}(BH^+/H_2) = E_{1/2}(BH^+/H_2) - \frac{RT}{2F} \ln \left(\frac{4\sqrt{D_{H_2}}}{\sqrt{D_{BH^+}}} \right) + \frac{RT}{2F} \ln[BH^+]_b \quad (24)$$

Again, $E_{1/2}(\text{BH}^+/\text{H}_2)$ can be estimated from a transient cyclic voltammogram using Eq. 22.

The $\text{p}K_{\text{a}}$ values calculated for all of the nitrogen acids are summarized in Table 4. In addition, experimental and simulated cyclic voltammograms obtained from the full spectrum of nitrogen acids investigated in the work are shown in Figure 5.

Table 4. $\text{p}K_{\text{a}}$ (IL) values calculated in this work and $\text{p}K_{\text{a}}$ (aq) values obtained from the literature for a range weak nitrogen acids.

Acid	$\text{p}K_{\text{a}}$ (SIM)	$\text{p}K_{\text{a}}$ (CV)	$\text{p}K_{\text{a}}$ (DCV)	$\text{p}K_{\text{a}}$ (aq) ¹⁸
[Pyr-H] ⁺	13.2	13.3	13.4	5.21
[ClPyr-H] ⁺	7.6	7.6	7.6	0.72
[dClPyr-H] ⁺	6.2	6.2	6.2	0.11 [†]
[An-H] ⁺	10.8	10.8	10.9	4.60
[MeIm-H] ⁺	16.1	16.1	16.2	6.95
[MePyrd-H] ⁺	19.5	19.5	19.8	10.46
[oPD-H] ⁺	11.3	11.3	11.4	4.74
[oPD-H ₂] ²⁺	5.3	5.4	5.4	0.6
SACC	13.0	13.3	13.0	1.31
DBSA	9.5	9.8	9.6	–

[†]Reliable literature data not available, $\text{p}K_{\text{a}}$ (aq) was estimated using MarvinSketch software

The $\text{p}K_{\text{a}}$ values estimated using numerical simulation are generally in excellent agreement with those determined directly from the cyclic voltammogram (CV) using Eqs. 21, and 24. The largest deviation between the two methods is approximately 0.3 $\text{p}K_{\text{a}}$ units for the neutral sulfonamide acid, DBSA. This is not surprising, since E_{mid} most closely approximates $E_{1/2}$ (see Eq. 22) when heterogeneous kinetics are reversible and the charge transfer coefficient (α) is equal to 0.5; neither of these conditions are met in the case of DBSA (see Table 3). Also included in the table are $\text{p}K_{\text{a}}$ values calculated using Eqs. 21 and 24 after estimating $E_{1/2}$ from the derivative peak potentials of a derivative cyclic voltammogram

(example shown in Figure S19). Although processing the data in this way (see Experimental Section) is unnecessary in the present case, it has been included here as a point of comparison because in our companion study on the reduction of oxyacids in [C₂mim][NTf₂], estimating $E_{1/2}$ directly from the CV is complicated by the effects of homoassociation.³⁴ In that study, we found that the differential response of the derivative cyclic voltammetry (DCV) technique resolved fine details that are not readily discernable on the normal cyclic voltammogram^{45, 46}, allowing $E_{1/2}$ to be estimated with greater accuracy. As expected, the pK_a values calculated using DCV method are in excellent agreement with those determined directly with CV or with CV plus numerical simulation.

Where available, aqueous pK_a values have also been included in Table 4. In all cases the nitrogen acids dissociate less readily in [C₂mim][NTf₂] than in water. This is not surprising, since [C₂mim][NTf₂] is a weak hydrogen bond donating/accepting solvent compared to water⁴⁷ and the [NTf₂]⁻ anion is very weakly basic due to extensive charge delocalization.^{47, 48} In addition, aprotic ILs are only considered to be ‘moderately polar’ solvents, with reported static dielectric constants being in the 10 to 20 range⁴⁹, compared to 80.1 for water⁵⁰. Nonetheless, there is a good correlation between the pK_a (aq) and pK_a (IL) data (see Figure S20) for the monocationic protonated amine acids, with pK_a increasing in the order [dClPyr-H]⁺ < [ClPyr-H]⁺ < [An-H]⁺ < [oPD-H]⁺ < [Pyr-H]⁺ < [MeIm-H]⁺ < [MePyrd-H]⁺ in both solvents. [oPD-H₂]²⁺ is a stronger acid than [dClPyr-H]⁺ in IL media, whereas the opposite is predicted in aqueous media. This is almost certainly a charge effect, reflecting the relative stability (or instability) of dications (BH₂²⁺) and monocations (BH⁺) in [C₂mim][NTf₂] compared to H₂O. The neutral sulfonamide acid, SACC, is the outlier in the pK_a (aq) vs. pK_a (IL) trend, having a considerably higher pK_a (IL) value than expected relative to the cationic protonated amine acids. A similar observation was made with neutral oxyacids and has been explored in further detail in our companion study.³⁴

Finally, by combining Eqs. 20, 21 and 24, the following relationship can be derived:

$$\begin{aligned}
 -\frac{2.303RT}{F} \text{p}K_a = E_{1/2}(\text{BH}^+/\text{H}_2) - E_{1/2}(\text{H}^+/\text{H}_2) + \frac{RT}{2F} \ln \left(\frac{\sqrt{D_{\text{BH}^+}}}{\sqrt{D_{\text{H}^+}}} \right) \\
 + \frac{RT}{2F} \ln \left(\frac{[\text{BH}^+]_b [\text{H}^+]_b}{4} \right)
 \end{aligned} \tag{25}$$

In order to apply this equation in practice, a solution containing H[NTf₂] and pyridine in a 2:1 ratio was prepared and characterized voltammetrically, as is shown in Figure 6. There are two reduction processes observable with cyclic voltammetry (see Figure 6a); the more positive process corresponds to the H⁺/H₂ couple and the more negative process corresponds to the [Pyr-H]⁺/H₂ couple. $E_{1/2}(\text{H}^+/\text{H}_2)$ and $E_{1/2}(\text{BH}^+/\text{H}_2)$ can be readily estimated from the peak potentials labeled in Figure 6a using Eq. 22. D_{BH^+} and D_{H^+} can be readily estimated by performing a potential step past each of the peaks (indicated in Figure 6a); chronoamperograms are shown in Figure 6b. The potential step to -0.323 V vs. Fc/Fc⁺ corresponds to the mass-transport controlled reduction of H⁺ to H₂ (see Eq. 6), and from this chronoamperogram, D_{H^+} was estimated to be $3.0 \times 10^{-7} \text{ cm}^2 \text{ s}^{-1}$. The potential step to -1.023 V vs. Fc/Fc⁺ corresponds to mass-transport controlled proton reduction from both H[NTf₂] and [Pyr-H][NTf₂]; D_{BH^+} was estimated to be $3.6 \times 10^{-7} \text{ cm}^2 \text{ s}^{-1}$ from the chronoamperogram obtained by subtracting the $I-t$ transient at -0.323 V vs. Fc/Fc⁺ from the one at -1.023 V vs. Fc/Fc⁺.

Substituting the appropriate values into Eq. 25, the p*K*_a of pyridine was calculated to be 13.4, which is in excellent agreement with the previously determined values (see Table 4). This method has a number of advantages over the previously outlined methods, namely: (a) numerical simulation is not required; (b) only a single solution containing a 2:1 mixture of HA_{IL} and B is required and; (c) preparation of [BH][A_{IL}] is not required, the solution can be prepared simply by adding B directly to a HA_{IL}/IL mixture. It should be noted that a similar

set of experiments have been previously reported by Doherty and co-workers⁷, where they calculated the pK_a value of $[\text{Pyr-H}]^+$ to be 10.5 in $[\text{C}_4\text{mim}][\text{NTf}_2]$. Changing the alkyl chain length on the imidazolium cation is expected to have a minimal impact on pK_a ^{9, 10}, so the large discrepancy between our value, 13.4, and their value, 10.5, is predominantly attributable to the method in which pK_a was calculated from the voltammogram. In their work, the authors assumed $\Delta E_{1/2} \approx \Delta E^0$, neglecting the two additional logarithmic terms shown in Eq. 25. Although the first logarithmic term is somewhat negligible because $D_{H^+} \cong D_{BH^+}$ (see Table 3), the second term is significant when working at millimolar concentrations, equaling -0.1 V or $+1.7$ pK_a units when $[\text{H}^+]_b = [\text{BH}^+]_b = 40$ mM. Furthermore, the authors assumed that $\text{H}[\text{OTf}]$ behaves as a strong acid (*i.e.*, undergoes 100% ionization) in $[\text{C}_4\text{mim}][\text{NTf}_2]$; we have shown in our companion study³⁴ that this is not likely to be the case.

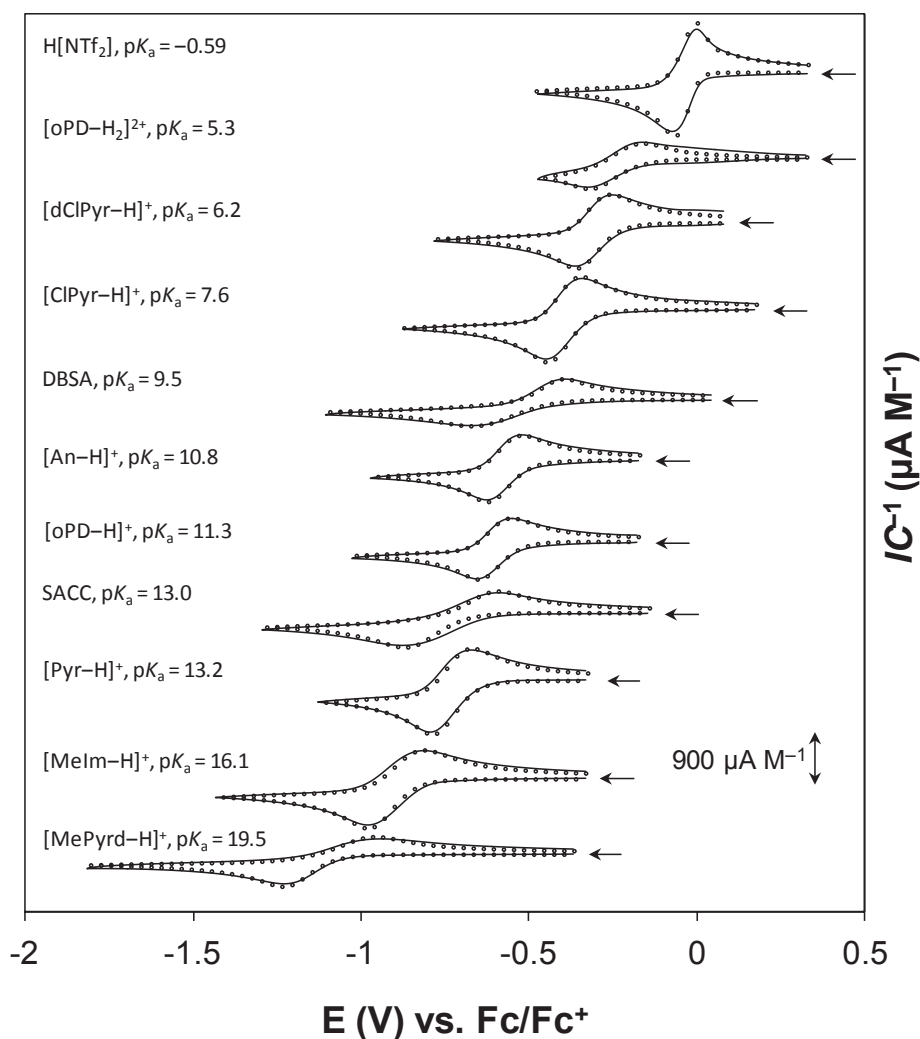


Figure 5. Simulated (\circ) and experimental ($—$) concentration-normalized cyclic voltammograms showing the proton reduction process obtained from (top to bottom) 49.8 mM H[NTf₂], 33.0 mM [oPD-H₂][NTf₂]₂, 38.7 mM [dClPyr-H][NTf₂], 62.4 mM [ClPyr-H][NTf₂], 37.6 mM DBSA, 30.4 mM [An-H][NTf₂], 28.2 mM [oPD-H][NTf₂], 58.3 mM SACC, 50.2 mM [Pyr-H][NTf₂], 49.3 mM [MeIm-H][NTf₂] and 29.4 mM [MePyrd-H][NTf₂] in [C₂mim][NTf₂] at a 1.6 mm dia. Pt macrodisk electrode with a scan rate of 100 mV s⁻¹. The arrows indicate zero current for each of the voltammograms. Simulation parameters are available in Table 3.

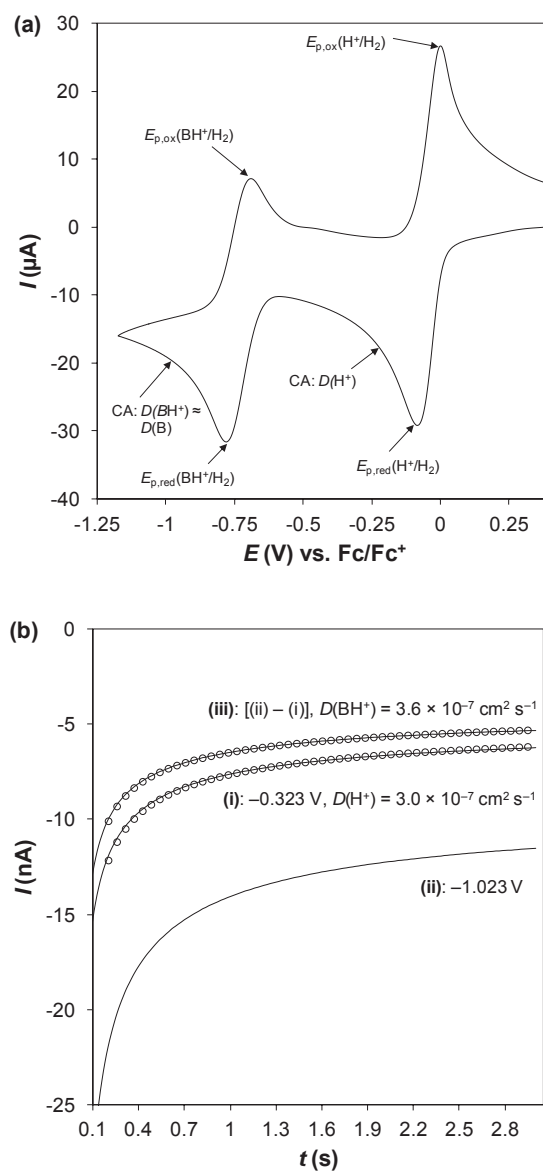


Figure 6. (a) A cyclic voltammogram obtained from the reduction of 33.1 mM H[NTf₂] and 24.3 mM [Pyr-H][NTf₂] in [C₂mim][NTf₂] at a 1.6 mm dia. Pt macrodisk electrode with a scan rate of 100 mV s⁻¹. (b) Experimental (—) and Shoup-Szabo theoretical chronoamperograms (○) obtained from the solution outlined in (a) at a 20 μm dia. Pt microdisk electrode by (i) stepping the potential to -0.323 V vs. Fc/Fc⁺, (ii) stepping the potential to -1.023 V vs. Fc/Fc⁺ and (iii) subtracting curve (i) from curve (ii).

Conclusions

The thermodynamics, kinetics and mechanisms for the proton reduction (hydrogen evolution) reaction at a platinum electrode have been investigated in ionic liquid media using a range of nitrogen acids (protonated amines or sulfonamides) as the proton source. The formal potential of the H^+/H_2 process (where H^+ signifies a 'solvated proton' released from a strong acid) was found to be strongly dependent on the identity of the IL anion, making direct comparison of pK_a data between ILs with different constituent anions impossible. Proton reduction from weak nitrogen acids (*i.e.*, HA/H_2 or BH^+/H_2) was found to be a diffusion controlled process which occurs in the potential region negative of the H^+/H_2 process (proportional to pK_a). Numerical simulations, performed by combining the classical Volmer and Tafel reactions, revealed that weak acid dissociation is limiting on the voltammetric timescale when $pK_a > 4$, meaning proton reduction *via* a *CE* mechanism cannot account for the experimentally observed mass-transport limited currents. A parallel direct reduction (*DR*) pathway was considered in addition to the *CE* pathway and using this mechanism, the proton reduction response from ten weak nitrogen acids covering 14 orders of magnitude in acid strength ($5.2 < pK_a < 19.5$) was successfully simulated. All of the investigated nitrogen acids dissociated to a much lesser extent in $[C_2mim][NTf_2]$ compared to water, indicating that the H^+ solvating ability of the former solvent is considerably weaker than the latter. Finally, after estimating $E_{1/2}(HA/H_2) - E_{1/2}(H^+/H_2)$ or $E_{1/2}(BH^+/H_2) - E_{1/2}(H^+/H_2)$ from a transient cyclic voltammogram and D_{HA}/D_{H^+} or D_{BH^+}/D_{H^+} from a microdisk electrode chronoamperogram, the pK_a values for each of the ten weak nitrogen acids were calculated using a straightforward formula, demonstrating the utility of voltammetry as a convenient method for calculating equilibrium acidities.

Associated Content

Supporting information. Simulation-experiment comparisons for the electroreduction of solvated H^+ in $[C_2mim][NTf_2]$ and $[C_2mim][OTf]$ (Figures S1 to S3), simulation-experiment comparisons for the proton reduction process from a range of weak nitrogen acids in $[C_2mim][NTf_2]$ (Figures S4 to S13), simulations showing the contributions of the *CE* and *DR* pathways to proton reduction from weak acids with $1 \leq pK_a \leq 5$ (Figures S14 to S18), derivative cyclic voltammogram for the proton reduction process obtained from $[Pyr-H]^+$ in $[C_2mim][NTf_2]$ (Figure S19) and a plot of pK_a (aq) vs. pK_a (IL) (Figure S20). This material is available free of charge *via* the Internet at <http://pubs.acs.org>.

Author Information

Corresponding Authors

Notes

The authors declare no competing financial interest.

Acknowledgements

The authors thank Dr. Thomas R  ther for assistance in the preparation of the protonated amine salts.

References

- (1) Migliore, A.; Polizzi, N. F.; Therien, M. J.; Beratan, D. N., Biochemistry and Theory of Proton-Coupled Electron Transfer. *Chem. Rev.* **2014**.
- (2) Kreuer, K. D., Proton Conductivity: Materials and Applications. *Chem. Mat.* **1996**, *8*, 610-641.
- (3) Mikkelsen, M.; Jorgensen, M.; Krebs, F. C., The Teraton Challenge. A Review of Fixation and Transformation of Carbon Dioxide. *Energy Environ. Sci.* **2010**, *3*, 43-81.
- (4) Arico, A. S.; Srinivasan, S.; Antonucci, V., DMFCs: From Fundamental Aspects to Technology Development. *Fuel Cells* **2001**, *1*, 133-161.
- (5) Bard, A. J.; Fox, M. A., Artificial Photosynthesis - Solar Splitting of Water to Hydrogen and Oxygen. *Acc. Chem. Res.* **1995**, *28*, 141-145.
- (6) Perrin, D. D.; Dempsey, B.; Serjeant, E. P., *pK_a Prediction for Organic Acids and Bases*. Chapman and Hall: New York, 1981.
- (7) Barhdadi, R.; Troupel, M.; Comminges, C.; Laurent, M.; Doherty, A., Electrochemical Determination of pK_a of N-Bases in Ionic Liquid Media. *J. Phys. Chem. B* **2012**, *116*, 277-282.
- (8) Campbell, M. L.; Waite, B. A., The K_a Values of Water and the Hydronium Ion for Comparison with Other Acids. *J. Chem. Educ.* **1990**, *67*, 386.
- (9) Deng, H.; Li, X.; Chu, Y.; He, J.; Cheng, J.-P., Standard pK_a Scales of Carbon-Centered Indicator Acids in Ionic Liquids: Effect of Media and Structural Implication. *J. Org. Chem.* **2012**, *77*, 7291-7298.

- (10) Wang, Z.; Deng, H.; Li, X.; Ji, P. J.; Cheng, J. P., Standard and Absolute pK_a Scales of Substituted Benzoic Acids in Room Temperature Ionic Liquids. *J. Org. Chem.* **2013**, *78*, 12487-12493.
- (11) Bordwell, F. G., Equilibrium Acidities in Dimethyl Sulfoxide Solution. *Acc. Chem. Res.* **1988**, *21*, 456-463.
- (12) Barrette, W. C.; Johnson, H. W.; Sawyer, D. T., Voltammetric Evaluation of the Effective Acidities (pK_a') for Bronsted Acids in Aprotic-solvents. *Anal. Chem.* **1984**, *56*, 1890-1898.
- (13) Slater, A. M., The IUPAC Aqueous and Non-Aqueous Experimental pK_a Data Repositories of Organic Acids and Bases. *J. Comput.-Aided Mol. Des.* **2014**, *28*, 1031-1034.
- (14) Haynes, W., *CRC Handbook of Chemistry and Physics : a Ready-Reference Book of Chemical and Physical Data* 95th ed.; CRC Press: Boca Raton, Florida, 2014.
- (15) Kütt, A.; Leito, I.; Kaljurand, I.; Sooväli, L.; Vlasov, V. M.; Yagupolskii, L. M.; Koppel, I. A., A Comprehensive Self-Consistent Spectrophotometric Acidity Scale of Neutral Brønsted Acids in Acetonitrile. *J. Org. Chem.* **2006**, *71*, 2829-2838.
- (16) Treimer, S. E.; Evans, D. H., Electrochemical Reduction of Acids in Dimethyl Sulfoxide. CE Mechanisms and Beyond. *J. Electroanal. Chem.* **1998**, *449*, 39-48.
- (17) Treimer, S. E.; Evans, D. H., Electrochemical Reduction of Acids in Dimethyl Sulfoxide. Comparison of Weak C-H, N-H and O-H Acids. *J. Electroanal. Chem.* **1998**, *455*, 19-28.
- (18) Serjeant, E. P.; Dempsey, B., *Ionisation Constants of Organic Acids in Aqueous Solution*. Pergamon: Oxford, 1979.

- (19) Qiang, Z.; Adams, C., Potentiometric Determination of Acid Dissociation Constants (pK_a) for Human and Veterinary Antibiotics. *Water Res.* **2004**, *38*, 2874-2890.
- (20) Kütt, A.; Rodima, T.; Saame, J.; Raamat, E.; Mäemets, V.; Kaljurand, I.; Koppel, I. A.; Garlyauskayte, R. Y.; Yagupolskii, Y. L.; Yagupolskii, L. M.; Bernhardt, E.; Willner, H.; Leito, I., Equilibrium Acidities of Superacids. *J. Org. Chem.* **2010**, *76*, 391-395.
- (21) Wilkes, J. S., A Short History of Ionic Liquids - from Molten Salts to Neoteric Solvents. *Green Chem.* **2002**, *4*, 73-80.
- (22) Galinski, M.; Lewandowski, A.; Stepniak, I., Ionic Liquids as Electrolytes. *Electrochim. Acta* **2006**, *51*, 5567-5580.
- (23) Dean, P. M.; Pringle, J. M.; MacFarlane, D. R., Structural Analysis of Low Melting Organic Salts: Perspectives on Ionic Liquids. *Phys. Chem. Chem. Phys.* **2010**, *12*, 9144-9153.
- (24) Armand, M.; Endres, F.; MacFarlane, D. R.; Ohno, H.; Scrosati, B., Ionic-Liquid Materials for the Electrochemical Challenges of the Future. *Nat. Mater.* **2009**, *8*, 621-629.
- (25) Bard, A. J.; Faulkner, L. R., *Electrochemical Methods : Fundamentals and Applications*. 2nd ed.; Wiley: New York, 2001.
- (26) Barrette, W. C.; Sawyer, D. T., Determination of Dissolved Hydrogen and Effects of Media and Electrode Materials on the Electrochemical Oxidation of Molecular-Hydrogen. *Anal. Chem.* **1984**, *56*, 653-657.
- (27) Meng, Y.; Aldous, L.; Belding, S. R.; Compton, R. G., The Hydrogen Evolution Reaction in a Room Temperature Ionic Liquid: Mechanism and Electrocatalyst Trends. *Phys. Chem. Chem. Phys.* **2012**, *14*, 5222-5228.

(28) Meng, Y.; Aldous, L.; Belding, S. R.; Compton, R. G., The Formal Potentials and Electrode Kinetics of the Proton/Hydrogen Couple in Various Room Temperature Ionic Liquids. *Chem. Commun.* **2012**, *48*, 5572-5574.

(29) Kibler, L. A., Hydrogen Electrocatalysis. *Chemphyschem* **2006**, *7*, 985-991.

(30) Jaworski, A.; Donten, M.; Stojek, Z.; Osteryoung, J. G., Conditions of Strict Voltammetric Reversibility of the H⁺/H₂ Couple at Platinum Electrodes. *Anal. Chem.* **1999**, *71*, 243-246.

(31) Conway, B. E.; Tilak, B. V., Interfacial Processes Involving Electrocatalytic Evolution and Oxidation of H₂, and the Role of Chemisorbed H. *Electrochim. Acta* **2002**, *47*, 3571-3594.

(32) Rieger, P. H., *Electrochemistry*. 2nd ed.; Chapman & Hall: New York, 1994.

(33) Bentley, C. L.; Bond, A. M.; Hollenkamp, A. F.; Mahon, P. J.; Zhang, J., Mass Transport Studies and Hydrogen Evolution at a Platinum Electrode Using Bis(trifluoromethanesulfonyl)imide as the Proton Source in Ionic Liquids and Conventional Solvents. *J. Phys. Chem. C* **2014**, *118*, 22439–22449.

(34) Bentley, C. L.; Bond, A. M.; Hollenkamp, A. F.; Mahon, P. J.; Zhang, J., Electrochemical Proton Reduction and Equilibrium Acidity (pK_a) in Aprotic Ionic Liquids: Phenols, Carboxylic Acids and Sulfonic Acids. *In preparation* **2015**.

(35) Gritzner, G.; Kuta, J., Recommendations on Reporting Electrode-Potentials in Nonaqueous Solvents. *Pure Appl. Chem.* **1984**, *56*, 461-466.

(36) Rogers, E. I.; Silvester, D. S.; Poole, D. L.; Aldous, L.; Hardacre, C.; Compton, R. G., Voltammetric Characterization of the Ferrocene|Ferrocenium and

Cobaltocenium|Cobaltocene Redox Couples in RTILs. *J. Phys. Chem. C* **2008**, *112*, 2729-2735.

(37) Mahon, P. J.; Oldham, K. B., Convolution Modelling of Electrochemical Processes Based on the Relationship Between the Current and the Surface Concentration. *J. Electroanal. Chem.* **1999**, *464*, 1-13.

(38) Bentley, C. L.; Bond, A. M.; Hollenkamp, A. F.; Mahon, P. J.; Zhang, J., Applications of Convolution Voltammetry in Electroanalytical Chemistry. *Anal. Chem.* **2014**, *86*, 2073–2081.

(39) Bentley, C. L.; Bond, A. M.; Hollenkamp, A. F.; Mahon, P. J.; Zhang, J., Electrode Reaction and Mass-Transport Mechanisms Associated with the Iodide/Triiodide Couple in the Ionic Liquid 1-Ethyl-3-methylimidazolium Bis(trifluoromethanesulfonyl)imide. *J. Phys. Chem. C* **2014**, *118*, 29663–29673.

(40) Shoup, D.; Szabo, A., Chronoamperometric Current at Finite Disk Electrodes. *J. Electroanal. Chem.* **1982**, *140*, 237-245.

(41) Klymenko, O. V.; Evans, R. G.; Hardacre, C.; Svir, I. B.; Compton, R. G., Double Potential Step Chronoamperometry at Microdisk Electrodes: Simulating the Case of Unequal Diffusion Coefficients. *J. Electroanal. Chem.* **2004**, *571*, 211-221.

(42) Stojanovic, R. S.; Bond, A. M., Examination of Conditions under Which the Reduction of the Cobaltocenium Cation Can Be Used as a Standard Voltammetric Reference Process in Organic and Aqueous Solvents. *Anal. Chem.* **1993**, *65*, 56-64.

(43) Hultgren, V. M.; Mariotti, A. W. A.; Bond, A. M.; Wedd, A. G., Reference Potential Calibration and Voltammetry at Macrodisk Electrodes of Metallocene Derivatives in the Ionic Liquid BMIM PF₆. *Anal. Chem.* **2002**, *74*, 3151-3156.

(44) Shuman, M. S., Nonunity Electrode Reaction Orders and Stationary Electrode Polarography. *Anal. Chem.* **1969**, *41*, 142-&.

(45) Tilset, M., Derivative Cyclic Voltammetry: Applications in the Investigation of the Energetics of Organometallic Electrode Reactions. In *Energetics of Organometallic Species*, Martinho Simões, J. A., Ed. Springer Netherlands: 1992; Vol. 367, p 109-129.

(46) Murthy, A.; Manthiram, A., Application of Derivative Voltammetry in the Analysis of Methanol Oxidation Reaction. *J. Phys. Chem. C* **2012**, *116*, 3827-3832.

(47) Crowhurst, L.; Mawdsley, P. R.; Perez-Arlandis, J. M.; Salter, P. A.; Welton, T., Solvent-Solute Interactions in Ionic Liquids. *Phys. Chem. Chem. Phys.* **2003**, *5*, 2790-2794.

(48) Schmeisser, M.; Illner, P.; Puchta, R.; Zahl, A.; van Eldik, R., Gutmann Donor and Acceptor Numbers for Ionic Liquids. *Chem.-Eur. J.* **2012**, *18*, 10969-10982.

(49) Barrosse-Antle, L. E.; Bond, A. M.; Compton, R. G.; O'Mahony, A. M.; Rogers, E. I.; Silvester, D. S., Voltammetry in Room Temperature Ionic Liquids: Comparisons and Contrasts with Conventional Electrochemical Solvents. *Chem.-Asian J.* **2010**, *5*, 202-230.

(50) Creager, S., 3 - Solvents and Supporting Electrolytes. In *Handbook of Electrochemistry*, Zoski, C. G., Ed. Elsevier: Amsterdam, 2007; p 57-72.

Supporting information for

Electrochemical Proton Reduction and
Equilibrium Acidity (pK_a) in Aprotic Ionic
Liquids: Protonated Amines and Sulfonamide
Acids

*Cameron L. Bentley,^{†,‡} Alan M. Bond,[†] Anthony F. Hollenkamp,[‡] Peter J. Mahon[§] and Jie
Zhang[†]*

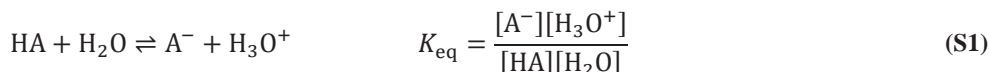
[†]School of Chemistry, Monash University, Clayton, Vic 3800, Australia

[‡]CSIRO Energy Flagship, Box 312, Clayton South, Vic 3169, Australia

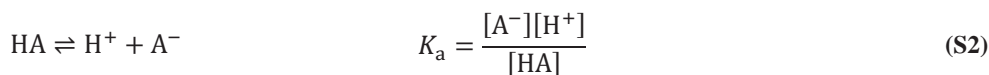
[§]Faculty of Science, Engineering and Technology, Swinburne University of Technology,
Hawthorn, Vic 3122, Australia

Calculation of pK_a (H_3O^+) in H_2O

Take the general Brønsted acid, HA. In water, ionization occurs:



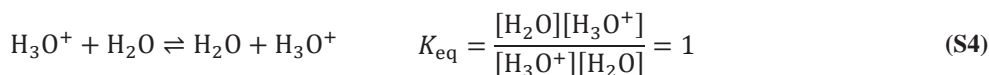
where $[H_2O]$ in pure water is equal to $(997.05 \text{ g/L})/(18.02 \text{ g/mol}) = 55.3 \text{ mol/L}$ at 25°C . In dilute aqueous solution, $[H_2O]$ is enormous and essentially constant. Consequently, the acid dissociation constant, K_a , is defined without regard to this entity:



As defined above, K_a and K_{eq} are related as follows:

$$K_a = K_{eq}[H_2O] \quad (S3)$$

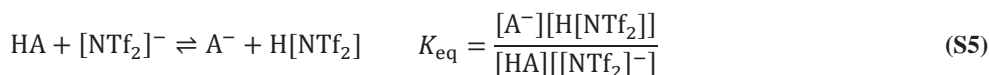
For the special case when $HA = H_3O^+$:



And therefore, $K_a = 1 \times 55.3 = 55.3$ and $pK_a(H_3O^+) = -\log_{10}(55.3) = -1.74$

Calculation of pK_a ($H[NTf_2]$) in $[C_2mim][NTf_2]$

Using the same logic as above, we get:



Given that the density and molecular weight of $[C_2mim][NTf_2]$ are 1520 g/L and 391.31 g/mol , $pK_a(H[NTf_2]) = -\log_{10}(1520/391.31) = -0.59$ at 25°C .

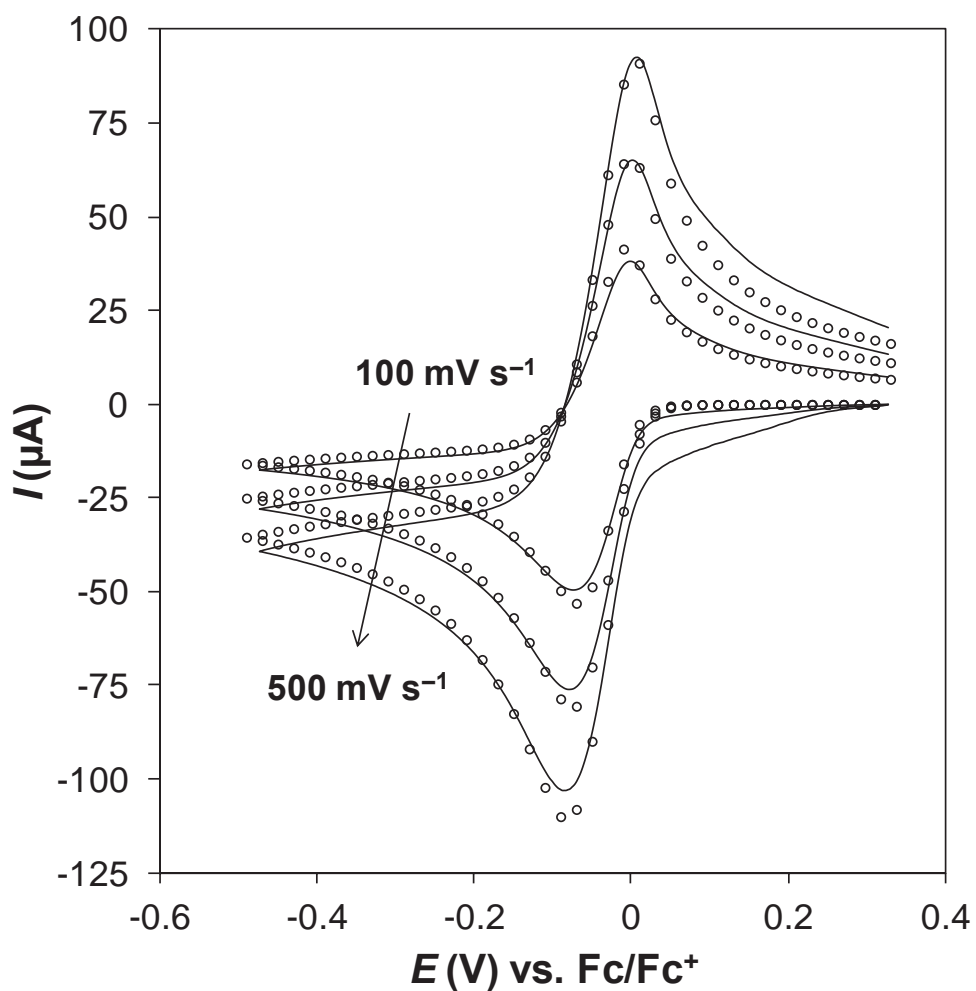


Figure S1. Comparison of the simulated (\circ) and experimental (—) cyclic voltammograms showing the proton reduction process obtained from 49.8 mM H[NTf₂] in [C₂mim][NTf₂] at a 1.6 mm dia. Pt macrodisk electrode with scan rates of 100, 250 and 500 mV s⁻¹. Simulation parameters are available in Table 2 of the main text.

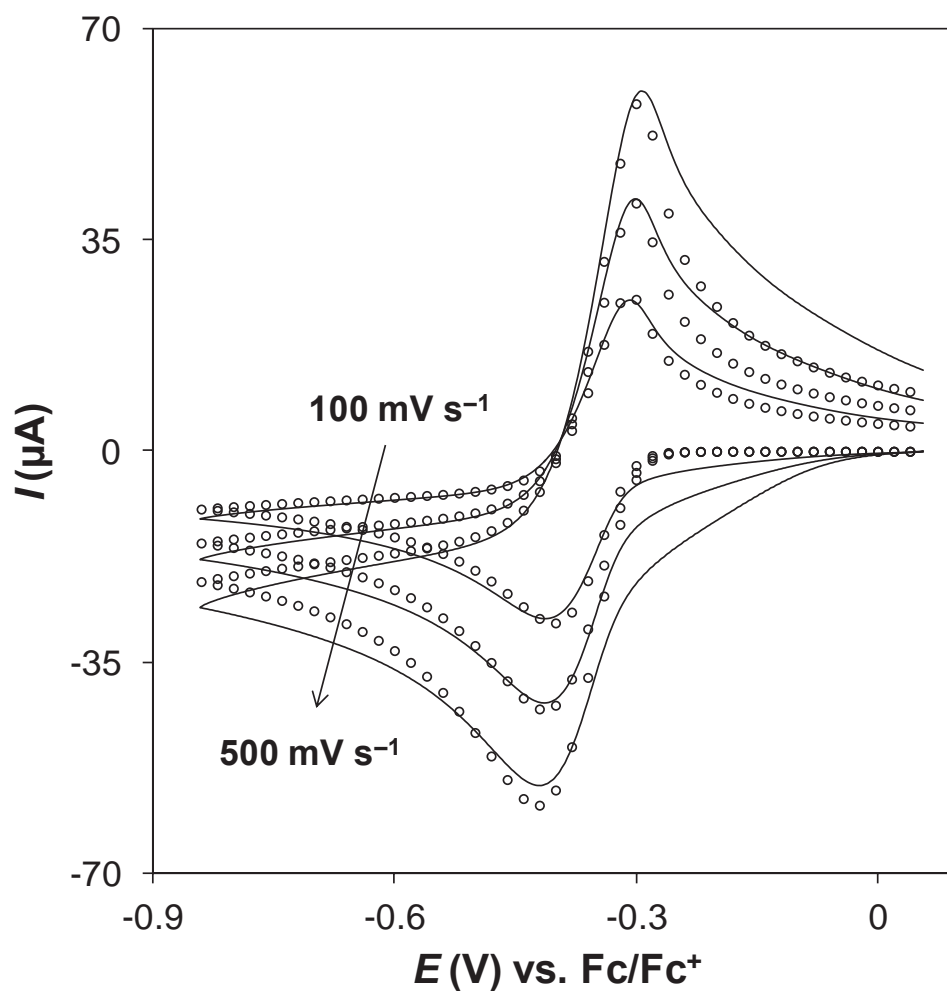


Figure S2. Comparison of the simulated (\circ) and experimental (—) cyclic voltammograms showing the proton reduction process obtained from 41.1 mM H[OTf] in $[\text{C}_2\text{mim}][\text{OTf}]$ at a 1.6 mm dia. Pt macrodisk electrode with scan rates of 100, 250 and 500 mV s^{-1} . Simulation parameters are available in Table 2 of the main text.

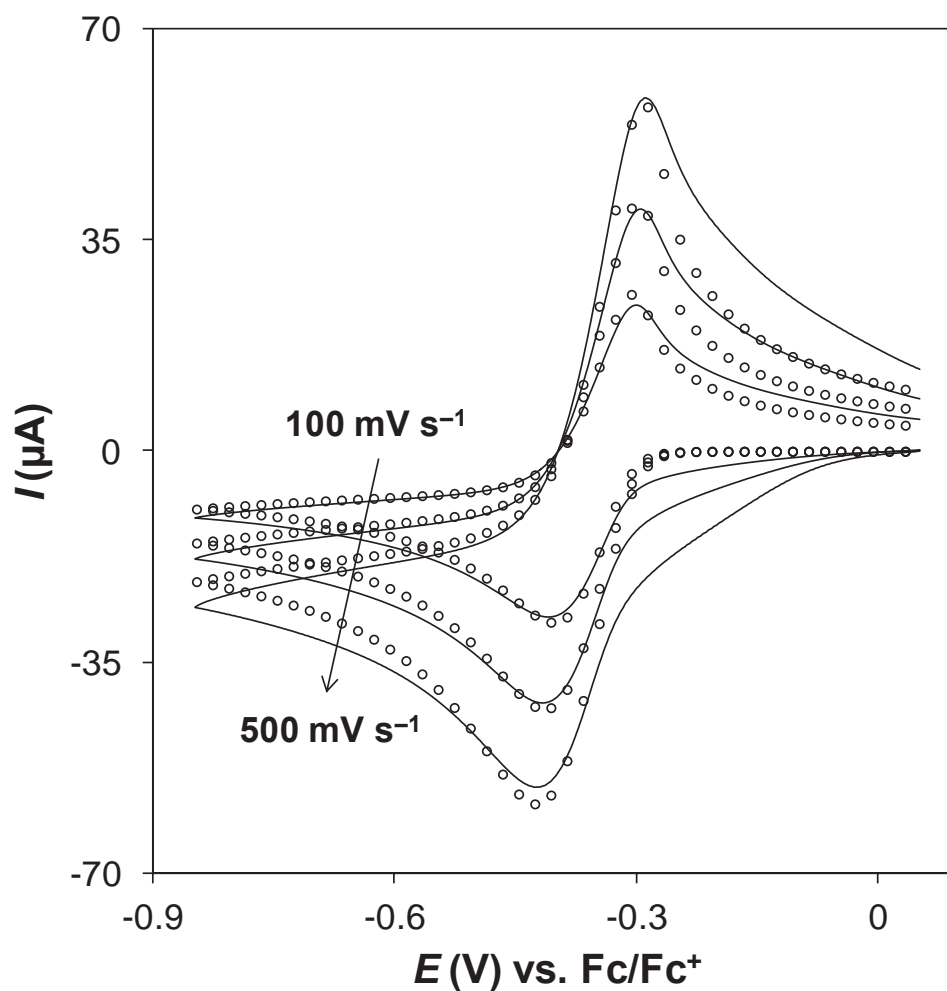


Figure S3. Comparison of the simulated (\circ) and experimental (—) cyclic voltammograms showing the proton reduction process obtained from 42.0 mM H[NTf₂] in [C₂mim][OTf] at a 1.6 mm dia. Pt macrodisk electrode with scan rates of 100, 250 and 500 mV s⁻¹. Simulation parameters are available in Table 2 of the main text.

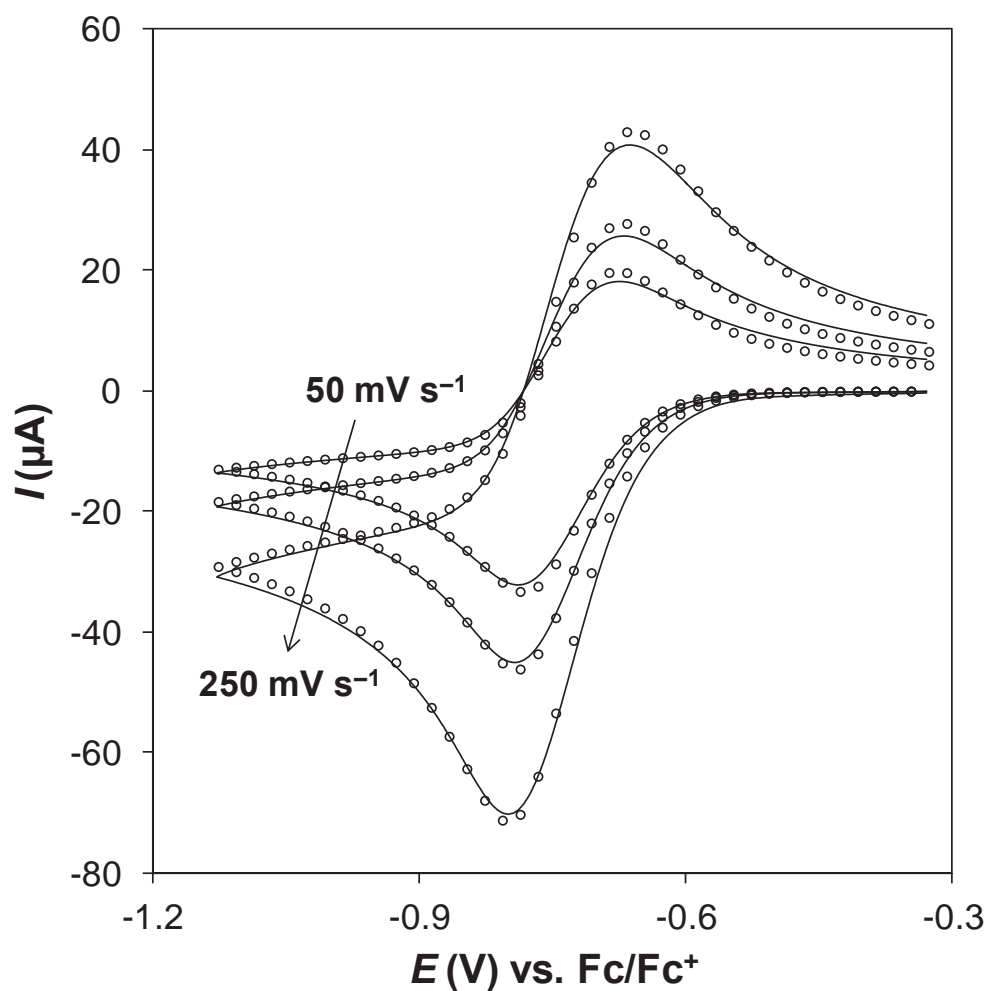


Figure S4. Comparison of the simulated (\circ) and experimental (—) cyclic voltammograms showing the proton reduction process obtained from 50.2 mM [Pyr-H][NTf₂] in [C₂mim][NTf₂] at a 1.6 mm dia. Pt macrodisk electrode with scan rates of 50, 100 and 250 mV s⁻¹. Simulation parameters are available in Table 3 of the main text.

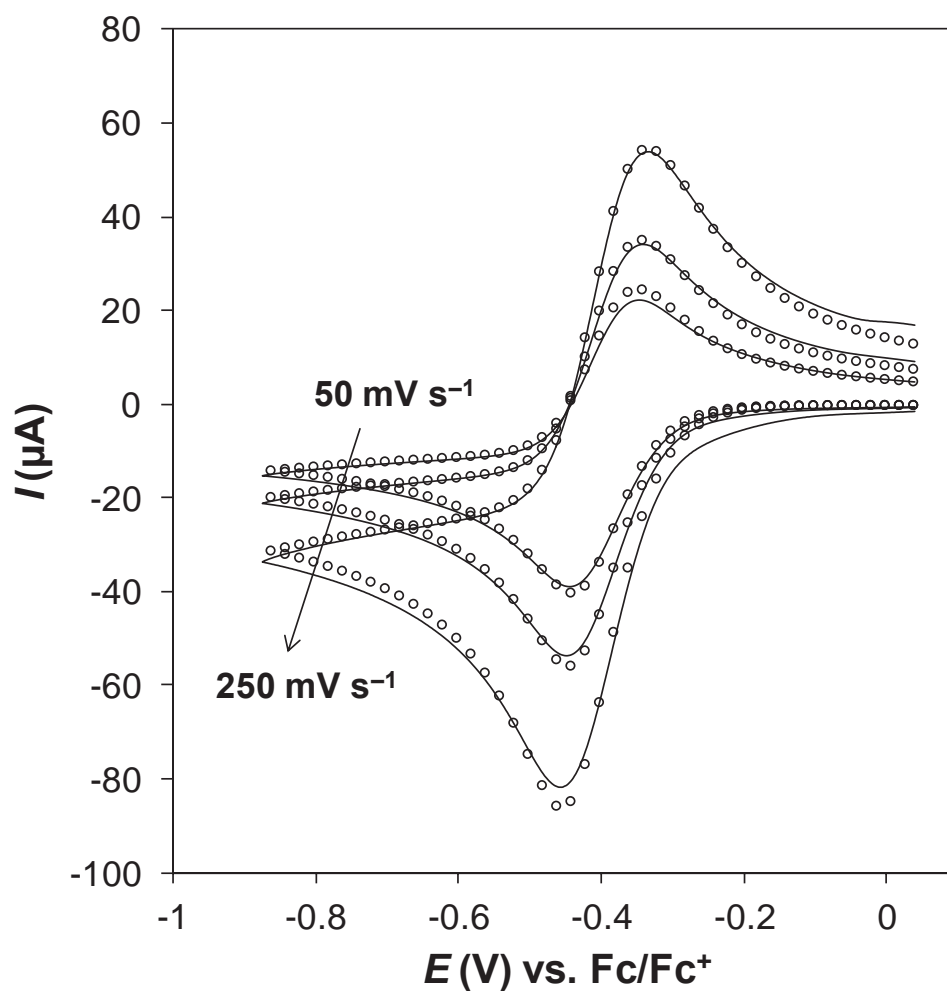


Figure S5. Comparison of the simulated (\circ) and experimental (—) cyclic voltammograms showing the proton reduction process obtained from 62.4 mM $[\text{CIPyr-H}][\text{NTf}_2]$ in $[\text{C}_2\text{mim}][\text{NTf}_2]$ at a 1.6 mm dia. Pt macrodisk electrode with scan rates of 50, 100 and 250 mV s^{-1} . Simulation parameters are available in Table 3 of the main text.

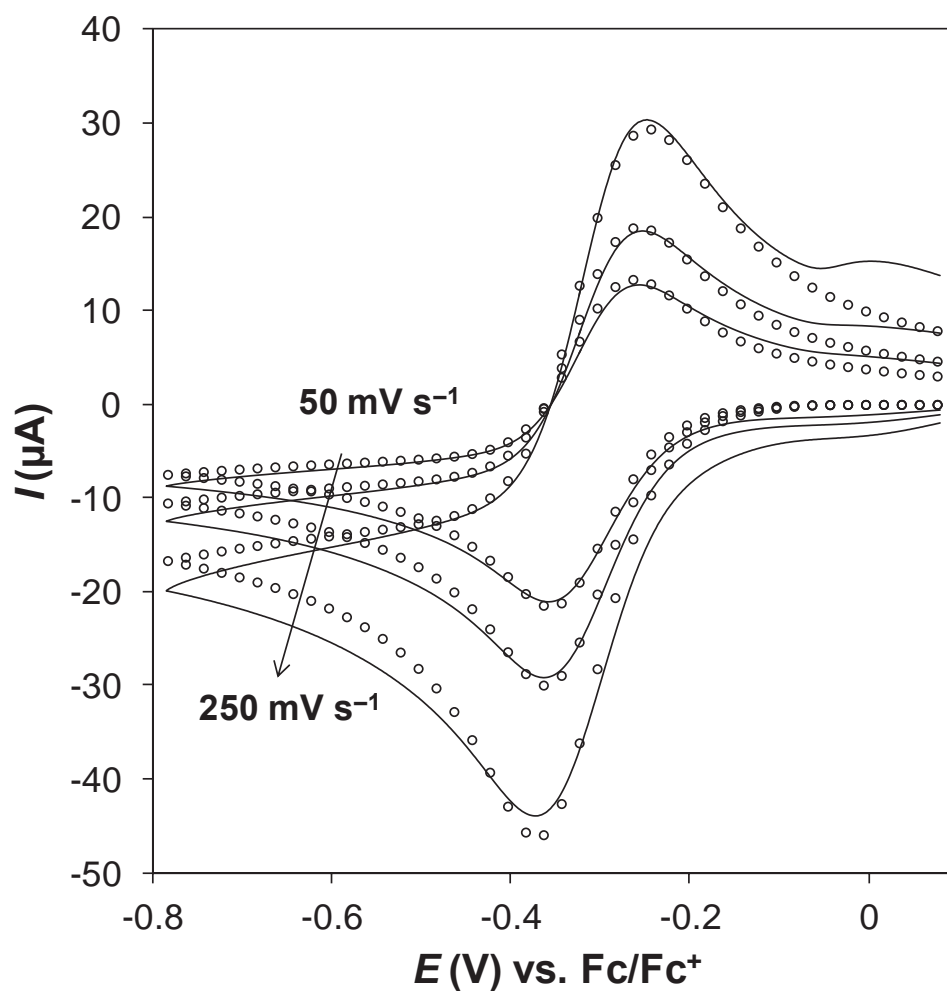


Figure S6. Comparison of the simulated (\circ) and experimental (—) cyclic voltammograms showing the proton reduction process obtained from 38.7 mM [dCIPyr-H][NTf₂] in [C₂mim][NTf₂] at a 1.6 mm dia. Pt macrodisk electrode with scan rates of 50, 100 and 250 mV s^{-1} . Simulation parameters are available in Table 3 of the main text.

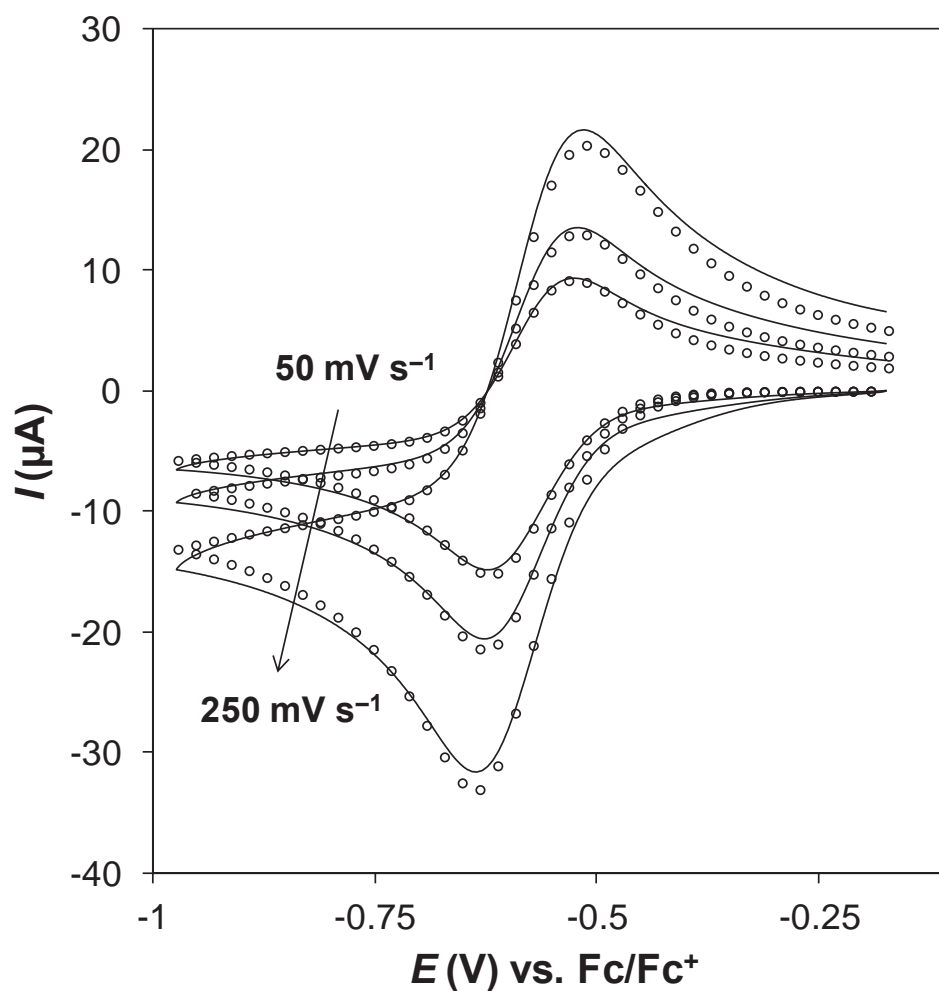


Figure S7. Comparison of the simulated (\circ) and experimental (—) cyclic voltammograms showing the proton reduction process obtained from 30.4 mM [An-H][NTf₂] in [C₂mim][NTf₂] at a 1.6 mm dia. Pt macrodisk electrode with scan rates of 50, 100 and 250 mV s⁻¹. Simulation parameters are available in Table 3 of the main text.

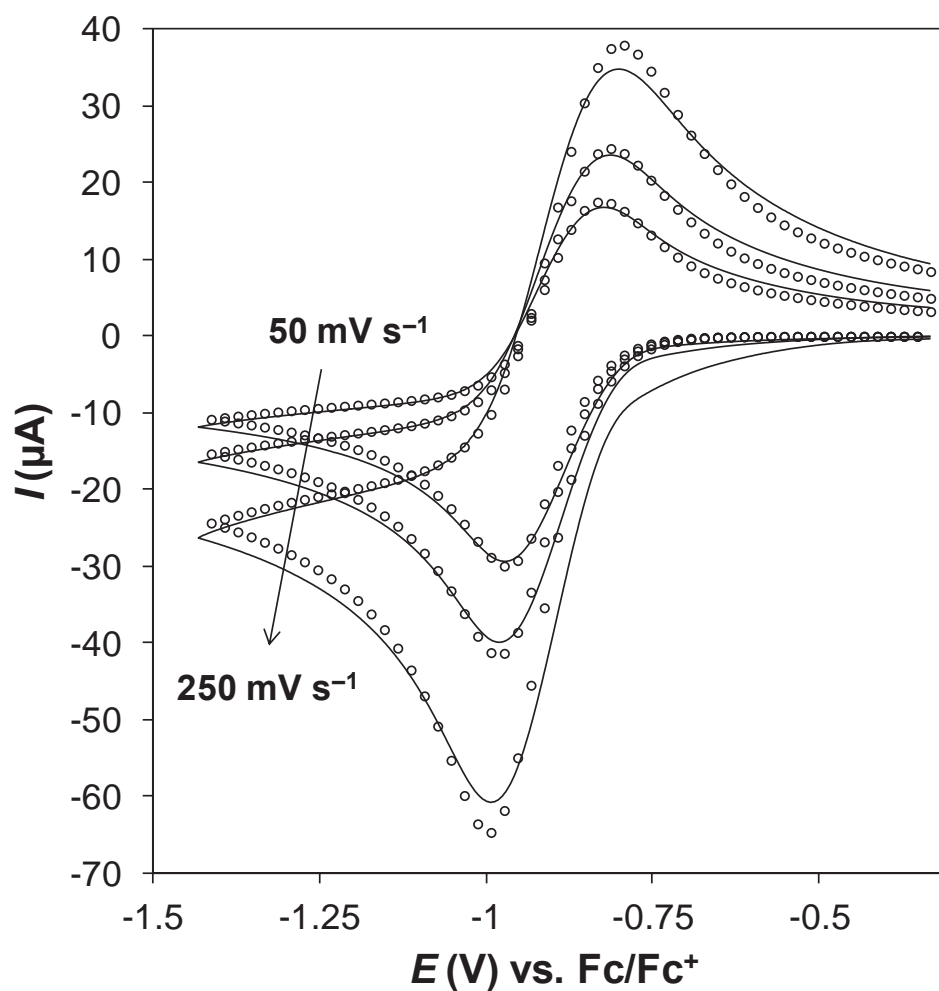


Figure S8. Comparison of the simulated (\circ) and experimental (—) cyclic voltammograms showing the proton reduction process obtained from 49.3 mM [MeIm-H][NTf₂] in [C₂mim][NTf₂] at a 1.6 mm dia. Pt macrodisk electrode with scan rates of 50, 100 and 250 mV s⁻¹. Simulation parameters are available in Table 3 of the main text.

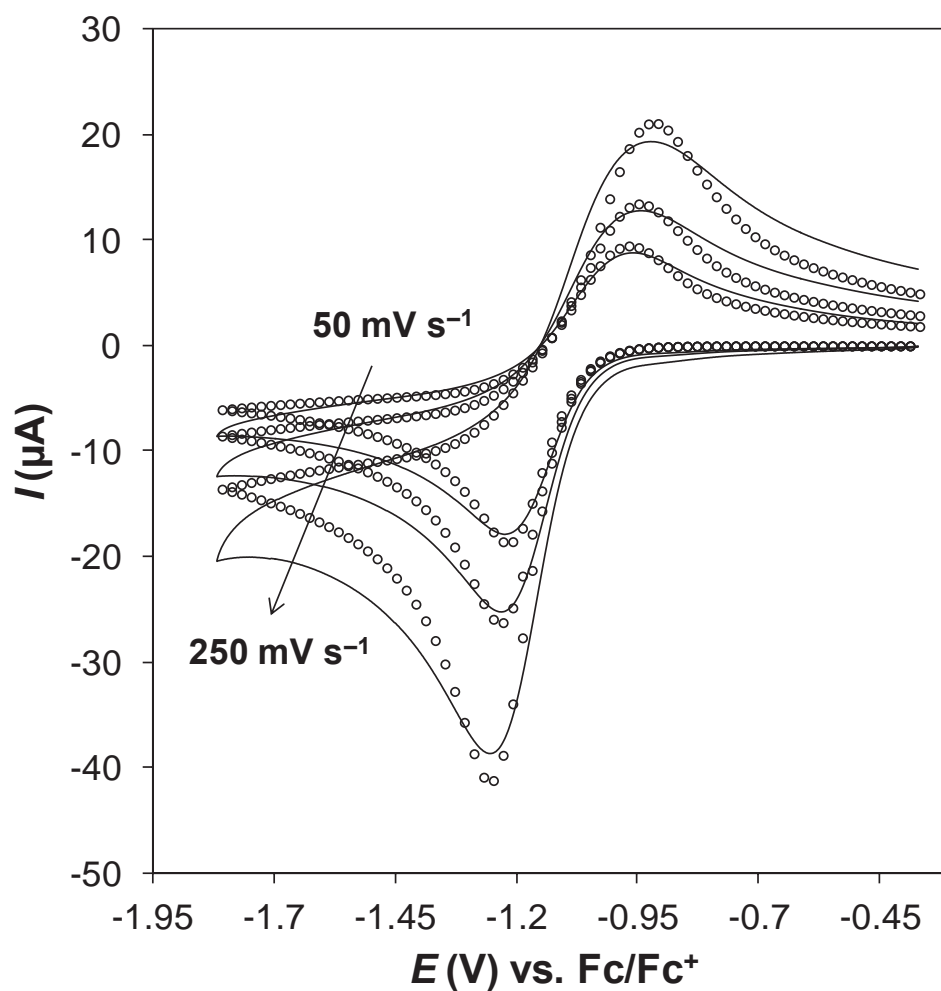


Figure S9. Comparison of the simulated (\circ) and experimental ($—$) cyclic voltammograms showing the proton reduction process obtained from 29.4 mM [MePyrd-H][NTf₂] in [C₂mim][NTf₂] at a 1.6 mm dia. Pt macrodisk electrode with scan rates of 50, 100 and 250 mV s⁻¹. Simulation parameters are available in Table 3 of the main text.

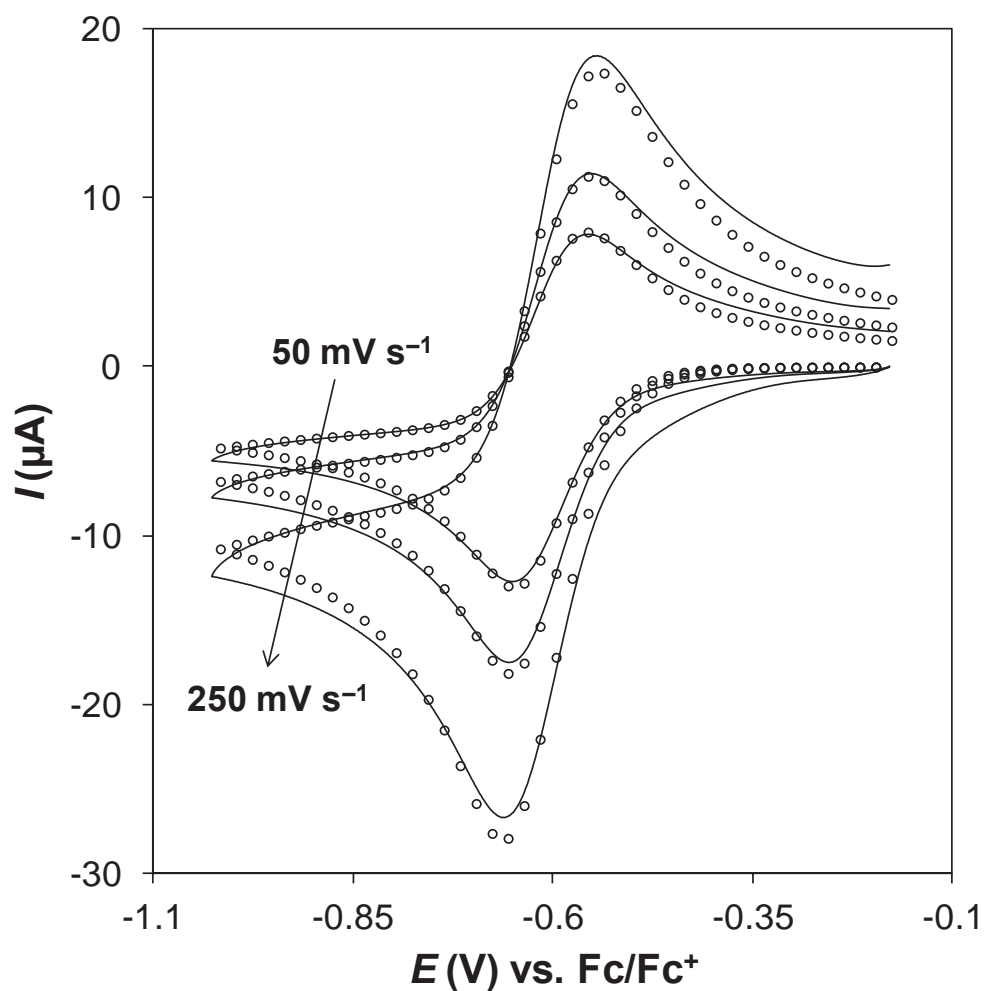


Figure S10. Comparison of the simulated (\circ) and experimental (—) cyclic voltammograms showing the proton reduction process obtained from 28.2 mM [oPD-H][NTf₂] in [C₂mim][NTf₂] at a 1.6 mm dia. Pt macrodisk electrode with scan rates of 50, 100 and 250 mV s^{-1} . Simulation parameters are available in Table 3 of the main text.

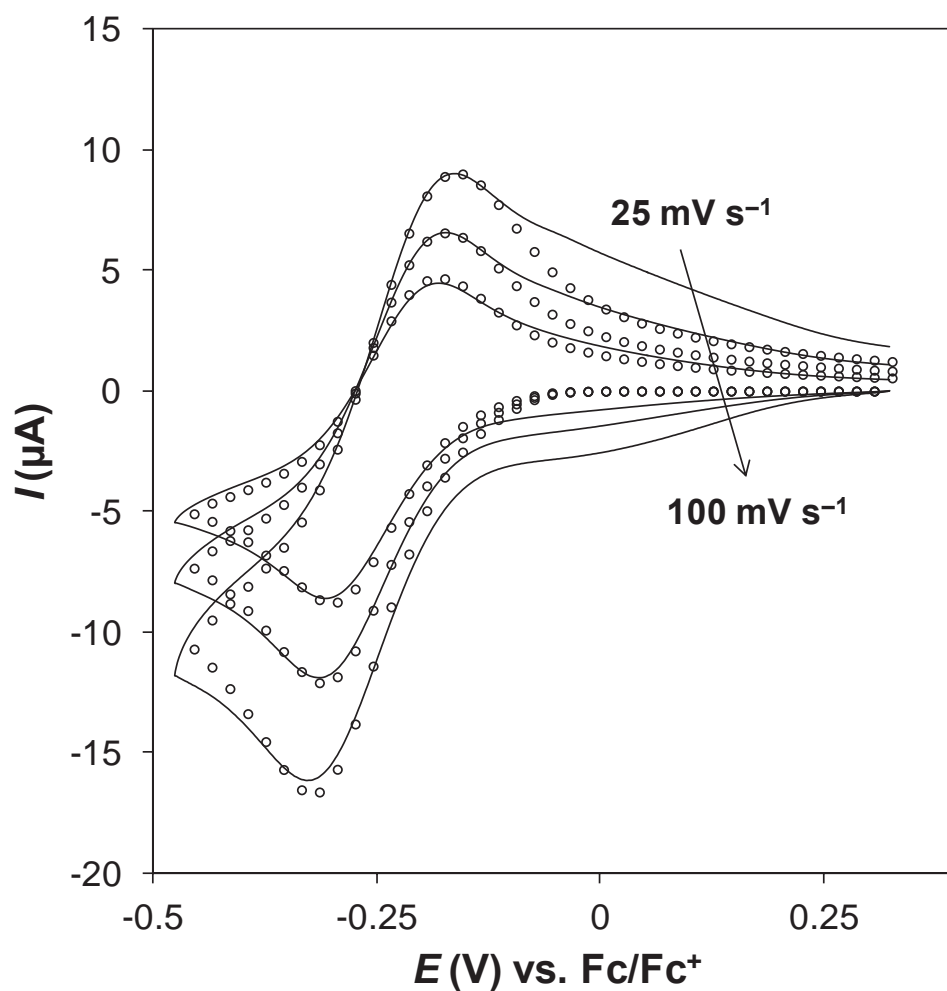


Figure S11. Comparison of the simulated (\circ) and experimental ($—$) cyclic voltammograms showing the proton reduction process obtained from 33.0 mM $[\text{oPD-H}_2][\text{NTf}_2]_2$ in $[\text{C}_2\text{mim}][\text{NTf}_2]$ at a 1.6 mm dia. Pt macrodisk electrode with scan rates of 25, 50 and 100 mV s^{-1} . Simulation parameters are available in Table 3 of the main text.

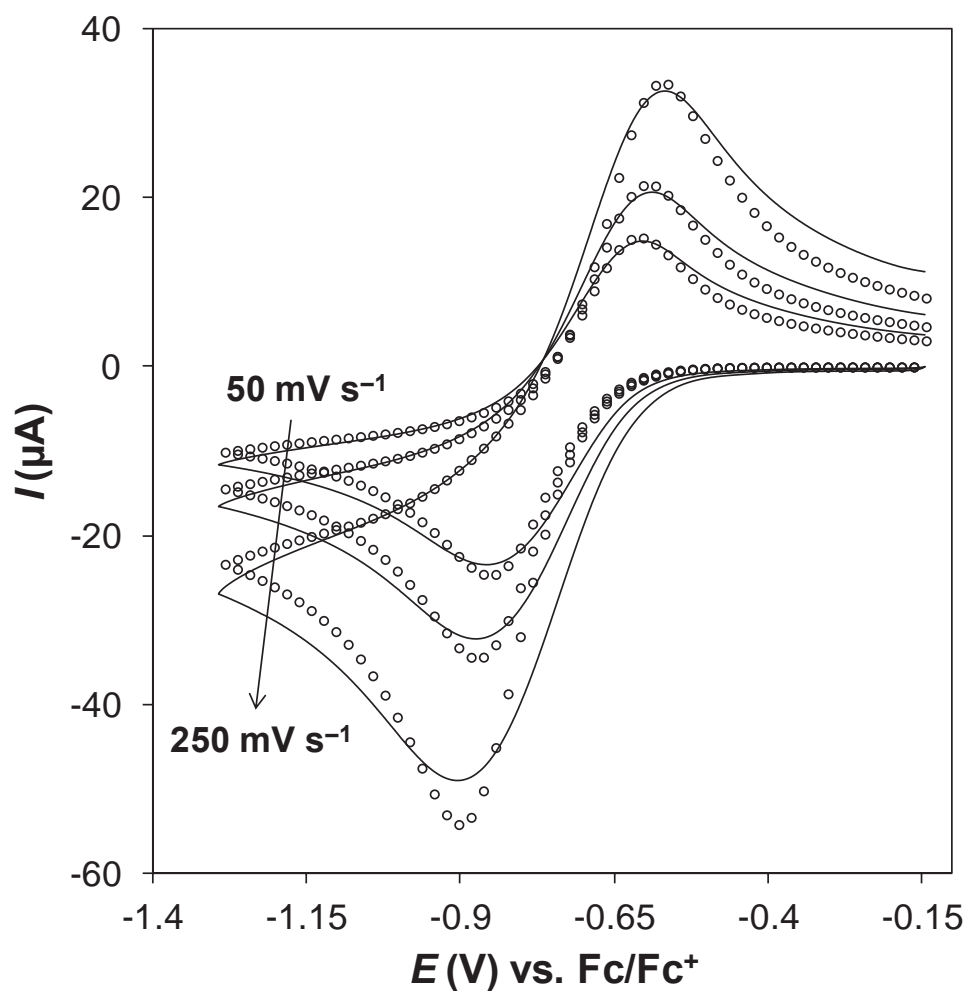


Figure S12. Comparison of the simulated (\circ) and experimental (—) cyclic voltammograms showing the proton reduction process obtained from 58.3 mM SACC in $[\text{C}_2\text{mim}][\text{NTf}_2]$ at a 1.6 mm dia. Pt macrodisk electrode with scan rates of 50, 100 and 250 mV s^{-1} . Simulation parameters are available in Table 3 of the main text.

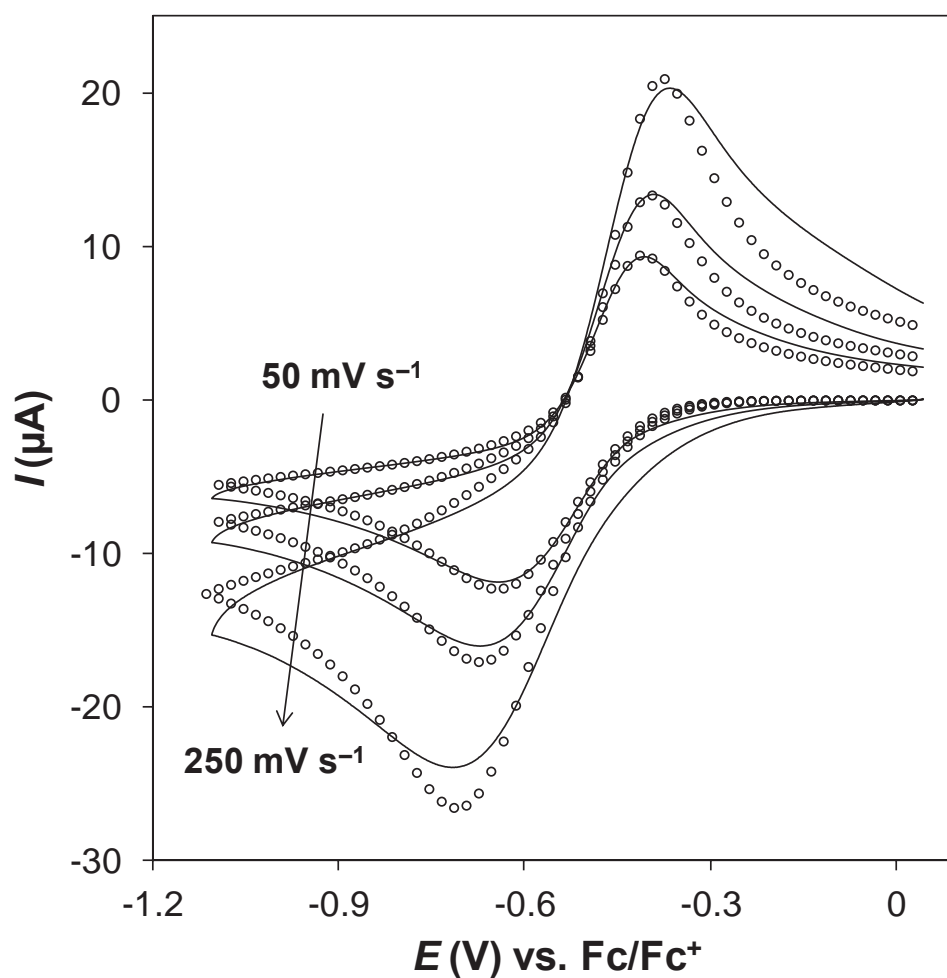
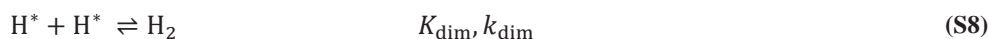


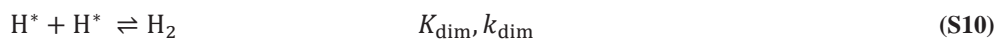
Figure S13. Comparison of the simulated (\circ) and experimental ($—$) cyclic voltammograms showing the proton reduction process obtained from 37.6 mM DBSA in $[\text{C}_2\text{mim}][\text{NTf}_2]$ at a 1.6 mm dia. Pt macrodisk electrode with scan rates of 50, 100 and 250 mV s^{-1} . Simulation parameters are available in Table 3 of the main text.

Simulations: *CE* vs. *DR* pathway

Chemical-Electrochemical (*CE*) Mechanism:



Direct Reduction (*DR*) Mechanism:



Simulation Parameters:

Table S1. Simulation parameters for the reactions shown in Eqs. S6 – S10.

Parameter	Value
K_a	10^{-1} to 10^{-5}
k_{dissoc}	$5 \times 10^8 \text{ M}^{-1} \text{ s}^{-1}$
$E_{\text{CE}}^{0'}$	-0.144 V
$k_{\text{s,CE}}$	0.022 cm/s
$\alpha_{\text{CE}} = \alpha_{\text{DR}}$	0.5
$E_{\text{DR}}^{0'}$	$E_{\text{CE}}^{0'} + \frac{RT}{F} \ln K_a$
$k_{\text{s,DR}}$	0.05 cm/s
K_{dim}	10^4
k_{dim}	$10^{16} \text{ M}^{-1} \text{ s}^{-1}$
$D_{\text{H}^+} = D_{\text{BH}^+} = D_{\text{B}}$	$3 \times 10^{-7} \text{ cm}^2 \text{ s}^{-1}$
D_{H_2}	$2 \times 10^{-5} \text{ cm}^2 \text{ s}^{-1}$
D_{H^*}	$1 \times 10^{-15} \text{ cm}^2 \text{ s}^{-1}$
$[\text{BH}^+]_{\text{b}}$	0.05 M

S16

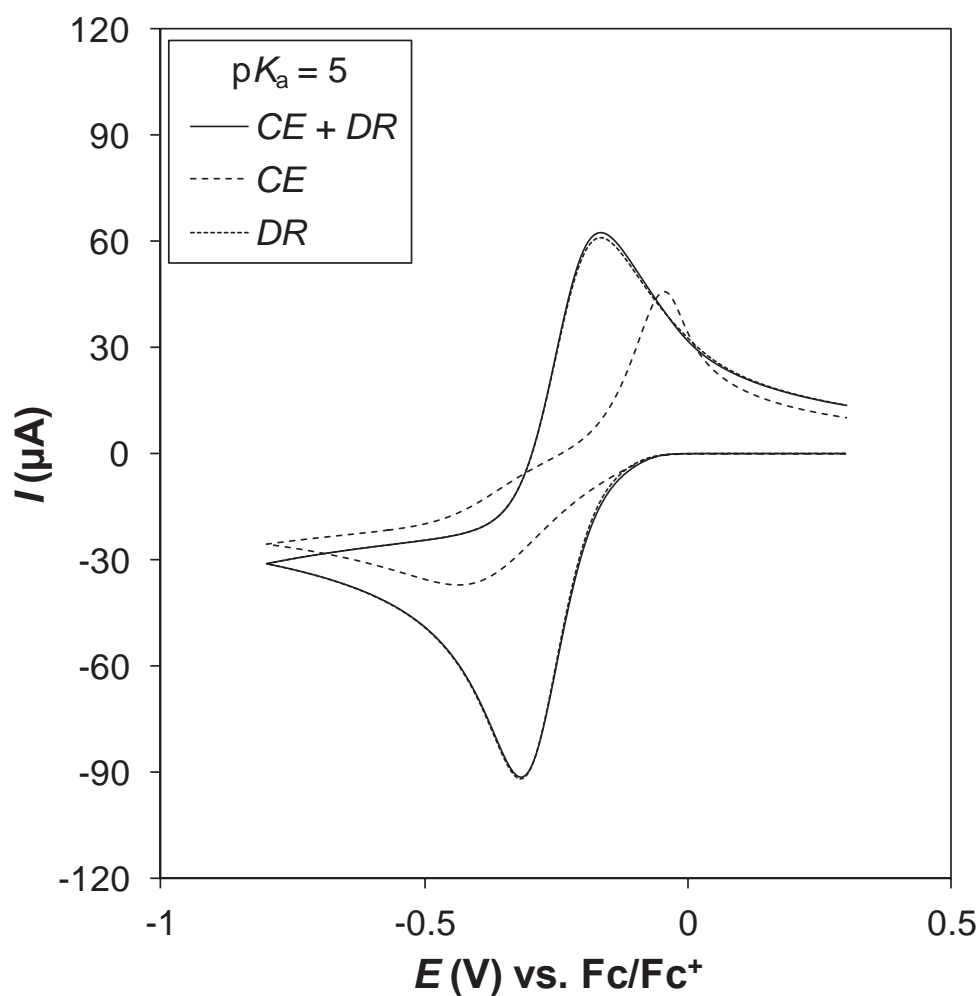


Figure S14. Simulated cyclic voltammograms mimicking proton reduction from a weak acid ($\text{p}K_a = 5$) in $[\text{C}_2\text{mim}][\text{NTf}_2]$ at a 1.6 mm dia. Pt macrodisk electrode with a scan rate of 500 mV s^{-1} . Three different mechanisms were employed in the simulations, CE (Eqs. S6 – S8, dashed line), DR (Eqs. S9 and S10, dotted line) and $\text{CE} + \text{DR}$ (Eqs. S6 – S10, solid line). Simulation parameters are available in Table S1.

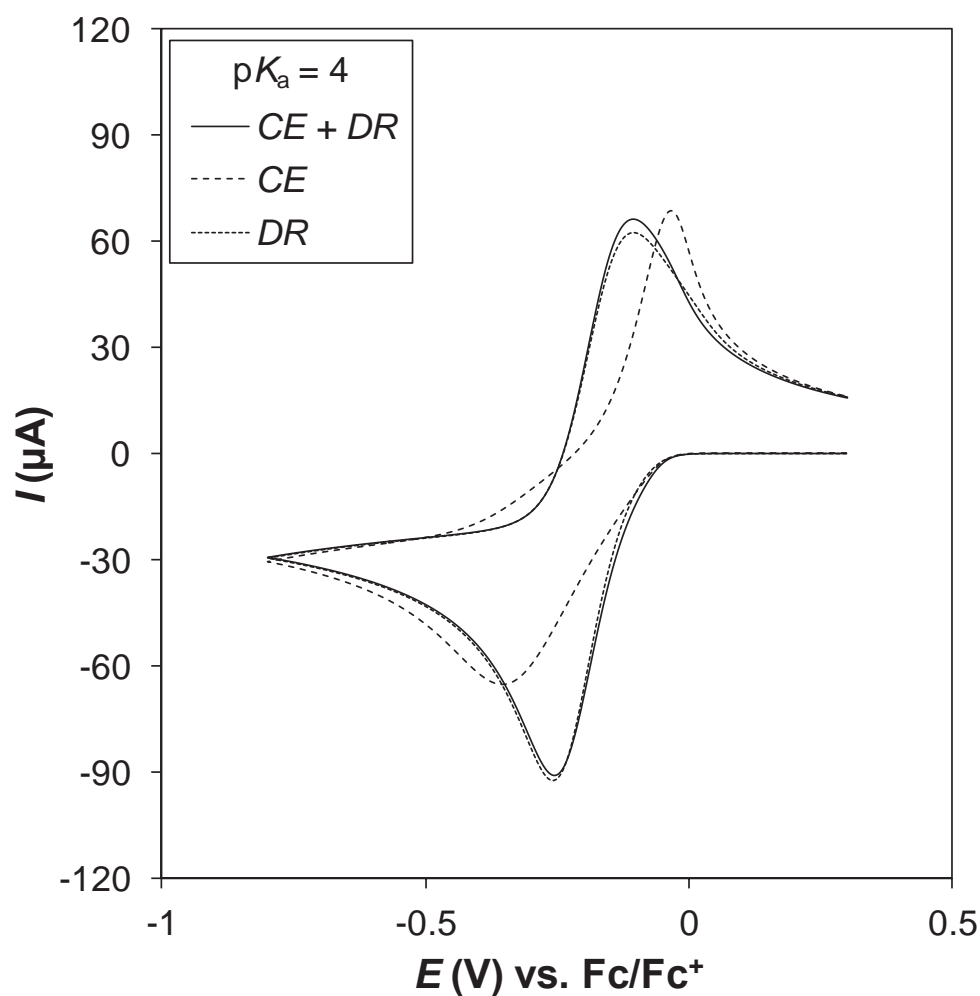


Figure S15. Simulated cyclic voltammograms mimicking proton reduction from a weak acid ($\text{p}K_a = 4$) in $[\text{C}_2\text{mim}][\text{NTf}_2]$ at a 1.6 mm dia. Pt macrodisk electrode with a scan rate of 500 mV s^{-1} . Three different mechanisms were employed in the simulations, CE (Eqs. S6 – S8, dashed line), DR (Eqs. S9 and S10, dotted line) and $\text{CE} + \text{DR}$ (Eqs. S6 – S10, solid line). Simulation parameters are available in Table S1.

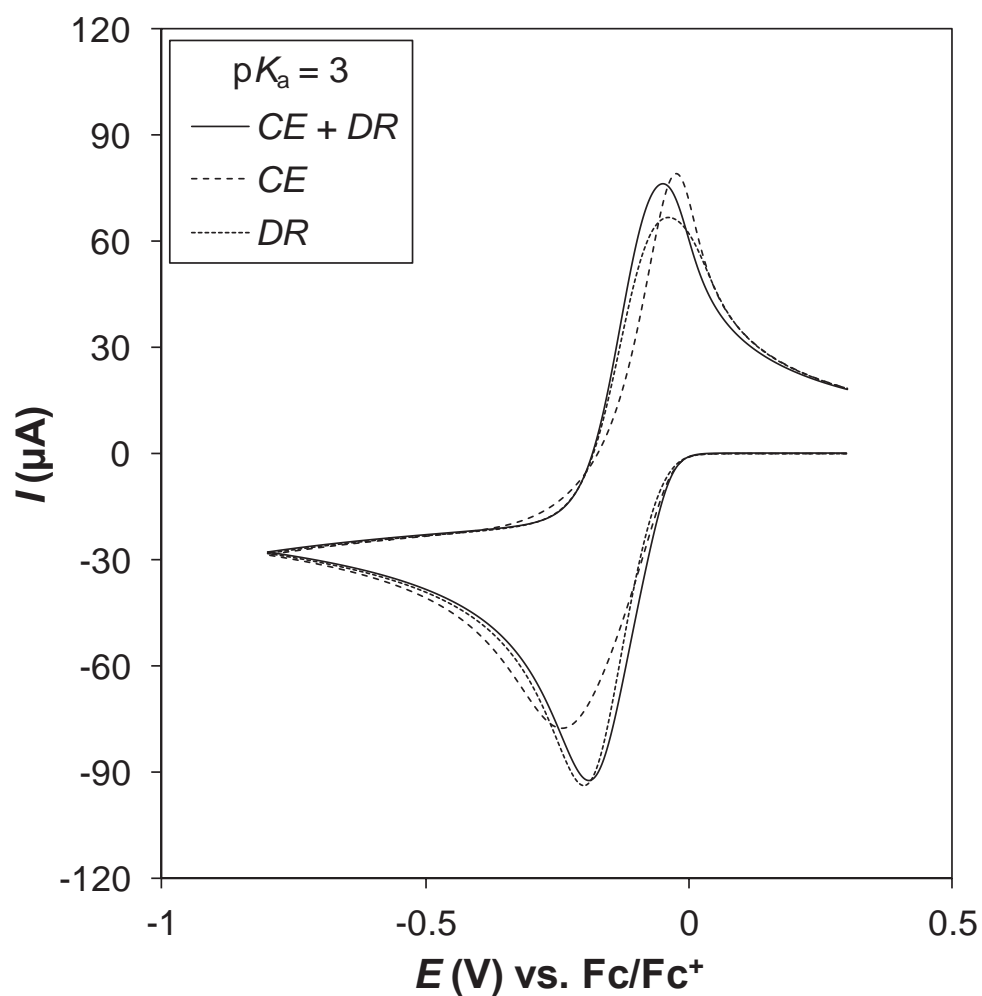


Figure S16. Simulated cyclic voltammograms mimicking proton reduction from a weak acid ($pK_a = 3$) in $[\text{C}_2\text{mim}][\text{NTf}_2]$ at a 1.6 mm dia. Pt macrodisk electrode with a scan rate of 500 mV s^{-1} . Three different mechanisms were employed in the simulations, CE (Eqs. S6 – S8, dashed line), DR (Eqs. S9 and S10, dotted line) and $CE + DR$ (Eqs. S6 – S10, solid line). Simulation parameters are available in Table S1.

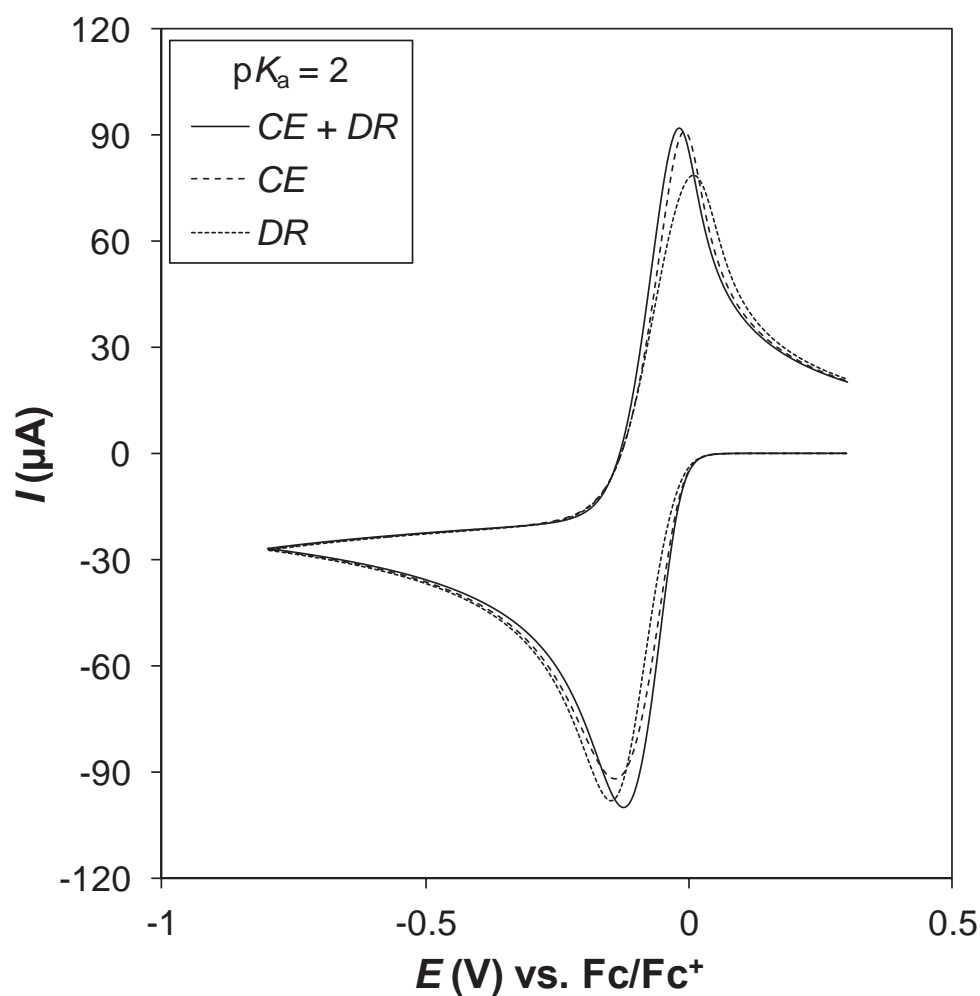


Figure S17. Simulated cyclic voltammograms mimicking proton reduction from a weak acid ($\text{p}K_a = 2$) in $[\text{C}_2\text{mim}][\text{NTf}_2]$ at a 1.6 mm dia. Pt macrodisk electrode with a scan rate of 500 mV s^{-1} . Three different mechanisms were employed in the simulations, CE (Eqs. S6 – S8, dashed line), DR (Eqs. S9 and S10, dotted line) and $\text{CE} + \text{DR}$ (Eqs. S6 – S10, solid line). Simulation parameters are available in Table S1.

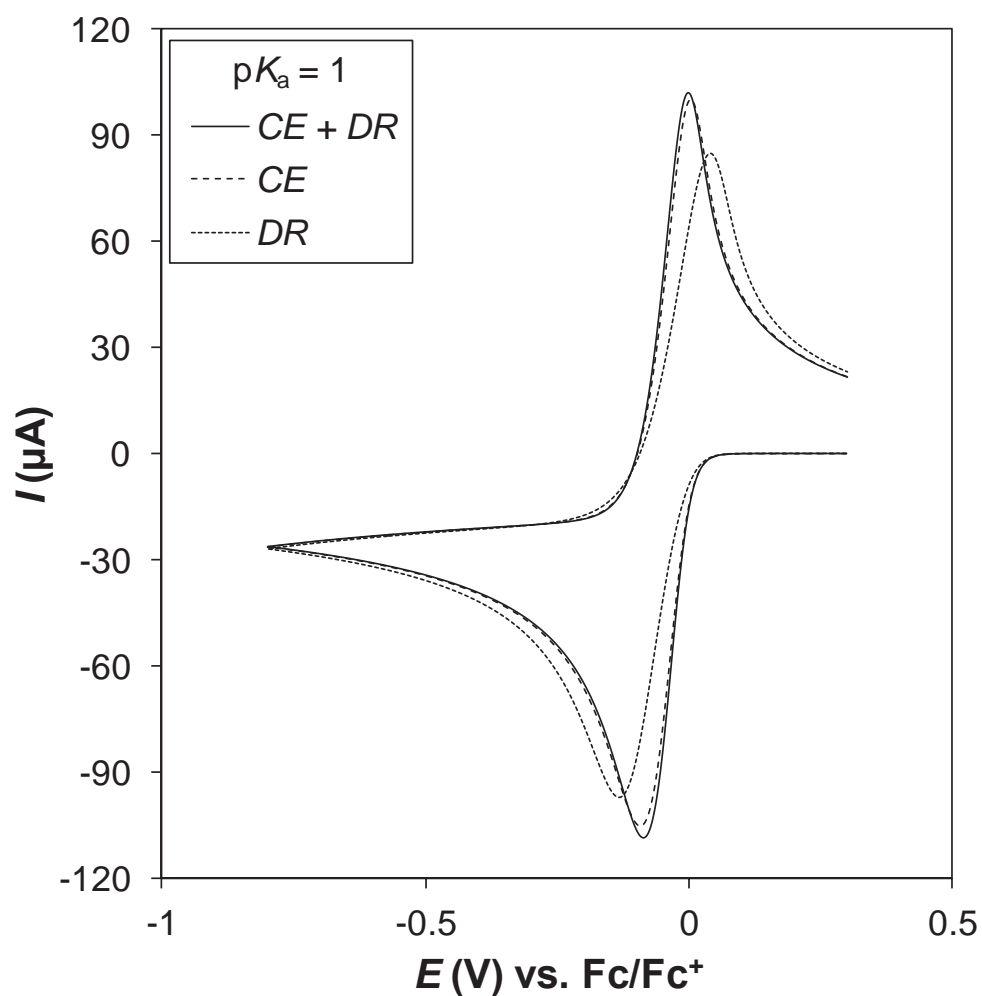


Figure S18. Simulated cyclic voltammograms mimicking proton reduction from a weak acid ($pK_a = 1$) in $[\text{C}_2\text{mim}][\text{NTf}_2]$ at a 1.6 mm dia. Pt macrodisk electrode with a scan rate of 500 mV s^{-1} . Three different mechanisms were employed in the simulations, CE (Eqs. S6 – S8, dashed line), DR (Eqs. S9 and S10, dotted line) and $CE + DR$ (Eqs. S6 – S10, solid line). Simulation parameters are available in Table S1.

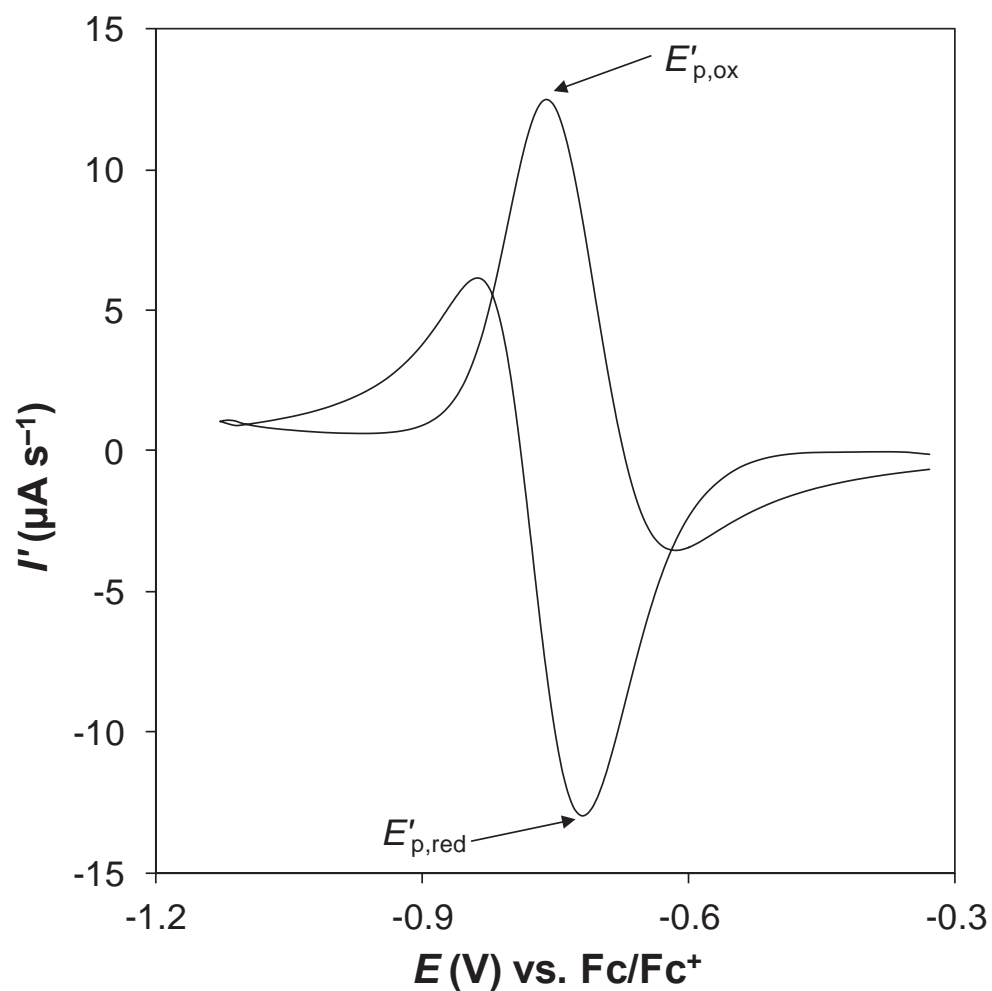


Figure S19. A derivative cyclic voltammogram showing the proton reduction process obtained from 50.2 mM [Pyr-H][NTf₂] in [C₂mim][NTf₂] at a 1.6 mm dia. Pt macrodisk electrode with a scan rate of 50 mV s⁻¹.

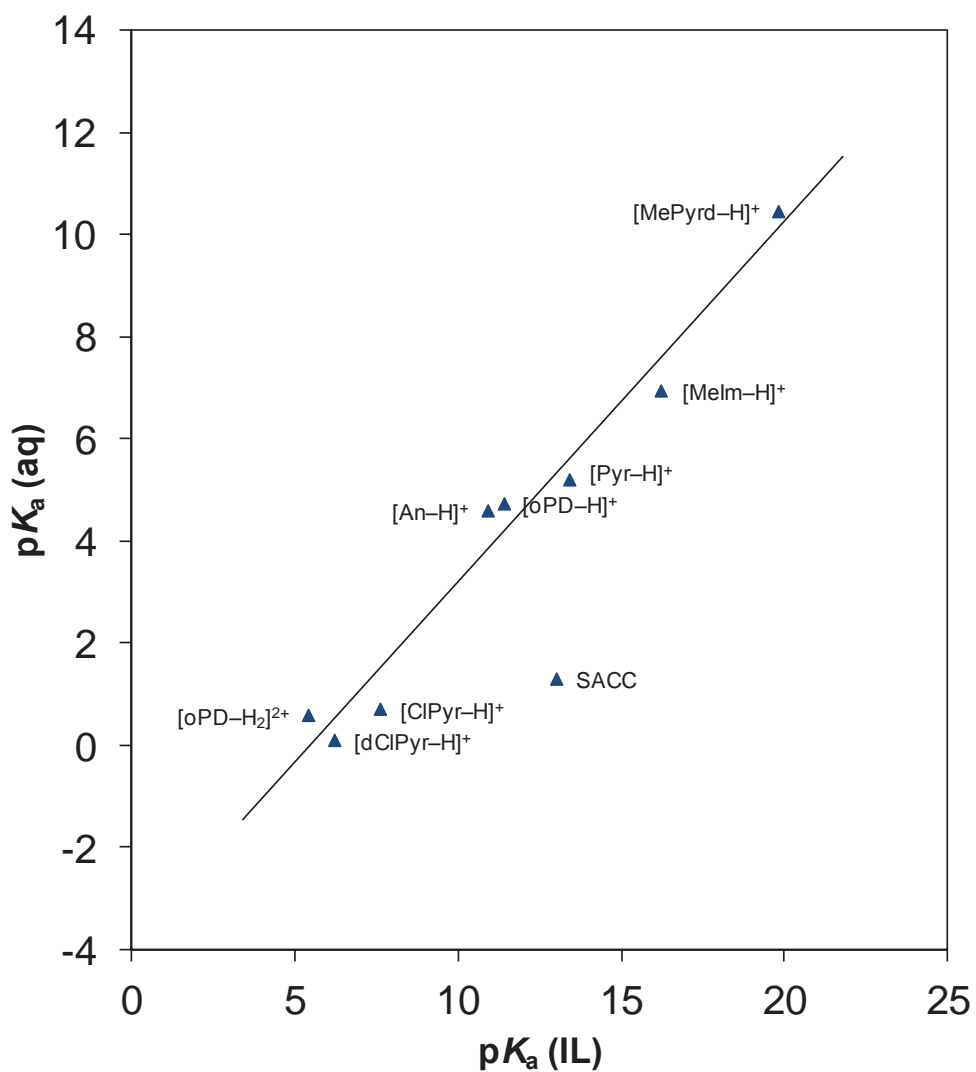


Figure S20. Plot of pK_a (aq) vs. pK_a (IL) for a range of nitrogen acids (protonated amines or sulfonamides). The regression line has been included to guide the reader's eye. SACC was not considered when calculating the regression line.

Electrochemical Proton Reduction and
Equilibrium Acidity (pK_a) in Aprotic Ionic
Liquids: Phenols, Carboxylic Acids and Sulfonic
Acids

*Cameron L. Bentley,^{†,‡} Alan M. Bond,[†] Anthony F. Hollenkamp,[‡] Peter J. Mahon[§] and Jie
Zhang[†]*

[†]School of Chemistry, Monash University, Clayton, Vic 3800, Australia

[‡]CSIRO Energy, Box 312, Clayton South, Vic 3169, Australia

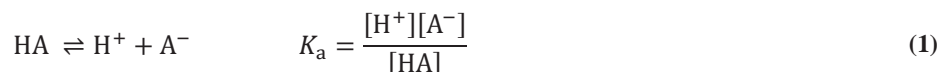
[§]Faculty of Science, Engineering and Technology, Swinburne University of Technology,
Hawthorn, Vic 3122, Australia

Abstract. Many organic compounds contain acidic and/or basic functional groups that dictate their physical, chemical and biological properties. For this reason, the acid dissociation constant, K_a , a quantitative measure of acid strength in solution, is a fundamentally important parameter. In this study, the thermodynamics, kinetics and mechanisms of the proton reduction (hydrogen evolution) reaction at a platinum electrode have been investigated in the room temperature ionic liquid (IL) 1-ethyl-3-methylimidazolium bis(trifluoromethanesulfonyl)imide, $[C_2mim][NTf_2]$, using a range of oxyacids (phenols, carboxylic acids or sulfonic acids) as the proton source. Triflic acid, $H[OTf]$, a well known superacid in aqueous media, has been shown to be a weak acid in $[C_2mim][NTf_2]$ with a pK_a of 2.0. Hydrogen evolution from $H[OTf]$ has been simulated using a CE mechanism, where acid dissociation, $HA \rightleftharpoons H^+ + A^-$ (where H^+ is a 'solvated' proton) is followed by proton reduction *via* the classical Volmer, $H^+ + e^- \rightleftharpoons H^*$ and Tafel reactions, $H^* + H^* \rightleftharpoons H_2$. Proton reduction from a range of other sulfonic or carboxylic acids has been shown to occur in two steps with an electron stoichiometry of 1:1, which has been attributed to the formation of a stable intermediate species through homo hydrogen bonding (homoassociation) between the acid (HA) and its conjugate anion base (A^-). Simulations confirm that the experimental voltammetric response is consistent with an ECE mechanism, where C is the anionic homoassociation step, $HA + A^- \rightleftharpoons [HA_2]^-$. Homoassociation can be suppressed by changing the constituent cation/anion of the IL or by mixing the IL with a hydrogen bond donating/accepting solvent, such as propylene glycol. Finally, the pK_a and homoassociation equilibrium constant (K_{homo}) of ten weak oxyacids, covering sixteen orders of magnitude in acid strength ($2.0 \leq pK_a \leq 17.8$), has been calculated using a voltammetric method and compared with data from conventional solvents (acetonitrile and water) in order to gain an insight into how the nature of the solvent (*i.e.*, dielectric properties, Lewis acidity/basicity, hydrogen donating/accepting ability etc.) influences equilibrium acidity.

Keywords: hydrogen evolution reaction, acid dissociation constant, homoassociation, homoconjugation, voltammetry

Introduction

Proton (H^+) transfer reactions are a fundamental step in many biologically and technologically important processes.¹⁻⁵ Indeed, many organic compounds contain acidic and/or basic functional groups that have a strong bearing on their physicochemical and/or biological properties. The strength of a Brønsted acid in solution is measured by its acid dissociation constant (K_a), formally defined as follows:



K_a or pK_a (where $pK_a = -\log_{10}K_a$) describes the Gibbs energy of 'R-H' bond heterolysis in solution, a critical step in many bond transformation processes.⁶⁻⁸ The pK_a of a given Brønsted acid is dependent upon structural factors (*i.e.*, mesomeric and inductive effects) and the nature of the solvent, specifically its ability to stabilize (solvate) or destabilize each of the species outlined in Eq. 1 (HA , H^+ and A^-). It follows that solvent acidity/basicity, dielectric properties and ability to donate/accept hydrogen bonds can all influence the pK_a of an acid in solution.^{8,9}

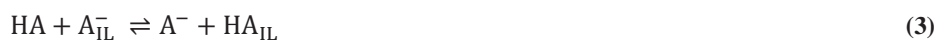
The concept of Brønsted acidity/basicity is well established in aqueous media¹⁰, where the solvent, water, is able to act as a Brønsted acid or base. The acidity of all strong acids in aqueous media is effectively 'leveled' through the formation of the hydronium (H_3O^+) ion:



It follows that the 'solvated proton' species, H_3O^+ , is the origin of the aqueous pK_a scale.¹¹⁻¹⁴ pK_a scales have also been established in a range of non-aqueous solvents, including

acetonitrile¹⁵, dimethylsulfoxide (DMSO)^{8, 16, 17} and 1,2-dichloroethane¹⁵. A variety of methods¹⁸ are commonly employed to quantify K_a , including potentiometry¹⁹, spectrophotometry^{8, 20} and voltammetry^{9, 16, 17}.

In the past two decades, air/water stable non-haloaluminate room temperature ionic liquids (ILs) have emerged as promising replacements for volatile molecular solvents (such as those listed above) in a range of applications.²¹ ILs are typically made by combining a bulky, asymmetric organic cation with a large, charge delocalized inorganic anion and, due to relatively strong electrostatic (cohesive) forces, the resulting liquids often tend to be highly viscous and non-volatile. They are commonly referred to as ‘designer solvents’ because their physicochemical properties can be ‘tuned’ to an extent by changing their constituent cation and/or anion.^{22, 23} When a Brønsted acid is dissolved in an IL, the protons released upon dissociation must associate or be ‘solvated’ by the most basic component of the IL, which is usually the anion (A_{IL}^-):



HA_{IL} effectively levels the acidity of strong acids in IL media, comparable to H_3O^+ in aqueous media. In other words, HA_{IL} is the origin of the pK_a scale in IL media and for this reason pK_a data are not directly comparable between ILs with different constituent anions.^{6, 7}

¹¹ From this point forward, ‘ H^+ ’, which refers to the ‘solvated’ proton species (*i.e.*, H_3O^+ in H_2O), is equivalent to HA_{IL} in the context of ILs.

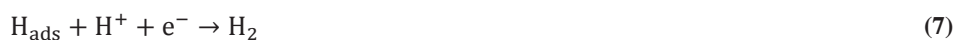
At this point in time, absolute pK_a data for weak acids in ILs is scarce, with only a few key studies available.^{6, 7, 11} Cheng *et al.*^{6, 7} have previously established the equilibrium acidity of 18 carbon acids⁶ and 15 substituted benzoic acids⁷ in a range of ILs using an overlapping indicator method. After carefully calibrating for intermolecular hydrogen bonding interactions between oxygen acids (oxyacids) and oxyanions, the authors found that

the pK_a (IL) data correlated linearly with corresponding pK_a (DMSO) and pK_a (GP) data (where GP signifies ‘gas phase’, determined using mass spectrometry²⁴). In addition, the identity of both the IL anion and (to a lesser extent) cation was found to influence the pK_a of a given acid, with the effect being more prominent for the oxyacids than for the carbon acids.

It can be shown^{9, 11, 25, 26} that the pK_a of a weak acid, HA, is proportional to difference between the formal potentials (E^0) of the H^+/H_2 and HA/H_2 processes. Therefore, in this study, we will employ electrochemical methods such as cyclic voltammetry²⁵ to probe the thermodynamics, kinetics and mechanisms of the H^+/H_2 and HA/H_2 processes. The proton reduction reaction or hydrogen evolution reaction (HER) is a conceptually simple, one-electron per proton process²⁷⁻³²:



However, this reaction is subject to significant kinetic barriers and therefore requires an electrocatalyst to proceed at an economically viable rate.³³ The HER is thought to proceed *via* a combination of the following three elementary reactions in acidic aqueous media^{28, 30, 33}:

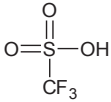
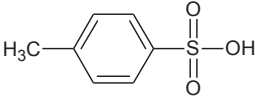
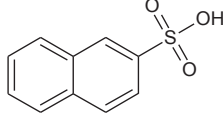
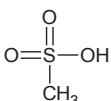
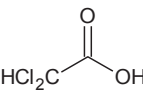
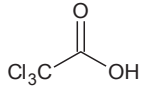
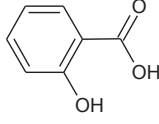
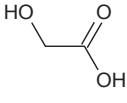
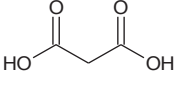
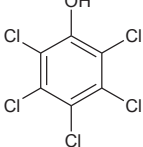


where H_{ads} is a chemisorbed hydrogen atom and Eqs. 5, 6 and 7 are known as the Volmer, Tafel and Heyrovsky reactions, respectively.²⁸ We have previously investigated the proton reduction reaction at a platinum electrode in a range of bis(trifluoromethanesulfonyl)imide ILs using $H[NTf_2]$ as the proton source (*i.e.*, the H^+/H_2 process).³⁴ In that study, we established that $E^0(H^+/H_2)$ is essentially insensitive to the identity of the constituent cation of the IL and that the Volmer reaction (see Eq. 5) is the rate determining step for the proton

reduction reaction in ILs. Surprisingly, there are few detailed studies^{35, 36} available on the proton reduction process from weak oxyacids in IL media.

In this paper, the thermodynamics, kinetics and mechanisms of the proton reduction (hydrogen evolution) reaction at a platinum electrode have been investigated in the room temperature ionic liquid 1-ethyl-3-methylimidazolium bis(trifluoromethanesulfonyl)imide using ten oxyacids (phenols, carboxylic acids or sulfonic acids, structures shown in Table 1) that cover a wide range of acidities as the proton source. The proton reduction process has been characterized predominantly using cyclic voltammetry with computational simulation (where appropriate). We also present a relatively straightforward method for calculating the pK_a of weak oxyacids acids in IL media, based on a combination of cyclic voltammetry and chronoamperometry. A companion study has also been undertaken with a range of nitrogen acids (protonated amines or sulfonamides), which will be presented elsewhere.²⁶

Table 1. Names and structures of the phenols, carboxylic acids and sulfonic acids (known collectively as oxygen acids or oxyacids) investigated in this work.

Name of the parent compound	Acid structure	Abbreviation
Trifluoromethanesulfonic (triflic) acid		H[OTf]
<i>p</i> -toluenesulfonic (tosylic) acid		H[OTs]
Napthalene-2-sulfonic acid		NSA
Methanesulfonic acid		MSA
Dichloroacetic acid		DCAA
Trichloroacetic acid		TCAA
<i>o</i> -hydroxybenzoic (salicylic) acid		<i>o</i> HBA
Glycolic acid		GA
Malonic acid		MA
Pentachlorophenol		PCP

Experimental Section

Reagents. 1-ethyl-3-methylimidazolium bis(trifluoromethanesulfonyl)imide ([C₂mim][NTf₂], Iolitec), 1-ethyl-3-methylimidazolium dicyanamide ([C₂mim][N(CN)₂], Solvent Innovation) and 1-butyl-1-methylpyrrolidinium bis(trifluoromethanesulfonyl)imide ([C₄mpyr][NTf₂], Merck) were commercial samples. Triethylammonium bis(trifluoromethanesulfonyl)imide ([N_{H,2,2,2}][NTf₂]) was prepared by a metathesis reaction between lithium bis(trifluoromethanesulfonyl)imide (Li[NTf₂], 3M Fluorad) and triethylammonium chloride ([N_{H,2,2,2}]Cl, Sigma-Aldrich, recrystallized from ethanol) as previously reported.³⁴ 1-ethyl-3-methylimidazolium *p*-toluenesulfonate ([C₂mim][OTs]) was prepared by alkylation of *N*-methylimidazole (Sigma-Aldrich, vacuum distilled over lithium) with ethyl *p*-toluenesulfonate (Sigma-Aldrich, recrystallized from *n*-pentane) in toluene, as reported in the literature.³⁷ Before use, each of the ILs was dried under high vacuum ($\leq 10^{-1}$ mbar) at 45°C for 48 hours. The residual water content was less than 100 ppm as determined by Karl Fischer titration (Metrohm 831 KF Coulometer).

Bis(trifluoromethanesulfonyl)imide (H[NTf₂], Sigma-Aldrich, 95%) was purified by sublimation under high vacuum. *p*-toluenesulfonic acid monohydrate (Acros, 99%) was recrystallized from ethyl acetate. Ferrocene (Fc, Fluka, >98%) was recrystallized from *n*-pentane. 1,2-propanediol (propylene glycol, Acros, 99%) was distilled under high vacuum over lithium. Trifluoromethanesulfonic (triflic) acid (H[OTf], Sigma-Aldrich, 98%), naphthalene-2-sulfonic acid monohydrate (TCI, 98%), methanesulfonic acid (Sigma-Aldrich, $\geq 99.5\%$), dichloroacetic acid (Fluka, 99.5%), trichloroacetic acid (Univar, 99%), *o*-hydroxybenzoic acid (Univar, 99.9%), glycolic acid (Sigma-Aldrich, 99%), malonic acid (Sigma-Aldrich, 99%), pentachlorophenol (Sigma-Aldrich, 99%), 2,3,4-trichlorophenol (Sigma-Aldrich, 99%), acetonitrile (Alfa-Aesar, anhydrous, 99.7%) and tetra-*n*-butylammonium hexafluorophosphate ([NBu₄][PF₆], Sigma-Aldrich) were used as supplied

by the manufacturer. All water-sensitive reagents were stored and handled under a dry argon atmosphere in a glovebox.

Electrochemical systems and procedures. All voltammetric experiments were carried out under benchtop conditions at ambient temperature ($24 \pm 1^\circ\text{C}$) with a Gamry Reference 600 Potentiostat/Galvanostat/ZRA (Gamry Instruments, USA). All solvents were degassed with N_2 prior to experimentation and a blanket of N_2 was maintained during the course of the voltammetric experiments. A faraday cage was employed to minimize noise in all microelectrode experiments. Positive feedback iR_u compensation (R_u = uncompensated resistance) was employed in macroelectrode experiments (R_u was estimated by electrochemical impedance spectroscopy). All voltammetric experiments were carried out using a standard 3-electrode arrangement with a working and reference electrode as described below and a Pt wire auxiliary electrode. An Ag wire which had been immersed in the IL under investigation (neat) and sealed in a fritted (Vycor glass frit) glass tube served as the pseudo reference electrode. The pseudo reference electrode potential was calibrated against the formal potential of the IUPAC recommended Fc/Fc^+ process³⁸ in the electrolyte of interest, taking into careful consideration the difference in the diffusion coefficients of Fc and Fc^+ .^{28, 39}

The Pt macrodisk with a nominal diameter of 1.6 mm was purchased from BASi (Bioanalytical Systems, USA) and the Pt microdisk with a nominal diameter of 20 μm was purchased from Metrohm (Switzerland). The Pt macrodisk electrode was activated by polishing with successively smaller (1 and 0.3 μm) aqueous alumina slurries (Kemet, UK) on a clean polishing cloth (Buehler, USA). Adherent alumina was removed by sonication in de-ionized water. The Pt microdisk electrode was activated by polishing with an aqueous slurry of 0.3 μm alumina and rinsed thoroughly with de-ionized water. The working electrode was preconditioned prior to sweeping by anodic polarization at 1.5 to 2.2 V vs. Fc/Fc^+ for ≤ 10 ms

as has been previously reported.³⁴ The active electrode area (A) of each of the electrodes was calibrated with convolution voltammetry⁴⁰⁻⁴², using the oxidation of a Fc solution of known concentration (2.0 mM in acetonitrile containing 0.10 M [NBu₄][PF₆]) and adopting a diffusion coefficient of $2.4 \times 10^{-5} \text{ cm}^2 \text{ s}^{-1}$, as published under these conditions.²⁵

Data treatment and processing. The algorithm used to calculate the convolved currents is the same as used previously.⁴¹ Derivative cyclic voltammograms (*i.e.*, 1st order derivative of current or 2nd order derivative of charge) were constructed by differentiating experimental current data with respect to time using the differentiate function available in OriginPro 9.0 software. Savitzky-Golay data smoothing (polynomial order 2) was performed prior to estimating the derivative peak potentials. The diffusion coefficients (D) of H⁺, HA and [HA₂]⁻ were estimated from chronoamperometric ($I-t$) decay curves obtained at a microdisk electrode using the Shoup and Szabo⁴³ method, as reported elsewhere.^{34, 39} The diffusion coefficient (D) of H₂ was estimated from the second (oxidative) step of a double-step chronoamperogram using numerical simulation as has been previously described.⁴⁴ The sample time used in all chronoamperometric experiments was 0.01 s. Voltammetric simulations were undertaken using the DigiElch software package (v. 7F, Elchsoft, Germany). The pK_a of *p*-toluenesulfonic acid and methanesulfonic acid was estimated using the MarvinSketch software package (v. 14.12.15.0, Chemaxon).

Results and Discussion

Proton reduction from H[OTf] in [C₂mim][NTf₂]. The name and structure of all of the oxyacids investigated in this work were previously shown in Table 1. The first oxyacid investigated in detail was H[OTf], a well known superacid²⁰ in aqueous media. [OTf]⁻ is a commonly used IL anion as it is weakly coordinating (and weakly basic) due to extensive charge delocalization. In our companion study²⁶, we have shown that the following equilibrium lies to the right in [C₂mim][OTf]:



in other words, H[NTf₂] behaves as a ‘strong acid’ in [C₂mim][OTf]. We therefore anticipate that H[OTf] will behave as a weak acid in [C₂mim][NTf₂]. Cyclic voltammograms obtained from H[OTf] at a platinum macrodisk electrode in [C₂mim][NTf₂] are shown in Figure 1. Proton reduction from H[OTf] is a one-electron quasi-reversible process, as the voltammetric peak-to-peak separation (ΔE_p) increases with scan rate, with values of 85.6, 87.7 and 99.7 mV at 50, 100 and 250 mV s⁻¹, respectively (R_u is expected to be negligible, see Experimental Section). The H[OTf]/H₂ process occurs at potentials approximately 0.1 V negative of the H⁺/H₂ process (shown in Figure S1), where H⁺ signifies a ‘solvated proton’ (*i.e.*, H[NTf₂]), confirming that H[OTf] is a weak acid in [C₂mim][NTf₂].

The pK_a of H[OTf] in [C₂mim][NTf₂] can be estimated using the following equation:

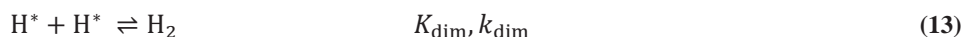
$$-\frac{2.303RT}{F}pK_a = E_{1/2}(\text{HA}/\text{H}_2) - E_{1/2}(\text{H}^+/\text{H}_2) + \frac{RT}{2F} \ln \left(\frac{\sqrt{D_{\text{HA}}}}{\sqrt{D_{\text{H}^+}}} \right) + \frac{RT}{2F} \ln \left(\frac{[\text{HA}]_b [\text{H}^+]_b}{4} \right) \quad (9)$$

where R is the gas constant, T is temperature, F is Faraday's constant, $E_{1/2}$ is the reversible half-wave potential and the subscript 'b' signifies 'bulk concentration'.²⁶ $E_{1/2}(\text{HA}/\text{H}_2)$ and $E_{1/2}(\text{H}^+/\text{H}_2)$ can be estimated from Figures 1 and S1, respectively, as follows:

$$E_{1/2} \cong \frac{E_{\text{p,ox}} + E_{\text{p,red}}}{2} = E_{\text{mid}} \quad (10)$$

and D can be estimated using microdisk electrode chronoamperometry (see Experimental Section). Substituting the appropriate values into Eq. 9, the $\text{p}K_{\text{a}}$ of $\text{H}[\text{OTf}]$ is estimated to be 2.0 in $[\text{C}_2\text{mim}][\text{NTf}_2]$. Thus, $\text{H}[\text{OTf}]$ is approximately 35% dissociated when dissolved in $[\text{C}_2\text{mim}][\text{NTf}_2]$ under the conditions used.

In our companion study²⁶, we proposed that proton reduction from weak acids can proceed *via* two pathways. One pathway is a *CE* process, where proton reduction *via* the classical Volmer-Tafel reactions (see Eqs. 5 and 6) is preceded by an acid dissociation step:



where k_{dissoc} is the dissociation rate constant, k_{assoc} is the association rate constant, $k_{\text{s}}^{\text{app}}$ is the apparent standard heterogeneous electron-transfer rate constant and α is the charge transfer coefficient. Considering only the *CE* pathway (Eqs. 11 to 13), we performed simulations where k_{assoc} was set to the diffusion controlled limit and showed that when $\text{p}K_{\text{a}} > 4$, weak acid dissociation (Eq. 11) is too slow on the voltammetric timescale to support the experimentally observed mass-transport controlled currents. To account for this, an alternative direct reduction (*DR*) pathway was considered, where the weak acid undergoes direct discharge at the platinum electrode, forming surface adsorbed H^* :



In the above scheme, Eq. 14 is followed by surface dimerization (Eq. 13). In the simulations, Eq. 13 was treated as a homogeneous process with arbitrarily defined dimerization equilibrium constant (K_{dim}) and dimerization rate constant (k_{dim}) values. Accordingly, the process shown in Eq. 13 has no physical significance (H^* is likely to be a surface confined species in reality^{30, 32}) and the following parameters: k_s^{app} , K_{dim} , k_{dim} and D_{H^*} are not quantitatively meaningful.¹⁶ Nonetheless, considering these two pathways outlined above, the proton reduction response from ten weak nitrogen acids (protonated amines or sulfonamides) covering 14 orders of magnitude in acid strength ($5.2 < \text{p}K_{\text{a}} < 19.5$) was successfully simulated.²⁶

Since $\text{H}[\text{OTf}]$ has a $\text{p}K_{\text{a}} < 4$ in $[\text{C}_2\text{mim}][\text{NTf}_2]$, simulations considering only the *CE* pathway (Eqs. 11 to 13) were performed; the results are also included in Figure 1. The simulation parameters (available in Table 2) for Eqs. 12 and 13 were taken (unmodified) from our companion study.²⁶ In all simulations, it was taken that $D_{\text{H}^*} = 10^{-10} \text{ cm}^2 \text{ s}^{-1}$, $k_{\text{assoc}} = 5 \times 10^8 \text{ M}^{-1} \text{ s}^{-1}$ (diffusion controlled, as justified in a previous publication⁴²), $K_{\text{dim}} = 10^4$, $k_{\text{dim}} = 10^{16} \text{ M}^{-1} \text{ s}^{-1}$, uncompensated resistance (R_{u}) = 0 Ω and double layer capacitance (C_{dl}) = 0 F. There is excellent agreement between the simulated and experimental data when only the *CE* mechanism is considered. Clearly, k_{dissoc} ($6.6 \times 10^6 \text{ s}^{-1}$) is large enough under these conditions to attain diffusion control at scan rates up to at least 250 mV s^{-1} . As was highlighted in a previous publication³⁴, the main discrepancy between the experimental and simulated data is in the hydrogen underpotential deposition (UPD) region, prior to the main (solution based) reduction process.⁹ The $\text{p}K_{\text{a}}$ value derived from the simulations, 1.9, is in excellent agreement with the value determined directly from the cyclic voltammogram using Eq. 9.

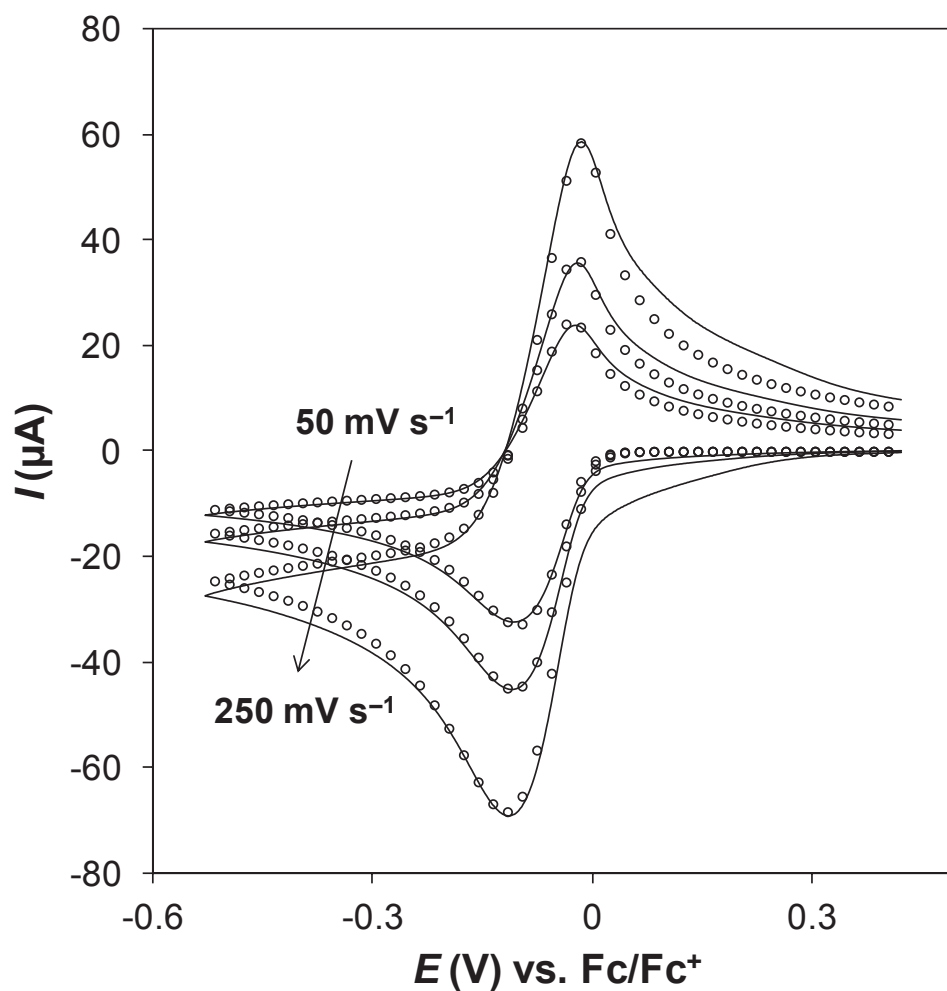


Figure 1. Comparison of the simulated (\circ) and experimental ($—$) cyclic voltammograms showing the proton reduction process obtained from 52.6 mM H[OTf] in $[\text{C}_2\text{mim}][\text{NTf}_2]$ at a 1.6 mm dia. Pt macrodisk electrode with scan rates of 50, 100 and 250 mV s^{-1} . Simulation parameters are available in Table 2.

Table 2. Parameters extracted from the comparison of experimental cyclic voltammetric data for the proton reduction process from H[OTf] in [C₂mim][NTf₂] and simulated data, based on the CE mechanism described by Eqs. 11 to 13.

Parameter	Value
K_a	1.33×10^{-2}
$E^{0'}(\text{H}^+/\text{H}_2)$	-0.026 V
$E^{0'}(\text{HA}/\text{H}_2)$	-0.137 V
k_s^{app}	0.022 cm/s
α	0.5
D_{H^+}	$3.1 \times 10^{-7} \text{ cm}^2 \text{ s}^{-1}$
$D_{\text{H}[\text{OTf}]} = D_{[\text{OTf}]^-}$	$2.4 \times 10^{-7} \text{ cm}^2 \text{ s}^{-1}$
D_{H_2}	$2.2 \times 10^{-5} \text{ cm}^2 \text{ s}^{-1}$

Proton reduction from sulfonic acids (RSO₃H) in [C₂mim][NTf₂]. The proton reduction process from a range of sulfonic acids (see Table 1) was investigated in [C₂mim][NTf₂]. Representative cyclic voltammograms obtained from H[OTs] at a platinum macrodisk electrode in [C₂mim][NTf₂] are shown in Figure 2a. In contrast to H[NTf₂] (see Figure S1), H[OTf] (see Figure 1) and all of the weak nitrogen acids investigated in our companion study²⁶, proton reduction from H[OTs] is split into two processes which are spaced approximately 0.2 V apart. This was also found to be the case with NSA (see Figure S2) and MSA (see Figure S3). In order to determine the electron stoichiometry of the two processes, the forward sweep of the voltammogram shown in Figure 2a ($\nu = 50 \text{ mV s}^{-1}$) was semiintegrated^{45, 46} (see Experimental Section), as shown in Figure 2b. There is an inflection point on the $M-E$ curve at $-0.32 \text{ V vs. Fc/Fc}^+$, which is midway between zero current and the mass-transport limited semiintegrated current plateau (M_L), indicating an electron stoichiometry of 1:1. In other words, for every proton (from HA) which is reduced, half an electron is taken in each process. The same was found for NSA and MSA.

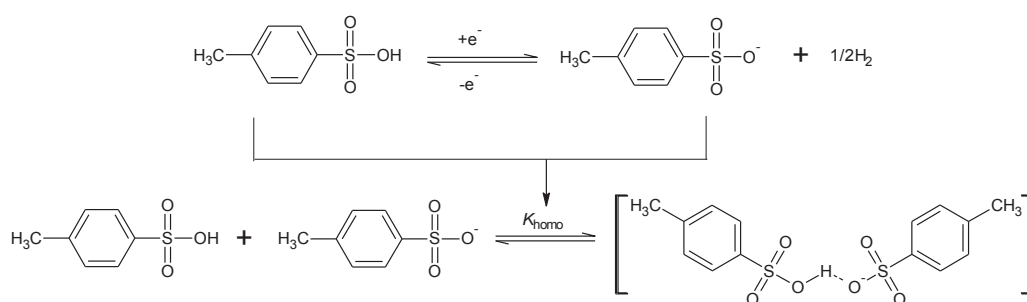
Based on the electron stoichiometry and what is known about oxyacids in aprotic media⁴⁷, including ILs⁷, we propose that the splitting of the proton reduction wave is caused by intermolecular hydrogen bonding between H[OTs] and its conjugate base, [OTs]⁻. This is a well-documented phenomenon^{48, 49} known as homoassociation or homoconjugation:



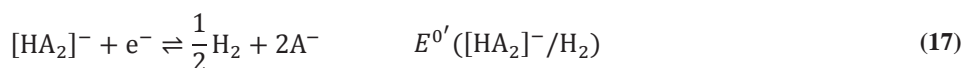
where $[\text{HA}_2]^-$ is a stable intermediate species formed by the interaction between an acid, HA and its conjugate base, A⁻. Homoassociation between H[OTs] and [OTs]⁻ is thought to occur in the diffusion layer adjacent to the electrode surface during the proton reduction process (see Scheme 1) in the potential region where the concentration of both species is comparable. As shown in Figure 1, in the case of H[OTf], homoassociation is not experimentally observable. Extensive charge delocalization on the conjugate base anion, [OTf]⁻, is expected

to result in extremely weak [RO-H---⁻OR] interactions, destabilizing the [HA₂]⁻ species (see Eq. 15). In addition, unlike H[OTs], which is essentially undissociated in [C₂mim][NTf₂] (see below), H[OTf] dissociates to a significant extent ($pK_a = 2.0$), making the interaction between H[OTf] and [OTf]⁻ less likely. As a result, the contribution from the homoassociation reaction between H[OTf] and [OTf]⁻ to the overall reaction pathway is insignificant.

Scheme 1. Proton reduction from H[OTs] and homoassociation between H[OTs] and [OTs]⁻.



Proton reduction from H[OTs] or any acid which undergoes homoassociation is expected to proceed *via* an *ECE* mechanism, where *C* is the homoassociation step. We therefore propose that the two processes observed experimentally are:



and the overall process remains unchanged:



$E^{0'}(\text{HA}/[\text{HA}_2]^-)$, $E^{0'}([\text{HA}_2]^-/\text{H}_2)$, $E^{0'}(\text{HA}/\text{H}_2)$ and K_{homo} are related as follows:

$$E^{0'}(\text{HA}/\text{H}_2) - E^{0'}(\text{HA}/[\text{HA}_2]^-) = -\frac{RT}{F} \ln(K_{\text{homo}}) \quad (19)$$

$$E^{0'}(\text{HA}/\text{H}_2) - E^{0'}([\text{HA}_2]^-/\text{H}_2) = \frac{RT}{F} \ln(K_{\text{homo}}) \quad (20)$$

$$E^{0'}(\text{HA}/\text{H}_2) = \frac{E^{0'}(\text{HA}/[\text{HA}_2]^-) + E^{0'}([\text{HA}_2]^-/\text{H}_2)}{2} \quad (21)$$

The reaction mechanism shown in Eqs. 16 and 17 accounts for the 1:1 electron stoichiometry observed experimentally. Additionally, adding $[\text{OTs}]^-$ to a $\text{H}[\text{OTs}]/[\text{C}_2\text{mim}][\text{NTf}_2]$ mixture should drive the equilibrium shown in Eq. 15 (or Scheme 1) to the right, forming $(\text{H}[\text{OTs}]_2)^-$ at the expense of $\text{H}[\text{OTs}]$. This was observed experimentally, as is shown in Figure 3. The proton reduction wave was also found to shift towards negative potentials at increasing $[\text{OTs}]^-$, consistent with the proposed mechanism.

Simulations (also shown in Figure 3) were performed by combining the reactions described by Eqs. 13 to 15 (*i.e.*, the *DR* pathway). The simulation parameters are available in Table 3. There is excellent agreement between the simulated and experimental data using the proposed homoassociation mechanism. $\text{H}[\text{OTs}]$ is only 0.4% dissociated under the conditions investigated. The mechanism outlined by Eqs. 13 to 15 also accounts for the scan rate dependence of the proton reduction process from $\text{H}[\text{OTs}]$, as is shown in Figure S4. Again, the main discrepancy between the experimental and simulated data is in the hydrogen UPD region.¹⁶ It should be noted that simulations have not been performed for any of the other oxyacids investigated in this work (see Table 1) because soluble conjugate base salts (*i.e.*, $[\text{C}_2\text{mim}][\text{A}]$) are not readily available.

The driving force for anionic homoassociation (*i.e.*, K_{homo}) is intermolecular hydrogen bonding, as shown in Scheme 1. This phenomenon is apparent in the present case because $[\text{C}_2\text{mim}][\text{NTf}_2]$ is a relatively poor hydrogen bond donating/accepting solvent compared to conventional polar solvents, such as water or methanol.⁵⁰ Anionic homoassociation is suppressed in the presence of hydrogen bonding solvents because solvent-solute hydrogen bonds form in preference to solute-solute. This can be easily demonstrated experimentally by

18

adding ~5% (v/v) propylene glycol to [C₂mim][NTf₂], as is shown in Figure 4a. Alternatively, the hydrogen bond donating/accepting ability can be enhanced by varying the constituent cation/anion of the IL. This has been demonstrated in Figure 4b, where the proton reduction process from H[OTs] in triethylammonium bis(trifluoromethanesulfonyl)imide ([N_{H,2,2,2}][NTf₂]) is shown. [N_{H,2,2,2}][NTf₂] is a protic ionic liquid, formed through the transfer of a proton from a Brønsted acid (*i.e.*, H[NTf₂]) to a Brønsted base (*i.e.*, [N_{2,2,2}]).^{51, 52} Although the anion ([NTf₂]⁻) is still a poor hydrogen bond acceptor, the cation is a good hydrogen bond donor through its [N–H]⁺ functionality. Interestingly, the proton reduction process from H[OTs] occurs at less negative potentials when [N_{H,2,2,2}]⁺ is the cation ($E_{\text{mid}} = -0.138 \text{ V vs. Fc/Fc}^+$) compared to [C₂mim]⁺ ($E_{\text{mid}} = -0.310 \text{ V vs. Fc/Fc}^+$). Since the position of the ‘solvated’ proton reduction wave (*i.e.*, H⁺/H₂ process) is cation independent³⁴, H[OTs] must be approximately 10³ times stronger in [N_{H,2,2,2}][NTf₂] compared to [C₂mim][NTf₂]. The reason for this is discussed in further detail below.

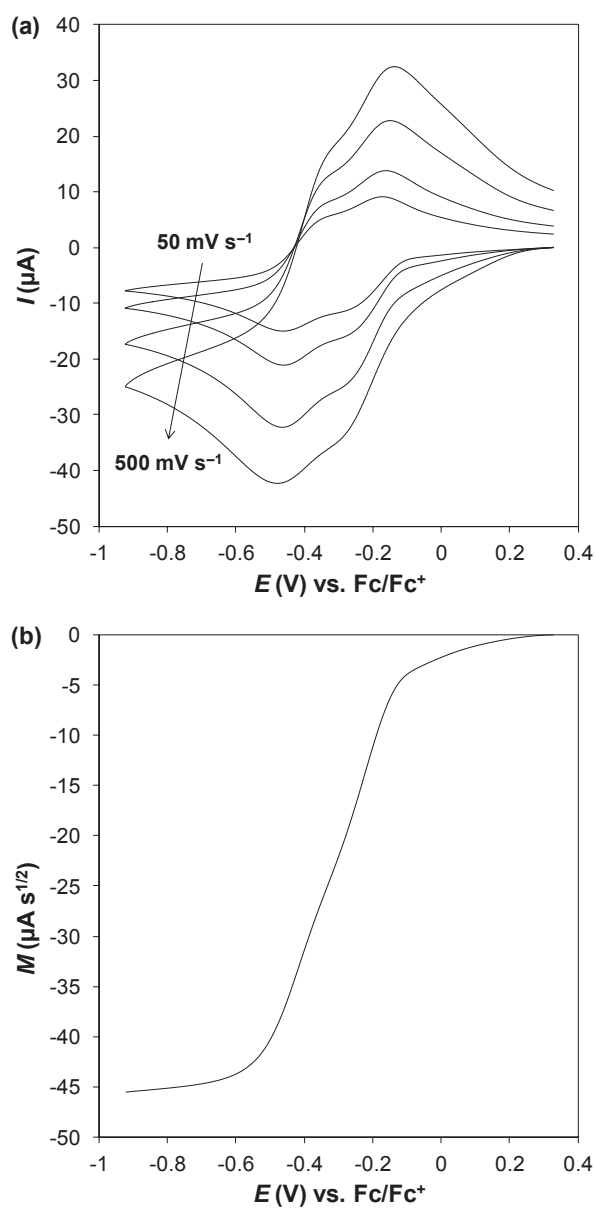


Figure 2. (a) Cyclic voltammograms showing the proton reduction process obtained from 41.6 mM H[OTs] in $[\text{C}_2\text{mim}][\text{NTf}_2]$ at a 1.6 mm dia. Pt macrodisk electrode with scan rates of 50, 100, 250 and 500 mV s^{-1} . (b) M - E curve obtained by semiintegrating the I - E data ($v = 50 \text{ mV s}^{-1}$) shown in (a).

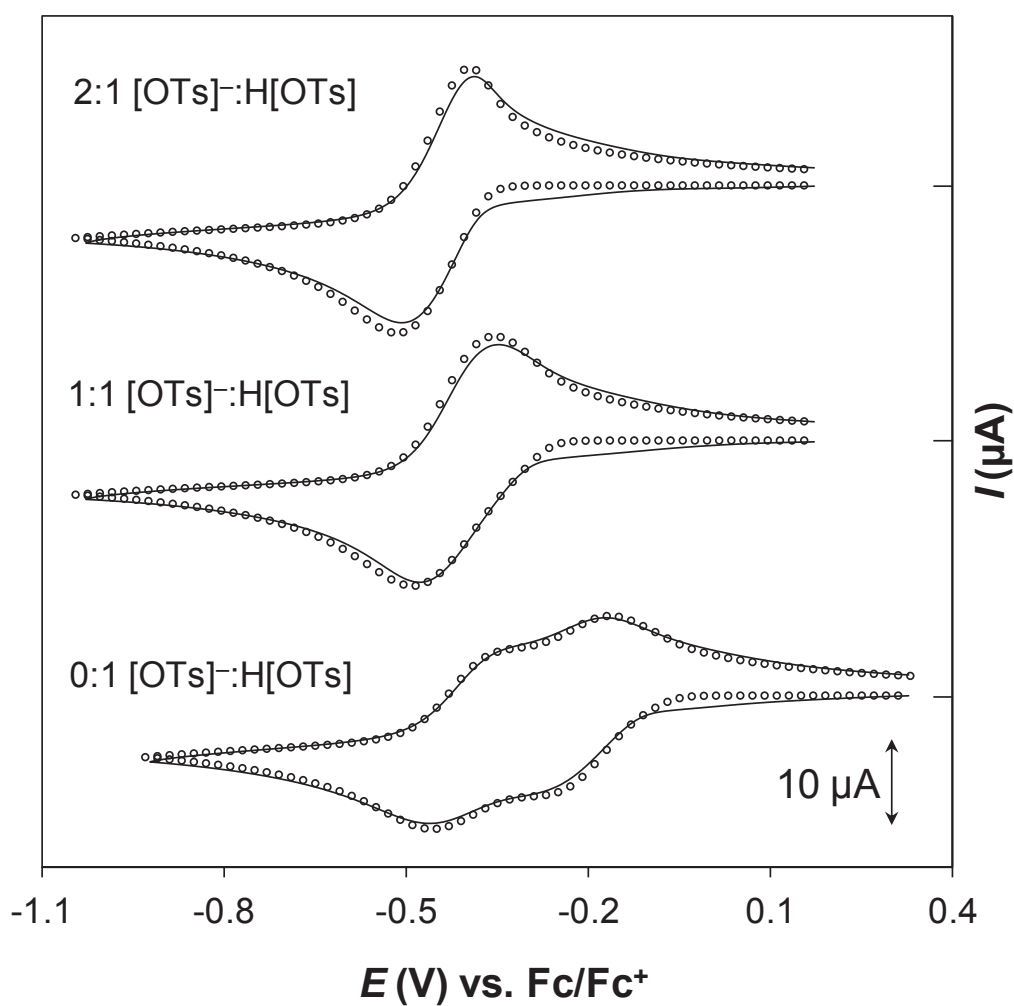


Figure 3. Comparison of the simulated (\circ) and experimental ($—$) cyclic voltammograms showing the proton reduction process obtained from: (a) 41.6 mM H[OTs], (b) 41.6 mM H[OTs] + 44.0 mM [C₂mim][OTs] and (c) 41.2 mM H[OTs] + 86.1 mM [C₂mim][OTs]; in [C₂mim][NTf₂] at a 1.6 mm dia. Pt macrodisk electrode with a scan rate of 50 mV s⁻¹. Simulation parameters are available in Table 3.

Table 3. Data extracted from the comparison of experimental cyclic voltammetric data for the proton reduction process from H[OTs] in [C₂mim][NTf₂] and simulated data, based on the DR mechanism described by Eqs. 13 to 15.

Parameter	Value
K_a	6.0×10^{-7}
$E^{0'}(\text{HA}/\text{H}_2)$	-0.394 V
$k_s^{\text{app}}(\text{DR})$	0.09 cm/s
α_{DR}	0.4
K_{homo}	950
k_{homo}	$5 \times 10^8 \text{ M}^{-1} \text{ s}^{-1}$
$D_{\text{H[OTs]}} = D_{\text{[OTs]}^-}$	$2.6 \times 10^{-7} \text{ cm}^2 \text{ s}^{-1}$
$D_{\text{(H[OTs]}_2)^-}$	$1.85 \times 10^{-7} \text{ cm}^2 \text{ s}^{-1}$
D_{H_2}	$2.2 \times 10^{-5} \text{ cm}^2 \text{ s}^{-1}$

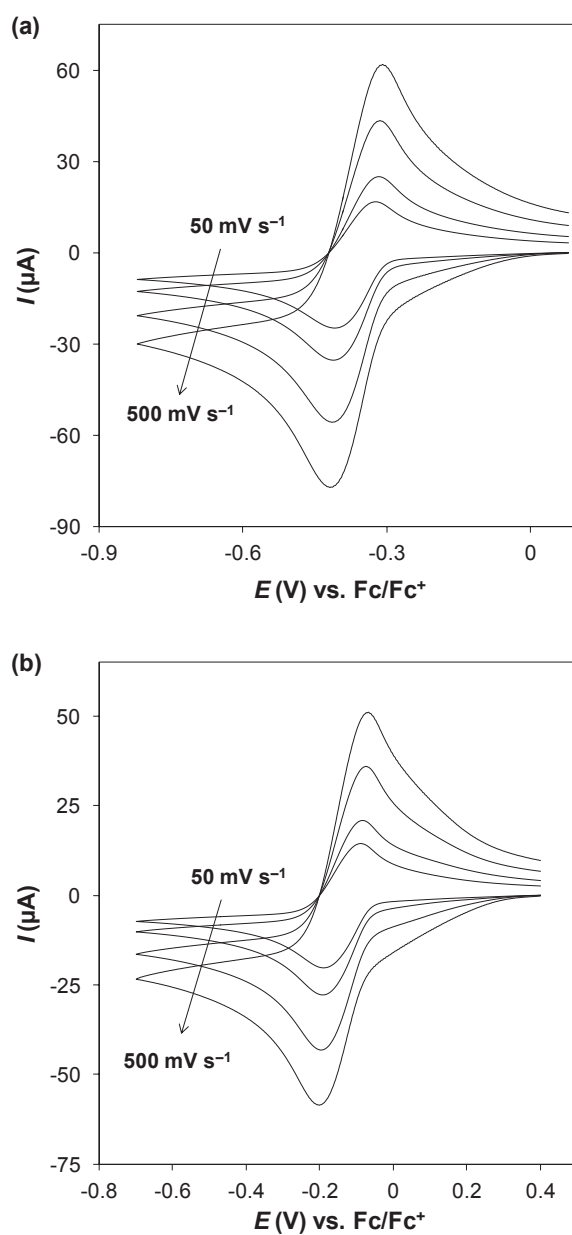


Figure 4. Cyclic voltammograms showing the proton reduction process obtained from: (a) 39.4 mM H[OTs] in $[\text{C}_2\text{mim}][\text{NTf}_2]$ + 5.2 vol% propylene glycol and (b) 42.0 mM H[OTs] in $[\text{NH},2,2,2][\text{NTf}_2]$; at a 1.6 mm dia. Pt macrodisk electrode with scan rates of 50, 100, 250 and 500 mV s^{-1} .

Proton reduction from carboxylic acids (RCOOH) in [C₂mim][NTf₂]. The next group of oxyacids investigated were the carboxylic acids; representative cyclic voltammograms obtained from DCAA and MA (see Table 1) at a platinum macrodisk electrode in [C₂mim][NTf₂] are shown in Figure 5a and b, respectively. All of the carboxylic acids underwent anionic (carboxylate) homoassociation, evidenced by the characteristic split proton reduction response (see Figures S5 to S7). Compared to the sulfonic acids (see above), the monoprotic carboxylic acids gave rise to significantly broader proton reduction responses, as is evident in Figure 5a. In all cases, ΔE_p for the first process (shown in Eq. 16) is small compared to the second process (shown in Eq. 17), indicating that the former process is more kinetically facile than the latter. This is especially evident for oHBA (Figure S6) and GA (Figure S7). Changing the IL anion from [NTf₂]⁻ to dicyanamide ([N(CN)₂]⁻), a relatively good hydrogen bond acceptor⁵³, was found to suppress anionic homoassociation, as is shown in Figure S8 for GA. The dicarboxylic acid MA also underwent anionic homoassociation (first deprotonation shown in Figure 5b) in [C₂mim][NTf₂] but the intermolecular interaction is weak, evidenced by the small potential gap between the two processes. This is not surprising since MA is capable of forming an intramolecular hydrogen bond⁵⁴, which would be expected to stabilize the monoanion in a similar way to intermolecular hydrogen bonding (*i.e.*, anionic homoassociation).

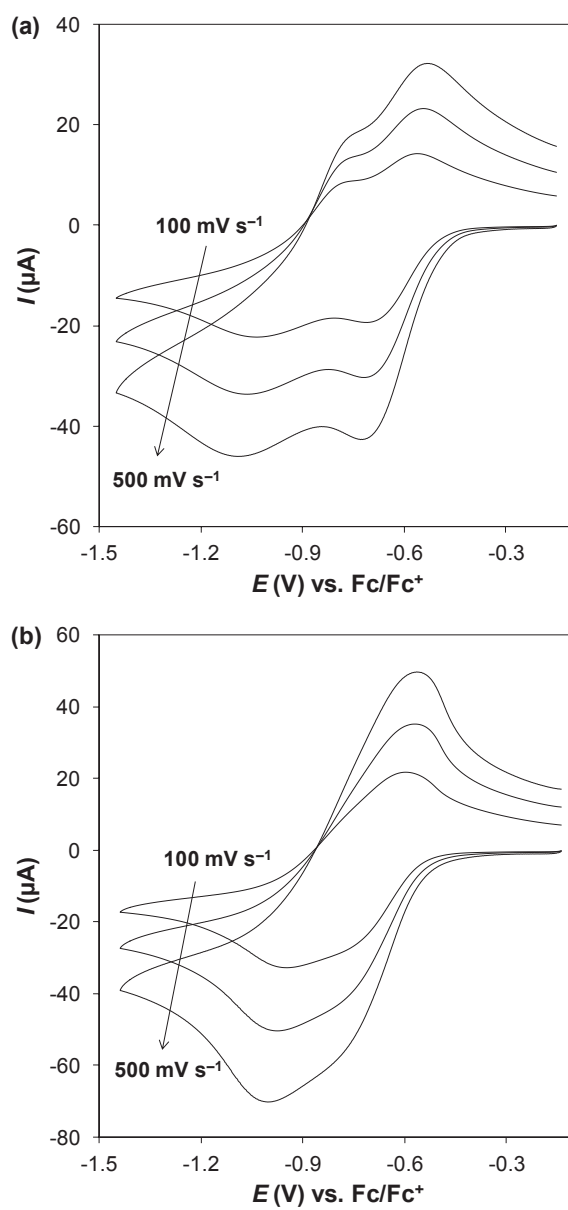


Figure 5. Cyclic voltammograms showing the proton reduction process obtained from: (a) 39.4 mM DCAA and (b) 56.4 mM MA; in $[\text{C}_2\text{mim}][\text{NTf}_2]$ at a 1.6 mm dia. Pt macrodisk electrode with scan rates of 100, 250 and 500 mV s^{-1} .

Proton reduction from phenols (ROH) in [C₂mim][NTf₂]. The last oxyacid investigated in this work was pentachlorophenol; cyclic voltammograms obtained at a platinum macrodisk electrode in [C₂mim][NTf₂] are shown in Figure 6. In stark contrast to the sulfonic and carboxylic acids, PCP gives rise to an uncomplicated, one-electron, quasi-reversible proton reduction process which is comparable to that obtained from neutral sulfonamide acids of similar strength, as shown in our companion study.²⁶ From this, it is evident that K_{homo} for PCP must be negligibly small. A similar observation was made by Chmurzyński *et. al*⁵⁵ when investigating the acid dissociation and anionic homoassociation equilibria of substituted phenols in dimethyl sulfoxide. The suppression of K_{homo} is likely due to steric crowding around acidic phenol group on the phenyl ring in the 2,6-positions. In order to test this hypothesis, the proton reduction response from a less substituted arenol, 2,3,4-trichlorophenol (TCP) was investigated, as shown in Figure S9. As expected, TCP underwent anionic homoassociation as evidenced by the characteristic split proton reduction response. It should be noted that due to complications arising from solvent breakdown, the proton reduction process from TCP was characterized in [C₄mpyr][NTf₂], which has a considerably larger electrochemical window than [C₂mim][NTf₂], particularly in the negative potential region.²² We anticipate that changing the cation from [C₂mim]⁺ to [C₄mpyr]⁺ would not significantly influence K_{homo} , so similar results would be expected in [C₂mim][NTf₂].

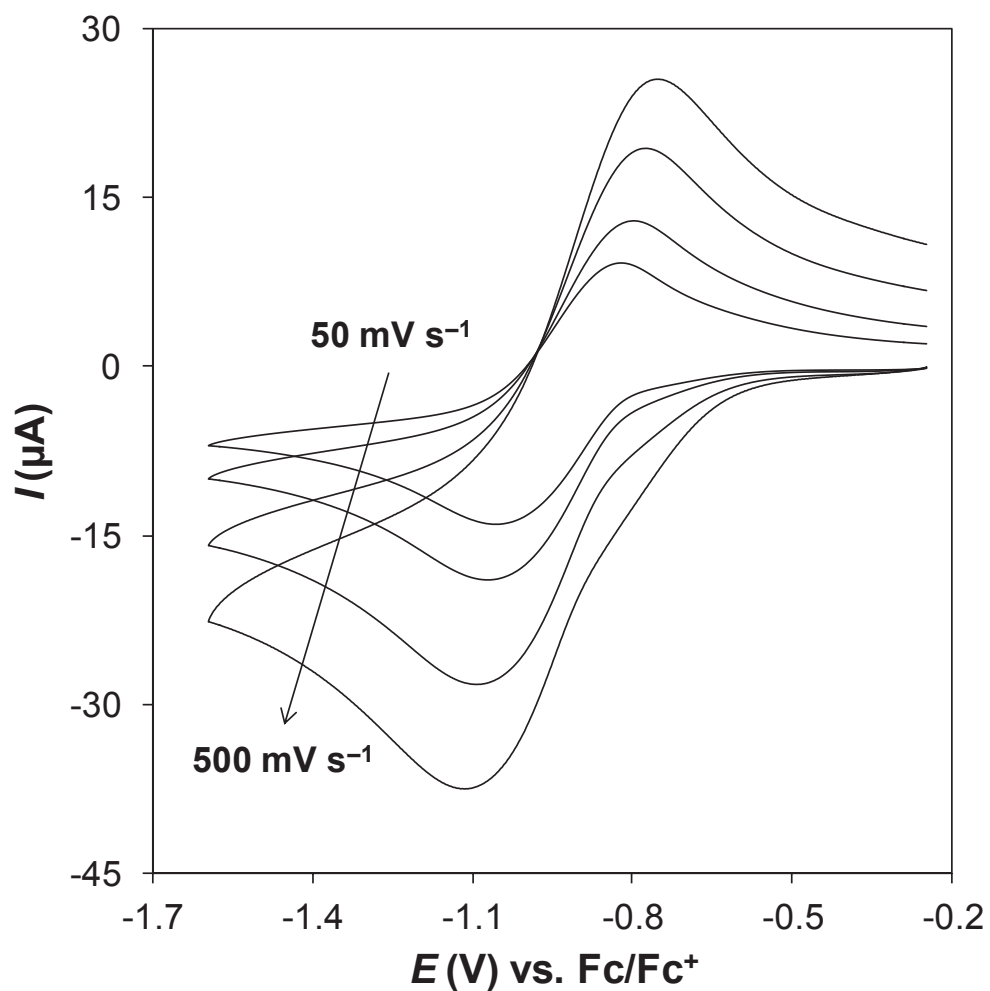


Figure 6. Cyclic voltammograms showing the proton reduction process obtained from 33.1 mM PCP in $[\text{C}_2\text{mim}][\text{NTf}_2]$ at a 1.6 mm dia. Pt macrodisk electrode with scan rates of 50, 100, 250 and 500 mV s^{-1} .

Calculating pK_a and K_{homo} of oxyacids in $[\text{C}_2\text{mim}][\text{NTf}_2]$. Despite the complications from anionic homoassociation, the overall proton reduction process (shown in Eq. 18) remains the same. Consequently, pK_a can still be calculated using Eq. 9 from $E_{1/2}(\text{HA}/\text{H}_2)$, which is located mid-way between $E_{1/2}(\text{HA}/[\text{HA}_2]^-)$ and $E_{1/2}([\text{HA}_2]^-/\text{H}_2)$. However, because $E^0(\text{HA}/[\text{HA}_2]^-)$ and $E^0([\text{HA}_2]^-/\text{H}_2)$ vary by less than 0.2 V, there is significant overlap between the two processes shown Eqs. 16 and 17, making it very difficult to estimate $E_{1/2}(\text{HA}/[\text{HA}_2]^-)$ and $E_{1/2}([\text{HA}_2]^-/\text{H}_2)$ directly from the cyclic voltammogram. Fortunately, the differential response of derivative cyclic voltammetry (DCV)^{56, 57} is able to resolve the two processes, as is shown for H[OTs] in Figure S10. pK_a values calculated using Eq. 9 from the $E_{1/2}$ values estimated with DCV are summarized in Table 4. In our companion study²⁶, pK_a values calculated using the DCV technique were in excellent agreement with those derived either directly with CV or with CV plus numerical simulation. For details on how the derivative currents were calculated, see the Experimental Section.

K_{homo} can also be estimated from the voltammogram using Eqs. 19 or 20 if $E^0(\text{HA}/\text{H}_2)$ and $E^0(\text{HA}/[\text{HA}_2]^-)$ or $E^0([\text{HA}_2]^-/\text{H}_2)$ are known. $E^0(\text{HA}/\text{H}_2)$ can be calculated as follows²⁶:

$$E^0(\text{HA}/\text{H}_2) = E_{1/2}(\text{HA}/\text{H}_2) - \frac{RT}{2F} \ln \left(\frac{4\sqrt{D_{\text{H}_2}} D_{\text{A}^-}}{\sqrt{D_{\text{HA}}^3}} \right) + \frac{RT}{2F} \ln[\text{HA}]_{\text{b}} \quad (22)$$

and from the Nernst expression for Eq. 16, the following relationship can be derived using the diffusion layer method^{17, 25}:

$$E^0(\text{HA}/[\text{HA}_2]^-) = E_{1/2}(\text{HA}/[\text{HA}_2]^-) - \frac{RT}{2F} \ln \left(\frac{8\sqrt{D_{\text{H}_2}} D_{[\text{HA}_2]^-}}{\sqrt{D_{\text{HA}}^3}} \right) + \frac{RT}{2F} \ln[\text{HA}]_{\text{b}} \quad (23)$$

Both of these derivations assume mass transport to the electrode surface is governed solely by semi-infinite planar diffusion and HA is the only species initially present in solution. Subtracting Eq. 23 from Eq. 22 and combining with Eq. 19, gives:

$$-\frac{2.303RT}{F} \log_{10}(K_{\text{homo}}) = \Delta E_{1/2} + \frac{RT}{2F} \ln\left(\frac{D_{[\text{HA}_2]^-}}{D_{\text{A}^-}}\right) + \frac{RT}{2F} \ln(2[\text{HA}]_b^2) \quad (24)$$

where $\Delta E_{1/2} = E_{1/2}(\text{HA}/\text{H}_2) - E_{1/2}(\text{HA}/[\text{HA}_2]^-)$. Unfortunately, D_{A^-} cannot be calculated easily using electrochemical methods and $D_{[\text{HA}_2]^-}$ can only be estimated from a mixture of HA and A^- . Nonetheless, as shown above for H[OTs] (see Table 3), D_{A^-} and $D_{[\text{HA}_2]^-}$ should be comparable ($D_{(\text{H}[\text{OTs}]_2)^-}/D_{[\text{OTs}]^-} = 0.7$), so this term is negligible compared to the concentration term when working at millimolar concentrations. K_{homo} values estimated using Eq. 24, assuming $D_{[\text{HA}_2]^-}/D_{\text{A}^-} = 0.7$ are also included in Table 4. In addition, cyclic voltammograms obtained from the full spectrum of oxyacids investigated in the work are shown in Figure 7. The values of $\text{p}K_{\text{a}}$ and K_{homo} for H[OTs], calculated using Eqs. 9 and 24 respectively, are in excellent agreement with the values determined using numerical simulation (see Table 3). Additionally, the K_{homo} values shown in Table 4 are comparable to the values previously calculated by Cheng *et. al*⁷ for a range of substituted benzoic acids in [C₄mim][NTf₂] ($2.7 < \log K_{\text{homo}} < 3.7$).

Where available, $\text{p}K_{\text{a}}$ data in acetonitrile (AN) also have been included in Table 4. In addition, $\text{p}K_{\text{a}}$ (IL) has been plotted against $\text{p}K_{\text{a}}$ (AN) in Figure 8a. There is a good correlation between $\text{p}K_{\text{a}}$ (IL) and $\text{p}K_{\text{a}}$ (AN) for the neutral HA species; in [C₂mim][NTf₂] and AN, acid strength increases in the order: H[OTf] > H[OTs] > MSA > DBSA > TCAA > SACC > DCAA > oHBA > PCP. DBSA and SACC are the respective neutral sulfonamide acids di(benzenesulfonyl)amide and saccharin taken from our companion study.²⁶ In all cases except H[OTf] (the outlier in Figure 8a), the $\text{p}K_{\text{a}}$ of HA is 1 to 2 units higher in

[C₂mim][NTf₂] than AN. Although the dielectric constant of AN (38.0⁵⁸) is higher than that of [C₂mim][NTf₂] (11.5⁵⁹), favoring ionization of neutral acids (see Eq. 1) in the former solvent, AN is a weaker Lewis acid than [C₂mim]⁺ (Gutmann acceptor numbers are 27.4 for [C₂mim][NTf₂]⁵³, and 18.9 for AN⁵⁸), allowing for stronger stabilization of A⁻ in the latter solvent. Additionally, both solvents are similarly protophobic, with Gutmann donor numbers of 14.1 and 11.2 for AN⁵⁸ and [C₂mim][NTf₂]⁵³ respectively. In reality, it is difficult to pin down the exact cause(s) of the observed p*K*_a (IL) < p*K*_a (AN) trend, as the following factors may also influence the p*K*_a of HA: solvent polarity, electrostatic interactions and specific interactions, such as hydrogen bonding.⁶⁰

Table 4. Summary of the p*K*_a (IL), *K*_{homo} (IL), p*K*_a (AN) and p*K*_a (aq) values for the range oxyacids investigated in this work.

Acid	p <i>K</i> _a (IL) ^a	<i>K</i> _{homo} (IL) ^a	p <i>K</i> _a (AN)	p <i>K</i> _a (aq) ¹⁸
H[OTf]	2.0 ^b	^c	0.7 ²⁰	^d
NSA	5.9	2.8	–	–
H[OTs]	6.2	3.0	8.5 ²⁰	–2.1 ^e
MSA	7.4	3.3	9.97 ⁶¹	–1.6 ^e
TCAA	11.0	3.2	12.4 ⁶²	0.51
DCAA	13.6	3.6	15.81 ⁶²	1.48
MA	13.9 ^b	^f	–	3.6
oHBA	15.3	3.3	16.7 ⁶²	2.97
PCP	16.8 ^b	^c	18.02 ¹⁵	4.5
GA	17.8	3.5	–	4.65

^aDetermined in this work. ^b*E*_{1/2} estimated directly from cyclic voltammetry. ^cHomoassociation not detected experimentally. ^dH[OTf] is a superacid in aqueous media. ^eReliable literature data not available, p*K*_a (aq) was estimated using MarvinSketch software. ^f*K*_{homo} could not be estimated due to the difficulty in resolving the two processes represented by Eqs. 16 and 17.

Where available, pK_a data in water also have been included in Table 4. In addition, pK_a (IL) has been plotted against pK_a (aq) in Figure 8b. The order of acidities for the carboxylic acids is different in $[C_2mim][NTf_2]$ (DCAA > MA > oHBA) and water (DCAA > oHBA > MA). The ‘enhanced’ acidity of MA in $[C_2mim][NTf_2]$ is thought to be due to stabilization of the monoanion conjugate base (A^-) by intramolecular hydrogen bonding (previously discussed). Aside from that, there is a good correlation between pK_a (IL) and pK_a (aq) for the neutral acids, increasing in the order $H[OTf] > H[OTs] > MSA > TCAA > SACC > DCAA > oHBA > PCP > GA$. The pK_a of each of the neutral acids is orders of magnitude higher in $[C_2mim][NTf_2]$ compared to water. This is not surprising, since water has a high dielectric constant (80.1), Gutmann donor number ($18.0 \text{ kcal mol}^{-1}$) and Gutmann acceptor number (54.8), meaning it can solvate (stabilize) H^+ and A^- to a greater extent than $[C_2mim][NTf_2]$. In addition, it is well known that water is able to form strong hydrogen bonds with oxyanions (*i.e.*, sulfonates and carboxylates), further promoting ionization *via* Eq. 1.⁸ A similar effect was achieved by changing from $[C_2mim][NTf_2]$ to the protic IL, $[N_{H,2,2,2}][NTf_2]$. As previously eluded too, the pK_a of $H[OTs]$ is 3.3 in $[N_{H,2,2,2}][NTf_2]$ compared to 6.2 in $[C_2mim][NTf_2]$ due to the stabilization of $[OTs]^-$ through hydrogen bonding with $[N_{H,2,2,2}]^+$ (which also suppresses K_{homo}). Hydrogen bonding is most effective when the charge on the anion (*i.e.*, A^-) is highly localized, which is why the difference between $pK_a(\text{IL})$ and $pK_a(\text{aq})$ increases with decreasing acid strength (see Table 4).

The intrinsic acidity of a compound is represented in its gas phase acidity. If a solution phase acidity scale correlates linearly with the corresponding gas phase data, it is said to be an intrinsic acidity scale as it reflects the intrinsic order of ionization. A solution phase pK_a scale will be non-intrinsic if the solvent preferentially stabilizes (solvates) or destabilizes the acid (*i.e.*, BH^+ or HA) or its conjugate base (*i.e.*, B or A^-), which will skew the dissociation (ionization) equilibrium (see Eq. 1) relative to the gas phase. Unfortunately,

there is insufficient gas phase acidity data available on the acids investigated in this study and the companion study²⁶ to make a judgment on whether the pK_a scale in $[C_2mim][NTf_2]$ is intrinsic. The aqueous pK_a scale is well known to correlate poorly with gas phase data (*i.e.*, is non-intrinsic) due to prejudicial solvation of the water molecule towards different ions. For example, as discussed above, in water the acidities of neutral oxyacids (HA) are ‘enhanced’ relative to the protonated amines (BH^+) through the stabilization of oxyanions (A^-) by hydrogen bonding. In addition, due to its high dielectric constant, water favors the dissociation of neutral HA (two ions are produced upon dissociation) over cationic BH^+ (no net increase in the number of charged species upon dissociation).

From Figure 8b, it is evident that the acids can be divided into two groups; cationic and neutral. There is good correlation between pK_a (aq) and pK_a (IL) within the groups (*i.e.*, cationic *vs.* cationic or neutral *vs.* neutral), but not between the groups (*i.e.*, cationic *vs.* neutral). As previously discussed, $[C_2mim][NTf_2]$ is made up of ions with strongly delocalized (diffuse) charge densities and is therefore a poor hydrogen bond donor/acceptor (or Lewis acid/base) relative to water. As a result, $[C_2mim][NTf_2]$ is not expected to interact strongly and thus preferentially ‘solvate’ the monocharged ions (BH^+ or A^-) versus the neutral molecules (B or HA). For this reason, the trends seen in Figure 8b are not surprising, as the ‘enhanced’ acidity of the neutral acids (HA) in water makes them appear to be ‘weaker’ relative to the cationic acids (BH^+) in the absence of strong solute-solvent hydrogen bonding interactions, as is the case in $[C_2mim][NTf_2]$. Finally, we anticipate that the pK_a (IL) scale would correlate more closely with the pK_a (aq) scale in a protic IL composed of a hydrogen bond donating cation (*i.e.*, $[R_xH_{(4-x)}N]^+$) with a hydrogen bond accepting anion (*i.e.*, $[CH_3COO]^-$ or $[H_2PO_4]^-$).^{63, 64}

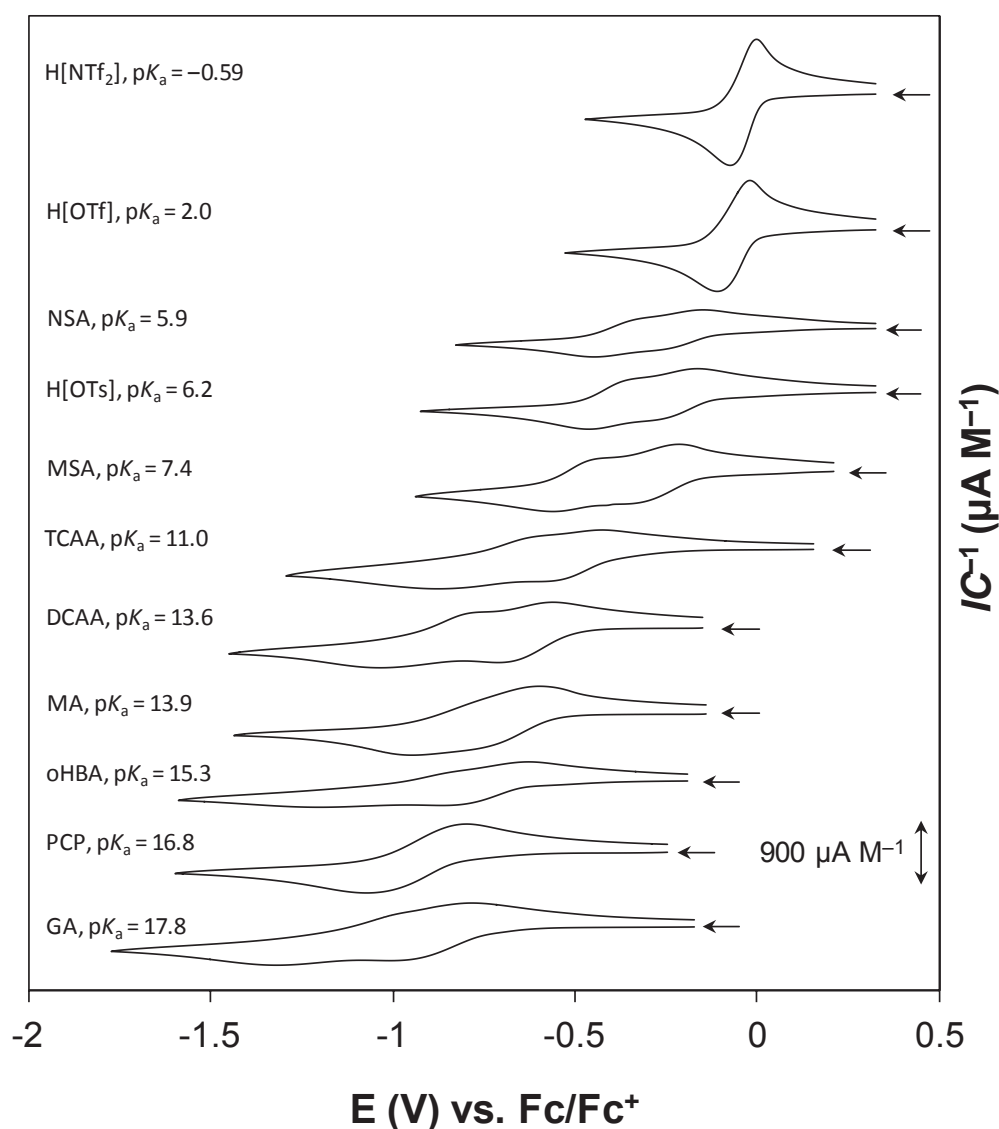


Figure 7. Concentration-normalized cyclic voltammograms showing the proton reduction process obtained from (top to bottom) 49.8 mM H[NTf₂], 52.6 mM H[OTf], 47.6 mM NSA, 41.6 mM H[OTs], 50.4 mM MSA, 48.3 mM TCAA, 39.4 mM DCAA, 56.4 mM MA, 81.7 mM oHBA, 33.1 mM PCP and 55.5 mM GA in [C₂mim][NTf₂] at a 1.6 mm dia. Pt macrodisk electrode with a scan rate of 100 mV s⁻¹. The arrows indicate zero current for each of the voltammograms.

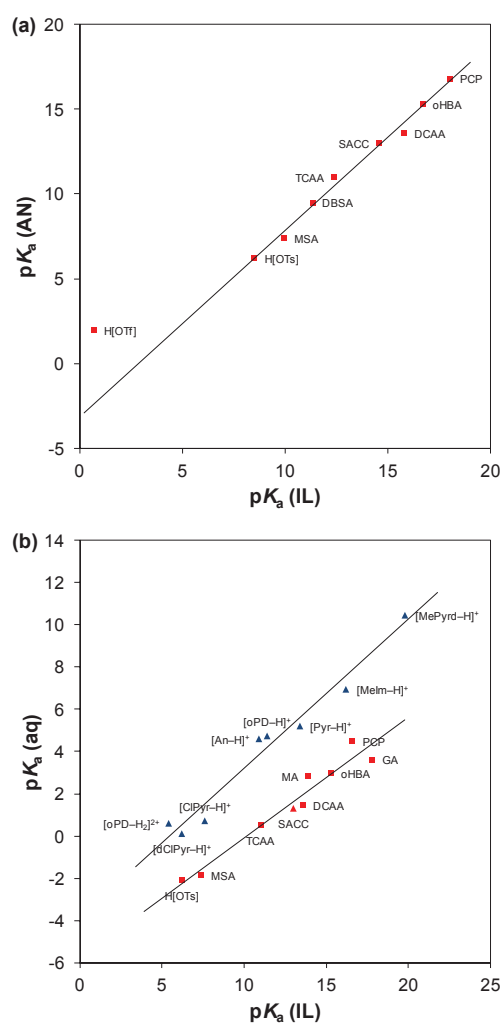


Figure 8. (a) Plot of pK_a (AN) vs. pK_a (IL) for a range of neutral acids (structures available in Table 1 of the main text). (b) Plot of pK_a (aq) vs. pK_a (IL) for a range of nitrogen (triangles) and oxygen (squares) acids. Regression lines for the uncharged (red symbols) and charged (blue symbols) acids have been included to guide the reader's eye. H[OTf] not considered when calculating the regression line in (a). Abbreviations are as follows: SACC = saccharin, DBSA = di(benzenesulfonyl)imide, dClPyr = 2,4-dichloropyridine, oPD = o-phenylenediamine, ClPyr = 2-chloropyridine, An = aniline, Pyr = pyridine, MeIm = N-methylimidazole and MePyrd = N-methylpyrrolidine.

Conclusions

The thermodynamics, kinetics and mechanisms for the proton reduction (hydrogen evolution) reaction at a platinum electrode have been investigated in [C₂mim][NTf₂] using a range of oxyacids (phenols, carboxylic acids or sulfonic acids) as the proton source. H[OTf], a well known superacid in aqueous media, was found to behave as a weak acid in [C₂mim][NTf₂]. Numerical simulations revealed that proton reduction from H[OTf] is likely to be a *CE* process, where hydrogen evolution *via* the classical Volmer-Tafel route is preceded by an acid dissociation (ionization) step. The proton reduction process from sulfonic (excluding H[OTf]) and carboxylic acids was found to occur in two steps (electron stoichiometry = 1:1), consistent with the formation of a stable intermediate species through homo hydrogen bonding (homoassociation) between the acid and its conjugate anion base. Simulations confirmed that the experimental voltammetric response is consistent with an *ECE* mechanism. Homoassociation was able to be suppressed by changing the constituent cation/anion of the IL or by mixing the IL with a hydrogen bonding solvent, such as propylene glycol. Finally, we have estimated the pK_a and K_{homo} values of ten oxyacids covering sixteen orders of magnitude in acid strength ($2.0 \leq pK_a \text{ (IL)} \leq 17.8$) from $E_{1/2}$ and D values derived using voltammetric methods. Comparison of the $pK_a \text{ (IL)}$ data with that from conventional solvents, such as acetonitrile and water has given us an insight into how the nature of the solvent (*i.e.*, dielectric properties, Lewis acidity/basicity, hydrogen donating/accepting ability etc.) can influence the strength of an acid (pK_a), which, as we have shown, has a strong bearing on the thermodynamics, kinetics and mechanism of the proton reduction process.

Associated Content

Supporting information. Simulation-experiment comparisons for the electro-reduction of solvated H^+ in $[C_2mim][NTf_2]$ (Figure S1), proton reduction process from the sulfonic acids NSA (Figure S2) and MSA (Figure S3) in $[C_2mim][NTf_2]$, simulation-experiment comparison for the proton reduction process from $H[OTs]$ in $[C_2mim][NTf_2]$ (Figure S4), proton reduction process from the carboxylic acids TCAA (Figure S5) and oHBA (Figure S6) in $[C_2mim][NTf_2]$, proton reduction process from GA in $[C_2mim][NTf_2]$ (Figure S7) and $[C_2mim][N(CN)_2]$ (Figure S8), proton reduction process from 2,3,4-trichlorophenol in $[C_4mpyr][NTf_2]$ (Figure S9) and derivative cyclic voltammogram for the proton reduction process obtained from $H[OTs]$ in $[C_2mim][NTf_2]$ (Figure S10). This material is available free of charge *via* the Internet at <http://pubs.acs.org>.

Author Information

Corresponding Authors

Notes

The authors declare no competing financial interest.

Acknowledgements

The authors thank Dr. Thomas R  ther for assistance in the preparation of 1-ethyl-3-methylimidazolium *p*-toluenesulfonate.

References

- (1) Migliore, A.; Polizzi, N. F.; Therien, M. J.; Beratan, D. N., Biochemistry and Theory of Proton-Coupled Electron Transfer. *Chem. Rev.* **2014**.
- (2) Kreuer, K. D., Proton Conductivity: Materials and Applications. *Chem. Mat.* **1996**, *8*, 610-641.
- (3) Mikkelsen, M.; Jorgensen, M.; Krebs, F. C., The Teraton Challenge. A Review of Fixation and Transformation of Carbon Dioxide. *Energy Environ. Sci.* **2010**, *3*, 43-81.
- (4) Arico, A. S.; Srinivasan, S.; Antonucci, V., DMFCs: From Fundamental Aspects to Technology Development. *Fuel Cells* **2001**, *1*, 133-161.
- (5) Bard, A. J.; Fox, M. A., Artificial Photosynthesis - Solar Splitting of Water to Hydrogen and Oxygen. *Acc. Chem. Res.* **1995**, *28*, 141-145.
- (6) Deng, H.; Li, X.; Chu, Y.; He, J.; Cheng, J.-P., Standard pK_a Scales of Carbon-Centered Indicator Acids in Ionic Liquids: Effect of Media and Structural Implication. *J. Org. Chem.* **2012**, *77*, 7291-7298.
- (7) Wang, Z.; Deng, H.; Li, X.; Ji, P. J.; Cheng, J. P., Standard and Absolute pK_a Scales of Substituted Benzoic Acids in Room Temperature Ionic Liquids. *J. Org. Chem.* **2013**, *78*, 12487-12493.
- (8) Bordwell, F. G., Equilibrium Acidities in Dimethyl Sulfoxide Solution. *Acc. Chem. Res.* **1988**, *21*, 456-463.
- (9) Barrette, W. C.; Johnson, H. W.; Sawyer, D. T., Voltammetric Evaluation of the Effective Acidities (pK_a') for Bronsted Acids in Aprotic-solvents. *Anal. Chem.* **1984**, *56*, 1890-1898.

- (10) Perrin, D. D.; Dempsey, B.; Serjeant, E. P., *pK_a Prediction for Organic Acids and Bases*. Chapman and Hall: New York, 1981.
- (11) Barhdadi, R.; Troupel, M.; Comminges, C.; Laurent, M.; Doherty, A., Electrochemical Determination of pK_a of N-Bases in Ionic Liquid Media. *J. Phys. Chem. B* **2012**, *116*, 277-282.
- (12) Campbell, M. L.; Waite, B. A., The K_a Values of Water and the Hydronium Ion for Comparison with Other Acids. *J. Chem. Educ.* **1990**, *67*, 386.
- (13) Slater, A. M., The IUPAC Aqueous and Non-Aqueous Experimental pK_a Data Repositories of Organic Acids and Bases. *J. Comput.-Aided Mol. Des.* **2014**, *28*, 1031-1034.
- (14) Haynes, W., *CRC Handbook of Chemistry and Physics : a Ready-Reference Book of Chemical and Physical Data* 95th ed.; CRC Press: Boca Raton, Florida, 2014.
- (15) Kütt, A.; Leito, I.; Kaljurand, I.; Sooväli, L.; Vlasov, V. M.; Yagupolskii, L. M.; Koppel, I. A., A Comprehensive Self-Consistent Spectrophotometric Acidity Scale of Neutral Brønsted Acids in Acetonitrile. *J. Org. Chem.* **2006**, *71*, 2829-2838.
- (16) Treimer, S. E.; Evans, D. H., Electrochemical Reduction of Acids in Dimethyl Sulfoxide. CE Mechanisms and Beyond. *J. Electroanal. Chem.* **1998**, *449*, 39-48.
- (17) Treimer, S. E.; Evans, D. H., Electrochemical Reduction of Acids in Dimethyl Sulfoxide. Comparison of Weak C-H, N-H and O-H Acids. *J. Electroanal. Chem.* **1998**, *455*, 19-28.
- (18) Serjeant, E. P.; Dempsey, B., *Ionisation Constants of Organic Acids in Aqueous Solution*. Pergamon: Oxford, 1979.

- (19) Qiang, Z.; Adams, C., Potentiometric Determination of Acid Dissociation Constants (pK_a) for Human and Veterinary Antibiotics. *Water Res.* **2004**, *38*, 2874-2890.
- (20) Kütt, A.; Rodima, T.; Saame, J.; Raamat, E.; Mäemets, V.; Kaljurand, I.; Koppel, I. A.; Garlyauskayte, R. Y.; Yagupolskii, Y. L.; Yagupolskii, L. M.; Bernhardt, E.; Willner, H.; Leito, I., Equilibrium Acidities of Superacids. *J. Org. Chem.* **2010**, *76*, 391-395.
- (21) Wilkes, J. S., A Short History of Ionic Liquids - from Molten Salts to Neoteric Solvents. *Green Chem.* **2002**, *4*, 73-80.
- (22) Galinski, M.; Lewandowski, A.; Stepniak, I., Ionic Liquids as Electrolytes. *Electrochim. Acta* **2006**, *51*, 5567-5580.
- (23) Dean, P. M.; Pringle, J. M.; MacFarlane, D. R., Structural Analysis of Low Melting Organic Salts: Perspectives on Ionic Liquids. *Phys. Chem. Chem. Phys.* **2010**, *12*, 9144-9153.
- (24) McMahon, T. B.; Kebarle, P., Intrinsic Acidities of Substituted Phenols and Benzoic Acids Determined by Gas-Phase Proton-Transfer Equilibriums. *J. Am. Chem. Soc.* **1977**, *99*, 2222-2230.
- (25) Bard, A. J.; Faulkner, L. R., *Electrochemical Methods : Fundamentals and Applications*. 2nd ed.; Wiley: New York, 2001.
- (26) Bentley, C. L.; Bond, A. M.; Hollenkamp, A. F.; Mahon, P. J.; Zhang, J., Electrochemical Proton Reduction and Equilibrium Acidity (pK_a) in Aprotic Ionic Liquids: Protonated Amines and Sulfonamide Acids. *In preparation* **2015**.
- (27) Barrette, W. C.; Sawyer, D. T., Determination of Dissolved Hydrogen and Effects of Media and Electrode Materials on the Electrochemical Oxidation of Molecular-Hydrogen. *Anal. Chem.* **1984**, *56*, 653-657.

(28) Meng, Y.; Aldous, L.; Belding, S. R.; Compton, R. G., The Hydrogen Evolution Reaction in a Room Temperature Ionic Liquid: Mechanism and Electrocatalyst Trends. *Phys. Chem. Chem. Phys.* **2012**, *14*, 5222-5228.

(29) Meng, Y.; Aldous, L.; Belding, S. R.; Compton, R. G., The Formal Potentials and Electrode Kinetics of the Proton/Hydrogen Couple in Various Room Temperature Ionic Liquids. *Chem. Commun.* **2012**, *48*, 5572-5574.

(30) Kibler, L. A., Hydrogen Electrocatalysis. *Chemphyschem* **2006**, *7*, 985-991.

(31) Jaworski, A.; Donten, M.; Stojek, Z.; Osteryoung, J. G., Conditions of Strict Voltammetric Reversibility of the H⁺/H₂ Couple at Platinum Electrodes. *Anal. Chem.* **1999**, *71*, 243-246.

(32) Conway, B. E.; Tilak, B. V., Interfacial Processes Involving Electrocatalytic Evolution and Oxidation of H₂, and the Role of Chemisorbed H. *Electrochim. Acta* **2002**, *47*, 3571-3594.

(33) Rieger, P. H., *Electrochemistry*. 2nd ed.; Chapman & Hall: New York, 1994.

(34) Bentley, C. L.; Bond, A. M.; Hollenkamp, A. F.; Mahon, P. J.; Zhang, J., Mass Transport Studies and Hydrogen Evolution at a Platinum Electrode Using Bis(trifluoromethanesulfonyl)imide as the Proton Source in Ionic Liquids and Conventional Solvents. *J. Phys. Chem. C* **2014**, *118*, 22439–22449.

(35) Silvester, D. S.; He, W.; Aldous, L.; Hardacre, C.; Compton, R. G., Electrochemical Reduction of Benzoic Acid and Substituted Benzoic Acids in Some Room Temperature Ionic Liquids. *J. Phys. Chem. C* **2008**, *112*, 12966-12973.

(36) Meng, Y.; Norman, S.; Hardacre, C.; Compton, R. G., The Electroreduction of Benzoic Acid: Voltammetric Observation of Adsorbed Hydrogen at a Platinum Microelectrode in Room Temperature Ionic Liquids. *Phys. Chem. Chem. Phys.* **2013**, *15*, 2031-2036.

(37) Holbrey, J. D.; Reichert, W. M.; Swatloski, R. P.; Broker, G. A.; Pitner, W. R.; Seddon, K. R.; Rogers, R. D., Efficient, Halide Free Synthesis of New, Low Cost Ionic Liquids: 1,3-Dialkylimidazolium Salts Containing Methyl- and Ethyl-Sulfate Anions *Green Chem.* **2002**, *4*, 407-413.

(38) Gritzner, G.; Kuta, J., Recommendations on Reporting Electrode-Potentials in Nonaqueous Solvents. *Pure Appl. Chem.* **1984**, *56*, 461-466.

(39) Rogers, E. I.; Silvester, D. S.; Poole, D. L.; Aldous, L.; Hardacre, C.; Compton, R. G., Voltammetric Characterization of the Ferrocene|Ferrocenium and Cobaltocenium|Cobaltocene Redox Couples in RTILs. *J. Phys. Chem. C* **2008**, *112*, 2729-2735.

(40) Mahon, P. J.; Oldham, K. B., Convulsive Modelling of Electrochemical Processes Based on the Relationship Between the Current and the Surface Concentration. *J. Electroanal. Chem.* **1999**, *464*, 1-13.

(41) Bentley, C. L.; Bond, A. M.; Hollenkamp, A. F.; Mahon, P. J.; Zhang, J., Applications of Convolution Voltammetry in Electroanalytical Chemistry. *Anal. Chem.* **2014**, *86*, 2073-2081.

(42) Bentley, C. L.; Bond, A. M.; Hollenkamp, A. F.; Mahon, P. J.; Zhang, J., Electrode Reaction and Mass-Transport Mechanisms Associated with the Iodide/Triiodide Couple in

the Ionic Liquid 1-Ethyl-3-methylimidazolium Bis(trifluoromethanesulfonyl)imide. *J. Phys. Chem. C* **2014**, *118*, 29663–29673.

(43) Shoup, D.; Szabo, A., Chronoamperometric Current at Finite Disk Electrodes. *J. Electroanal. Chem.* **1982**, *140*, 237-245.

(44) Klymenko, O. V.; Evans, R. G.; Hardacre, C.; Svir, I. B.; Compton, R. G., Double Potential Step Chronoamperometry at Microdisk Electrodes: Simulating the Case of Unequal Diffusion Coefficients. *J. Electroanal. Chem.* **2004**, *571*, 211-221.

(45) Grenness, M.; Oldham, K. B., Semiintegral Electroanalysis: Theory and Verification. *Anal. Chem.* **1972**, *44*, 1121-1129.

(46) Bentley, C. L.; Bond, A. M.; Hollenkamp, A. F.; Mahon, P. J.; Zhang, J., Advantages Available in the Application of the Semi-Integral Electroanalysis Technique for the Determination of Diffusion Coefficients in the Highly Viscous Ionic Liquid 1-Methyl-3-Octylimidazolium Hexafluorophosphate. *Anal. Chem.* **2012**, *85*, 2239-2245.

(47) Bordwell, F. G.; McCallum, R. J.; Olmstead, W. N., Acidities and Hydrogen-bonding of Phenols in Dimethylsulfoxide. *J. Org. Chem.* **1984**, *49*, 1424-1427.

(48) Roses, M., Ionic Equilibria in Nonaqueous Solvents .3. Effect of Homoconjugation. *Anal. Chim. Acta* **1994**, *285*, 391-399.

(49) Zielinska, J.; Makowski, M.; Maj, K.; Liwo, A.; Chmurzynski, L., Acid-Base and Hydrogen-bonding Equilibria in Aliphatic Amine and Carboxylic Acid Systems in Non-Aqueous Solutions. *Anal. Chim. Acta* **1999**, *401*, 317-321.

(50) Crowhurst, L.; Mawdsley, P. R.; Perez-Arlandis, J. M.; Salter, P. A.; Welton, T., Solvent-Solute Interactions in Ionic Liquids. *Phys. Chem. Chem. Phys.* **2003**, *5*, 2790-2794.

- (51) Belieres, J.-P.; Angell, C. A., Protic Ionic Liquids: Preparation, Characterization, and Proton Free Energy Level Representation. *J. Phys. Chem. B* **2007**, *111*, 4926-4937.
- (52) Bautista-Martinez, J. A.; Tang, L.; Belieres, J. P.; Zeller, R.; Angell, C. A.; Friesen, C., Hydrogen Redox in Protic Ionic Liquids and a Direct Measurement of Proton Thermodynamics. *J. Phys. Chem. C* **2009**, *113*, 12586-12593.
- (53) Schmeisser, M.; Illner, P.; Puchta, R.; Zahl, A.; van Eldik, R., Gutmann Donor and Acceptor Numbers for Ionic Liquids. *Chem.-Eur. J.* **2012**, *18*, 10969-10982.
- (54) Nguyen, T. H.; Hibbs, D. E.; Howard, S. T., Conformations, Energies, and Intramolecular Hydrogen Bonds in Dicarboxylic Acids: Implications for the Design of Synthetic Dicarboxylic Acid Receptors. *J. Comput. Chem.* **2005**, *26*, 1233-1241.
- (55) Czaja, M.; Kozak, A.; Makowski, M.; Chmurzyński, L., Potentiometric Investigation of Acid Dissociation and Anionic Homoconjugation Equilibria of Substituted Phenols in Dimethyl Sulfoxide. *J. Chem. Thermodyn.* **2003**, *35*, 1645-1655.
- (56) Tilset, M., Derivative Cyclic Voltammetry: Applications in the Investigation of the Energetics of Organometallic Electrode Reactions. In *Energetics of Organometallic Species*, Martinho Simões, J. A., Ed. Springer Netherlands: 1992; Vol. 367, p 109-129.
- (57) Murthy, A.; Manthiram, A., Application of Derivative Voltammetry in the Analysis of Methanol Oxidation Reaction. *J. Phys. Chem. C* **2012**, *116*, 3827-3832.
- (58) Gutmann, V., Solvent Effects on the Reactivities of Organometallic Compounds. *Coord. Chem. Rev.* **1976**, *18*, 225-255.

- (59) Singh, T.; Kumar, A., Static Dielectric Constant of Room Temperature Ionic Liquids: Internal Pressure and Cohesive Energy Density Approach. *J. Phys. Chem. B* **2008**, *112*, 12968-12972.
- (60) Augustin-Nowacka, D.; Makowski, M.; Chmurzynski, L., Acid-Base Equilibria in Systems Involving Substituted Pyridines in Polar Aprotic Protophobic Media and in the Amphiprotic Methanol. *Anal. Chim. Acta* **2000**, *418*, 233-240.
- (61) Eckert, F.; Leito, I.; Kaljurand, I.; Kütt, A.; Klamt, A.; Diedenhofen, M., Prediction of Acidity in Acetonitrile Solution with COSMO-RS. *J. Comput. Chem.* **2009**, *30*, 799-810.
- (62) Kim, H. S.; Chung, T. D.; Kim, H., Voltammetric Determination of the pK(a) of Various Acids in Polar Aprotic Solvents Using 1,4-Benzoquinone. *J. Electroanal. Chem.* **2001**, *498*, 209-215.
- (63) Greaves, T. L.; Drummond, C. J., Protic Ionic Liquids: Properties and Applications. *Chem. Rev.* **2008**, *108*, 206-237.
- (64) MacFarlane, D. R.; Pringle, J. M.; Johansson, K. M.; Forsyth, S. A.; Forsyth, M., Lewis Base Ionic Liquids. *Chem. Commun.* **2006**, 1905-1917.

Supporting information for

Electrochemical Proton Reduction and
Equilibrium Acidity (pK_a) in Aprotic Ionic
Liquids: Phenols, Carboxylic Acids and Sulfonic
Acids

*Cameron L. Bentley,^{†,‡} Alan M. Bond,[†] Anthony F. Hollenkamp,[‡] Peter J. Mahon[§] and Jie
Zhang[†]*

[†]School of Chemistry, Monash University, Clayton, Vic 3800, Australia

[‡]CSIRO Energy Flagship, Box 312, Clayton South, Vic 3169, Australia

[§]Faculty of Science, Engineering and Technology, Swinburne University of Technology,
Hawthorn, Vic 3122, Australia

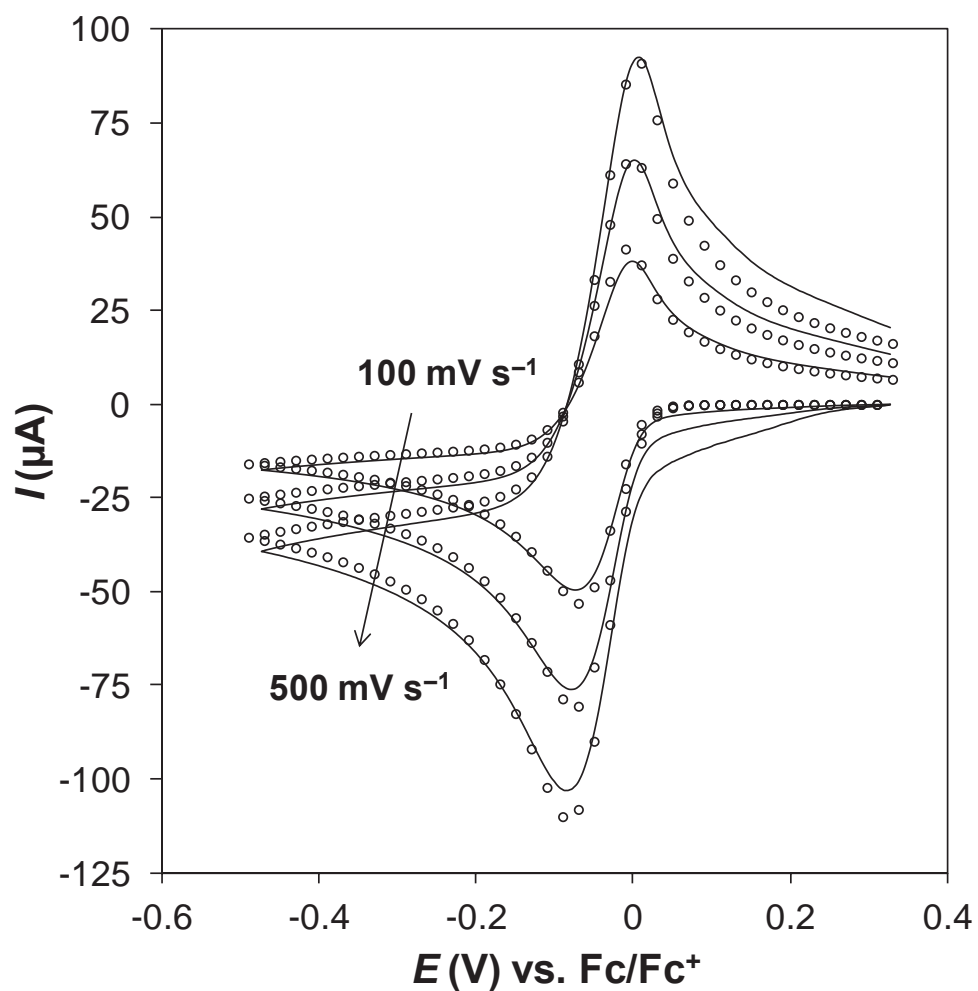


Figure S1. Comparison of the simulated (\circ) and experimental ($—$) cyclic voltammograms showing the proton reduction process obtained from 49.8 mM $\text{H}[\text{NTf}_2]$ in $[\text{C}_2\text{mim}][\text{NTf}_2]$ at a 1.6 mm dia. Pt macrodisk electrode with scan rates of 100, 250 and 500 mV s^{-1} . Simulation parameters are available in Table 2 of the main text.

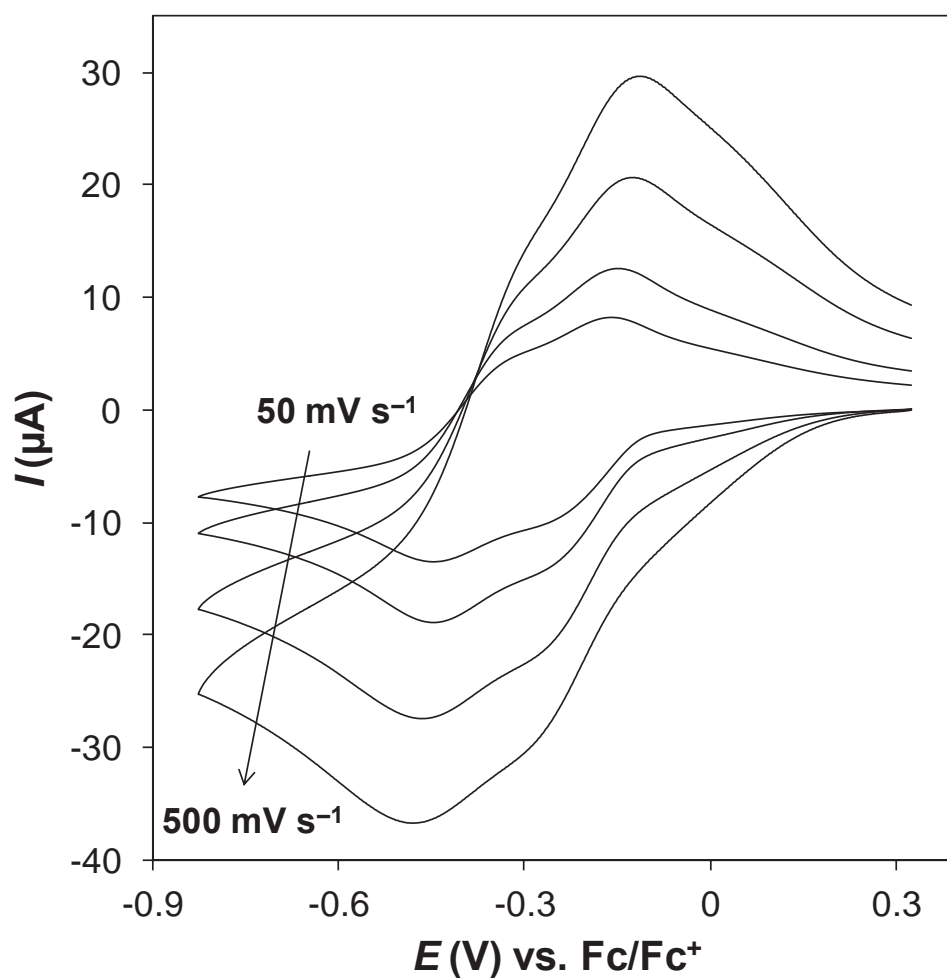


Figure S2. Cyclic voltammograms showing the proton reduction process obtained from 47.6 mM NSA in $[\text{C}_2\text{mim}][\text{NTf}_2]$ at a 1.6 mm dia. Pt macrodisk electrode with scan rates of 50, 100, 250 and 500 mV s^{-1} .

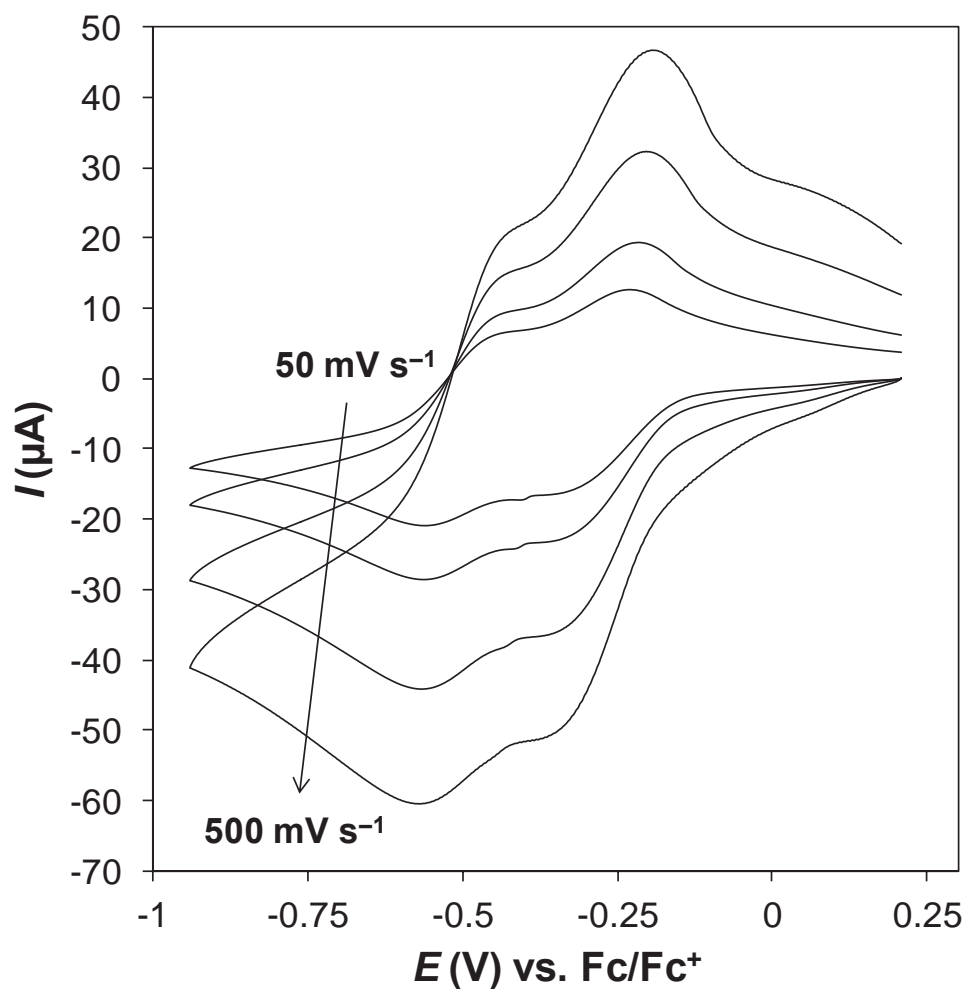


Figure S3. Cyclic voltammograms showing the proton reduction process obtained from 50.4 mM MSA in $[\text{C}_2\text{mim}][\text{NTf}_2]$ at a 1.6 mm dia. Pt macrodisk electrode with scan rates of 50, 100, 250 and 500 mV s^{-1} .

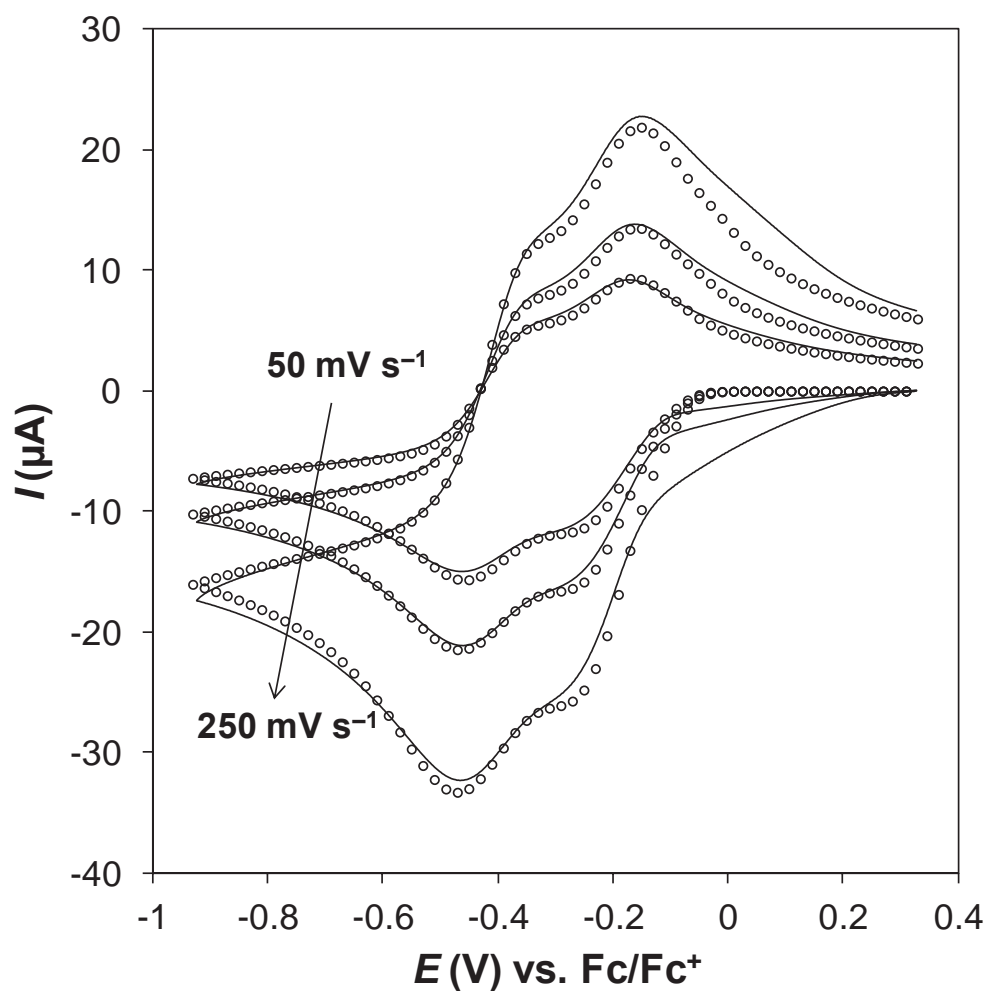


Figure S4. Comparison of the simulated (\circ) and experimental (—) cyclic voltammograms showing the proton reduction process obtained from 41.6 mM H[OTs] in $[\text{C}_2\text{mim}][\text{NTf}_2]$ at a 1.6 mm dia. Pt macrodisk electrode with scan rates of 50, 100 and 250 mV s^{-1} . Simulation parameters are available in Table 3 of the main text.

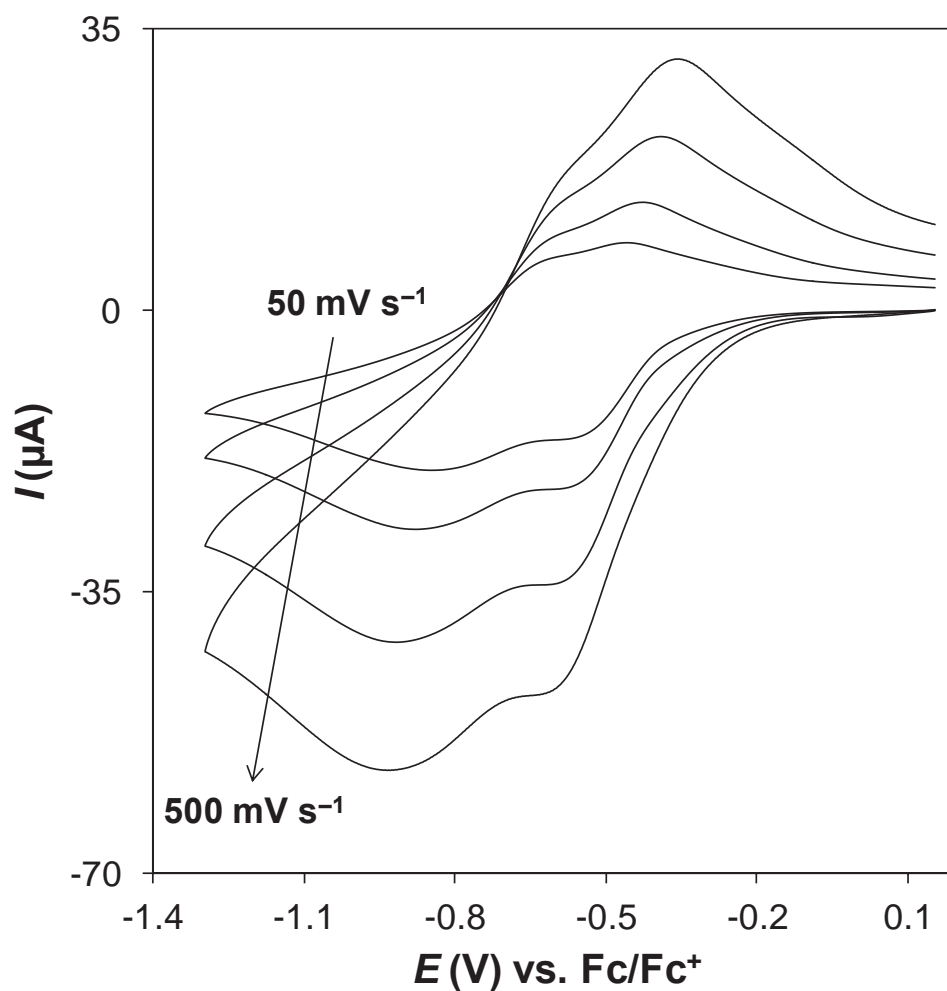


Figure S5. Cyclic voltammograms showing the proton reduction process obtained from 48.3 mM TCAA in $[\text{C}_2\text{mim}][\text{NTf}_2]$ at a 1.6 mm dia. Pt macrodisk electrode with scan rates of 50, 100, 250 and 500 mV s^{-1} .

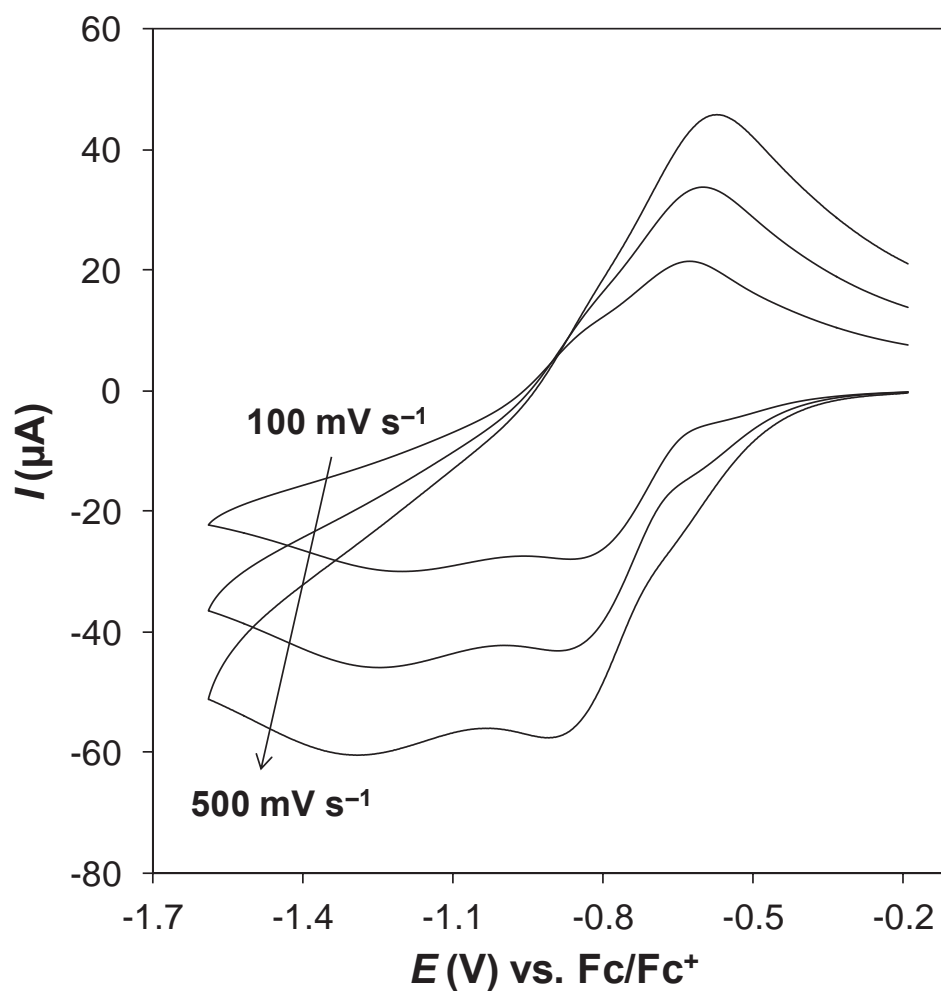


Figure S6. Cyclic voltammograms showing the proton reduction process obtained from 81.7 mM oHBA in $[\text{C}_2\text{mim}][\text{NTf}_2]$ at a 1.6 mm dia. Pt macrodisk electrode with scan rates of 100, 250 and 500 mV s^{-1} .

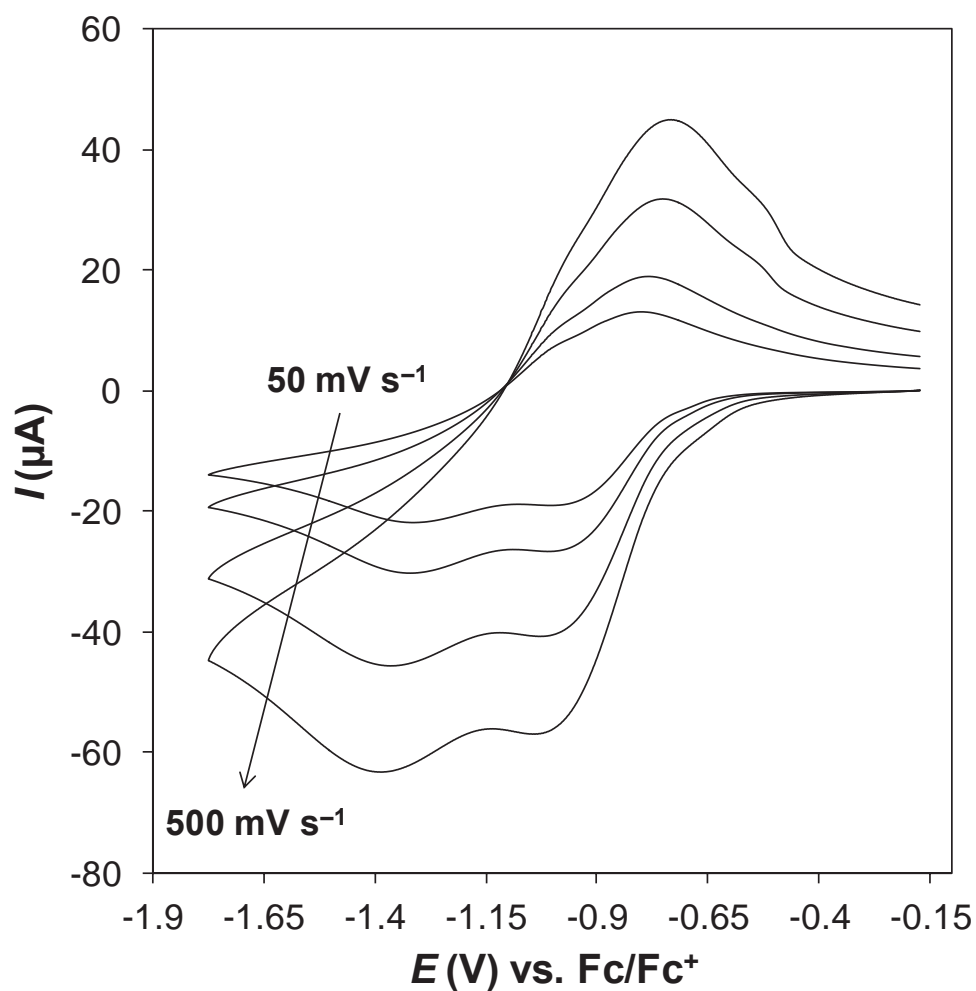


Figure S7. Cyclic voltammograms showing the proton reduction process obtained from 55.5 mM GA in $[\text{C}_2\text{mim}][\text{NTf}_2]$ at a 1.6 mm dia. Pt macrodisk electrode with scan rates of 50, 100, 250 and 500 mV s^{-1} .

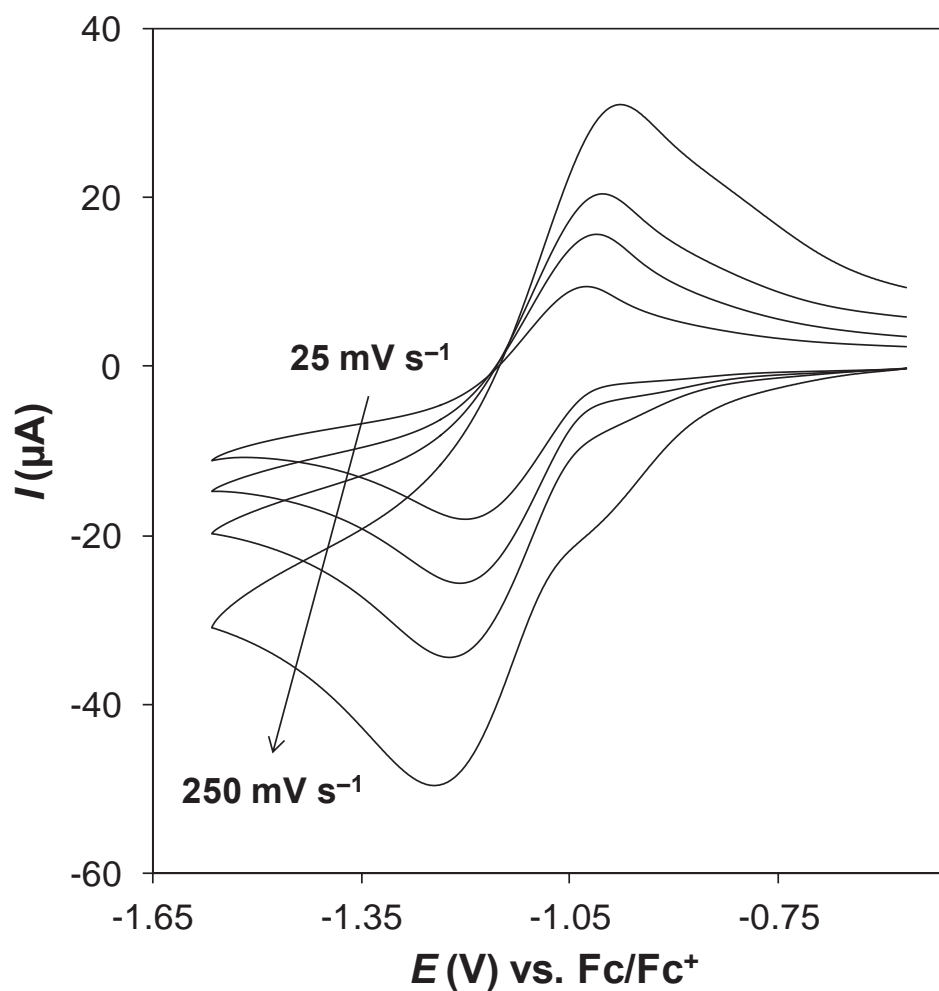


Figure S8. Cyclic voltammograms showing the proton reduction process obtained from 46.8 mM GA in $[\text{C}_2\text{mim}][\text{N}(\text{CN})_2]$ at a 1.6 mm dia. Pt macrodisk electrode with scan rates of 25, 50, 100 and 250 mV s^{-1} .

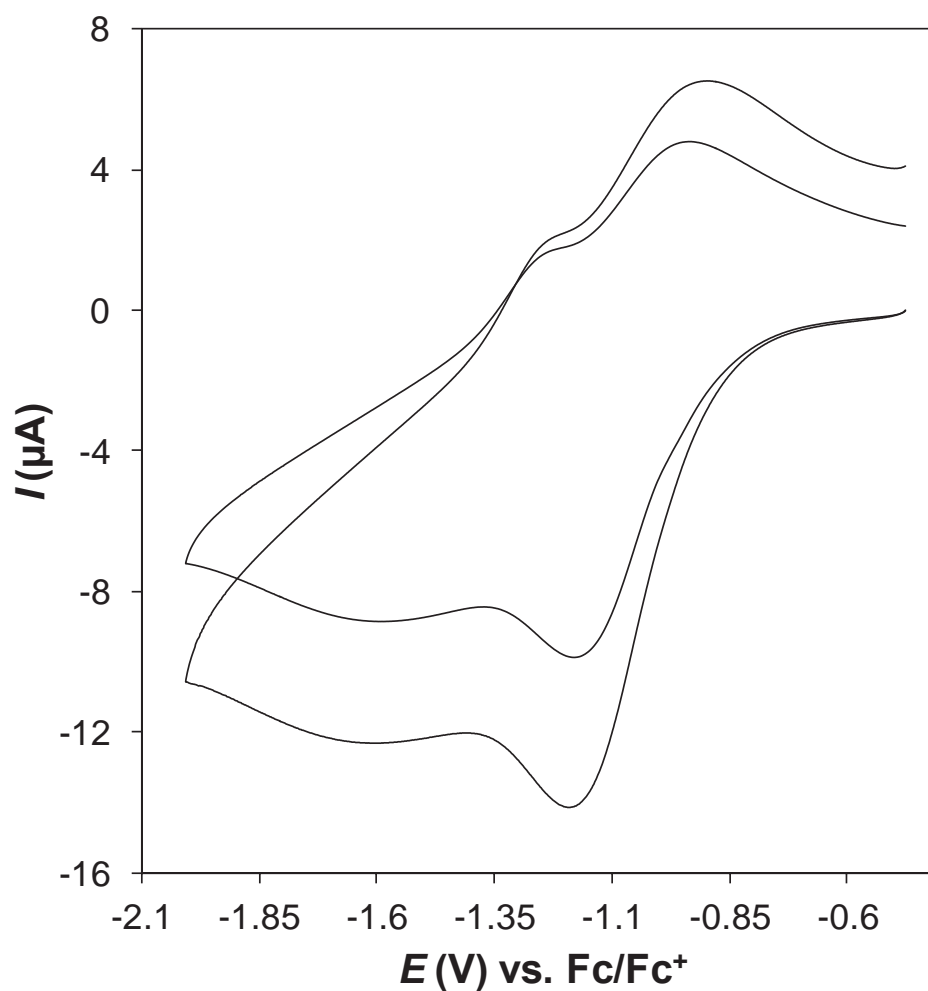


Figure S9. Cyclic voltammograms showing the proton reduction process obtained from 41.9 mM 2,3,4-trichlorophenol in $[\text{C}_4\text{mpyr}][\text{NTf}_2]$ at a 1.6 mm dia. Pt macrodisk electrode with scan rates of 50 and 100 mV s^{-1} .

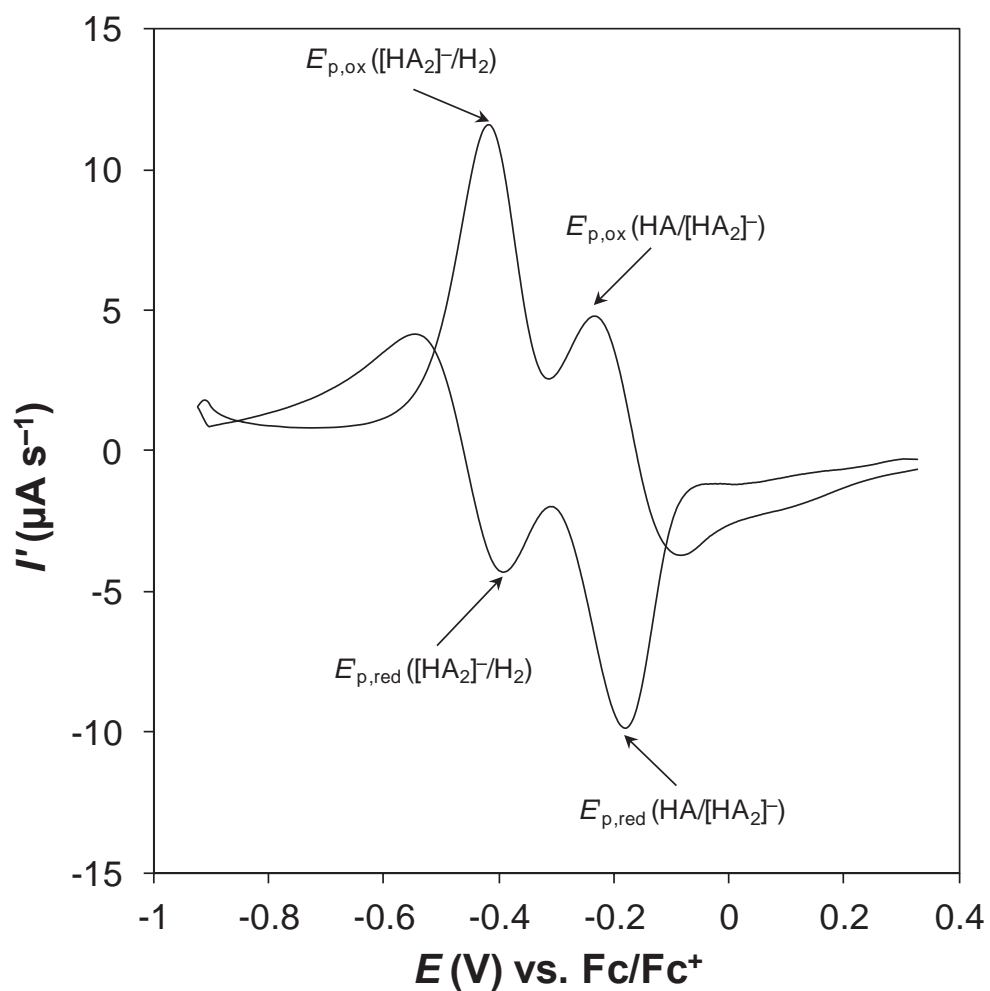


Figure S10. Derivative cyclic voltammogram showing the proton reduction process obtained from 41.6 mM H[OTs] in $[\text{C}_2\text{mim}][\text{NTf}_2]$ at a 1.6 mm dia. Pt macrodisk electrode with a scan rate of 100 mV s^{-1} .

6. Conclusions and Future Work

Room temperature ionic liquids have received considerable attention over the past two decades as promising replacements for volatile molecular solvents in a range of applications. They are intrinsic ionic conductors and have been successfully employed as non-flammable/non-reactive electrolyte media in a range of electrochemical devices. As the use of these novel electrolytes continues to expand, the limits to our knowledge on fundamental processes such as mass-transport; reaction kinetics and thermodynamics; and (electro)chemical reaction mechanisms in this type of medium has become apparent. To this end, the work presented here endeavoured to compare and contrast the electrode reaction and mass-transport mechanisms associated with suitable ‘model’ redox systems in ionic liquid and conventional molecular-solvent media.

In Chapter 3, the utility of several voltammetric methods were evaluated for the purpose of quantifying the parameters (*i.e.*, D , n , and/or C) associated with a range of electroactive species in ionic liquid media. The application of conventional steady-state methods in this kind of medium was found to be problematic, due to the difficulty in approaching a true steady-state under highly viscous conditions. In addition, analysis on the basis of the relationships outlined by the Randles-Sevcik equation was ruled out, because the peak currents of dc cyclic voltammograms are sensitive to heterogeneous kinetics/uncompensated resistance and although numerical simulation is relatively straightforward and represents a robust method of analysis, on some occasions it was found to be hampered by mechanistic complexities and/or other uncertainties.

Semiintegral voltammetry, a convolution method specific to conditions under which mass transport occurs solely by semi-infinite planar diffusion, is a powerful and also robust electroanalytical method which was applied under highly viscous conditions to quantify the diffusivity of a range of electroactive species. Unfortunately, the fully-planar diffusion

requirement of semiintegration limits the use of this technique to conditions where background charging current is significant, and thus background subtraction was essential for quantitative work. Fortunately, an extension of this method, known generally as convolution voltammetry, accommodates radial diffusion, and thus it was shown that the experimental conditions can be tailored to minimize charging current, avoiding the need to subtract the background contribution.

Overall, the convolutive techniques discussed in Chapter 3 provide powerful analytical tools which have great versatility, being applicable under experimental conditions where the direct use of conventional steady-state and transient voltammetry is severely limited. Although convolutive techniques have not been widely adopted in the literature, potential applications of these techniques in the field of electroanalytical chemistry are diverse. The most obvious avenue for future work in this area could be to apply them for quantitative analysis with a wide range of electrochemical systems at electrodes with geometries other than the standard inlaid disk (*i.e.*, spherical, cylindrical etc.).¹ For example, recently the semiintegral electroanalysis method has been used to calculate the diffusivity of metal complexes (dysprosium and niobium) in ionic liquid media.^{2,3}

In Chapter 4, the electrode reaction and mass-transport mechanisms associated with the Γ/I_2 couple was investigated in 1-ethyl-3-methylimidazolium bis(trifluoromethanesulfonyl)imide. Two processes with a relative electron stoichiometry of 2:1 were observed at a platinum electrode, and were assigned to the Γ/I_3^- and I_3^-/I_2 processes at lower and higher potentials respectively (confirmed by UV/visible spectroscopy), comparable to the case in acetonitrile. An analogous mechanism was observed on glassy carbon and boron-doped diamond electrodes, albeit with significant overpotentials when compared with the behaviour at platinum. In contrast to platinum or carbon electrodes, two processes with a relative electron stoichiometry of 1:1 were observed at a gold electrode. Dissolution of the gold electrode, detected *in situ* using an electrochemical quartz crystal

microbalance technique, was found to coincide with the first iodide oxidation process and the oxidation state of the soluble gold species was found to be (+1) using coulometry/electrogravimetric analysis. Quantitative treatment of the coulometric data suggested that iodide oxidation to molecular iodine on gold occurs predominantly *via* a diiodoaurate intermediate, and to a lesser extent, *via* a triiodide intermediate. Diiodoaurate was further confirmed as the intermediate by investigating the voltammetric response of an authentic sample of this species at a gold electrode.

The electro-oxidation of iodide on platinum macro- and microdisk electrodes was simulated using a termolecular charge-transfer mechanism and the apparent stability constant of triiodide in this media, estimated from experiment-simulation comparisons, was found to be comparable to that previously reported in acetonitrile. The diffusivity of iodide was found to be directly proportional to the concentration of triiodide present, showing up to a $\approx 50\%$ enhancement under the conditions investigated. This enhancement in mass transport could not be explained by a decrease in solution viscosity (*i.e.*, is non-Stokesian), and was therefore attributed to electron-hopping and/or a Grotthuss-type bond-exchange reaction between iodide and triiodide.

There is great scope for further work in this area, since only a limited number of electrode materials were investigated and in only a single class of ionic liquid. A systematic study on the mass-transport of iodide in ionic liquids made up of various combinations of anion and cation could give an insight into which physicochemical properties (*i.e.*, viscosity, Lewis acidity/basicity, etc.) influence the non-Stokesian transport mechanism in this type of media. In addition, because the stability constant of triiodide is solvent dependent⁴, it is expected that changing the constituent anion/cation would strongly influence this parameter, which can be conveniently measured using cyclic voltammetry. It is also possible that the iodide-oxidation mechanism may change depending on the nature of the anion and/or cation. For example, it has been reported that the (+1) oxidation state of iodine is stabilized in the

presence of chloride (*i.e.*, in chloroaluminate melts⁵) through the formation of interhalogen compounds of the type $I_mCl_n^{(m-n)}$. Finally, the electrocatalytic performance of a given electrode material towards the I^-/I_3^- process (relevant in the context of dye-sensitized solar cells) can be assessed in a relatively quick and straightforward manner by characterizing the electro-oxidation of iodide with cyclic voltammetry. There are many possibilities in this area, as numerous noble metal-free materials that show good electrocatalytic activity towards to the I^-/I_3^- process have been reported in recent years⁶, one notable example being cobalt sulfide.⁷

In Chapter 5, proton transport, hydrogen evolution (at a platinum electrode) and equilibrium acidity (pK_a) was investigated in a broad range of ionic liquids. It was found that regardless of the nature of the proton source, the hydrogen evolution reaction is very sensitive to the surface-state of the platinum electrode, requiring preconditioning at oxidative potentials to achieve a well-defined and reproducible cyclic voltammetric response. In bis(trifluoromethanesulfonyl)imide ionic liquids, when the conjugate acid of the anion (*i.e.*, $H[NTf_2]$) is used as the proton source, it was shown that proton transport obeys the relationships outlined by the Stokes-Einstein equation (*i.e.*, $D \propto 1/\eta$). Furthermore, correlation of the proton diffusivity data (derived electrochemically) with bis(trifluoromethanesulfonyl)imide self-diffusion data (derived with ^{19}F NMR) revealed that the acid is not dissociated in this environment (*i.e.*, the protons diffuse as $H[NTf_2]$).

The formal potential of the H^+/H_2 process (where H^+ signifies a ‘solvated proton’ released from a strong acid) was found to be sensitive to the anion component of the ionic liquid and insensitive to the cation component. Proton reduction from a range of weak acids (*i.e.*, protonated amines, sulfonamides, phenols, sulfonic acids or carboxylic acids) was found to be a diffusion controlled process that occurs in the potential region negative of the H^+/H_2 process (proportional to pK_a). When the proton source is a sulfonic acid or carboxylic acid, proton reduction was found to occur in two steps (electron stoichiometry = 1:1),

consistent with the formation of a stable intermediate species through homo hydrogen bonding (homoassociation) between the acid and its conjugate anion base. Computational simulations, performed by combining the classical Volmer (rate determining step) and Tafel reactions, revealed that weak acid dissociation is limiting on the voltammetric timescale when $\text{p}K_{\text{a}} > 4$, meaning proton reduction *via* a *CE* mechanism cannot account for the experimentally observed mass-transport limited currents. Under these conditions, proton reduction must proceed *via* an alternate pathway, which was proposed to involve the direct reduction (*DR*) of the weak acid at the platinum electrode surface.

Finally, a straightforward voltammetric method for calculating $\text{p}K_{\text{a}}$ values was devised and the equilibrium acidities ($\text{p}K_{\text{a}}$) of twenty weak acids covering eighteen orders of magnitude in acid strength ($2.0 \leq \text{p}K_{\text{a}} \leq 19.5$) was quantified in 1-ethyl-3-methylimidazolium bis(trifluoromethanesulfonyl)imide. Comparison of the $\text{p}K_{\text{a}}$ (IL) data with that from conventional solvents, such as acetonitrile and water has provided an insight into how the nature of the solvent (*i.e.*, dielectric properties, Lewis acidity/basicity, hydrogen donating/accepting ability etc.) can influence the strength of an acid ($\text{p}K_{\text{a}}$), which has a strong bearing on the thermodynamics, kinetics and mechanism of the proton reduction process.

Once again, there is great scope for further work in this area, since proton reduction from only a few classes of acids (*i.e.*, nitrogen and oxygen acids) was carried out almost exclusively in aprotic ionic liquid media. In terms of proton transport, the ultimate goal would be to develop an ionic liquid formulation which facilitates anhydrous proton conduction over a large temperature range. Protic ionic liquids are a clear candidate for this purpose, since certain combinations of Brønsted acid/base can produce liquids with water-like properties (*i.e.*, a 3D hydrogen bonded network).⁸ An alternative approach could be to dope either aprotic or protic ionic liquids with low-volatility protic molecular solvents such as polyalcohols to achieve water-like proton-conduction properties. Further studies on the

hydrogen evolution reaction mechanism and proton thermodynamics (pK_a) could be carried out with a broader range of weak acids, for example carbon acids⁹, which are well known to possess sluggish dissociation kinetics in molecular solvents. Lastly, calculating the pK_a of a model acid species in a series of ionic liquids with a fixed anion and varying cations (aprotic or protic) could provide a valuable insight into the influence of solvent properties (*i.e.*, Lewis acidity/basicity, hydrogen bonding, polarity etc.) on equilibrium acidity.

In conclusion, the work presented here has shed light on two fundamental processes in ionic liquid media: heterogeneous electron transfer (*i.e.*, thermodynamics, kinetics and mechanisms) and mass-transport (*i.e.*, Stokesian and non-Stokesian). Aprotic ionic liquids were predominantly investigated in this work, and in many ways they resemble conventional aprotic molecular solvents such as acetonitrile or propylene carbonate, although some phenomena are seemingly unique to this type of media, for example the iodide/triiodide exchange mechanism. In reality however, the properties of an ionic liquid are determined by its unique combination of cation and anion, and can therefore be ‘tuned’ to an extent to resemble different classes of molecular solvent.

With the use of ionic liquids in electrochemical devices and a growing range of processing technologies continuing to expand, it is important that fundamental research such as that presented here continues to be undertaken by researchers in the field. Aside from the Γ/I_3^- couple, there are a number of other redox systems which have found application as mediators in dye-sensitized solar cells that may be suitable for investigating charge- and mass-transfer phenomena in ionic liquids, including pseudohalides (*i.e.*, SCN^- or $SeCN^-$)¹⁰,¹¹, metallocenes^{12, 13} and cobalt complexes (*i.e.*, polypyridyl or ethylenediamine)^{14, 15}. Finally, ongoing research on fundamental topics such as interfacial (electrical ‘double-layer’) structure¹⁶; intermolecular ordering and solvation^{17, 18}; and Lewis acidity/basicity (*i.e.*, donor/acceptor numbers)¹⁹; will be invaluable in gaining a comprehensive understanding of (electro)chemical reactivity²⁰ and mass-transport in ionic liquid media.

References

- (1) Mahon, P. J.; Oldham, K. B., Convolutive Modelling of Electrochemical Processes Based on the Relationship Between the Current and the Surface Concentration. *J. Electroanal. Chem.* **1999**, *464*, 1-13.
- (2) Kazama, R.; Matsumiya, M.; Tsuda, N.; Tsunashima, K., Electrochemical Analysis of Diffusion Behavior and Nucleation Mechanism for Dy(II) and Dy(III) in Phosphonium-Based Ionic Liquids. *Electrochim. Acta* **2013**, *113*, 269-279.
- (3) Matsumiya, M.; Ishii, M.; Kazama, R.; Kawakami, S., Electrochemical Analyses of Diffusion Behaviors and Nucleation Mechanisms for Neodymium Complexes in [DEME][TFSA] Ionic Liquid. *Electrochim. Acta* **2014**, *146*, 371-377.
- (4) Iwamoto, R. T., Solvent Effects on the Electro-Oxidation of Iodide Ion. *Anal. Chem.* **1959**, *31*, 955-955.
- (5) Marassi, R.; Chambers, J. Q.; Mamantov, G., Electrochemistry of Iodine and Iodide in Chloroaluminate Melts. *J. Electroanal. Chem.* **1976**, *69*, 345-359.
- (6) Hagfeldt, A.; Boschloo, G.; Sun, L. C.; Kloo, L.; Pettersson, H., Dye-Sensitized Solar Cells. *Chem. Rev.* **2010**, *110*, 6595-6663.
- (7) Wang, M.; Anghel, A. M.; Marsan, B.; Cevey Ha, N.-L.; Pootrakulchote, N.; Zakeeruddin, S. M.; Grätzel, M., CoS Supersedes Pt as Efficient Electrocatalyst for Triiodide Reduction in Dye-Sensitized Solar Cells. *J. Am. Chem. Soc.* **2009**, *131*, 15976-15977.
- (8) Greaves, T. L.; Drummond, C. J., Protic Ionic Liquids: Properties and Applications. *Chem. Rev.* **2008**, *108*, 206-237.
- (9) Deng, H.; Li, X.; Chu, Y.; He, J.; Cheng, J.-P., Standard pK_a Scales of Carbon-Centered Indicator Acids in Ionic Liquids: Effect of Media and Structural Implication. *J. Org. Chem.* **2012**, *77*, 7291-7298.
- (10) Solangi, A.; Bond, A. M.; Burgar, I.; Hollenkamp, A. F.; Horne, M. D.; Ruther, T.; Zhao, C., Comparison of Diffusivity Data Derived from Electrochemical and NMR investigations of the SeCN⁻/(SeCN)₂/(SeCN)₃⁻ System in Ionic Liquids. *J. Phys. Chem. B* **2011**, *115*, 6843-6852.
- (11) Wang, P.; Zakeeruddin, S. M.; Moser, J. E.; Humphry-Baker, R.; Grätzel, M., A Solvent-Free, SeCN⁻/(SeCN)₃⁻ Based Ionic Liquid Electrolyte for High-Efficiency Dye-Sensitized Nanocrystalline Solar Cells. *J. Am. Chem. Soc.* **2004**, *126*, 7164-7165.

(12) Sukardi, S. K.; Zhang, J.; Burgar, I.; Horne, M. D.; Hollenkamp, A. F.; MacFarlane, D. R.; Bond, A. M., Prospects for a Widely Applicable Reference Potential Scale in Ionic Liquids Based on Ideal Reversible Reduction of the Cobaltocenium Cation. *Electrochem. Commun.* **2008**, *10*, 250-254.

(13) Daeneke, T.; Mozer, A. J.; Kwon, T. H.; Duffy, N. W.; Holmes, A. B.; Bach, U.; Spiccia, L., Dye Regeneration and Charge Recombination in Dye-sensitized Solar Cells with Ferrocene Derivatives as Redox Mediators. *Energy Environ. Sci.* **2012**, *5*, 7090-7099.

(14) Hamann, T. W., The End of Iodide? Cobalt Complex Redox Shuttles in DSSCs. *Dalton Trans.* **2012**, *41*, 3111-3115.

(15) Powar, S.; Daeneke, T.; Ma, M. T.; Fu, D.; Duffy, N. W.; Götz, G.; Weidelener, M.; Mishra, A.; Bäuerle, P.; Spiccia, L.; Bach, U., Highly Efficient p-Type Dye-Sensitized Solar Cells based on Tris(1,2-diaminoethane)Cobalt(II)/(III) Electrolytes. *Angew. Chem., Int. Ed.* **2013**, *52*, 602-605.

(16) Fedorov, M. V.; Kornyshev, A. A., Ionic Liquids at Electrified Interfaces. *Chem. Rev.* **2014**.

(17) Hardacre, C.; Holbrey, J. D.; Nieuwenhuyzen, M.; Youngs, T. G. A., Structure and Solvation in Ionic Liquids. *Acc. Chem. Res.* **2007**, *40*, 1146-1155.

(18) Ueki, T.; Watanabe, M., Macromolecules in Ionic Liquids: Progress, Challenges, and Opportunities. *Macromolecules* **2008**, *41*, 3739-3749.

(19) Schmeisser, M.; Illner, P.; Puchta, R.; Zahl, A.; van Eldik, R., Gutmann Donor and Acceptor Numbers for Ionic Liquids. *Chem.-Eur. J.* **2012**, *18*, 10969-10982.

(20) Hapiot, P.; Lagrost, C., Electrochemical Reactivity in Room-Temperature Ionic Liquids. *Chem. Rev.* **2008**, *108*, 2238-2264.

7. Publications

- (1) Bentley, C. L.; Bond, A. M.; Hollenkamp, A. F.; Mahon, P. J.; Zhang, J., Advantages Available in the Application of the Semi-Integral Electroanalysis Technique for the Determination of Diffusion Coefficients in the Highly Viscous Ionic Liquid 1-Methyl-3-Octylimidazolium Hexafluorophosphate. *Anal. Chem.* **2012**, *85*, 2239-2245.
- (2) Bentley, C. L.; Bond, A. M.; Hollenkamp, A. F.; Mahon, P. J.; Zhang, J., Concentration and Electrode Material Dependence of the Voltammetric Response of Iodide on Platinum, Glassy Carbon and Boron-doped Diamond in the Room Temperature Ionic Liquid 1-ethyl-3-methylimidazolium Bis(Trifluoromethanesulfonyl)imide. *Electrochim. Acta* **2013**, *109*, 554-561.
- (3) Bentley, C. L.; Bond, A. M.; Hollenkamp, A. F.; Mahon, P. J.; Zhang, J., Unexpected Complexity in the Electro-Oxidation of Iodide on Gold in the Ionic Liquid 1-Ethyl-3-methylimidazolium bis(trifluoromethanesulfonyl)imide. *Anal. Chem.* **2013**, *85*, 11319–11325.
- (4) Bentley, C. L.; Bond, A. M.; Hollenkamp, A. F.; Mahon, P. J.; Zhang, J., Applications of Convolution Voltammetry in Electroanalytical Chemistry. *Anal. Chem.* **2014**, *86*, 2073–2081.
- (5) Bentley, C. L.; Bond, A. M.; Hollenkamp, A. F.; Mahon, P. J.; Zhang, J., Electrode Reaction and Mass-Transport Mechanisms Associated with the Iodide/Triiodide Couple in the Ionic Liquid 1-Ethyl-3-methylimidazolium Bis(trifluoromethanesulfonyl)imide. *J. Phys. Chem. C* **2014**, *118*, 29663–29673.
- (6) Bentley, C. L.; Bond, A. M.; Hollenkamp, A. F.; Mahon, P. J.; Zhang, J., Mass Transport Studies and Hydrogen Evolution at a Platinum Electrode Using Bis(trifluoromethanesulfonyl)imide as the Proton Source in Ionic Liquids and Conventional Solvents. *J. Phys. Chem. C* **2014**, *118*, 22439–22449.
- (7) Bentley, C. L.; Bond, A. M.; Hollenkamp, A. F.; Mahon, P. J.; Zhang, J., Electrochemical Proton Reduction and Equilibrium Acidity (pK_a) in Aprotic Ionic Liquids: Phenols, Carboxylic Acids and Sulfonic Acids. *In preparation* **2015**.

(8) Bentley, C. L.; Bond, A. M.; Hollenkamp, A. F.; Mahon, P. J.; Zhang, J., Electrochemical Proton Reduction and Equilibrium Acidity (pK_a) in Aprotic Ionic Liquids: Protonated Amines and Sulfonamide Acids. *In preparation* **2015**.

(9) Bentley, C. L.; Bond, A. M.; Hollenkamp, A. F.; Mahon, P. J.; Zhang, J., 5 - Electroanalytical Applications of Semiintegral and Convolution Voltammetry in Room Temperature Ionic Liquids, In *Electrochemistry in Ionic Liquids*, accepted by Springer International Publishing: Switzerland, **2015**.

(10) Zhao S. F.; Bentley C. L.; Horne M. D.; Bond A. M.; Zhang J., 14 - Voltammetry of Adhered Microparticles in Contact with Ionic Liquids: Principles and Applications, In *Electrochemistry in Ionic Liquids*, accepted by Springer International Publishing: Switzerland, **2015**.